The Emerging Mechanochemistry of Naphthopyran

Thesis by

Molly Elizabeth McFadden

In Partial Fulfillment of the
Requirements for the Degree of
Doctor of Philosophy

CALIFORNIA INSTITUTE OF TECHNOLOGY
Pasadena, California

2023
(Defended April 12, 2023)

Molly Elizabeth McFadden
ORCID: 0000-0003-3174-6385

ACKNOWLEDGEMENTS

This work would not have been possible without a degree of community support that I have felt humbled and privileged to receive. I am eternally grateful for the opportunity to study, learn, and grow at Caltech; I imagine (and have been often told) that there are few places quite like it. The people here have made this a home, and while I am so excited for what the future will bring, it is bittersweet to leave. While it has had challenges, my years in graduate school have been some of the best in my life. In writing this document and reflecting on my time here, I find so many people are to thank for their love, friendship, and support. I cannot put into words how much I appreciate you all, but I will try. It won't be succinct.

I firstly would not have even known to consider graduate school as an option without the support of the IU chemistry department, of Laura and Kevin Brown and the entirety of the Brown lab at IU. I thank my grad student mentor Yao Xu for her enduring patience in teaching a talkative freshman the fundamentals of benchwork from scratch. I have also realized in retrospect what a gift it was that she washed all of my glassware for me. I am grateful my friendship with Stephen Sardini has lasted all these years, and am so glad he has been here at Caltech for some of my time here. I am continuously impressed by his knowledge, humbleness, and incomparably good attitude. Kevin and Laura were and continue to be wonderful mentors. In combination with working in his lab, Kevin's organic chemistry class (and beautiful chalkboard work) made me switch my major to (bio)chemistry. I thank Laura for numerous memorable, warm chats in and out the lab. I also would like to thank Martha Oakley and Sara Skrabalak for helpful guidance, and Megan Porter for guidance, support, and friendship. I also thank Dr. deSouza for his kindness and support in S117, a course that induced significant personal and intellectual growth. Many great friendships came from bonding experiences in that class: Alex, David, Bryce, Sam, Sarah, Angely, Abby, Grant, Justine… Alex and David, your comradery and calls throughout grad school have been a blessing and I am so glad we have kept in touch. I am so excited to see where your careers take you. Bryce, Allison, Sarah, Sam, Susan, Andy, Eric, Adrian, MaryAnn, your friendship and the pandemic return of Game Night kept me sane, and thanks to Bryce, Allison, Adrian, and MaryAnn for wonderful visits over the years.

Laura encouraged me to apply for a summer research experience in a totally different field, and in doing so gave me one of my favorite summers on memory working at the Columbia MRSEC. I thank Xiaoyang Zhu for letting an organic chemist work in a pchem lab, my mentors Kihong and Xinjue, and the entire XYZ lab for being so kind and welcoming. I am grateful for friends made that summer, including Alexis, Brandon, and Derek, but most of all for Maria Paley, who has become one of my best and most enduring friends. Even when with months between chats, it feels like no time has passed every time we talk.

My time at Caltech has been great because the people here are great. The CCE staff have been a joy to work with. Thanks in particular to Allison Ross and Rebecca Fox, who have all the answers, to Joe Drew, a cheerful presence in the building who makes sure that literally everything that gets done, to Greg and Armando for their helpfulness and friendliness, to Nate and Ricardo for fixing what breaks and enjoyable chats, and to Mona Shahgoli for mass spec expertise and good chats about cats. To Dave Vander Velde, for unparalleled NMR expertise and enthusiasm: I love your emails, and it was a major thrill of my graduate career to make a compound with NMR properties that were exciting to you. To Scott Virgil, for your willingness to deep dive into a problem you've only just heard about, to Silva Virgil for friendly midday chats and too high of praise, and to both of you for your warmth, friendship, and excellent wine and travel advice. To Annette Luymes, for so many things but mostly friendship and guidance. I greatly admire you. I will miss the wonderful sense of community among all the tenants of Crellin and Church.

I owe much to the faculty at Caltech. The way they engage with students stood out to me on visit weekend and was a major part of my decision to come here, but I couldn't have known what an accurate first impression that would turn out to be. Everyone here has been so supportive of me and my goals and my science, and I'm so thankful for the time and care invested in me. I cannot believe the number of professors here who allowed me to just drop in and get their thoughts on my ongoing projects. My thesis committee is comprised of truly inspiring people, and really has gone above and beyond what I could have hoped for in their support and guidance, as well as insightful comments and questions at all of our meetings. I am so grateful Dennis Dougherty let me come to his office as a first year and ramble incoherently about my reaction's mechanism, and that he found a way to make sense of it and help me through. I have since greatly benefitted from his guidance and support, and am perpetually impressed by his humility and kindness. I am lucky to have fallen in love with physical organic chemistry while working down the hall from the person who literally wrote the book on it. Sarah Reisman is an inspiration, and her support, friendliness and candor are greatly appreciated. At every professional networking event I have attended with her, she has gone out of her way to say kind and supportive things. Greg Fu has provided invaluable discussion and given so generously of his time and attention over the years – once even discussing the mechanistic implications of some data over zoom at dinnertime. I am grateful for his advice on several of the projects reported herein. Beyond my committee, I have benefitted greatly from scientific guidance and support from Mikhail Shapiro, who throughout our collaborative project has so generously included me in all of the wonderful Shapiro group events. Brian Stoltz has provided much appreciated general career guidance and support. I admire and am very grateful to have gotten to know Kim See through all of the Robb-See joint events, and I appreciate her support and kindness. Lastly, while not *Caltech* faculty, I am glad to have gotten to know my fellow Evansville native Geoff Coates during his sabbatical here in 2022, and am grateful for his advice and support during that time and since then.

I have grown greatly as a scientist by working closely with the greatest collaborators one could ask for. Soren Holm and Rui Xu at Stanford have brought so much depth of thought to our project and I learn something new every time we meet. I am so impressed by Soren's dedication and work ethic. Yuxing Yao is a shining beacon of positivity and I am so lucky to have gotten to work with him. No one else can tell you you're dead wrong about something as graciously and kindly as Yuxing. Yuxing has a genuine love and enthusiasm for science that is infectious and inspiring – it is hard to be stressed when around him. Our monthly collaboration dinners were a wonderful idea of his, and were a great way to keep up group morale on a project that took a long time to come together.

I am lucky to have worked with the excellent scientists and people that make up the Robb group. I have enjoyed getting to work and grow with each of you. Seeing Xiaoran Hu's dedication and commitment to his science was very formative for me, and I am so excited to continue watching his independent work. Brooke Versaw, my first naphthopyran collaborator, has provided years of flawless baked good to boost group morale, and has been a great person to chat with particularly throughout the thesis writing process. Anna Overholts and Corey Husic have provided invaluable feedback and insightful comments in and out of group meeting on the work described herein that is greatly appreciated. In addition to being an excellent chemist, May Zeng can brighten the mood of any room she's in and brings a cheerful levity to even the most stressful times. I am so glad to have gotten to know her. I am glad to have known Peng Liu, who provided helpful feedback during my fellowship application process and has a wonderful positive attitude. Jolly Patro, yet another wonderfully positive person, is the most impressive undergraduate scientist I've met and I am glad to have worked alongside her, and even learned from her. Debbie Tseng is a powerhouse of a synthetic chemist and a joy to work alongside. Quan Gan is our resident polymer expert and chromatography wizard and I am glad for his time spend in the Robb group. The fellow occupants of Church 311 have become some of my very best friends. Stella Luo is a kind and thoughtful friend, and has done a phenomenal job as the group's lab manager. I am grateful for all her help in the last year on our collaboration with the Shapiro group, and I am leaving confident that these projects are in good hands with her. I am grateful to have worked with and become friends with Yan Sun, a major contributor to our naphthopyran subgroup, who is an impressively hard worker and has shown tremendous dedication and creativity in solving difficult problems. He brings kindness, enthusiasm, and positivity to interactions in and out of work, and I'm so excited to see what comes next for him. Skylar Osler was the first real permanent addition to the naphthopyran subgroup, and I am so grateful that she chose to do so. She has been my closest collaborator, and I couldn't dream of anyone better to have worked with. I cannot overstate the value of her enthusiasm, thoughtful and deep insights, and meticulous work. She has been a wonderful and supportive close friend, and I hope her visits to the Bay area continue. I have loved my time thinking deeply about naphthopyran with Skylar and Yan, and the future of this subgroup couldn't be in better hands. Lastly, my cohort-mate Ross Barber has been my ride-or-die throughout the entirety of graduate school. This would have been immeasurably harder or maybe impossible to do without his comradery. I can't put into words how valuable our friendship has been: he has become like a brother to me, and I am so grateful to have met him.

I don't know where to start in describing my thanks and appreciation to my advisor Max Robb. I thank him first for taking a chance on a very nervous first year, and for playing a truly huge role in my growth from that point. Max has been a better mentor than I could ever have hoped for, scientific and otherwise. I so appreciate his support and encouragement of my science, my career, and me in general. I thank him for tolerating too-long conversations, unannounced drop-ins, and engaging in deep-dives into scientific rabbit holes. I thank him for letting me explore my interests, and for helping me develop and work on projects that I have loved. I have learned so much from Max, and I frequently reflect on what a good choice it was to work with him. It has made me so happy to watch the growth and success of the Robb group and I am grateful to have been a member. I can't wait to see what the future brings for Max and for his group, and I hope that we can stay in touch.

Outside the Robb group at Caltech, my friendships with Gracie Zhang and Alex Barth have been so supportive and rewarding and I look forward to their continued friendship as we move on to the next stages of our lives and careers. I am also grateful for other good friends from our cohort Alex Shimozono, Nick Hafeman, Ailiena Maggiolo and Felix, Juner Zhang and Tim, Sarah Bevilacqua, Axl Levan, Morgan Abernathy and Veeral. I glad to have known Veronica Hubble, Jay Barbor and Jessie, Melinda Chan, Chloe Williams, Sepand Nistanaki, Tyler Casselman and Janelle, Stanna Dorn, Mark Legendre, temporary Crellin residents Samir Rezgui and Elliot Hicks, and many others.

I could not have done this without the love of my family. Their support and efforts to visits have meant the world to me and kept me sane. I am so thankful for their perpetual encouragement and faith in me. My dad told me as I was starting high school that he was sure I was going to love chemistry, and that organic chemistry was by far his favorite college class. At the time, I didn't even really like science, and as a teenager took this as evidence that he didn't "get" me at all. It's so funny how things shake out. I thank him for checking in during my time here and giving great movie suggestions. My mom has been my strongest supporter and my greatest role model, and striving to be more like her has allowed me to appreciate even the hardest times here. I thank her for everything.

I'm grateful for the friendship of my wonderful siblings Colin, Grace, and Aidan, and while the distance has been hard on all of us, I am so proud of the young adults they have become, and I appreciate their support during my time here. My grandparents have been another strong source of love and support, as well as my wonderful cousins that I'm so glad to be close with. My Great Uncle Paul, who lives just down the road in Orange county, has made being far from family so much easier, and has really adopted me during my time here. I'm grateful for his friendship, time, fun conversations and easygoing nature.

I finally must thank my best friend and fiancé William Hargis. He has been phenomenally supportive throughout this entire process, and I could not have ever done this without him. In fact, I would not have even applied to Caltech – days before the application deadline, he convinced me I had a worthwhile chance of getting in here. He has repeatedly put my career aspirations ahead of his own, and has continually believed in me when I have not believed in myself. He is kind and supportive, and I am so glad to get to spend my life with him. I will lastly also thank our wonderful cat Murph, the light of my life, who has napped steadfastly by my side through the majority of the thesis writing process.

ABSTRACT

Asserting remote control over reactivity is a pervasive goal in modern chemistry. Several external stimuli can supply energy to facilitate productive chemical transformations. In recent years, that list has grown to include mechanical force. In the growing field of polymer mechanochemistry, privileged, mechanically sensitive molecules called mechanophores undergo desirable chemical reactions under force. Force is transduced to mechanophores through covalently attached polymer chains. Among many applications, mechanophores that react to produce colored species can be used for visual stress and damage detection in plastics. Naphthopyran is a highly modular molecular switch that can undergo ring-opening reaction to generates intensely colored merocyanine dyes. The studies described in this dissertation have thoroughly established the versatility and complexity of naphthopyran-based mechanochromic mechanophores.

In Chapter 1, the history of naphthopyran molecular switches is summarized with particular emphasis on the exhaustive and generalizable merocyanine structure-property relationships established for photochromic naphthopyrans. Naphthopyran mechanochemistry is reviewed and contextualized among other mechanochromic mechanophores. Mechanochromic structure-function relationships are highlighted, as well as a series of studies using the naphthopyran platform for illustration of the unusual reaction pathways accessible under force, and studies demonstrating that multimodal naphthopyrans are an ideal platform for multicolor mechanochromism.

As discussed extensively in Chapter 1, merocyanines are typically susceptible to thermal recyclization. However, Chapter 2 describes a scissile naphthopyran mechanophore that undergoes an unusual secondary mechanochemical ester cleavage after the ring-opening reaction. By revealing a β-hydroxy ketone group with a stable intramolecular hydrogen bonding interaction, mechanical force uniquely generates persistent merocyanine species.

The irreversible reaction sequence described in Chapter 2 enables determination of mechanochemical reaction kinetics under solution-phase ultrasound-mediated mechanical force. However, common methods for determining reaction rate constants under these conditions are time-intensive and convoluted by the competitive side reaction of nonspecific polymer backbone scission. In Chapter 3, through model studies on the highly efficient scissile naphthopyran and a comparatively inefficient coumarin dimer mechanophore, we validate a time-efficient and accurate initial rates method for determination of selective mechanophore reaction kinetics under ultrasonication.

The ability to colorimetrically report on the magnitude of applied stress is a grand challenge in the field of mechanochromism. Chapter 4 describes the first single mechanophore capable of such behavior. Mechanical force induces unexpectedly simultaneous ring-opening reactions from a bis-naphthopyran mechanophore, biasing a dynamic equilibrium between two distinct merocyanine states to effect gradient force-dependent multicolor mechanochromism.

In further studies seeking multicolor mechanochromic systems, it was discovered that mechanical force facilitates the first reported dual-ring-opening reaction of naphthodipyran. Chapter 5 describes the mechanochemical generation of an unusual dimerocyanine species with near-IR absorption that is not formed photochemically.

PUBLISHED CONTENT AND CONTRIBUTIONS

1. McFadden, M. E.; Robb, M. J. Generation of an Elusive Permanent Merocyanine via a Unique Mechanochemical Reaction Pathway. *J. Am. Chem. Soc.* **2021**, *143*, 7925–7929. DOI: 10.1021/jacs.1c03865

   M. E. M. participated in the conception and design of the project, synthesis of reported compounds, data collection and analysis, and manuscript preparation.
2. McFadden, M. E.; Overholts, A. C.; Osler, S. K.; Robb, M. J. Validation of an Accurate and Expedient Initial Rates Method for Characterizing Mechanophore Reactivity. *ACS Macro. Lett.* **2023**, *12*, 440–445. DOI: https://doi.org/10.1021/acsmacrolett.3c00054

   M. E. M. participated in the conception and design of the project, data collection and analysis, and manuscript preparation.
3. McFadden, M. E.; Robb, M. J. Force-Dependent Multicolor Mechanochromism from a Single Mechanophore. *J. Am. Chem. Soc.* **2019**, *141*, 11388–11392. DOI: 10.1021/jacs.9b05280

   M. E. M. participated in the design of the project, synthesis of reported compounds, data collection and analysis, and manuscript preparation.
4. McFadden, M. E.; Osler, S. K.; Sun, Y.; Robb, M. J. Mechanical Force Enables an Anomalous Dual Ring-Opening Reaction of Naphthodipyran. *J. Am. Chem. Soc.* **2022**, *144*, 22391–22396. DOI: 10.1021/jacs.2c08817

   M. E. M. participated in the conception and design of the project, synthesis of reported compounds, data collection and analysis, and manuscript preparation.

TABLE OF CONTENTS

Chapter 1

NAPHTHOPYRAN MOLECULAR SWITCHES AND THEIR EMERGING MECHANOCHEMICAL REACTIVITY

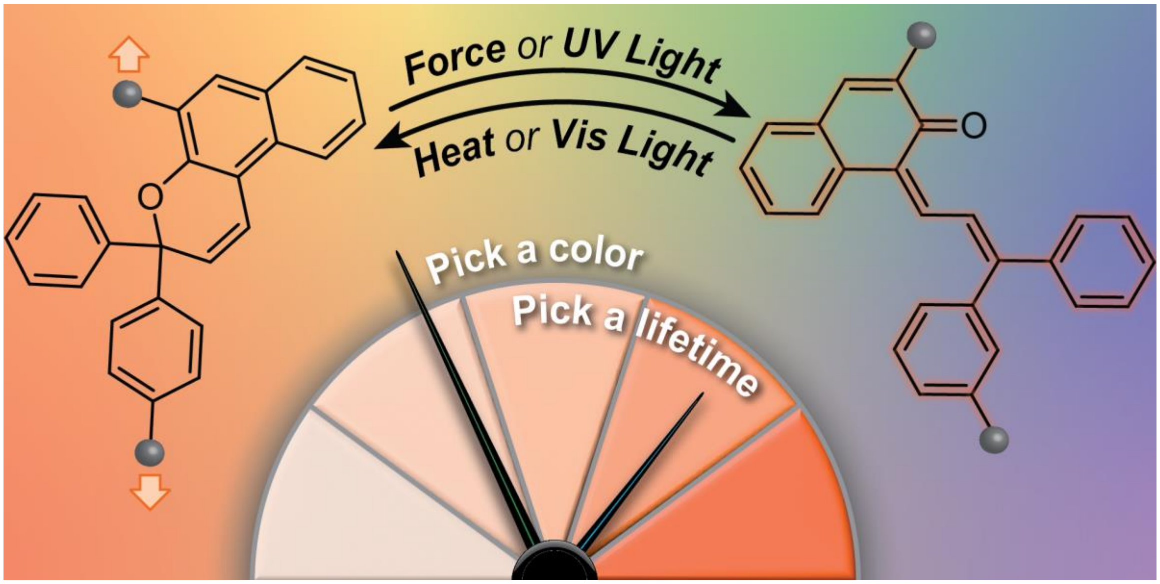

ABSTRACT: Naphthopyran molecular switches undergo a stimulus-induced ring-opening reaction to yield intensely colored merocyanine dyes. Their privileged degree of modularity and synthetic accessibility afford the platform exceptional functional control. Widespread commercial applications of naphthopyran photoswitches in photochromic ophthalmic lenses have led to production of an extensive body of work exploring merocyanine structure–property relationships. More recently, the use of force-responsive naphthopyrans in the emerging field of polymer mechanochemistry has enabled both groundbreaking advances for stimuli-responsive materials and fundamental discoveries in force-mediated reactivity. Mechanochromism is a robust strategy for remote visual stress sensing, and the structure–property relationships established in the photochemical literature have translated seamlessly to the design of naphthopyran stress sensors with predictable and precisely tunable properties, including elusive multicolor mechanochromism. The modularity of naphthopyran additionally facilitates investigations into the laws of mechanochemical reactivity. Substantial prior research and straightforward diversification render the naphthopyran platform a promising candidate for the continued study of mechanochemistry and for the development of highly tailored and complex molecular force probes.

This work was composed in collaboration with Ross W. Barber and Anna C. Overholts.

Introduction

I. Polymer Mechanochemistry

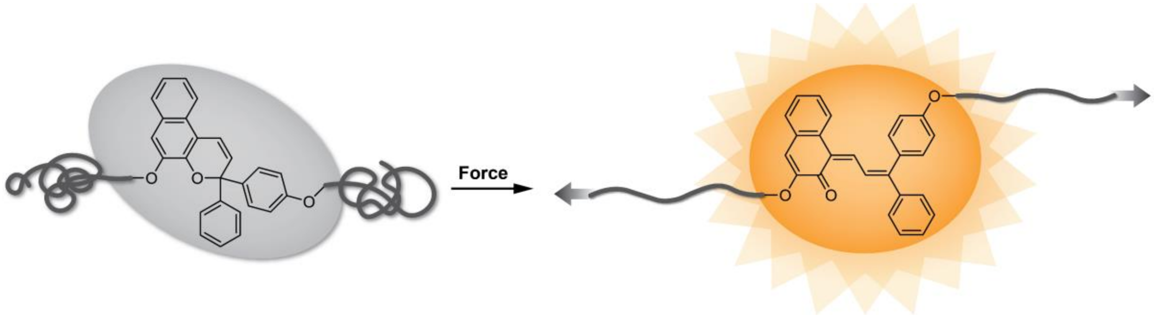

Figure 1.1. Mechanophores like naphthopyran that are covalently embedded within polymer chains undergo predictable and productive chemical reactions in response to applied mechanical force.

The development of force-sensitive molecules termed mechanophores has revolutionized the capabilities of mechanical force as a stimulus for responsive behavior in smart materials. Polymer chains transduce externally applied force to mechanically labile bonds in covalently incorporated mechanophores, inducing specific and selective chemical reactivity. (Figure 1.1).[1] Since the first report of site-specific mechanical activation of covalent bonds in 2005,[2] judicious mechanophore design has enabled a diverse range of responses including catalyst activation,[3] electrical conductivity switching,[4] chemiluminescence,[5] and cargo release,[6] among many others. Mechanochromic mechanophores are a well-studied group of molecules that change color in response to force, making them highly suitable for stress sensing in bulk materials.[7–12] Mechanical stress typically causes nonspecific chain cleavage in polymeric materials and degrades their overall mechanical properties.[13–16] Because this damage is often invisible, mechanochromic mechanophores are valuable for convenient signaling of material deterioration to the naked eye. Furthermore, mechanochromic transformations are easy to monitor, facilitating studies into mechanisms of force-mediated reactivity[17] which often proceed through unusual pathways inaccessible under other stimuli.[18–20]

Among mechanochromic mechanophores, naphthopyran shows great promise as a highly modular force-driven molecular switching and visual stress-sensing platform. In response to ultraviolet light or mechanical force, naphthopyran undergoes a ring-opening reaction to produce a highly colored merocyanine.[21,17] Due to its modular synthetic pathway and highly tunable photophysical properties of the associated merocyanine, naphthopyran has been described as "the most industrially relevant" photochromic dye, and has been extensively studied in the context of its photochemical applications.[22–24] We assert that these qualities make naphthopyran an ideal candidate for the investigation of mechanochemical structure–property relationships and the study of fundamental aspects of mechanochemical reactivity. In this perspective, we first briefly provide context for naphthopyran among mechanochromic mechanophores. We will next discuss in detail the synthetic accessibility and modularity of naphthopyrans, and then briefly review the photochemistry of naphthopyran with a strong emphasis on the extensive and generalizable knowledge regarding merocyanine structure–property relationships. Lastly, we offer commentary on the mechanochemical reactivity of naphthopyrans studied thus far, highlighting the promise of this platform for accessible and versatile molecular force probes.

II. Mechanochromic Mechanophores

Scheme 1.2. Examples of mechanochromic mechanophores that fracture into two distinct species upon exposure to mechanical force

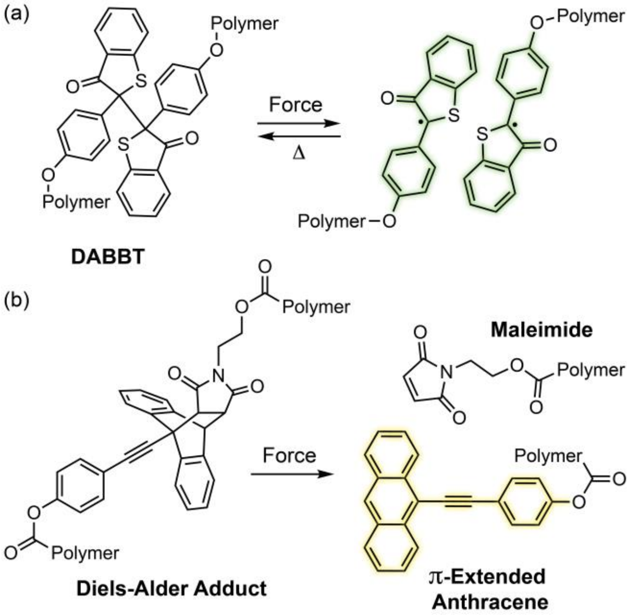

Stress sensing is a salient goal in the context of functional materials. Due to the enormous variety of existing polymer compositions and properties, wide range of stress loads typically experienced by materials, and differing needs for permanent versus reversible damage detection, developing a general molecular stress reporter is a deceptively difficult challenge. As such, the available toolbox of molecular stress reporters must respond under an equally wide range of force sensitivities, generate a variety of colors to account for differences in material color and application, and form colored products with variable and tunable lifetimes. Reported mechanochromic mechanophores exhibit a variety of activation mechanisms and resulting dye structures. The Otsuka group has developed a series of symmetric dimer mechanophores that produce stable colored radical species following force-induced bond homolysis[25–30] such as diarylbibenzothiophenonyl (**DABBT**), shown in Scheme 1.2a.[28] The reaction is scissile but thermally reversible, and thus radical lifetime is highly dependent on the surrounding environment. For example, fluid environments like solutions,

Scheme 1.1. Ladderene mechanophores undergo a force-induced unzipping reaction to produce blue semiconducting polyacetylene.

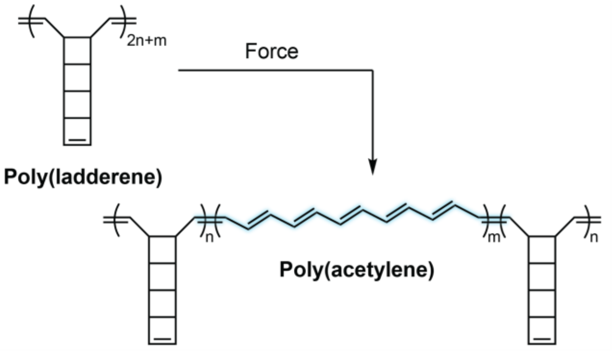

hydrogels, or rubbery materials afford the products a high degree of movement and facilitate recombination under ambient conditions[25] while more rigid crystalline or glassy materials prevent recombination.[27,30,31] In some cases, only partial recombination occurs.[32] Constructing a library of these dimer mechanophores has enabled access to colored products spanning a spectrum of distinct colors and product lifetimes. However, each mechanophore is completely structurally distinct, necessitating an entirely new mechanophore design to access new colors or product stabilities. Another example of scissile mechanochromic mechanophores includes π-extended anthracene–maleimide Diels–Alder adducts developed by Göstl and Sijbesma, in which the extended π system of the anthracene products was cleverly employed to both enhance their fluorescence quantum yield and shift their absorption into the visible range (Scheme 1.2b).[33–35] Unlike the dimer mechanophores discussed previously, the anthracene products are stable and their color can be adjusted via straightforward substitution, although the range of accessible colors is somewhat limited. Notably, Xia and coworkers developed a series of ladderene mechanophores whose mechanical activation, though primarily intended to generate conducting polymers, inherently involves the generation of colored polyacetylene oligomers (Scheme 1.1).[36–38] Significant strides have recently been made towards improving the stability of the colored, conjugated products.[39]

Naphthopyran is one among several mechanochromic mechanophores that produce colored species through conjugation-extending ring-opening reactions, alongside spiropyran,[40–42] spirothiopyran,[43,44] rhodamine,[45] and oxazine[46] (Scheme 1.3). These mechanophores are often particularly force-sensitive, are typically non-scissile, and produce merocyanine species that recyclize thermally or with visible light. Their inherent reversibility enables multiple cycles of reactivation. The merocyanines are usually zwitterionic, with the quinoidal dye derived from naphthopyran being a notable exception. Spiropyran in particular is among the most labile force probes, but its application is limited by its sensitivity to several other stimuli; its ring-opening reaction can be triggered by heat, light, metal ions, redox potential, pH changes, or polar solvent environments.[47,48] Spirothiopyran,[47] rhodamine,[49] and oxazine[46] exhibit similarly broad sensitivity. Additionally, synthetic modification of substituents on spiropyran, which can be challenging, concurrently alters its thermal reactivity, making it difficult to develop modular or selective force probes based on this scaffold. While certain substitution patterns have been shown to eliminate its susceptibility to light and heat, these modifications also rendered the associated merocyanine nearly thermally transient.[50] In general, clear gaps in functional modularity and behavioral control exist among spiropyran, spirothiopyran, rhodamine, and oxazine mechanophores. Naphthopyran, on the other hand, exhibits a higher degree of chemical stability and typically only responds to UV light or mechanical force, making it a much more convenient platform for selective force-sensing applications.

Scheme 1.3. Thermally reversible mechanochromic mechanophores that proceed through ring-opening reactions

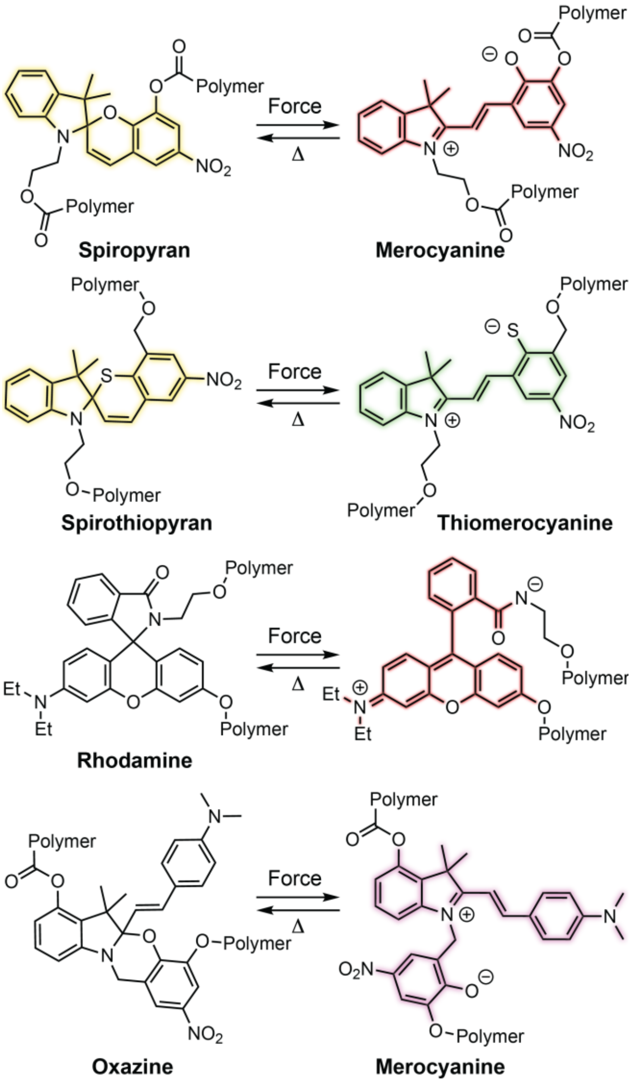

Improved stimulus specificity and control distinguish naphthopyran from the comparatively sensitive spiropyran and its relatives. Color generation for each switch shown in Scheme 1.3 is facilitated by a conjugated amine: the nitrogen provides anchimeric assistance during the ring-opening reaction and stabilizes the merocyanine product by extending the length of the resulting conjugated π system.[47,51] Naphthopyran-derived merocyanines are instead stabilized by the extended conjugation offered by the naphthalene core.[52] The absence of a nitrogen atom, and therefore anchimeric assistance during the ring-opening reaction, significantly reduces the relative susceptibility of naphthopyran to spontaneous coloration without sacrificing merocyanine stability. Furthermore, as naphthopyran-based merocyanines are neutral and quinoidal in nature rather than zwitterionic, their thermal equilibrium is substantially less variable with solvent or material polarity.[53]

III. Naphthopyran Molecular Switches

Scheme 1.4. Reversible electrocyclic ring-opening reaction of diaryl naphthopyran

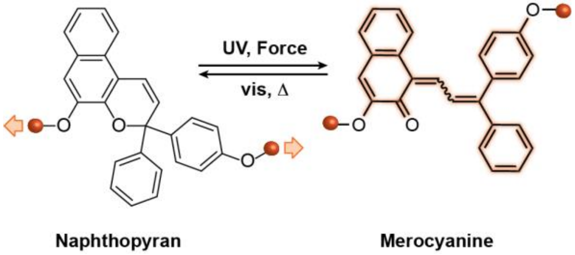

Naphthopyrans, or benzo-annulated benzopyrans, are a class of chromene molecular switches that undergo a reversible 6*π* electrocyclic ring-opening reaction to convert colorless naphthopyran into a colored merocyanine dye (Scheme 1.4).[54] There are three possible orientations the pyran ring can assume about the naphthalene core. However, only the angular 2*H*-naphtho[1,2-*b*]pyran and 3*H*-naphtho[2,1-*b*]pyran regioisomers display appreciable photochromic activity under ambient conditions (Scheme 1.5).[55] Naphthopyrans photoswitches have diverse applications as reversible coloring agents and have been commercially developed for use in plastic ophthalmic lenses, with other notable uses in textiles, anti-counterfeiting measures,[56] and cosmetics.[57,22] In research settings, naphthopyrans have been harnessed for use as conductivity switches,[58–63] logic gates,[64–67] molecular actuators, chemodosimeters,[68] and dynamic models of photo-excitable neurons.[67]

Scheme 1.5. Three diaryl naphthopyran regioisomers.

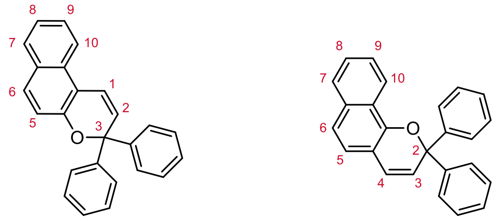

3,3-diphenyl-3*H*-benzo[*f*]chromene
or: **3*H*-naphtho[2,1-*b*]pyran**

2,2-diphenyl-2*H*-benzo[*h*]chromene
or: **2*H*-naphtho[1,2-*b*]pyran**

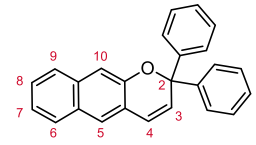

2,2-diphenyl-2*H*-benzo[*g*]chromene
or: **2*H*-naphtho[2,3-*b*]pyran**

To date, most reported naphthopyrans respond exclusively to UV light, and their photochemistry has been extensively studied since its discovery in 1966.[21] However, judicious structural modifications have also enabled activation by other stimuli. Our focus in this perspective is the force-mediated ring-opening reaction of naphthopyran, first realized in 2016.[17] Building off the vast knowledge of their photochemistry and structure–function relationships, naphthopyran mechanophores for use as force sensors have been easily diversified into a broad palette of accessible colors and thermal reversitivon rates. Further studies have provided insights into the nature of general force-mediated reactivity. Naphthopyran mechanophores can be scissile or non-scissile, reversible or irreversible, and their color, lifetime, and mechanochemical reactivity is precisely tunable.

Synthesis

Naphthopyran's industrial relevance and versatility is facilitated by its modular construction through simple, established synthetic routes. Facile modification of the naphthopyran scaffold enables access to merocyanine dyes that display a wide range of properties. Unless otherwise stated, all methods described herein are applicable to the formation of both angular 2*H*- and 3*H*-naphthopyrans.

I. Acid-Catalyzed Coupling of Propargyl Alcohols and Naphthols

The most straightforward and robust method of synthesizing naphthopyrans relies on the thermal rearrangement of naphthyl propargyl ethers (Scheme 1.6).[69] These substrates are typically generated *in situ* via the condensation of a naphthol with a propargyl alcohol under acidic conditions. *para*-Toluenesulfonic acid (TsOH), for example, is an ideal catalyst due to its solubility in organic media.[58,59,70–75] Heterogeneous catalysis using acidic alumina is also exceedingly common and efficient, enabling facile synthesis on large scale.[17,76–81] Protonation of the propargyl alcohol and loss of water forms a propargyl cation that is intercepted by the nucleophilic naphthol. A Claisen rearrangement and subsequent enolization generates the intermediate allenyl naphthol, which undergoes a 1,5-hyride transfer to form the naphthopyran in its merocyanine form. Finally, a thermal 6π-electrocyclization closes the merocyanine to generate the colorless naphthopyran.[82] Due to the relatively mild conditions employed here, a wide range of substituents on both the naphthol and propargyl alcohol are tolerated. It should be noted, however, that because the mechanism necessarily involves the thermal electrocyclization of the open merocyanine, substituents that strongly stabilize the merocyanine can decrease the yield of the thermally cyclized naphthopyran.

The simple propargyl alcohol and naphthol building blocks are commercially abundant and easily modified, which reinforces the popularity of this synthetic approach. Many inexpensive 1- and 2-naphthols are commercially available; for example, at the time this perspective was written, Sigma Aldrich carried 74 such compounds. The propargyl alcohol coupling partners are also often

Scheme 1.6. Naphthopyran formation via acid-catalyzed condensation of naphthols and diaryl propargyl alcohols

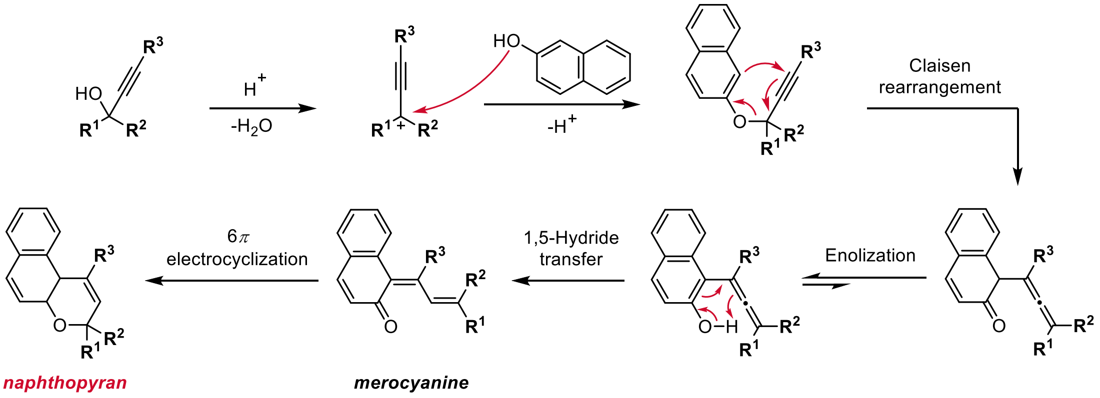

commercially available, but when not, they are efficiently synthesized by treating commercially abundant and diverse benzophenones with an alkali metal acetylide.[58,79,83,84] Specialty benzophenones, in turn, can be produced in one step by the Friedel-Crafts acylation of an aromatic nucleophile with an acyl halide. The modularity of this strategy has enabled the construction of diverse libraries of naphthopyran derivatives displaying a range of substitution patterns, both on the naphthalene core and on the peripheral aryl groups, from a relatively small collection of simple yet customizable building blocks.

Scheme 1.7. Acid-catalyzed naph*th*opyran syntheses suffer from side reactions including the Meyer-Schuster rearrangement (blue arrows) and trapping of the propargyl cation by the 4-position of 1-naphthols (red arrows)

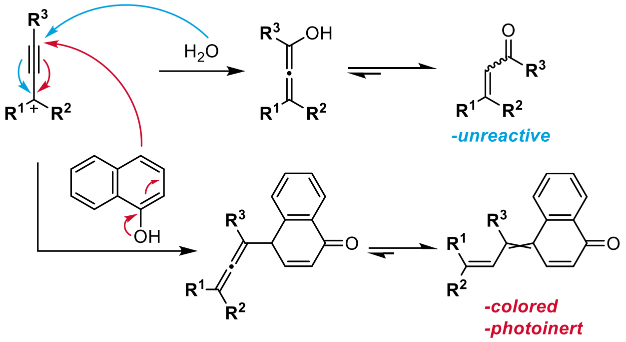

In certain cases, this synthetic route can involve the formation of undesired byproducts. If naphthol condensation does not occur rapidly after acid-mediated dehydration, the propargyl carbocation can be intercepted by adventitious water and undergo a Meyer–Shuster rearrangement to produce disubstituted α,β-unsaturated carbonyls that cannot react with the naphthol to produce naphthopyran (Scheme 1.7, blue arrows).[85] Electron-rich diaryl propargyl alcohols form relatively stable carbocations and are particularly susceptible to this rearrangement.[79] Additionally, the synthesis of 2*H*-naphthopyrans is complicated by the nucleophilic activity of the carbon *para-* to the naphthol. Trapping of the carbocation by this carbon produces a colored propylidenenaphthalenone dye that displays no photoswitching activity (Scheme 1.7, red arrows).[79,86] The yield of this product is heightened when increasingly electron-rich propargyl alcohols are used, or if the nucleophilic activity of the naphthol is particularly low.

II. Improved Acid-Catalyzed Synthesis of Naphthopyran

Scheme 1.8. Conditions developed by Zhao and Carreira to minimize side reactions in the acid-catalyzed formation of naphthopyrans.

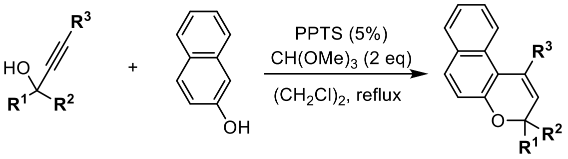

- minimal side reactivity
- high yields
- short reaction times

An optimized one-pot procedure that minimizes these side reactions was developed by Zhao and Carreira in 2003 with pyridinium *para*-toluenesulfonate (PPTS), a milder acid than TsOH (Scheme 1.8).[87] High-boiling, polar aprotic 1,2-dichloroethane was found to be an ideal solvent for facilitating formation of the carbocation intermediate. Importantly, the inclusion of trimethylorthoformate as a dehydrating agent greatly increased the yield of the desired product while significantly decreasing the reaction time. Typically, these conditions produce the desired naphthopyran in excess of 90% yield in one to three hours. Several naphthopyrans with a variety of aryl and core substituents were produced more cleanly and in higher yields than by other methods. Of note, bis-naphthopyrans, whose construction had traditionally suffered from low yields,[88] were synthesized cleanly enough that simple filtration provided pure material. The high yields, clean conversion, and fast reaction times make this method superior to traditional methods in nearly every regard.[77,89–100] We note, however, that the dehydrating conditions will not tolerate all functional groups, and in particular primary alcohols are incompatible with this method.

III. Alternative Synthetic Routes

A variety of other methods have historically been used to synthesize substituted naphthopyrans, including Grignard addition to unsubstituted benzocoumarins,[101–104] the reduction of substituted naphthopyranones,[104,105] and the addition of a lithiated naphthol to cinnamaldehyde derivatives.[104,106,107] However, these outdated routes involve the use of harsh reagents, which severely limit the scope of accessible naphthopyrans, or suffer from low yields. Additionally, the starting materials are often not commercially available and require cumbersome synthesis. Although there may be niche applications in which these methods may provide useful, they can be thought of as generally inferior to the more modular, functional-group-tolerant, and straightforward modern methods discussed above.

One exception is a route involving treatment of a naphthol with a substituted cinnamaldehyde derivative in the presence of titanium tetraethoxide, affording the naphthopyran in one step (Scheme 1.9)[70,76,104,108] First, the naphthol displaces one of the ethoxide ligands to form a titanium phenoxide. Following coordination of the aldehyde to the titanium center, the adduct undergoes a pericyclic rearrangement, dearomatizing the naphthol and forming a bond between the carbonyl carbon and the carbon β- to the naphthol. Elimination of the titanium alkoxide produces the open merocyanine that ultimately undergoes a thermal electrocyclization to produce the desired naphthopyran. Although the requisite cinnamaldehyde is typically not commercially available, it can be synthesized from propargyl alcohols under acidic conditions as shown above in Scheme 1.7. The robust nature and functional group tolerance of this method enables it to succeed where others fail. For example, heterocycle-fused naphthopyrans and similar chromenes are synthesized more efficiently and with fewer byproducts than with acidic conditions.[70,109]

More recent developments have focused on improvements in synthesis of these highly commercialized compounds from an environmental perspective. Because solvents are often the major component of organic reactions, which is particularly problematic on industrial scale, some efforts

Scheme 1.9. Titanium-mediated synthesis of angular naphthopyrans from naphthols and substituted cinnamaldehydes

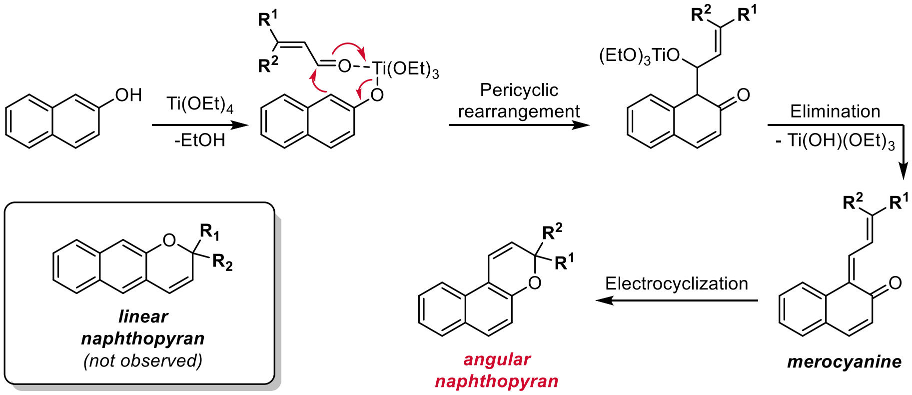

have focused on the use of both environmentally and economically friendly solvents. Several naphtho- and benzopyrans were attained in very good yields by treating an aqueous mixture of the propargyl alcohol and naphthol starting materials with a β-cyclodextrin hydrate catalyst.[110] The authors demonstrated significant catalytic activity even when the cyclodextrin was reused in subsequent reactions. Better still, solid-state syntheses have successfully eliminated the need for solvent in naphthopyran production. Tanaka et al. demonstrated that grinding the standard propargyl alcohol, naphthol, and TsOH components at room temperature with a mortar and pestle yielded the desired naphthopyrans, albeit in poor to fair yields (Scheme 1.10).[88] Substantial improvement to the method was made in a subsequent report by Dong et al., in which the two starting materials were ball-milled in the presence of catalytic $InCl_3$.[111] Under these conditions, most naphthopyrans were formed in excellent or quantitative yields with minimal side product formation. Additionally, exclusion of a Brønsted acid catalyst, which is typically necessary for the most efficient naphthopyran syntheses, lends this method to the construction of naphthopyrans containing acid-sensitive functional groups. The authors also demonstrated the mechanochemical synthesis of the propargyl alcohol starting materials by ball-milling a terminal alkyne with a benzophenone, circumventing the use of potentially dangerous pyrophoric alkali metal acetylide species.

Scheme 1.10. Solvent-free syntheses of naphthopyrans mediated by mechanical forces associated with physical grinding or ball-milling

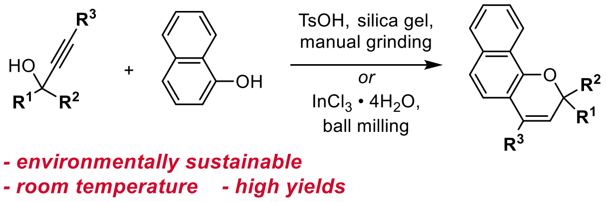

IV. Tolerance to Post-Synthetic Modification

The widespread use of naphthopyran as a molecular switch is enabled by its tolerance to a wide range of reaction conditions. Naphthopyran libraries are easily constructed via a divergent synthetic strategy in which a single naphthopyran core is diversified with several different substituents at a late stage. The most versatile of these strategies are those in which halide or triflate substituents on the naphthopyran core or aryl rings serve as cross-coupling handles. Notably, Suzuki,[71,112–114] Sonogashira,[115] and Buchwald–Hartwig[116] couplings have been used to install aryl/vinyl, alkynyl, or amino substituents, respectively. Further diversity can be afforded by copper catalyzed Ullman-type[117] or Grignard coupling.[71] Appropriate cross-coupling handles may be installed via selective halogenations.[45,51] Copper-catalyzed azide–alkyne cycloadditions involving pendant azide or alkynyl groups have also been successful.[118] More generally, naphthopyrans are stable under reaction conditions including acids or bases,[71,117,119] strong nucleophiles[71,118] and electrophiles,[118,120] organolithium species,[119] and reducing agents.[121]

The chemical resistance of the naphthopyran scaffold enables its facile covalent incorporation into polymers and polymeric matrices, which is often a requirement in the construction of responsive materials. Naphthopyran is highly tolerant of organic radicals, enabling naphthopyran-based initiators and comonomers to be used in the synthesis of linear polymers via the controlled radical copolymerization of polyacrylates, polystyrene, and polybutadiene.[114,118,120,122] Additionally, naphthopyrans have been incorporated into siloxane polymers via platinum-catalyzed hydrosilylation,[54–56] and in organic/inorganic composites via tin-catalyzed sol-gel formation.[118] As the needs for stimuli-responsive materials evolve, the tolerance of naphthopyran to several reaction types including those discussed above make it an ideal candidate for the construction of such materials.

Merocyanine Formation and Structure-Activity Relationships Derived from Photochemical Studies

Becker and Michl first alluded to the photochromism of naphthopyrans in 1966 in their seminal report on comparatively unstable photochromic benzopyrans,[21] with formal structural details and experimentation on naphthopyran photochromism provided in a subsequent patent.[125] Whereas the benzene core of benzopyran undergoes complete loss of aromaticity in its merocyanine form, the naphthalene core maintains partial aromaticity in the ring-opened state of the analogous naphthopyran. This additional degree of stabilization enables naphthopyran to access comparatively intense coloration and significantly improved fatigue resistance.[54] As the thermal barrier to the naphthopyran ring-opening reaction is significantly greater than that of the ring-closing reaction, naphthopyrans exhibit little to no thermochromism[54,126] in contrast to closely related spiropyrans.[127] These properties, combined with its synthetic accessibility, have made naphthopyran a particularly robust and practical photoswitch suitable for a number of applications. Given its industrial relevance, studies of naphthopyran photochemistry are abundant. Thorough and numerous investigations of merocyanine structure–property relationships have facilitated their use as commercial coloring agents;[22–24] since the same merocyanines are produced in response to mechanical force, these studies are valuable resources for designing mechanochromic mechanophores with predictable colored products with tunable characteristics. Furthermore, studies of the mechanisms of photochemically and thermally mediated naphthopyran ring opening (vide infra) serve as valuable points of comparison by which to compare the analogous mechanically mediated process, serving to provide general insights into the nature of force-driven chemical reactivity. While this review will highlight key discoveries in naphthopyran photochemistry, more exhaustive reviews dedicated to the topic are available.[22,54,104,128,129]

I. Photochemical Ring-Opening and Alkene Isomerization Reactions

Excitation of naphthopyran with UV light induces a 6π electrocyclic ring-opening reaction to generate a π-extended, conjugated merocyanine dye (Scheme 1.11).[130–134] Upon merocyanine formation, rotation about the central single bond from a *cisoid* to *transoid* conformation occurs rapidly to reduce steric interactions between the aryl substituents and the naphthalene core.[135] The *cis-transoid* (**CT**) species, wherein the alkene bond exocyclic to the naphthalene core is in the *cis* configuration, can revert to the colorless naphthopyran either thermally or with visible light irradiation. Alternatively, under extended UV irradiation **CT** will undergo a *cis*-to-*trans* isomerization of the exocyclic olefin to produce the much more thermally stable *trans-transoid* (**TT**) merocyanine. While thermal *trans*-to-*cis* isomerization does occur, photochemical isomerization with visible light is significantly more efficient.[74,131,133,136]

Careful analysis of reaction kinetics with UV-vis absorption spectroscopy has uncovered critical information on the reaction mechanism and rates, as well as the quantum yields and extinction coefficients for naphthopyran and its associated merocyanines. However, photochemical activation can produce mixtures of up to seven species, including several with overlapping absorption spectra. Analytical[137] or even numerical[62,94,119,138,139] solutions to such kinetic systems are complex, and often assumptions must be introduced to simplify analysis.[94,138,139] Kinetic and mechanistic studies of naphthopyran photochemistry are dramatically simplified by monitoring reaction progress using NMR spectroscopy, which allows the evolution of each isomeric form to be monitored separately. Particularly elegant studies have employed fluorinated naphthopyrans to track each species through sensitive ^{19}F NMR.[94,119,130,140,140–144] A single ^{19}F signal for each species in the equilibrium, combined with the broader spectral range of ^{19}F compared to ^{1}H, results in excellent resolution of individual signals. A critical finding from this body of work is that irradiation of a typical naphthopyran results in immediate formation of **CT**, and extended irradiation triggers olefin isomerization to generate **TT**.[63] Flash photolysis experiments support these conclusions.[133]

Scheme 1.11. Photochemical ring-opening reaction and isomerization of naphthopyran

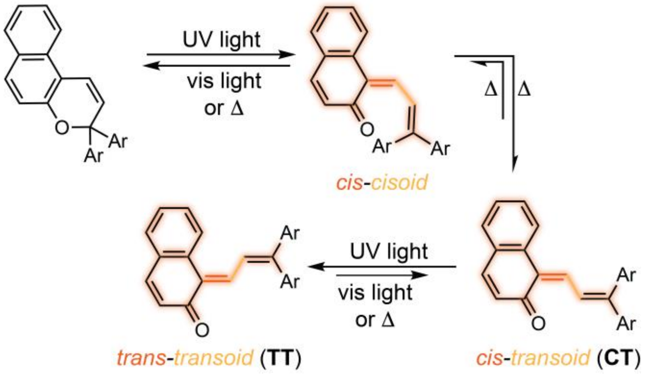

The large number of isomers produced under photochemical activation derive from the two merocyanine bridge olefins, which can both isomerize, resulting in a maximum of two observable constitutional stereoisomers of the merocyanine if the pendant aryl groups are symmetric and a maximum of four if the pendant aryl groups are asymmetric. Stereoisomers of the olefin exocyclic to the naphthalene core (*i.e.,* **CT** vs **TT**) are known to exhibit modest differences in spectroscopic features: λ_{max} values for the *cis* versus *trans* isomers are typically within approximately 10 nm of one another,[95,99,131,132] although comparisons of these species' extinction coefficients are often complicated by short lifetimes that render isolation difficult. In the case of 3,3-diphenyl-3*H*-naphtho[2,1-*b*]pyran, the extinction coefficients of the two exocyclic isomers could be determined after careful isolation of each species by chromatography at reduced temperatures. The difference was found to be less than 10%: ε for **CT** is 18,100 M^{-1} cm^{-1} in toluene, while that of **TT** is 16,900 M^{-1} cm^{-1}.[145] In addition to a few other examples of isolation via cold chromatography,[95,99,146] other studies have applied complex kinetic fitting procedures to absorption profiles,[96,131,147–149] computational simulations,[96,150] or simply ambiently stable merocyanines[96,100,146,151] to obtain or estimate these extinction coefficients. Notably, similar determination of the extinction coefficient of **TT** from kinetic analysis is significantly more prone to error and underestimation as **TT** typically comprises only a small fraction of the photochemically generated merocyanine mixture.[131] Given the general difficulty in selectively monitoring these stereoisomers, it is often assumed that these species have roughly the same extinction coefficient to simplify kinetic analysis.[62,71,97,151,152] To the best of our knowledge, no studies have investigated photophysical differences between stereoisomers of the distal diaryl merocyanine olefin, but these are likely even less distinct than isomers of the olefin exocyclic to the naphthalene core.

Evidence that naphthopyran-derived merocyanine dyes assume a charge-neutral quinoidal form in the ground state is derived from spectroscopic data,[54,74,100,130,153–156] x-ray crystallography for especially thermally stable species,[96,100,151] and solvatochromic behavior.[70,132,136,151,155,157–160] These merocyanines exhibit positive solvatochromism, or bathochromic shifts in λ_{max} with increasing solvent polarity, and respond to changes in polymeric environment or in some cases pH with shifts in l_{max} due to conformational distortions.[91,114,158,161–166] Whereas merocyanines generated from 3*H*-naphthopyrans typically display only one spectral absorption feature in the visible region, 2*H*-naphthopyrans exhibit two. The more intense of the two peaks is typically bathochromically shifted by approximately 45 nm when compared to that of similarly substituted 3*H*-naphthopyran analog (Figure 1.2).[167] Consequently, the effective perceived color of 2*H*-naphthopyrans is red-shifted from constitutionally isomeric 3*H*-naphthopyrans. 3*H*-Naphthopyrans can generate red, orange, yellow, blue, or purple merocyanines. While 2*H*-

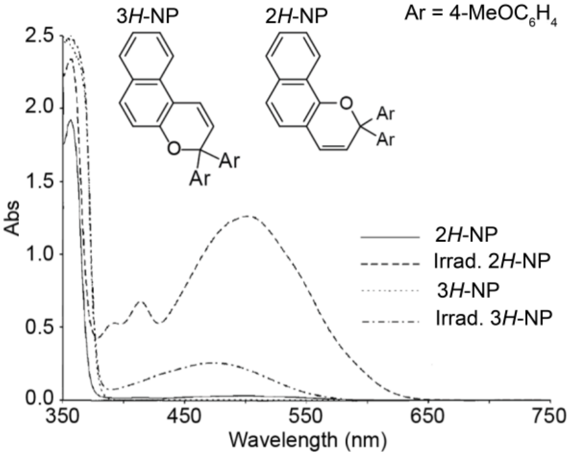

Figure 1.2. UV-vis spectra of 2,2-bis(4-methoxyphenyl)-2*H* -naphtho[l,2-*b*]pyran and 3,3-bis(4-methoxyphenyl)-3*H*-naphtho[2,l-b]pyran in toluene before and after UV irradiation. [Adapted from Hepworth and Heron 2006] Photoirradiation conditions not disclosed.

naphthopyran-derived merocyanines span these colors, their dual absorption peaks also enable access to commercially desirable neutral hues such as brown and grey.[23,168–171]

Greater mechanistic detail has been elucidated using transient spectroscopy techniques, which have been employed to study the productive forward reaction pathway for various naphthopyrans. Here, we discuss such findings for the simple 3,3-diphenyl 3*H*-naphtho[2,1-*b*]pyran (Scheme 1.11, Ar = Ph). It should be noted that while changes in solvent and temperature are known to alter the lifetimes of the individual mechanistic states, the overall photochemical pathway has been shown to be unaffected by solvent polarity, a notable distinction from closely related spiropyran.[134,172] Photochemical naphthopyran ring-opening reactions proceed from a singlet excited state.[134,135,153,173–175] Upon absorption of a photon, the closed form (**NP**) is excited to the Franck-Condon (**FC**) region of the lowest energy excited state **NP(S$_1$)** or to a higher energy state, all of which rapidly relax to the **NP(S$_1$)** excited state minimum **M*** on the femtosecond timescale (Figure 1.3). **M*** has a relatively short lifetime of ~1.8 ps and has structural features of the closed form of naphthopyran. Although many excited state pathways have been postulated,[132,153,173,176,177] the work of Herzog et al. suggests that from **M***, an insignificant energy barrier (<2 kcal/mol) must be overcome before transition through a conical intersection into ground state ring-opened form **CT(S$_0$)**.[174,178] Pyran C–O bond scission does not occur until the transition to the conical intersection, an observation backed by computational results for similar molecules.[175] While the quantum yield of the ring-opening reaction is typically high (~0.7–0.8), it is not impossible for the excited species **M*** to undergo internal conversion back to the **NP** ground state. A notable rarity within photochemistry, the

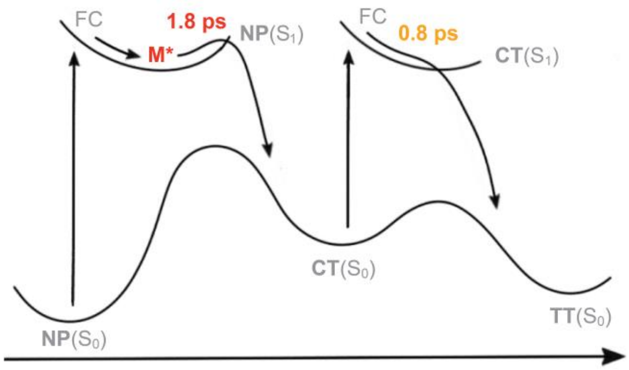

Figure 1.3. Proposed reaction pathway for the photochemical ring-opening reaction of a generic naphthopyran.

ring-opening reaction of chromenes has been found to be vibrational mode-dependent by both experimental and computational methods.[63,153,175,179–183] Whereas vibrationally excited states (within the electronic excited state) are typically so short-lived that excited photoswitches first relax to a vibronic ground state before undergoing productive reaction, the essentially barrierless photochemical transformation of naphthopyran to merocyanine proceeds so rapidly that such vibronic relaxation cannot occur. Therefore, the ring-opening reaction can proceed from any of several distinct vibronic states whose identity can affect the photochemical reaction and its quantum yield.

Exocyclic *cis* to *trans* isomerization also occurs through a singlet excited state. It is generally accepted that **TT** only arises from **CT** after a second photon absorption event, rather than directly from **NP(S_1)**, a conclusion backed by mathematical models as well as flash photolysis experiments that show minimal formation of **TT** under brief irradiation.[62,184,185] Brazevic et al. recently showed that excitation of **CT(S_0)** leads to an excited singlet state **CT(S_1)** with a sub-picosecond lifetime in acetonitrile.[174] However, for the 3*H*-naphthopyran we focus on in this section, conversion from **CT(S_1)** to **TT** is low because the dominant pathway for this species is internal conversion back to **CT(S_0)**.

While photoexcitation of **CT(S_0)** can also induce merocyanine ring closure from **CT(S_1)**,[174] the yield of this transformation is so much lower than that of the photo-induced ring-opening of **NP** that closure can only be significantly achieved by irradiating in the visible region where **NP** does not absorb.[136] **CT** can also undergo photoenolization. The resulting allene intermediate was discovered and extensively studied by Delbaere and coworkers by NMR, and Brazevic et al. recently determined that the reaction occurs through **CT(S_1)**. A thermally mediated proton transfer regenerates **CT(S_0)** from the allene. Interestingly, this allene intermediate has only been reported during photoexcitation of 3*H*-naphtho[2,1-*b*]pyrans, not 2*H*-naphtho[1,2-*b*]pyrans.

II. Thermal Reversion of the Merocyanine

Thermal transformations play an important role in naphthopyran equilibria. While heat can induce the ring-opening reaction of naphthopyran, the process is extremely inefficient. By comparison, thermal reversion is so rapid that no accumulation of colored product (*i.e.*, thermochromism) is typically observed.[82] Therefore, electrocyclic ring-closure of the merocyanine is the most kinetically relevant thermally mediated reaction in naphthopyran chemistry. The rate of this process is heavily dependent upon the regiochemistry and geometry of the merocyanine, which will be the focus of this section.

The geometry of the exocyclic double bond greatly impacts on merocyanine stability and, therefore, its ability to revert to the closed naphthopyran. NMR studies have found that the ring-closure of **TT** cannot occur directly and necessitates an initial isomerization to **CT**.[133] While such isomerization is possible thermally, this process is orders of magnitude slower than the thermal electrocyclization of **CT**, and thus reversion of **TT** is comparatively slow.[62,74,96,97,100,119,130–133,136,151,186] In some cases, **TT** is even stable enough to isolate and characterize under ambient conditions.[96,100,136,141,151] The *trans*-to-*cis* isomerization is much more efficiently facilitated through the visible light-mediated pathways discussed previously. Therefore, while naphthopyran is generally considered to be a T-type (*i.e.,* thermally reversible) photoswitch, partial P-type (*i.e.,* photochemically reversible) behavior is observed if its extended exposure to UV light generates a significant amount of the thermally stable **TT**.[74] As thermal *cis*-to-*trans* isomerization of the exocyclic olefin has only been observed in very limited and unique cases,[119,144] electrocyclization of **CT** is the dominant thermal process operative for naphthopyran switches and their merocyanine isomers. While thermal reversion rates can sometimes vary between isomers of the distal, diaryl-substituted olefin, these values usually lie within one order of magnitude of each other[63,94,187] in contrast to the 1–3 orders of magnitude spanned by geometric isomers of the exocyclic naphthyl olefin.[62,74,96,97,119,130,131,133,141,147,185,186,188]

Reversion kinetics can be reliably determined using multiple methods, but most often by fitting time-dependent absorption-loss data to a biexponential decay function.[71,91,93,94,97,130,131,185,187] The smaller rate constant obtained is attributed to **TT**, the more thermally stable isomer. Analyses by both absorption and NMR spectroscopy have enabled determination of activation enthalpy and activation entropy for isomerization and ring-closure using Eyring-type analysis.[119,138,161,189]

Thermal reversion behavior represents a key functional divergence between 2*H*- and 3*H*-naphthopyrans. Merocyanines arising from 2*H*-naphtho[1,2-*b*]pyran are typically more stable than those from 3*H*-naphtho[2,1-*b*]pyrans, which experiences higher degrees of steric crowding between the alkene and naphthalene hydrogens in both **CT** and **TT** (Scheme 1.12).[55] As a result, 3*H*-naphthopyran merocyanines typically recyclize at rates roughly two orders of magnitude faster than those derived from 2*H*-naphthopyrans.[70,133]

The thermal behavior of naphthopyrans and their merocyanines are somewhat susceptible to environmental effects, though significantly less so than other molecular switches like spiropyran. Polar solvents can destabilize the quinoidal merocyanine and accelerate the rate of thermal reversion.[70,71,157,158,160,190] Interestingly, the thermal ring-opening reaction, which is thought to proceed through a polar, heterolytic mechanism, is also accelerated by polar solvents that may enable more

Scheme 1.12. The ring-opening reactions of 3H- and 2H- naphthopyrans generate merocyanine isomers with varying degrees of steric repulsion, which strongly influences absorption and reversion

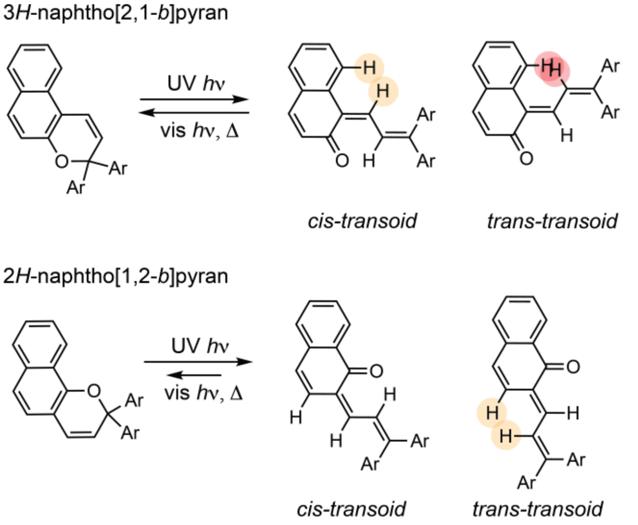

pronounced polarization of the reactive pyran C–O bond.[160] Even so, this does not lead to significant thermochromism. Relatively viscous solvents like toluene have been found to slow the rate of thermal merocyanine electrocyclization via interactions with the alkylidene bridge, changing its position in the solvent sphere during cyclization while the naphthalene unit remains unmoved.[104,191,192] Thermal reversion is analogously slowed when the merocyanine is incorporated into certain bulk polymeric materials[22,91,93,123,128,154,185,189] or sol-gel films[193,194] where conformational changes are restricted by spatial constraints. Accordingly, photochromism within bulk polymeric materials is most efficient in polymers with low flexural moduli (*i.e.*, below 2 GPa) and T_g like polyolefins and polyvinyls as opposed to rigid, glassy matrices like polycarbonates and styrene-acrylonitriles.[22] A rarity among photochromic species, naphthopyrans do exhibit photochromism in the bulk crystalline state.[151,189] The resulting merocyanines are thermally stable, but can still be photobleached with visible light.

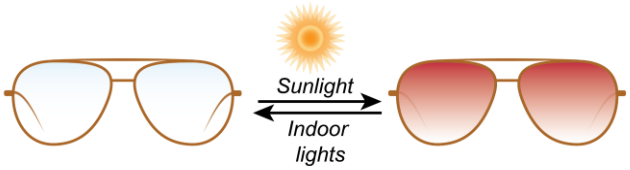

Figure 1.4. Naphthopyrans have been extensively used as UV-responsive coloring agents in plastic ophthalmic lenses.

III. Synthetic Modulation of Merocyanine Color, Intensity, and Lifetime

Commercial interest in the development of naphthopyran derivatives as photoswitches for use in ophthalmic lenses has culminated in a vast library of structures whose resulting merocyanine dyes exhibit a wide range of colors and thermal bleaching rates (Figure 1.4). Extensive work in this area has been carried out in particular by Gabbutt, Hepworth, and Heron.[65,75,78,81,84,90,104,114,128,150,163,164,195–199] As mechanochemical stimulation of naphthopyrans can generate these same merocyanine dyes, the established structure–property relationships for photochemically generated merocyanines provide a convenient point of reference for mechanophore design.

***Para*-aryl Substitution**

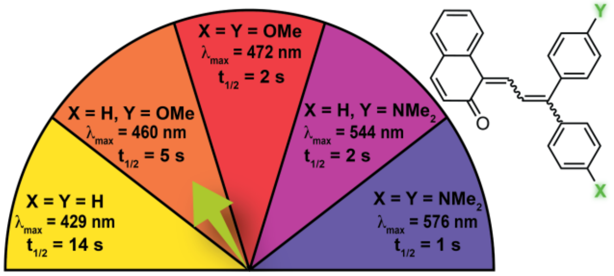

Figure 1.5. Electron-donating para-aryl substituents produce significant bathochromic shifts in merocyanines and drastically increase fade rates. Inspired by Towns.[23]

The modular syntheses described previously enable the development of diverse naphthopyrans through facile installation of property-altering substituents. Specifically, significant changes to merocyanine absorption properties and reversion kinetics may be affected by substituting the phenyl rings at the *para*-position (Figure 1.5).[75,128] Such substitution is easily introduced through modification of the benzophenone starting material (see section 2a). 2*H*- and 3*H*-naphthopyrans with electron-donating *para*-substituents both exhibit significant bathochromic shifts in l_{max} that can be greater than 100 nm. Careful control over electron-donating character enables precise tuning of merocyanine color. For example, incorporation of a *para*-pyrrolidine substituent transforms the color of the merocyanine from yellow to purple. Notably, symmetrical *para*-substitution of both phenyl rings on a 3*H*-naphthopyran can cause formation of a shorter-wavelength shoulder in the UV-vis spectrum, resulting in significant changes to the dye's color. Further tuning of merocyanine color can be achieved by adding a bulky *meta*-aryl substituent to a *para*-pyrrolidinated phenyl ring.[196] Steric interactions from the *meta*-substituent force the pyrrolidine to twist out of plane, reducing its degree of conjugation with the rest of the molecule (Figure 1.6). In addition

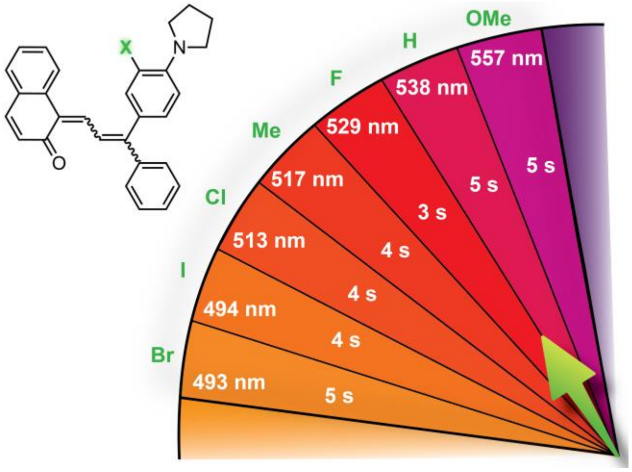

Figure 1.6. Fine control of merocyanine color is enabled through sterically crowding a para-pyrrolidine substituent at the neighboring meta-position. Wavelengths (in nm) and half-lives (in seconds) are given for various meta-substituents.

to these effects on merocyanine color, *para*-substitution also dramatically alters the rate of thermal reversion. Studies on 2*H*- and 3*H*-naphthopyrans have shown that ring-closing of their respective merocyanine forms is accelerated with increasing electron-donating character of the *para*-substituent, with amino substituents typically eliciting the greatest effects.

The *ortho*-Aryl Effect

ortho-Aryl substitution in 3*H*-naphthopyrans significantly reduces merocyanine thermal reversion rates compared to their unmodified counterparts.[78,81,104,128,196] Regardless of electronic considerations, the degree of impedance to merocyanine recyclization scales with the size of the *ortho*-substituent, indicating that this is a primarily steric effect (Table 1.1). Larger substituents hinder rotation of the aryl rings, a necessary step in merocyanine reversion. These effects compound for aryl rings bearing substituents at both *ortho*-positions on a single ring, resulting in even slower fade rates. *ortho*-Substitution can slow merocyanine bleaching to such a degree that it substantially mitigates the reversion-accelerating effect of an electron-rich *para*-substituent when both substituents lie on the same aryl ring. Critically, this substitution pattern can decouple the accelerating effect of electron-donating *para*-aryl substituents on merocyanine reversion kinetics from its effect on color, accessing long-lived purple

Table 1.1. Effect of remote *ortho*-substituents on the color and lifetime of *para*-pyrrolidinated merocyanines

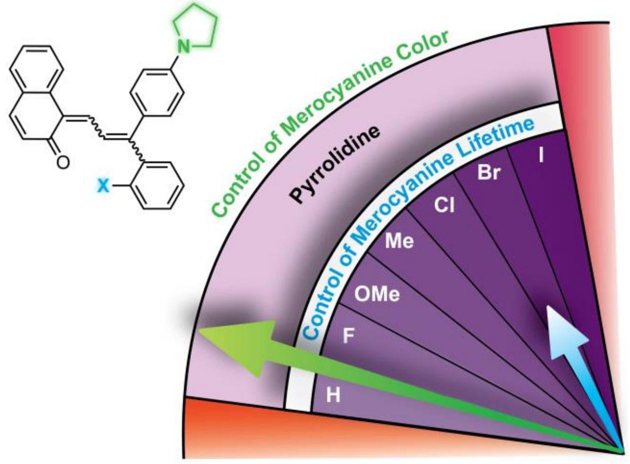

Entry	X	λ_{max} (nm)	$t_{1/2}$ (s)
1	H	538	5
2	F	554	40
3	Cl	554	741
4	Br	554	1024
5	I	553	1167
6	OMe	555	351
7	Me	555	639

merocyanines. While the systematic studies summarized in Table 1.1 were conducted on naphthopyrans with *para*-pyrrolidine substituents, the *ortho*-effect can be considered to apply generally regardless of specific substitution patterns.[23,94,120,123,200] It is also notable that the synthesis of naphthopyrans bearing significantly bulky *ortho*-substituents can suffer from reduced yield because thermal reversion of the open merocyanine is a necessary step in reaching the desired naphthopyran.

Table 1.2. Effect of sterically crowding *ortho*-substituents on the color and lifetime of *para*-pyrrolidinated merocyanines

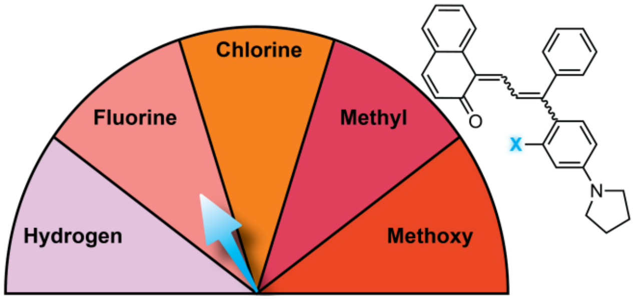

Entry	X	λ_{max} (nm)	$t_{1/2}$ (s)
1	H	538	5
2	F	394, 501	21
3	Cl	403, 480	44
4	OMe	399, 519	73
5	Me	410, 507	104

Ortho-substitution has moderate effects on the absorption properties of the open merocyanine, although not to the same degree as *para*-substitution. If located remotely on the phenyl ring geminal to a *para*-pyrrolidine substituted phenyl ring, an *ortho*-substituent induces a moderate bathochromic shift in λ_{max} regardless of its size or electronics (Table 1.1).[78] In this case, the pyrrolidine-substituted ring adopts a coplanar conformation with the merocyanine bridge to maximize its degree of conjugation with the rest of the π system. Steric crowding between the two rings then forces *ortho*-substituted ring to rotate out of that plane, minimizing its steric interactions with the pyrrolidine-substituted ring and greatly reducing its effect on merocyanine color. However, if the two substituents reside on the same aryl ring , the bathochromic shift in absorption imbued by the *para*-pyrrolidine substituent is dampened (Table 1.2).[81] Its *ortho*-substituent forces the ring to rotate out of the plane of the merocyanine bridge, reducing its conjugation to the rest of the molecule. This substitution pattern also results in a second major absorbance feature in the visible spectrum around 400 nm. For each peak, increasing substituent size generally produces larger hypsochromic shifts, likely due to increased out-of-plane twisting. Electron-donating *ortho*-substituents can counteract this shift; while the *ortho*-chlorinated merocyanine absorbs most strongly at 480 nm (Table 1.2, entry 3), the merocyanine with a comparatively sized *ortho*-methyl substituent absorbs at 507 nm (Table 1.2, entry 5). The interplay of these steric and electronic effects has been harnessed to precisely modify color and fading behavior.

Core Substitution

Unlike pendant phenyl substitution patterns, core substitution patterns are not generalizable between 2*H*- and 3*H*-naphthopyrans.[54,128] Typically, substituents in conjugation with the merocyanine bridge produce the greatest effects on merocyanine photophysical properties and thermal stability. Electron donating alkoxy and amino substituents at the 5- and 8- positions of 3*H*-naphthopyrans significantly slow thermal reversion by stabilizing the conjugated merocyanine form.[200] These positions can also moderately affect the absorption properties, with 8-methoxy substitution resulting in a bathochromic shift in λ_{max} (Table 1.3, entry 4).[154] Conjugation with the merocyanine carbonyl alters λ_{max} in the opposite way, producing minor hypsochromic shifts with electron donation at the 6- and 9- positions (Table 1.3, entries 2 and 5). More importantly, donating substituents at the 6-position drastically reduce merocyanine reversion rates. In the case of 6-amino substitution, a second major resonance form can drastically alter merocyanine properties (Scheme 1.13).[54] This resonance form is not able to undergo the ring-closing reaction to form the

Table 1.3. Electron-donating core substituent effects on the color of 3H-naphthopyran-derived merocyanines

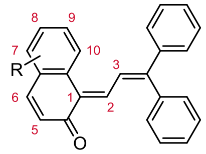

Entry	R	λ_{max} (nm)
1	5-OMe	435
2	6-OMe	423
3	7-OMe	435
4	8-OMe	477
5	9-OMe	432
6	H	436

naphthopyran, resulting in reduced overall merocyanine fading. Core substituent modifications on 2*H*-naphthopyrans are summarized in Table 1.4. In this case, electron donating and withdrawing substituents produce only slight changes in λ_{max}.[128] The fade rate is dictated by the degree of steric interaction between the 5- position substituent and 4- position proton on the merocyanine bridge (Table 1.4., entries 1-4). Weaker effects on fading can be introduced by mildly donating substituents at the 6- position (Table 1.4., entries 5-7). The disparate reversion kinetics between **CT** and **TT** are undesirable for commercial applications, particularly in photochromic ophthalmic lenses. Thus, significant efforts have been undertaken to design naphthopyrans that either cannot access **TT** or generate **TT** species with accelerated reversion due to unfavorable steric interactions, ensuring that rapid coloration and decoloration is achieved when transitioning between sunlight and indoor environments. For example, the thermal stability of merocyanines derived from 3*H*-naphthopyrans can be modulated via the introduction of bulky substituents at the 2- or 10- position. Larger substituents like bromo or phenyl suppress the formation and lifetime of **TT** due to steric repulsion with the merocyanine bridge, constraining the merocyanine to exist only in the **CT** form (**Scheme 1.14**a).[112,178] Naphthopyrans with these substitution

Table 1.4. Core substituent effects on the color and lifetime of 2H-naphthopyran-derived merocyanines

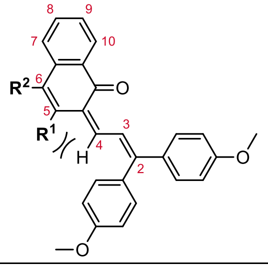

Entry	R_1	R_2	λ_{max} (nm)	$t_{1/2}$ (s)
1	H	H	412, 508	> 1800
2	Me	H	416, 496	178
3	Me	Me	421, 494	66
4	Ph	Ph	418, 508	20
5	CO_2Me	H	492	2
6	CO_2Me	Me	416, 492	4
7	CO_2Me	Ph	416, 506	7

Scheme 1.13. Amine substituents stabilize 3H-naphthopyran-derived merocyanines by contributing a new significant resonance form resistant to cyclization.

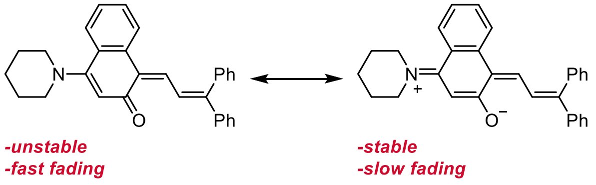

patterns produce quickly fading merocyanine forms with sub-millisecond half-lives. In another example, the 10- position is substituted by a methyl ether, enabling a hydrogen bonding interaction between the proton at the 2- position and the ether oxygen that heavily favors the open **CT** form and, in several cases, almost completely suppresses **TT** accumulation (Scheme 1.14b).[112]

Scheme 1.14. (a) Substituents at the 2- and 10- positions of 3H-naphthopyrans sterically clash in TT, destabilizing that isomer (b) Hydrogen bond acceptors at the 10- position of 3H-naphthopyrans stabilize CT

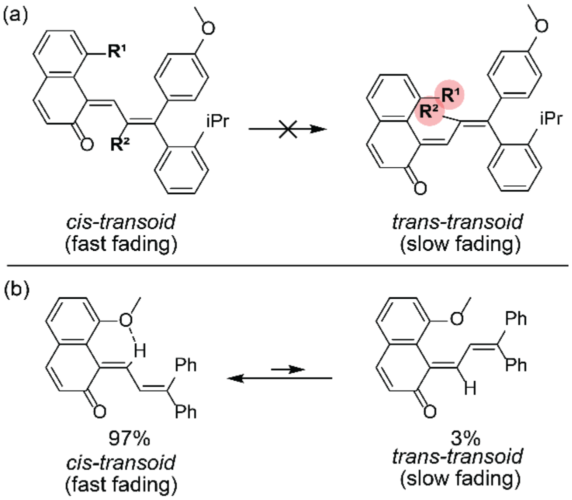

Other Modification Patterns

More synthetically intensive modifications to naphthopyran scaffolds can have drastic effects on fading behavior. As above, these typically involve suppression of the long-lived **TT** merocyanine isomer, conformationally restricting the merocyanine to exist solely as the more short-lived **CT**. For example, fusing the 4- and 5- positions of a 2*H*-naphthopyran with an alkyl bridge prevents isomerization of the exocyclic olefin, resulting in exclusive **CT** production upon irradiation. There merocyanines exhibit fading half-lives on the order of seconds to minutes even in the presence of fade-reducing functionalities like *ortho*-aryl substituents (Scheme 1.15).[201–205] Conversely, a few core substitution patterns strongly stabilize TT upon photoirradiation, resulting in merocyanines dyes with thermal half-lives on the order of days to years.[96,141,201] For example, fusing a benzopyrrole or phenanthrene ring system to the naphthopyran core produces a nonplanar, helical naphthopyran whose **TT** merocyanine is significantly stabilized through favorable

Scheme 1.15. Fusing the 4- and 5- positions of 2H-naphthopyrans locks the exocyclic olefin, preventing isomerization to TT

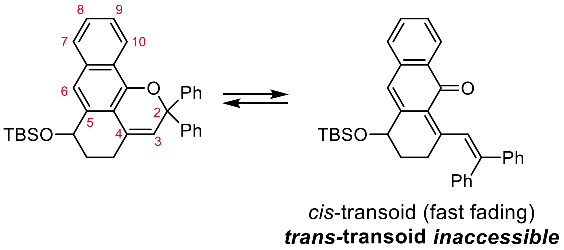

electronic interactions between the extended core and the bis-aryl substituents.[96] Consequently, thermal reversion to **CT** is strongly disfavored.

Significant extension of the naphthopyran's conjugated π system can give rise to merocyanines displaying colors not accessible using the modification patterns discussed previously. For example, use of an anthracene core instead of naphthalene produces merocyanines that are green through combination of two absorption features between 400–480 nm and 580–620 nm.[202] Similar colors can be accessed by extending the length of conjugation of the pendant aryl substituents.[203]

Privileged substituent patterns that have significant effects on the fading and absorption properties of both 3*H*- and 2*H*-naphthopyran-derived merocyanines have been summarized in Table 1.5 and Table 1.6, respectively. However, many more handles for controlling merocyanine lifetime and color exist than have been discussed in this review. The addition of the pendant aryl ring substitutions discussed above on top of these core variations vastly expands the scope of accessible properties. The breadth and variety of attainable synthetic modifications explored here cement naphthopyran as a versatile, highly studied molecular switch whose characteristics can be tuned to meet a wide variety of applications.[22,23,54,104,128]

Table 1.5. Summary of significant substituent effects on the properties of 3H-naphthopyran- derived merocyanines

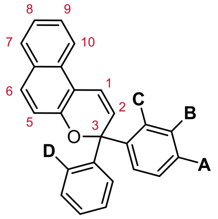

Position	**Substituent Property**	**Fading Effect**	**Shift in λ_{max}**	**Section**
A	↑ e$^-$ donation	Faster	Bathochromic	**3ci**
B	↑ size	--	Hypsochromic (if **A** = pyrrolidine)	**3ci**
C	↑ size	Slower	Hypsochromic (if **A** = pyrrolidine)	**3cii**
D	↑ size	Slower	Bathochromic	**3cii**
2	↑ size	Faster	--	**3civ**
5	↑ e$^-$ donation	Slower	--	**3ciii**
6	↑ e$^-$ donation	Slower	Hypsochromic	**3ciii**
8	↑ e$^-$ donation	Slower	Bathochromic	**3ciii**
10	↑ size	Faster	--	**3civ**

Table 1.6. Summary of significant substituent effects on the properties of 2H-naphthopyran-derived merocyanines

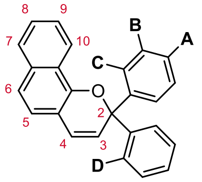

Position	**Substituent Property**	**Fading Effect**	**Shift in λ_{max}**	**Section**
A	↑ e$^-$ donation	Faster	Bathochromic	**3ci**
B	↑ size	--	Hypsochromic (if **A** = pyrrolidine)	**3ci**
C	↑ size	Slower	Hypsochromic (if **A** = pyrrolidine)	**3cii**
D	↑ size	Slower	Bathochromic	**3cii**
5	↑ size	Faster	--	**3civ**
6	↑ e$^-$ donation	Slower	--	**3ciii**

The Emerging Mechanochemistry of Naphthopyran

I. Discovery of Naphthopyran Mechanochemistry

The mechanically triggered ring-opening reaction of naphthopyran was first demonstrated by Moore and coworkers in 2016.[17] The authors hypothesized that properly aligning applied mechanical force with the reactive pyran C–O bond would lengthen and eventually break it, inducing the 6*π* electrocyclic ring-opening reaction and yielding the colored merocyanine product. To vary the alignment of applied force with the labile bond, three 3*H*-naphtho[2,1-*b*]pyran regioisomers were designed, each with one polymer attachment handle at the *para*-position of one of the pendant phenyl rings and the second at either the 5-, 8-, or 9-position on the naphthopyran core (Figure 1.7a). Density functional theory (DFT) calculations performed on **NP5** predicted the desired ring-opening reaction to occur in response to mechanical force while calculations on **NP8** and **NP9** predicted

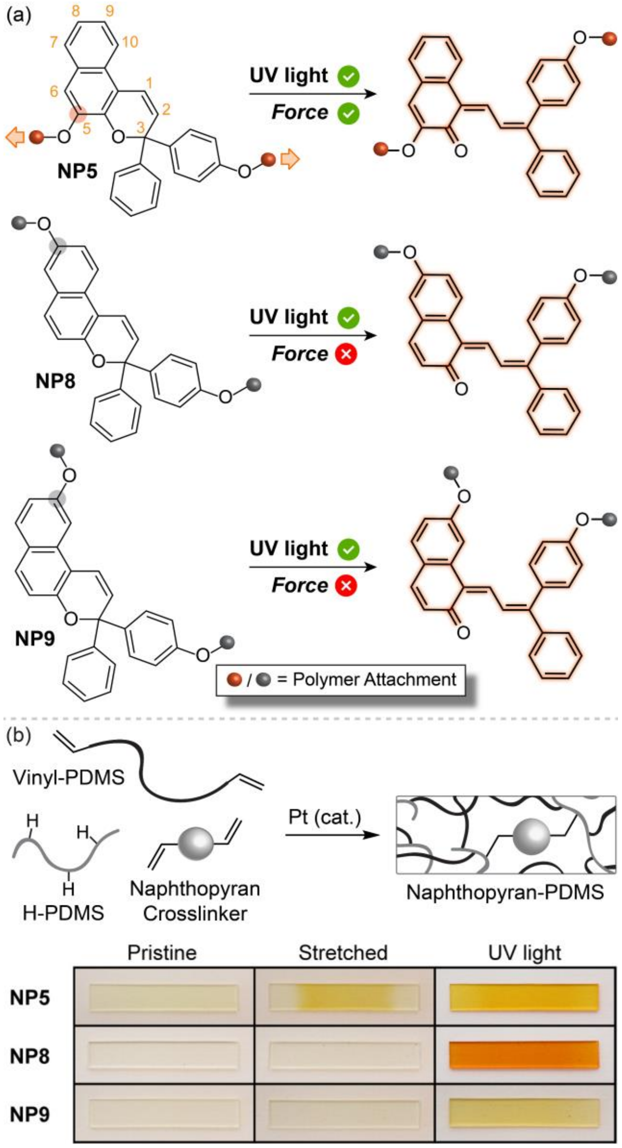

Figure 1.7. Mechanochemical activity or inertness of three naphthopyran regioisomers. (a) While naphthopyran regioisomers with various pulling positions all demonstrate photochemical activity, only the isomer that aligns the transduced force with the mechanically labile C–O bond (**NP5**) is mechanochemically active. (b) PDMS films covalently crosslinked with each of the three isomers were exposed to uniaxial mechanical stress by manual pulling, effecting successful activation and associated color change only in the film containing **NP5**.

non-specific bond cleavage elsewhere in the molecules, suggesting that proper pulling geometry is critical for mechanochemical activation.

When incorporated as crosslinkers into solid poly(dimethyl siloxane) (PDMS) films, all naphthopyran isomers exhibited photoswitching behavior under irradiation with UV light as evidenced by orange/yellow coloration characteristic of their merocyanine forms (Figure 1.7b). However, when uniaxial tension was applied to the films, only **NP5** generated merocyanine, consistent with the DFT predictions. The authors rationalized these results by examining the degree of alignment between the scissile pyran C-O bond vector and the force vector, defined as that between the two pulling positions. In the mechanochemically active **NP5**, these vectors were more closely aligned than those in **NP8** and **NP9**. It is likely that agreement between these two vectors is, in the case of 3*H*-naphthopyrans, a major determinant of mechanochemical activity. Later work on a different mechanophore supported these conclusions; the mechanochemical activity of scissile Diels–Alder adduct regioisomers was found to similarly depend on the alignment of applied mechanical force with labile bonds.[204] This initial report indicated that naphthopyran held promise both a mechanical force sensor and a platform for studying fundamental aspects of polymer mechanochemistry.

II. Structure-Property Relationships

Our group sought to harness the synthetic modularity and highly tunable properties of naphthopyran molecular switches highlighted earlier in this perspective to elicit precisely controllable and predictable mechanochromic behavior. By carefully selecting substituent patterns to assert control over merocyanine color and lifetime, we found that the established structure-property relationships for photochemically generated merocyanines translate seamlessly to mechanochemically-generated merocyanines (Figure 1.8a).[205] For example, we predicted that *ortho*-fluorine substitution would increase the lifetime and intensity of mechanically generated color through steric interactions, while *para*-pyrrolidine substitution would significantly alter merocyanine color and concomitantly accelerate thermal reversion kinetics. We also investigated whether the electronic nature of the polymer attachment site at the 5-position of the naphthalene core, *i.e.*, a comparatively electron-rich ether versus a methylene, affected merocyanine behavior. A library of naphthopyran derivatives containing varied combinations of these substituents were covalently incorporated as crosslinkers into PDMS elastomers (Figure 1.8b). The generally colorless films were activated by manual stretching and were monitored for a short period to observe their thermal fading behavior. As intended, the pyrrolidinated naphthopyrans produced purple coloration under mechanical force, while mechanophores without this substituent exhibited yellow/orange coloration. Additionally, *ortho*-fluorine substitution successfully intensified mechanochromism and slowed thermal fading of color regardless of *para*-substitution, evidenced by their comparatively dark and persistent coloration. Lastly, electron-rich substitution at the 5-position (Figure 1.8, **1a**/ **2a** vs **1c**/**2c**) prolonged merocyanine lifetime, a structure-property relationship previously unreported in the photochemical literature. These findings provide strong support that the design principles established

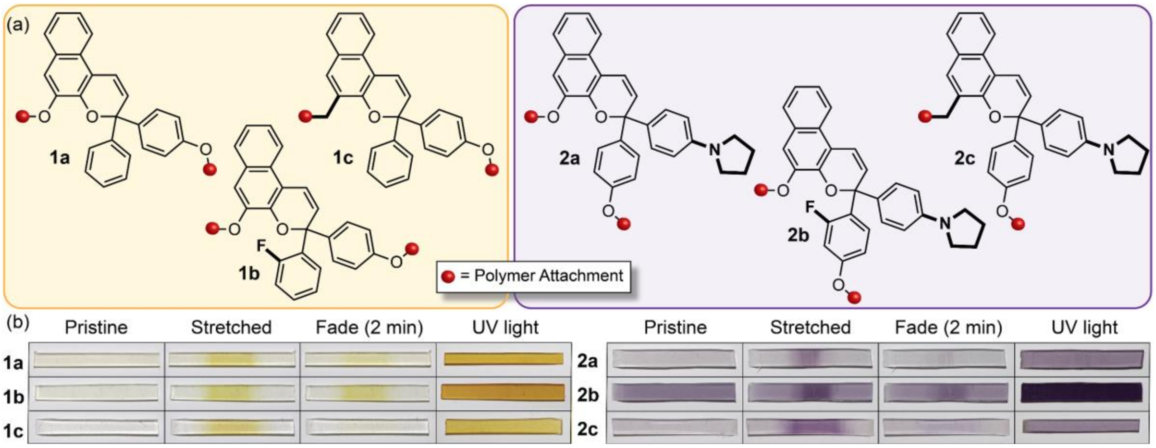

Figure 1.8. Naphthopyran mechanophore crosslinkers with varied functional substitution patterns. (a) Substitution patterns that engendered a spectrum of different steric and electronic properties were harnessed to design modular force sensors with modular color and thermal fading behavior. (b) Mechanical activation of the PDMS films containing covalently incorporated naphthopyran crosslinkers revealed successful translation of the desired photochemical properties in a mechanochemical context.

for naphthopyran photoswitches can be generalized and harnessed for the construction of naphthopyran mechanophores.

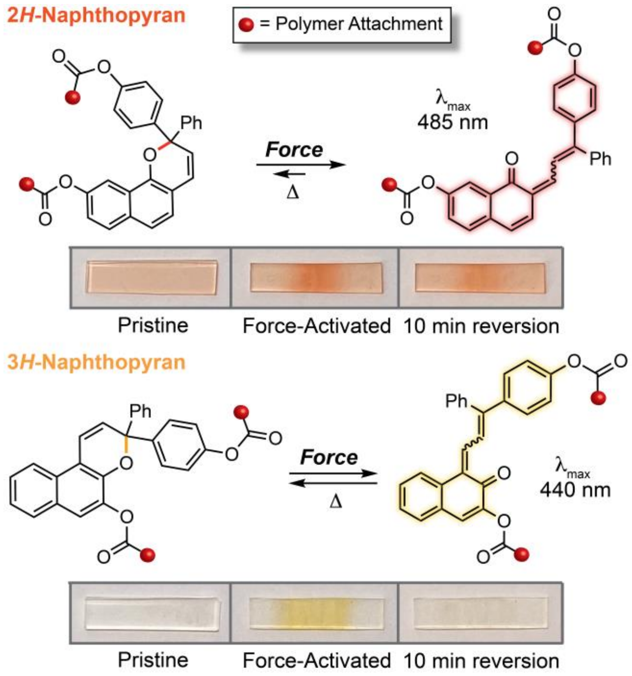

Figure 1.9. Constitutionally isomeric naphthopyran mechanophores with varied regiochemistry of the pyran ring about the naphthalene core generate merocyanines with distinct coloration and thermal stability. 2H-naphthopyrans yield slow fading red merocyanines, while 3H-naphthopyrans produce rapidly reverting yellow merocyanines.

As discussed previously, two constitutional isomers of naphthopyran have been widely investigated as photoswitches, though initial studies of naphthopyran mechanochromism were limited to the 3*H*-naphthopyran scaffold. We were intrigued by the potential of mechanophores based on angular 2*H*-naphthopyrans to generate merocyanine dyes with unique absorption features and slower reversion rates than those derived from 3*H*-naphthopyrans. Intense and long-lived coloration is an attractive characteristic for reporting a material's force history. To investigate regiochemistry as a handle for modulating mechanophore behavior, two constitutionally isomeric 2*H*- and 3*H*-naphthopyran mechanophores were synthesized.[206] Initial investigations of mechanochemical activity were carried out using solution-phase ultrasonication, which causes formation and immediate collapse of bubbles in solution. Dissolved linear polymers in proximity to the collapsing bubbles experience elongational shear forces maximized at the chain center.[2] Two poly(methyl acrylate) (PMA) polymers covalently incorporating each mechanophore at the chain center were exposed to ultrasonication. Similar to findings from photochemical studies on analogous molecules, the merocyanine generated from the 2*H*-

naphthopyran displayed bathochromically shifted absorption features from those of the yellow merocyanine generated from the 3*H*-naphthopyran, resulting in intense red coloration (Figure 1.9). 3*H*-Naphthopyran-derived merocyanines reverted rapidly, while those generated from 2*H*-naphthopyrans exhibited lifetimes an order of magnitude longer. We were pleased to find that this trend was also observed when the two naphthopyrans were incorporated as crosslinkers in PDMS bulk materials. Interestingly, we noticed that while a fraction of photochemically generated merocyanine is persistent, no persistent merocyanine is generated under mechanical force. This result may suggest that the merocyanines whose exocyclic olefin displays *trans* geometry (**TT**, see Section 3II above) can be generated photochemically but are not accessed mechanically. Indeed, mechanochemical *cis* to *trans* isomerizations of alkenes are uncommon.[207,208,38] This study confirmed that pyran regiochemistry is a synthetically accessible handle for diversifying naphthopyran mechanophore functionality. Future work from our group will investigate whether mechanical force elicits this unusual stereospecificity in naphthopyran molecular switches. We note that the third possible naphthopyran constitutional isomer, the linear 2*H*-naphtho[2,3-*b*]pyran (see Scheme 1.5), has yet to be investigated as a potential mechanophore. Given that this species does not typically exhibit photochromism,[52,54] this platform could be valuable as a force-selective molecular switch.

III. Unique Naphthopyran Reactivity Accessed by Mechanical Force

Mechanical force is a unique stimulus known to facilitate unusual reaction pathways and form unexpected products. For example, the Moore and Craig groups have both shown that mechanical force can override Woodward–Hoffman orbital symmetry rules and promote thermally forbidden reaction pathways for *cis*-benzocyclobutene and *trans*-*gem*-difluoroyclopropane mechanophores, respectively.[18,19] The naphthopyran scaffold’s modular construction and thoroughly studied photochemical behavior lends it to further investigations into the unique nature of force-driven reactivity. The following section will describe three cases where mechanical force promotes reaction pathways and the formation of products from naphthopyrans that are inaccessible under photochemical activation.

Mechanochemical Generation of an Elusive Persistent Merocyanine

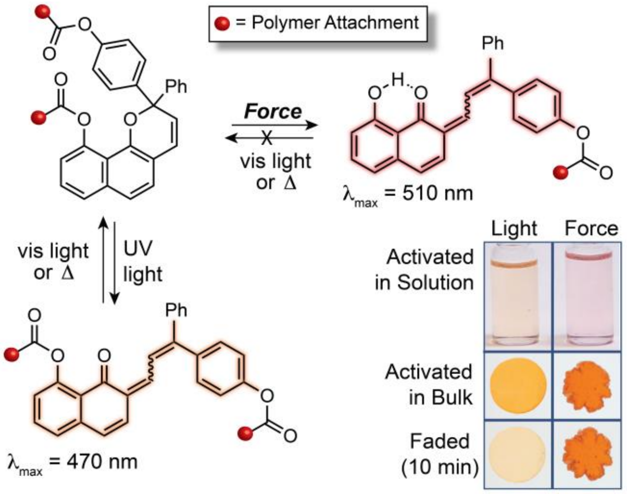

Figure 1.10. In solution and in bulk materials, mechanochemical activation of a 2H-naphthopyran mechanophore generates a merocyanine locked in the ring-opened state through an intramolecular hydrogen bond that is not accessed photochemically. This is made possible by a β-hydroxy ketone moiety revealed by an unexpected mechanochemical ester C(O)-O bond scission.

The vast majority of mechanochromic mechanophores, including most naphthopyrans, produce transient colored species (see Section 1I). While this is advantageous for real-time assessment of stress, thermal reversion is undesirable when the permanent recording of a material's force history or accurate kinetic analysis of mechanochemical reactions is needed. To this end, we constructed a 2*H*-naphthopyran mechanophore with a polymer attachment point at the 10-position of the naphthalene core instead of the 9-position (see Figure 1.8).[209] Photochemical activation of this species with UV light produces a vibrant orange merocyanine (λ_{max} = 470 nm) that typically reverts to a colorless state at room temperature (Figure 1.10). However, we discovered that this functionalization pattern facilitates an unusual mechanochemical transformation that yields an elusive thermally stable merocyanine, resistant to both thermal and photochemical recyclization. Ultrasound-mediated mechanochemical activation generates an intense red merocyanine (λ_{max} = 510 nm) that persists indefinitely at room temperature. We hypothesized that mechanochemical scission of the ester C–O bond could reveal a β-hydroxy ketone moiety that would stabilize the merocyanine via an intramolecular H-bond, preventing its recyclization. Bolstered by computational support of this theory, we synthesized a small-molecule model merocyanine bearing this functionality and indeed found it to be locked in the ring-opened state. The model compound exhibited the same λ_{max} (510 nm) as the mechanochemical product and, critically, ^{1}H NMR spectral features diagnostic of the H-bonded β-hydroxy ketone were observed in both products, thereby confirming the identity of the stable merocyanine. Ester scission was found to occur immediately after the ring-opening reaction even at low forces, resulting in little to no accumulation of the reversible merocyanine that has not undergone ester scission. The locked merocyanine was also successfully generated in bulk polymeric materials. The permanent coloration achieved by this unique naphthopyran mechanophore enables opportunities for stress sensing and force-recording applications, as well as fundamental studies of naphthopyran mechanochemistry and its kinetics that are typically complicated by merocyanine reversion.

Force-Dependent Color from a Bis-Naphthopyran Mechanophore

Bis-naphthopyrans (BNPs), wherein two naphthopyran units are joined by a conjugated linker, are among the few multiphotochromic systems known to access distinctly colored states based on the duration of exposure to light.[95,98,99,197–199,210,210,211] Pioneering work primarily led by Zhao and Carreira found that short periods of photoirradiation induce a single ring-opening reaction to form a mono-merocyanine with short-wavelength absorption features, while extended photoirradiation induces a second, sequential ring-opening reaction that produces a distinctly-colored bis-merocyanine displaying longer-wavelength absorption. Most mechanochromic mechanophores can only access one colored state in response to stress, and thus can only binarily indicate whether or not they have sustained a certain critical force; developing multimodal stress sensors that can produce distinct visual outputs in response to different magnitudes of applied force is therefore a grand challenge in the field of polymer mechanochemistry. Based on their established photochemical behavior, we hypothesized that BNPs could enable multicolor, force-dependent mechanochromism. In 2019, our group demonstrated mechanochemical activation of a thiophene-linked BNP that achieved this goal and

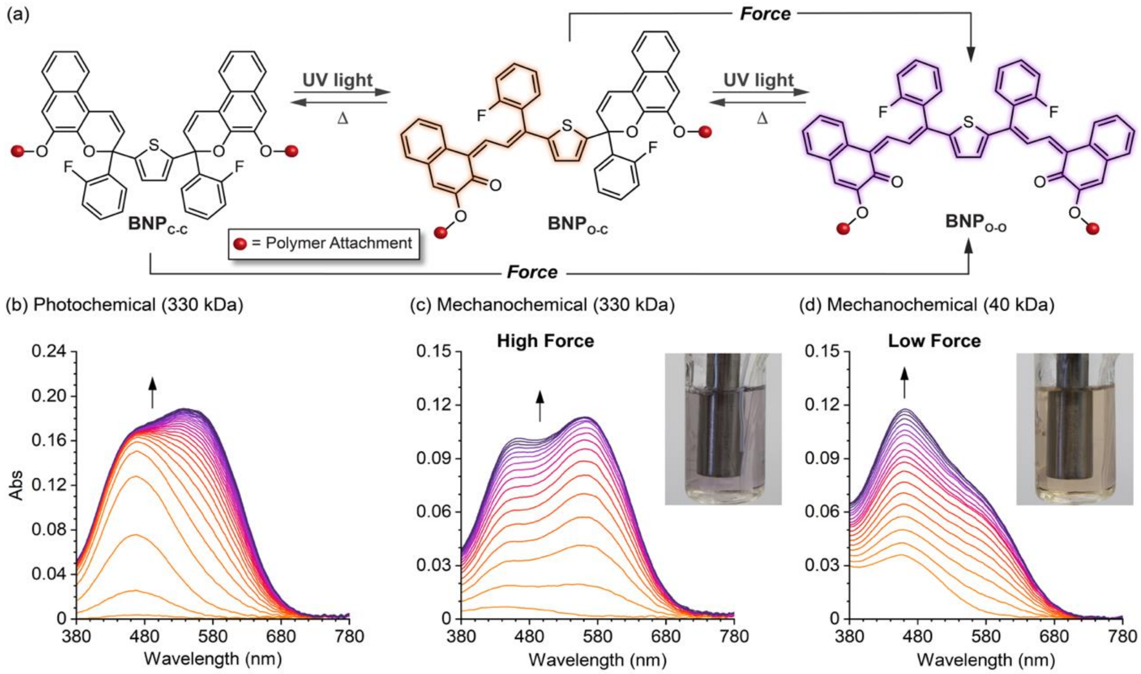

Figure 1.11. Force-dependent gradient multicolor mechanochromism from a bis-naphthopyran mechanophore. (a) While photoirradiation with UV light triggers sequential ring-opening reactions, mechanical force directly generates **BNP$_{O\text{-}O}$**, while **BNP$_{O\text{-}C}$** is formed subsequently from thermal fading. (b) Photochemical activation of a 330 kDa PMA chain-centered BNP demonstrates sequential-ring opening behavior observed using UV-vis spectroscopy. Mechanochemical activation of the same polymer (c) and a 40 kDa polymer (d) that transduces weaker force demonstrate non-sequential ring opening. The kinetic equilibrium is biased towards **BNP$_{O\text{-}O}$** with increasing force, as demonstrated by spectral features and visible color (see insets).

found that the mechanochemical reaction pathway is unexpectedly distinct from that observed under photochemical activation (Figure 1.11a).[212]

Consistent with prior reports, a BNP incorporated at the center of a linear PMA chain undergoes sequential ring-opening reactions when irradiated with UV light (Figure 1.11b). Initially, a single visible absorption peak corresponding to the orange open-closed species (**BNP$_{O\text{-}C}$**) appears at 460 nm. A longer-wavelength peak characteristic of the purple open-open species (**BNP$_{O\text{-}O}$**) emerges at 580 nm after extended irradiation. While mechanical activation of the same polymer produces these same absorption features, their order of appearance is surprisingly different (Figure 1.11c). In response to force, the spectral features of **BNP$_{O\text{-}O}$** appear immediately. Kinetic analysis and modeling experiments indicate that force directly converts $\mathbf{BNP_{C\text{-}C}}$ to $\mathbf{BNP_{O\text{-}O}}$, and $\mathbf{BNP_{O\text{-}C}}$ is generated by thermal electrocyclization of $\mathbf{BNP_{O\text{-}O}}$. This drastic deviation from the sequential photochemical mechanism is consistent with recent findings that extrinsic force can cause some reactions to completely bypass reactive intermediates – in this case, $\mathbf{BNP_{O\text{-}C}}$.[20]

We next investigated how the multicolor mechanochromism of BNP varied with force magnitude. In solution-phase ultrasonication experiments, the force transduced to the chain-centered mechanophore increases with polymer backbone length.[213,214] To systematically investigate the effects of a broad range of forces on product distribution, we synthesized and ultrasonicated a series of BNP-functionalized PMAs that spanned an order of magnitude in size (22–330 kDa). The longest polymers, which delivered the largest forces, produced spectra that strongly displayed the absorbance features of the purple $\mathbf{BNP_{O\text{-}O}}$ (Figure 1.11c), while shorter polymers that transduced lower forces produced spectra dominated by those of the orange $\mathbf{BNP_{O\text{-}C}}$ (Figure 1.11d). The kinetic equilibrium of the three BNP species, which involves thermal fading of $\mathbf{BNP_{O\text{-}C}}$ and $\mathbf{BNP_{O\text{-}O}}$ and force-induced ring-opening of $\mathbf{BNP_{C\text{-}C}}$ and $\mathbf{BNP_{O\text{-}C}}$, was biased towards higher amounts $\mathbf{BNP_{O\text{-}O}}$ under larger stress loads. Overall, different forces were found to predictably alter the color of the solution along a gradient resulting from different kinetic equilibria that were described by a simple kinetic model. This work represented the first report of force-dependent, multicolor mechanochromism from a single mechanophore.

Mechanical Force Enables an Anomalous Dual Ring-Opening Reaction of Naphthodipyran

Given the exceptional behavior exhibited by BNP, we sought to investigate other potentially multichromic species that could elicit complex mechanochromic outputs. While BNPs are comprised of two complete naphthopyran units joined by a conjugated thiophene linker, naphthodipyrans (NDPs) are comprised of two separate pyran rings fused to a shared naphthalene core (Figure 1.12a). In contrast to BNPs, concurrent opening of both pyran rings is photochemically inaccessible.[52,104,215]

As mechanical force is often able to facilitate otherwise inaccessible reactivity, we hypothesized that mechanochemical activation could enable the opening of rings, generating naphthodipyran's elusive dimerocyanine and unlocking its multichromic potential. Anticipating that the dimerocyanine would be thermally unstable, we designed a naphthodipyran bearing electron-rich pyrrolidine groups that enable trapping of the merocyanine with BF$_3$.[89] Promisingly, DFT calculations on this structure predicted dual ring-opening reactions following mechanochemical elongation.

Even in the presence of BF$_3$, UV irradiation of NDP incorporated at the center of a linear PMA chain produced only the BF$_3$-coordinated mono-merocyanine, **NDP$_{O–C}$·*n*BF$_3$** (Figure 1.12b),

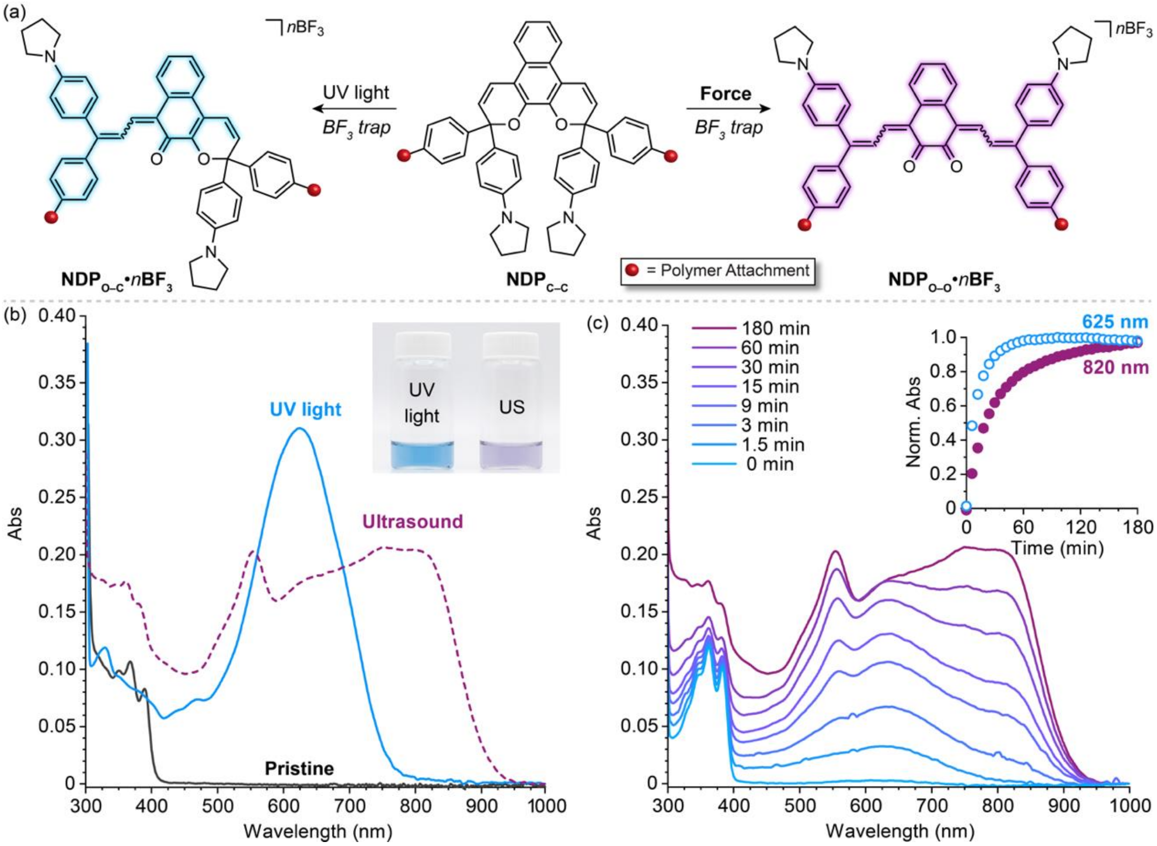

Figure 1.12. (a) Divergent photochemical and mechanochemical reactivity of a 3H-naphthodipyran moiety incorporated near the center of a polymer chain. (b) UV−vis−near-infrared absorption spectra of a PMA polymer incorporating a NDP molecular switch before and after photoirradiation with 365 nm UV light or ultrasonication. The photograph shows the two solutions after activation with UV light or ultrasound. (c) Spectral evolution during sonication of the same polymer and time-dependent absorption profiles at 625 and 820 nm characteristic of monomerocyanine **NDP$_{O–C}$·nBF$_3$** and dimerocyanine **NDP$_{O–O}$·nBF$_3$**, respectively.

consistent with prior literature. However, mechanochemical activation generated new near-IR absorption features indicative of the BF_3-trapped dimerocyanine, **$NDP_{O\text{–}O}\cdot n BF_3$**. This structural assignment was confirmed by ^{1}H NMR and high-resolution mass spectrometry of a small-molecule model compound, which notably determined that the dimerocyanine was trapped through formation of a stable 5-membered borocycle involving bonding of BF_2 to both oxygens of the 1,2-dicarbonyl.

In a surprising deviation from the kinetic behavior of other multimodal mechanophores like the scissile 2*H*-naphthopyran and BNP, the absorption profile of **NDP** evolves over the course of ultrasonication (Figure 1.12c). At early reaction times, only the short-wavelength absorption features of **$NDP_{O\text{–}C}\cdot n BF_3$** are observed. The longer-wavelength absorption features of **$NDP_{O\text{–}O}\cdot n BF_3$** emerge later in the reaction and increase with extended ultrasonication time. NDP hereby reports colorimetrically on its duration of exposure to ultrasound-induced mechanical force. However, we hypothesize that this behavior derives from diffusion limitations in trapping the especially thermally transient dimerocyanine, rather than truly sequential ring-opening reactions.

The mechanochemically mediated ring-opening reactions of NDP demonstrate that mechanical force can promote transformations inaccessible by light or heat alone, complementing previously discussed findings that force can override orbital symmetry rules governing conventional electrocyclic ring-opening reactions. We have demonstrated that mechanical force causes **NDP** to exhibit unprecedented ring-opening kinetics, culminating in force-specific and time-dependent coloration behavior. Future work will investigate other naphthopyran-based multichromic species in the hope of discovering new forms of mechanochemical activity with unique kinetic profiles.

IV. Complex Stimuli-Responsive Materials

Naphthopyran force probes have been incorporated into bulk polymeric materials alongside other mechanophores to construct complex stimuli-responsive plastics. Blending mechanophores with complementary reactivities enables a single material to differentiate multiple stimuli without the need to design an entirely new molecular switch. The Otsuka and Moore groups developed a polymer/silica blend capable of displaying variable force-dependent color outputs, as well as orthogonal responses to light and solvent swelling (Figure 1.13a).[216] A naphthopyran mechanophore was incorporated in the "soft" polymer domain while the interface between the "hard" silica and "soft" polymer domains was functionalized with a diarylbibenzofuranone (**DABBF**) mechanophore, which undergoes force-induced homolytic cleavage to form a colored radical species. Weak forces cause only the **DABBF** mechanophores to activate, coloring the material blue. Higher forces activate both mechanophores and a green color, resulting from the combination of blue and orange dyes, is observed. Treating the dually activated material with specific stimuli can selectively reverse each mechanophore, bleaching their associated color: irradiation with visible light reverts the merocyanine species back to the colorless naphthopyran, leaving only the blue **DABBF** fragments that recombine thermally. The opposite effect was achieved by swelling the material with solvent, providing the cleaved **DABBF** radical fragments with enough mobility to recombine while preserving the orange merocyanine dye. Effectively, this polymer/silica composite records not only the material's force history but also the peak load experienced by the material. The simple combination of two existing mechanophores substantially increased in the amount of information encoded in a material following mechanical deformation.

While composite materials create distinctly reactive domains, different strategies can be employed to achieve multi-stimuli responsiveness in homogeneous polymeric materials. Our group constructed a PDMS film with orthogonal visual responses to light and force by blending photochemically active naphthopyran and non-photochromic spiropyran mechanophores.[205] Mechanical stress activates both mechanophores and generates a blue-purple color arising from the dominant spiropyran coloration, whereas UV irradiation selectively produces the orange naphthopyran-derived merocyanine. In a second film, two differently substituted naphthopyran

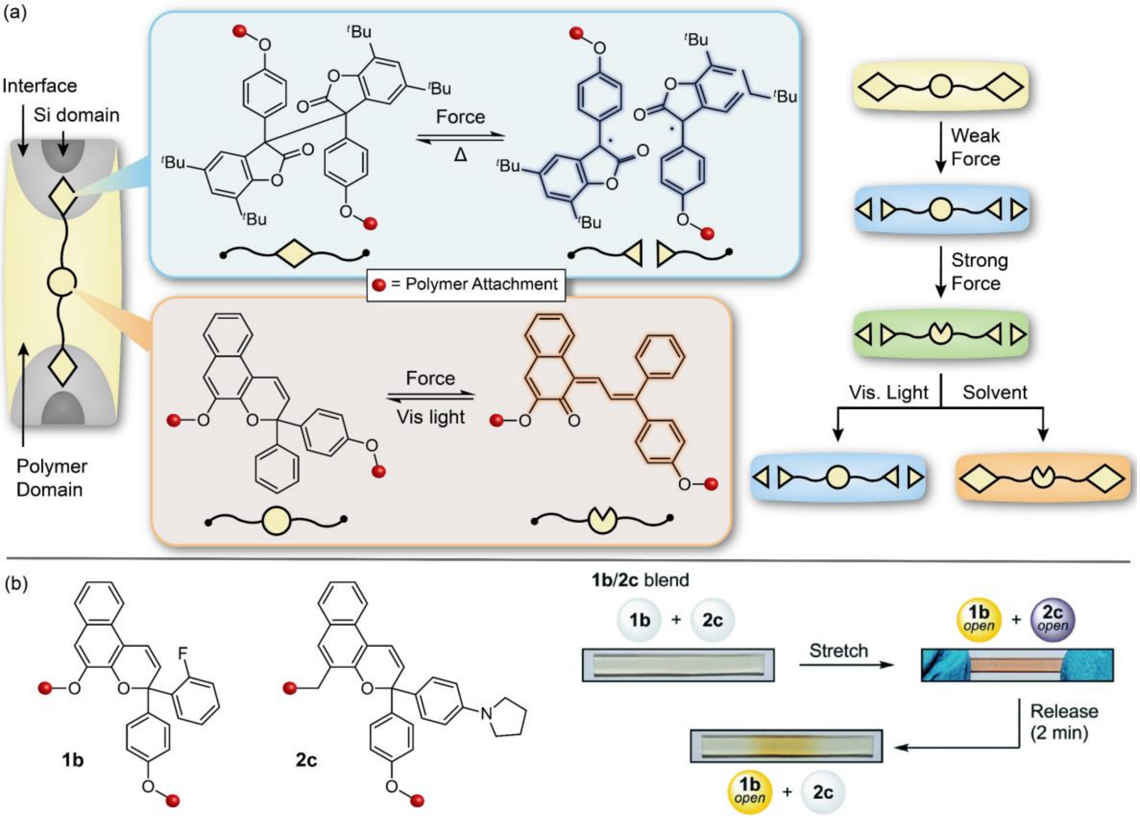

Figure 1.13. Complex stimuli-responsive materials incorporating a naphthopyran mechanophore. (a) Blending of diarylbibenzofuranone and naphthopyran mechanophores into a polymer/silica composite allows for force-dependent mechanochromism, as well as orthogonal responses to visible light and swelling of the material by solvent. (b) Multicolor mechanochromism is achieved in a PDMS film by blending two naphthopyran mechanophores with different color and fading kinetics.

mechanophores were blended to exploit established structure–property relationships (*vide supra*) (Figure 1.13b). Extended durations of stretching produce a red color arising from generation of both an orange and a purple merocyanine. Upon release of force, the fast-fading purple merocyanine quickly reverts, resulting in transient orange color indicative of the thermally persistent, slow-fading merocyanine. Incorporating multiple mechanophores with different fade rates expanded the material's recorded force history by providing visual indication of the time elapsed since mechanical stress was sustained. These early examples demonstrate that blending distinct mechanophores like naphthopyrans is a powerful method for achieving materials that can differentiate complex stimuli.

Outlook

The modularity, synthetic accessibility, and rich literature precedent associated with naphthopyran molecular switches afford this platform an unusually high degree of functional control. Their versatility and photoswitching behavior led to widespread use in photochromic polymeric materials beginning in the late 20th century, and this intense commercial demand precipitated the development of expansive literature on merocyanine structure–property relationships. More recently, the use of naphthopyrans in the emerging field of polymer mechanochemistry has garnered widespread attention for both fundamental discoveries in chemical reactivity and groundbreaking advances in stimuli-responsive materials applications. Mechanochromism is versatile strategy for remote visual stress sensing, and the clean translation of naphthopyran's photochemical structure–property relationships has enabled design of naphthopyran stress sensors with predictable and precisely tunable properties. These compounds have demonstrated robust and versatile molecular force sensing behavior harnessed for the fabrication of complex stimuli-responsive materials. In addition to their applications in damage reporting, naphthopyrans have been instrumental in studying and discovering fundamental concepts in mechanochemical reactivity. The precision with which the properties of naphthopyran can be modulated allows the subtleties of mechanochemistry to be probed through elegant physical organic chemistry studies. We believe the vast precedent of knowledge and ease of diversification of the naphthopyran molecular switch render it a promising candidate for the continued study of fundamental mechanochemistry as well as for the development of highly tailored molecular force probes.

Acknowledgements

Financial support from Caltech and an NSF CAREER award (CHE-2145791) is gratefully acknowledged. M.E.M. and A.C.O. were supported by NSF Graduate Research Fellowships (DGE-1745301). Support from a Barbara J. Burger Graduate Fellowship (M.E.M. and A.C.O.) and Institute Fellowships (A.C.O.) at Caltech is also gratefully acknowledged. M.J.R. is an Alfred P. Sloan Research Fellow and a Camille Dreyfus Teacher-Scholar.

References

(1) Li, J.; Nagamani, C.; Moore, J. S. Polymer Mechanochemistry: From Destructive to Productive. *Acc. Chem. Res.* **2015**, *48*, 2181–2190.

(2) Berkowski, K. L.; Potisek, S. L.; Hickenboth, C. R.; Moore, J. S. Ultrasound-Induced Site-Specific Cleavage of Azo-Functionalized Poly(Ethylene Glycol). *Macromolecules* **2005**, *38*, 8975–8978.

(3) Piermattei, A.; Karthikeyan, S.; Sijbesma, R. P. Activating Catalysts with Mechanical Force. *Nat. Chem.* **2009**, *1*, 133–137.

(4) Chen, Z.; Mercer, J. A. M.; Zhu, X.; Romaniuk, J. A. H.; Pfattner, R.; Cegelski, L.; Martinez, T. J.; Burns, N. Z.; Xia, Y. Mechanochemical Unzipping of Insulating Polyladderene to Semiconducting Polyacetylene. *Science* **2017**, *357*, 475–479.

(5) Chen, Y.; Spiering, A. J. H.; Karthikeyan, S.; Peters, G. W. M.; Meijer, E. W.; Sijbesma, R. P. Mechanically Induced Chemiluminescence from Polymers Incorporating a 1,2-Dioxetane Unit in the Main Chain. *Nature Chemistry* **2012**, *4*, 559–562.

(6) Hu, X.; Zeng, T.; Husic, C. C.; Robb, M. J. Mechanically Triggered Small Molecule Release from a Masked Furfuryl Carbonate. *J. Am. Chem. Soc.* **2019**, *141*, 15018–15023.

(7) Traeger, H.; Kiebala, D. J.; Weder, C.; Schrettl, S. From Molecules to Polymers—Harnessing Inter- and Intramolecular Interactions to Create Mechanochromic Materials. *Macromol. Rapid Commun.* **2021**, *42*, 2000573.

(8) Calvino, C.; Neumann, L.; Weder, C.; Schrettl, S. Approaches to Polymeric Mechanochromic Materials. *J. Pol. Sci. Part A: Polym. Chem.* **2017**, *55*, 640–652.

(9) Stratigaki, M.; Göstl, R. Methods for Exerting and Sensing Force in Polymer Materials Using Mechanophores. *ChemPlusChem* **2020**, *85*, 1095–1103.

(10) Jiang, Y. An Outlook Review: Mechanochromic Materials and Their Potential for Biological and Healthcare Applications. *Materials Science and Engineering: C* **2014**, *45*, 682–689.

(11) Guo, Q.; Zhang, X. A Review of Mechanochromic Polymers and Composites: From Material Design Strategy to Advanced Electronics Application. *Composites Part B: Engineering* **2021**, *227*, 109434.

(12) Barber, R. W.; McFadden, M. E.; Hu, X.; Robb, M. J. Mechanochemically Gated Photoswitching: Expanding the Scope of Polymer Mechanochromism. *Synlett* **2019**, *30*, 1725–1732.

(13) Staudinger, H.; Bondy, H. F. Über Isopren Und Kautschuk, 19. Mitteil.: Über Die Molekülgröße Des Kautschuks Und Der Balata. *Berichte der deutschen chemischen Gesellschaft (A and B Series)* **1930**, *63*, 734–736.

(14) Staudinger, H.; Bondy, H. F. Über Isopren Und Kautschuk, 17. Mitteil.: Über Die Fraktionierung Der Balata. *Berichte der deutschen chemischen Gesellschaft (A and B Series)* **1930**, *63*, 724–730.

(15) Staudinger, H.; Heuer, W. Über Hochpolymere Verbindungen, 93. Mitteil.: Über Das Zerreißen Der Faden-Moleküle Des Poly-Styrols. *Berichte der deutschen chemischen Gesellschaft (A and B Series)* **1934**, *67*, 1159–1164.

(16) Sohma, J. Mechanochemistry of Polymers. *Progress in Polymer Science* **1989**, *14*, 451–596.

(17) Robb, M. J.; Kim, T. A.; Halmes, A. J.; White, S. R.; Sottos, N. R.; Moore, J. S. Regioisomer-Specific Mechanochromism of Naphthopyran in Polymeric Materials. *J. Am. Chem. Soc.* **2016**, *138*, 12328–12331.

(18) Hickenboth, C. R.; Moore, J. S.; White, S. R.; Sottos, N. R.; Baudry, J.; Wilson, S. R. Biasing Reaction Pathways with Mechanical Force. *Nature* **2007**, *446*, 423–427.

(19) Lenhardt, J. M.; Ong, M. T.; Choe, R.; Evenhuis, C. R.; Martinez, T. J.; Craig, S. L. Trapping a Diradical Transition State by Mechanochemical Polymer Extension. *Science* **2010**, *329*, 1057–1060.

(20) Liu, Y.; Holm, S.; Meisner, J.; Jia, Y.; Wu, Q.; Woods, T. J.; Martinez, T. J.; Moore, J. S. Flyby Reaction Trajectories: Chemical Dynamics under Extrinsic Force. *Science* **2021**, *373*, 208–212.

(21) Becker, R. S.; Michl, J. Photochromism of Synthetic and Naturally Occurring 2H-Chromenes and 2H-Pyrans. *J. Am. Chem. Soc.* **1966**, *88*, 5931–5933.

(22) Corns, S. N.; Partington, S. M.; Towns, A. D. Industrial Organic Photochromic Dyes. *Color. Technol.* **2009**, *125*, 249–261.

(23) Towns, A. Naphthopyran Dyes. *Physical Sciences Reviews* **2020**, *5*, 20190085.

(24) Towns, A. Photochromic Dyes. *Physical Sciences Reviews* **2021**, *6*, 477–511.

(25) Imato, K.; Irie, A.; Kosuge, T.; Ohishi, T.; Nishihara, M.; Takahara, A.; Otsuka, H. Mechanophores with a Reversible Radical System and Freezing-Induced Mechanochemistry in Polymer Solutions and Gels. *Angewandte Chemie International Edition* **2015**, *54*, 6168–6172.

(26) Verstraeten, F.; Göstl, R.; Sijbesma, R. P. Stress-Induced Colouration and Crosslinking of Polymeric Materials by Mechanochemical Formation of Triphenylimidazolyl Radicals. *Chemical Communications* **2016**, *52*, 8608–8611.

(27) Ishizuki, K.; Aoki, D.; Goseki, R.; Otsuka, H. Multicolor Mechanochromic Polymer Blends That Can Discriminate between Stretching and Grinding. *ACS Macro Letters* **2018**, *7*, 556–560.

(28) Ishizuki, K.; Oka, H.; Aoki, D.; Goseki, R.; Otsuka, H. Mechanochromic Polymers That Turn Green Upon the Dissociation of Diarylbibenzothiophenonyl: The Missing Piece toward Rainbow Mechanochromism. *Chemistry - A European Journal* **2018**, *24*, 3170–3173.

(29) Kato, S.; Ishizuki, K.; Aoki, D.; Goseki, R.; Otsuka, H. Freezing-Induced Mechanoluminescence of Polymer Gels. **2018**, *12*, 28.

(30) Sakai, H.; Sumi, T.; Aoki, D.; Goseki, R.; Otsuka, H. Thermally Stable Radical-Type Mechanochromic Polymers Based on Difluorenylsuccinonitrile. *ACS Macro Letters* **2018**, *7*, 1359–1363.

(31) Kato, S.; Furukawa, S.; Aoki, D.; Goseki, R.; Oikawa, K.; Tsuchiya, K.; Shimada, N.; Maruyama, A.; Numata, K.; Otsuka, H. Crystallization-Induced Mechanofluorescence for Visualization of Polymer Crystallization. *Nat Commun* **2021**, *12*, 126.

(32) Watabe, T.; Aoki, D.; Otsuka, H. Polymer-Network Toughening and Highly Sensitive Mechanochromism via a Dynamic Covalent Mechanophore and a Multinetwork Strategy. *Macromolecules* **2022**, *55*, 5795–5802.

(33) Göstl, R.; Sijbesma, R. P. π-Extended Anthracenes as Sensitive Probes for Mechanical Stress. *Chem. Sci.* **2016**, *7*, 370–375.

(34) Baumann, C.; Göstl, R. Triazole-Extended Anthracenes as Optical Force Probes. *Synlett* **2021**, *32*, DOI: 10.1055/s-0040-1720924.

(35) Baumann, C.; Stratigaki, M.; Centeno, S. P.; Göstl, R. Multicolor Mechanofluorophores for the Quantitative Detection of Covalent Bond Scission in Polymers. *Angew. Chem., Int. Ed.* **2021**, *60*, 13287–13293.

(36) Yang, J.; Horst, M.; Werby, S. H.; Cegelski, L.; Burns, N. Z.; Xia, Y. Bicyclohexene- *Peri* -Naphthalenes: Scalable Synthesis, Diverse Functionalization, Efficient Polymerization, and Facile Mechanoactivation of Their Polymers. *J. Am. Chem. Soc.* **2020**, *142*, 14619–14626.

(37) Boswell, B. R.; Mansson, C. M. F.; Cox, J. M.; Jin, Z.; Romaniuk, J. A. H.; Lindquist, K. P.; Cegelski, L.; Xia, Y.; Lopez, S. A.; Burns, N. Z. Mechanochemical Synthesis of an Elusive Fluorinated Polyacetylene. *Nature Chemistry* **2021**, *13*, 41–46.

(38) Chen, Z.; Mercer, J. A. M.; Zhu, X.; Romaniuk, J. A. H.; Pfattner, R.; Cegelski, L.; Martinez, T. J.; Burns, N. Z.; Xia, Y. Mechanochemical Unzipping of Insulating Polyladderene to Semiconducting Polyacetylene. *Science* **2017**, *357*, 475–479.

(39) Boswell, B. R.; Mansson, C. M. F.; Cox, J. M.; Jin, Z.; Romaniuk, J. A. H.; Lindquist, K. P.; Cegelski, L.; Xia, Y.; Lopez, S. A.; Burns, N. Z. Mechanochemical Synthesis of an Elusive Fluorinated Polyacetylene. *Nat. Chem.* **2021**, *13*, 41–46.

(40) Potisek, S. L.; Davis, D. A.; Sottos, N. R.; White, S. R.; Moore, J. S. Mechanophore-Linked Addition Polymers. *Journal of the American Chemical Society* **2007**, *129*, 13808–13809.

(41) Davis, D. A.; Hamilton, A.; Yang, J.; Cremar, L. D.; Van Gough, D.; Potisek, S. L.; Ong, M. T.; Braun, P. V.; Martínez, T. J.; White, S. R.; Moore, J. S.; Sottos, N. R. Force-Induced Activation of Covalent Bonds in Mechanoresponsive Polymeric Materials. *Nature* **2009**, *459*, 68–72.

(42) Barbee, M. H.; Kouznetsova, T.; Barrett, S. L.; Gossweiler, G. R.; Lin, Y.; Rastogi, S. K.; Brittain, W. J.; Craig, S. L. Substituent Effects and Mechanism in a Mechanochemical Reaction. *J. Am. Chem. Soc.* **2018**, *140*, 12746–12750.

(43) Yao, R.; Li, X.; Xiao, N.; Weng, W.; Zhang, W. Single-Molecule Observation of Mechanical Isomerization of Spirothiopyran and Subsequent Click Addition. *Nano Res.* **2021**, *14*, 2654–2658.

(44) Zhang, H.; Gao, F.; Cao, X.; Li, Y.; Xu, Y.; Weng, W.; Boulatov, R. Mechanochromism and Mechanical-Force-Triggered Cross-Linking from a Single Reactive Moiety Incorporated into Polymer Chains. *Angew. Chem., Int. Ed.* **2016**, *55*, 3040–3044.

(45) Wang, Z.; Ma, Z.; Wang, Y.; Xu, Z.; Luo, Y.; Wei, Y.; Jia, X. A Novel Mechanochromic and Photochromic Polymer Film: When Rhodamine Joins Polyurethane. *Advanced Materials* **2015**, *27*, 6469–6474.

(46) Qian, H.; Purwanto, N. S.; Ivanoff, D. G.; Halmes, A. J.; Sottos, N. R.; Moore, J. S. Fast, Reversible Mechanochromism of Regioisomeric Oxazine Mechanophores: Developing in Situ Responsive Force Probes for Polymeric Materials. *Chem* **2021**.

(47) Minkin, V. I. Photo-, Thermo-, Solvato-, and Electrochromic Spiroheterocyclic Compounds. *Chem. Rev.* **2004**, *104*, 2751–2776.

(48) Paramonov, S. V.; Lokshin, V.; Fedorova, O. A. Spiropyran, Chromene or Spirooxazine Ligands: Insights into Mutual Relations between Complexing and Photochromic Properties. *J. Photochem. Photobiol. C: Photochem. Rev.* **2011**, *12*, 209–236.

(49) Kim, H. N.; Lee, M. H.; Kim, H. J.; Kim, J. S.; Yoon, J. A New Trend in Rhodamine-Based Chemosensors: Application of Spirolactam Ring-Opening to Sensing Ions. *Chem. Soc. Rev.* **2008**, *37*, 1465–1472.

(50) Peterson, G. I.; Larsen, M. B.; Ganter, M. A.; Storti, D. W.; Boydston, A. J. 3D-Printed Mechanochromic Materials. *ACS Appl. Mater. Interfaces* **2015**, *7*, 577–583.

(51) Swansburg, S.; Buncel, E.; Lemieux, R. P. Thermal Racemization of Substituted Indolinobenzospiropyrans: Evidence of Competing Polar and Nonpolar Mechanisms. *J. Am. Chem. Soc.* **2000**, *122*, 6594–6600.

(52) Hepworth, J. D.; Heron, B. M. Photochromic Naphthopyrans. Photochromic Naphthopyrans. In *Functional Dyes*; Elsevier Science, 2006; pp 85–135.

(53) Hobley, J.; Lear, M. J.; Fukumura, H. Photo-Switching Spiropyrans and Related Compounds. Photo-Switching Spiropyrans and Related Compounds. In *Photochemistry of Organic Molecules in Isotropic and Anisotropic Media*; CRC Press, 2003.

(54) Van Gemert, B. Benzo and Naphthopyrans (Chromenes). Benzo and Naphthopyrans (Chromenes). In *Organic Photochromic and Thermochromic Compounds*; Springer: Boston, MA, 2002; pp 111–140.

(55) Van Gemert, B.; Kumar, A.; Knowles, D. B. Naphthopyrans. Structural Features and Photochromic Properties. *Mol. Cryst. and Liq. Cryst.* **1997**, *297–298*, 131–138.

(56) Jin, K.; Ji, X.; Yang, T.; Zhang, J.; Tian, W.; Yu, J.; Zhang, X.; Chen, Z.; Zhang, J. Facile Access to Photo-Switchable, Dynamic-Optical, Multi-Colored and Solid-State Materials from Carbon Dots and Cellulose for Photo-Rewritable Paper and Advanced Anti-Counterfeiting. *Chemical Engineering Journal* **2021**, *406*, 126794.

(57) Blin, X.; Simon, J. C. Cosmetic Composition Containing Oil Phase and Naphthopyran Photochromic Dye, Useful e.g. as Make up, Provides Rapid and Reversible Color Change on Exposure to Sunlight. Cosmetic Composition Containing Oil Phase and Naphthopyran Photochromic Dye, Useful e.g. as Make up, Provides Rapid and Reversible Color Change on Exposure to Sunlight. FR2845910A1, April 23, 2004.

(58) Moustrou, C.; Rebière, N.; Samat, A.; Guglielmetti, R.; Yassar, A. E.; Dubest, R.; Aubard, J. Synthesis of Thiophene-Substituted 3H-Naphtho[2,1-b]Pyrans, Precursors of Photomodulated Materials. *Helv. Chim. Acta* **1998**, *81*, 1293–1302.

(59) Yassar, A.; Rebière-Galy, N.; Frigoli, M.; Moustrou, C.; Samat, A.; Guglielmetti, R.; Jaafari, A. Molecular Switch Devices Realised by Photochromic Oligothiophenes. Molecular Switch Devices Realised by Photochromic Oligothiophenes. In *Synthetic Metals*; Elsevier, 2001; Vol. 124, pp 23–27.

(60) Yassar, A.; Garnier, F.; Jaafari, H.; Rebière-Galy, N.; Frigoli, M.; Moustrou, C.; Samat, A.; Guglielmetti, R. Light-Triggered Molecular Devices Based on Photochromic Oligothiophene Substituted Chromenes. *Applied Physics Letters* **2002**, *80*, 4297–4299.

(61) Yassar, A.; Jaafari, H.; Rebière-Galy, N.; Frigoli, M.; Moustrou, C.; Samat, A.; Guglielmetti, R. Photochromic Oligothiophene Substituted Chromenes a New Approach towards a Molecular Switch: Electrical Characterisation. *Eur. Phys. J. AP* **2002**, *18*, 3–8.

(62) Frigoli, M.; Pimienta, V.; Moustrou, C.; Samat, A.; Guglielmetti, R.; Aubard, J.; Maurel, F.; Micheau, J.-C. Continuous Irradiation and Flash-Photolysis Studies of New[3H]Naphtho[2,1-b]Pyrans Linked by Covalent Bonds to Oligothiophene Units. Effect of Thiophene Substituents on the Photochromism. *Photochem. Photobiol. Sci.* **2003**, *2*, 888–892.

(63) Ortica, F.; Smimmo, P.; Favaro, G.; Mazzucato, U.; Delbaere, S.; Venec, D.; Vermeersch, G.; Frigoli, M.; Moustrou, C.; Samat, A. Effect of Oligothiophene Substituents on the Photophysical and Photochromic Properties of a Naphthopyran. *Photochem. Photobiol. Sci.* **2004**, *3*, 878–885.

(64) Gentili, P. L.; Rightler, A. L.; Heron, B. M.; Gabbutt, C. D. Discriminating between the UV-A, UV-B and UV-C Regions by Novel Biologically Inspired Photochromic Fuzzy Logic (BIPFUL) Systems: A Detailed Comparative Study. *Dyes and Pigments* **2016**, *135*, 169–176.

(65) Gentili, P. L.; Rightler, A. L.; Heron, B. M.; Gabbutt, C. D. Extending Human Perception of Electromagnetic Radiation to the UV Region through Biologically Inspired Photochromic Fuzzy Logic (BIPFUL) Systems. *Chem. Commun.* **2016**, *52*, 1474–1477.

(66) Gentili, P. L.; Giubila, M. S.; Heron, B. M. Processing Binary and Fuzzy Logic by Chaotic Time Series Generated by a Hydrodynamic Photochemical Oscillator. *ChemPhysChem* **2017**, *18*, 1831–1841.

(67) Gentili, P. L.; Giubila, M. S.; Germani, R.; Heron, B. M. Photochromic and Luminescent Compounds as Artificial Neuron Models. *Dyes and Pigments* **2018**, *156*, 149–159.

(68) Dong, Z. M.; Ren, H.; Wang, J. N.; Wang, Y. A New Naphthopyran-Based Chemodosimeter with Aggregation-Induced Emission: Selective Dual-Channel Detection of Cyanide Ion in Aqueous Medium and Test Strips. *Microchemical Journal* **2020**, *155*, 104676.
(69) Iwai, I.; Ide, J. Studies on Acetylenic Compounds. XXIII. A New Ring Closure of 2-Propynyl Ethers. *Chem. Pharm. Bull.* **1962**, *10*, 926–933.
(70) Pozzo, J.-L.; Samat, A.; Guglielmetti, R.; Dubest, R.; Aubard, J. Synthesis and Photochromic Behaviour of Naphthopyrans, Pyranoquinolines, Pyranoquinazolines and Pyranoquinoxalines. *Helv. Chim. Acta* **1997**, *80*, 725–738.
(71) Inagaki, Y.; Kobayashi, Y.; Mutoh, K.; Abe, J. A Simple and Versatile Strategy for Rapid Color Fading and Intense Coloration of Photochromic Naphthopyran Families. *Journal of the American Chemical Society* **2017**, *139*, 13429–13441.
(72) Kuroiwa, H.; Inagaki, Y.; Mutoh, K.; Abe, J. On-Demand Control of the Photochromic Properties of Naphthopyrans. *Advanced Materials* **2019**, *31*.
(73) Ushakov, E. N.; Nazarov, V. B.; Fedorova, O. A.; Gromov, S. P.; Chebun'kova, A. V.; Alfimov, M. V.; Barigelletti, F. Photocontrol of Ca 2+ Complexation with an Azacrown-Containing Benzochromene. *J. Phys. Org. Chem.* **2003**, *16*, 306–309.
(74) Sallenave, X.; Delbaere, S.; Vermeersch, G.; Saleh, A.; Pozzo, J. L. Photoswitch Based on Remarkably Simple Naphthopyrans. *Tetrahedron Lett.* **2005**, *46*, 3257–3259.
(75) Gabbutt, C. D.; Gelbrich, T.; Hepworth, J. D.; Heron, B. M.; Hursthouse, M. B.; Partington, S. M. Synthesis and Photochromic Properties of Some Fluorine-Containing Naphthopyrans. *Dyes and Pigments* **2002**, *54*, 79–93.
(76) Harié, G.; Samat, A.; Guglielmetti, R.; van Parys, I.; Saeyens, W.; de Keukeleire, D.; Lorenz, K.; Mannschreck, A. Chiral 2-Aryl-2-Methyl-2 H -1-Benzopyrans: Synthesis, Characterization of Enantiomers, and Barriers to Thermal Racemization. *Helv. Chim. Acta* **1997**, *80*, 1122–1132.
(77) Aiken, S.; de Azevedo, O. D. C. C.; Chauhan, K.; Driscoll, T.; Elliott, P. I.; Gabbutt, C. D.; Heron, B. M. Base-Mediated Ring-Contraction of Pyran Systems Promoted by Palladium and Phase-Transfer Catalysis. *J. Org. Chem.* **2020**, *85*, 952–966.
(78) Gabbutt, C. D.; Heron, B. M.; Instone, A. C. Control of the Fading Properties of Photochromic 3,3-Diaryl-3H-Naphtho[2,1-b]Pyrans. *Heterocycles* **2003**, *60*, 843–855.
(79) Gabbutt, C. D.; Heron, B. M.; Instone, A. C.; Thomas, D. A.; Partington, S. M.; Hursthouse, M. B.; Gelbrich, T. Observations on the Synthesis of Photochromic Naphthopyrans. *Eur. J. Org. Chem.* **2003**, *2003*, 1220–1230.
(80) Gabbutt, C. D.; Heron, B. M.; Kolla, S. B.; Kilner, C.; Coles, S. J.; Horton, P. N.; Hursthouse, M. B. Ring Contraction during the 6π-Electrocyclisation of Naphthopyran Valence Tautomers. *Org. Biomol. Chem.* **2008**, *6*, 3096–3104.
(81) Gabbutt, C. D.; Heron, B. M.; Instone, A. C. The Synthesis and Electronic Absorption Spectra of 3-Phenyl-3(4- Pyrrolidino-2-Substituted Phenyl)-3H-Naphtho[2,1-b]Pyrans: Further Exploration of the Ortho Substituent Effect. *Tetrahedron* **2006**, *62*, 737–745.
(82) Harie, G.; Samat, A.; Guglielmetti, R. Comparative Study of Chromenes Containing Different Spiro-Carbocyclic Moieties. *Mol. Cryst. and Liq. Cryst.* **1997**, *297*, 263–268.
(83) Gemert, B. V.; Bergomi, M. P. Photochromic Naphthopyran Compounds. Photochromic Naphthopyran Compounds. US5066818A, November 19, 1991.
(84) Gabbutt, C. D.; Hepworth, J. D.; Mark Heron, B.; Partington, S. M.; Thomas, D. A. Synthesis and Spectroscopic Properties of Some Merocyanine Dyes. *Dyes and Pigments* **2001**, *49*, 65–74.
(85) Swaminathan, S.; Narayanan, K. V. Rupe and Meyer-Schuster Rearrangements. *Chem. Rev.* **1971**, *71*, 429–438.

(86) Carvalho, L. M.; Silva, A. M. S.; Martins, C. I.; Coelho, P. J.; Oliveira-Campos, A. M. F. Structural Elucidation of the Red Dye Obtained from Reaction of 1,8-Naphthalenediol with 1,1-Diphenylprop-2-Yn-1-Ol. A Correction. *Tetrahedron Lett.* **2003**, *44*, 1903–1905.

(87) Zhao, W.; Carreira, E. M. Facile One-Pot Synthesis of Photochromic Pyrans. *Org. Lett.* **2003**, *5*, 4153–4154.

(88) Tanaka, K.; Aoki, H.; Hosomi, H.; Ohba, S. One-Pot Synthesis of Photochromic Naphthopyrans in the Solid State. *Org. Lett.* **2000**, *2*, 2133–2134.

(89) Guo, K.; Chen, Y. ‘Locking and Unlocking Control’ of Photochromism of Naphthopyran Derivative. *J. Phys. Org. Chem.* **2010**, *23*, 207–210.

(90) Aiken, S.; Allsopp, B.; Booth, K.; Gabbutt, C. D.; Heron, B. M.; Rice, C. R. 5-Hydroxy Substituted Naphthofurans and Naphthothiazoles as Precursors of Photochromic Benzochromenes. *Tetrahedron* **2014**, *70*, 9352–9358.

(91) Guo, K.; Chen, Y. A Strategy for the Design of Photochromic Naphthopyrans with Large Optical Density at Photosteady State and Fast Fading Speed at Ambient Temperature in the Dark. *J. Mater. Chem.* **2010**, *20*, 4193–4197.

(92) Delbaere, S.; Vermeersch, G.; Frigoli, M.; Mehl, G. H. Bridging the Visible: The Modulation of the Absorption by More than 450 Nm. *Organic Letters* **2010**, *12*, 4090–4093.

(93) Han, S.; Chen, Y. Modification of a Photochromic 3-Aryl-3-(α-Naphthalene)-3H-Naphtho[2, 1-b]Pyran System with a Fast Fading Speed in Solution and in a Rigid Polymer Matrix. *J. Mater. Chem.* **2011**, *21*, 4961–4965.

(94) Delbaere, S.; Micheau, J.-C.; Teral, Y.; Bochu, C.; Campredon, M.; Vermeersch, G. NMR Structural and Kinetic Assignment of Fluoro-3H-Naphthopyran Photomerocyanines¶. *Photochem. Photobiol.* **2001**, *74*, 694.

(95) Zhao, W.; Carreira, E. M. Oligothiophene-Linked Bisnaphthopyrans: Sequential and Temperature- Dependent Photochromism. *Eur. J. Chem.* **2007**, *13*, 2671–2688.

(96) Frigoli, M.; Marrot, J.; Gentili, P. L.; Jacquemin, D.; Vagnini, M.; Pannacci, D.; Ortica, F. P-Type Photochromism of New Helical Naphthopyrans: Synthesis and Photochemical, Photophysical and Theoretical Study. *ChemPhysChem* **2015**, *16*, 2447–2458.

(97) Coelho, P. J.; Salvador, M. A.; Oliveira, M. M.; Carvalho, L. M. Photochemical and Thermal Behaviour of New Photochromic Indeno-Fused Naphthopyrans. *J. Photochem. Photobiol. A: Chem.* **2005**, *172*, 300–307.

(98) Zhao, W.; Carreira, E. M. Synthesis and Photochromism of Novel Phenylene-Linked Photochromic Bispyrans. *Organic Letters* **2006**, *8*, 99–102.

(99) Lu, X.; Dong, Q.; Dong, X.; Zhao, W. Synthesis and Sequential Photochromism of Thiophene-Linked Bis-Pyrans. *Tetrahedron* **2015**, *71*, 4061–4069.

(100) Aiken, S.; Booth, K.; Gabbutt, C. D.; Mark Heron, B.; Rice, C. R.; Charaf-Eddin, A.; Jacquemin, D. The First Structural and Spectroscopic Characterisation of a Ring-Opened Form of a 2H-Naphtho[1,2-b]Pyran: A Novel Photomerocyanine. *Chemical Communications* **2014**, *50*, 7900–7903.

(101) Cotterill, W. D.; Livingstone, R. 1,3-and 3,3-Bis(MethoxyphenyI)Naphtho[2,1,-b]Pyrans. *J. Chem. Soc.* **1758**, No. 13, 7.

(102) Livingstone, R.; Miller, D.; Morris, S. 2-Methoxy-2,4-Diphenylchroman and 5,6-Dihydro-6-Methoxy-4,6-Diphenyl-4H- and 6,6-Diphenyl-6H-Naphtho(2’,1’:2,3)Pyran. *J. Chem. Soc.* **1960**, No. 0, 5148–5152.

(103) Cottam, J.; Livingstone, R. 6,6-DiPhenylnaphtho(1’,2‘:2,3)Pyran and 1,3-Diphenyl-3-(1-Hydroxy-2-Naphthyl)Propan-1-One. *Journal of the Chemical Society (Resumed)* **1964**, No. 0, 5228–5231.

(104) Hepworth, J. D.; Heron, B. M. Synthesis and Photochromic Properties of Naphthopyrans. Synthesis and Photochromic Properties of Naphthopyrans. In *Progress in Heterocyclic Chemistry*; Elsevier Ltd, 2005; Vol. 17, pp 33–62.

(105) Kabbe, H. J. Eine einfache Synthese von 4-Chromanonen. *Synthesis* **1978**, *1978*, 886–887.

(106) Talley, J. J. Synthesis of 4- and 6-Substituted 2,2-Dimethyl-2H-Chromenes. *Synthesis* **1983**, *10*, 845–847.

(107) Heller, H. G.; Levell, J. R.; Hibbs, D. E.; Hughes, D. S.; Hursthouse, M. B. Novel Photochromic Naphthopyran Derivatives via New General Synthetic Methodology. *Mol. Cryst. and Liq. Cryst.* **1997**, *297*, 123–130.

(108) Sartori, G.; Casiraghi, G.; Bolzoni, L.; Casnati, G. General Synthesis of 2H-Benzo[b]Pyrans (Chrom-3-Enes) from Metal Phenoxides and .Alpha.,.Beta.-Unsaturated Carbonyl Compounds. *J. Org. Chem.* **1979**, *44*, 803–805.

(109) Pozzo, J.-L.; Lokshin, V. A.; Guglielmetti, R. A Convenient Synthesis of Azolo-Fused 2H-[1] Benzopyrans. *J. Chem. Soc., Perkin Trans. 1* **1994**, No. 18, 2591–2595.

(110) Ghatak, A.; Khan, S.; Bhar, S. Catalysis by β-Cyclodextrin Hydrate – Synthesis of 2,2-Disubstituted 2H-Chromenes in Aqueous Medium. *Advanced Synthesis & Catalysis* **2016**, *358*, 435–443.

(111) Dong, Y. W.; Wang, G. W.; Wang, L. Solvent-Free Synthesis of Naphthopyrans under Ball-Milling Conditions. *Tetrahedron* **2008**, *64*, 10148–10154.

(112) Arai, K.; Kobayashi, Y.; Abe, J. Rational Molecular Designs for Drastic Acceleration of the Color-Fading Speed of Photochromic Naphthopyrans. *Chem. Commun.* **2015**, *51*, 3057–3060.

(113) Frigoli, M.; Moustrou, C.; Samat, A.; Guglielmetti, R. Synthesis of New Thiophene-Substituted 3,3-Diphenyl-3H-Naphtho[2,1-b]Pyrans by Cross-Coupling Reactions, Precursors of Photomodulated Materials. *Eur. J. Org. Chem.* **2003**, *2003*, 2799–2812.

(114) Blackwell, C. J.; Gabbutt, C. D.; Guthrie, J. T.; Heron, B. M. The Synthesis and Properties of Vinyl Substituted Naphthopyrans and Their Styrene Copolymers. *Dyes and Pigments* **2012**, *95*, 408–420.

(115) Frigoli, M.; Moustrou, C.; Samat, A.; Guglielmetti, R. Photomodulable Materials. Synthesis and Properties of Photochromic 3H-Naphtho[2,1-b]Pyrans Linked to Thiophene Units via an Acetylenic Junction. *Helv. Chim. Acta* **2000**, *83*, 3043–3052.

(116) Demadrille, R.; Moustrou, C.; Samat, A.; Guglielmetti, R. Palladium-Catalyzed Amination of Photochromic Triflate-Substituted 3H-Naphtho[2, 1-b]Pyrans. *Heterocycl. Commun.* **1999**, *5*, 123–126.

(117) Naga Venkata Sastry, M.; Claessens, S.; Habonimana, P.; De Kimpe, N. Synthesis of the Natural Products 3-Hydroxymollugin and 3-Methoxymollugin. *J. Org. Chem.* **2010**, *75*, 2274–2280.

(118) Kosuge, T.; Zhu, X.; Lau, V. M.; Aoki, D.; Martinez, T. J.; Moore, J. S.; Otsuka, H. Multicolor Mechanochromism of a Polymer/Silica Composite with Dual Distinct Mechanophores. *J. Am. Chem. Soc.* **2019**, *141*, 1898–1902.

(119) Delbaere, S.; Micheau, J.-C.; Frigoli, M.; Vermeersch, G. Unexpected Halogen Substituent Effects on the Complex Thermal Relaxation of Naphthopyrans after UV Irradiation. *The Journal of Organic Chemistry* **2005**, *70*, 5302–5304.

(120) McFadden, M. E.; Robb, M. J. Force-Dependent Multicolor Mechanochromism from a Single Mechanophore. *J. Am. Chem. Soc.* **2019**, *141*, 11388–11392.

(121) Gabbutt, C. D.; Heron, B. M.; Thomas, D. A.; Light, M. E.; Hursthouse, M. B. Carbenoid Induced Irreversible Ring Opening of Naphthopyrans. *Tetrahedron Lett.* **2004**, *45*, 6151–6154.

(122) Sriprom, W.; Néel, M.; Gabbutt, C. D.; Heron, B. M.; Perrier, S. Tuning the Color Switching of Naphthopyrans via the Control of Polymeric Architectures. *J. Mater. Chem.* **2007**, *17*, 1885–1893.

(123) Versaw, B.; McFadden, M.; Husic, C.; Robb, M. Designing Naphthopyran Mechanophores with Tunable Mechanochromic Behavior. *Chem. Sci.* **2020**, *11*, 4525–4530.

(124) Kim, G.; Lau, V. M.; Halmes, A. J.; Oelze, M. L.; Moore, J. S.; Li, K. C. High-Intensity Focused Ultrasound-Induced Mechanochemical Transduction in Synthetic Elastomers. *Proc Natl Acad Sci USA* **2019**, *116*, 10214–10222.

(125) Becker, R. S. Photochemical Process. Photochemical Process. US3567605A, March 2, 1971.

(126) Harié, G.; Samat, A.; Guglielmetti, R.; van Parys, I.; Saeyens, W.; de Keukeleire, D.; Lorenz, K.; Mannschreck, A. Chiral 2-Aryl-2-Methyl-2 H -1-Benzopyrans: Synthesis, Characterization of Enantiomers, and Barriers to Thermal Racemization. *Helvetica Chimica Acta* **1997**, *80*, 1122–1132.

(127) Kortekaas, L.; Browne, W. R. The Evolution of Spiropyran: Fundamentals and Progress of an Extraordinarily Versatile Photochrome. *Chem. Soc. Rev.* **2019**, *48*, 3406–3424.

(128) Hepworth, J. D.; Heron, B. M. Photochromic Naphthopyrans. Photochromic Naphthopyrans. In *Functional Dyes*; Elsevier Science, 2006; pp 85–135.

(129) Helmy, S.; Read de Alaniz, J. Photochromic and Thermochromic Heterocycles. *Adv. Heterocycl. Chem.* **2015**, *117*, 131–177.

(130) Delbaere, S.; Luccioni-Houze, B.; Bochu, C.; Teral, Y.; Campredon, M.; Vermeersch, G. Kinetic and Structural Studies of the Photochromic Process of 3H-Naphthopyrans by UV and NMR Spectroscopy. *J. Chem. Soc., Perkin Trans. 2* **1998**, *2*.

(131) Ottavi, G.; Favaro, G.; Malatesta, V. Spectrokinetic Study of 2,2-Diphenyl-5,6-Benzo(2H)Chromene: A Thermoreversible and Photoreversible Photochromic System. *J. Photochem. Photobiol. A: Chem.* **1998**, *115*, 123–128.

(132) Görner, H.; Chibisov, A. K. Photoprocesses in 2,2-Diphenyl-5,6-Benzo(2H)Chromene. *J. Photochem. Photobiol. A: Chem.* **2002**, *149*, 83–89.

(133) Jockusch, S.; Turro, N. J.; Blackburn, F. R. Photochromism of 2H-Naphtho[1,2-b]Pyrans: A Spectroscopic Investigation. *J. Phys. Chem. A* **2002**, *106*, 9236–9241.

(134) Herzog, T. T.; Ryseck, G.; Ploetz, E.; Cordes, T. The Photochemical Ring Opening Reaction of Chromene as Seen by Transient Absorption and Fluorescence Spectroscopy. *Photochem. Photobiol. Sci.* **2013**, *12*, 1202–1209.

(135) Brown, R. G.; Maafi, M.; Foggi, P.; Bussotti, L. The Ultrafast Dynamics of Some Photochromic Naphthopyrans. The Ultrafast Dynamics of Some Photochromic Naphthopyrans. In *Femtochemistry and Femtobiology: Ultrafast Events in Molecular Science*; 2004; pp 283–286.

(136) Hobley, J.; Malatesta, V.; Hatanaka, K.; Kajimoto, S.; L. Williams, S.; Fukumura, H. Picosecond and Nanosecond Photo-Dynamics of a Naphthopyran Merocyanine. *Phys. Chem. Chem. Phys.* **2002**, *4*, 180–184.

(137) Maafi, M.; Brown, R. G. Photophysics and Kinetics of Naphthopyran Derivatives, Part 1 : General Analytical Solutions for the Kinetics of AB(k,φ) and ABC(k,φ) Systems. *Int. J. Chem. Kinet.* **2005**, *37*, 162–174.

(138) Delbaere, S.; Vermeersch, G.; Micheau, J. C. Quantitative Analysis of the Dynamic Behaviour of Photochromic Systems. *J. Photochem. Photobiol. C: Photochem. Rev.* **2011**, *12*, 74–105.

(139) Maafi, M.; Brown, R. G. Photophysics and Kinetics of Naphthopyran Derivatives, Part 4: Investigation of [3H]-Naphthopyran Kinetics Considered as an ABC(2k, 6φ) System Yielding a Monoexponential Trace. *Int. J. Chem. Kinet.* **2006**, *38*, 431–438.

(140) Berthet, J.; Delbaere, S.; Levi, D.; Brun, P.; Guglielmetti, R.; Vermeersch, G. Investigations by NMR Spectroscopy of a Polyphotochromic System Involving Two Entities, Spirooxazine and Naphthopyran, Linked by a Z-Ethenic Bridge. **2002**.

(141) Berthet, J.; Coelho, P. J.; Carvalho, L. M.; Vermeersch, G.; Delbaere, S. NMR Investigation of the Dyes Formed under UV Irradiation of Some Photochromic Indeno-Fused Naphthopyrans. *J. Photochem. Photobiol. A: Chem.* **2009**, *208*, 180–185.

(142) Delbaere, S.; Vermeersch, G. NMR Proofs of the Involvement of an Allenyl-Naphthol as a Key-Intermediate in the Photochromic Process of [3H]-Naphthopyrans. *Tetrahedron Lett.* **2003**, *44*, 259–262.

(143) Delbaere, S.; Micheau, J. C.; Vermeersch, G. Multinuclear NMR Structural Characterization of an Unprecedented Photochromic Allene Intermediate. *Organic Letters* **2002**, *4*, 3143–3145.

(144) Delbaere, S.; Micheau, J.-C.; Vermeersch, G. NMR Kinetic Investigations of the Photochemical and Thermal Reactions of a Photochromic Chromene. *J. Org. Chem.* **2003**, *68*, 8968–8973.

(145) Zhao, W.; Carreira, E. M. Oligothiophene-Linked Bisnaphthopyrans: Sequential and Temperature- Dependent Photochromism. *Chem. Eur. J.* **2007**, *13*, 2671–2688.

(146) Favaro, G.; Romani, A.; Becker, R. S. Photochromic Behavior of 2,2-Spiro-Adamantylidene-2H-Naphtho[1,2-b]Pyran: A New Thermoreversible and Photoreversible Photochromic System¶. *Photochem. Photobiol.* **2000**, *72*, 632–638.

(147) Maafi, M.; Brown, R. G. Photophysics and Kinetics of Naphthopyran Derivatives, Part 2: Analysis of Diarylnaphthopyran Kinetics. Degeneracy of the Kinetic Solution. *Int. J. Chem. Kinet.* **2005**, *37*, 717–727.

(148) Maafi, M.; Brown, R. G. Photophysics and Kinetics of Naphthopyran Derivatives, Part 3: A General Procedure to Uniquely Identify the Kinetic and Spectroscopic Parameters of ABC(2k,2φ) Systems and Application to Naphthopyran Reactions. *Int. J. Chem. Kinet.* **2006**, *38*, 421–430.

(149) Maafi, M. Useful Spectrokinetic Methods for the Investigation of Photochromic and Thermo-Photochromic Spiropyrans. *Molecules* **2008**, *13*, 2260–2302.

(150) Christie, R. M.; Hepworth, J. D.; Gabbutt, C. D.; Rae, S. An Investigation of the Electronic Spectral Properties of the Coloured Photoproducts Derived from Some Photochromic Naphtho[2,1-b]Pyrans. *Dyes and Pigments* **1997**, *35*, 339–346.

(151) Hobley, J.; Malatesta, V.; Millini, R.; Giroldini, W.; Wis, L.; Goto, M.; Kishimoto, M.; Fukumura, H. Photochromism of Chromene Crystals; a New Property of Old Chromenes. *Chemical Communications* **2000**, No. 14, 1339–1340.

(152) Lenoble, C.; Becker, R. S. Photophysics, Photochemistry, and Kinetics of Photochromic 2H-Pyrans and Chromenes. *J. Photochem.* **1986**, *33*, 187–197.

(153) Gentili, P. L.; Danilov, E.; Ortica, F.; Rodgers, M. A. J.; Favaro, G. Dynamics of the Excited States of Chromenes Studied by Fast and Ultrafast Spectroscopies. *Photochem. Photobiol. Sci.* **2004**, *3*, 886–891.

(154) Crano, J. C.; Flood, T.; Knowles, D.; Kumar, A.; Van Gemert, B. Photochromic Compounds: Chemistry and Application in Ophthalmic Lenses. *Pure and Applied Chemistry* **1996**, *68*, 1395–1398.

(155) Ramamurthy, V.; Schanze, K. S. *Photochemistry of Organic Molecules in Isotropic and Anisotropic Media*. *Photochemistry of Organic Molecules in Isotropic and Anisotropic Media*; CRC Press, 2003.

(156) Kolc, J.; Becker, R. S. Proof of Structure of the Colored Photoproducts of Chromenes and Spiropyrans. *J. Phys. Chem.* **1967**, *71*, 4045–4048.

(157) Pozzo, J.-L.; Lokshin, V.; Samat, A.; Guglielmetti, R.; Dubest, R.; Aubard, J. Effect of Heteroaromatic Annulation with Five-Membered Rings on the Photochromism of 2H- [1] -Benzopyrans. *J. Photochem. Photobiol. A: Chem.* **1998**, *114*, 185–191.

(158) Ortica, F.; Romani, A.; Blackburn, F.; Favaro, G. Effects of the Environment on the Photochromic Behaviour of a Novel Indeno-Fused Naphthopyran. *Photochemical and Photobiological Sciences* **2002**, *1*, 803–808.

(159) Pan, G.-L.; Wei, J.-Q.; Fan, P.; Zhu, A.-P.; Ming, Y.-F.; Fan, M.-G.; Yao, S. D. Laser Induced Photochromic Mechanism of 3-Phenyl-3-[1,2-Dimethylindol-3-YL]-3H-Naphtho[2,1-B]Pyran. *Res. Chem. Intermed.* **2000**, *26*, 829–838.

(160) Harié, G.; Samat, A.; Guglielmetti, R.; De Keukeleire, D.; Saeyens, W.; Van Parys, I. Photochromic Behaviour of Bis[4-(N,N-Dimethylamino)Phenyl]-Substituted 3H-Naphtho[2,1-b]Pyran and 2H-1-Benzopyran. *Tetrahedron Lett.* **1997**, *38*, 3075–3078.

(161) Rumi, M.; White, T. J.; Bunning, T. J. Phototropic Guest-Host Liquid Crystal Systems: Environmental Effects on Naphthopyran Kinetics. *Journal of Physical Chemistry B* **2016**, *120*, 12755–12767.

(162) Clarke, David, A.; Herno, Bernard, M.; Gabuutt, Christopher, D.; Hepworth, John, D.; Partington, Steven, M.; Corns, Stephen, N. PH Sensitive Photochromic Dyes. PH Sensitive Photochromic Dyes. WO 99/31081, June 24, 1999.

(163) Aiken, S.; Clayton, D.; Gabbutt, C. D.; Heron, B. M.; Kolla, S. B. Cationic Merocyanine Dyes by Photomodulation of [4-(Naphthopyran-3-Yl)Phenyl]Methines. *Dyes and Pigments* **2013**, *97*, 118–123.

(164) Gabbutt, C. D.; Gibbons, L. V.; Heron, B. M.; Kolla, S. B. The Intramolecular Capture of Thermally Generated Merocyanine Dyes Derived from Naphthopyrans: Photochromism of 5-(Diarylhydroxymethyl)-2H-Naphtho[1,2-b]Pyrans. *Dyes and Pigments* **2012**, *92*, 995–1004.

(165) Gabbutt, C. D.; Heron, B. M.; Kolla, S. B.; Mcgivern, M. Two Stage Colour Modulation of Triarylmethine Dyes Derived from a Photochromic Naphthopyran. *Eur. J. Org. Chem.* **2008**, *2008*, 2031–2034.

(166) Gabbutt, C. D.; Heron, B. M.; Kilner, C.; Kolla, S. B. Benzopentalenonaphthalenones from the Intramolecular Capture of a Merocyanine Derived from a Naphthopyran. *Chem. Commun.* **2010**, *46*, 8481.

(167) Kumar, A.; Van Gemert, B.; Knowles, D. B. Color Tunability in Photochromic Naphthopyrans. *Mol. Cryst. and Liq. Cryst.* **2000**, *344*, 217–222.

(168) Chan, Y.-P.; Jean, P. Naphthopyrans Annelated in C6-C7, Their Preparation and Compositions and (CO)Polymer Matrices Containing Them. Naphthopyrans Annelated in C6-C7, Their Preparation and Compositions and (CO)Polymer Matrices Containing Them. US6207084B1, March 27, 2001.

(169) Clarke, D. A.; Heron, B. M.; Gabbutt, C. D.; Hepworth, J. D.; Partington, S. M.; Corns, S. N. Grey Colouring Photochromic Fused Pyrans. Grey Colouring Photochromic Fused Pyrans. WO2000018755A1, April 6, 2000.

(170) Clarke, D. A.; Heron, B. M.; Gabbutt, C. D.; Hepworth, J. D.; Partington, S. M.; Corns, S. N. Neutral Colouring Photochromic 2H-Naphtho[1,2-b]Pyrans and Heterocyclic Pyrans.

Neutral Colouring Photochromic 2H-Naphtho[1,2-b]Pyrans and Heterocyclic Pyrans. WO1998042693A2, October 1, 1998.

(171) Gemert, B. V. Novel Photochromic Indeno-Fused Naphthopyrans. Novel Photochromic Indeno-Fused Naphthopyrans. WO1996014596A1, May 17, 1996.

(172) Kortekaas, L.; Browne, W. R. The Evolution of Spiropyran: Fundamentals and Progress of an Extraordinarily Versatile Photochrome. *Chem. Soc. Rev.* **2019**, *48*, 3406–3424.

(173) Aubard, J.; Maurel, F.; Buntinx, G.; Poizat, O.; Levi, G.; Guglielmetti, R.; Samat, A. Femto/Picosecond Transient Absorption Spectroscopy of Photochromic 3,3-Diphenylnaphtho[2,1-b]Pyran. *Mol. Cryst. and Liq. Cryst.* **2000**, *345*, 215–220.

(174) Brazevic, S.; Baranowski, M.; Sikorski, M.; Rode, M.; Burdzinski, G. Ultrafast Dynamics of the Transoid-Cis Isomer Formed in Photochromic Reaction from 3H-Naphthopyran. *ChemPhysChem* **2020**, *n/a*.

(175) Migani, A.; Gentili, P. L.; Negri, F.; Olivucci, M.; Romani, A.; Favaro, G.; Becker, R. S. The Ring-Opening Reaction of Chromenes: A Photochemical Mode-Dependent Transformation. *J. Phys. Chem. A* **2005**, *109*, 8684–8692.

(176) Moine, B.; Réhault, J.; Aloïse, S.; Micheau, J.-C.; Moustrou, C.; Samat, A.; Poizat, O.; Buntinx, G. Transient Absorption Studies of the Photochromic Behavior of 3H-Naphtho[2,1-b]Pyrans Linked to Thiophene Oligomers via an Acetylenic Junction. *J. Phys. Chem. A* **2008**, *112*, 4719–4726.

(177) Moine, B.; Buntinx, G.; Poizat, O.; Rehault, J.; Moustrou, C.; Samat, A. Transient Absorption Investigation of the Photophysical Properties of New Photochromic 3H-Naphtho[2,1-b]Pyran. *J. Phys. Org. Chem.* **2007**, *20*, 936–943.

(178) Brazevic, S.; Sliwa, M.; Kobayashi, Y.; Abe, J.; Burdzinski, G. Disclosing Whole Reaction Pathways of Photochromic 3H-Naphthopyrans with Fast Color Fading. *J. Phys. Chem. Lett.* **2017**, *8*, 909–914.

(179) Gentili, P. L.; Romani, A.; Becker, R. S.; Favaro, G. The Photoinduced Ring Opening Reaction of Benzo(2H)Chromenes: A Kinetic and Thermodynamic Approach. *Chem. Phys.* **2005**, *309*, 167–175.

(180) Becker, R. S.; Favaro, G.; Romani, A.; Gentili, P. L.; Dias, F. M. B. Vibronic Effects in Pathways of Photochemistry and Vibrational Relaxation. *Chem. Phys.* **2005**, *316*, 108–116.

(181) Favaro, G.; Romani, A.; Becker, R. S. Competition Between Vibrational Relaxation and Photochemistry: Relevance of Vibronic Quantum Effects†¶. *Photochem. Photobiol.* **2001**, *74*, 378–384.

(182) Becker, R. S.; Pellliccioli, A. P.; Romani, A.; Favaro, G. Vibronic Quantum Effects in Fluorescence and Photochemistry. Competition between Vibrational Relaxation and Photochemistry and Consequences for Photochemical Control. *J. Am. Chem. Soc.* **1999**, *121*, 2104–2109.

(183) Becker, R. S.; Dolan, E.; Balke, D. E. Vibronic Effects in Photochemistry—Competition between Internal Conversion and Photochemistry. *J. Chem. Phys.* **1969**, *50*, 239–245.

(184) Maafi, M.; Brown, R. G. Photophysics and Kinetics of Naphthopyran Derivatives, Part 5: An Analytical Model Utilizing Temperature Effects to Evaluate ABC(2k,3–5ϕ) Kinetic Parameters. *Int. J. Chem. Kinet.* **2007**, *39*, 472–479.

(185) Brazevic, S.; Nizinski, S.; Szabla, R.; Rode, M. F.; Burdzinski, G. Photochromic Reaction in 3H-Naphthopyrans Studied by Vibrational Spectroscopy and Quantum Chemical Calculations. *Phys. Chem. Chem. Phys.* **2019**, *21*, 11861–11870.

(186) Luccioni-Houzé, B.; Campredon, M.; Guglielmetti, R.; Giusti, G. Kinetic Analysis of Fluoro-[2H]-Chromenes at the Photostationary States. *Mol. Cryst. and Liq. Cryst.* **1997**, *297*, 161–165.

(187) Pan, G.; Jingqiang, W.; Zhu, A.; Yangfu, M.; Meigong, F.; Side, Y. *SCIENCE IN CHINA (Series B) Photochromic Properties and Reaction Mechanism of Naphthopyran*. *SCIENCE IN CHINA (Series B) Photochromic Properties and Reaction Mechanism of Naphthopyran*; 2001; Vol. 44.

(188) Venec, D.; Delbaere, S.; Micheau, J. C.; Frigoli, M.; Moustrou, C.; Samat, A.; Vermeersch, G. Photochromism of 8-Thienyl-Naphthopyrans Investigated by NMR Spectroscopy. *J. Photochem. Photobiol. A: Chem.* **2006**, *181*, 174–179.

(189) di Nunzio, M. R.; Gentili, P. L.; Romani, A.; Favaro, G. Photochromism and Thermochromism of Some Spirooxazines and Naphthopyrans in the Solid State and in Polymeric Film. *J. Phys. Chem. C* **2010**, *114*, 6123–6131.

(190) Fan, P.; Pan, G.; Wei, J.; Ming, Y.; Zhu, A.; Fan, M. G.; Hung, W. M. Synthesis and Photochromic Mechanism of 3-Phenyl-3-[1,2-Dimethylindol-3-Yl]-3H-Naphtho[2,1-b]Pyran. *Mol. Cryst. and Liq. Cryst.* **2000**, *344*, 283–288.

(191) Goto, Y.; Sugita, K.; Takahashi, T.; Ohga, Y.; Asano, T. An Experimental Attempt to Identify a Moving Molecular Moiety in a Solvent Matrix. *Chem. Lett.* **2003**, *32*, 618–619.

(192) Sugita, K.; Goto, Y.; Ono, M.; Yamashita, K.; Hayase, K.; Takahashi, T.; Ohga, Y.; Asano, T. A New Application of High-Viscosity Kinetics. An Attempt to Identify a Site of Solvent Reorganizations around a Reactant. *BCSJ* **2004**, *77*, 1803–1806.

(193) Zayat, M.; Levy, D. Photochromic Naphthopyrans in Sol–Gel Ormosil Coatings. *J. Mater. Chem.* **2003**, *13*, 727–730.

(194) Pardo, R.; Zayat, M.; Levy, D. The Influence of Sol–Gel Processing Parameters on the Photochromic Spectral and Dynamic Behaviour of a Naphthopyran Dye in an Ormosil Coating. *J. Mater. Chem.* **2005**, *15*, 703–708.

(195) Mark Heron, B.; D. Gabbutt, C.; D. Hepworth, J.; A. Thomas, D.; Kilner, C.; M. Partington, S. Synthesis and Photochromic Properties of Methoxy Substituted 2,2-Diaryl-2H-Naphtho[1,2-b]Pyrans. *Heterocycles* **2004**, *63*, 567.

(196) Gabbutt, C. D.; Heron, B. M.; Instone, A. C.; Horton, P. N.; Hursthouse, M. B. Synthesis and Photochromic Properties of Substituted 3H-Naphtho[2,1-b]Pyrans. *Tetrahedron* **2005**, *61*, 463–471.

(197) Gabbutt, C. D.; Heron, B. M.; Instone, A. C.; Kolla, S. B.; Mahajan, K.; Coelho, P. J.; Carvalho, L. M. Synthesis and Photochromic Properties of Symmetrical Aryl Ether Linked Bi- and Tri-Naphthopyrans. *Dyes and Pigments* **2008**, *76*, 24–34.

(198) Aiken, S.; Gabbutt, C. D.; Heron, B. M.; Kolla, S. B. Photochromic Bi-Naphthopyrans. *Dyes and Pigments* **2015**, *113*, 239–250.

(199) Coelho, P. J.; Salvador, M. A.; Heron, B. M.; Carvalho, L. M. Spectrokinetic Studies on New Bi-Photochromic Molecules Containing Two Naphthopyran Entities. *Tetrahedron* **2005**, *61*, 11730–11743.

(200) Gemert, B. V.; Bergomi, M.; Knowles, D. Photochromism of Diarylnaphthopyrans. *Mol. Cryst. and Liq. Cryst.* **1994**, *246*, 67–73.

(201) Sousa, C. M.; Coelho, P. J.; Vermeersch, G.; Berthet, J.; Delbaere, S. Synthesis and Photochemical Reactivity of New 4-Substituted Naphtho[1,2-b]Pyran Derivatives. *J. Photochem. Photobiol. A: Chem.* **2010**, *216*, 73–78.

(202) Gorelik, A. M.; Venidiktova, O. V.; Kobeleva, O. I.; Valova, T. M.; Barachevsky, V. A. Spectral Manifestation of Protonation of Photochromic Naphthopyrans. *Dyes and Pigments* **2021**, *184*, 108833.

(203) Mwalukuku, V. M.; Liotier, J.; Riquelme, A. J.; Kervella, Y.; Huaulmé, Q.; Haurez, A.; Narbey, S.; Anta, J. A.; Demadrille, R. Strategies to Improve the Photochromic Properties

and Photovoltaic Performances of Naphthopyran Dyes in Dye-Sensitized Solar Cells. *Advanced Energy Materials* **2023**, *13*, 2203651.

(204) Stevenson, R.; De Bo, G. Controlling Reactivity by Geometry in Retro-Diels–Alder Reactions under Tension. *Journal of the American Chemical Society* **2017**, *139*, 16768–16771.

(205) Versaw, B. A.; McFadden, M. E.; Husic, C. C.; Robb, M. J. Designing Naphthopyran Mechanophores with Tunable Mechanochromic Behavior. *Chem. Sci.* **2020**, *11*, 4525–4530.

(206) Osler, S. K.; McFadden, M. E.; Robb, M. J. Comparison of the Reactivity of Isomeric 2H- and 3H-Naphthopyran Mechanophores. *J. Pol. Sci. 59*, 2537–2544.

(207) Radiom, M.; Kong, P.; Maroni, P.; Schäfer, M.; Kilbinger, A. F. M.; Borkovec, M. Mechanically Induced Cis-to-Trans Isomerization of Carbon–Carbon Double Bonds Using Atomic Force Microscopy. *Phys. Chem. Chem. Phys.* **2016**, *18*, 31202–31210.

(208) Huang, W.; Zhu, Z.; Wen, J.; Wang, X.; Qin, M.; Cao, Y.; Ma, H.; Wang, W. Single Molecule Study of Force-Induced Rotation of Carbon–Carbon Double Bonds in Polymers. *ACS Nano* **2017**, *11*, 194–203.

(209) McFadden, M. E.; Robb, M. J. Generation of an Elusive Permanent Merocyanine via a Unique Mechanochemical Reaction Pathway. *J. Am. Chem. Soc.* **2021**, *143*, 7925–7929.

(210) Ortica, F.; Moustrou, C.; Berthet, J.; Favaro, G.; Samat, A.; Guglielmetti, R.; Vermeersch, G.; Mazzucato, U. Comprehensive Photokinetic and NMR Study of a Biphotochromic Supermolecule Involving Two Naphthopyrans Linked to a Central Thiophene Unit Through Acetylenic Bonds¶. *Photochem. Photobiol.* **2003**, *78*, 558–566.

(211) Zhao, W.; Carreira, E. M. A Smart Photochromophore through Synergistic Coupling of Photochromic Subunits. *J. Am. Chem. Soc.* **2002**, *124*, 1582–1583.

(212) McFadden, M. E.; Robb, M. J. Force-Dependent Multicolor Mechanochromism from a Single Mechanophore. *J. Am. Chem. Soc.* **2019**, *141*, 11388–11392.

(213) May, P. A.; Munaretto, N. F.; Hamoy, M. B.; Robb, M. J.; Moore, J. S. Is Molecular Weight or Degree of Polymerization a Better Descriptor of Ultrasound-Induced Mechanochemical Transduction? *ACS Macro Lett.* **2016**, *5*, 177–180.

(214) Odell, J. A.; Keller, A. Flow-Induced Chain Fracture of Isolated Linear Macromolecules in Solution. *J. Polym. Sci. Pol. Phys.* **1986**, *24*, 1889–1916.

(215) Van Gemert, B.; Kumar, A.; Knowles, D. B. Naphthopyrans. Structural Features and Photochromic Properties. *Mol. Cryst. Liq. Cryst.* **1997**, *297–298*, 131–138.

(216) Kosuge, T.; Zhu, X.; Lau, V. M.; Aoki, D.; Martinez, T. J.; Moore, J. S.; Otsuka, H. Multicolor Mechanochromism of a Polymer/Silica Composite with Dual Distinct Mechanophores. *J. Am. Chem. Soc.* **2019**, *141*, 1898–1902.

Chapter 2

GENERATION OF AN ELUSIVE PERMANENT MEROCYANINE VIA A UNIQUE MECHANOCHEMICAL REACTION PATHWAY

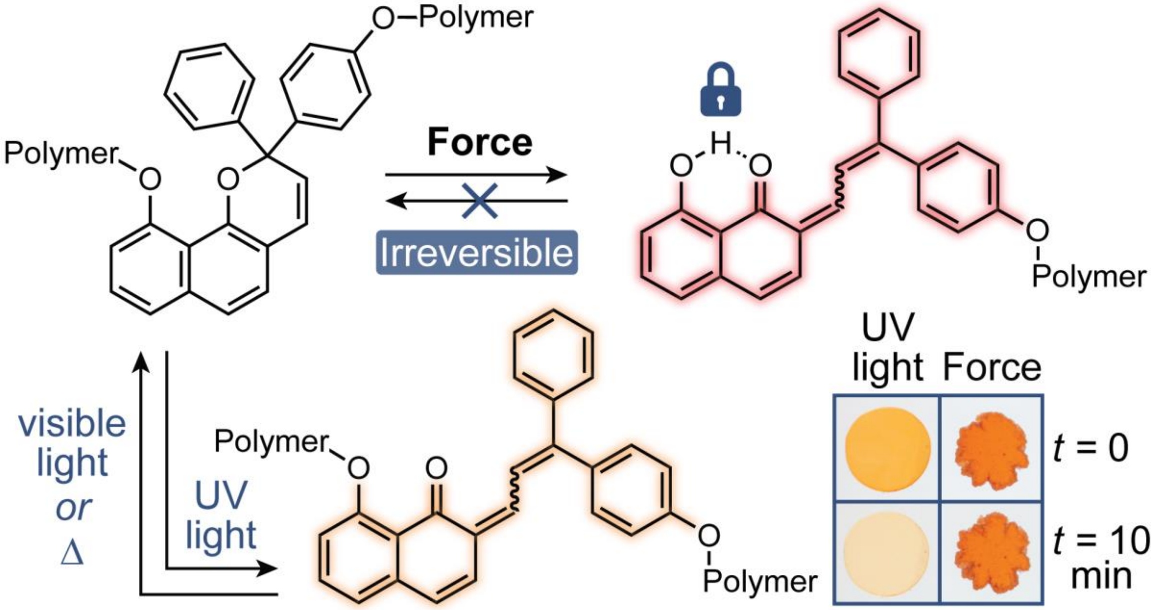

ABSTRACT: We report the discovery of a 2*H*-naphtho[1,2-*b*]pyran mechanophore that produces a permanent merocyanine dye upon mechanochemical activation, in contrast to the reversible product generated photochemically. Experiments suggest that the irreversibility of the mechanically generated merocyanine is due to a unique reaction in which the scission of an ester C–O bond reveals a β-hydroxy ketone that locks the merocyanine through an intramolecular H-bonding interaction. In addition to demonstrating the reactivity using solution-phase ultrasonication, permanent merocyanine generation is also achieved in solid polymeric materials. The permanent coloration achieved with the naphthopyran mechanophore affords unique opportunities for sensing and force-recording applications as well as fundamental studies limited by the reversibility of typical colorimetric force probes.

This chapter has been adapted with permission from McFadden, M. E.; Robb, M. J. Generation of an Elusive Permanent Merocyanine via a Unique Mechanochemical Reaction Pathway. *J. Am. Chem. Soc.* **2021**, *143*, 7925–7929. DOI: 10.1021/jacs.1c03865

Investigation

Naphthopyrans undergo a 6π electrocyclic ring-opening reaction to generate intensely colored merocyanine dyes.[1] Due to their synthetic accessibility and modularity, naphthopyrans have been extensively studied and developed as photoswitches, notably for commercial applications in photochromic lenses.[2] Recently, naphthopyrans have also been identified as a versatile class of mechanophores that generate the merocyanine dye under mechanical force. The mechanochemical activation of naphthopyrans incorporated covalently into polymers has been achieved under tension in bulk polymeric materials,[3,4] using solution-phase ultrasonication,[5] grinding of polymer composites,[6] and with high intensity focused ultrasound.[7] The modularity of the naphthopyran scaffold enables access to structurally diverse mechanophores with highly tunable mechanochromic properties, making naphthopyrans particularly attractive as molecular force probes enabling visualization of critical stress and/or strain in materials.

While several different constitutional isomers of naphthopyran have been widely investigated as photoswitches, mechanochemical reactivity has only been demonstrated for the 3*H*-naphtho[2,1-*b*]pyran (3*H*-NP) scaffold. However, 2*H*-naphtho[1,2-*b*]pyrans (2*H*-NPs) generate merocyanine dyes with unique absorption features that are more intensely colored with slower reversion compared to merocyanines derived from 3*H*-NPs.[1] These characteristics are attractive for many stress sensing applications. In addition, most mechanochromic mechanophores reported to date are reversible or produce transiently colored species that revert to a colorless state via oxidative decomposition under ambient conditions on relatively short timescales.[8]

Scheme 2.1. Mechanochemical Activation of a 2*H*-Naphtho[1,2-b]Pyran Mechanophore Generates a Permanent Merocyanine that is not Accessed Photochemically.

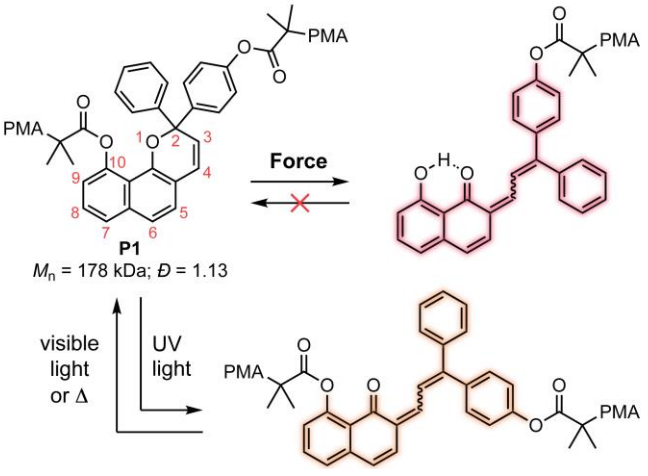

This transience is advantageous in situations where real-time assessment of stress and/or strain is desired,[9,10] but it also limits the intensity of the signal and precludes the use of such mechanophores in applications where a more permanent record of the mechanical history of a material is required.

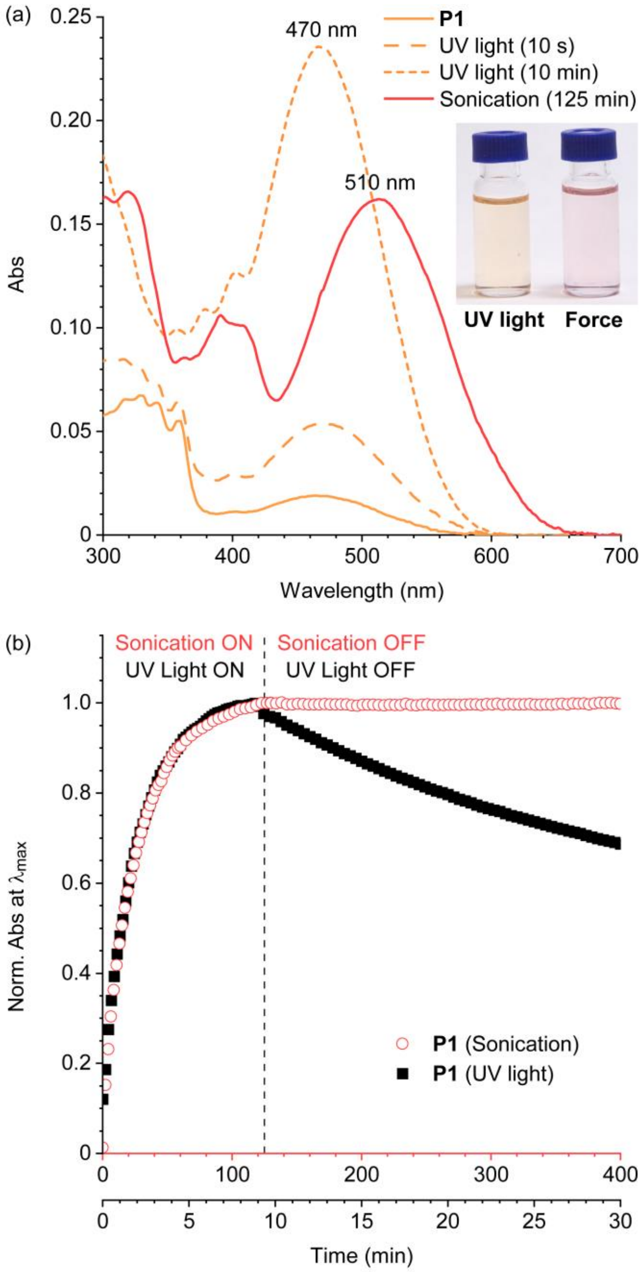

Figure 2.1. Mechanical activation of P1 produces a distinct merocyanine species from that produced under UV irradiation. (a) UV-vis absorption spectra and photographs of P1 after photoirradiation ($\lambda = 311$ nm) and ultrasound-induced mechanochemical activation. (b) Mechanical activation of P1 produces a permanent merocyanine in contrast to the thermally reversible photochemical product.

Interested in expanding the repertoire of naphthopyran mechanophores, we set out to explore the mechanochemistry of 2*H*-NPs. We envisioned that polymer attachment at the 10-position of the naphthopyran in conjunction with a second pulling position on one of the phenyl groups attached at the 3-position of the substrate would provide an effective geometry for efficient force transmission across the labile C–O bond of the pyran (Scheme 2.1). While we find that this particular 2*H*-NP is indeed mechanochemically active, the transformation unexpectedly produces a permanent merocyanine species distinct from the thermally reversible merocyanine generated via photochemical activation. Here we characterize the unusual mechanochemical reactivity of this 2*H*-NP mechanophore in solution and further demonstrate that the same reactivity is accessed in solid polymeric materials under force.

The mechanochemical reactivity of the 2*H*-NP mechanophore in polymer **P1** was investigated using solution-phase ultrasonication methods and compared directly to its photochemical reactivity under UV light. Polymer chains are subjected to elongational forces upon ultrasonication that are maximized near the chain midpoint.[11] Poly(methyl acrylate) (PMA) polymer **P1** (M_n = 178 kDa; $Đ$ = 1.13) containing a chain-centered mechanophore was synthesized by controlled radical polymerization starting from the naphthopyran bis-initiator (see the Supporting Information (SI) for details). Both the photochemical and mechanochemical reactions were monitored in real-time by UV−vis absorption spectroscopy using a continuous flow setup.[5,12] Irradiation of **P1** (2 mg/mL in THF) with 311 nm UV light at 19–22 °C produces a yellow-orange colored merocyanine with λ_{max} = 470 nm (Figure 2.1a). In contrast, when **P1** (2 mg/mL in THF with 30 mM BHT) is subjected to mechanical force via continuous ultrasonication at a similar solution temperature of 15–20 °C, a unique, red-colored species is generated (λ_{max} = 510 nm) with an absorption spectrum distinct from the photochemical product. Ultrasonication of an analogous chain-end functional control polymer does not result in color generation, confirming the mechanical origin of the reaction observed with **P1** (Figure 2.2).

In addition to the distinct differences in the color of the products generated photochemically or mechanochemically, we observe a striking discrepancy in the thermal reversion properties of the two dyes. Under the same conditions, the two reactions were monitored at the respective λ_{max} for each product during mechanochemical or photochemical activation, and then after cessation of ultrasound or UV irradiation (Figure 2.1b). After UV irradiation is stopped, the absorbance measured at 470 nm immediately begins to attenuate, corresponding to the thermal reversion of the merocyanine dye. On the other hand, the mechanically generated product is persistent. Furthermore, subjecting **P1** to alternating "on–off" cycles of ultrasonication results in minimal fading during the early "off" periods,

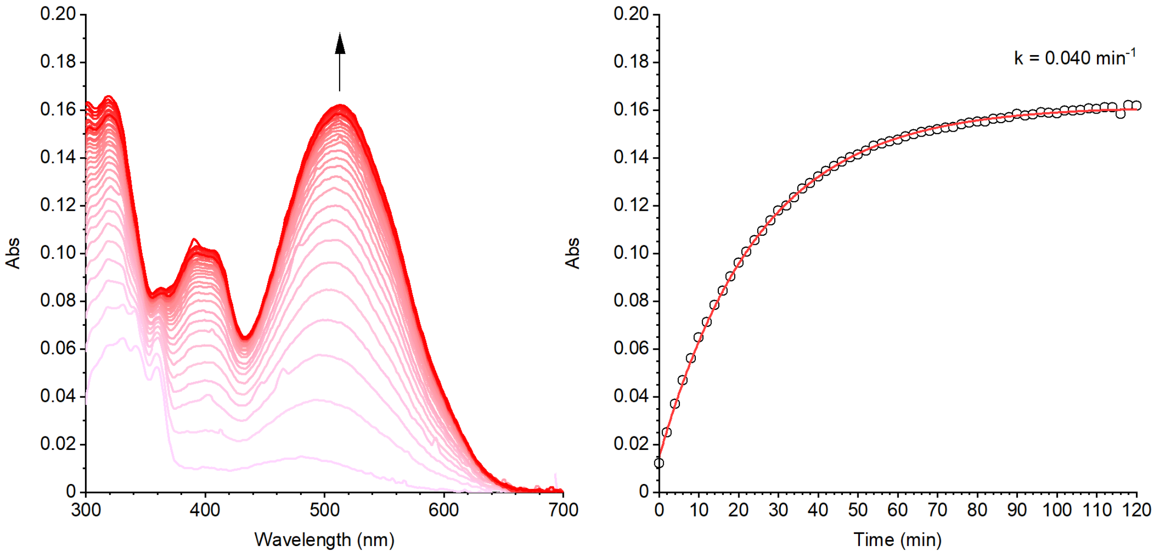

(a) Spectral evolution during sonication of **P1**

(b) Time-dependent absorbance at 510 nm during sonication of **P1**

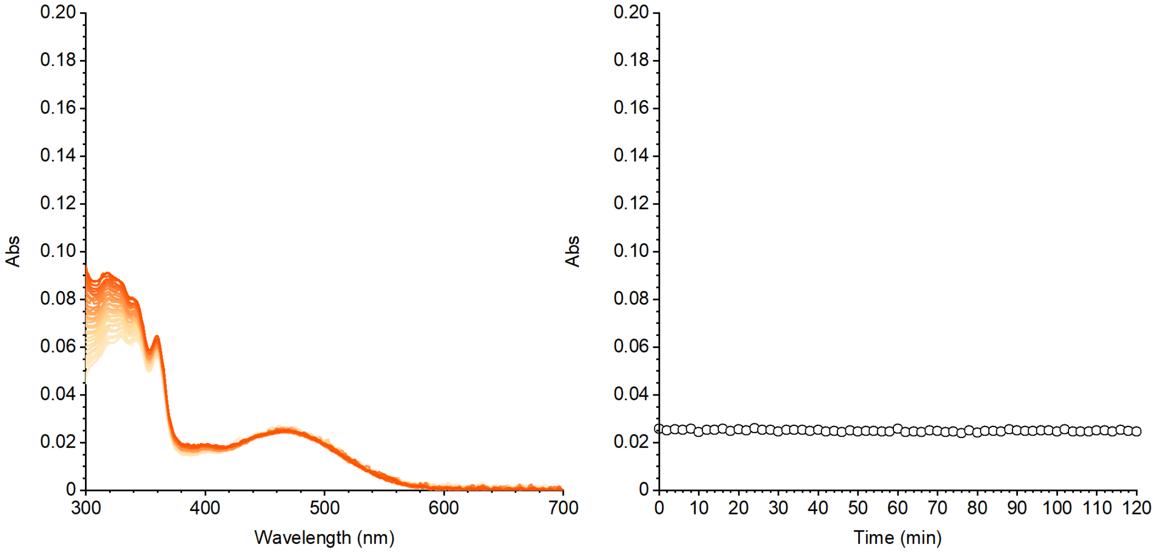

(c) Spectral evolution during sonication of **P3**

(d) Time-dependent absorbance at 470 nm during sonication of **P3**

Figure 2.2. Comparison of sonication experiments performed on solutions (2 mg/mL in THF with 30 mM BHT) of polymer **P1** containing a chain-centered mechanophore and chain-end functional control polymer **P3**. (a) UV-vis spectra acquired at regular intervals during ultrasound-induced mechanical activation of **P1** exhibit an increase in visible absorption with λ_{max} of 510 nm. (b) Fitting time-dependent absorbance at 510 nm to eq. 2.1myields a rate constant for merocyanine formation of 0.040 min^{-1}. (c,d) No change in visible absorption is observed upon sonication of a solution of chain-end functional control polymer **P3**.

indicating that the irreversible product is formed rapidly upon mechanochemical activation (Figure 2.4). We note that differences in alkene isomerization are unlikely to account for these observations.

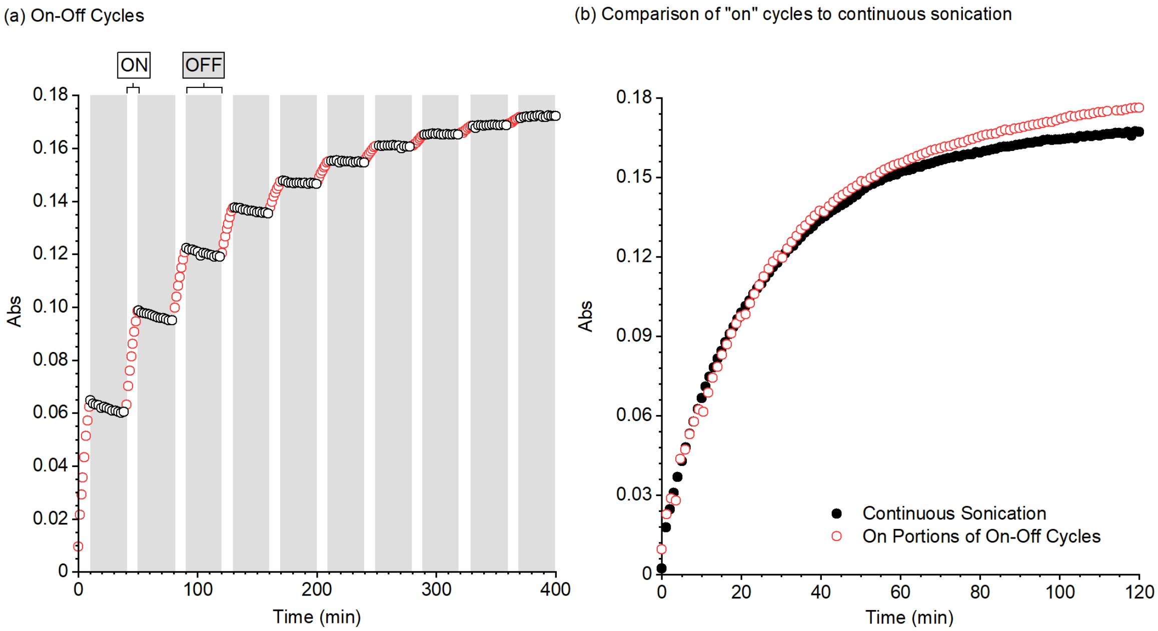
(a) On-Off Cycles

(b) Comparison of "on" cycles to continuous sonication

Figure 2.4. Investigation of the temporal dependence of permanent merocyanine formation. (a) A solution of P1 (2 mg/mL with 30 mM BHT) was exposed to “on–off” cycles of ultrasonication, alternating between 10 min “on” and 30 min “off.’ (b) Minimal loss of color is observed during the “off” periods, as demonstrated by comparing only the “on” time from panel a to the mechanochemical activation of P1 under continuous ultrasonication. Absorbance measured at 510 nm.

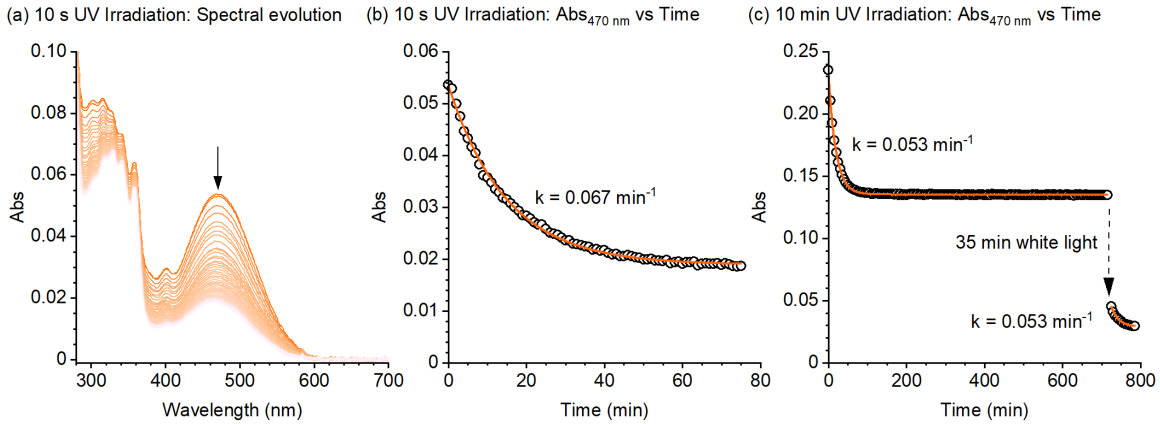
(a) 10 s UV Irradiation: Spectral evolution

(b) 10 s UV Irradiation: $Abs_{470\ nm}$ vs Time

(c) 10 min UV Irradiation: $Abs_{470\ nm}$ vs Time

Figure 2.3. Demonstration of reversion of the photochemically generated merocyanine under ambient conditions or upon irradiation with white light. (a,b) Brief photoactivation of a solution of P1 with UV light (10 s) produces a merocyanine with λmax of 470 nm that fully reverts after approximately 1 h at room temperature. Fitting the time dependent absorbance at 470 nm to eq. 2.2 yields a reversion rate of 0.067 min-1. (c) Extended irradiation of a solution of P1 with UV light (10 min) generates a merocyanine with the same λ_{max} of 470 nm, which fades to half the initial absorbance in approximately 1 h, leaving a persistent merocyanine attributed to the exocyclic trans isomer. Subsequent irradiation with white light for 35 min leads to additional reversion. Further thermal reversion occurs with the same rate constant observed initially.

The *cis* and *trans* stereoisomers of naphthopyran-derived merocyanine dyes have different rates of thermal reversion; however, they typically display variances in λ_{max} that are < 10 nm.[13–15] Extended UV irradiation of **P1** does produce a greater fraction of slower fading *trans* isomers than that observed after brief UV irradiation (Figure 2.3), but λ_{max} is invariant. Moreover, the photochemical product completely reverts upon irradiation with white light, while the same treatment of the mechanochemical product results in < 10% decrease in the absorbance at 510 nm (Figure 2.5). Together, these results suggest that the mechanochemical reaction product is not simply a different stereoisomer than the merocyanine produced photochemically.

Density functional theory (DFT) calculations using the CoGEF method[16,17] performed on a truncated model of the 2*H*-NP mechanophore in **P1** predict the expected ring-opening reaction upon mechanical elongation, which occurs with a maximum force (F_{max}) of 4.1 nN (Figure 2.6). Extending the simulation beyond the initial ring-opening reaction, however, provided additional insight into the possible identity of the mechanochemical reaction product observed experimentally. Upon further molecular elongation, the next bond predicted to break is the ester C(O)–O bond derived from the hydroxyl group at the 10-position of the naphthopyran, which occurs at a moderate F_{max} value of 4.8 nN.[17] This result is surprising given that CoGEF calculations typically predict the C–C(O) bond

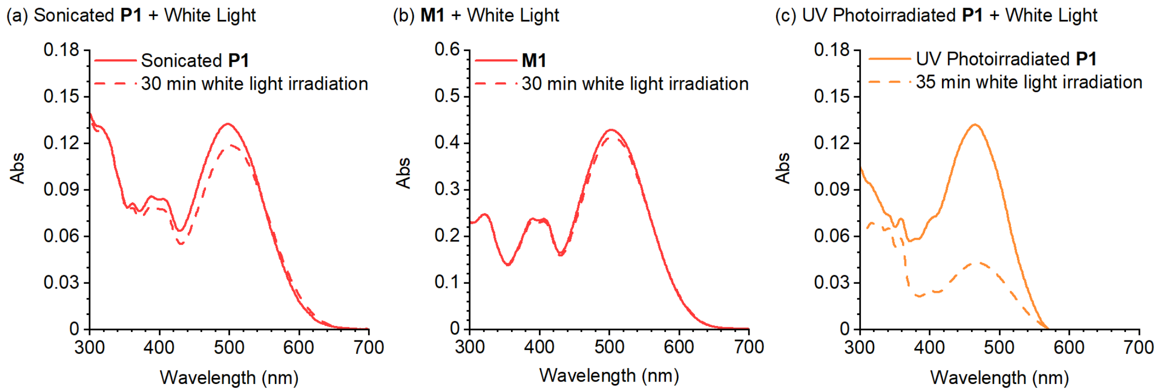

Figure 2.5. Irradiation of (a) the merocyanine derived from ultrasound-induced mechanochemical activation of **P1** and (b) **M1** (vida infra) with white light for 30 min results in negligible (< 10%) change in visible absorption. (c) Irradiation of the thermally persistent merocyanine generated from photochemical activation of **P1** with white light for 35 min under the same conditions results in 67% attenuation of the visible absorbance at 470 nm (see Figure 2.4c above).

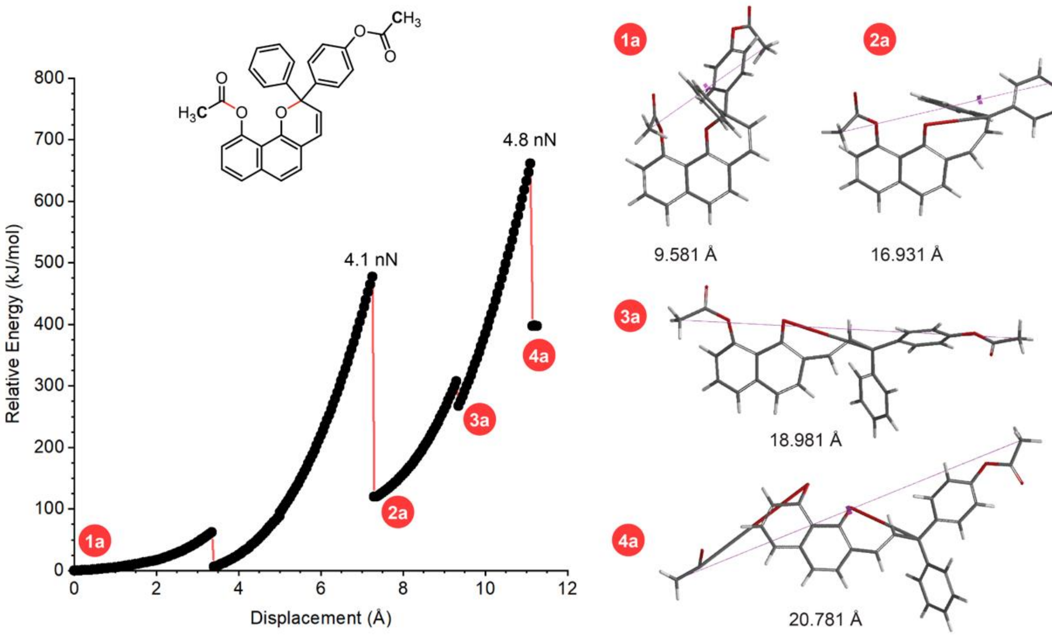

Figure 2.6. DFT calculations using the constrained geometries simulate external force (CoGEF) method at the B3LYP/6-31G* level of theory for a truncated model reflecting the mechanophore in polymer **P1**. CoGEF calculations predict the ring-opening reaction with an $F_{\max}$ value of 4.1 nN followed by further elongation that results in C–O bond scissile at a predicted $F_{\max}$ value of 4.8 nN. The corresponding computed structures at various points of elongation are shown at right along with the associated constraint distance between the terminal methyl groups.

within terminal acetoxy groups to be more labile, with the exception of a similar phenyl ester that has been demonstrated to undergo C(O)–O bond cleavage under mechanical force.[17,18] In addition, 1-naphthyl esters undergo photo-Fries rearrangements, whereby the ester C(O)–O bond is cleaved homolytically to furnish the naphthol.[19,20] We therefore suspected that cleavage of the ester C(O)–O bond on the merocyanine could be occurring during the mechanochemical activation of **P1**. Such a reaction is remarkable because it would lead to a merocyanine stabilized by an intramolecular H-bond between the ketone and the newly generated β-hydroxyl group.[21] In fact, the supposed synthesis of a similar permanent naphthopyran-derived merocyanine was reported previously,[22] but the obtained dye was later determined to be the product of a different reaction entirely.[23]

To further explore the possibility that mechanochemical activation of **P1** produces an intramolecularly H-bonded merocyanine, we synthesized model compound **M1** (Figure 2.7a, see the Experimental section for details). Despite being protected from UV light during synthesis, deprotection of the 10-hydroxyl group on the naphthopyran precursor generated a mixture of merocyanine stereoisomers with only a small amount of 10-hydroxynaphthopyran, suggesting that the presence of the β-hydroxyl group dramatically shifts the thermal equilibrium between the naphthopyran and merocyanine (see the Experimental section for details). Merocyanine **M1** is an intensely colored dye with an absorption spectrum that closely matches that of the product obtained from mechanochemical activation of **P1** (Figure 2.7a). Furthermore, diagnostic resonances in the ^{1}H NMR spectrum associated with the H-bonded hydroxyl proton on the various merocyanine stereoisomers are observed at approximately 13.3 and 13.6 ppm (Figure 2.7b). The set of doublets around 8.75 ppm (*J* = ~12 Hz) is attributed to protons on the two exocyclic *cis* alkene isomers deshielded by a weak intramolecular interaction with the nearby carbonyl.[24] Significantly, the ^{1}H NMR spectrum of **P1** after ultrasonication displays peaks matching those of model compound **M1**, further indicating that the mechanochemical reaction generates an analogous product (Figure 2.7c and Figure 2.8). Extended irradiation of compound **M1** with white light results

(a) UV-vis spectra

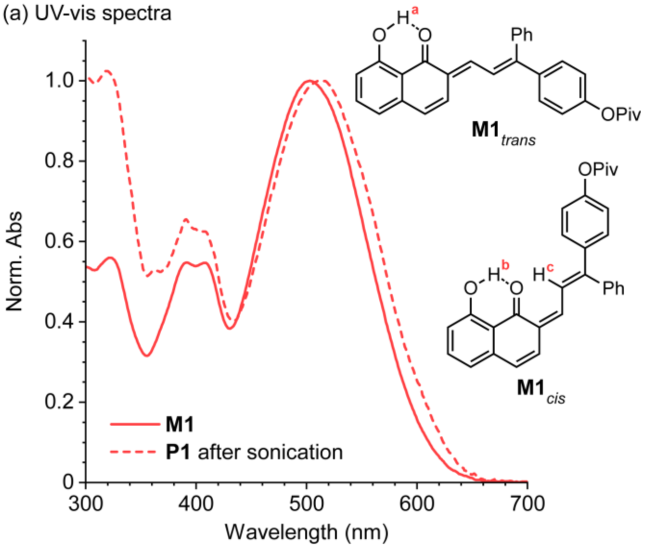

(b) **M1**, ^{1}H NMR (400 MHz, Acetone-d_6)

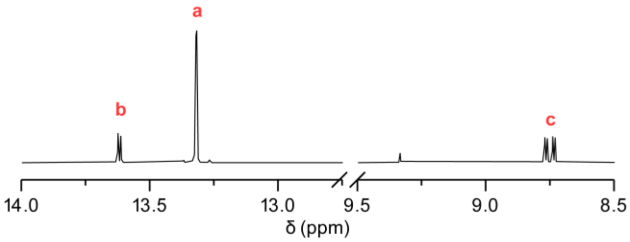

(c) **P1** after sonication, ^{1}H NMR (400 MHz, Acetone-d_6)

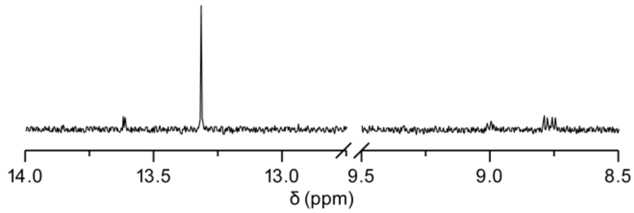

Figure 2.7. (a) UV-vis absorption spectra of **P1** after ultrasound-induced mechanical activation compared to **M1** in THF. ^{1}H NMR spectra of (b) **M1** and (c) **P1** after ultrasonication.

in only approximately 3% attenuation of the total absorbance, consistent with the results presented above for the product derived from mechanochemical activation of **P1** (see Figure 2.5b above).

(a) Sonicated **P1**, ^{1}H (400 MHz, acetone-d_6)

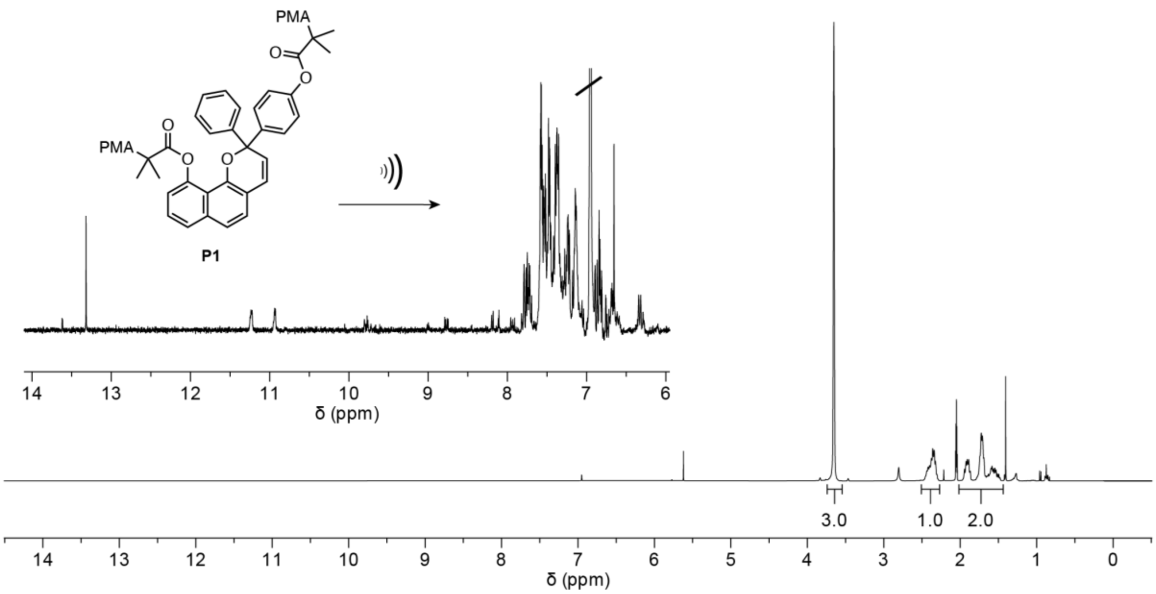

(b) **M1**, ^{1}H (400 MHz, acetone-d_6)

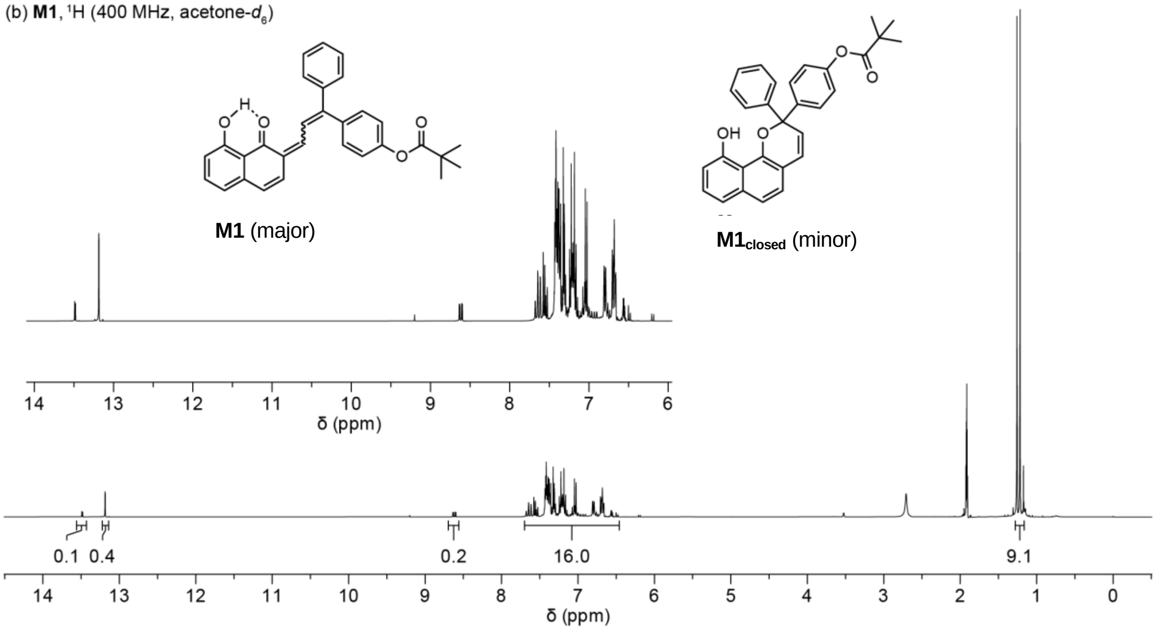

Figure 2.8. ^{1}H NMR spectra of (a) **P1** after ultrasonication (125 min), and (b) **M1**. Polymer **P1** was precipitated into hexanes and dried under vacuum prior to analysis. In the spectrum for **P1**, the peak at 6.95 ppm is residual BHT and peaks at 10.94 and 11.23 ppm are attributed to peroxide impurities resulting from the decomposition of THF. The small singlet at 9.34 ppm in the spectrum of **M1** is attributed to the significantly more shielded hydroxyl proton of the minor ring-closed naphthopyran (**M1**$_{\text{closed}}$).

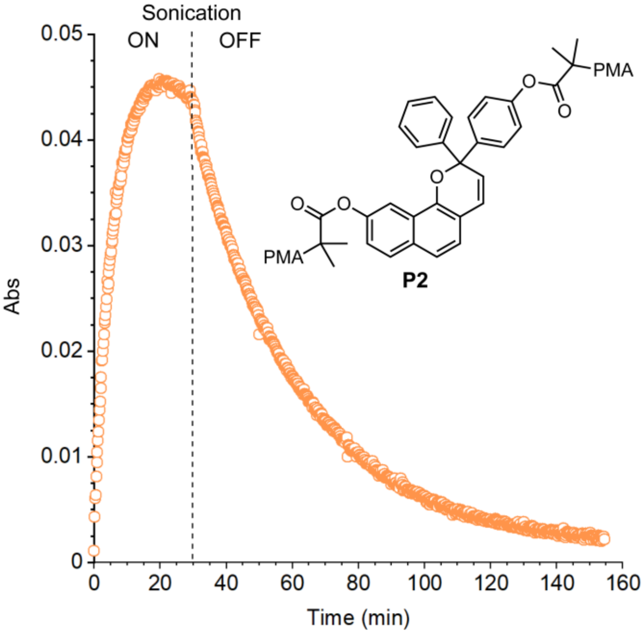

Figure 2.9. Ultrasound-induced mechanical activation and subsequent reversion of control polymer **P2** containing an isomeric naphthopyran mechanophore with polymer attachment at the 9-position. Absorption monitored at λ_{max} = 485 nm.

Formation of the proposed merocyanine locked by an intramolecular H-bond is dictated by the presence of a β-hydroxy ketone. To further test the hypothesis that this β-hydroxyl group confers permanence to the merocyanine accessed mechanochemically from **P1**, we synthesized polymer **P2** (M_n = 178 kDa, $Đ$ = 1.06) containing an analogous chain-centered naphthopyran, but with the polymer attached via an ester linkage at the 9-position instead of the 10-position (Figure 2.9). Scission of the C(O)–O ester bond at the 9-position of this naphthopyran would lead to a γ-hydroxy ketone in the merocyanine, which would not be expected to engage in a H-bonding interaction. Indeed, ultrasound-induced mechanical activation of **P2** produces a thermally transient merocyanine that reverts rapidly upon cessation of ultrasound with a half-life of ~22 min, providing further evidence for the mechanism and structure of the permanent merocyanine produced from mechanochemical activation of **P1**.

Photo-Fries rearrangements of 1-naphthyl esters are often carried out in bulk polymeric materials,[25] and given the propensity for mechanochemical activation of naphthopyran in similar environments,[3,4] we were interested to see if the permanent merocyanine could be generated in the solid state. A polydimethylsiloxane (PDMS) elastomer[26] was prepared with a 2*H*-NP crosslinker analogous to the structure of the mechanophore in **P1** (see the Experimental section for details). Irradiation of the material with UV light (λ = 365 nm, 2 min) produces the anticipated yellow-orange color, which fades rapidly under ambient conditions (Figure 2.10). Mechanochemical activation of

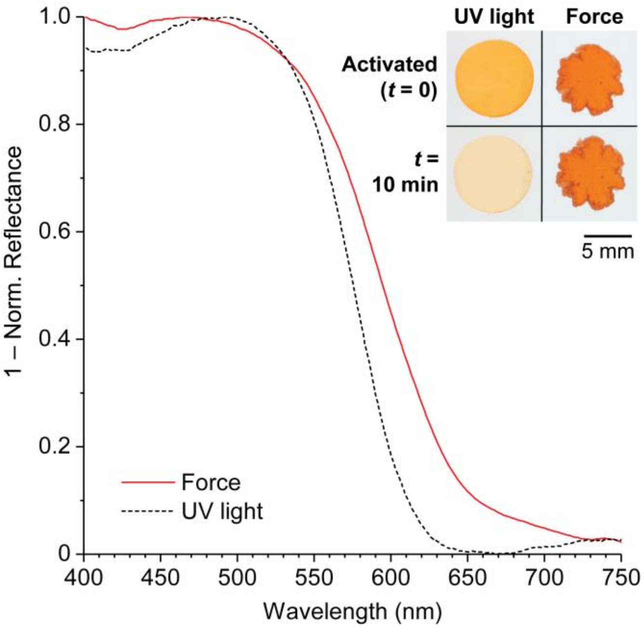

Figure 2.10. UV-vis spectra and photographs of a photochemically and mechanochemically activated PDMS network crosslinked with a 2*H*-NP mechanophore analogous to the structure in **P1**. Spectra were obtained via reflectance measurements and plotted for comparison with solution-phase absorption data. Photographs were acquired immediately after activation and 10 min post-activation.

the material under manual tension yields the same yellow-orange coloration, which again quickly fades upon stress relaxation (Figure 2.11). However, when the film is repeatedly struck by hammer, a distinct red color is observed that persists indefinitely. The difference in the behavior of the products generated from these two mechanical activation experiments may indicate a strain rate dependence for scission of the C(O)–O ester bond in the merocyanine relative to the ring-opening reaction of naphthopyran, and is consistent with the high strain rates achieved during ultrasound-induced mechanochemical activation.[27] Reflectance measurements confirm that the color of the hammered film is bathochromically shifted compared to the UV-activated material, consistent with the absorption spectra from solution-phase activation experiments. Finally, control experiments performed on an analogous PDMS material containing a non-crosslinked, but otherwise identical 2*H*-NP molecule in which mechanical force is not transferred across the labile C–O pyran bond illustrate a similar response to UV light, but do not produce any color with mechanical force (Figure 2.12). Furthermore, when the control material is subjected to repeated hammering after UV irradiation, complete loss of color is still observed, supporting that the putative cleavage of the merocyanine C(O)–O ester bond is a mechanochemical and not a thermal process.

In summary, we have demonstrated the mechanochemical reactivity of a new class of naphthopyran mechanophores based on the *2H*-naphtho[1,2-*b*]pyran scaffold. Remarkably, mechanochemical activation of a 2*H*-NP mechanophore with polymer attachment via an ester group at the 10-position of the substrate leads to the generation of a unique, permanent merocyanine dye distinct from the thermally reversible merocyanine product accessed photochemically. An intramolecular H-bond formed via mechanochemical scission of the C(O)–O ester bond that establishes a β-hydroxy ketone is implicated in the permanence of the mechanochemical merocyanine product. Generation of the permanent merocyanine is also demonstrated in bulk polymeric materials under stress, with experiments potentially indicating a strain rate dependence on the C(O)–O bond scission reaction that accompanies ring opening of the naphthopyran. A naphthopyran mechanophore that provides permanent coloration after mechanical activation offers a promising platform for stress

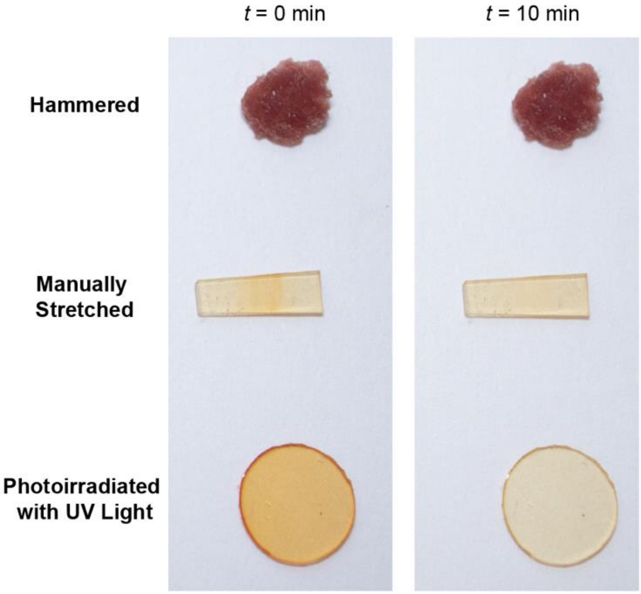

Figure 2.11. Photographs of **PDMS$_{\textbf{active}}$** films containing a mechanophore crosslinker after being subjected to repeated hammering, manual tension, and UV irradiation (365 nm) immediately after activation and then 10 min later. Manual stretching and UV light generate a transient yellow-orange color that quickly fades. In contrast, mechanical activation using a hammer generates a distinct red coloration that does not fade.

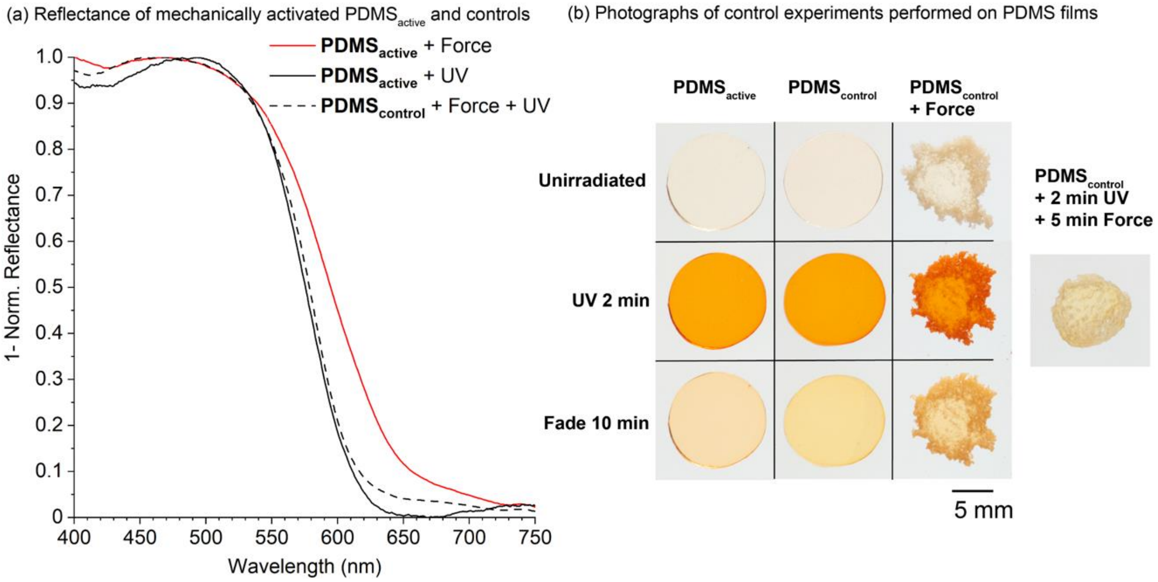

Figure 2.12. (a) Reflectance measurements and (b) photographs of a mechanophore-crosslinked active PDMS material (**PDMS$_{\text{active}}$**) and a control PDMS network incorporating a mono-functional naphthopyran moiety (**PDMS$_{\text{control}}$**) after being subjected to combinations of mechanical force by repeated hammering and UV light (365 nm). The control material exhibits similar reflection after being subjected to mechanical force and UV light as **PDMS$_{\text{active}}$** after UV irradiation, in contrast to the bathochromically shifted reflection observed for **PDMS$_{\text{active}}$** following mechanical activation. The control film turns yellow-orange under UV light and the color quickly fades in all cases. Fading is accelerated in the photoactivated control film after being hammered for 5 min.

sensing and recording applications in materials as well as fundamental studies limited by the reversibility of typical mechanochromic mechanophores.

Acknowledgements

Financial support from Caltech is gratefully acknowledged. M.E.M. was supported by an NSF Graduate Research Fellowship (DGE-1745301). We thank the Molecular Materials Research Center and the Center for Catalysis and Chemical Synthesis of the Beckman Institute at Caltech for access to equipment. We also thank Dr. Bruce Brunschwig, Dr. Mona Shahgholi, and Dr. David VanderVelde for technical assistance.

EXPERIMENTAL DETAILS

I. General Experimental Details

Reagents from commercial sources were used without further purification unless otherwise stated. Methyl acrylate was passed through a short plug of basic alumina to remove inhibitor immediately prior to use. Dry THF was obtained from a Pure Process Technology solvent purification system. All reactions were performed under a N_2 or argon atmosphere unless specified otherwise. Column chromatography was performed on a Biotage Isolera system using SiliCycle SiliaSep HP flash cartridges.

NMR spectra were recorded using a 400 MHz Bruker Avance III HD with Prodigy Cryoprobe. All ^1H NMR spectra are reported in δ units, parts per million (ppm), and were measured relative to the signals for residual $CHCl_3$ (7.26 ppm), acetone (2.05 ppm), or acetonitrile (1.94 ppm) in deuterated solvent. All ^{13}C NMR spectra were measured in deuterated solvents and are reported in ppm relative to the signals for $^{13}CDCl_3$ (77.16 ppm) or acetone-d_6 (206.26 ppm). Multiplicity and qualifier abbreviations are as follows: s = singlet, d = doublet, m = multiplet, br = broad, app = apparent.

High resolution mass spectra (HRMS) were obtained from a Waters Corp. LCT Premier XE time-of-flight mass spectrometer equipped with an electrospray ionization (ESI) probe, or a JEOL JMS-600H magnetic sector mass spectrometer equipped with a FAB+ probe.

Analytical gel permeation chromatography (GPC) was performed using an Agilent 1260 series pump equipped with two Agilent PLgel MIXED-B columns (7.5 x 300 mm), an Agilent 1200 series diode array detector, a Wyatt 18-angle DAWN HELEOS light scattering detector, and a Optilab rEX differential refractive index detector. The mobile phase was THF at a flow rate of 1 mL/min. Molecular weights and molecular weight distributions were calculated by light scattering using a dn/dc value of 0.062 mL/g (25 °C) for poly(methyl acrylate).

UV-Vis absorption spectra were recorded on a Thermo Scientific Evolution 220 spectrometer. Reflection measurements were performed on a Cary 5000 UV/Vis/NIR spectrophotometer equipped with an integrating sphere diffuse reflectance accessory (Internal DRA 1800). All reflection measurements were referenced to a LabSphere Spectralon 99% certified reflectance standard. The samples were illuminated through a Spectralon-coated aperture with a diameter of 1 cm, with a beam area of approximately 0.5 cm^2.

Ultrasound experiments were performed using a Vibra Cell 505 liquid processor equipped with a 0.5-inch diameter solid probe (part #630-0217), sonochemical adapter (part #830-00014), and a Suslick reaction vessel made by the Caltech glass shop (analogous to vessel #830-00014 from Sonics and Materials). Polymer solutions were continuously sampled for UV-vis analysis using a Cole Parmer Masterflex L/S pump system (item #EW-77912-10) composed of an L/S pump head (part #77390-00) and L/S precision variable speed drive (part #07528-20) using 4x6 mm PTFE tubing (part #77390-60) and a quartz flow-through cell (Starna, part #583.4-Q-10/Z8.5), which was connected using M6-threaded PTFE tubing (Starna, part #M6-SET).

Photoirradiation with UV light was performed using either a Philips PL-S 9W/01/2P UVB bulb with a narrow emission of 305–315 nm and a peak at 311 nm, or a DR/9W-UVA bulb with peak at 365 nm under ambient conditions unless indicated otherwise. Irradiation with white light was carried out using a 13 W broadband fluorescent lamp (Bayco Model BA-506) filtered through a 425 nm bandpass filter. Irradiation with blue light was applied to PDMS films using a 470 nm LED (ThorLabs M470L3), driver (ledd1B), and collimator (SM1U25-A).

II. Synthetic Details

Scheme 2.2. Synthesis of all compounds used in this study.

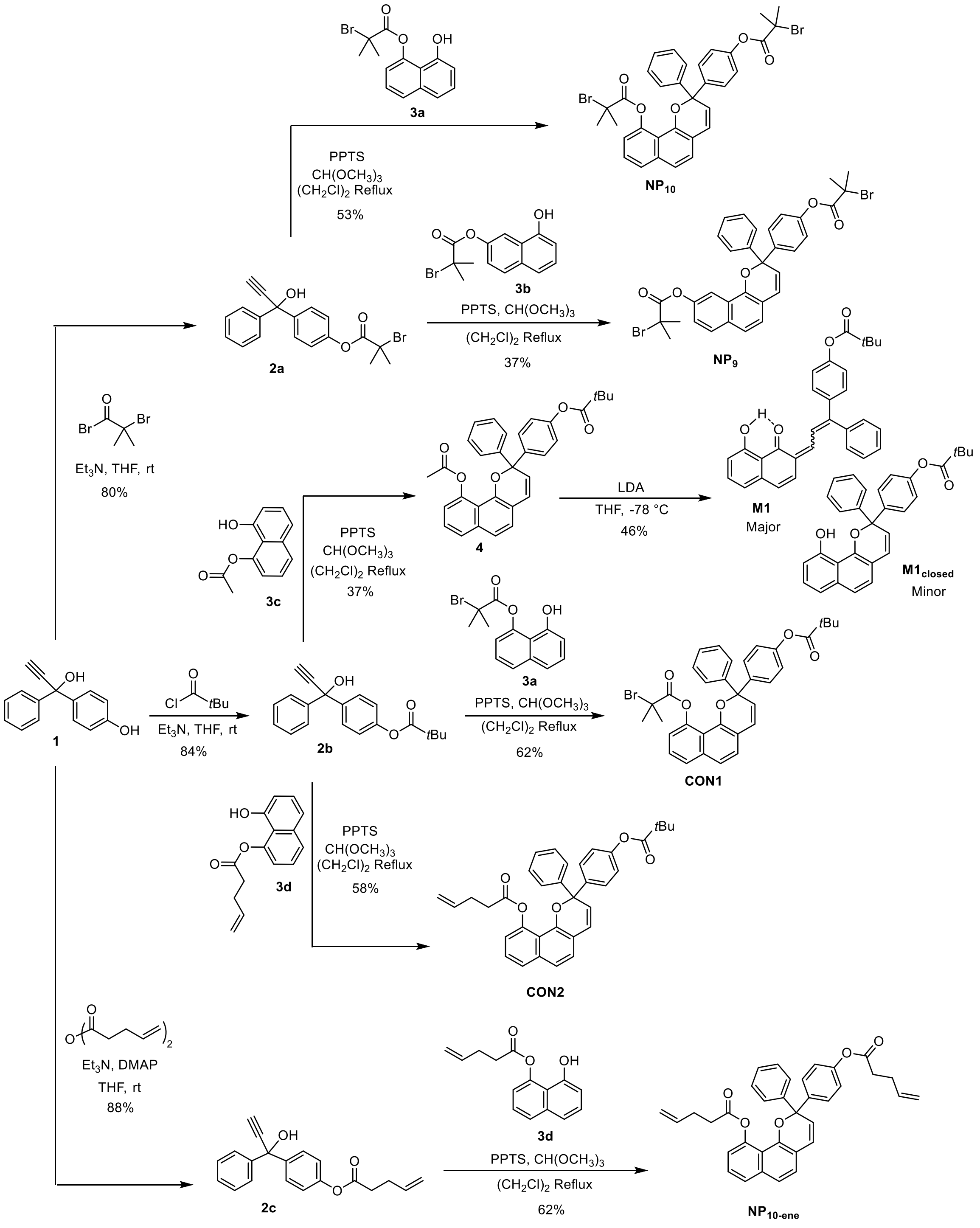

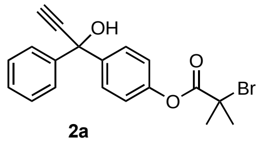

2a

4-(1-hydroxy-1-phenylprop-2-yn-1-yl)phenyl 2-bromo-2-methylpropanoate (2a). To a flame-dried 2-neck 50 mL RBF equipped with a stir bar was added **1** (773 mg, 3.45 mmol). The flask was evacuated and backfilled with N_2 three times. Anhydrous THF (20 mL) and then triethylamine (0.65 mL, 4.7 mmol) were added via syringe under N_2. α-bromoisobutyryl bromide (0.42 mL, 3.4 mmol) was added dropwise via syringe over 10 min under N_2 at room temperature. After stirring for 19 h, the reaction was diluted with EtOAc (100 mL), washed with DI water (100 mL), saturated aqueous $NaHCO_3$ (100 mL), and brine (50 mL). The organic layer was dried over $MgSO_4$, filtered, and concentrated. The crude yellow oil was purified by column chromatography on silica gel (5–30% EtOAc/hexanes) to yield the product as a pale yellow oil that solidified upon trituration with hexanes (1.01 g, 78%).

TLC (25% EtOAc/hexanes): $R_f = 0.57$

^{1}H NMR (400 MHz, $CDCl_3$) δ: 7.68 – 7.57 (m, 4H), 7.38 – 7.26 (m, 3H), 7.13 – 7.07 (m, 2H), 2.89 (s, 1H), 2.86 (s, 1H), 2.06 (s, 6H).

$^{13}C\{^1H\}$ NMR (101 MHz, $CDCl_3$) δ: 170.3, 150.4, 144.2, 142.5, 128.5, 128.2, 127.5, 126.1, 120.9, 86.2, 76.0, 74.0, 55.4, 30.7.

HRMS (FAB, *m/z*): calcd for $[C_{19}H_{17}BrO_3]^+$ $(M)^+$, 372.0361; found, 372.0372.

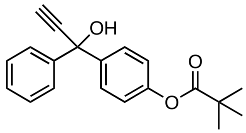

2b

4-(1-hydroxy-1-phenylprop-2-yn-1-yl)phenyl pivalate (2b). To a flame-dried 2-neck 100 mL RBF equipped with a stir bar was added **1** (922 mg, 4.11 mmol). The flask was evacuated and backfilled with N_2 three times. Anhydrous THF (30 mL) and subsequently triethylamine (0.80 mL, 5.7 mmol) was added via syringe under N_2. Pivaloyl chloride (0.58 mL, 4.7 mmol) was added dropwise via syringe over 10 min at room temperature. After stirring for 20 h, the reaction was diluted with 100 mL EtOAc, washed with 10% aqueous NH_4Cl (100 mL), saturated aqueous $NaHCO_3$ (100 mL) and brine (50 mL). The organic layer was dried over $MgSO_4$, filtered, and concentrated to a yellow oil. The crude material purified by column chromatography on silica gel (10–30% EtOAc/hexanes) to yield the product as a pale yellow solid (1.06 g, 83%).

TLC (25% EtOAc/hexanes): $R_f = 0.53$

^{1}H NMR (400 MHz, $CDCl_3$) δ: 7.64 – 7.57 (m, 4H), 7.37 – 7.27 (m, 3H), 7.05 – 7.00 (m, 2H), 2.88 (s, 1H), 2.86 (s, 1H), 1.35 (s, 9H).

$^{13}C\{^1H\}$ NMR (101 MHz, $CDCl_3$) δ: 177.1, 150.8, 144.3, 141.8, 128.5, 128.1, 127.3, 126.1, 121.4, 86.3, 75.8, 74.1, 39.2, 27.2.

HRMS (FAB, *m/z*): calcd for $[C_{20}H_{20}O_3]^+$ $(M)^+$, 309.1491; found, 309.1471.

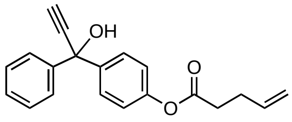

2c

4-(1-hydroxy-1-phenylprop-2-yn-1-yl)phenyl pent-4-enoate (2c). To a flame-dried 2-neck 50 mL RBF equipped with a stir bar was added **1** (307 mg, 1.37 mmol) and catalytic N,N-dimethylaminopyridine (10 mg, 0.08 mmol). The flask was evacuated and backfilled with N_2 three times. Anhydrous THF (20 mL) and subsequently triethylamine (0.23 mL, 1.6 mmol) was added via syringe under N_2. Pentenoic anhydride (0.28 mL, 1.5 mmol) was added dropwise via syringe over 10 min room temperature. After stirring for 22 h, the reaction was diluted with 100 mL EtOAc, washed with DI water (50 mL), saturated aqueous $NaHCO_3$ (50 mL) and brine (30 mL). The organic layer was dried over $MgSO_4$, filtered, and concentrated. The crude material purified by column chromatography on silica gel (0–30% EtOAc/hexanes) to yield the product as a pale yellow oil (371 mg, 88%).

TLC (25% EtOAc/hexanes): $R_f = 0.51$

^{1}H NMR (400 MHz, Acetone-d_6) δ: 7.69 – 7.62 (m, 4H), 7.37 – 7.30 (m, 2H), 7.28 – 7.22 (m, 1H), 7.10 – 7.05 (m, 2H), 5.92 (ddt, *J* = 16.9, 10.2, 6.5 Hz, 1H), 5.77 (s, 1H), 5.13 (dq, *J* = 17.2, 1.7 Hz, 1H), 5.03 (dq, *J* = 10.2, 1.4 Hz, 1H), 3.38 (d, *J* = 0.6 Hz, 1H), 2.67 (t, *J* = 7.3 Hz, 2H), 2.50 – 2.39 (m, 2H).

$^{13}C\{^1H\}$ NMR (101 MHz, Acetone-d_6) δ: 171.8, 151.1, 146.7, 144.4, 137.7, 128.9, 128.2, 127.9, 126.7, 122.1, 116.0, 87.8, 76.5, 74.0, 34.0.

HRMS (FAB, *m/z*): calcd for $[C_{20}H_{19}O_3]^+$ $(M+H)^+$, 307.1334; found, 307.1327.

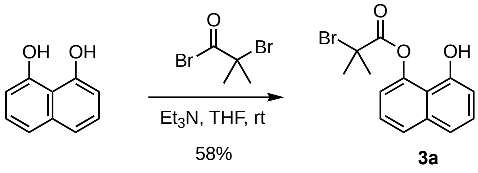

8-hydroxynaphthalen-1-yl 2-bromo-2-methylpropanoate (3a). To a flame-dried 2-neck 100 mL RBF equipped with a stir bar was added 1,8-dihydroxynaphthalene (2.31 g, 14.4 mmol). The flask was evacuated and backfilled with N_2 three times. Anhydrous THF (40 mL) and then triethylamine (2.60 mL, 18.6 mmol) were added via syringe under N_2, followed by the dropwise addition of α-bromoisobutyryl bromide (2.00 mL, 16.3 mmol) via syringe over 10 min at room temperature. After stirring for 19 h, the reaction was diluted with 100 mL EtOAc, washed with aqueous 10% NH_4Cl (2 x 100 mL), saturated aqueous $NaHCO_3$ (100 mL), and brine (50 mL). The organic layer was dried over $MgSO_4$, filtered, and concentrated. The crude material was dissolved in hot toluene (50 mL) and recrystallized in the dark to yield the product as grey crystals (2.57 g, 58%).

TLC (25% EtOAc/hexanes): $R_f = 0.49$

^1H NMR (400 MHz, $CDCl_3$) δ: 7.70 (dd, J = 8.3, 1.1 Hz, 1H), 7.44 – 7.38 (m, 2H), 7.32 (dd, J = 8.3, 7.6 Hz, 1H), 7.17 (dd, J = 7.6, 1.1 Hz, 1H), 7.06 (s, 1H), 6.85 (dd, J = 7.6, 1.1 Hz, 1H), 2.43 (s, 3H).

$^{13}C\{^1H\}$ NMR (101 MHz, $CDCl_3$) δ: 169.8, 151.6, 146.3, 137.0, 127.3, 127.0, 125.5, 120.6, 117.8, 117.0, 111.8, 55.5, 31.0.

HRMS (ESI, *m/z*): calcd for $[C_{14}H_{13}BrO_3]^+$ $(M+H)^+$, 309.0126; found, 309.0151.

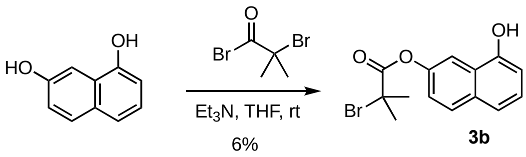

3b

8-hydroxynaphthalen-2-yl 2-bromo-2-methylpropanoate (3b). To a flame-dried 2-neck 100 mL RBF equipped with a stir bar was added 1,7-dihydroxynaphthalene (2.99 g, 18.7 mmol). The flask was evacuated and backfilled with N_2 three times. Anhydrous THF (60 mL) and subsequently triethylamine (3.40 mL, 24.4 mmol) was added via syringe under N_2. α-bromoisobutyryl bromide (2.25 mL, 18.5 mmol) was added dropwise via syringe over 10 min under N_2 at room temperature. After stirring for 17 h, the reaction was diluted with 150 mL EtOAc, washed with DI water (100 mL, aqueous layer turns pink), saturated aqueous $NaHCO_3$ (100 mL), and brine (50 mL). The organic layer was dried over $MgSO_4$, filtered, and concentrated onto celite. The material was partially purified by column chromatography on silica gel (10–100% EtOAc/hexanes), then product-containing fractions were loaded onto a plug of basic alumina and washed with 25% EtOAc/hex to remove diester side product, and lastly the product and its constitutional isomer were eluted with 5% MeOH/CH_2Cl_2. A second silica column was run (10–50% EtOAc/hexanes with 1% triethylamine) and then a third (25–100% 10–50% EtOAc/hexanes with 1% triethylamine) to finally yield the pure product as a grey solid (341 mg, 6%).

TLC (25% EtOAc/hexanes): $R_f = 0.45$

^{1}H NMR (400 MHz, Acetone-d_6) δ: 9.20 (br s, 1H), 7.99 (d, J = 2.5 Hz, 1H), 7.92 (d, J = 8.8 Hz, 1H), 7.44 (d, J = 8.3 Hz, 1H), 7.34 (d, J = 7.5 Hz, 1H), 7.31 (dd, J = 8.8, 2.5 Hz, 1H), 6.99 (dd, J = 7.5, 1.0 Hz, 1H), 2.13 (s, 6H).

^{13}C{^{1}H} NMR (101 MHz, Acetone-d_6) δ: 170.9, 153.7, 148.8, 133.9, 130.0, 127.2, 125.9, 121.7, 119.8, 113.8, 109.6, 57.2, 30.8.

HRMS (FAB, *m/z*): calcd for $[C_{14}H_{13}BrO_3]^+$ $(M)^+$, 308.0048; found, 308.0076.

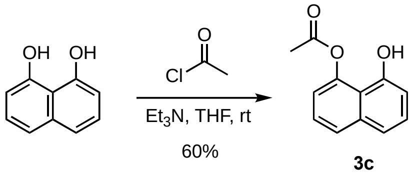

3c

8-hydroxynaphthalen-1-yl acetate (3c). To a flame-dried 2-neck 50 mL RBF equipped with a stir bar was added 1,8-dihydroxynaphthalene (1.01 g, 6.30 mmol). The flask was evacuated and backfilled with N_2 three times. Anhydrous THF (20 mL) and subsequently triethylamine (1.10 mL, 7.89 mmol) was added via syringe under N_2. Acetyl chloride (0.50 mL, 7.0 mmol) was added dropwise via syringe over 10 min at room temperature. After stirring for 3.5 h, the reaction was diluted with 100 mL EtOAc, washed with DI water (50 mL), 10% aqueous NH_4Cl (50 mL), and brine (50 mL). The organic layer was dried over $MgSO_4$, filtered, and concentrated. The crude material was recrystallized from toluene in the dark to yield the product as beige crystals (0.76 g, 60%).

TLC (25% EtOAc/hexanes): $R_f = 0.26$

^{1}H NMR (400 MHz, $CDCl_3$) δ: 7.70 (dd, *J* = 8.3, 1.1 Hz, 1H), 7.44 – 7.38 (m, 2H), 7.32 (dd, *J* = 8.3, 7.6 Hz, 1H), 7.17 (dd, *J* = 7.6, 1.1 Hz, 1H), 7.06 (s, 1H), 6.85 (dd, *J* = 7.6, 1.1 Hz, 1H), 2.43 (s, 3H).

$^{13}C\{^1H\}$ NMR (101 MHz, $CDCl_3$) δ: 168.8, 151.8, 146.0, 137.0, 127.2, 126.6, 125.6, 120.6, 118.6, 117.1, 111.5, 21.6.

HRMS (FAB, *m/z*): calcd for $[C_{12}H_{10}O_3]^+$ $(M)^+$, 202.0630; found, 202.0638.

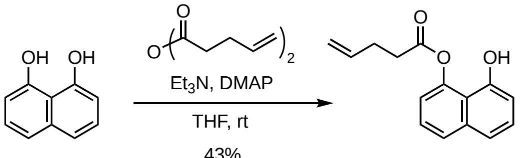

3d

8-hydroxynaphthalen-1-yl pent-4-enoate (3d). To a flame-dried 2-neck 50 mL RBF equipped with a stir bar was added 1,8-dihydroxynaphthalene (687 mg, 4.29 mmol) and catalytic N,N-dimethylaminopyridine (5.5 mg, 0.045 mmol). The flask was evacuated and backfilled with N_2 three times. Anhydrous THF (15 mL) and subsequently triethylamine (0.72 mL, 5.2 mmol) was added via syringe under N_2. Pentenoic anhydride (0.89 mL, 4.7 mmol) was added dropwise via syringe over 10 min room temperature. After stirring for 15 h, the reaction was diluted with 100 mL EtOAc, washed with DI water (50 mL), saturated aqueous $NaHCO_3$ (50 mL) and brine (30 mL). The organic layer was dried over $MgSO_4$, filtered, and concentrated. The crude material purified by column chromatography on silica gel (5–30% EtOAc/hexanes) and subsequently recrystallized from toluene to yield the product as colorless crystals (444 mg, 43%).

TLC (25% EtOAc/hexanes): $R_f = 0.56$

^{1}H NMR (400 MHz, $CDCl_3$) δ: 7.69 (dd, *J* = 8.2, 1.2 Hz, 1H), 7.44 – 7.37 (m, 2H), 7.33 (app t, *J* = 7.9 Hz, 1H), 7.16 (dd, *J* = 7.6, 1.2 Hz, 1H), 7.11 (d, *J* = 2.1 Hz, 1H), 6.86 (dd, *J* = 7.6, 1.2 Hz, 1H), 5.93 (ddt, *J* = 16.9, 10.1, 6.4 Hz, 1H), 5.19 (dq, *J* = 17.2, 1.5 Hz, 1H), 5.12 (dq, *J* = 10.2, 1.4 Hz, 1H), 2.87 – 2.77 (m, 2H), 2.63 – 2.53 (m, 2H).

^{13}C{^{1}H} NMR (101 MHz, $CDCl_3$) δ: 170.7, 151.9, 146.0, 137.0, 136.1, 127.2, 126.6, 125.6, 120.5, 118.6, 117.0, 116.5, 111.5, 34.1, 28.7.

HRMS (FAB, *m/z*): calcd for $[C_{15}H_{14}O_3]^+$ $(M)^+$, 242.0943; found, 242.0930.

General Procedure A for Naphthopyran Synthesis. Naphthopyrans were synthesized following the procedure by Zhao and Carreira.[28] To a flame-dried 2-neck round bottom flask equipped with a stir bar and reflux condenser was added the appropriate propargyl alcohol, naphthol, and a catalytic amount of pyridinium *p*-toluenesulfonate (PPTS). The flask was evacuated and backfilled with N_2 three times followed by the sequential addition of 1,2-dichloroethane and trimethyl orthoformate via syringe. The reaction was heated to reflux and stirred for the indicated amount of time. Upon completion, the reaction was cooled to room temperature, concentrated with celite, and purified by column chromatography on silica gel.

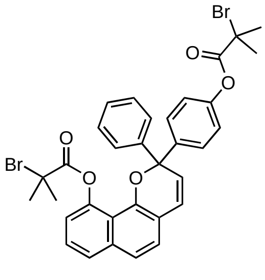

NP$_{10}$

4-(10-((2-bromo-2-methylpropanoyl)oxy)-2-phenyl-2H-benzo[h]chromen-2-yl)phenyl 2-bromo-2-methylpropanoate (NP$_{10}$). The title compound was prepared using General Procedure A with **3a** (283 mg, 0.915 mmol), **2a** (475 mg, 1.27 mmol) added as a solution in 1,2-dichloroethane, PPTS (22 mg, 0.088 mmol), trimethyl orthoformate (0.30 mL, 2.7 mmol), and 1,2-dichloroethane (10 mL) for 7 h. Purification by column chromatography on silica gel (5–40% EtOAc/hexanes) yielded the title compound as a pink foamy solid (322 mg, 53%).

TLC (25% EtOAc/hexanes): R_f = 0.57 (Merocyanine R_f = 0.50)

^{1}H NMR (400 MHz, CDCl$_3$) δ: 7.64 (dd, *J* = 8.3, 1.2 Hz, 1H), 7.56 – 7.50 (m, 2H), 7.46 – 7.35 (m, 4H), 7.35 – 7.27 (m, 3H), 7.17 (dd, *J* = 7.5, 1.2 Hz, 1H), 7.14 (d, *J* = 8.3 Hz, 1H), 7.11 – 7.05 (m, 2H), 6.66 (d, *J* = 9.6 Hz, 1H), 6.11 (d, *J* = 9.6 Hz, 1H), 2.04 (s, 6H), 1.55 (s, 3H), 1.54 (s, 3H).

^{13}C{^{1}H} NMR (101 MHz, CDCl$_3$) δ: 170.7, 170.2, 150.4, 147.4, 147.0, 144.4, 142.2, 137.1, 129.1, 128.6, 128.3, 128.2, 127.8, 127.2, 126.1, 125.6, 124.0, 121.6, 120.8, 119.5, 118.8, 117.5, 83.6, 57.1, 55.4, 30.7, 29.7, 29.6.

HRMS (ESI, *m/z*): calcd for $[C_{33}H_{29}Br_2O_5]^+$ $(M+H)^+$, 663.0382; found, 663.0399.

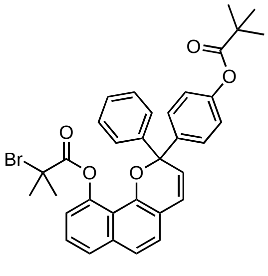

CON1

4-(10-((2-bromo-2-methylpropanoyl)oxy)-2-phenyl-2H-benzo[h]chromen-2-yl)phenyl pivalate (CON1). The title compound was prepared using General Procedure A with **3a** (181 mg, 0.585 mmol), **2b** (204 mg, 0.662 mmol), PPTS (8.0 mg, 0.032 mmol), trimethyl orthoformate (0.20 mL, 1.8 mmol), and 1,2-dichloroethane (9 mL) for 17 h. Purification by column chromatography on silica gel (10–60% CH_2Cl_2/hexanes) yielded the title compound as a pink foamy solid (219 mg, 62%).

TLC (25% EtOAc/hexanes): R_f = 0.66 (Merocyanine form R_f = 0.60)

^{1}H NMR (400 MHz, $CDCl_3$) δ: 7.64 (dd, *J* = 8.3, 1.2 Hz, 1H), 7.53 – 7.48 (m, 2H), 7.47 – 7.35 (m, 4H), 7.35 – 7.27 (m, 3H), 7.18 (dd, *J* = 7.5, 1.2 Hz, 1H), 7.13 (d, *J* = 8.3 Hz, 1H), 7.04 – 6.98 (m, 2H), 6.65 (d, *J* = 9.6 Hz, 1H), 6.11 (d, *J* = 9.6 Hz, 1H), 1.56 (s, 3H), 1.54 (s, 3H), 1.34 (s, 9H).

$^{13}C\{^1H\}$ NMR (101 MHz, $CDCl_3$) δ: 177.1, 170.7, 150.8, 147.4, 147.0, 144.5, 141.6, 137.1, 128.9, 128.7, 128.2, 128.1, 127.9, 127.2, 126.0, 125.5, 123.8, 121.6, 121.2, 119.5, 118.8, 117.5, 83.6, 57.1, 39.2, 29.7, 29.6, 27.2.

HRMS (ESI, *m/z*): calcd for $[C_{34}H_{32}BrO_5]^+$ $(M+H)^+$, 599.1433; found, 599.1441.

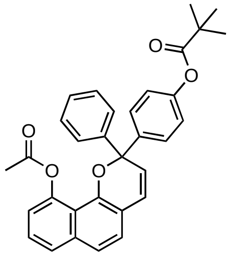
4

4-(10-acetoxy-2-phenyl-2H-benzo[h]chromen-2-yl)phenyl pivalate (4). The title compound was prepared using General Procedure A with **3c** (519 mg, 2.57 mmol), **2b** (905 mg, 2.93 mmol), PPTS (32.7 mg, 0.130 mmol), trimethyl orthoformate (0.70 mL, 6.4 mmol), and 1,2-dichloroethane (20 mL) for 19 h. The crude reaction mixture was filtered over basic alumina, eluted with EtOAc, and purification by column chromatography on silica gel (0–25% EtOAc/hexanes) yielded the title compound as pink foamy solid (466 mg, 37%).

TLC (25% EtOAc/hexanes): R_f = 0.47

^{1}H NMR (400 MHz, Acetone-d_6) δ: 7.69 (dd, *J* = 8.3, 1.2 Hz, 1H), 7.59 – 7.52 (m, 4H), 7.47 – 7.30 (m, 5H), 7.26 (d, *J* = 8.3 Hz, 1H), 7.14 – 7.08 (m, 3H), 6.83 (d, *J* = 9.7 Hz, 1H), 6.34 (d, *J* = 9.7 Hz, 1H), 1.68 (s, 3H), 1.32 (s, 9H).

<u>^{13}C{^{1}H} NMR (101 MHz, Acetone-*d*$_6$) δ:</u> 177.2, 170.4, 152.0, 148.1, 147.7, 145.5, 142.9, 138.0, 129.7, 129.4, 129.0, 128.9, 128.4, 127.3, 127.1, 126.3, 124.7, 122.24, 122.22, 121.1, 120.2, 118.3, 84.5, 39.7, 27.4, 20.8.

<u>HRMS (ESI, *m/z*):</u> calcd for [$C_{32}H_{29}O_5$]$^+$ (M+H)$^+$, 493.2015; found, 493.2005.

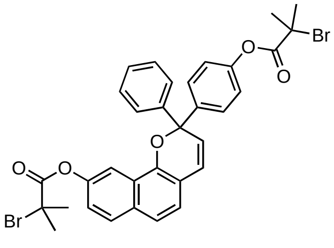
NP$_9$

4-(9-((2-bromo-2-methylpropanoyl)oxy)-2-phenyl-2H-benzo[h]chromen-2-yl)phenyl 2-bromo-2-methylpropanoate (NP$_9$). The title compound was prepared using General Procedure A with **3b** (308 mg, 0.997 mmol), **2a** (436 mg, 1.17 mmol), which was added as a solid, PPTS (34.5 mg, 0.137 mmol), trimethyl orthoformate (0.33 mL, 3.0 mmol), and 1,2-dichloroethane (10 mL) for 18 h. Purification by column chromatography on silica gel (5–40% EtOAc/hexanes) yielded the title compound as a pink foamy solid (246 mg, 37%).

<u>TLC (25% EtOAc/hexanes):</u> R$_f$ = 0.57 (Merocyanine R$_f$ = 0.50)

<u>^{1}H NMR (400 MHz, CDCl$_3$) δ:</u> 7.97 (d, *J* = 2.5 Hz, 1H), 7.76 (d, *J* = 8.9 Hz, 1H), 7.57 – 7.46 (m, 4H), 7.39 – 7.27 (m, 4H), 7.23 (dd, *J* = 8.9, 2.4 Hz, 1H), 7.16 (d, *J* = 8.4 Hz, 1H), 7.14 – 7.08 (m, 2H), 6.75 (d, *J* = 9.8 Hz, 1H), 6.17 (d, *J* = 9.7 Hz, 1H), 2.13 (s, 6H), 2.04 (s, 6H).

<u>^{13}C{^{1}H} NMR (101 MHz, CDCl$_3$) δ:</u> 170.5, 170.3, 150.2, 148.7, 147.5, 144.7, 142.8, 132.9, 129.5, 128.5, 128.4, 127.9, 127.8, 127.1, 125.0, 124.7, 123.9, 121.0, 120.8, 120.7, 116.2, 112.7, 83.3, 55.7, 55.4, 30.9, 30.7.

<u>HRMS (ESI, *m/z*):</u> calcd for [$C_{33}H_{29}Br_2O_5$]$^+$ (M+H)$^+$, 663.0382; found, 663.0390.

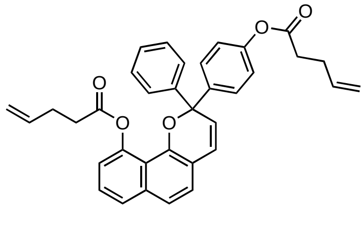

NP$_{10\text{-ene}}$

4-(10-(pent-4-enoyloxy)-2-phenyl-2H-benzo[h]chromen-2-yl)phenyl pent-4-enoate (NP$_{10\text{-ene}}$). The title compound was prepared using General Procedure A with **3d** (102 mg, 0.420 mmol), **2c** (148 mg, 0.483 mmol) added as a solution in 1,2-dichloroethane, PPTS (9.4 mg, 0.037 mmol), trimethyl orthoformate (0.14 mL, 1.3 mmol), and 1,2-dichloroethane (6 mL) for 2 h. Purification by column chromatography on silica gel (0–10% EtOAc with 1% triethylamine/hexanes) yielded the title compound as a dark orange-red oil (138 mg, 62%).

<u>TLC (25% EtOAc/hexanes):</u> R$_f$ = 0.57 (Merocyanine R$_f$ = 0.50)

<u>^{1}H NMR (400 MHz, CDCl$_3$) δ:</u> 7.60 (dd, *J* = 8.3, 1.2 Hz, 1H), 7.56 – 7.45 (m, 4H), 7.40 – 7.27 (m, 5H), 7.12 (d, *J* = 8.3 Hz, 1H), 7.08 – 6.98 (m, 3H), 6.66 (d, *J* = 9.7 Hz, 1H), 6.12 (d, *J* = 9.6 Hz, 1H), 5.89 (ddt, *J* = 16.8, 10.2, 6.4 Hz, 1H), 5.70 – 5.57 (m, 1H), 5.13 (dq, *J* = 17.1, 1.6 Hz, 1H), 5.07 (dq, *J* = 10.3, 1.4 Hz, 1H), 4.99 – 4.95 (m, 1H), 4.93 (dt, *J* = 2.6, 1.7 Hz, 1H), 2.65 (td, *J* = 7.3, 0.8 Hz, 2H), 2.49 (tdd, *J* = 7.6, 6.0, 1.1 Hz, 2H), 2.20 – 2.06 (m, 2H), 2.06 – 1.94 (m, 2H).

<u>^{13}C{^{1}H} NMR (101 MHz, CDCl$_3$) δ:</u> 172.6, 171.6, 150.4, 147.5, 146.6, 144.6, 142.1, 137.3, 136.9, 136.5, 129.0, 128.3, 128.2, 128.0, 127.8, 126.8, 126.1, 125.6, 124.1, 121.5, 121.3, 1220.2, 119.3, 117.3, 116.2, 115.5, 83.7, 33.8, 33.1, 29.1, 28.6.

<u>HRMS (FAB, *m/z*):</u> calcd for [$C_{35}H_{30}O_5$]$^+$ (M)$^+$, 530.2093; found, 530.2094.

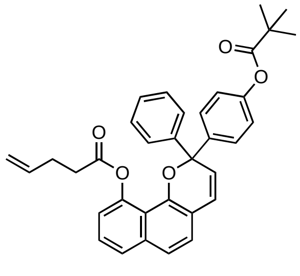

CON2

2-phenyl-2-(4-(pivaloyloxy)phenyl)-2H-benzo[h]chromen-10-yl pent-4-enoate (CON2). The title compound was prepared using General Procedure A with **3d** (180 mg, 0.743 mmol), **2b** (309 mg, 1.00 mmol) added as a solid, PPTS (9.6 mg, 0.038 mmol), trimethyl orthoformate (0.25 mL, 2.3 mmol), and 1,2-dichloroethane (6 mL) for 2 h. Purification by column chromatography on silica gel (0–10% EtOAc with 1% triethylamine/hexanes) yielded the title compound as a pink foamy solid (229 mg, 58%).

TLC (25% EtOAc/hexanes): $R_f = 0.66$

^{1}H NMR (400 MHz, Acetone-d_6) δ: 7.73 – 7.66 (m, 1H), 7.59 – 7.51 (m, 5H), 7.48 – 7.30 (m, 6H), 7.26 (dd, *J* = 8.3, 1.0 Hz, 1H), 7.15 – 7.07 (m, 3H), 6.83 (dd, *J* = 9.7, 1.1 Hz, 1H), 6.34 (dd, *J* = 9.7, 1.0 Hz, 1H), 5.75 – 5.60 (m, 1H), 5.01 – 4.88 (m, 2H), 2.17 – 2.07 (m, 4H), 1.32 (d, *J* = 0.7 Hz, 9H).

^{13}C{^{1}H} NMR (101 MHz, Acetone-d_6) δ: 177.1, 172.5, 152.0, 148.2, 147.7, 145.5, 142.8, 138.0, 137.9, 129.7, 129.6, 129.1, 129.0, 128.5, 127.4, 127.1, 126.4, 124.7, 122.30, 122.27, 121.2, 120.3, 118.4, 115.7, 84.6, 39.7, 33.7, 29.3, 27.4.

HRMS (FAB, *m/z*): calcd for $[C_{35}H_{33}O_5]^+$ $(M+H)^+$, 533.2328; found, 533.2345.

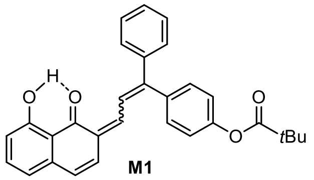

M1
Major

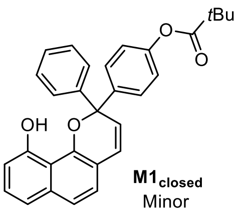

M1$_{closed}$
Minor

4-(3-(8-hydroxy-1-oxonaphthalen-2(1H)-ylidene)-1-phenylprop-1-en-1-yl)phenyl pivalate (M1). Lithium diisopropylamine was freshly prepared in a flame-dried 25 mL round bottom flask. Anhydrous THF (7 mL) and diisopropylamine (0.50 mL, 3.5 mmol) were added via syringe under N_2. The flask was cooled to –78 °C and n-butyllithium (2.5 M in hexanes, 1.4 mL, 3.5 mmol) was added via syringe under N_2. The reaction was stirred for 2 h. To a separate flame dried 100 mL 2-neck round bottom flask equipped with a stir bar was added **4** (210 mg, 0.426 mmol) and the vessel was evacuated and backfilled with N_2 three times. Anhydrous THF (10 mL) was added via syringe under N_2, the solution was cooled to –78 °C, and LDA solution (1.0 mL, 0.39 mmol) was added dropwise via syringe, upon which the coral pink solution immediately turned yellow. After 2 h, the reaction was removed from the cooling bath and immediately diluted with EtOAc (100 mL) and 10% aqueous NH_4Cl solution (120 mL). Upon dilution, the organic layer initially becomes deep indigo in color, but the organic layer becomes a deep burgundy red color upon washing with aqueous acid. The organic layer was washed with brine (50 mL), dried over Na_2SO_4, filtered, and concentrated. Purification by column chromatography on silica gel (0–25% EtOAc/hexanes) yielded the product as a red foamy solid (80.3 mg, 46%). The product is a mixture of merocyanine stereoisomers that readily interconvert and contains ~10% ring-closed naphthopyran as a minor product based on integrations of the hydroxyl resonances in the ^1H NMR spectrum measured in acetonitrile-d_3.

TLC (25% EtOAc/hexanes): R_f = 0.66, 0.58 (stereoisomers)

^1H NMR (400 MHz, acetone-d_6) δ: 13.63 (s, 0.04H, -O*H*), 13.61 (s, 0.04H, -O*H*), 13.322 (s, 0.2H, -O*H*), 13.319 (s, 0.2H, -O*H*), 9.34 (s, 0.01H, -O*H*, **M1$_{closed}$**), 8.76 (d, *J* = 12.2 Hz, 0.09H), 8.75 (d, *J* = 12.3 Hz, 0.09H), 7.85 – 6.59 (m, 16H), 6.33 (d, *J* = 9.9 Hz, 0.03H, **M1$_{closed}$**) 1.40 – 1.30 (m, 9H).

^1H NMR (400 MHz, acetonitrile-d_3) δ: 13.60 (s, 0.2H, -O*H*), 13.58 (s, 0.2H, -O*H*), 13.24 (s, 0.5H, -O*H*), 9.25 (s, 0.1H, -O*H*, **M1$_{closed}$**), 8.67 (d, *J* = 12.1 Hz, 0.2H), 8.64 (d, *J* = 12.2 Hz, 0.2H), 7.69 – 6.55 (m, 16H), 6.25 (d, *J* = 9.8 Hz, 0.1H, **M1$_{closed}$**), 1.38 – 1.30 (m, 9H).

$^{13}C\{^1H\}$ NMR (101 MHz, Acetone-d_6) δ: 189.30, 189.26, 176.13, 176.12, 164.5, 164.2, 163.8, 157.5, 155.82, 155.78, 155.7, 152.7, 152.6, 152.0, 146.8, 141.4, 141.2, 140.1, 140.0, 139.83, 139.79, 138.82, 138.80, 138.78, 138.6, 138.4, 136.70, 136.67, 136.65, 136.62, 135.8, 132.4, 132.1, 132.0, 131.3, 131.0, 130.93, 130.88, 130.84, 130.82, 130.80, 130.0, 129.9, 129.8, 129.6, 129.2, 128.9, 128.8, 128.7, 128.63, 128.57, 128.5, 128.4, 128.2, 126.8, 126.5, 126.2, 125.1, 125.0, 124.8, 124.12, 124.07 123.6, 123.54, 123.51, 122.5, 122.3, 122.1, 121.91, 121.86, 121.84, 121.79, 121.7, 119.20, 119.17, 119.13, 119.10, 118.5, 116.34, 116.30, 116.24, 116.20, 116.0, 115.9, 115.4, 38.83, 38.80, 26.5, 26.42, 26.38.

HRMS (ESI, *m/z*): calcd for $[C_{30}H_{27}O_4]^+$ $(M+H)^+$, 451.1909; found, 451.1921

General Procedure B for the Synthesis of Poly(Methyl Acrylate) (PMA) Polymers Incorporating a 2*H*-Naphthopyran. Polymers were synthesized by controlled radical polymerization following the procedure by Nguyen *et al*.[29] A flame-dried Schlenk flask was charged with freshly cut 20 G copper wire (2 cm), initiator, DMSO, and methyl acrylate. The flask was sealed and the solution was degassed via three freeze-pump-thaw cycles, then backfilled with nitrogen and warmed to room temperature. Me_6TREN was added via microsyringe and the reaction was stirred at room temperature for the indicated amount of time. Upon completion of the polymerization, the flask was opened to atmosphere and diluted with a minimal amount of CH_2Cl_2. The polymer was precipitated 3x into methanol cooled with dry ice and then dried under vacuum to afford the polymer.

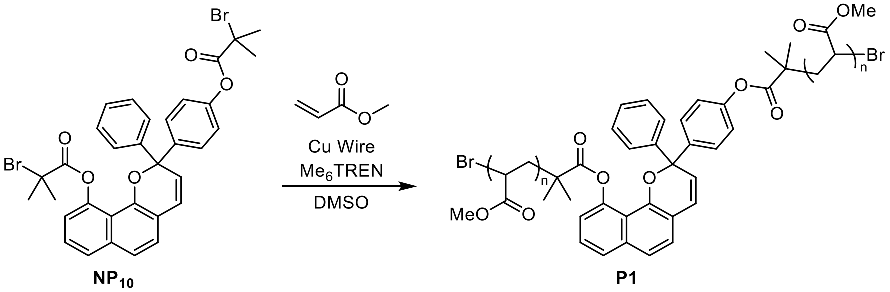

Polymer **P1.** Synthesized using General Procedure B with initiator **NP₁₀** (14.0 mg, 0.021 mmol), methyl acrylate (6.8 mL, 76 mmol), DMSO (6.8 mL), and Me_6TREN (28 µL, 0.10 mmol). Polymerization for 5 h provided the title polymer as a tacky orange solid (1.6 g, 25%). M_n = 178 kg/mol, $Đ$ = 1.13.

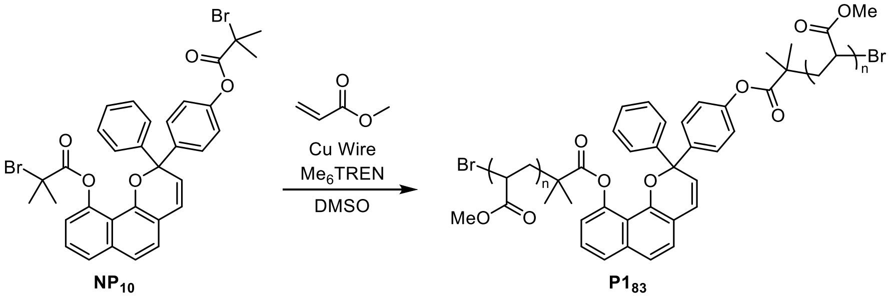

Polymer **P1$_{83}$.** Synthesized using General Procedure B with initiator **NP$_{10}$** (16.7 mg, 0.0251 mmol), methyl acrylate (2.6 mL, 29 mmol), DMSO (2.6 mL), and Me$_6$TREN (34 µL, 0.13 mmol). Polymerization for 2.5 h provided the title polymer as a tacky orange solid (440 mg, 25%). M_n = 83.1 kg/mol, $Đ$ = 1.15.

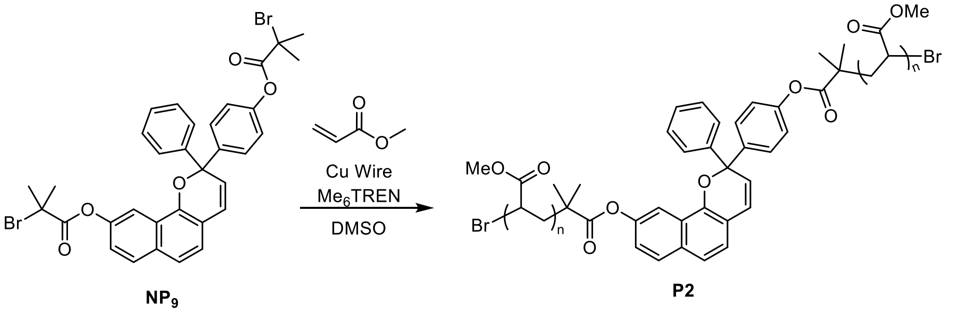

Polymer **P2.** Synthesized using General Procedure B with initiator **NP$_9$** (13.9 mg, 0.0209 mmol), methyl acrylate (6.7 mL, 74 mmol), DMSO (6.7 mL), and Me$_6$TREN (30 µL, 0.11 mmol). Polymerization for 4.5 h provided the title polymer as a tacky orange solid (2.5 g, 39%). M_n = 174 kg/mol, $Đ$ = 1.06.

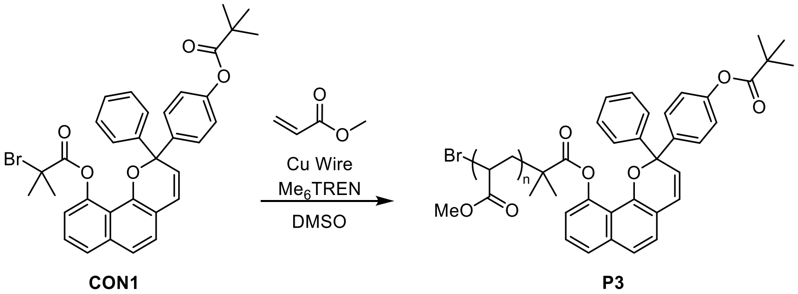

Polymer **P3.** Synthesized using General Procedure B with initiator **CON1** (9.1 mg, 0.015 mmol), methyl acrylate (5.3 mL, 59 mmol), DMSO (5.3 mL), and Me$_6$TREN (20 µL, 0.075 mmol).

Polymerization for 3 h provided the title polymer as a tacky orange solid (1.2 g, 24%). M_n = 183 kg/mol, $Đ$ = 1.07.

Characterization of Linear PMA Polymers.

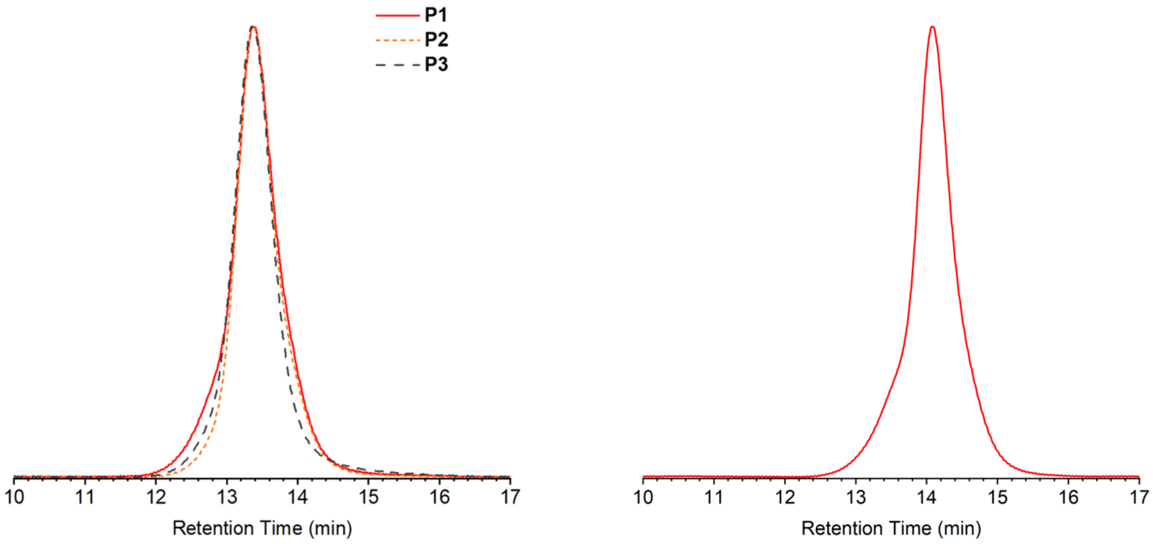

Figure 2.13. GPC traces (refractive index response) normalized to peak height for **P1**, **P2**, and **P3** (left), and **P1$_{83}$** (right).

(a) **NP$_{10}$**, ^{1}H (400 MHz, acetone-d_6)

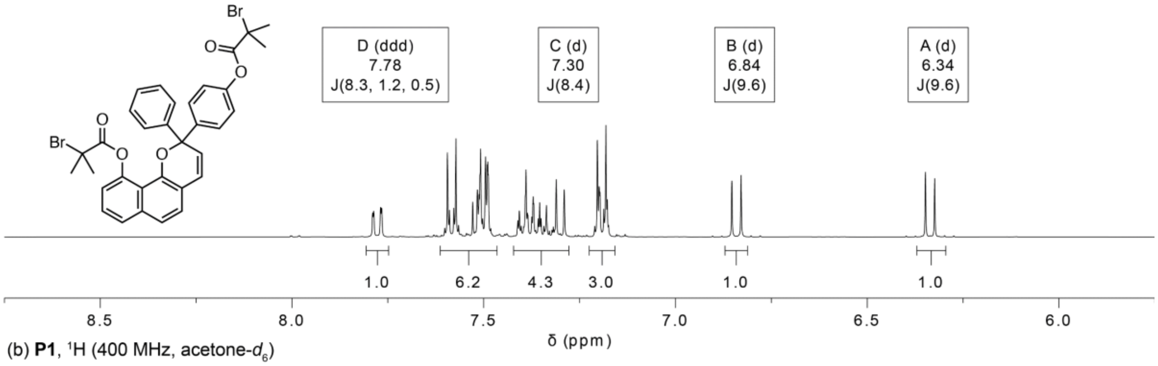

(b) **P1**, ^{1}H (400 MHz, acetone-d_6)

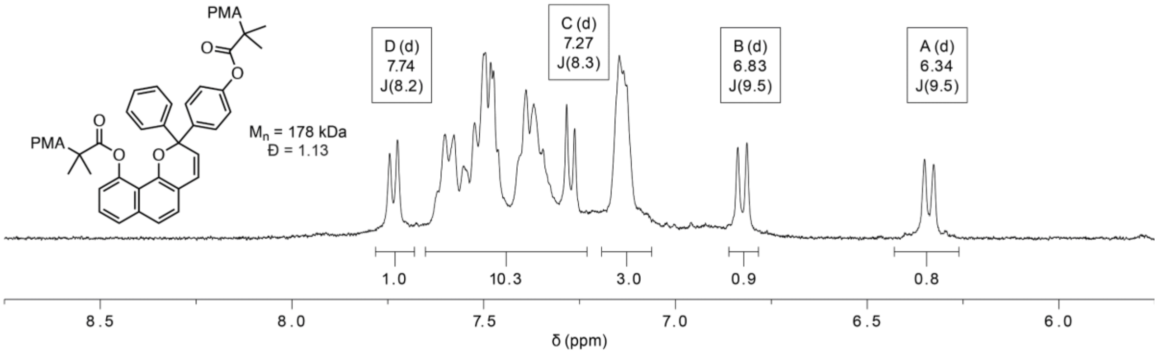

Figure 2.14. Partial ^{1}H NMR spectra of (a) small molecule initiator **NP$_{10}$**, and (b) polymer **P1** demonstrating successful incorporation of the initiator into the polymer chain.

III. Preparation of PDMS Materials

PDMS materials incorporating naphthopyran (1.5 wt%) were prepared following previously reported procedures using the two-part Sylgard® 184 elastomer kit (Dow Corning).[3,26] PDMS films approximately 0.5 mm thick were cut into 8 mm diameter disks using a hole punch unless otherwise specified.

General Procedure for Preparation of PDMS Materials. A representative procedure is provided for the preparation of $\mathbf{PDMS_{active}}$ incorporiating naphthopyran crosslinker $\mathbf{NP_{10\text{-}ene}}$. Naphthopyran crosslinker **NP10-ene** (30.4 mg) was dissolved in xylene (0.3 mL) in a 20 mL scintillation vial. Sylgard® 184 prepolymer base (1.93 g) was added and the contents were thoroughly mixed in a vortex mixer with intermittent gentle heating to form a homogeneous, orange dispersion. Sylgard® 184 curing agent (0.193 g) was added and the contents were mixed thoroughly using a vortex mixer. The mixture was pipetted onto a clean 5 cm x 5 cm delrin plate, which was placed inside a vacuum chamber and evacuated under high vacuum (~30 mTorr) for 3 h. The delrin plate was then transferred to an oven and cured at 80 °C overnight. After curing, the plate was removed from the oven and the PDMS film was peeled off and either cut into strips with a razor blade or cut into uniform 8 mm circles using a hole punch. A similar procedure was followed for preparation of $\mathbf{PDMS_{control}}$ using **CON2**. A sample of PDMS without any additional naphthopyran was also prepared similarly as a blank. PDMS samples containing naphthopyran were irradiated with blue light (470 nm) for 30 min to reduce initial coloration.

IV. DFT Calculations (CoGEF)

CoGEF calculations were performed using Spartan ′18 Parallel Suite according to previously reported methods.[16,17] Ground state energies were calculated using DFT at the B3LYP/6-31G* level of theory. For each mechanophore, the equilibrium conformations of the unconstrained molecule was initially calculated using molecular mechanics (MMFF) followed by optimization of the equilibrium geometries using DFT (B3LYP/6-31G*). Starting from the equilibrium geometry of the unconstrained molecules (energy = 0 kJ/mol), the distance between the terminal methyl groups of the truncated structures was increased in increments of 0.05 Å and the energy was minimized at each step. The maximum force associated with the mechanochemical reaction was calculated from the slope of the curve immediately prior to bond cleavage. CoGEF results are shown in Figure 2.6 for a truncated model reflecting the mechanophore in **P1**, while the results for a truncated model reflecting the mechanophore in **P2** with attachment at the 9-position of the naphthopyran are illustrated below in Figure 2.15. In contrast to the C–O bond scission reaction predicted for the naphthopyran in **P1**, the naphthopyran in **P2** is predicted to undergo cleavage of the terminal C–C bond upon full extension.

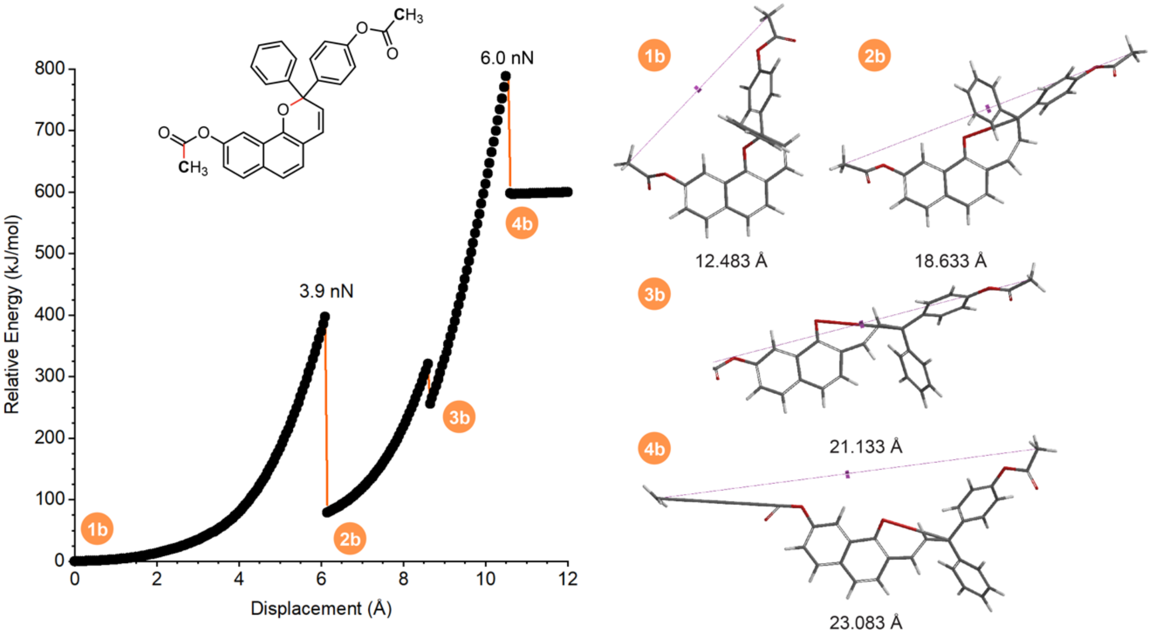

Figure 2.15. DFT calculations using the constrained geometries simulate external force (CoGEF) method at the B3LYP/6-31G* level of theory for a truncated model reflecting the mechanophore in polymer **P2**. CoGEF calculations predict the ring-opening reaction with an F_{max} value of 3.9 nN followed by further elongation that results in C–C bond scission at a predicted F_{max} value of 6.0 nN. The corresponding computed structures at various points of elongation are shown at right along with the associated constraint distance between the terminal methyl groups.

V. Details for Photoirradiation and Sonication Experiments

In order to continuously monitor reaction progress by UV-vis absorption spectroscopy, a previously reported experimental setup[5,12] was assembled using a peristaltic pump to transport solution from the reaction vessel through a quartz flow cell in a UV-vis spectrometer and return the solution to the reaction vessel. The flow rate through the system was maintained at 8 mL/min, corresponding to a setting of 50 RPM on the peristaltic pump at the selected occlusion. The UV-vis spectrometer was programmed to acquire either full spectra or absorbance at predefined wavelengths at regular time intervals. Absorbance measurements at wavelengths of 470, 485, 510 nm, and 700 nm were acquired every 10 s during continuous photoirradiation or sonication of polymer solutions. The absorbance values measured at 700 nm were subtracted from the absorbance values monitored at 470, 485, or 510 nm at each time point to account for drift during the experiments. The two traces in Figure 2.1b are normalized to their respective maximum absorbance values.

General Procedure for Sonication Experiments. A sonication vessel was placed onto the sonication probe and allowed to cool under a stream of N_2. The vessel was charged with THF, which contained 30 mM BHT (19.0 mL) to avoid decomposition side reactions resulting from free radicals generated during sonication.[30] An additional 6.2 mL of stabilized THF was pumped into the dead space of the circulatory setup. Teflon inlet and outlet tubes were inserted into the solution in the sonication vessel through punctured septa, and the pump was engaged to start the flow of solution through the system. The sonication vessel was submerged in an ice bath and the solution was sparged with N_2 for 30 min. The system was then maintained under an inert atmosphere for the duration of sonication. Continuous sonication at 20 kHz (8.77 ± 0.19 W/cm^2) was initiated and run for approximately 5 min to allow the temperature inside the reaction vessel to equilibrate to 15–20 °C, as measured by a thermocouple inserted into the solution (Digi-Sense EW-91428-02 thermometer with Digi-Sense probe EW-08466-83). Separately, a concentrated solution of polymer (1.0 mL, 52.4 mg/mL in stabilized THF) was sparged with N_2 for 30 min. This solution was then injected into the sonication vessel to provide a total system volume of 26.2 mL (2.0 mg/mL of polymer) and reaction progress was monitored by UV-vis absorption spectroscopy. Sonication intensity was calibrated via the literature method.[31] The entire system was kept in the dark for the duration of the experiment.

General Procedure for Photoirradiation Experiments. To monitor thermal reversion of the photochemically generated merocyanine, a two-sided quartz cuvette was charged with a solution of the polymer in THF (2.0 mg/mL, 1.0 mL, with 1 mM BHT) and then exposed to a UV light source (λ = 311 nm) positioned 2 in away for either 10 s or 10 min (see Figure 2.4). The cuvette was immediately placed into the spectrometer and absorption was monitored over time. To monitor the photochemical ring-opening reaction, a four-sided quartz cuvette was fitted with a septum with holes for inlet and outlet tubes. The cuvette was charged with a solution of the polymer in THF (2.0 mg/mL, 3.0 mL, with 1 mM BHT). An additional 6.2 mL of polymer solution was pumped into the dead space of the circulatory setup. Teflon inlet and outlet tubes were inserted into the solution in the cuvette through the septum and the pump was engaged to start the flow of solution through the system. Photoirradiation experiments were performed at room temperature (19–22 °C). The cuvette was then exposed to a UV light source (λ = 311 nm) positioned 2 in away. The total volume of the apparatus was 9.2 mL, with 3.0 mL contained in the cuvette. At any given time, only 3.0 mL of solution (out of the total 9.2 mL) was inside of the cuvette and exposed to UV irradiation. The entire system was protected from outside light for the duration of the experiment.

VI. Description of Control Experiments

Sonication of lower molecular weight polymer $\mathbf{P1_{83}}$. To explore whether a persistent colored species is still generated at lower forces than those experienced by **P1** (M_n = 178 kDa, $Đ$ = 1.13), a lower molecular weight PMA polymer with the same chain-centered mechanophore was synthesized ($\mathbf{P1_{83}}$, M_n = 83.1 kDa, $Đ$ = 1.15). $\mathbf{P1_{83}}$ was subjected to ultrasound-induced mechanical force for 2 h under identical conditions as those used for **P1**, and then the solution was monitored for 5 h after cessation of ultrasound. As shown below in Figure 2.16, minimal reversion is observed after sonication was stopped as evidenced by the nearly constant absorbance monitored at 470 and 510 nm. These results indicate that at lower forces transduced by shorter polymer chains,[32] generation of the permanent merocyanine species is still nearly exclusively observed. Note that only partial conversion is achieved after sonication for 2 h due to the slower reaction kinetics compared to that of **P1**.

Sonication of chain-end functional control polymer P3. To confirm that the ring-opening and ester C(O)–O cleavage reactions observed for **P1** containing a chain-centered 2*H*-naphthopyran mechanophore were due to mechanical force, a chain-end functional control polymer (**P3**) was synthesized and exposed to ultrasound-induced mechanical force under identical conditions. As shown in Figure 2.2, no changes in absorption were detected during sonication of chain-end functional control polymer **P3**, supporting that the ring-opening reaction is mechanically mediated.[33] In order to rule out that the ester C(O)–O cleavage is a thermally or otherwise non-mechanically mediated process, a second control experiment was devised. Chain-end functional control polymer **P3** was first irradiated with UV light (311 nm, 5 min) as a 52.4 mg/mL solution, and subsequently injected into the sonication vessel and subjected to continuous ultrasonication as described above. As shown below in Figure 2.17, the photochemically generated merocyanine steadily reverts during

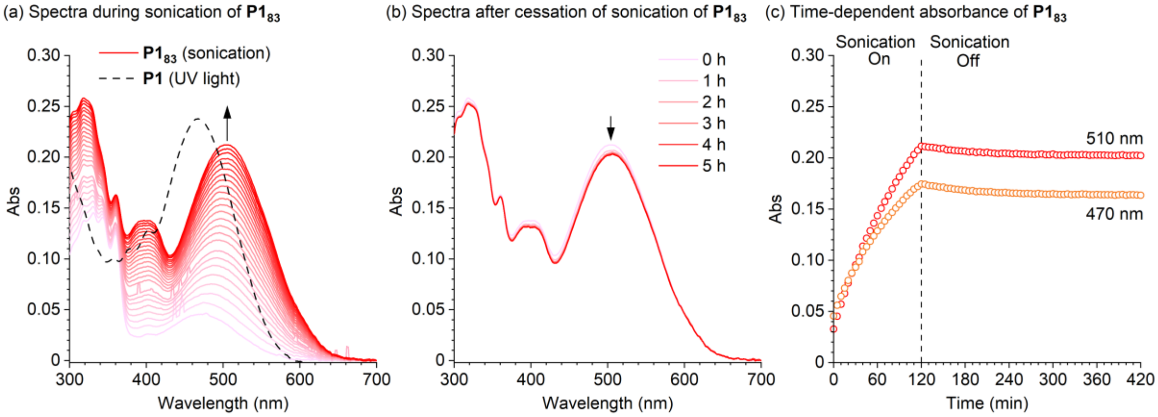

Figure 2.16. Characterization of ultrasound-induced mechanical activation and subsequent thermal reversion for a lower molecular weight polymer (**P1$_{83}$**) with a chain-centered 2H-NP mechanophore analogous to **P1**. (a) UV-vis absorption spectra acquired at regular intervals during ultrasound-induced mechanical activation of **P1$_{83}$** (pink and red solid traces) exhibit an increase in visible absorption that is significantly bathochromically shifted compared to the photochemical merocyanine product. Note that only partial conversion is achieved after sonication for 2 h. The absorption spectrum of **P1** after irradiation with UV light (311 nm, 10 min) is included for comparison with a λ_{max} of 470 nm (black dashed trace). (b,c) Spectra and time-dependent absorbance at 470 and 510 nm acquired over a period of 5 h after cessation of ultrasound illustrating minimal thermal reversion.

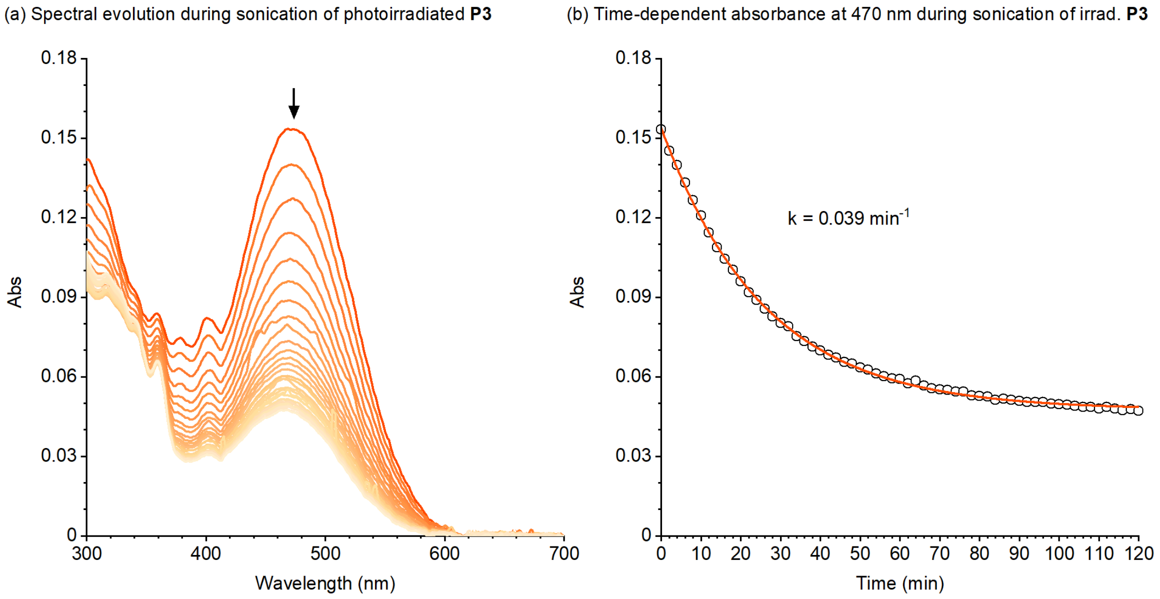

Figure 2.17. Sonication of chain-end control polymer **P3** after initial photochemical activation with UV light does not result in a permanent merocyanine. A solution of **P3** was irradiated with UV light (311 nm, 5 min) and subsequently subjected to ultrasound. In addition, no bathochromic shift in λ_{max} is observed, which would occur upon ester C(O)–O bond cleavage.

sonication as evidenced by the attenuation of visible absorption. In addition, a shift in λ_{max} is not observed, indicating that the C(O)–O ester bond is not cleaved.

VII. Kinetic Analysis

Determination of reaction kinetics from UV-vis spectroscopy. The kinetics of mechanochemical product formation, or thermal ring-closure after UV irradiation, was evaluated by fitting time-dependent absorbance traces at λ_{max} to first-order exponential decay using OriginPro 2020. For tracking mechanochemical product formation, the data is fit to eq. 2.1:

$$A(t) = A\left(1 - e^{-kt}\right) + c \qquad (2.1)$$

For tracking thermal ring-closure (UV-vis) or ultrasound-induced mechanical chain scission (GPC-RI), the time-dependent signal is fit to eq. 2.2:

$$A(t) = A\left(e^{-kt}\right) + c \qquad (2.2)$$

Determination of polymer chain scission kinetics from GPC measurements. To determine relative rates of polymer chain scission, sonication experiments were performed on **P1** and **P2**, during which aliquots (1 mL) were taken at regular time intervals for GPC analysis. Aliquots were removed from the sonication reactions via a N_2-flushed syringe during continuous sonication as described in section V, filtered through a 0.45 μm PTFE syringe filter, and submitted for GPC analysis. GPC traces for the ultrasound-induced chain scission of **P1** and **P2** are shown in Figure 2.18. GPC traces were normalized by area and the rate of chain scission was determined by plotting the attenuation of the RI response at the retention time (t_R) corresponding to the initial polymer peak as a function of sonication time. The time dependent GPC-RI response is fit to eq. 2.2 to determine the rate of chain scission.[34]

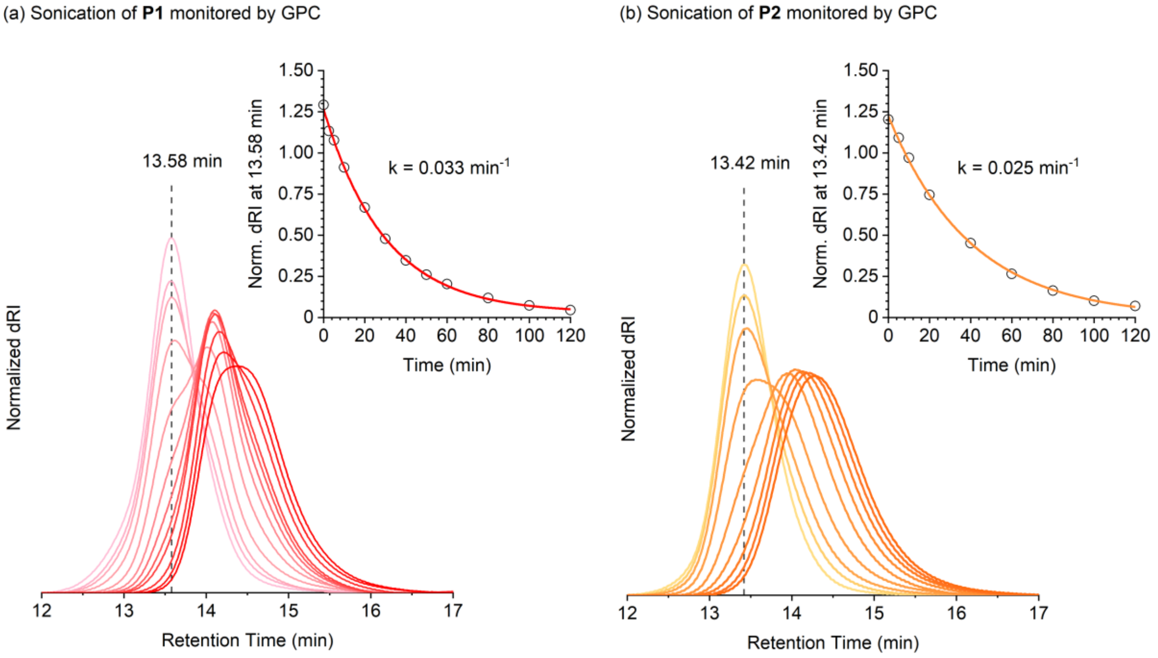
(a) Sonication of **P1** monitored by GPC

(b) Sonication of **P2** monitored by GPC

Figure 2.18. Ultrasound-induced mechanical chain cleavage of **P1** and **P2** monitored by GPC. (a) The rate of chain scission for **P1** determined from time-dependent attenuation of the RI signal at t_R = 13.58 min was found to be 0.033 min^{-1}. (b) The rate of chain scission for **P2** was found to be 0.025 min^{-1} by monitoring the RI signal at t_R = 13.42 min.

VIII. Characterization of Activation and Fading in PDMS Materials

PDMS films were activated mechanically either manually in tension or by repeated strikes with a hammer with the film placed between sheets of weigh paper on a hard flat surface, or photochemically by irradiation with UV light (λ_{max} = 365 nm). Films were placed between two vertical glass slides and photographed against a white background. Digital images were acquired in RAW mode with a Nikon D3200 DSLR camera. Images were cropped and standardized to a white balance temperature of 5300 and tint of +34 and an exposure of +1.50 in Adobe Photoshop using the Adobe Color profile. Reflectance measurements were performed to spectroscopically characterize the color of the PDMS materials. Spectra were acquired using an integrating sphere accessory to account for variation in surface roughness and scattering. Samples were loaded against a black sample holder. Reflectance spectra were normalized by defining the maximum and minimum value between 450 and 800 nm as 1 and 0, respectively (see Figure 2.19). In order to make a clear comparison to solution-phase absorption data, reflectance data are plotted in Figure 2.10 as the inverse, *i.e.*, "1 − norm. reflectance".

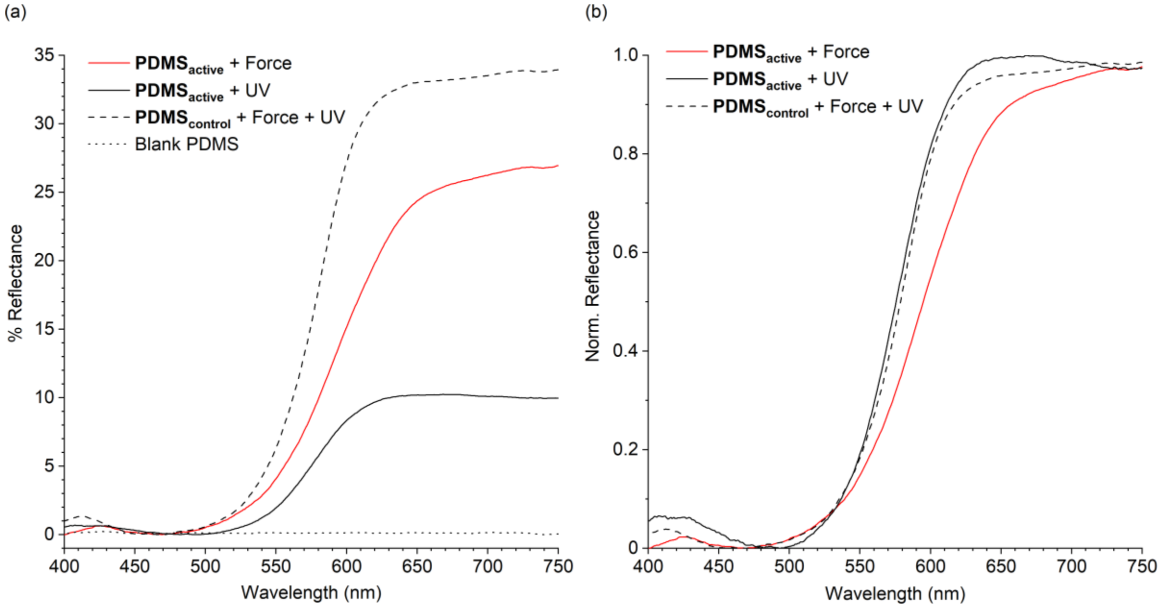

Figure 2.19. (a) UV-vis reflectance spectra acquired using an integrating sphere for samples of **PDMS$_{\text{active}}$** and **PDMS$_{\text{control}}$** after being subjected to combinations of mechanical force by repeated hammering and/or irradiation with UV light (365 nm). These are the same spectra depicted in Figure 2.12. The reflectance spectrum of a blank PDMS sample that does not contain naphthopyran is also shown. (b) The reflectance spectra shown in panel (a) after normalization to define the maximum value between 450–800 nm as 1.

References

(1) Hepworth, J. D.; Heron, B. M. Photochromic Naphthopyrans. Photochromic Naphthopyrans. In *Functional Dyes*; Elsevier Science, 2006; pp 85–135.

(2) Nigel Corns, S.; Partington, S. M.; Towns, A. D. Industrial Organic Photochromic Dyes. *Coloration Technology* **2009**, *125*, 249–261.

(3) Robb, M. J.; Kim, T. A.; Halmes, A. J.; White, S. R.; Sottos, N. R.; Moore, J. S. Regioisomer-Specific Mechanochromism of Naphthopyran in Polymeric Materials. *J. Am. Chem. Soc.* **2016**, *138*, 12328–12331.

(4) Versaw, B. A.; McFadden, M. E.; Husic, C. C.; Robb, M. J. Designing Naphthopyran Mechanophores with Tunable Mechanochromic Behavior. *Chem. Sci.* **2020**, *11*, 4525–4530.

(5) McFadden, M. E.; Robb, M. J. Force-Dependent Multicolor Mechanochromism from a Single Mechanophore. *J. Am. Chem. Soc.* **2019**, *141*, 11388–11392.

(6) Kosuge, T.; Zhu, X.; Lau, V. M.; Aoki, D.; Martinez, T. J.; Moore, J. S.; Otsuka, H. Multicolor Mechanochromism of a Polymer/Silica Composite with Dual Distinct Mechanophores. *J. Am. Chem. Soc.* **2019**, *141*, 1898–1902.

(7) Kim, G.; Lau, V. M.; Halmes, A. J.; Oelze, M. L.; Moore, J. S.; Li, K. C. High-Intensity Focused Ultrasound-Induced Mechanochemical Transduction in Synthetic Elastomers. *Proc Natl Acad Sci USA* **2019**, *116*, 10214–10222.

(8) Barber, R. W.; McFadden, M. E.; Hu, X.; Robb, M. J. Mechanochemically Gated Photoswitching: Expanding the Scope of Polymer Mechanochromism. *Synlett* **2019**, *30*, 1725–1732.

(9) Sagara, Y.; Karman, M.; Verde-Sesto, E.; Matsuo, K.; Kim, Y.; Tamaoki, N.; Weder, C. Rotaxanes as Mechanochromic Fluorescent Force Transducers in Polymers. *J. Am. Chem. Soc.* **2018**, *140*, 1584–1587.

(10) Qian, H.; Purwanto, N. S.; Ivanoff, D. G.; Halmes, A. J.; Sottos, N. R.; Moore, J. S. Fast, Reversible Mechanochromism of Regioisomeric Oxazine Mechanophores: Developing in Situ Responsive Force Probes for Polymeric Materials. *Chem* **2021**, *7*, 1080–1091.

(11) Berkowski, K. L.; Potisek, S. L.; Hickenboth, C. R.; Moore, J. S. Ultrasound-Induced Site-Specific Cleavage of Azo-Functionalized Poly(Ethylene Glycol). *Macromolecules* **2005**, *38*, 8975–8978.

(12) May, P. A.; Munaretto, N. F.; Hamoy, M. B.; Robb, M. J.; Moore, J. S. Is Molecular Weight or Degree of Polymerization a Better Descriptor of Ultrasound-Induced Mechanochemical Transduction? *ACS Macro Lett.* **2016**, *5*, 177–180.

(13) Görner, H.; Chibisov, A. K. Photoprocesses in 2,2-Diphenyl-5,6-Benzo(2H)Chromene. *J. Photochem. Photobiol. A: Chem.* **2002**, *149*, 83–89.

(14) Zhao, W.; Carreira, E. M. Oligothiophene-Linked Bisnaphthopyrans: Sequential and Temperature- Dependent Photochromism. *Chem. Eur. J.* **2007**, *13*, 2671–2688.

(15) Lu, X.; Dong, Q.; Dong, X.; Zhao, W. Synthesis and Sequential Photochromism of Thiophene-Linked Bis-Pyrans. *Tetrahedron* **2015**, *71*, 4061–4069.

(16) Beyer, M. K. The Mechanical Strength of a Covalent Bond Calculated by Density Functional Theory. *J. Chem. Phys.* **2000**, *112*, 7307–7312.

(17) Klein, I. M.; Husic, C. C.; Kovács, D. P.; Choquette, N. J.; Robb, M. J. Validation of the CoGEF Method as a Predictive Tool for Polymer Mechanochemistry. *J. Am. Chem. Soc.* **2020**, *142*, 16364–16381.

(18) Karman, M.; Verde-Sesto, E.; Weder, C. Mechanochemical Activation of Polymer-Embedded Photoluminescent Benzoxazole Moieties. *ACS Macro Lett.* **2018**, *7*, 1028–1033.

(19) Ohto, Y.; Shizuka, H.; Sekiguchi, S.; Matsui, K. The Photo-Fries Rearrangement of Aryloxy-1,3,5-Triazines. *BCSJ* **1974**, *47*, 1209–1214.

(20) Crouse, D. J.; Hurlbut, S. L.; Wheeler, D. M. S. Photo Fries Rearrangements of 1-Naphthyl Esters in the Synthesis of 2-Acylnaphthoquinones. *J. Org. Chem.* **1981**, *46*, 374–378.

(21) Guo, Z.-Q.; Chen, W.-Q.; Duan, X.-M. Highly Selective Visual Detection of Cu(II) Utilizing Intramolecular Hydrogen Bond-Stabilized Merocyanine in Aqueous Buffer Solution. *Org. Lett.* **2010**, *12*, 2202–2205.

(22) Martins, C. I.; Coelho, P. J.; Carvalho, L. M.; Oliveira-Campos, A. M. F. First Report of a Permanent Open Form of a Naphthopyran. *Tetrahedron Lett.* **2002**, *43*, 2203–2205.

(23) Carvalho, L. M.; Silva, A. M. S.; Martins, C. I.; Coelho, P. J.; Oliveira-Campos, A. M. F. Structural Elucidation of the Red Dye Obtained from Reaction of 1,8-Naphthalenediol with 1,1-Diphenylprop-2-Yn-1-Ol. A Correction. *Tetrahedron Lett.* **2003**, *44*, 1903–1905.

(24) Aiken, S.; Booth, K.; Gabbutt, C. D.; Mark Heron, B.; Rice, C. R.; Charaf-Eddin, A.; Jacquemin, D. The First Structural and Spectroscopic Characterisation of a Ring-Opened Form of a 2H-Naphtho[1,2-b]Pyran: A Novel Photomerocyanine. *Chemical Communications* **2014**, *50*, 7900–7903.

(25) Gu, W.; Bi, S.; Weiss, R. G. Photo-Fries Rearrangements of 1-Naphthyl Esters in the Glassy and Melted States of Poly(Vinyl Acetate). Comparisons with Reactions in Less Polar Polymers and Low-Viscosity Solvents. *Photochem. Photobiol. Sci.* **2002**, *1*, 52–59.

(26) Gossweiler, G. R.; Hewage, G. B.; Soriano, G.; Wang, Q.; Welshofer, G. W.; Zhao, X.; Craig, S. L. Mechanochemical Activation of Covalent Bonds in Polymers with Full and Repeatable Macroscopic Shape Recovery. *ACS Macro Letters* **2014**, *3*, 216–219.

(27) May, P. A.; Moore, J. S. Polymer Mechanochemistry: Techniques to Generate Molecular Force via Elongational Flows. *Chem. Soc. Rev* **2013**, *42*, 7497–7506.

(28) Zhao, W.; Carreira, E. M. Facile One-Pot Synthesis of Photochromic Pyrans. *Org. Lett.* **2003**, *5*, 4153–4154.

(29) Nguyen, N. H.; Rosen, B. M.; Lligadas, G.; Percec, V. Surface-Dependent Kinetics of Cu(0)-Wire-Catalyzed Single-Electron Transfer Living Radical Polymerization of Methyl Acrylate in DMSO at 25 °C. *Macromolecules* **2009**, *42*, 2379–2386.

(30) Yang, J.; Horst, M.; Werby, S. H.; Cegelski, L.; Burns, N. Z.; Xia, Y. Bicyclohexene- *Peri* -Naphthalenes: Scalable Synthesis, Diverse Functionalization, Efficient Polymerization, and Facile Mechanoactivation of Their Polymers. *J. Am. Chem. Soc.* **2020**, *142*, 14619–14626.

(31) Berkowski, K. L.; Potisek, S. L.; Hickenboth, C. R.; Moore, J. S. Ultrasound-Induced Site-Specific Cleavage of Azo-Functionalized Poly(Ethylene Glycol). *Macromolecules* **2005**, *38*, 8975–8978.

(32) May, P. A.; Moore, J. S. Polymer Mechanochemistry: Techniques to Generate Molecular Force via Elongational Flows. *Chem. Soc. Rev.* **2013**, *42*, 7497–7506.

(33) Li, J.; Nagamani, C.; Moore, J. S. Polymer Mechanochemistry: From Destructive to Productive. *Acc. Chem. Res.* **2015**, *48*, 2181–2190.

(34) Church, D. C.; Peterson, G. I.; Boydston, A. J. Comparison of Mechanochemical Chain Scission Rates for Linear versus Three-Arm Star Polymers in Strong Acoustic Fields. *ACS Macro Lett.* **2014**, *3*, 648–651.

^{1}H and ^{13}C NMR Spectra

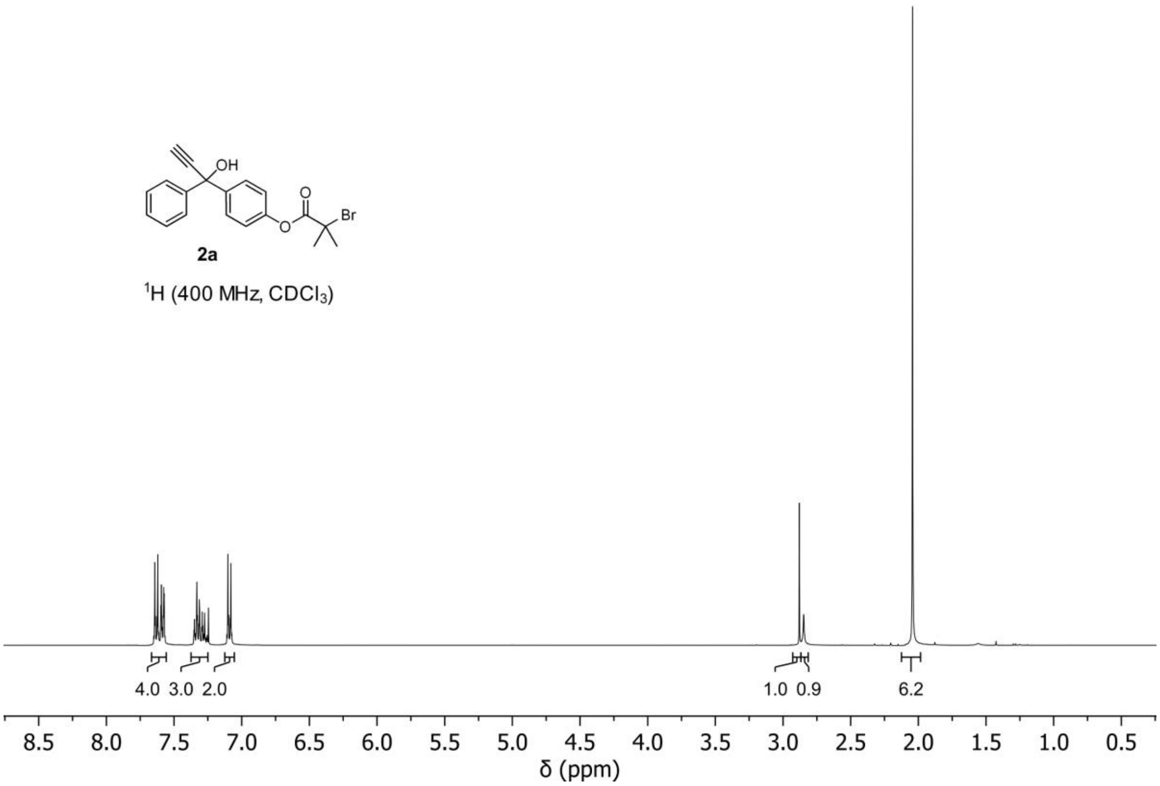

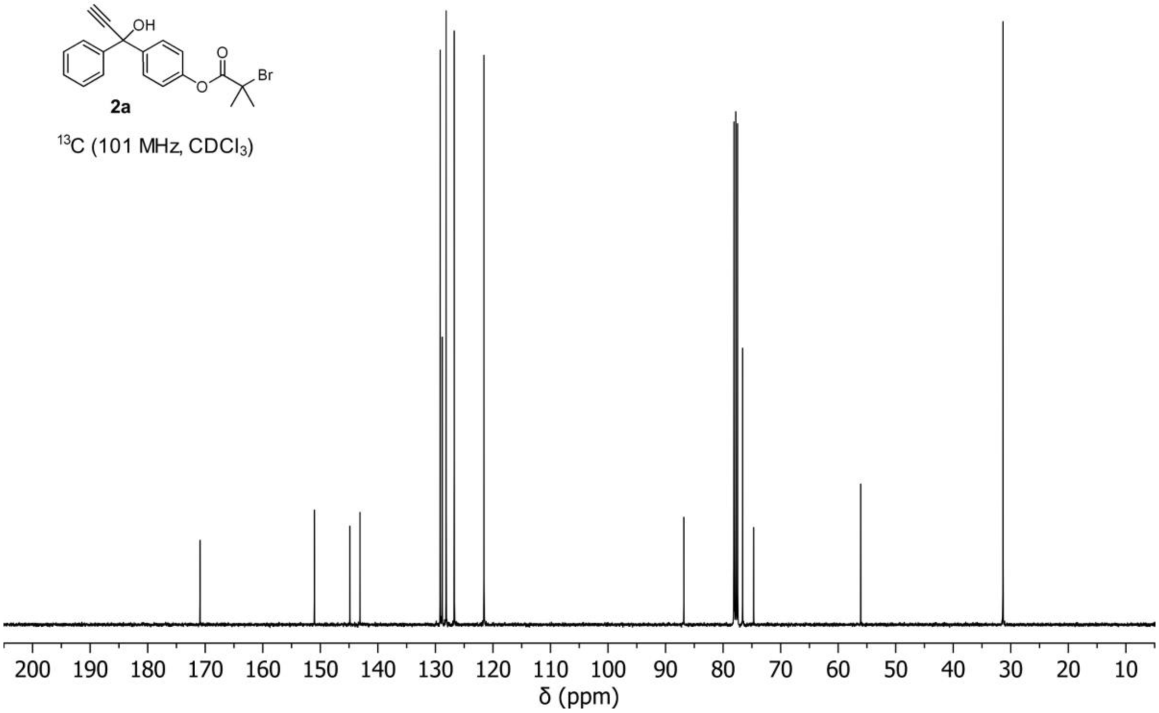

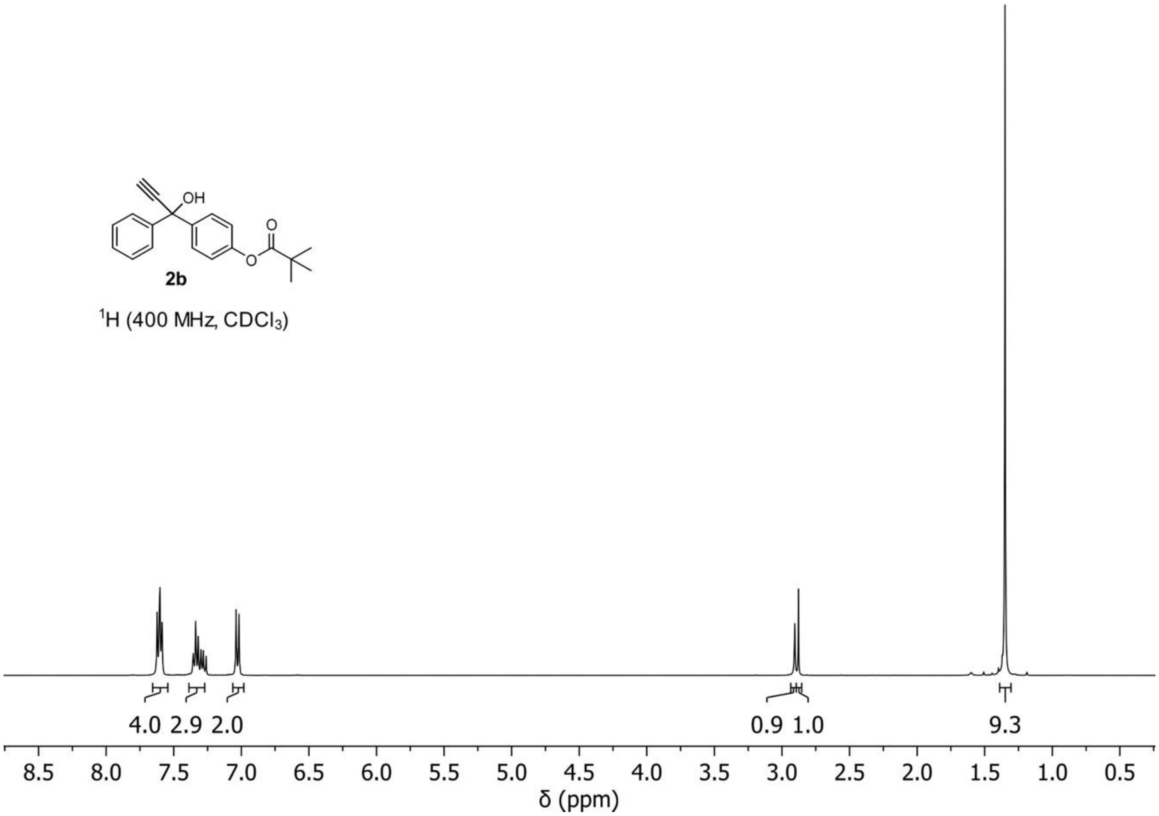
OH
O
O
2b
1H (400 MHz, CDCl3)
4.0 2.9 2.0
0.9 1.0
9.3
8.5 8.0 7.5 7.0 6.5 6.0 5.5 5.0 4.5 4.0 3.5 3.0 2.5 2.0 1.5 1.0 0.5
δ (ppm)

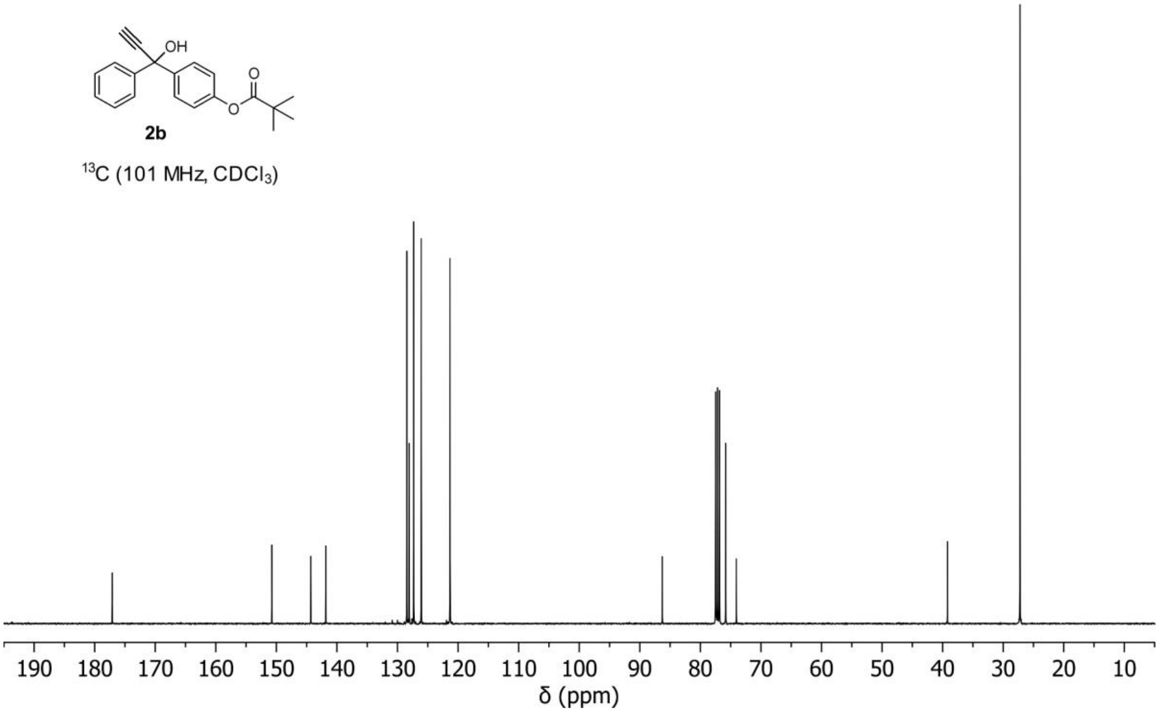
OH
O
O
2b
13C (101 MHz, CDCl3)
190 180 170 160 150 140 130 120 110 100 90 80 70 60 50 40 30 20 10
δ (ppm)

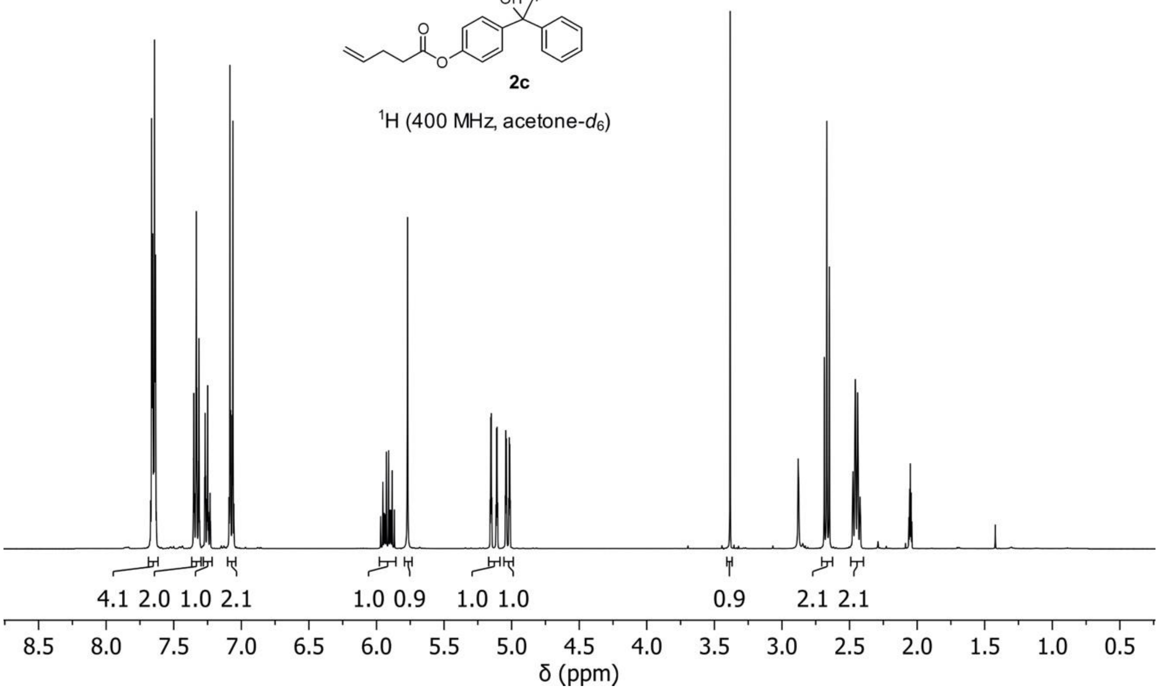

2c

^{1}H (400 MHz, acetone-d_6)

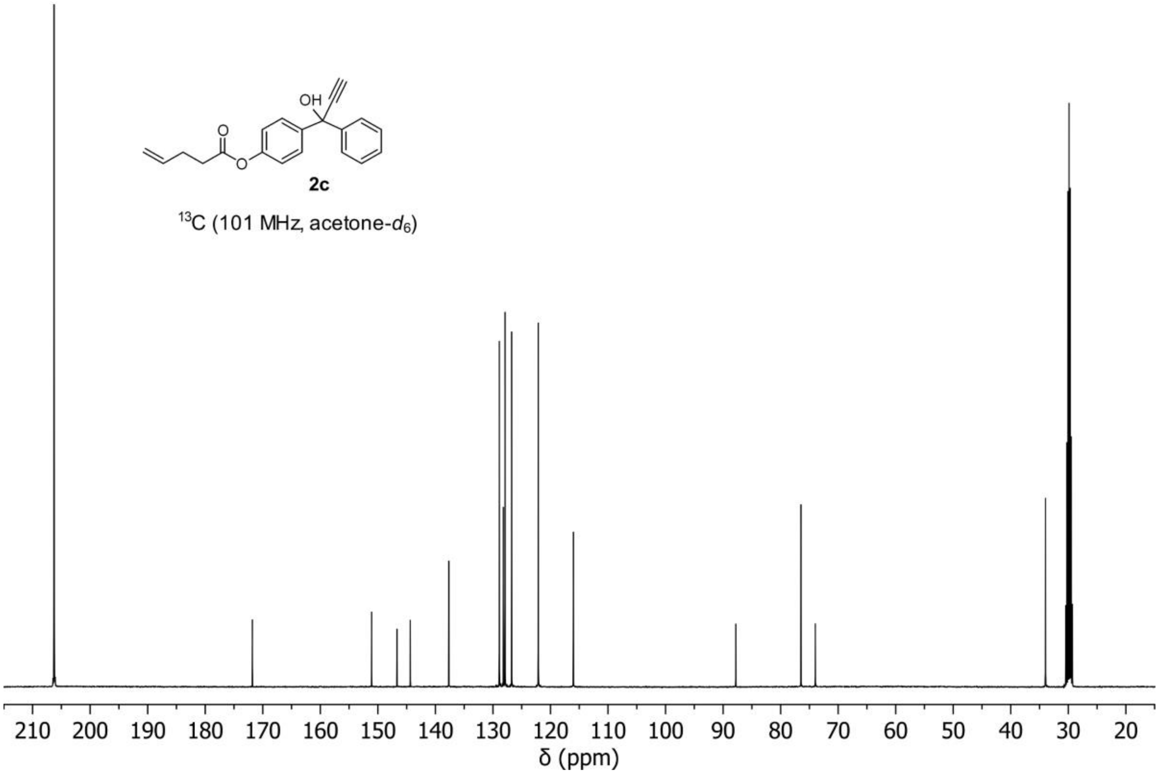

2c

^{13}C (101 MHz, acetone-d_6)

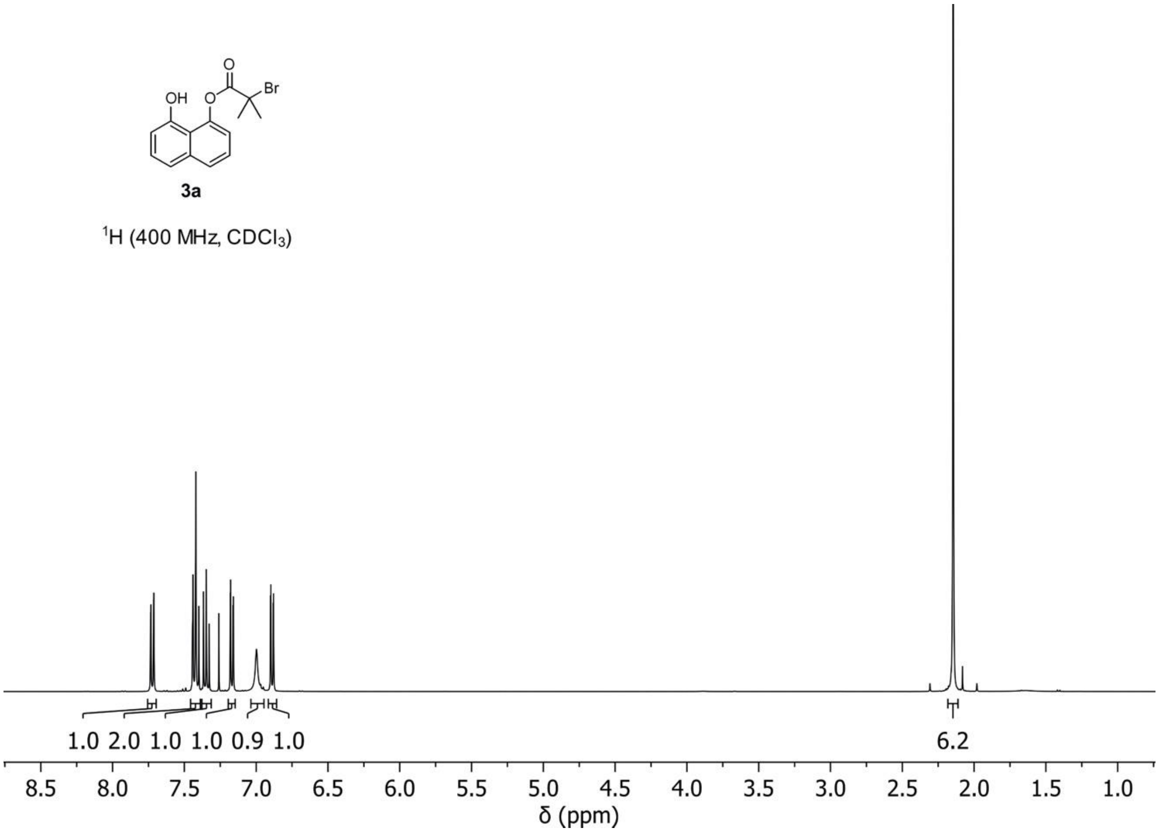
OH
O
O
Br
3a
^{1}H (400 MHz, CDCl$_3$)
1.0 2.0 1.0 1.0 0.9 1.0
6.2
8.5 8.0 7.5 7.0 6.5 6.0 5.5 5.0 4.5 4.0 3.5 3.0 2.5 2.0 1.5 1.0
δ (ppm)

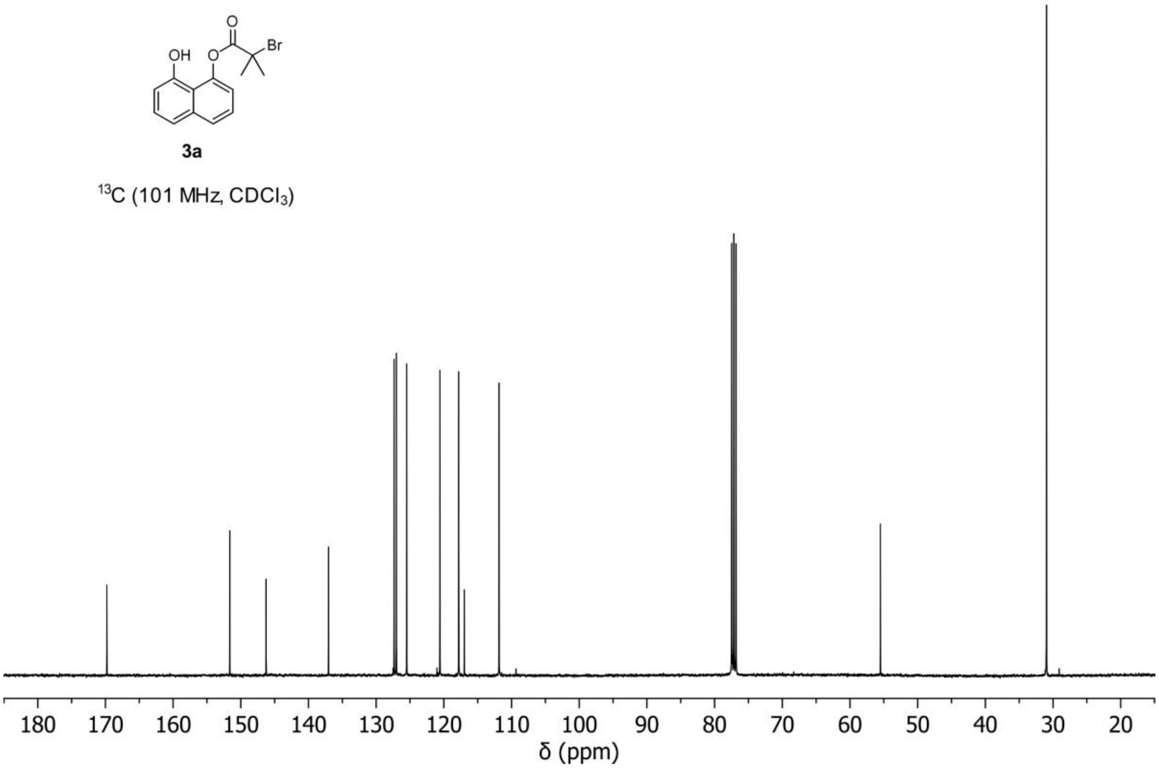
OH
O
O
Br
3a
^{13}C (101 MHz, CDCl$_3$)
180 170 160 150 140 130 120 110 100 90 80 70 60 50 40 30 20
δ (ppm)

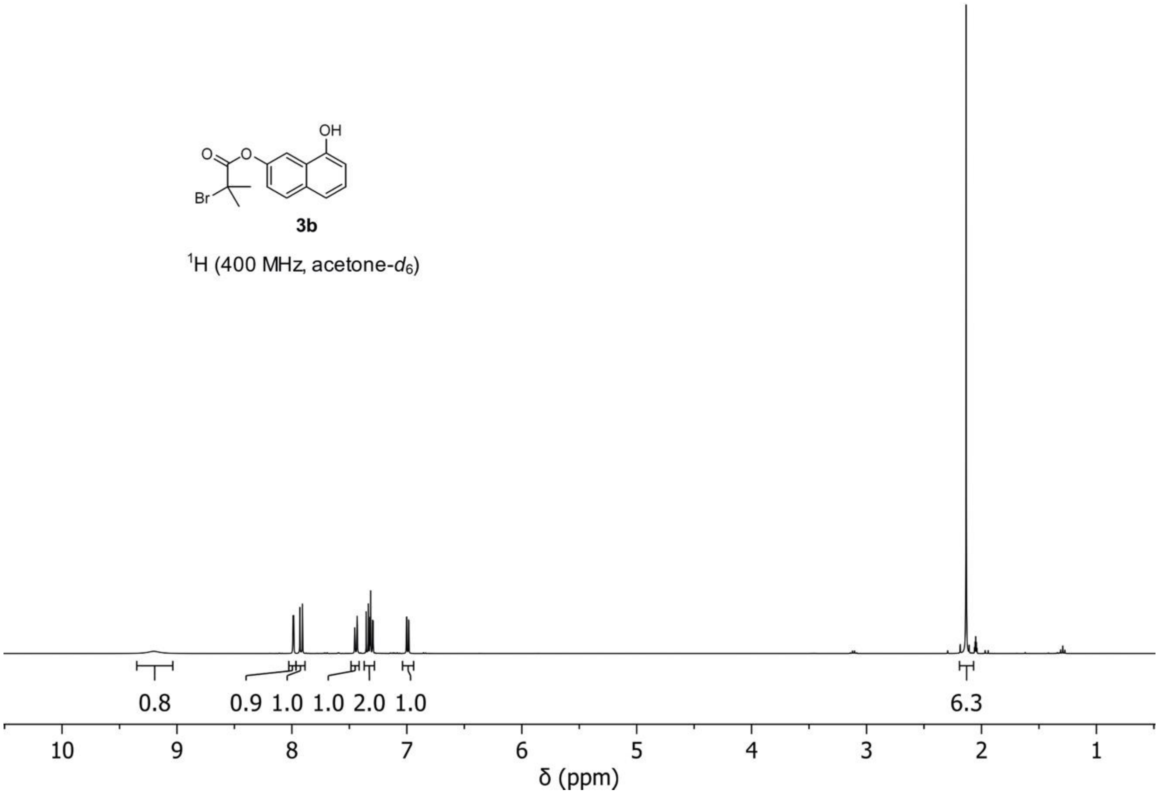
OH
O
O
Br
3b
^{1}H (400 MHz, acetone-d_6)
0.8
0.9
1.0
1.0
2.0
1.0
6.3
10
9
8
7
6
5
4
3
2
1
δ (ppm)

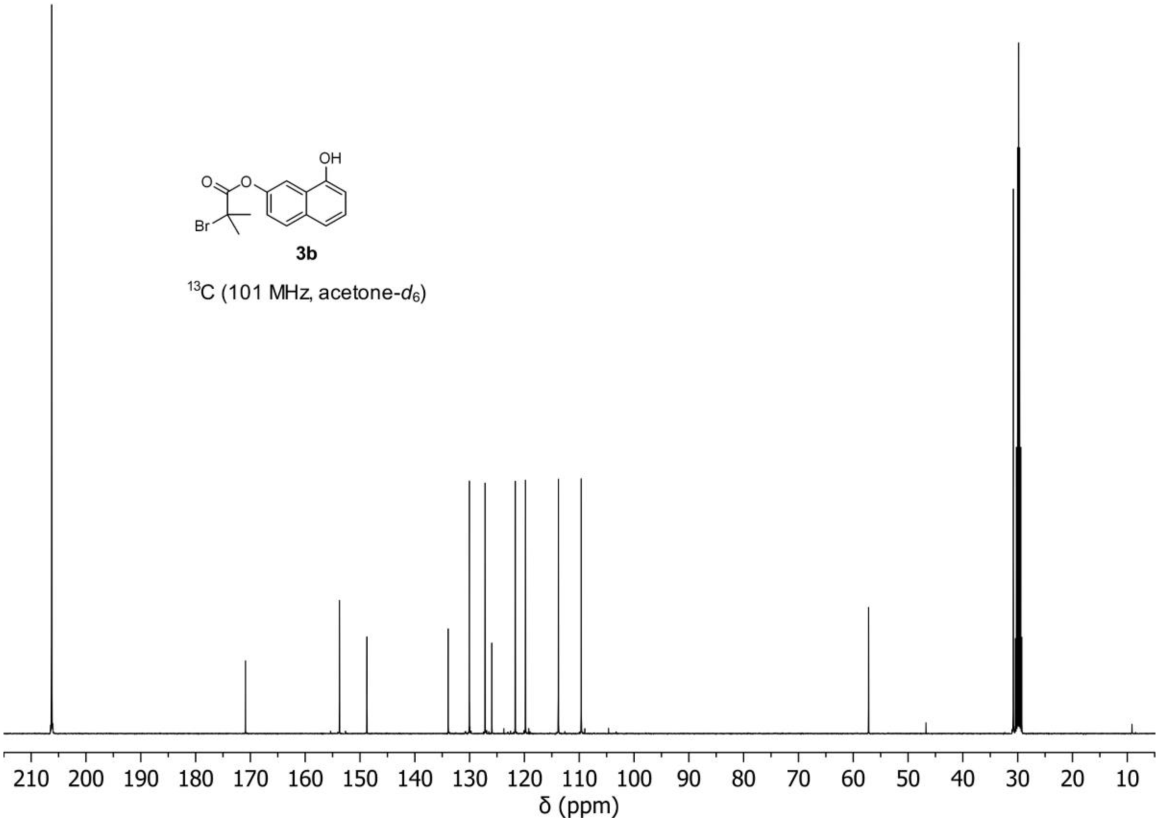
OH
O
O
Br
3b
^{13}C (101 MHz, acetone-d_6)
210
200
190
180
170
160
150
140
130
120
110
100
90
80
70
60
50
40
30
20
10
δ (ppm)

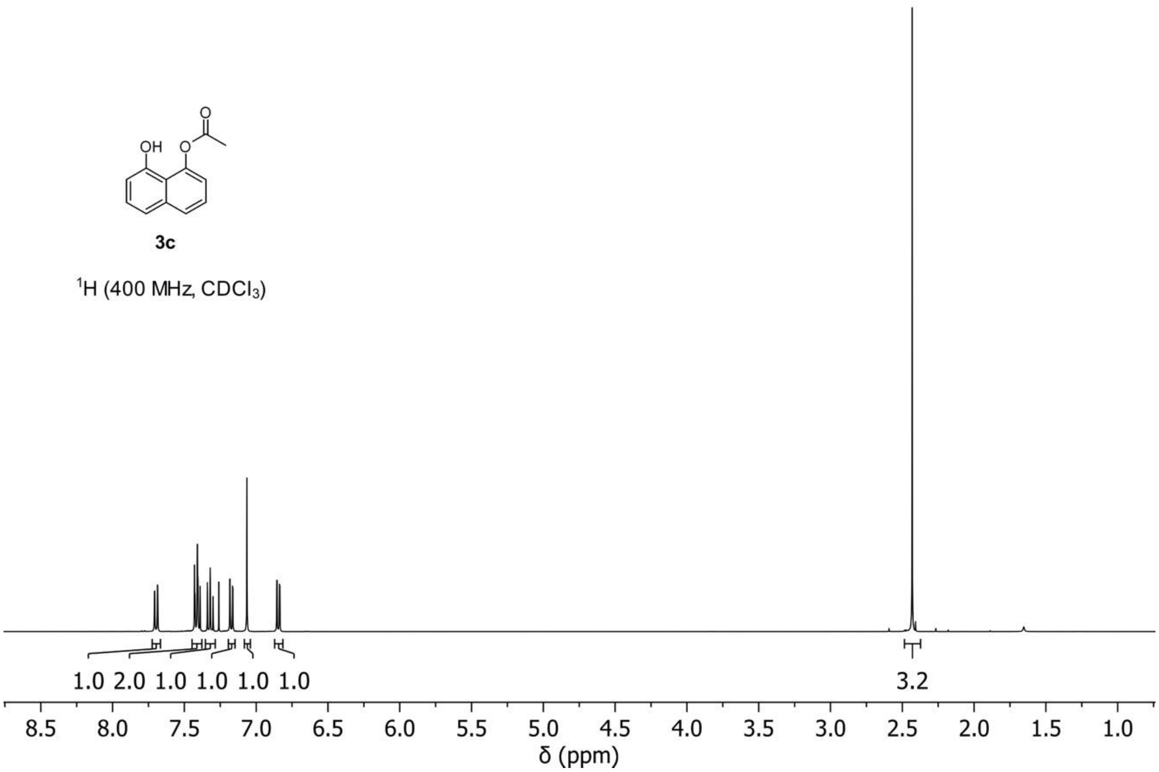
OH
O
O
3c
1H (400 MHz, CDCl3)
1.0 2.0 1.0 1.0 1.0 1.0
3.2
8.5 8.0 7.5 7.0 6.5 6.0 5.5 5.0 4.5 4.0 3.5 3.0 2.5 2.0 1.5 1.0
δ (ppm)

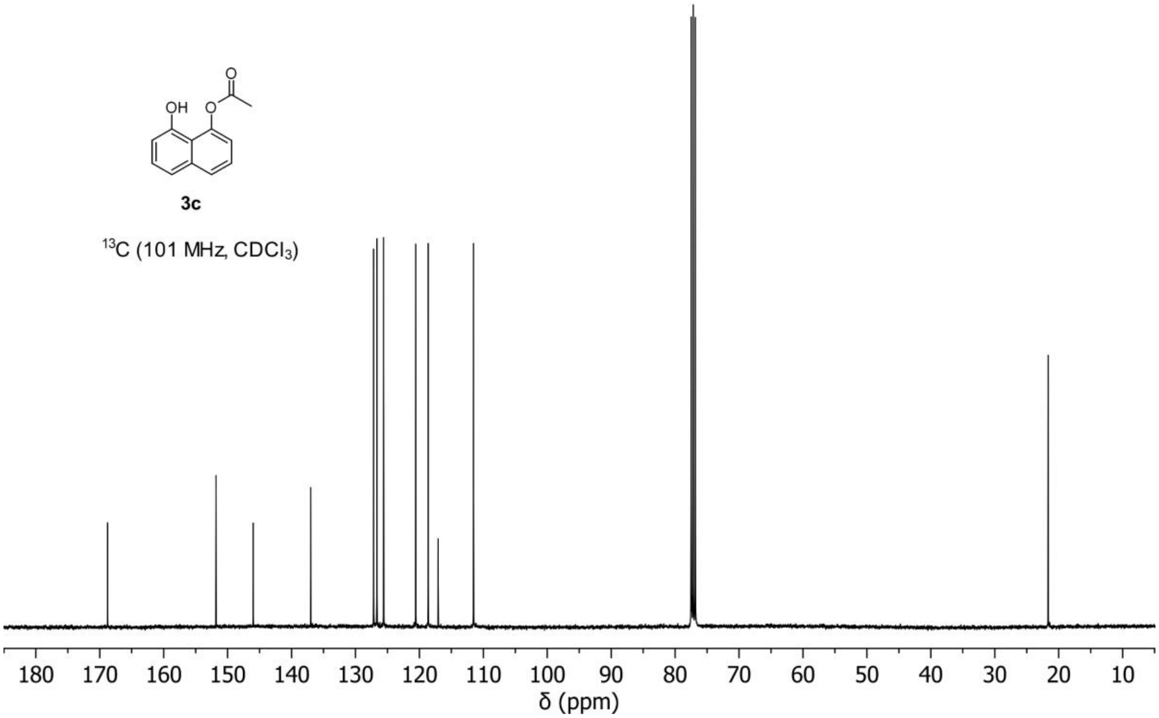
OH
O
O
3c
13C (101 MHz, CDCl3)
180 170 160 150 140 130 120 110 100 90 80 70 60 50 40 30 20 10
δ (ppm)

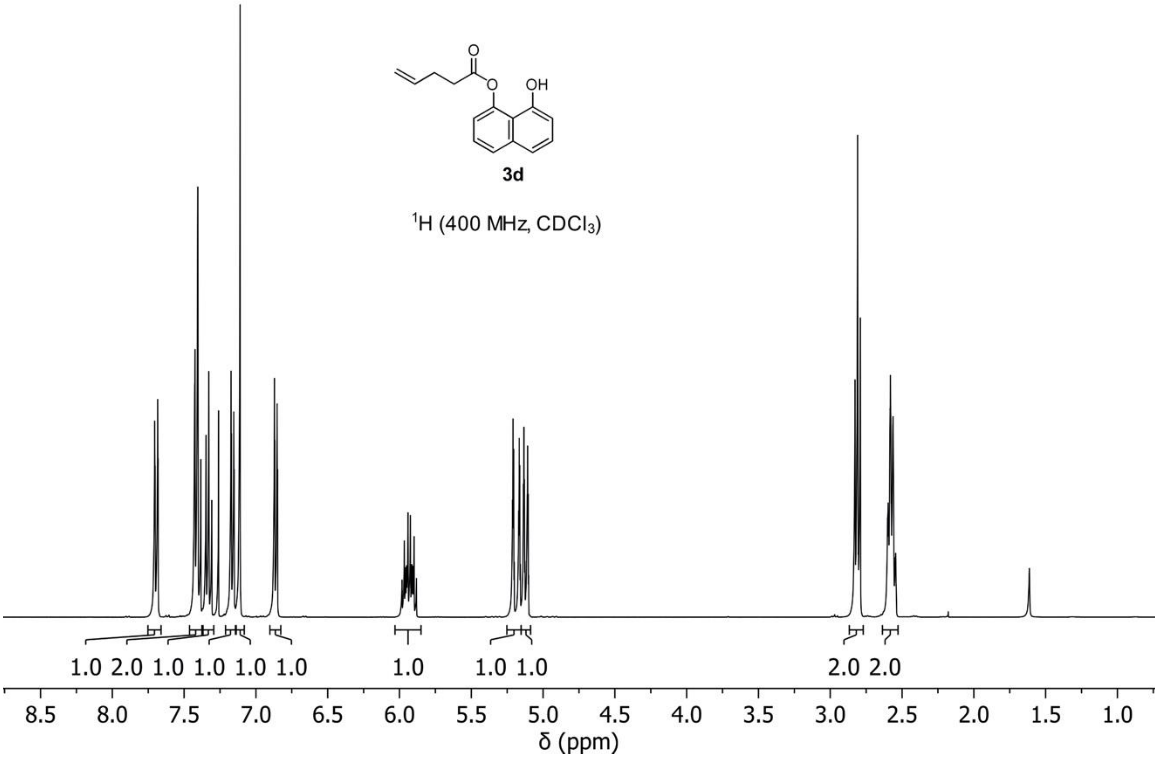

O
OH
3d
^{1}H (400 MHz, CDCl$_3$)
1.0 2.0 1.0 1.0 1.0 1.0
1.0
1.0 1.0
2.0 2.0
8.5 8.0 7.5 7.0 6.5 6.0 5.5 5.0 4.5 4.0 3.5 3.0 2.5 2.0 1.5 1.0
δ (ppm)

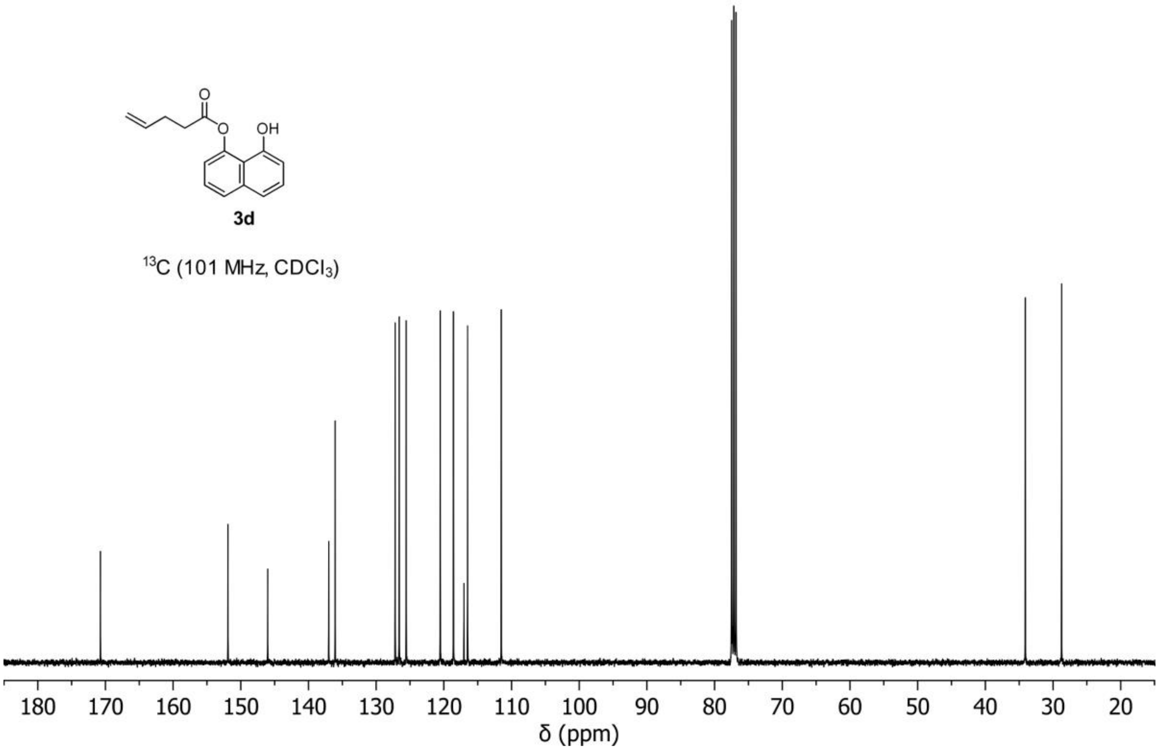

O
OH
3d
^{13}C (101 MHz, CDCl$_3$)
180 170 160 150 140 130 120 110 100 90 80 70 60 50 40 30 20
δ (ppm)

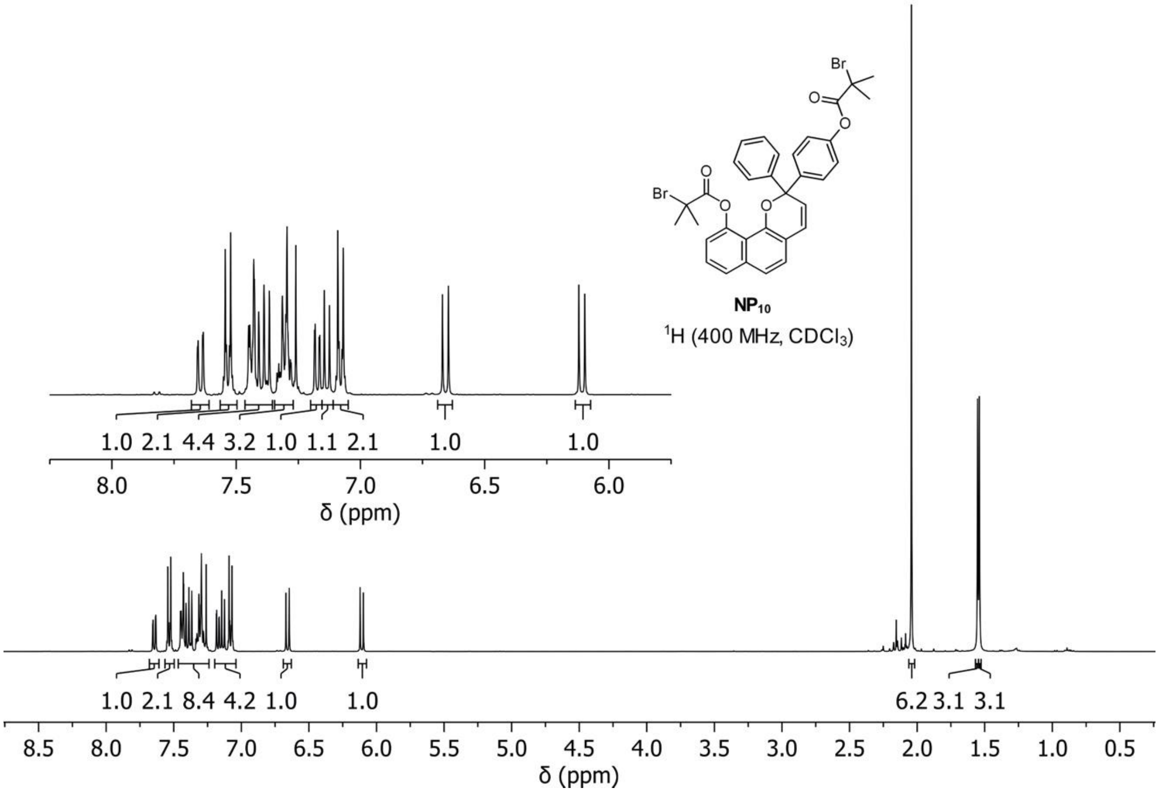
Br
O
O
Br
O
O
O
O
NP10
¹H (400 MHz, CDCl₃)
1.0 2.1 4.4 3.2 1.0 1.1 2.1 1.0 1.0
8.0 7.5 7.0 6.5 6.0
δ (ppm)
1.0 2.1 8.4 4.2 1.0 1.0 6.2 3.1 3.1
8.5 8.0 7.5 7.0 6.5 6.0 5.5 5.0 4.5 4.0 3.5 3.0 2.5 2.0 1.5 1.0 0.5
δ (ppm)

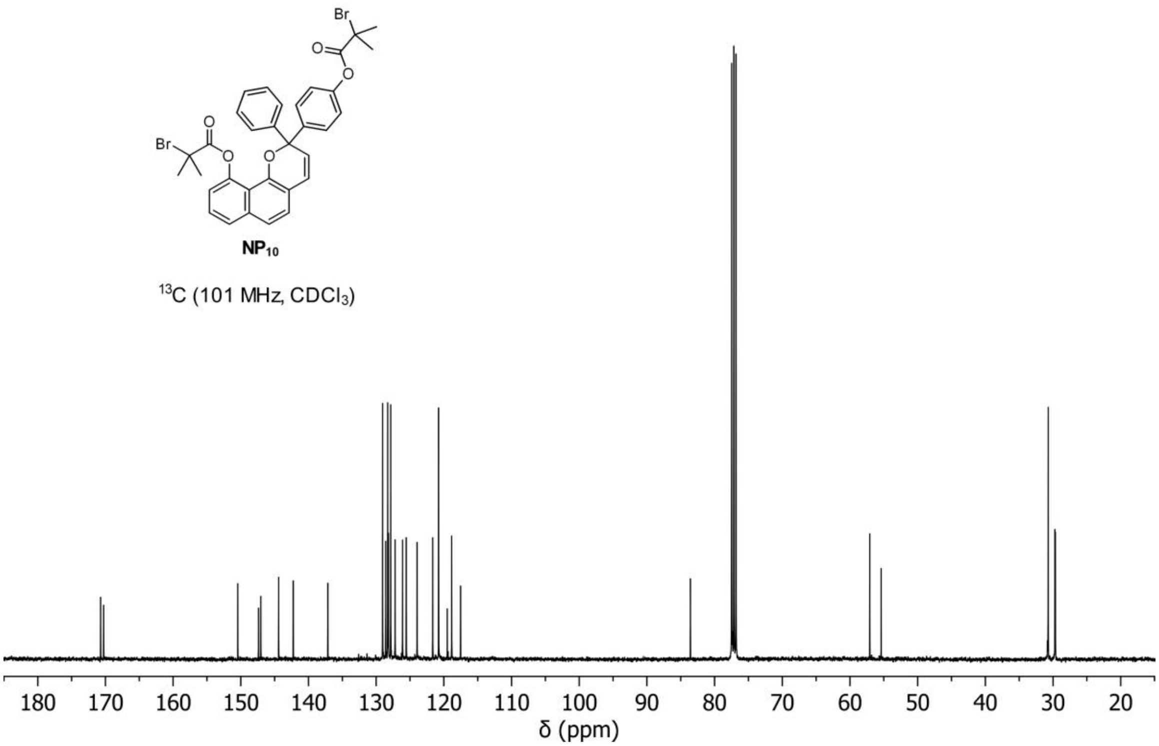
Br
O
O
Br
O
O
O
O
NP10
¹³C (101 MHz, CDCl₃)
180 170 160 150 140 130 120 110 100 90 80 70 60 50 40 30 20
δ (ppm)

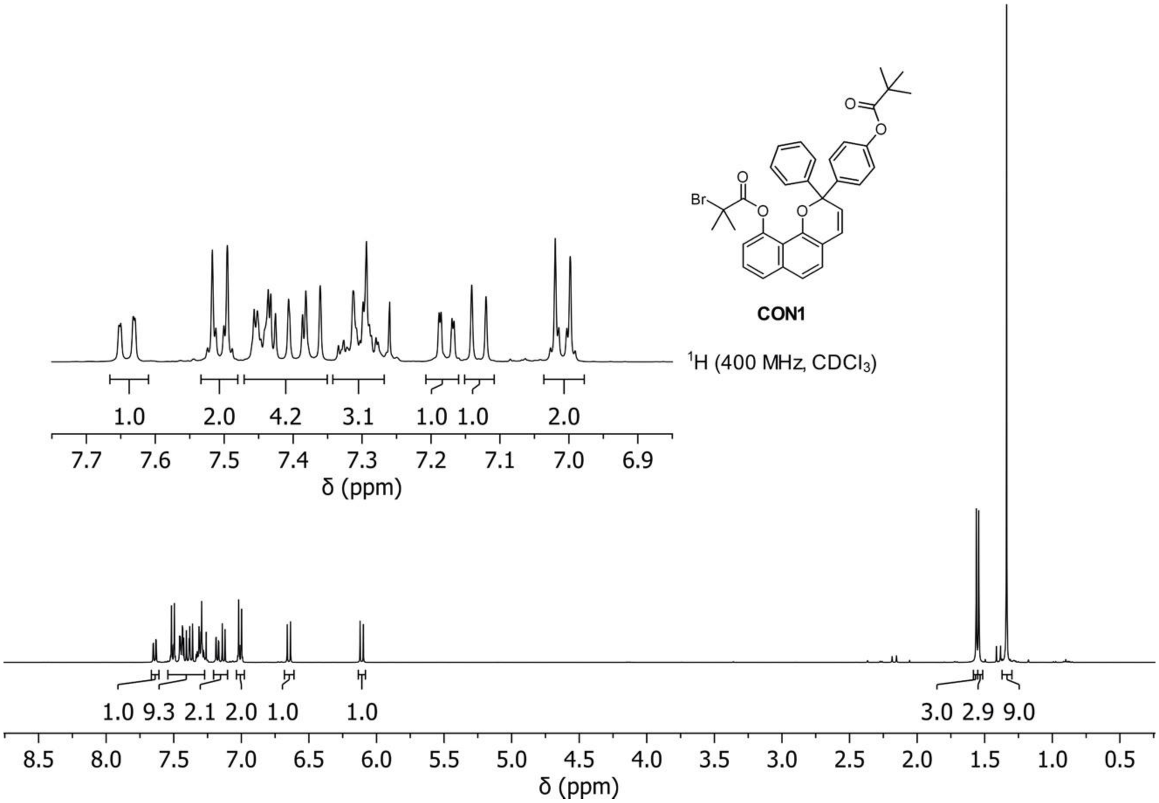
Br
O
O
O
O
O
CON1
1H (400 MHz, CDCl3)
1.0
2.0
4.2
3.1
1.0
1.0
2.0
7.7
7.6
7.5
7.4
7.3
7.2
7.1
7.0
6.9
δ (ppm)
1.0
9.3
2.1
2.0
1.0
1.0
3.0
2.9
9.0
8.5
8.0
7.5
7.0
6.5
6.0
5.5
5.0
4.5
4.0
3.5
3.0
2.5
2.0
1.5
1.0
0.5
δ (ppm)

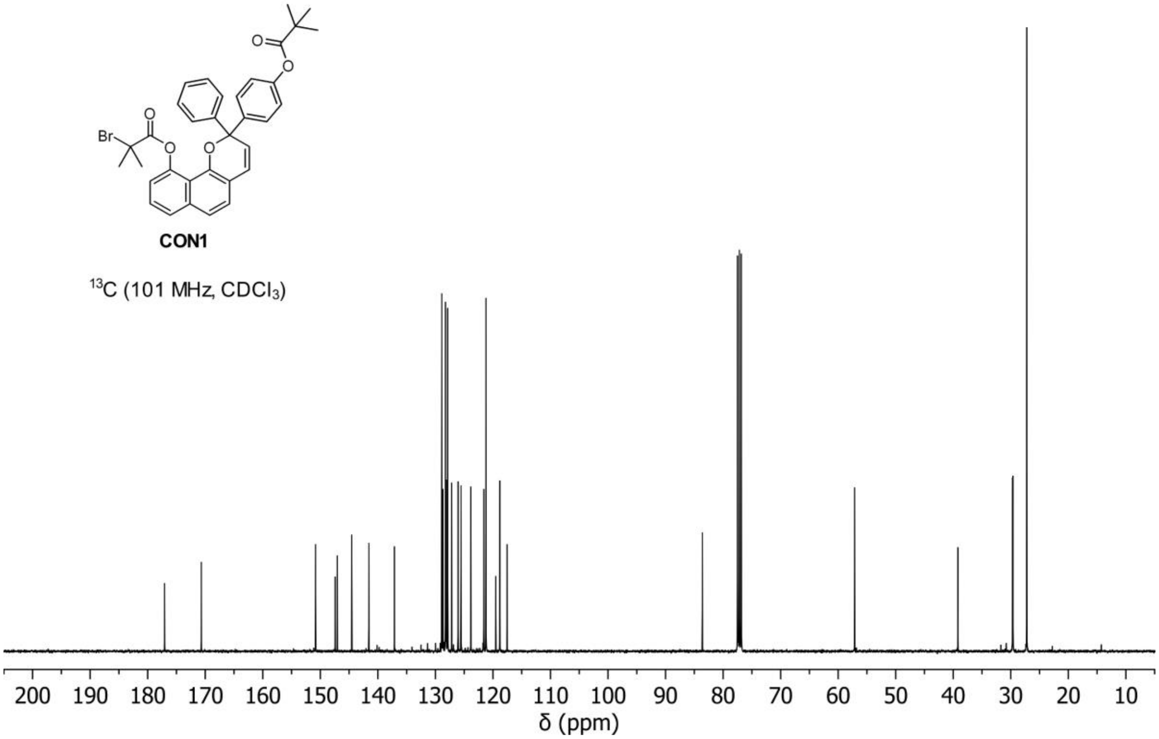
Br
O
O
O
O
O
CON1
13C (101 MHz, CDCl3)
200
190
180
170
160
150
140
130
120
110
100
90
80
70
60
50
40
30
20
10
δ (ppm)

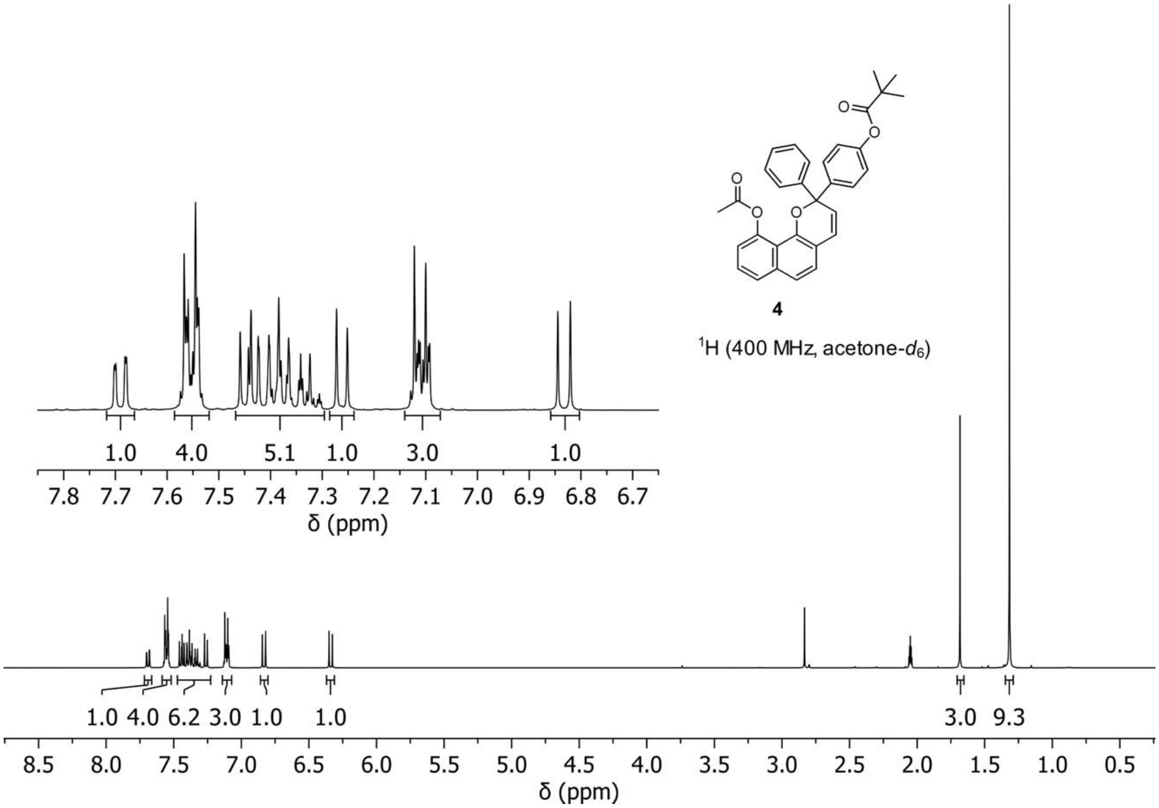
4
^{1}H (400 MHz, acetone-d_6)
1.0 4.0 5.1 1.0 3.0 1.0
7.8 7.7 7.6 7.5 7.4 7.3 7.2 7.1 7.0 6.9 6.8 6.7
δ (ppm)
1.0 4.0 6.2 3.0 1.0 1.0 3.0 9.3
8.5 8.0 7.5 7.0 6.5 6.0 5.5 5.0 4.5 4.0 3.5 3.0 2.5 2.0 1.5 1.0 0.5
δ (ppm)

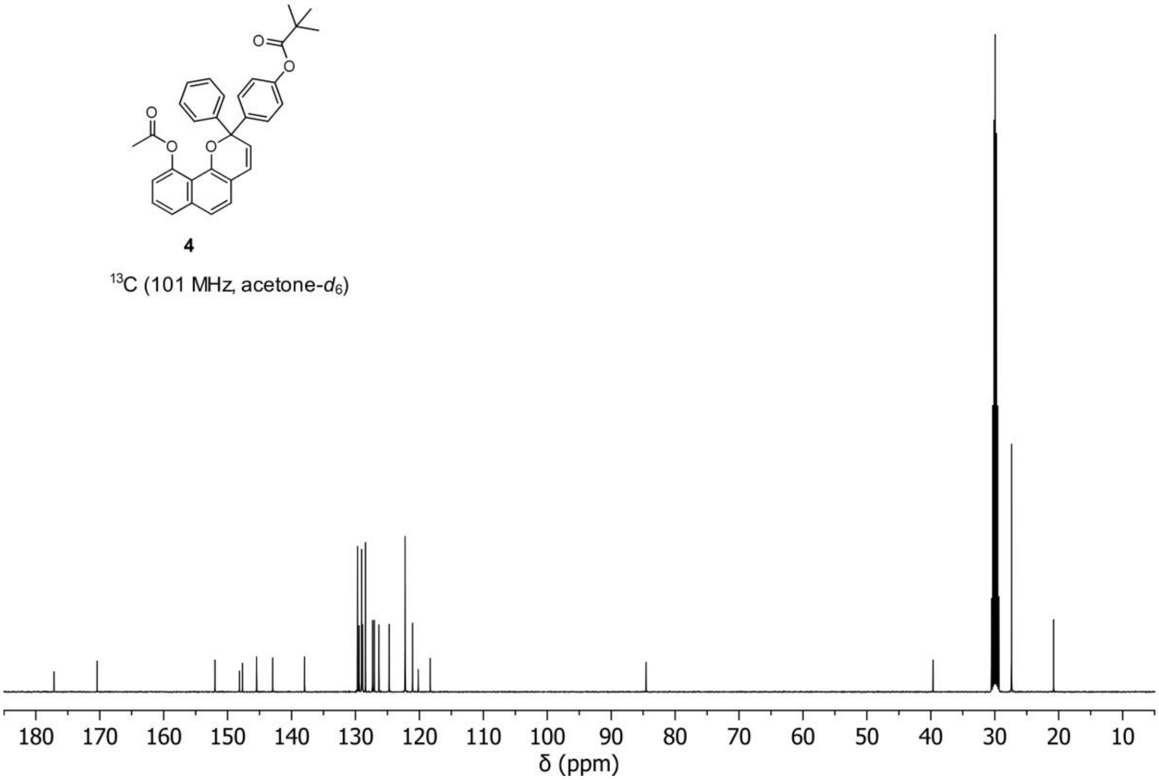
4
^{13}C (101 MHz, acetone-d_6)
180 170 160 150 140 130 120 110 100 90 80 70 60 50 40 30 20 10
δ (ppm)

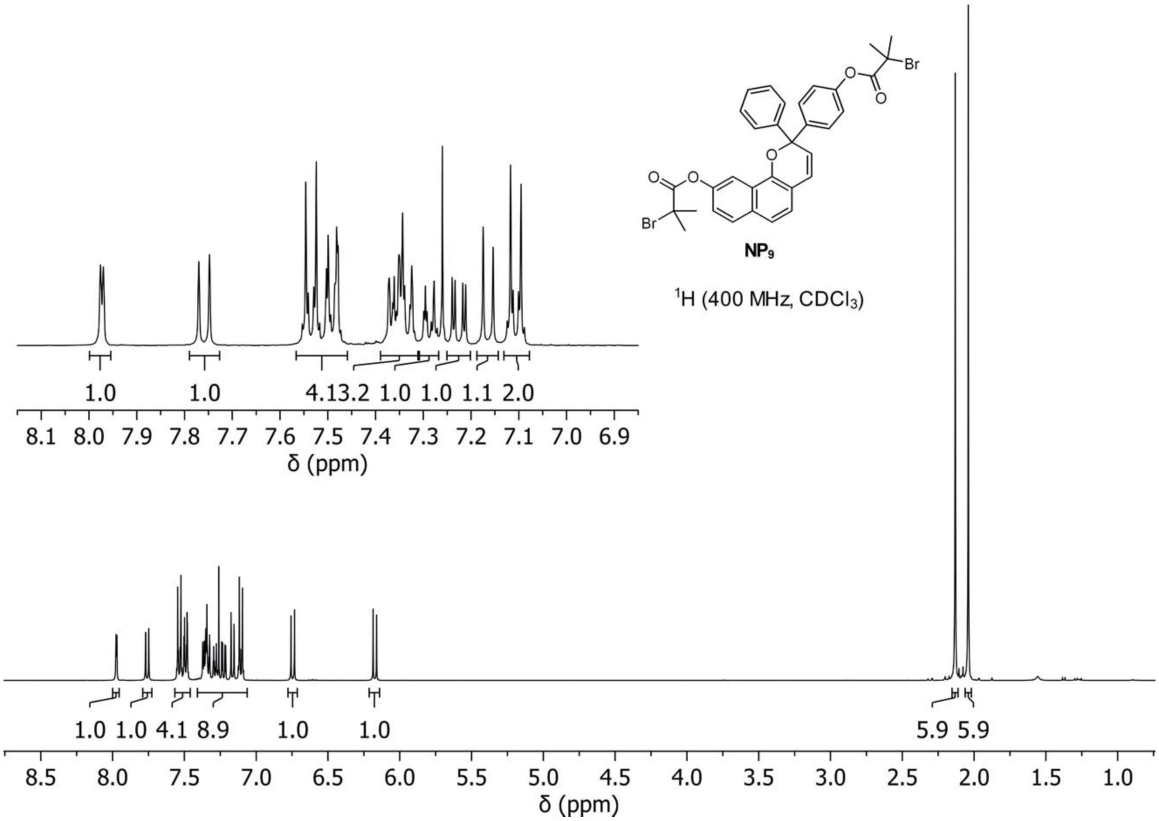
NP₉
¹H (400 MHz, CDCl₃)
1.0
1.0
4.1
3.2
1.0
1.0
1.1
2.0
8.1 8.0 7.9 7.8 7.7 7.6 7.5 7.4 7.3 7.2 7.1 7.0 6.9
δ (ppm)
1.0 1.0 4.1 8.9
1.0
1.0
5.9 5.9
8.5 8.0 7.5 7.0 6.5 6.0 5.5 5.0 4.5 4.0 3.5 3.0 2.5 2.0 1.5 1.0
δ (ppm)
O
Br
O
O
O
O
Br

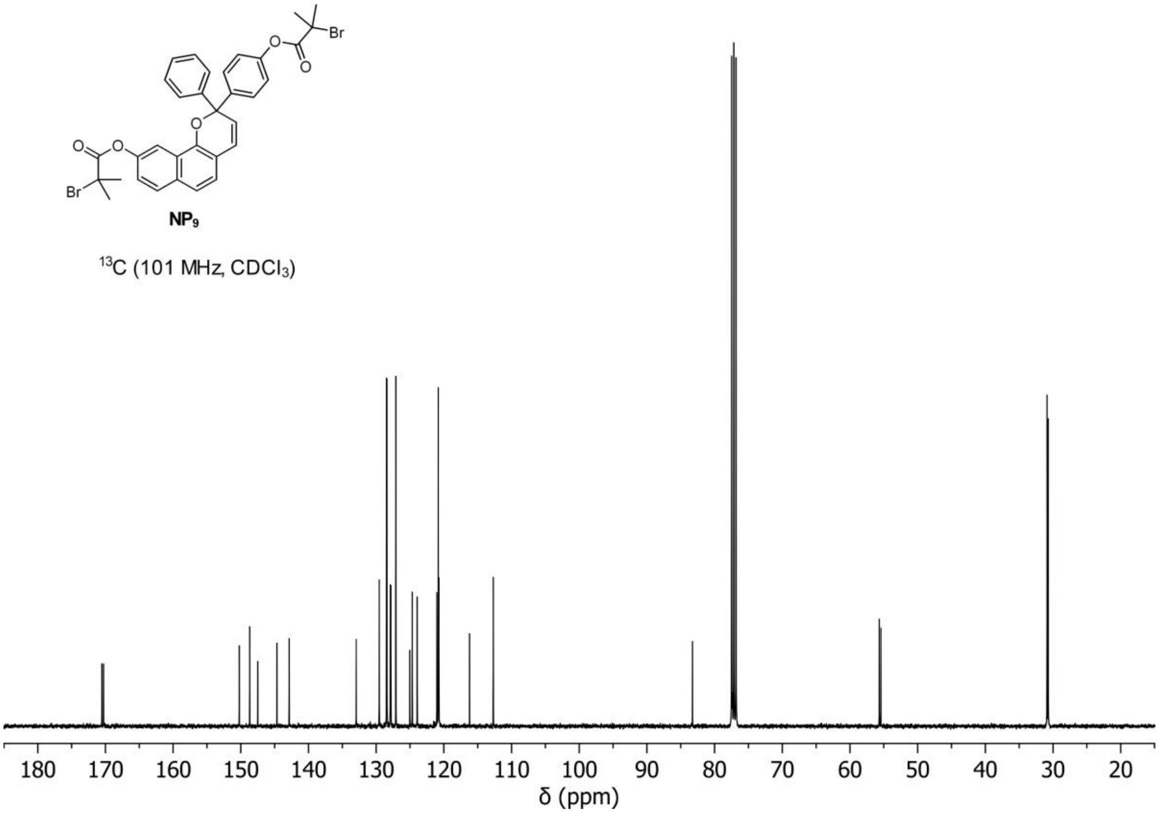
NP₉
¹³C (101 MHz, CDCl₃)
180 170 160 150 140 130 120 110 100 90 80 70 60 50 40 30 20
δ (ppm)
O
Br
O
O
O
O
Br

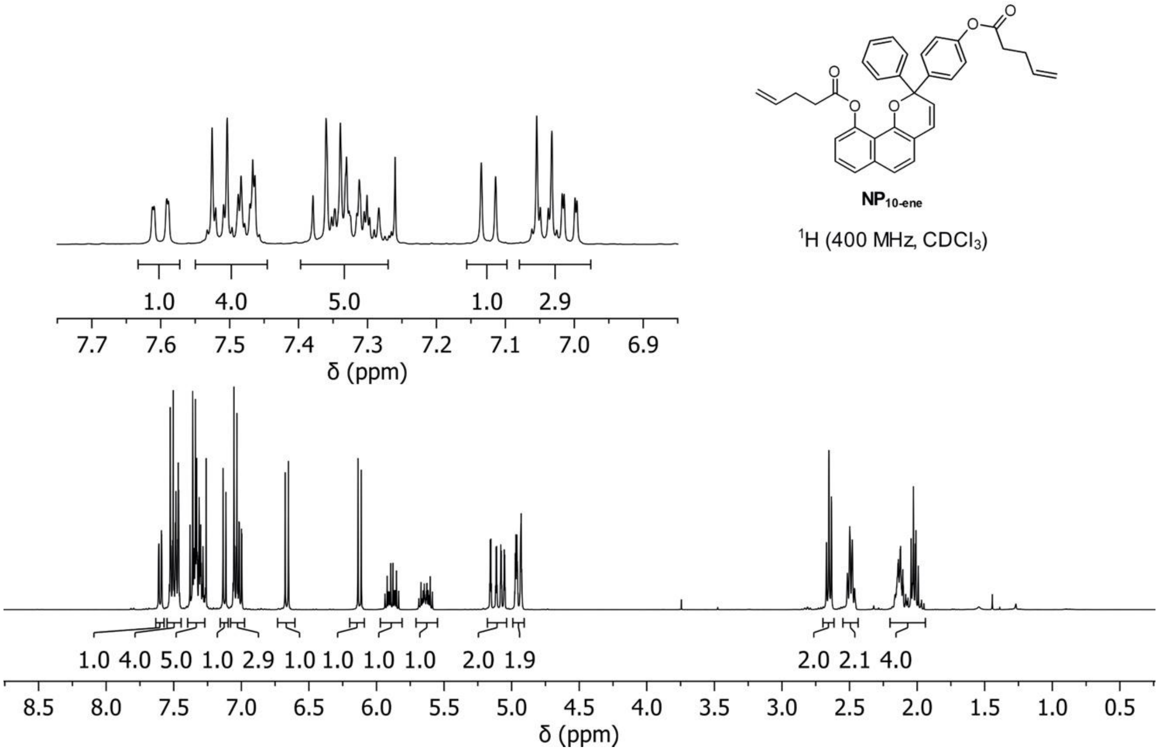
NP$_{10\text{-ene}}$
^{1}H (400 MHz, CDCl$_3$)
1.0
4.0
5.0
1.0
2.9
7.7
7.6
7.5
7.4
7.3
7.2
7.1
7.0
6.9
δ (ppm)
1.0 4.0 5.0 1.0 2.9 1.0 1.0 1.0 1.0 2.0 1.9
2.0 2.1 4.0
8.5
8.0
7.5
7.0
6.5
6.0
5.5
5.0
4.5
4.0
3.5
3.0
2.5
2.0
1.5
1.0
0.5
δ (ppm)

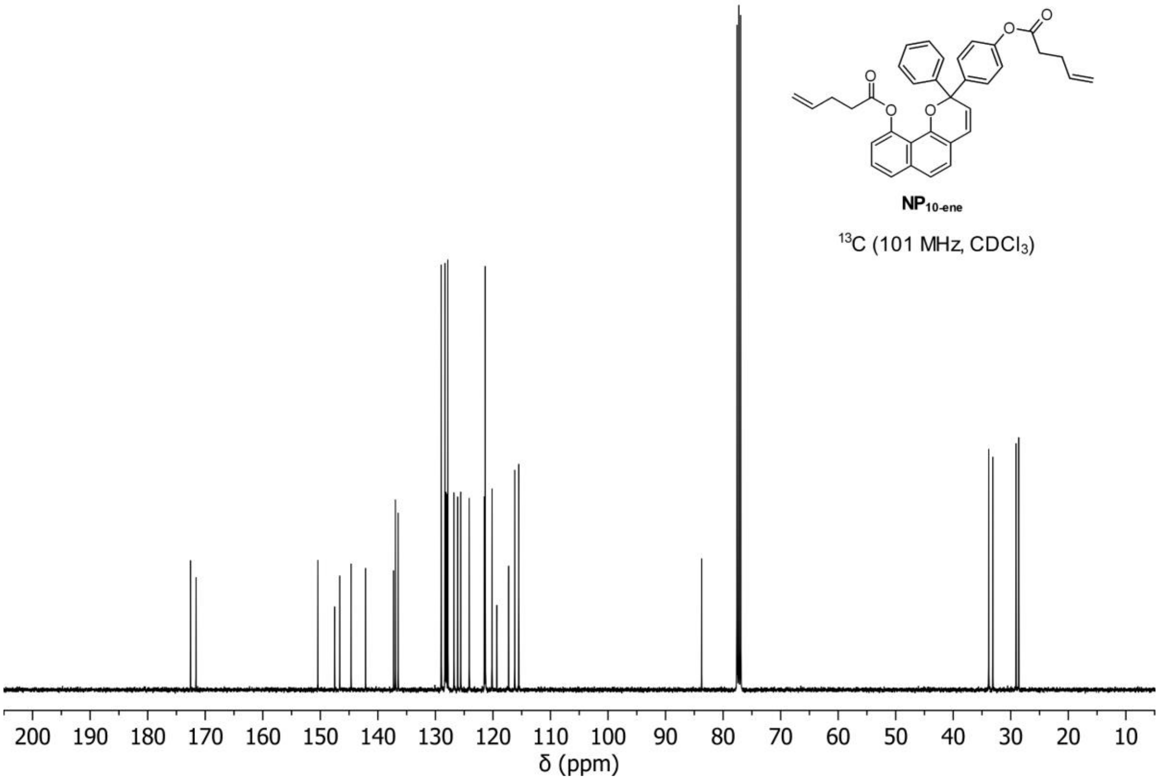
NP$_{10\text{-ene}}$
^{13}C (101 MHz, CDCl$_3$)
200
190
180
170
160
150
140
130
120
110
100
90
80
70
60
50
40
30
20
10
δ (ppm)

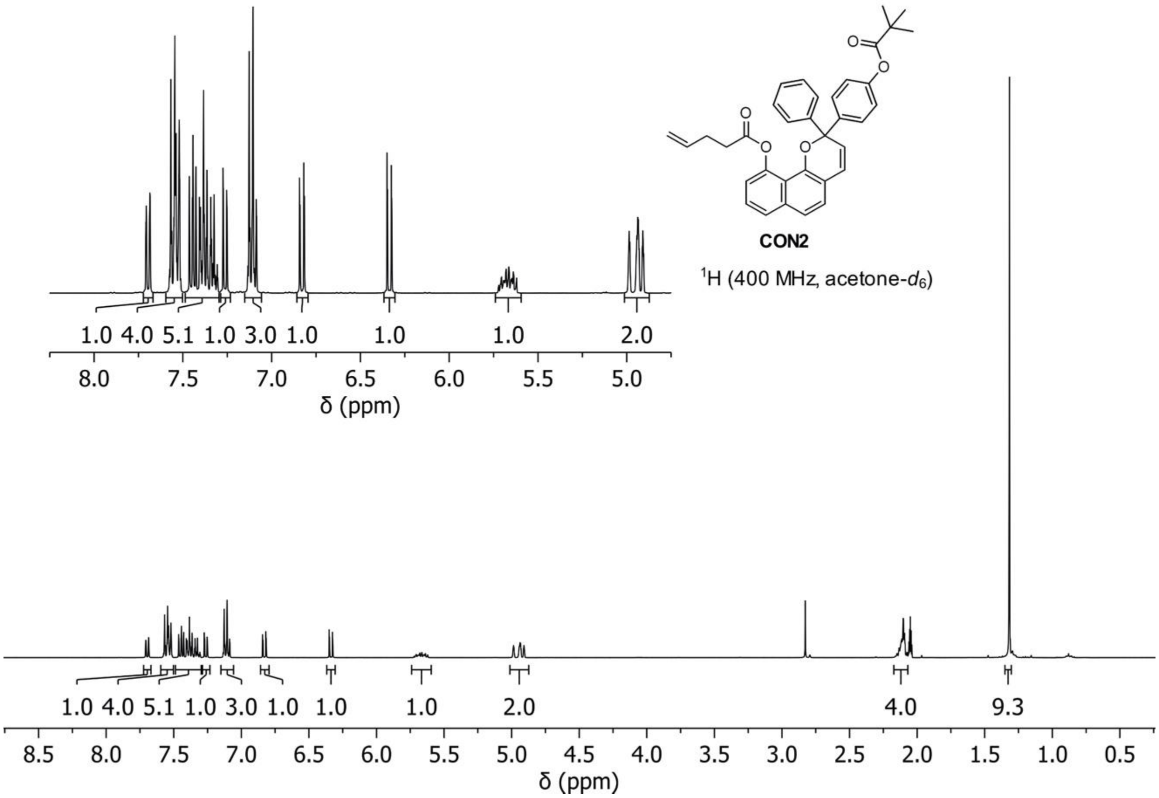
CON2
^{1}H (400 MHz, acetone-d_6)
1.0 4.0 5.1 1.0 3.0 1.0 1.0 1.0 2.0
8.0 7.5 7.0 6.5 6.0 5.5 5.0
δ (ppm)
1.0 4.0 5.1 1.0 3.0 1.0 1.0 1.0 2.0 4.0 9.3
8.5 8.0 7.5 7.0 6.5 6.0 5.5 5.0 4.5 4.0 3.5 3.0 2.5 2.0 1.5 1.0 0.5
δ (ppm)

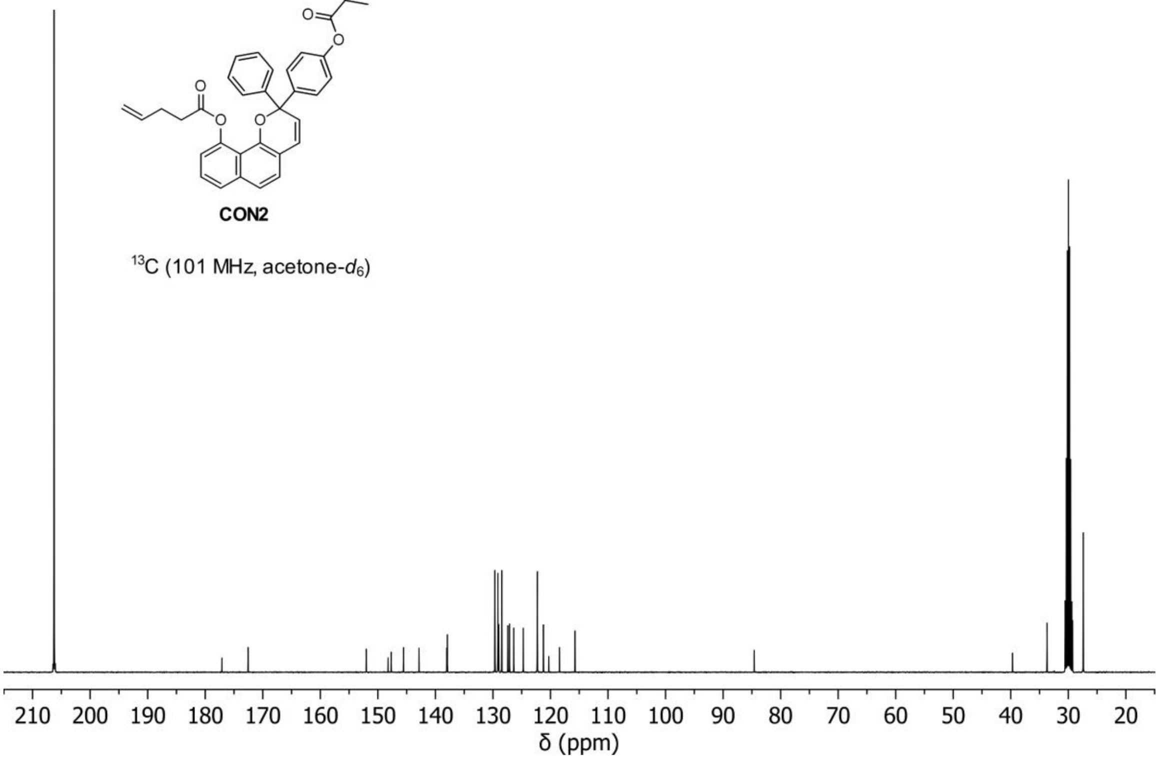
CON2
^{13}C (101 MHz, acetone-d_6)
210 200 190 180 170 160 150 140 130 120 110 100 90 80 70 60 50 40 30 20
δ (ppm)

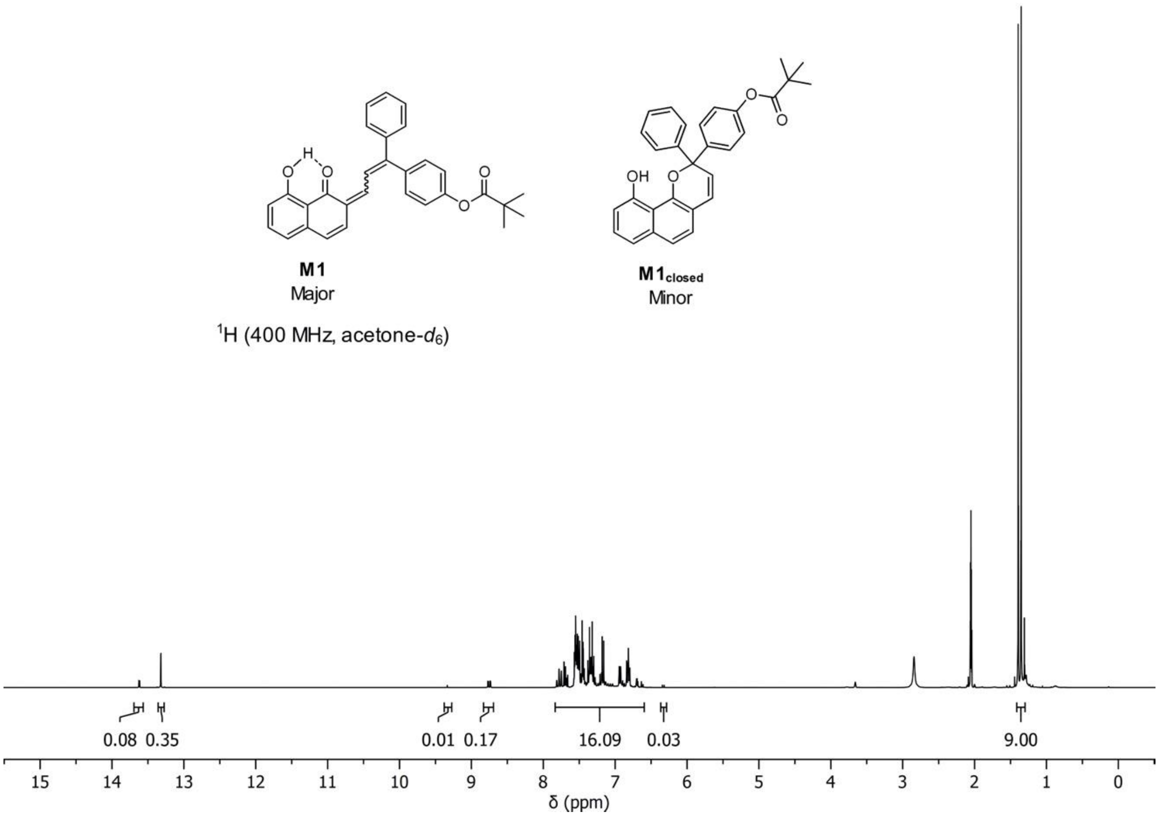
M1
Major
M1closed
Minor
1H (400 MHz, acetone-d6)
0.08
0.35
0.01
0.17
16.09
0.03
9.00
15 14 13 12 11 10 9 8 7 6 5 4 3 2 1 0
δ (ppm)

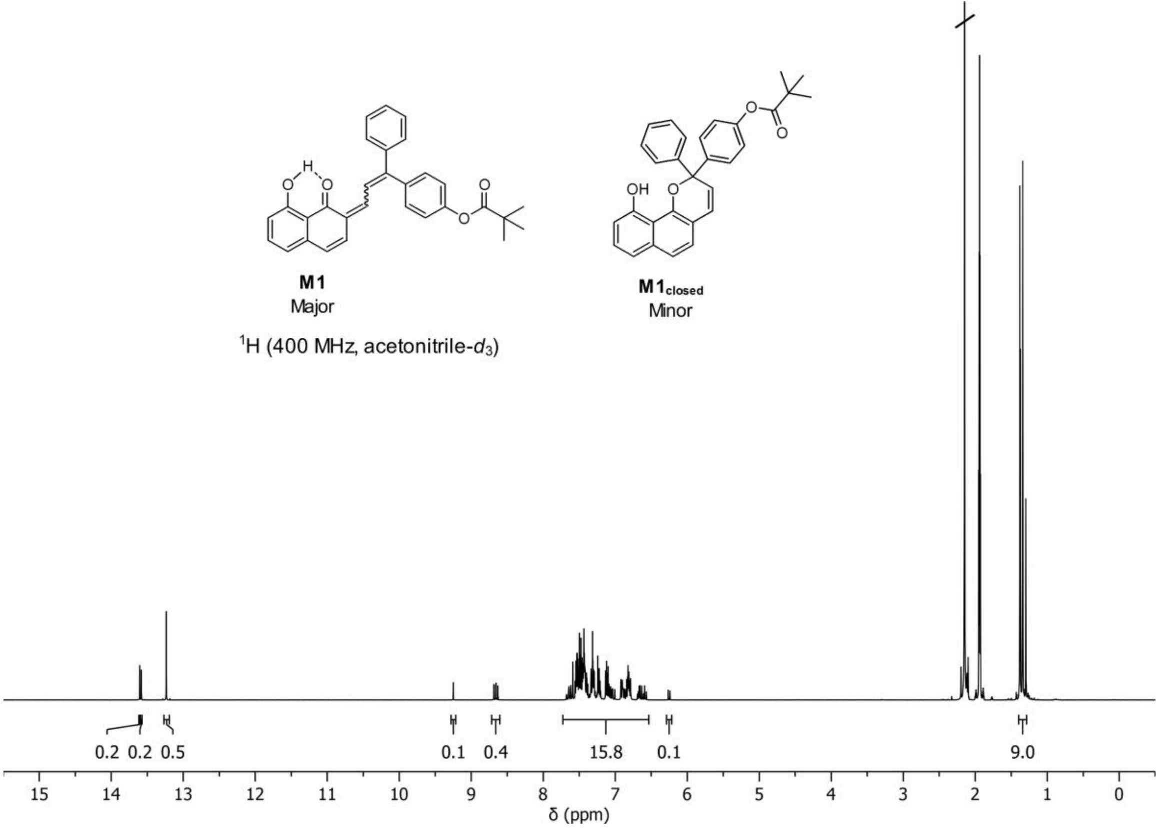
M1
Major
M1closed
Minor
1H (400 MHz, acetonitrile-d3)
0.2
0.2
0.5
0.1
0.4
15.8
0.1
9.0
15 14 13 12 11 10 9 8 7 6 5 4 3 2 1 0
δ (ppm)

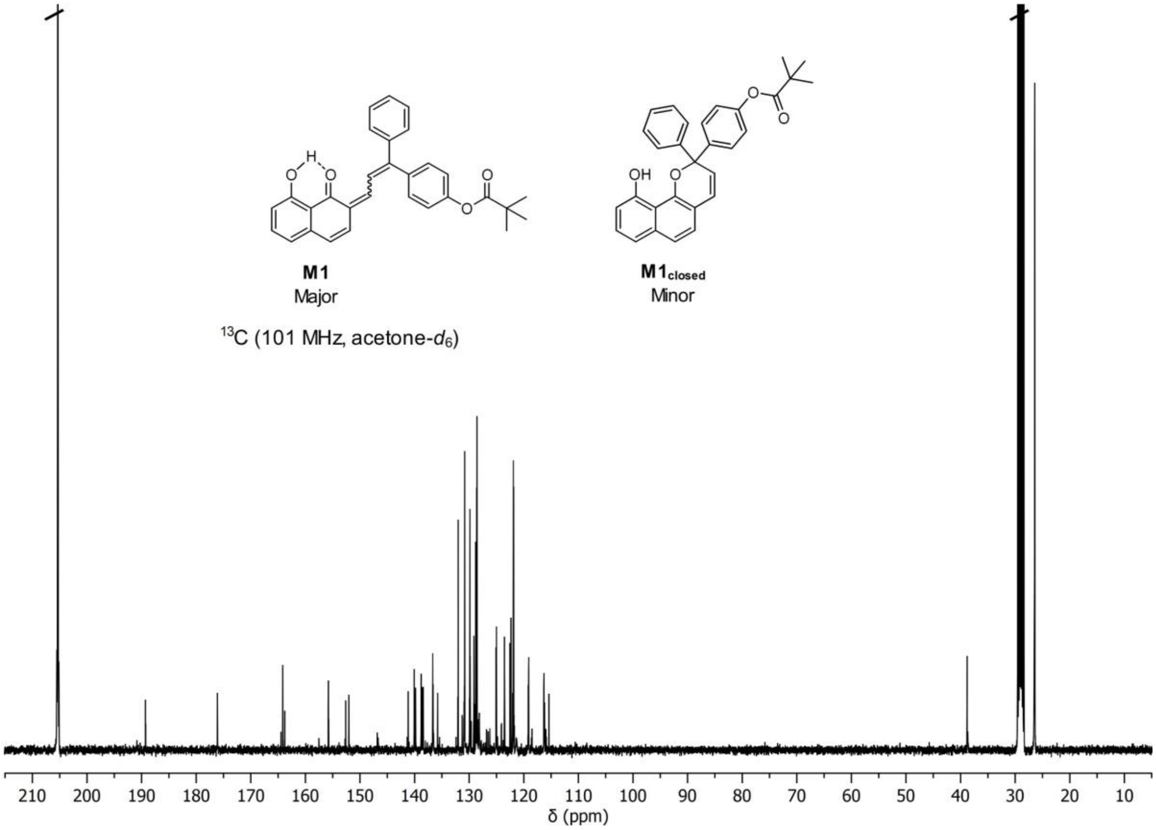
M1
Major
M1$_{closed}$
Minor
^{13}C (101 MHz, acetone-d_6)
210 200 190 180 170 160 150 140 130 120 110 100 90 80 70 60 50 40 30 20 10
δ (ppm)

Chapter 3

VALIDATION OF AN ACCURATE AND EXPEDIENT INITIAL RATES METHOD FOR CHARACTERIZING MECHANOPHORE REACTIVITY

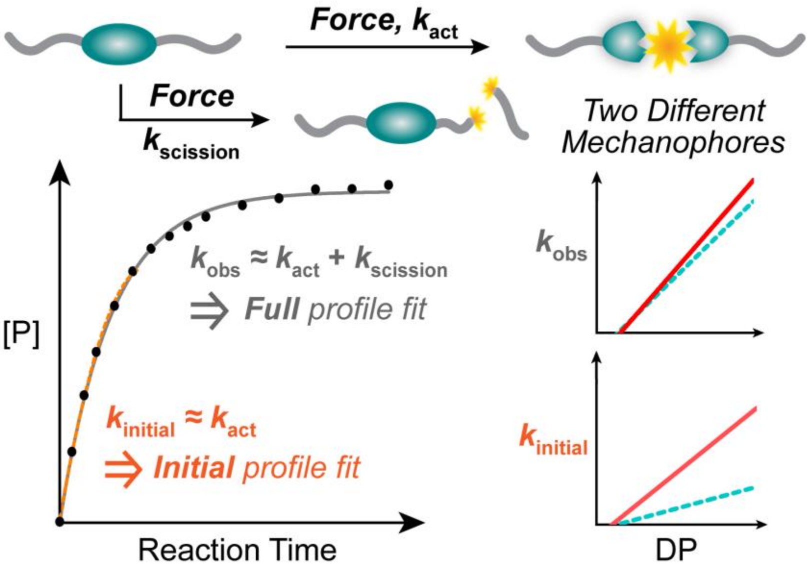

ABSTRACT: Understanding structure–mechanochemical reactivity relationships is important for informing the rational design of new stimuli-responsive polymers. To this end, establishing accurate reaction kinetics for mechanophore activation is a key objective. Here, we validate an initial rates method that enables the accurate and rapid determination of rate constants for ultrasound-induced mechanochemical transformations. Experimental reaction profiles are well-aligned with theoretical models, which support that the initial rates method can effectively deconvolute the kinetics of specific mechanophore activation from the competitive process of nonspecific chain scission.

This chapter has been adapted with permission from McFadden, M. E.; Overholts, A. C.; Osler, S. K.; Robb, M. J. Validation of an Accurate and Expedient Initial Rates Method for Characterizing Mechanophore Reactivity. *ACS Macro. Lett.* **2023**, *12*, 440–445. DOI: https://doi.org/10.1021/acsmacrolett.3c00054

Investigation

Mechanical force promotes a variety of chemical transformations including formal retro-cycloaddition reactions,[1–4] electrocyclic ring-opening reactions,[5–7] homolytic[8,9] and heterolytic[10–13] bond scission, and metal-ligand dissociation.[14,15] Mechanochemical reactions have been harnessed for a wide range of applications including visual force sensing,[16–19] catalyst activation,[20,21] conductivity switching,[22] and molecular release.[23] Fundamentally, understanding structure–mechanochemical activity relationships for mechanically sensitive moieties (*i.e.*, mechanophores) is critical for informing the rational design of new stimuli-responsive materials and their emergent applications.[1]

Solution-phase ultrasonication is a routine method for achieving mechanochemical activation of mechanophore-containing polymers because it is simple, reproducible, and enables the straightforward characterization of reactivity.[24,25] The force experienced by a polymer scales with chain length according to the Bead–Rod model,[26] and the rate of a mechanochemical reaction scales with chain length above a critical threshold.[1,27,28] Reaction progress is conveniently followed using techniques like UV–vis or photoluminescence (PL) spectroscopy for reactions that result in characteristic changes in absorption and emission, or alternatively, gel permeation chromatography (GPC) to monitor chain fragmentation for polymers containing a scissile mechanophore.[29] To characterize the rate of mechanophore activation, reactions are typically run until maximum product formation is achieved and the temporal profile is fit to the integral form of the rate law for a first-order reaction given by eq.3.1:

$$[P]_t = n \cdot [M]_0 \cdot (1 - e^{-k_{obs}t}) + [P]_0 \tag{3.1}$$

where $[P]_t$ and $[P]_0$ are the concentrations of product at time t and $t = 0$, respectively; n is the equivalents of product generated per mechanophore reaction; $[M]_0$ is the initial mechanophore concentration; and k_{obs} is the apparent rate constant (Figure 3.1). This treatment assumes that all mechanophore is fully converted to product, which is not appropriate for most mechanochemical reactions because nonspecific backbone cleavage often competes significantly with mechanophore activation.[30–33] While k_{obs} describes the effective kinetics of product accumulation, the specific kinetics of the mechanophore reaction are not accurately described by simple first-order kinetics when a significant competing reaction pathway exists.

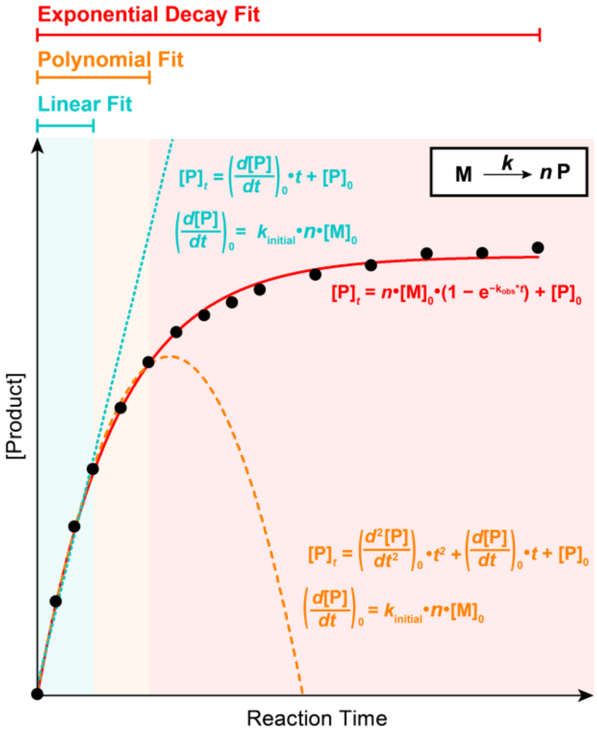

Figure 3.1. Comparisons of different fitting functions applied to a reaction profile for determining a rate constant. Fitting the data to the integrated first-order rate law (red curve) yields the rate constant, kobs. Alternatively, the initial rates method considers only the initial portion of the reaction profile for determining the rate constant, kinitial (blue dashed line). A polynomial fit improves the accuracy and reproducibility of the protocol (orange dashed curve).

In contrast to fitting the full reaction profile, the method of initial rates offers an expedient approach to reliably determine reaction rate constants (see Figure 3.1).[34–36] This approach requires that molar concentrations of species be determined but considers only the initial portion of the reaction profile, which is fit to the differential form of the rate law describing a first-order process given by eq. 3.2:

$$[P]_t = \left(\frac{d[P]}{dt}\right)_0 \cdot t + [P]_0 \tag{3.2}$$

The initial rate of product formation, $(\frac{d[P]}{dt})_0$, is related to the reaction rate constant according to eq. 3.3:

$$\left(\frac{d[P]}{dt}\right)_0 = k_{initial} \cdot n \cdot [M]_0 \tag{3.3}$$

where $k_{initial}$ specifically denotes the rate constant derived from the initial rate. In practice, fitting a slightly larger portion of the reaction profile to a second-order polynomial (eq. 3.4) minimizes variability associated with fitting an arbitrary region of the curve to a linear regression, improving the accuracy and reproducibility of the method (see Figure 3.1).[37]

$$[P]_t = \left(\frac{d^2[P]}{dt^2}\right)_0 \cdot t^2 + \left(\frac{d[P]}{dt}\right)_0 \cdot t + [P]_0 \tag{3.4}$$

The method of initial rates offers a number of advantages for the determination of reaction kinetics. From a practical perspective, running reactions to full conversion can be time-intensive. Since only the early portion of the reaction profile is fit, data collection time is reduced compared to integral methods that require a complete reaction profile. Furthermore, initial rates of product formation are minimally affected by competing pathways that consume reactant. Accurate rates are thus determined from this initial region since the rate of product formation for a first order reaction depends only on substrate concentration, which can be assumed to be nearly constant at early reaction times. We therefore hypothesized that an initial rates method could deconvolute mechanophore activation kinetics from degradative processes like nonspecific backbone scission, producing an accurate depiction of mechanophore reactivity while simultaneously streamlining experimentation. Here, we validate the use of the initial rates method as an accurate and time-efficient protocol for characterizing the kinetics of ultrasound-mediated mechanophore activation, enabling insights into the relative reactivity of different mechanophores.

We first analyzed kinetic data from a series of poly(methyl acrylate) (PMA) polymers containing a scissile and fluorogenic coumarin dimer mechanophore (**PMA-CD**). The coumarin dimer mechanophore in **PMA-CD** undergoes a formal retro-[2 + 2] cycloaddition reaction to generate two fluorescent coumarin moieties as illustrated in Figure 3.2.[30] In comparison to other mechanophores, the coumarin dimer is relatively unreactive, achieving only ~33% total activation upon ultrasound-induced mechanochemical activation.[33,30] This low activation efficiency can be

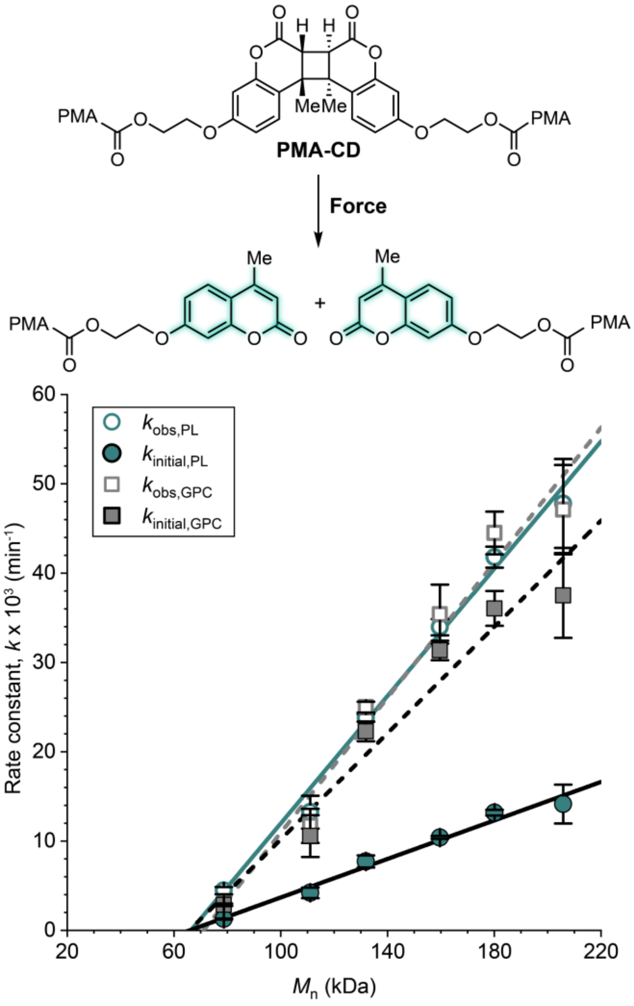

Figure 3.2. Comparison of rate constants for the ultrasound-induced mechanochemical activation of **PMA-CD**. Data were obtained from either PL or GPC-RI measurements and rate constants were determined by fitting the full reaction profile to the integrated rate law (k_{obs}) or by using the initial rates method (k_{initial}). Data points and error bars represent average values and standard deviation from three replicate experiments.

attributed to poor selectivity between nonspecific chain scission and mechanophore activation, and presents an excellent case study for the initial rates method as demonstrated below. Polymers were synthesized by controlled radical polymerization to install a coumarin dimer mechanophore near the chain midpoint, where mechanical force is maximized during ultrasonication.[25,30] Dilute solutions of each polymer were subjected to pulsed ultrasound in an ice bath and aliquots were removed periodically for analysis by PL spectroscopy and GPC. Experiments were performed in triplicate and sonication was applied until PL emission of the product reached an approximately constant maximum value (see the Experimental section for details).

Rate constants obtained from fitting the full reaction profiles to the integrated rate law (k_{obs}) and by using the initial rates method (k_{initial}) are presented in Figure 3.2 (see the Experimental section for details). Whereas PL measurements report specifically on product (*i.e.*, coumarin) formation, attenuation of the GPC refractive index (GPC-RI) signal of the initial polymer reports on chain scission and therefore substrate consumption.[29] Fitting the full reaction profiles produces similar rate constants when monitoring product formation via PL ($k_{\mathrm{obs,PL}}$) and substrate consumption by GPC-RI ($k_{\mathrm{obs,GPC}}$). While $k_{\mathrm{obs,PL}}$ describes the effective kinetics of product accumulation, the close agreement with $k_{\mathrm{obs,GPC}}$ illustrates that it is an imperfect descriptor of mechanophore activation. These two rate constants would be expected to diverge given the poor selectivity for coumarin dimer activation versus nonspecific backbone scission. Nonspecific backbone scission represents a significant competitive pathway for the consumption of starting polymer, which also ultimately suppresses the maximum attainable amount of product. In accordance with our hypotheses, applying the initial rates method to the PL data reveals significantly slower kinetics ($k_{\mathrm{initial,PL}}$) while the rate constants determined from the GPC-RI data ($k_{\mathrm{initial,GPC}}$) are only slightly smaller than the values of $k_{\mathrm{obs,GPC}}$. The faster consumption of substrate compared to product formation (*i.e.*, $k_{\mathrm{initial,GPC}} > k_{\mathrm{initial,PL}}$) indicates that chain scission occurs with a higher frequency than mechanophore activation, which is again consistent with the low activation efficiency observed for the coumarin dimer mechanophore. These results suggest that the initial rates method, applied to reaction profiles monitoring product formation, can readily deconvolute the kinetics of mechanophore activation from those of competitive nonproductive pathways that consume starting material.

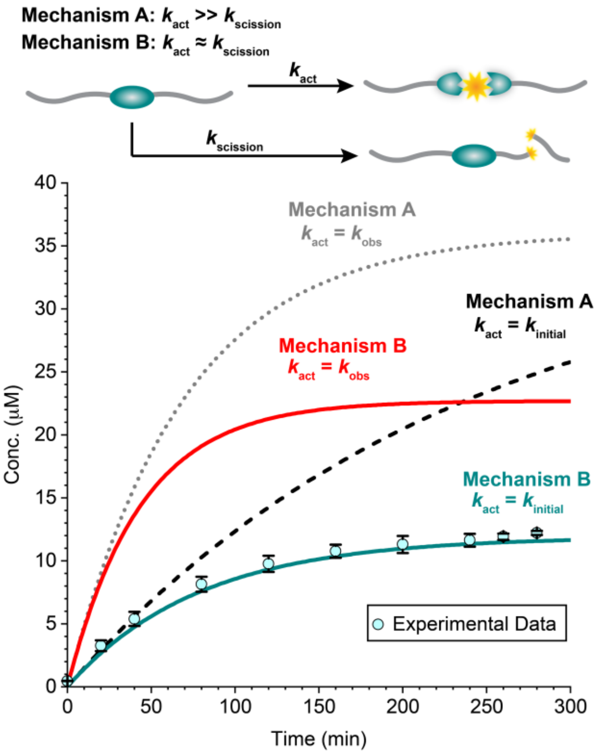

Figure 3.3. Experimental data for the mechanochemical activation of a 111 kDa **PMA-CD** polymer modeled by different theoretical rate expressions using either $k_{\mathrm{obs,PL}}$ or $k_{\mathrm{initial,PL}}$ for k_{act} under two different mechanistic scenarios assuming varying degrees of competition between mechanophore activation and nonspecific chain scission.

If we assume that nonspecific backbone scission is the dominant nonproductive reaction pathway that depletes starting material, as hypothesized, then a revised rate law that specifically accounts for this competing process should accurately reproduce the observed mechanophore reaction profile. To test this hypothesis and validate the accuracy of rate constants obtained using the initial rates method, Figure 3.3 compares experimental PL data for the mechanochemical generation of coumarin product from a 111 kDa **PMA-CD** polymer to theoretical kinetic profiles. We focus on two mechanistic scenarios in which the true rate constant for mechanophore activation, k_{act}, is either significantly greater than (mechanism A) or of comparable magnitude to (mechanism B) the effective rate constant for nonspecific polymer chain scission, k_{scission}. As described above, a simple first-order reaction would follow mechanism A according to eq. 3.1. Here we use n = 2 and $[M]_0$ = 30.4 μM based on the experimental quantity, along with experimentally determined values of $k_{\text{obs,PL}}$ and $k_{\text{initial,PL}}$. Using the rate constant determined by the initial rates method more accurately reflects the experimental reactivity, but both of these theoretical curves significantly overestimate the amount of product generation, which is consistent with the relatively low activation efficiency of the coumarin dimer mechanophore. On the other hand, mechanism B assumes that nonspecific backbone scission competes with mechanophore activation. Given these constraints, the integral form of the rate law is provided by eq. 3.5

$$[P]_t = \frac{n[M]_0 \cdot k_{act}(1 - e^{-(k_{act} + k_{scission})\cdot t})}{(k_{act} + k_{scission})} \tag{3.5}$$

Experimentally determined values of k_{scission} were obtained using a series of PMA polymers with a mechanochemically inactive, chain-centered bisphenol A moiety that was subjected to ultrasonication under the same conditions as the **PMA-CD** series (see Experimental section for details). Chain scission kinetics were obtained from GPC-RI measurements and values of k_{scission} were determined using the initial rates method (Figure 3.4). Using the appropriate values of k_{scission} for a 111 kDa polymer and $k_{\text{obs,PL}}$ for k_{act} in 3.5, the theoretical curve still significantly overestimates the experimental data (red solid trace in Figure 3.3). However, using the value of $k_{\text{initial,PL}}$ for k_{act} results in a curve that closely matches the experimental data. This trend is consistent for the other polymers of varying molecular weight in the **PMA-CD** series (Figure 3.5). The excellent agreement between theory and experiment support that the disparity observed between rate constants determined using the full reaction profile and those from the initial rates method is due to significant competition between mechanophore activation and nonspecific chain scission, as anticipated. As evident in the decay term of 3.5 (*i.e.*, $k_{act} + k_{scission}$), the observed rate constant obtained by fitting the profile for a reaction that involves a significant secondary pathway to simple first-order kinetics, as in 3.1, reflects the sum of the rate constants for the two constituent processes (Figure 3.6). This modeling exercise strongly supports that the initial rates method produces rate constants that accurately describe mechanophore activation kinetics, notably without any experimental characterization of $k_{scission}$. On the other hand, the results above demonstrate that if the molar concentrations of product cannot be determined, the experimental determination of $k_{scission}$ under comparable conditions allows accurate values of k_{act} to be obtained by fitting the full reaction profile to 3.5 (see Figure 3.7 and Figure 3.8).

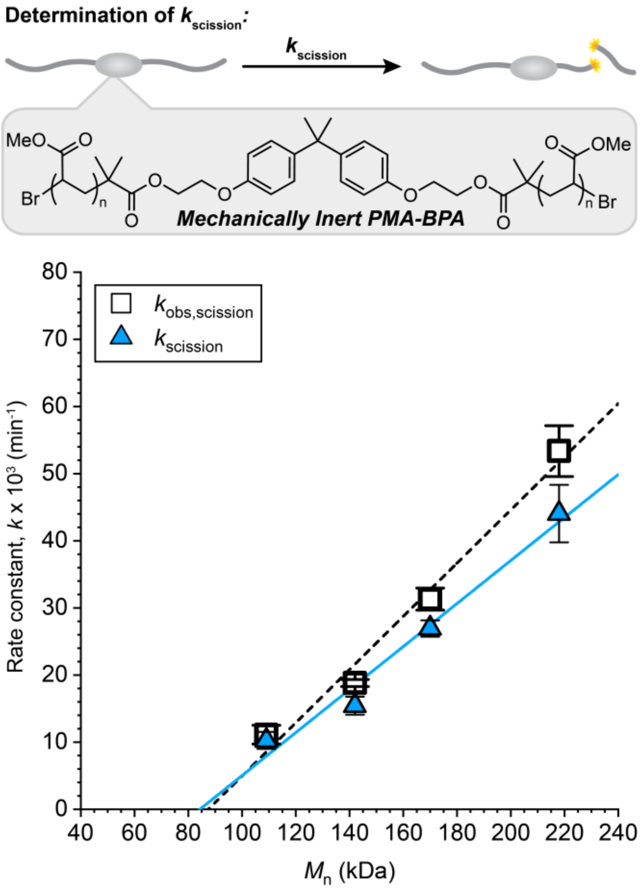

Figure 3.4. Effective rate constants for nonspecific backbone scission upon ultrasonication of PMA-BPA as a function of initial polymer molecular weight. Rate constants were determined from time-dependent GPC-RI measurements by fitting either the full reaction profile to the integrated rate law ($k_{obs,scission}$) or by using the initial rates method ($k_{scission}$). Data points and error bars represent average values and standard deviation from three replicate experiments. See Section V for details.

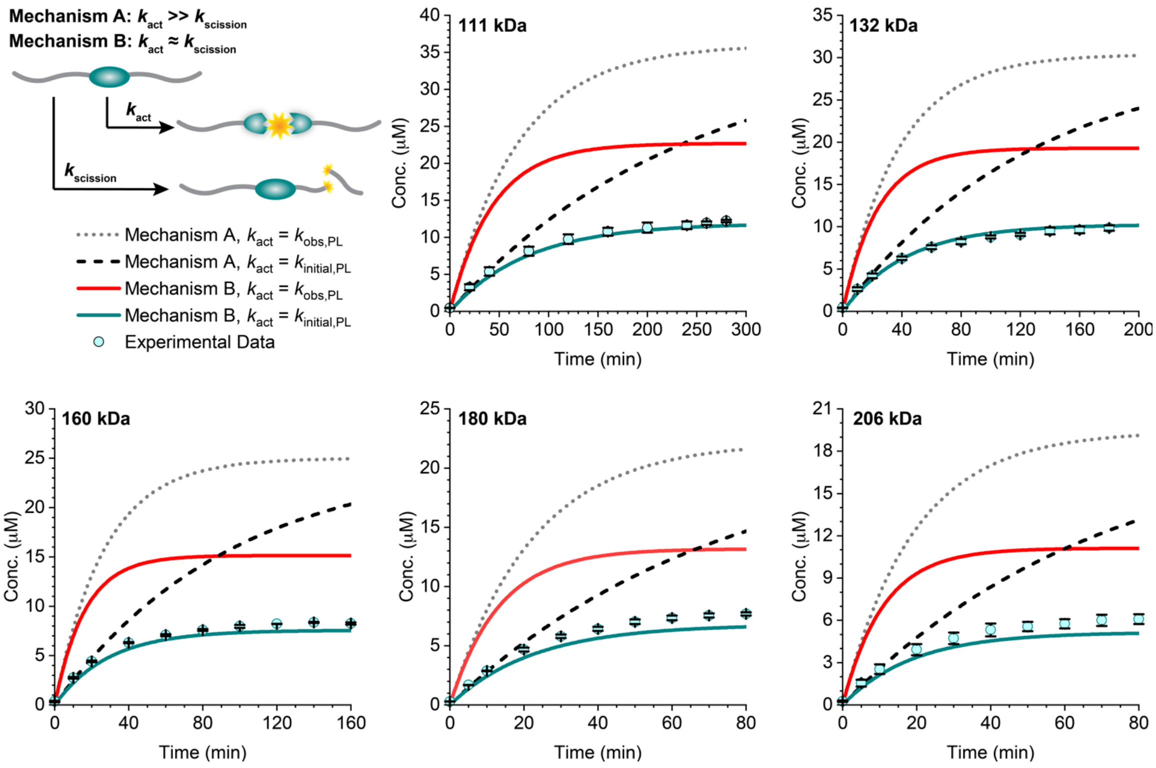

Figure 3.5. Experimental data for the mechanochemical activation of **PMA-CD** polymers of varying initial molecular weight compared to projected models for different theoretical rate expressions using either $k_{obs,PL}$ or $k_{initial\ PL}$ for k_{act} under two different mechanistic scenarios assuming different degrees of competition between mechanophore activation and nonspecific chain scission. Data points and error bars represent average values and standard deviation from three replicate experiments. See Section VI of the Experimental section for details.

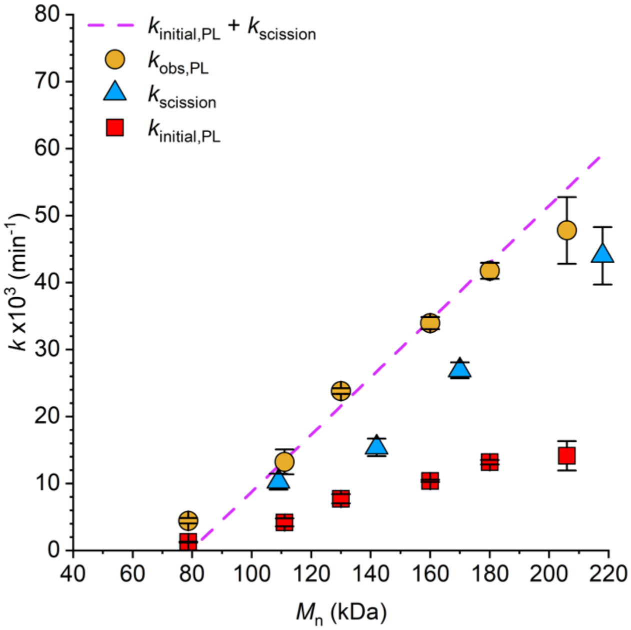

Figure 3.6. Rate constants obtained from time-dependent photoluminescence measurements for **PMA-CD** upon ultrasonication by fitting either the full reaction profile to the integrated rate law ($k_{obs,PL}$) or using the initial rates method ($k_{initial,PL}$), compared to the effective rate of nonspecific backbone scission ($k_{scission}$) determined from **PMA-BPA**. The dashed line represents the sum of the individual linear regressions for $k_{initial,PL}$ and $k_{scission}$ data sets as a function of polymer molecular weight, which closely matches the values of $k_{obs,PL}$. Data points and error bars represent average values and standard deviation from three replicate experiments.

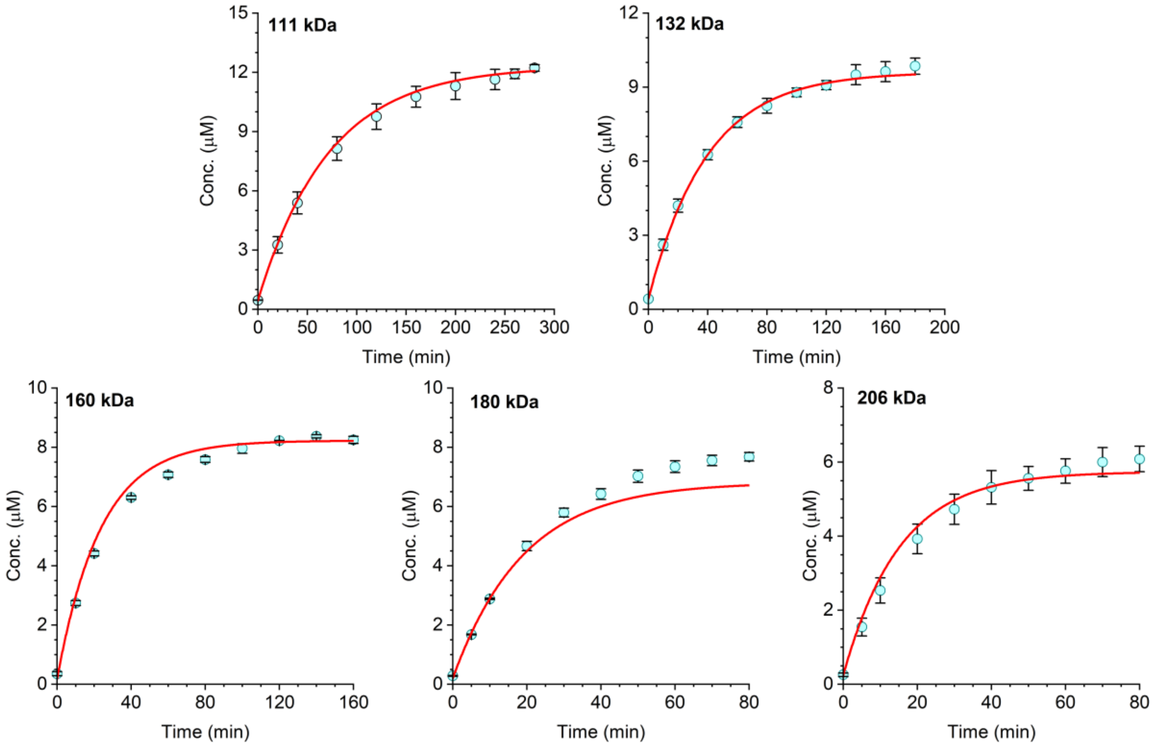

Figure 3.7. Experimental mechanochemical reaction profiles for **PMA-CD** determined by PL measurements fit to the integral form of a theoretical rate law (eq. 3.17) incorporating nonspecific backbone scission to obtain fit-determined values for k_{act}. Data points and error bars represent average values and standard deviation from three replicate experiments. See Section VI of the Experimental section for details.

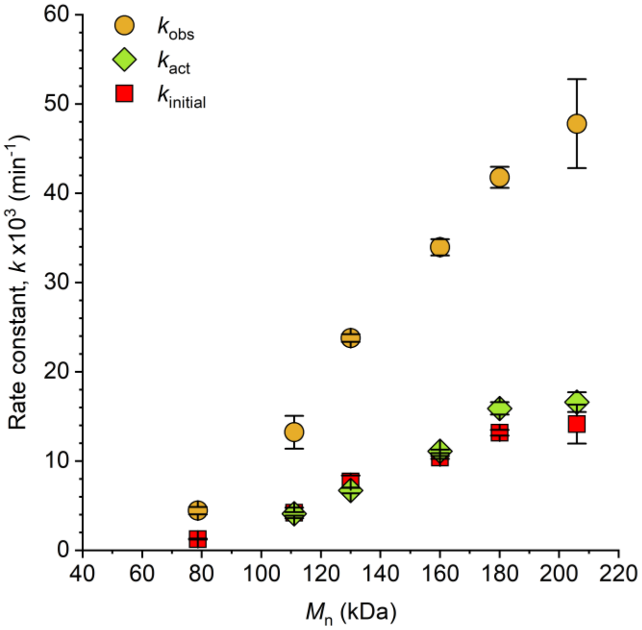

Figure 3.8. Rate constants obtained from time-dependent photoluminescence measurements for **PMA-CD** upon ultrasonication using three different fitting methods, plotted as a function of initial polymer molecular weight. Data points and error bars represent average values and standard deviation from three replicate experiments. See Section VI of the Experimental section for details.

To investigate the generality of the initial rates method for characterizing mechanophore activation kinetics, we turned our attention to a second mechanophore. A naphthopyran mechanophore reported by our group undergoes a ring-opening reaction upon mechanical activation that is accompanied by the scission of the naphthyl C(O)–O ester bond to reveal a β-hydroxy ketone moiety that locks the merocyanine in the ring-opened state (Figure 3.9).[38] Importantly, this naphthopyran mechanophore exhibits a significantly higher activation efficiency than the coumarin dimer (~77%, *vida infra*), providing breadth to this validation study (Figure 3.11). An analogous series of PMA polymers (**PMA-NP**) containing the naphthopyran mechanophore near the chain center was synthesized and dilute solutions of each polymer in THF were subjected to continuous ultrasonication (see Experimental section for details). Product formation was monitored synchronously by UV-vis absorption spectroscopy using a previously described flow setup (Figure 3.10).[39] Notably, the initial rates analysis required ~10× less total reaction time compared to the approach using the full reaction profiles (6 h vs 63 h) for the entire PMA-NP series, highlighting the distinct advantage in time efficiency.

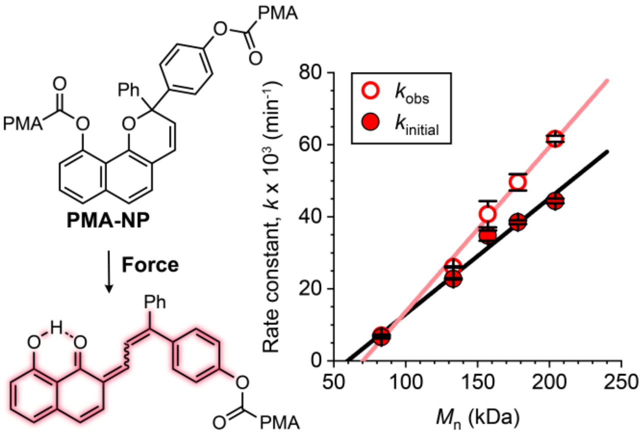

Figure 3.9. Comparison of rate constants for the ultrasound-induced mechanochemical activation of **PMA-NP**. Data were obtained from UV-vis absorption measurements and rate constants were determined by fitting the full reaction profile to the integrated rate law (k_{obs}) or by using the initial rates method ($k_{initial}$). Data points and error bars represent average values and standard deviation from two or three replicate experiments.

Analogous to the results presented above for the coumarin dimer mechanophore, the values of $k_{initial}$ determined for **PMA-NP** are consistently smaller than the values of k_{obs}, indicating that mechanophore activation efficiency is less than unity (Figure 3.9). The difference in the values of these rate constants, however, is less pronounced than for the coumarin dimer. The modeling exercise above supports that

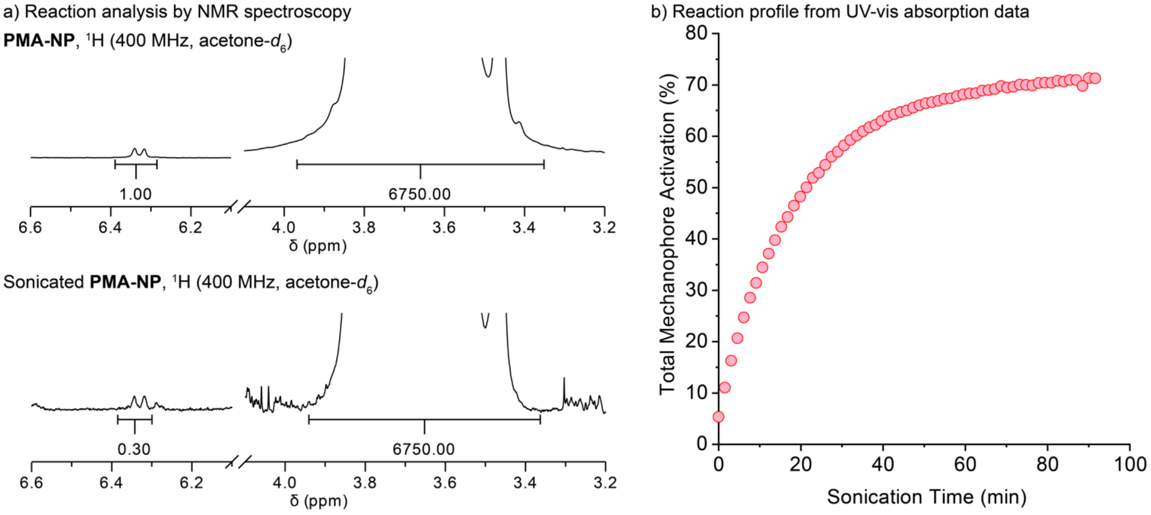

Figure 3.11. Determination of total mechanophore yield by either ^{1}H NMR spectroscopy or UV-vis absorption spectroscopy yields similar results for **PMA-NP** (M_n = 178 kDa; Đ = 1.14). (a) NMR analysis of **PMA-NP** before and after ultrasonication. The methyl ester group of PMA (3.65 ppm) is used as an internal standard. Integration of the pyran olefin resonance (6.33 ppm) is reduced from 1.00 to 0.30 H after extended sonication (~100 min), suggesting ~70% mechanophore conversion. (b) The reaction profile followed by UV-vis absorption spectroscopy at 510 nm (characteristic of the merocyanine) was converted to total mechanophore activation using the measured extinction coefficient of **M1** (see Section IV of the Experimental section for details). Consistent with the NMR analysis monitoring starting material consumption, the UV-vis absorption data indicate ~70% conversion to product.

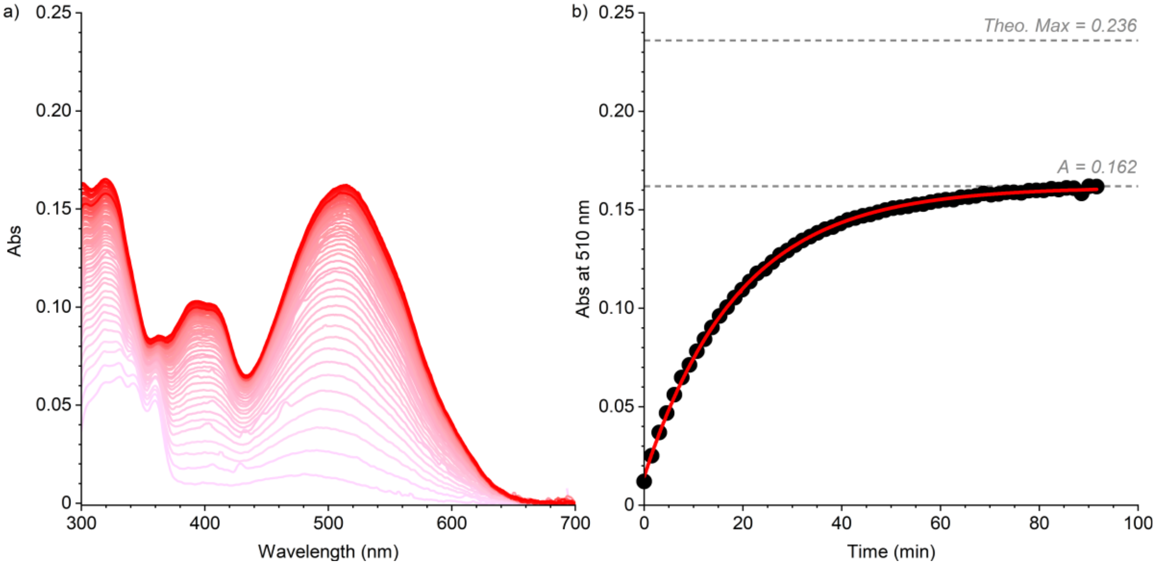

Figure 3.10. (a) Representative UV-vis absorption spectra acquired during ultrasonication of **PMA-NP** (M_n = 178 kDa; Đ = 1.14). Spectra were collected every 2 min (~1.5 min sonication time). (b) Absorbance at 510 nm as a function of sonication time, which is fitted to eq. 3.7 to determine the plateau absorbance, *A*. The projected plateau value is compared to the maximum theoretical absorbance calculated using the extinction coefficient of model compound **M1**. See Sections IV and V of the Experimental section for details.

rate constants determined using the initial rates method for product formation are not convoluted by competitive backbone scission and reflect the true rate of mechanophore activation. It follows that if k_{initial} provides an accurate representation of k_{act}, and k_{obs} is the sum of the rate constants for mechanophore activation and nonspecific chain scission (*i.e.*, the rate constant for starting material consumption), then the ratio $k_{\text{initial}}/k_{\text{obs}}$ should describe mechanophore activation efficiency, as depicted by the preexponential factor of eq. 3.5. Indeed, this ratio agrees well with measured mechanophore activation efficiencies for both the **PMA-CD** and **PMA-NP** series across a broad range of molecular weights (Figure 3.12a). These results further support the conclusions from modeling above and indicate that the rate constants determined using the initial rates method applied to time-dependent product formation profiles provide an accurate description of mechanophore reactivity. Figure 3.12b further illustrates this point by comparing the rate constants determined for **PMA-NP** to those of **PMA-CD**.

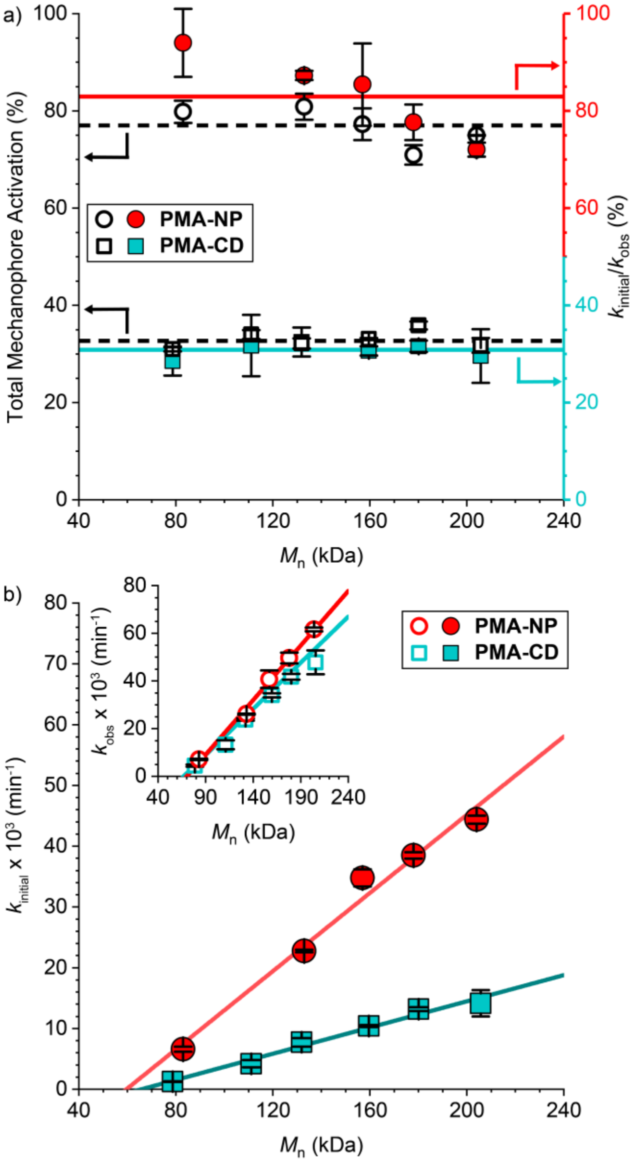

Figure 3.12. (a) Comparison of mechanophore activation efficiency to the ratio $k_{\text{initial}}/k_{\text{obs}}$ for **PMA-CD** and **PMA-NP**. Horizontal lines represent the average value for each series. (b) Comparison of the rate constants determined for the two mechanophores using the initial rates method (k_{intial}), or by fitting the full reaction profiles to the integrated rate law (k_{obs}). Data points and error bars represent average values and standard deviation from two or three replicate experiments.

While a comparison of k_{obs} implies similar reactivity between the naphthopyran and coumarin dimer mechanophores (Figure 3.12b inset), the trends in k_{initial} clearly highlight the differences in mechanophore activation kinetics that are consistent with measured activation efficiencies.

In summary, we validate an initial rates method for characterizing mechanophore reactivity in solution-phase ultrasonication experiments that provides accurate rate constants in a time-efficient protocol. We demonstrate that typical methods for kinetic evaluation of mechanochemical reactions are convoluted by competitive processes like nonspecific backbone scission, whereas the initial rates method produces rate constants that more accurately describe the specific kinetics of mechanophore activation. Though not tested here, the initial rates method may also prove to be useful for determining the forward rates of mechanochemical reactions in reversible processes. The accurate and rapid determination of rate constants for mechanochemical reactions will benefit the further development of structure–reactivity relationships to inform the rational design of new mechanophores and force-responsive materials.

Acknowledgements

Financial support from Caltech and an NSF CAREER award (CHE-2145791) is gratefully acknowledged. M.E.M. and A.C.O. were supported by NSF Graduate Research Fellowships (DGE-1745301). Support from a Barbara J. Burger Graduate Fellowship (M.E.M. and A.C.O.) and Institute Fellowships (A.C.O. and S.K.O.) at Caltech is also gratefully acknowledged. M.J.R. is an Alfred P. Sloan Research Fellow and a Camille Dreyfus Teacher-Scholar.

EXPERIMENTAL DETAILS

I. General Experimental Details

Reagents from commercial sources were used without further purification unless otherwise noted. Methyl acrylate was passed through a short plug of basic alumina to remove inhibitor immediately prior to use. Copper wire was soaked in 1 M HCl for 10 min and then rinsed consecutively with water and acetone immediately prior to use. Dry THF and MeCN were obtained from a Pure Process Technology solvent purification system. All reactions were performed under a N_2 atmosphere unless specified otherwise.

NMR spectra were recorded using a 400 MHz Bruker Avance III HD with Prodigy Cryoprobe. ^{1}H NMR spectra are reported in δ units, parts per million (ppm), and were measured relative to the signals for residual chloroform (7.26 ppm) in deuterated solvent. All ^{13}C NMR spectra were measured in deuterated solvents and are reported in ppm relative to the signals for chloroform (77.16 ppm). Multiplicity and qualifier abbreviations are as follows: s = singlet, d = doublet, m = multiplet.

High resolution mass spectra (HRMS) were obtained via direct injection on an Agilent 1260 Infinity II Series HPLC coupled to a 6230 LC/TOF system in electrospray ionization (ESI+) mode.

Analytical gel permeation chromatography (GPC) was performed using an Agilent 1260 series pump equipped with two Agilent PLgel MIXED-B columns (7.5 x 300 mm), an Agilent 1200 series diode array detector, a Wyatt 18-angle DAWN HELEOS light scattering detector, and an Optilab rEX differential refractive index detector. The mobile phase was THF at a flow rate of 1 mL/min. Molecular weights and molecular weight distributions were calculated by light scattering using a dn/dc value of 0.062 mL/g (25 °C) for poly(methyl acrylate).

UV-Vis absorption spectra were recorded on a Thermo Scientific Evolution 220 spectrometer. When applicable, polymer solutions were continuously sampled for UV-vis analysis using a Cole Parmer Masterflex L/S pump system (item #EW-77912-10) composed of an L/S pump head (part #77390-00) and L/S precision variable speed drive (part #07528-20) using 4x6 mm PTFE tubing (part #77390-60) and a quartz flow-through cell (Starna, part #583.4-Q-10/Z8.5) with a 1 cm pathlength, which was connected using M6-threaded PTFE tubing (Starna, part #M6-SET).

Photoluminescence spectra were recorded on a Shimadzu RF-6000 spectrofluorophotometer in a quartz microcuvette (Starna 18F-Q-10-GL14-S).

Photochemical reactions were performed using a 36 W UV100A Honeywell Air Treatment System with a Philips PL-L Hg lamp, or a 4 Watt UVLS-24 EL Series UV Lamp.

Ultrasound experiments were performed inside a sound abating enclosure using a Vibra Cell 505 liquid processor equipped with a 0.5-inch diameter solid probe (part #630-0217), sonochemical adapter (part #830-00014), and a Suslick reaction vessel made by the Caltech glass shop (analogous to vessel #830-00014 from Sonics and Materials).

Compounds **Init-NP**,[38] **Init-CD**,[29] **Diol-BPA,**[40] and **M1**[38] were synthesized following the procedures reported in the literature.

Chart 3.1. Structures of initiators (**Init-CD**, **Init-NP**, **Init-BPA**) and small molecule reference compound (**M1**) used in this study.

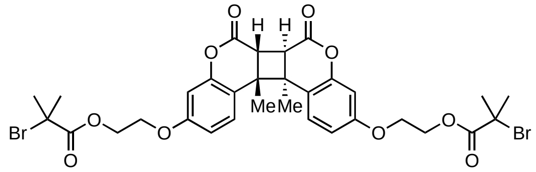

Init-CD

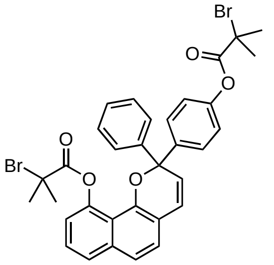

Init-NP

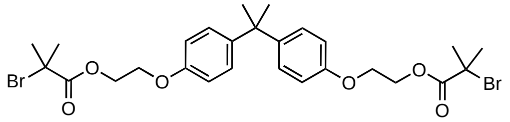

Init-BPA

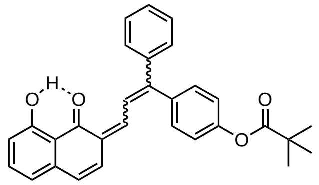

M1

Chart 3.2. Structures of polymers PMA-CD, PMA-NP, and PMA-BPA.

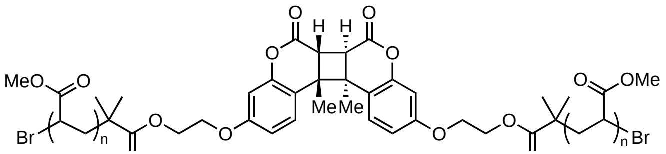

PMA-CD

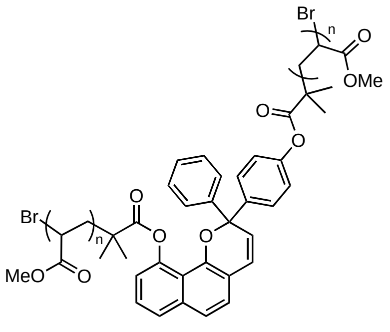

PMA-NP

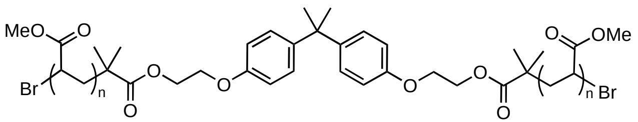

PMA-BPA

II. Synthetic Details

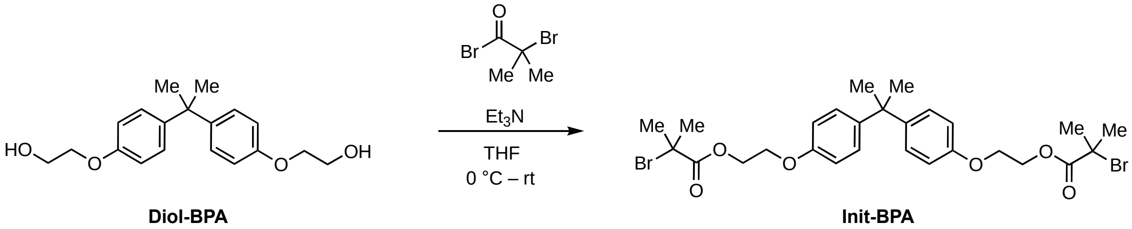

((propane-2,2-diylbis(4,1-phenylene))bis(oxy))bis(ethane-2,1-diyl) bis(2-bromo-2-methylpropanoate) (Init-BPA). To a flame-dried 25 mL round bottom flask equipped with a stir bar was added **Diol-BPA** (198.6 mg, 0.628 mmol). The flask was evacuated and backfilled with N_2 three times. Anhydrous THF (5 mL) and triethylamine (0.30 mL, 2.2 mmol) were added via syringe under N_2 and the flask was cooled to 0 °C. α-bromoisobutyryl bromide (0.25 mL, 2.0 mmol) was added dropwise via syringe under N_2 and the reaction was allowed to warm to room temperature overnight. After 12 h the reaction was diluted with EtOAc, washed twice with 10% aqueous NH_4Cl, twice with 10% aqueous $NaHCO_3$, and once with brine. The organic layer was dried over Na_2SO_4, filtered, and concentrated under reduced pressure. The material was purified by column chromatography on silica gel (0–20% EtOAc/hexanes) to afford the title product as a colorless oil (242 mg, 61% yield).

HRMS (ESI, *m/z*): calcd for $[C_{27}H_{38}Br_2NO_6]^+$ $(M+NH_4)^+$, 630.1060; found, 630.1065.

TLC (20% EtOAc/hexanes): $R_f = 0.55$

^{1}H NMR (400 MHz, $CDCl_3$) δ 7.14 (d, *J* = 8.8 Hz, 4H), 6.82 (d, *J* = 8.8 Hz, 4H), 4.54 – 4.46 (m, 4H), 4.22 – 4.18 (m, 4H), 1.93 (s, 12H), 1.63 (s, 6H).

^{13}C NMR (101 MHz, $CDCl_3$) δ 171.8, 156.4, 143.8, 127.9, 114.3, 65.7, 64.5, 55.7, 41.9, 31.2, 30.9.

Representative procedure for the synthesis of poly(methyl acrylate) (PMA) polymers. PMA polymers were synthesized by controlled radical polymerization following the procedure by Nguyen *et al.*[41] A 25 mL Schlenk flask equipped with a stir bar was charged with initiator **Init-CD** (16.7 mg, 0.226 mmol), DMSO (2 mL), methyl acrylate (2 mL), and freshly cut copper wire (2.0 cm length, 20 gauge). The flask was sealed, the solution was deoxygenated with three freeze-pump-thaw cycles, and then allowed to warm to rt and backfilled with nitrogen. Me$_6$TREN (17 μL, 0.0636 mmol) was added via microsyringe to initiate the polymerization. After stirring at rt for ~2 h, the flask was opened to air and the solution was diluted with dichloromethane. The polymer solution was precipitated into cold methanol (3x) and the isolated material was dried under vacuum to yield 1.46 g of **PMA-CD** (70%). M_n = 78.7 kDa, $Đ$ = 1.05. Characterization data for all polymers is provided below in Table 3.1.

Table 3.1. Summary of M_n and $Đ$ data for **PMA-NP, PMA-CD,** and **PMA-BPA**.

	M_n (kDa)	**$Đ$**		**M_n (kDa)**	**$Đ$**
PMA-NP	83.1	1.15	**PMA-CD**	78.7	1.05
	133	1.10		111	1.07
	158	1.11		132	1.06
	178	1.14		160	1.05
	204	1.12		180	1.05
				206	1.09
			PMA-BPA	109	1.05
				142	1.07
				170	1.06
				218	1.06

III. Description of Sonication Experiments

General Procedure for Ultrasonication Experiments of PMA-CD and PMA-BPA. An oven-dried sonication vessel was fitted with rubber septa, placed onto the sonication probe, and allowed to cool under a stream of dry argon. The vessel was charged with a dilute solution of the polymer (2.0 mg/mL, 20 mL) and submerged in an ice bath. Sonications were run in 3:1 MeCN/MeOH, which has been shown to provide reproducible photoluminescence spectra for the CD mechanophore.[29] The solution was sparged continuously with argon beginning 10 min prior to sonication and for the duration of the sonication experiment. Pulsed ultrasound (1 s on / 2 s off, 30% amplitude, 20 kHz, 13.6 W/cm^2) was then applied to the system. Aliquots (1.0 mL) were removed at specified time points (sonication "on" time) and filtered through a 0.45 μm PTFE syringe filter prior to analysis by GPC and/or fluorescence spectroscopy. Aliquots from the sonication experiment were added to a quartz microcuvette and emission spectra for **PMA-CD** were recorded at 330–500 nm using an excitation wavelength of λ_{ex} = 320 nm. For **PMA-CD**, sonications were run until the PL signal (λ_{em} = 375 nm) from the mechanically generated product reached a nearly constant value.

General Procedure for Ultrasonication Experiments of PMA-NP. In order to continuously monitor reaction progress by UV-vis absorption spectroscopy, a previously reportedsisetup[28,42] was assembled using a peristaltic pump to transport solution from the reaction vessel through a quartz flow cell in a UV-vis spectrometer and return the solution to the reaction vessel. The flow rate through the system was maintained at 8 mL/min, corresponding to a setting of 50 RPM on the peristaltic pump at the selected occlusion. The UV-vis spectrometer was programmed to acquire either full spectra or absorbance at predefined wavelengths at regular time intervals. Absorbance measurements at wavelengths of 510 and 700 nm were acquired every 10 s. The absorbance values measured at 700 nm were subtracted from the absorbance values monitored at 510 nm at each time point to account for drift during the experiments.

An oven-dried sonication vessel was fitted with rubber septa, placed onto the sonication probe, and allowed to cool under a stream of dry nitrogen. The vessel was charged with THF, which contained 30 mM BHT (19.0 mL) to avoid decomposition side reactions resulting from free radicals generated during sonication.[43] An additional 6.2 mL of stabilized THF was pumped into the dead space of the circulatory setup. Teflon inlet and outlet tubes were inserted into the solution in the sonication vessel through punctured septa, and the pump was engaged to start the flow of solution through the system. The polymer solution was sparged with N_2 for 30 min prior to sonication. During sonication, the gas line was moved into the headspace of the sonication vessel to maintain an inert atmosphere. Continuous sonication (20% amplitude, 20 kHz, 8.77 W/cm^2) was initiated during flow and run for approximately 5 min to allow the temperature inside the reaction vessel to equilibrate to 15–20 °C, as measured by a thermocouple (Digi-Sense EW-91428-02 thermometer with Digi-Sense probe EW-

08466-83). A concentrated solution of polymer (1.0 mL, 52.4 mg/mL in stabilized THF) was then injected to provide a total system volume of 26.2 mL of a 2.0 mg/mL polymer solution, and reaction progress was followed by UV-vis absorption spectroscopy (see Figure 3.10). Ultrasonic intensity was calibrated using the method described by Berkowski et al.[44] The entire system was kept in the dark for the duration of the experiment.

IV. Determination of Molar Response Factors and Percent Activation

Characterization of Coumarin PL Response Factor. The response factor for converting PL intensity of coumarin to molar concentration was determined based on the literature method.[29] For each sonication, an aliquot of polymer solution prior to sonication was added to a quartz cuvette and irradiated with 254 nm light for 60 s and a PL spectrum was acquired. Further irradiation did not lead to any increase in PL intensity, indicating that the coumarin dimer was fully cleaved after 60 s of UV irradiation. The PL intensity at the peak maximum for the photoirradiated sample was then used as the value for 100% activation. Data is provided below in Table 3.6–Table 3.11 for each sonication experiment.[29]

Characterization of Merocyanine Molar Extinction Coefficient. Samples of small molecule merocyanine model compound **M1** at various concentrations in THF containing 30 mM BHT were prepared and absorption spectra were acquired to construct the calibration curve shown below in Figure 3.13. The theoretical absorbance for each sonication experiment based on the concentration of mechanophore was determined from this calibration curve and used as the value for 100% activation. A representative example is shown above in Figure 3.10. Absorbance measurements from sonication experiments of **PMA-NP** were converted to merocyanine concentration (µM) using the extinction coefficient, $\varepsilon = 21{,}000\ \mathrm{M^{-1}\ cm^{-1}}$.

Calculation of Percent Activation for PMA-CD and PMA-NP. Time-dependent PL or absorption values at the relevant emission or absorption wavelength (375 nm for **PMA-CD,** 510 nm for **PMA-NP**) were fit to eq. 3.6 or 3.7 following the procedure described in the literature.[29] The fit-determined plateau value (*A*) was used as the maximum activation for that sonication experiment. The projected plateau value (*A*) was then divided by the maximum theoretical value calculated for full conversion (*i.e.*, 100% mechanophore activation) as described above for **PMA-CD** and **PMA-NP**. Percent activation for **PMA-NP** was also determined by NMR spectroscopy for a 178 kDa polymer (Figure 3.11). Solutions of **PMA-NP** exposed to approximately 100 min of continuous sonication in three separate trials were combined, concentrated, and precipitated from DCM into cold hexanes (dry ice). ^{1}H NMR analysis[38] referenced to the methyl groups of the PMA backbone demonstrate ~70% reduction of the pyran olefin integration after sonication, consistent with the ~71% activation

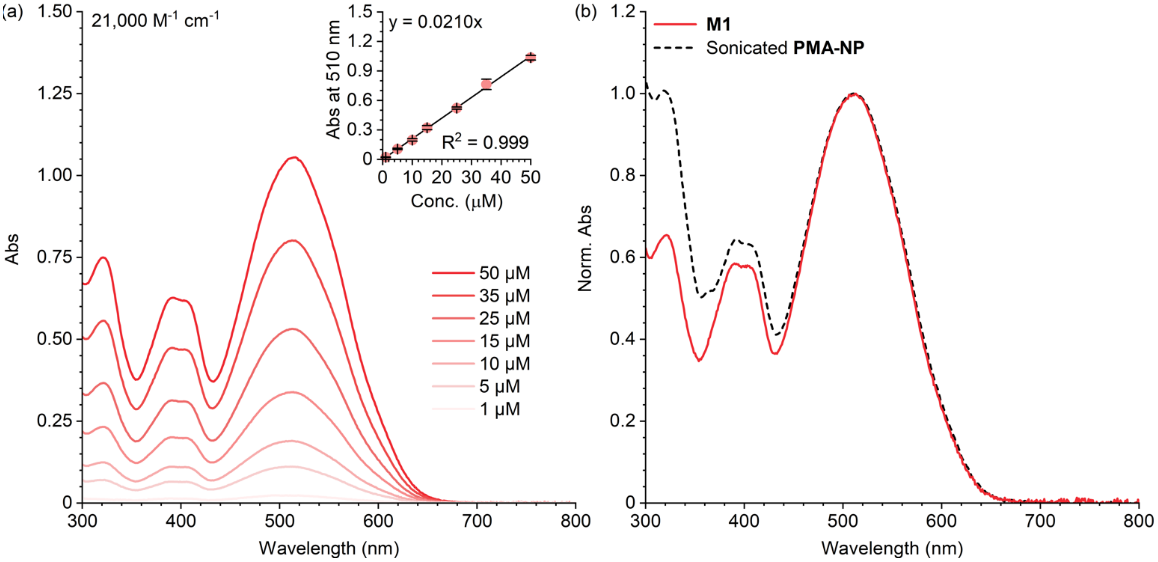

Figure 3.13. Construction of a calibration curve for experimental determination of the concentration of merocyanine. (a) Representative UV-vis absorption spectra are shown for a series of calibration standards of compound **M1** at varying concentration in THF with 30 mM BHT in a 1 cm pathlength cuvette. The inset depicts absorbance at 510 nm as a function of concentration. A linear regression of the data gives the calibration function y = 0.0210*x. Data points and error bars represent average values and standard deviation from two replicate experiments. (b) Comparison of absorption spectra for **M1** (10 µM) and **PMA-NP** (M_n = 204 kg/mol; Đ = 1.12) after sonication for 92 min, normalized to the maximum of the visible absorption peaks.

determined from UV-vis absorption measurements based on the extinction coefficient of model merocyanine **M1**.

V. Calculation of Reaction Rate Constants for PMA-NP, PMA-CD, and PMA-BPA.

Calculation of k_{obs} from time-dependent UV-vis absorption and PL emission measurements. For **PMA-CD**, time dependent PL emission profiles corresponding to coumarin product were fit to the integrated rate law for simple first-order kinetics given by eq. 3.6:

$$PL_t = A \cdot \left(1 - e^{-k_{obs,PL} \cdot t}\right) + PL_0 \tag{3.6}$$

where PL_t and PL_0 are the emission intensity at time t and $t = 0$, respectively; the pre-exponential factor A corresponds to the maximum PL signal attained upon extended sonication; and $k_{obs,PL}$ is the observed rate constant of product accumulation determined from fitting the spectroscopic data to the integrated rate law. PL_0, A, and $k_{obs,PL}$ are fit-determined quantities. Although values of PL_0 represent < 1.5% of the theoretical maximum yield (see Table 3.6–Table 3.11), incorporating this term

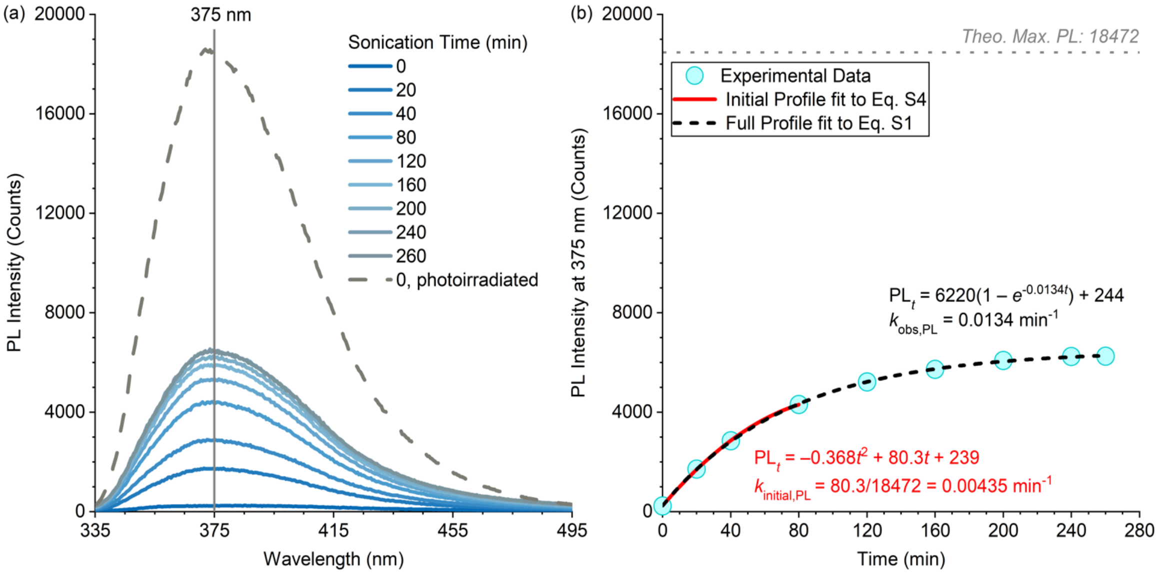

Figure 3.14. (a) Representative PL measurements for the ultrasound-mediated mechanochemical activation of polymer **PMA-CD** (M_n = 111 kg/mol; Đ = 1.07). The unsonicated sample is irradiated with 254 nm light for 60 s to fully cleave the coumarin dimer (gray dashed trace), providing the maximum theoretical PL intensity and facilitating calculation of coumarin concentration. (b) PL intensity at 375 nm as a function of ultrasonication time, for which the full reaction profile is fit to eq. 3.6 (black dashed trace) to obtain $k_{obs,PL}$ (0.0134 min^{-1}). The initial portion of the profile is fit to eq. 3.9 (red solid trace) to obtain the initial rate in terms of PL counts/min (80.3 counts/min), which is in turn converted to $k_{initial,PL}$ using eq. 3.10 (0.00435 min^{-1}).

improves the quality of the fit and therefore the accuracy of the determined rate constants. A representative example of this procedure is shown in Figure 3.14.

For **PMA-NP**, sonication time was defined to be $\frac{20}{26.2}$ of clock time to account for time spent in the flow cell dead space that does not experience sonication.[42] Time-dependent absorption profiles corresponding to merocyanine product were fit to the integrated rate law for simple first-order kinetics given in eq. 3.7:

$$Abs_t = A \cdot \left(1 - e^{-k_{obs} \cdot t}\right) + Abs_0 \tag{3.7}$$

where Abs_t and Abs_0 are the absorbance at 510 nm at time t and $t = 0$, respectively; the pre-exponential factor A corresponds to the maximum absorbance attained upon extended sonication; and k_{obs} is the observed rate constant of product accumulation determined from fitting the spectroscopic data to the integrated rate law. Abs_0, A, and k_{obs} are fit-determined quantities. Note that a small amount of merocyanine (with naphthyl ester intact) exists in the sample initially due to thermal equilibration (see Figure 3.16).[38] Additionally, as the concentrated polymer solution is added directly to the flask already under sonication, some mechanical activation occurs prior to the first measurement. Including the term Abs_0 accounts for this initial signal and improves the fitting characteristics.

Calculation of $k_{obs,GPC}$ from time-dependent GPC-RI measurements. The kinetics of substrate consumption were determined according to the literature method by monitoring the attenuation of the GPC-RI signal of the initial polymer.[29] GPC-RI curves were normalized to peak area for each sonication timepoint. Attenuation of the normalized GPC-RI response at the retention time corresponding to the maximum signal in the initial polymer was plotted as a function of sonication time and fit to eq. 3.8:

$$RI_t = A \cdot \left(e^{-k_{obs,GPC} \cdot t}\right) \tag{3.8}$$

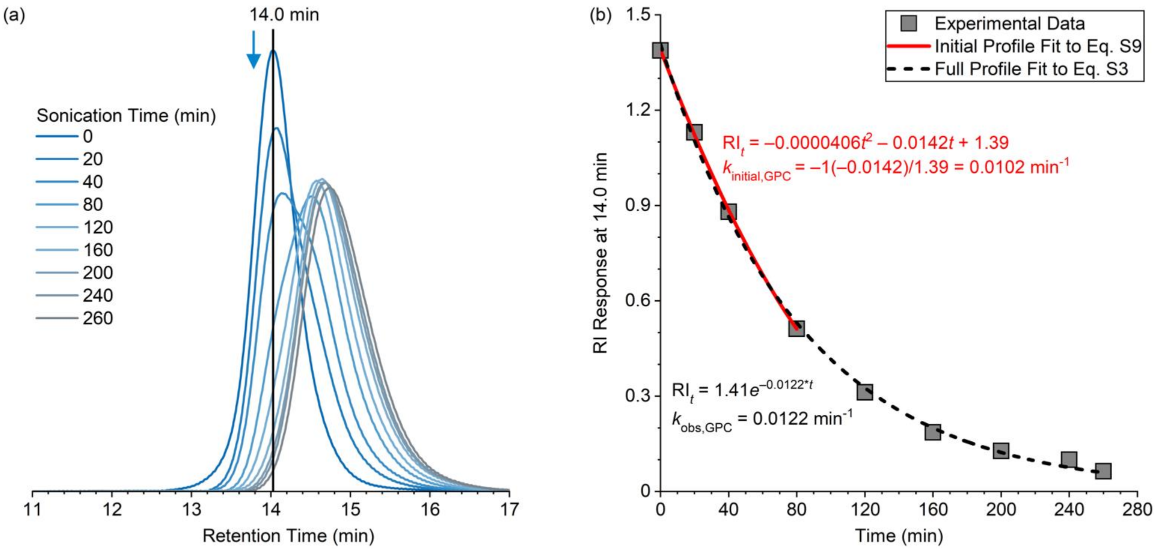

Figure 3.15. (a) Representative time-dependent GPC traces (RI response) normalized by integrated peak area for the ultrasound-mediated mechanochemical activation of polymer **PMA-CD** (M_n = 111 kg/mol; Đ = 1.07). (b) RI response at t_R = 14.0 min (corresponding to the peak maximum of the unsonicated polymer) as a function of ultrasonication time, for which the full reaction profile is fit to eq. 3.8 (black dashed trace) to obtain $k_{obs,GPC}$ (0.0122 min^{-1}). The initial portion of the profile is fit to eq. 3.14 (red solid trace) to obtain the initial rate of polymer scission in arbitrary units of RI response/min (0.0142 counts/min), which is in turn converted to $k_{initial,GPC}$ by eq. 3.15 (0.0102 min^{-1}) using the value of RI_0 (1.39) from Trial 2 in Table 3.5.

where RI_t is the normalized GPC-RI signal at time *t*, A corresponds to the experimental RI amplitude at $t = 0$, and $k_{obs,RI}$ is the rate constant of polymer consumption determined from fitting to the integrated rate law. A and $k_{obs,RI}$ are fit-determined quantities. A representative example of this procedure is shown in Figure 3.15.

Calculation of $k_{initial}$ from time-dependent PL emission and UV-vis absorption measurements. Initial rates of mechanochemical product accumulation were determined by fitting the early portion of the reaction profile spectroscopically monitoring product formation (absorption or PL) to a second order polynomial function following the procedure by Collum.[37]

For **PMA-CD**, the initial reaction profile (up to ~70% of the experimentally observed maximum PL intensity) was fit to eq. 3.9:

$$PL_t = \left(\frac{d^2PL}{dt^2}\right)_0 \cdot t^2 + \left(\frac{dPL}{dt}\right)_0 \cdot t + PL_0 \qquad (3.9)$$

where PL_t and PL_0 are the emission intensity at time *t* and *t* = 0, respectively; $(\frac{d^2PL}{dt^2})_0$ describes the negative acceleration of product formation; and $(\frac{dPL}{dt})_0$ represents the initial rate of change of the PL emission. PL_0, $(\frac{d^2PL}{dt^2})_0$, and $(\frac{dPL}{dt})_0$ are fit-determined quantities. The initial rate of change of the PL emission, $(\frac{dPL}{dt})_0$, is related to the rate constant, $k_{\text{initial,PL}}$, by eq. 3.10:

$$\left(\frac{dPL}{dt}\right)_0 = k_{initial,PL} \cdot PL_{max} \tag{3.10}$$

where PL_{max} is the theoretical maximum emission at 100% mechanophore activation (see Section IV above and Table 3.6–Table 3.11 below). A representative example of this procedure is shown in Figure 3.14.

For **PMA-NP**, the initial reaction profile (up until ~40% of the experimentally observed maximum absorption) was fit to eq. 3.11:

$$Abs_t = \left(\frac{d^2Abs}{dt^2}\right)_0 \cdot t^2 + \left(\frac{dAbs}{dt}\right)_0 \cdot t + Abs_0 \tag{3.11}$$

where Abs_t and Abs_0 are the product absorbance at time *t* and *t* = 0, respectively; $(\frac{d^2Abs}{dt^2})_0$ describes the negative acceleration of product formation; and $(\frac{dAbs}{dt})_0$ represents the initial rate of change of the absorbance. Abs_0, $(\frac{d^2Abs}{dt^2})_0$, and $(\frac{dAbs}{dt})_0$ are fit-determined quantities. The quantity $(\frac{dAbs}{dt})_0$ is related to the initial rate of product formation, $(\frac{d[P]}{dt})_0$, by the Beer–Lambert relationship (eq. 3.12):

$$\left(\frac{dAbs}{dt}\right)_0 = \left(\frac{d[P]}{dt}\right)_0 \cdot \varepsilon \cdot l \tag{3.12}$$

where ε is 0.021 μM^{-1} cm^{-1} (see Section IV above) and l is the cuvette pathlength (1 cm). The initial reaction rate, $(\frac{d[P]}{dt})_0$, is related to the rate constant, k_{initial}, by eq. 3.13:

$$\left(\frac{d[P]}{dt}\right)_0 = k_{initial} \cdot n \cdot [M]_0 \tag{3.13}$$

where *n* is the number of equivalents of product generated per mechanophore reaction and $[M]_0$ is the initial concentration of mechanophore.

Calculation of $k_{\text{initial,GPC}}$ from time-dependent GPC-RI measurements. Initial rates of starting polymer consumption were determined by fitting the early portion of the time-dependent normalized GPC-RI profile to the second order polynomial function given by eq. 3.14:

$$RI_t = \left(\frac{d^2RI}{dt^2}\right)_0 \cdot t^2 + \left(\frac{dRI}{dt}\right)_0 \cdot t + B \tag{3.14}$$

where $(\frac{d^2RI}{dt^2})_0$ describes the negative acceleration of signal attenuation, B is the RI signal at $t = 0$, and $(\frac{dRI}{dt})_0$ represents the initial rate of RI attenuation. $(\frac{d^2RI}{dt^2})_0$, $(\frac{dRI}{dt})_0$, and B are fit-determined quantities. The initial rate of RI signal attenuation is related to the rate constant, $k_{\text{initial,GPC}}$, and the initial experimental RI signal, RI_0, by eq. 3.15:

$$\left(\frac{dRI}{dt}\right)_0 = k_{initial,GPC} \cdot RI_0 \tag{3.15}$$

A representative example of this procedure is shown in Figure 3.15.

Determination of k_{scission} from PMA-BPA. To determine values of k_{scission}, a series of PMA polymers with a chain-centered, mechanically inert bisphenol A diester (**PMA-BPA**) was subjected to ultrasonication as described above. Polymer connectivity for **PMA-BPA** was designed to mimic that of **PMA-CD**, with chains attached to the molecule via similar alkyl ester linkages. Polymers were sonicated in 3:1 MeCN:MeOH and chain scission was followed by the GPC-RI method (See Sections III and V). Values of k_{scission} were determined using both the integral method from full profile fitting and the initial rates method as described previously (Figure 3.4). Values of k_{scission} determined from these two methods are similar, although the rate constants determined using the initial rates method are slightly smaller, consistent with the observed trend for **PMA-CD** (see Figure 3.2). This disparity may be due to the comparatively fast scission of longer polymer chains in the molecular weight distribution at early reaction times producing polymer fragments that elute at the retention time of the original polymer peak, thus dampening the observed rate of signal attenuation. This effect would be more pronounced for polymers with higher initial molecular weight where GPC resolution is lower. The plot of k_{scission} versus M_n was fit to a linear regression, and the resulting function (eq. 3.16) was used to obtain the rate constant (in units of min^{-1} x 10^{-3}) of nonspecific chain scission at a particular M_n. Estimated values of k_{scission} at each molecular weight in the **PMA-CD** series are tabulated below in Table 3.2.

$$k_{scission} = 0.320 \cdot M_n - 27.0 \tag{3.16}$$

We note that these values are *effective* rate constants for the cumulative probability of chain scission at any of many possible points in the chain, rather than the rate constant for mechanical scission of a specific bond. Given that there are many bonds in the **PMA-CD** chain but only one mechanophore, the effective rate constant for nonspecific backbone scission is larger than the rate constant for the mechanochemical activation of the coumarin dimer mechanophore, even though the coumarin dimer mechanophore is more mechanically sensitive than any particular bond in the polymer backbone.

This analysis predicts a value of the threshold molecular weight, M_{thresh}, of 84 kDa, which is greater than the M_n for the shortest polymer in the **PMA-CD** series (79 kDa). Therefore, analyses incorporating k_{scission} values into the rate law were not performed on this shorter polymer. However, we note that this does not indicate that the 79 kDa **PMA-CD** polymer does not experience nonspecific backbone scission. In fact, the activation efficiency for the 79 kDa **PMA-CD** polymer is comparable to that of polymers in the series with higher M_n (Figure 3.12b, Table 3.4). This is in part a consequence of the dispersity of synthetic polymers.[29] A polymer with M_n = 79 kDa inherently contains a significant fraction of chains above this molecular weight that are susceptible to mechanical activation.

VI. Full Reaction Profile Fitting to an Integrated Rate Law Incorporating k_{scission}

As shown in Figure 3.3 and Figure 3.5, theoretical reaction profiles assuming a rate law where nonspecific backbone scission is significant and that $k_{\text{initial,PL}}$ accurately reflects the rate constant for mechanophore activation are well-aligned with experimental values. To alternatively demonstrate the accuracy of this mechanism, experimental reaction profiles for **PMA-CD** (obtained from PL data) were fit to eq. 3.17 (a modified version of eq. 3.5 in the main text), and the rate constant for mechanophore activation, k_{act}, was obtained.

$$[P]_t = \frac{n[M]_0 \cdot k_{act}\left(1 - e^{-(k_{act} + k_{scission})\cdot t}\right)}{(k_{act} + k_{scission})} + [P]_0 \tag{3.17}$$

Here we constrain the values of k_{scission} to those determined in Section V above (Table 3.2), again with n=2 and $[M]_0$ based on the experimental quantities. $[P]_0$ and k_{act} are fit-determined quantities. Excellent fits are observed for each experiment (Figure 3.7), and the resulting values of k_{act} are tabulated in Table 3.2. The fit-determined values of k_{act} agree well with independently determined values of $k_{\text{initial,PL}}$, further supporting the validity of the initial rates method for determining accurate mechanophore activation kinetics in presence of competitive nonspecific backbone scission (Figure 3.8). Relative standard error (RSE) is provided at the 95% confidence interval (CI) for values of k_{act}.

Table 3.2. Constrained and fit-determined values from fitting experimental data to eq. 3.17 for **PMA-CD** with k_{scission} constrained.

M_n (kDa)	$[M]_0$ (μM) (constrained)	k_{scission} x 10^3 (min^{-1}) (constrained)	k_{act} x 10^3 (min^{-1}) (fit-determined)	RSE of k_{act} (%) (95% CI)
111 kDa	18.0	8.55	4.1 ± 0.2	2.2 ± 1.0
132 kDa	15.2	15.3	6.7 ± 0.3	2.6 ± 0.4
160 kDa	12.5	24.2	11.1 ± 0.2	2.5 ± 0.6
180 kDa	11.1	30.7	15.9 ± 0.7	2.1 ± 0.2
206 kDa	9.71	39.0	16.6 ± 1.1	3.1 ± 0.7

Values of k_{scission} can also be approximated using a bivariate function and solving for both k_{act} and k_{scission} with least squares fitting of the experimental data, although additional error can often be introduced with this type of multivariate analysis. Results of fitting the time-dependent experimental data to eq. 3.17 with both k_{act} and $k_{scission}$ as unconstrained variables are given in Figure 3.16 and Table 3.3. While many of the fit-determined values of $k_{scission}$ are similar to the experimentally determined values in Table 3.2, some deviation is observed for the highest molar mass polymers. Similarly, some deviation is also observed for values of k_{act} using this multivariate least squares fitting analysis.

Table 3.3. Constrained and fit-determined values from fitting experimental data to eq. 3.17 for **PMA-CD** with $k_{scission}$ unconstrained.

M_n (kDa)	**[M]$_0$ (μM)** (constrained)	**$k_{scission}$ x 10^3 (min^{-1})** (fit-determined)	**RSE of $k_{scission}$ (%) (95% CI)**	**k_{act} x 10^3 (min^{-1})** (fit-determined)	**RSE of k_{act} (%) (95% CI)**
78.7 kDa	25.4	3.1 ± 0.3	3.6 ± 1.3	1.3 ± 0.1	2.5 ± 0.7
111 kDa	18.0	8.9 ± 1.0	3.4 ± 1.8	4.3 ± 0.5	3.1 ± 1.5
132 kDa	15.2	16.6 ± 0.3	4.8 ± 1.5	7.2 ± 0.2	4.9 ± 1.5
160 kDa	12.5	23.3 ± 0.1	4.7 ± 1.4	10.7 ± 0.1	5.2 ± 1.5
180 kDa	11.1	27.3 ± 0.7	2.4 ± 0.7	14.5 ± 0.5	2.2 ± 0.6
206 kDa	9.71	33.3 ± 2.4	2.6 ± 1.1	14.5 ± 1.6	2.6 ± 1.1

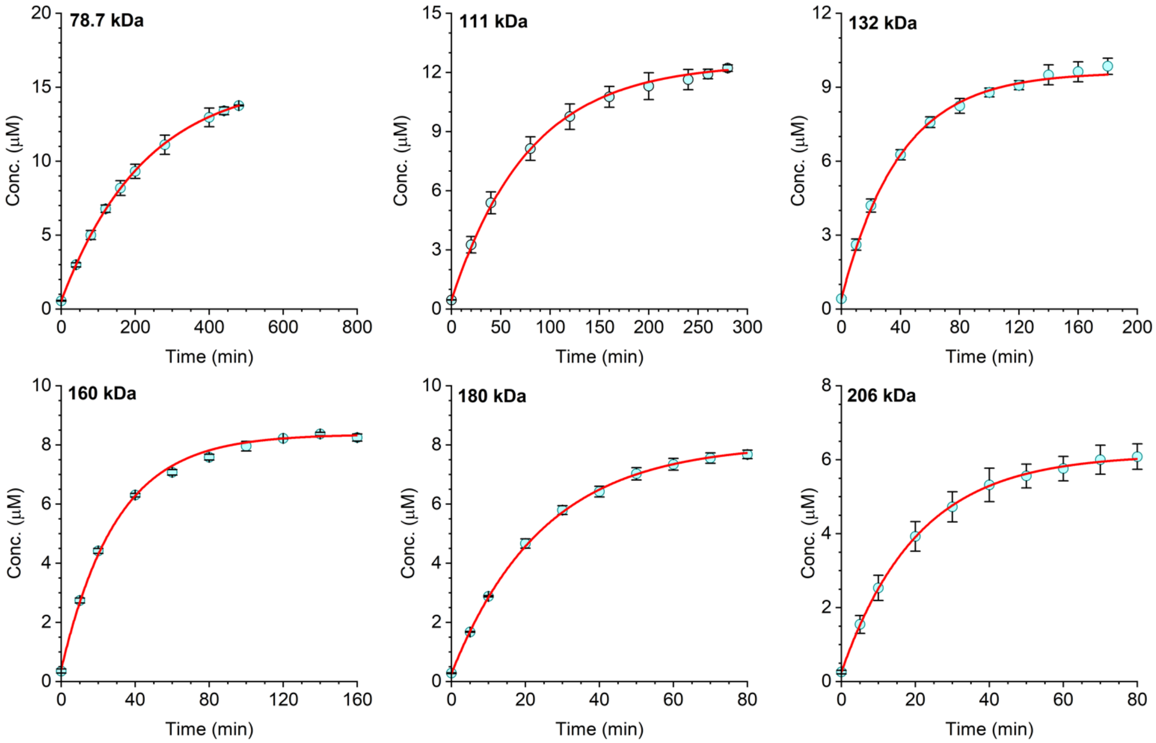

Figure 3.16. Experimental mechanochemical reaction profiles for **PMA-CD** determined by PL measurements fit to the integral form of a theoretical rate law (eq. 3.17) incorporating nonspecific backbone scission to obtain fit-determined values of k_{act} and $k_{scission}$. Data points and error bars represent average values and standard deviation from three replicate experiments.

VII. Plotted or Tabulated Characterization Data for Ultrasonication Experiments

The values of all determined rates constants are provided below in Table 3.4 and relative standard errors reported in Table 3.5. experimental data used to determine rate constants are provided below in Table 3.6–Table 3.15. For **PMA-CD**, only tabulated data highlighted in yellow were used to apply the initial rates method by fitting to eq. 3.9 or 3.14 to determine values of $k_{\text{initial,PL}}$ or $k_{\text{initial,GPC}}$, respectively. The reaction profiles measured using UV-vis absorption during ultrasonication of **PMA-NP** are illustrated in Figure 3.17. In Figure 3.17, the horizontal dashed lines denote the maximum theoretical absorbance value, and the vertical solid lines denote the upper limit of the data fit to eq. 3.11 to determine values of k_{initial}.

Table 3.4. Rate constants determined for ultrasonication experiments of **PMA-CD**, **PMA-NP**, or **PMA-BPA**. Reported rate constants are average values and standard deviation from three replicate trials for **PMA-CD** and **PMA-BPA**, and from two or three replicate trials for **PMA-NP**.

	$M_{\text{n,0}}$ (kDa)	Avg. k_{obs} x 10^3 (min^{-1}) from GPC-RI data	Avg. k_{initial} or k_{scission} x 10^3 (min^{-1}) from GPC-RI data	Avg. k_{obs} x 10^3 (min^{-1}) from PL or UV-vis data	Avg. k_{initial} x 10^3 (min^{-1}) from PL or UV-vis data	Activation Efficiency (%)
PMA-CD	78.7	2.9 ± 0.1	2.9 ± 0.2	4.5 ± 0.4	1.3 ± 0.1	31.0 ± 0.4
	111	11.7 ± 1.9	10.6 ± 2.3	13.2 ± 1.8	4.2 ± 0.6	34.0 ± 0.9
	132	25.0 ± 0.6	22.2 ± 1.1	23.8 ± 0.4	7.7 ± 0.7	32.2 ± 1.1
	160	35.4 ± 3.3	31.3 ± 1.1	34.0 ± 0.9	10.4 ± 0.2	33.1 ± 0.2
	180	44.5 ± 2.4	36.0 ± 1.9	41.8 ± 1.2	13.2 ± 0.3	35.9 ± 0.8
	206	47.1 ± 5.0	37.5 ± 4.7	47.8 ± 5.0	14.1 ± 2.2	31.8 ± 1.5
PMA-NP	83.1	-	-	7.0 ± 0.3	6.6 ± 0.4	79.8 ± 2.3
	133	-	-	26.1 ± 0.2	22.8 ± 0.2	80.8 ± 2.7
	158	-	-	40.7 ± 3.7	34.8 ± 1.4	77.3 ± 3.3
	178	-	-	49.6 ± 2.2	38.5 ± 0.5	70.9 ± 2.0
	204	-	-	61.6 ± 0.8	44.4 ± 0.7	75.0 ± 0.1
PMA-BPA	109	11.1 ± 2.1	10.3 ± 1.2	-	-	-
	142	18.9 ± 1.9	15.4 ± 1.3	-	-	-
	170	31.2 ± 2.1	26.9 ± 1.2	-	-	-
	218	53.4 ± 5.2	44.0 ± 4.3	-	-	-

Table 3.5. Values of relative standard error (RSE) at the 95% CI for rate constants determined from ultrasonication experiments of **PMA-CD**, **PMA-NP**, or **PMA-BPA** provided in Table 3.4. Values represent the average RSE and standard deviation of the error from the replicate trials.

	$M_{n,0}$ (kDa)	**Avg. RSE for k_{obs} from GPC-RI data (%)**	**Avg. RSE for $k_{initial}$ or $k_{scission}$ from GPC-RI data (%)**	**Avg. RSE for k_{obs} from PL or UV-vis data (%)**	**Avg. RSE for $k_{initial}$ from PL or UV-vis data (%)**
PMA-CD	78.7	1.5 ± 0.3	4.1 ± 1.6	3.2 ± 1.1	2.3 ± 0.5
	111	2.0 ± 0.2	3.3 ± 1.7	3.2 ± 1.7	2.0 ± 1.6
	132	1.5 ± 0.3	3.7 ± 1.5	4.7 ± 1.4	3.5 ± 1.3
	160	2.4 ± 0.1	2.0 ± 0.2	4.7 ± 1.4	3.2 ± 2.2
	180	2.6 ± 0.3	3.9 ± 2.2	2.3 ± 0.7	2.7 ± 0.6
	206	2.6 ± 0.1	2.7 ± 0.8	2.6 ± 1.1	2.6 ± 1.3
PMA-NP	83.1	-	-	0.1 ± 0.01	0.4 ± 0.1
	133	-	-	0.3 ± 0.02	1.5 ± 0.3
	158	-	-	0.2 ± 0.01	0.9 ± 0.1
	178	-	-	0.4 ± 0.1	2.8 ± 0.8
	204	-	-	0.7 ± 0.4	3.7 ± 2.6
PMA-BPA	109	2.2 ± 0.6	5.4 ± 2.9	-	-
	142	2.2 ± 0.6	6.6 ± 3.5	-	-
	170	2.7 ± 0.9	8.9 ± 5.2	-	-
	218	2.3 ± 0.2	2.0 ± 1.1	-	-

Table 3.6. Determined PL response (λ_{em} = 375 nm) for **PMA-CD** (M_n = 78.7 kDa) upon ultrasonication (1 s on, 2 s off) in 3:1 MeCN/MeOH.

	Trial 1		**Trial 2**		**Trial 3**	
Sonication time (min)	**PL**	**RI**	**PL**	**RI**	**PL**	**RI**
0	325	1.32	303	1.31	331	1.35
40	1753	1.18	1717	1.21	1651	1.23
80	2899	1.03	2907	1.06	2728	1.09
120	3909	0.91	3870	0.94	3763	0.96
160	4649	0.81	4746	0.82	4458	0.85
200	5365	0.72	5374	0.73	5117	0.77
280	6332	0.58	6438	0.57	6072	0.63
400	7286	0.42	7456	0.4	7131	0.45
440	7655	0.38	7561	0.38	7537	0.4
480	7783	0.32	7644	0.34	7854	0.36
0 (photoirradiated)	**28420**	**-**	**28272**	**-**	**28955**	**-**

Table 3.7. Determined PL response (λ_{em} = 375 nm) for **PMA-CD** (M_n = 111 kDa) upon ultrasonication (1 s on, 2 s off) in 3:1 MeCN/MeOH.

	Trial 1		**Trial 2**		**Trial 3**	
Sonication time (min)	**PL**	**RI**	**PL**	**RI**	**PL**	**RI**
0	230	1.41	234	1.39	249	1.31
20	1815	1.08	1710	1.13	1492	1.11
40	2913	0.81	2851	0.88	2533	0.91
80	4266	0.48	4308	0.51	3959	0.6
120	5027	0.27	5220	0.31	4792	0.4
160	5469	0.16	5725	0.19	5399	0.28
200	5744	0.12	6077	0.13	5605	0.19
240	5765	0.08	6246	0.1	5940	0.15
260	5920	0.06	6248	0.06	6222	0.13
0 (photoirradiated)	**17983**	**-**	**18472**	**-**	**19150**	**-**

Table 3.8. Determined PL response (λ_{em} = 375 nm) for **PMA-CD** (M_n = 132 kDa) upon ultrasonication (1 s on, 2 s off) in 3:1 MeCN/MeOH.

	Trial 1		**Trial 2**		**Trial 3**	
Sonication time (min)	**PL**	**RI**	**PL**	**RI**	**PL**	**RI**
0	209	1.31	222	1.3	238	1.3
10	1257	1.06	1418	1.03	1419	1.01
20	2083	0.83	2270	0.79	2220	0.8
40	3245	0.5	3350	0.46	3213	0.47
60	3983	0.29	4045	0.27	3848	0.29
80	4281	0.17	4434	0.16	4202	0.18
100	4622	0.1	4642	0.11	4501	0.11
120	4743	0.07	4754	0.07	4729	0.07
140	4875	0.05	5132	0.05	4875	0.05
160	4956	0.03	5203	0.03	4922	0.04
180	5080	0.03	5250	0.03	5098	0.02
0 (photoirradiated)	**16189**	**-**	**15651**	**-**	**15634**	**-**

Table 3.9. Determined PL response (λ_{em} = 375 nm) for **PMA-CD** (M_n = 160 kDa) upon ultrasonication (1 s on, 2 s off) in 3:1 MeCN/MeOH.

	Trial 1		**Trial 2**		**Trial 3**	
Sonication time (min)	**PL**	**RI**	**PL**	**RI**	**PL**	**RI**
0	152	1.27	179	1.27	218	1.27
10	1413	0.91	1412	0.91	1436	0.92
20	2260	0.61	2340	0.61	2259	0.66
40	3293	0.26	3276	0.27	3220	0.35
60	3754	0.12	3664	0.13	3569	0.19
80	4011	0.07	3919	0.07	3854	0.12
100	4266	0.04	4116	0.04	3985	0.08
120	4309	0.03	4300	0.03	4161	0.05
140	4354	0.02	4419	0.02	4228	0.03
160	4302	0.01	4266	0.02	4238	0.02
0 (photoirradiated)	**13087**	**-**	**13101**	**-**	**12645**	**-**

Table 3.10. Determined PL response (λ_{em} = 375 nm) for **PMA-CD** (M_n = 180 kDa) upon ultrasonication (1 s on, 2 s off) in 3:1 MeCN/MeOH.

	Trial 1		**Trial 2**		**Trial 3**	
Sonication time (min)	**PL**	**RI**	**PL**	**RI**	**PL**	**RI**
0	145	1.38	145	1.37	146	1.38
5	906	1.15	861	1.12	816	1.15
10	1549	0.94	1467	0.96	1414	0.92
20	2466	0.59	2469	0.61	2240	0.56
30	3072	0.36	3033	0.38	2807	0.33
40	3454	0.22	3370	0.24	3055	0.2
50	3763	0.15	3695	0.15	3347	0.11
60	3964	0.1	3847	0.09	3489	0.07
70	4047	0.06	3951	0.06	3625	0.04
80	4159	0.04	3982	0.04	3673	0.03
0 (photoirradiated)	**12046**	**-**	**11312**	**-**	**10821**	**-**

Table 3.11. Determined PL response (λ_{em} = 375 nm) for **PMA-CD** (M_n = 206 kDa) upon ultrasonication (1 s on, 2 s off) in 3:1 MeCN/MeOH.

	Trial 1		**Trial 2**		**Trial 3**	
Sonication time (min)	**PL**	**RI**	**PL**	**RI**	**PL**	**RI**
0	154	1.23	137	1.2	130	1.22
5	901	0.99	878	1	769	1.03
10	1450	0.76	1436	0.82	1293	0.83
20	2170	0.42	2262	0.51	2050	0.53
30	2567	0.24	2755	0.3	2490	0.33
40	2882	0.15	3124	0.19	2794	0.19
50	2935	0.09	3270	0.11	3005	0.13
60	3028	0.06	3413	0.08	3099	0.09
70	3187	0.03	3541	0.05	3207	0.07
80	3191	0.03	3624	0.03	3264	0.05
0 (photoirradiated)	**9638**	**-**	**11562**	**-**	**11048**	**-**

Table 3.12. Determined GPC-RI response for **PMA-BPA** (M_n = 109 kDa) upon ultrasonication (1 s on, 2 s off) in 3:1 MeCN/MeOH.

	Trial 1	**Trial 2**	**Trial 3**
Sonication time (min)	**RI**	**RI**	**RI**
0	1.44182	1.43375	1.37311
20	1.14041	1.13798	1.13014
40	0.90336	0.89997	0.94309
60	0.70139	0.68801	0.74629
90	0.46113	0.47893	0.53559
120	0.32649	0.34659	0.41939
150	0.22914	0.24782	0.32558
180	0.16912	0.20219	0.25961
210	0.12833	0.15448	0.22923
240	0.08872	0.12288	0.16536

Table 3.13. Determined GPC-RI response for **PMA-BPA** (M_n = 142 kDa) upon ultrasonication (1 s on, 2 s off) in 3:1 MeCN/MeOH.

	Trial 1	**Trial 2**	**Trial 3**
Sonication time (min)	**RI**	**RI**	**RI**
0	1.29469	1.31034	1.29477
20	0.91161	0.99133	0.90523
40	0.62433	0.65733	0.63954
60	0.40307	0.42264	0.42294
80	0.25908	0.283	0.27443
100	0.16452	0.19876	0.19229
120	0.11359	0.13037	0.13754
140	0.09663	0.10218	0.09267
160	0.0576	0.06856	0.07761
180	0.04876	0.04964	0.06057
200	0.0359	0.04518	0.04828

Table 3.14. Determined GPC-RI response for **PMA-BPA** (M_n = 170 kDa) upon ultrasonication (1 s on, 2 s off) in 3:1 MeCN/MeOH.

	Trial 1	**Trial 2**	**Trial 3**
Sonication time (min)	**RI**	**RI**	**RI**
0	1.26796	1.26072	1.25757
10	0.94252	0.91982	1.00031
20	0.69733	0.68863	0.68686
40	0.32185	0.36831	0.34554
60	0.16353	0.22276	0.17658
80	0.10001	0.12183	0.10617
100	0.05348	0.07791	0.05361
120	0.03213	0.04641	0.03013
140	0.02363	0.02634	0.01572

Table 3.15. Determined GPC-RI response for **PMA-BPA** (M_n = 218 kDa) upon ultrasonication (1 s on, 2 s off) in 3:1 MeCN/MeOH.

	Trial 1	**Trial 2**	**Trial 3**
Sonication time (min)	**RI**	**RI**	**RI**
0	1.29475	1.29243	1.2194
10	0.78136	0.78302	0.7899
20	0.42261	0.41228	0.47918
30	0.23054	0.23695	0.26131
40	0.13231	0.12944	0.1621
50	0.08123	0.0752	0.09469
60	0.04623	0.04801	0.05606
70	0.03494	0.02984	0.03399
80	0.0263	0.02047	0.02385

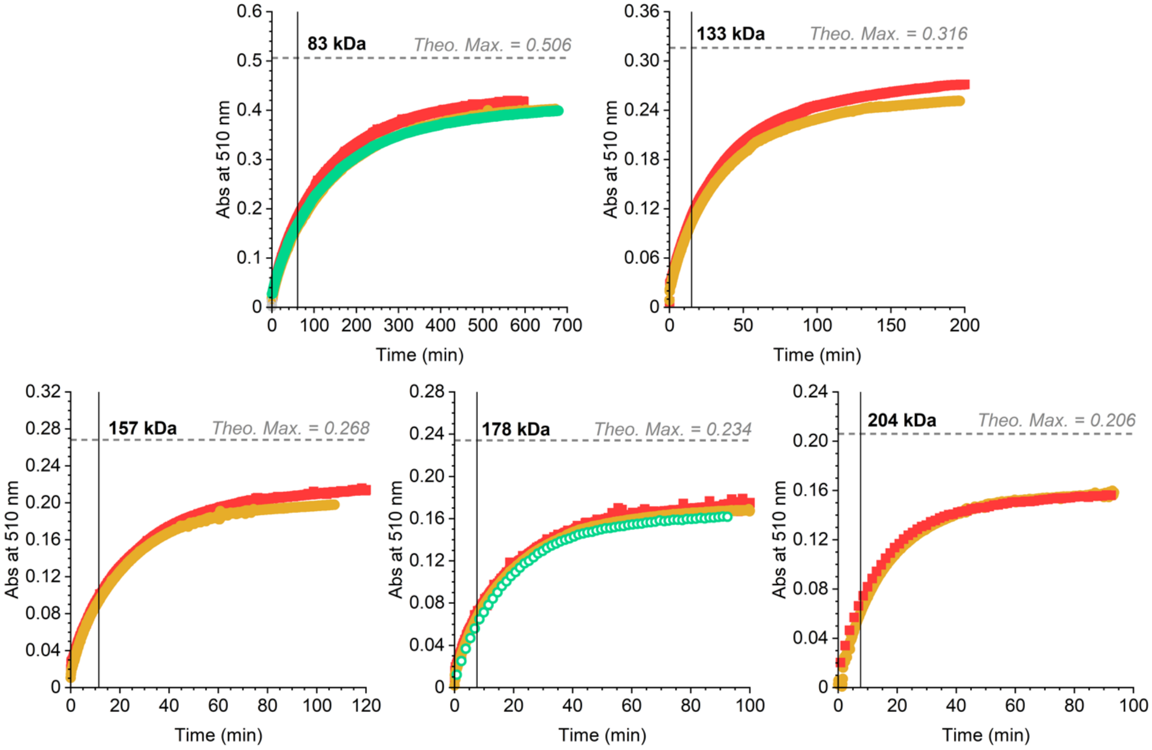

Figure 3.17. UV-vis absorption profiles for ultrasonication of **PMA-NP** (2–3 trials for each polymer). Dashed horizontal lines mark the theoretical maximum absorbance if 100% of mechanophore reacted to form the merocyanine product. Vertical solid lines mark the end of the region that was used to determine k_{initial} by the initial rates method.

References

(1) Kryger, M. J.; Munaretto, A. M.; Moore, J. S. Structure-Mechanochemical Activity Relationships for Cyclobutane Mechanophores. *J. Am. Chem. Soc* **2011**, *133*, 18992–18998.

(2) Konda, S. S. M.; Brantley, J. N.; Varghese, B. T.; Wiggins, K. M.; Bielawski, C. W.; Makarov, D. E. Molecular Catch Bonds and the Anti-Hammond Effect in Polymer Mechanochemistry. *J. Am. Chem. Soc.* **2013**, *135*, 12722–12729.

(3) Robb, M. J.; Moore, J. S. A Retro-Staudinger Cycloaddition: Mechanochemical Cycloelimination of a β-Lactam Mechanophore. *J. Am. Chem. Soc.* **2015**, *137*, 10946–10949.

(4) Luo, S. M.; Barber, R. W.; Overholts, A. C.; Robb, M. J. Competitive Activation Experiments Reveal Significantly Different Mechanochemical Reactivity of Furan–Maleimide and Anthracene–Maleimide Mechanophores. *ACS Polym. Au* **2023**, DOI: 10.1021/acspolymersau.2c00047.

(5) Potisek, S. L.; Davis, D. A.; Sottos, N. R.; White, S. R.; Moore, J. S. Mechanophore-Linked Addition Polymers. *J. Am. Chem. Soc.* **2007**, *129*, 13808–13809.

(6) Gossweiler, G. R.; Hewage, G. B.; Soriano, G.; Wang, Q.; Welshofer, G. W.; Zhao, X.; Craig, S. L. Mechanochemical Activation of Covalent Bonds in Polymers with Full and Repeatable Macroscopic Shape Recovery. *ACS Macro Lett.* **2014**, *3*, 216–219.

(7) Robb, M. J.; Kim, T. A.; Halmes, A. J.; White, S. R.; Sottos, N. R.; Moore, J. S. Regioisomer-Specific Mechanochromism of Naphthopyran in Polymeric Materials. *J. Am. Chem. Soc.* **2016**, *138*, 12328–12331.

(8) Berkowski, K. L.; Potisek, S. L.; Hickenboth, C. R.; Moore, J. S. Ultrasound-Induced Site-Specific Cleavage of Azo-Functionalized Poly(Ethylene Glycol). *Macromolecules* **2005**, *38*, 8975–8978.

(9) Imato, K.; Irie, A.; Kosuge, T.; Ohishi, T.; Nishihara, M.; Takahara, A.; Otsuka, H. Mechanophores with a Reversible Radical System and Freezing-Induced Mechanochemistry in Polymer Solutions and Gels. *Angew. Chem. Int. Ed.* **2015**, *54*, 6168–6172.

(10) Barbee, M. H.; Kouznetsova, T.; Barrett, S. L.; Gossweiler, G. R.; Lin, Y.; Rastogi, S. K.; Brittain, W. J.; Craig, S. L. Substituent Effects and Mechanism in a Mechanochemical Reaction. *J. Am. Chem. Soc.* **2018**, *140*, 12746–12750.

(11) Diesendruck, C. E.; Peterson, G. I.; Kulik, H. J.; Kaitz, J. A.; Mar, B. D.; May, P. A.; White, S. R.; Martínez, T. J.; Boydston, A. J.; Moore, J. S. Mechanically Triggered Heterolytic Unzipping of a Low-Ceiling-Temperature Polymer. *Nat. Chem.* **2014**, *6*, 623–628.

(12) Hemmer, J. R.; Rader, C.; Wilts, B. D.; Weder, C.; Berrocal, J. A. Heterolytic Bond Cleavage in a Scissile Triarylmethane Mechanophore. *J. Am. Chem. Soc.* **2021**, *143*, 18859–18863.

(13) Nixon, R.; De Bo, G. Three Concomitant C–C Dissociation Pathways during the Mechanical Activation of an N-Heterocyclic Carbene Precursor. *Nat. Chem.* **2020**, *12*, 826–831.

(14) Paulusse, J. M. J.; Sijbesma, R. P. Reversible Mechanochemistry of a PdII Coordination Polymer. *Angew. Chem. Int. Ed.* **2004**, *43*, 4460–4462.

(15) Yount, W. C.; Loveless, D. M.; Craig, S. L. Small-Molecule Dynamics and Mechanisms Underlying the Macroscopic Mechanical Properties of Coordinatively Cross-Linked Polymer Networks. *J. Am. Chem. Soc.* **2005**, *127*, 14488–14496.

(16) Davis, D. A.; Hamilton, A.; Yang, J.; Cremar, L. D.; Van Gough, D.; Potisek, S. L.; Ong, M. T.; Braun, P. V.; Martínez, T. J.; White, S. R.; Moore, J. S.; Sottos, N. R. Force-Induced Activation of Covalent Bonds in Mechanoresponsive Polymeric Materials. *Nature* **2009**, *459*, 68–72.

(17) Versaw, B. A.; McFadden, M. E.; Husic, C. C.; Robb, M. J. Designing Naphthopyran Mechanophores with Tunable Mechanochromic Behavior. *Chem. Sci.* **2020**, *11*, 4525–4530.

(18) Göstl, R.; Sijbesma, R. P. π-Extended Anthracenes as Sensitive Probes for Mechanical Stress. *Chem. Sci.* **2016**, *7*, 370–375.

(19) Sakai, H.; Sumi, T.; Aoki, D.; Goseki, R.; Otsuka, H. Thermally Stable Radical-Type Mechanochromic Polymers Based on Difluorenylsuccinonitrile. *ACS Macro Lett.* **2018**, *7*, 1359–1363.

(20) Piermattei, A.; Karthikeyan, S.; Sijbesma, R. P. Activating Catalysts with Mechanical Force. *Nat. Chem.* **2009**, *1*, 133–137.

(21) Michael, P.; Binder, W. H. A Mechanochemically Triggered "Click" Catalyst. *Angew. Chem. Int. Ed.* **2015**, *54*, 13918–13922.

(22) Chen, Z.; Mercer, J. A. M.; Zhu, X.; Romaniuk, J. A. H.; Pfattner, R.; Cegelski, L.; Martinez, T. J.; Burns, N. Z.; Xia, Y. Mechanochemical Unzipping of Insulating Polyladderene to Semiconducting Polyacetylene. *Science* **2017**, *357*, 475–479.

(23) Versaw, B. A.; Zeng, T.; Hu, X.; Robb, M. J. Harnessing the Power of Force: Development of Mechanophores for Molecular Release. *J. Am. Chem. Soc.* **2021**, *143*, 21461–21473.

(24) Li, J.; Nagamani, C.; Moore, J. S. Polymer Mechanochemistry: From Destructive to Productive. *Acc. Chem. Res.* **2015**, *48*, 2181–2190.

(25) May, P. A.; Moore, J. S. Polymer Mechanochemistry: Techniques to Generate Molecular Force via Elongational Flows. *Chem. Soc. Rev* **2013**, *42*, 7497–7506.

(26) Odell, J. A.; Keller, A. Flow-Induced Chain Fracture of Isolated Linear Macromolecules in Solution. *J. Polym. Sci. B Polym. Phys.* **1986**, *24*, 1889–1916.

(27) Schaefer, M.; Icli, B.; Weder, C.; Lattuada, M.; Kilbinger, A. F. M.; Simon, Y. C. The Role of Mass and Length in the Sonochemistry of Polymers. *Macromolecules* **2016**, *49*, 1630–1636.

(28) May, P. A.; Munaretto, N. F.; Hamoy, M. B.; Robb, M. J.; Moore, J. S. Is Molecular Weight or Degree of Polymerization a Better Descriptor of Ultrasound-Induced Mechanochemical Transduction? *ACS Macro Lett.* **2016**, *5*, 177–180.

(29) Overholts, A. C.; McFadden, M. E.; Robb, M. J. Quantifying Activation Rates of Scissile Mechanophores and the Influence of Dispersity. *Macromolecules* **2022**, *55*, 276–283.

(30) Kean, Z. S.; Gossweiler, G. R.; Kouznetsova, T. B.; Hewage, G. B.; Craig, S. L. A Coumarin Dimer Probe of Mechanochemical Scission Efficiency in the Sonochemical Activation of Chain-Centered Mechanophore Polymers. *Chem. Commun.* **2015**, *51*, 9157–9160.

(31) Duan, H.-Y.; Wang, Y.-X.; Wang, L.-J.; Min, Y.-Q.; Zhang, X.-H.; Du, B.-Y. An Investigation of the Selective Chain Scission at Centered Diels–Alder Mechanophore under Ultrasonication. *Macromolecules* **2017**, *50*, 1353–1361.

(32) Ayer, M. A.; Verde-Sesto, E.; Liu, C. H.; Weder, C.; Lattuada, M.; Simon, Y. C. Modeling Ultrasound-Induced Molecular Weight Decrease of Polymers with Multiple Scissile Azo-Mechanophores. *Polym. Chem.* **2021**, *12*, 4093–4103.

(33) Overholts, A. C.; Robb, M. J. Examining the Impact of Relative Mechanophore Activity on the Selectivity of Ultrasound-Induced Mechanochemical Chain Scission. *ACS Macro Lett.* **2022**, *11*, 733–738.

(34) Harvey, D. *Modern Analytical Chemistry*. *Modern Analytical Chemistry*; McGraw-Hill: Boston, 2000.

(35) Wentzell, P. D.; Crouch, S. R. Comparison of Reaction-Rate Methods of Analysis for Systems Following First-Order Kinetics. *Anal. Chem.* **1986**, *58*, 2855–2858.

(36) Larsson, J. A.; Pardue, H. L. Linearized Model for Error-Compensated Kinetic Determinations without Prior Knowledge of Reaction Order or Rate Constant. *Anal. Chem.* **1989**, *61*, 1949–1954.

(37) Collum, D. B. *Determining Initial Rates*. Collum Group Website (Cornell University): Initial Rates, 2009. https://collum.chem.cornell.edu/resources/kinetics/ (accessed August 16, 2022).

(38) McFadden, M. E.; Robb, M. J. Generation of an Elusive Permanent Merocyanine via a Unique Mechanochemical Reaction Pathway. *J. Am. Chem. Soc.* **2021**, *143*, 7925–7929.

(39) McFadden, M. E.; Robb, M. J. Force-Dependent Multicolor Mechanochromism from a Single Mechanophore. *J. Am. Chem. Soc.* **2019**, *141*, 11388–11392.

(40) Kem, K. M. Process for Alkoxylation of Phenols. Process for Alkoxylation of Phenols. US4261922A, April 14, 1981.

(41) Nguyen, N. H.; Rosen, B. M.; Lligadas, G.; Percec, V. Surface-Dependent Kinetics of Cu(0)-Wire-Catalyzed Single-Electron Transfer Living Radical Polymerization of Methyl Acrylate in DMSO at 25 °C. *Macromolecules* **2009**, *42*, 2379–2386.

(42) McFadden, M. E.; Robb, M. J. Force-Dependent Multicolor Mechanochromism from a Single Mechanophore. *J. Am. Chem. Soc.* **2019**, *141*, 11388–11392.

(43) Yang, J.; Horst, M.; Werby, S. H.; Cegelski, L.; Burns, N. Z.; Xia, Y. Bicyclohexene- *Peri* -Naphthalenes: Scalable Synthesis, Diverse Functionalization, Efficient Polymerization, and Facile Mechanoactivation of Their Polymers. *J. Am. Chem. Soc.* **2020**, *142*, 14619–14626.

(44) Berkowski, K. L.; Potisek, S. L.; Hickenboth, C. R.; Moore, J. S. Ultrasound-Induced Site-Specific Cleavage of Azo-Functionalized Poly(Ethylene Glycol). *Macromolecules* **2005**, *38*, 8975–8978.

^{1}H and ^{13}C NMR Spectra

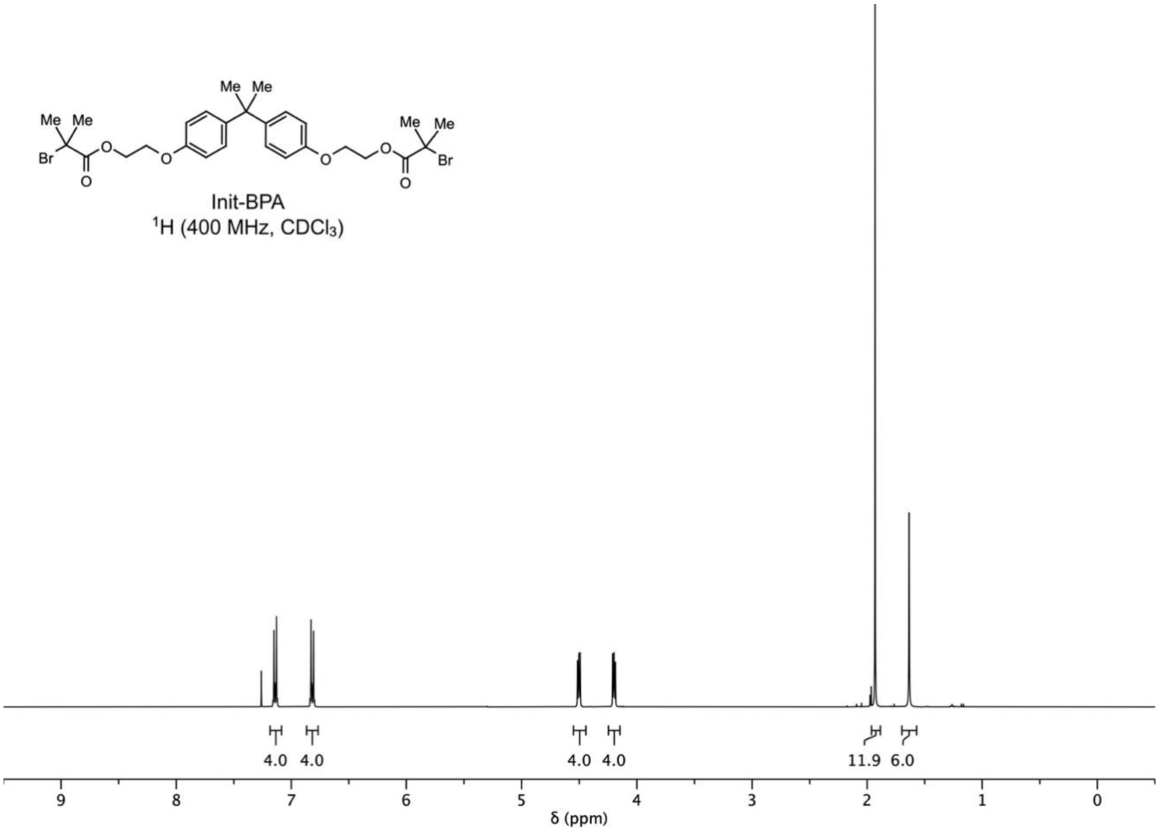

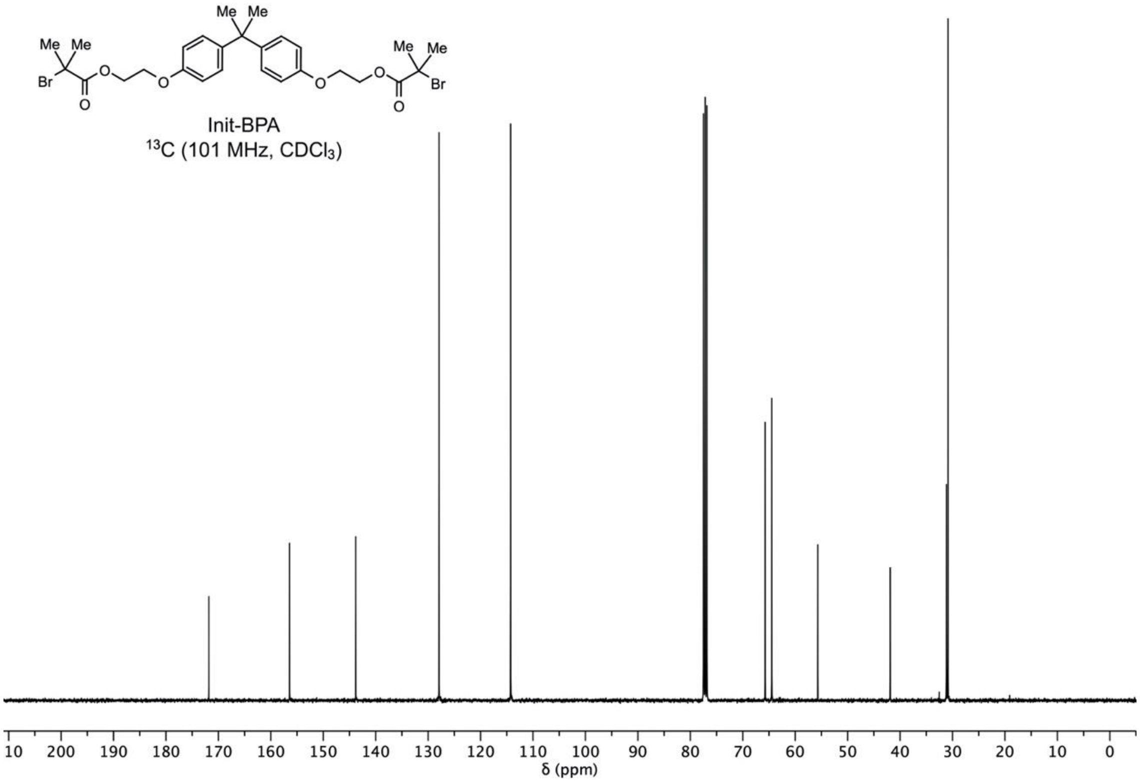

Chapter 4

FORCE-DEPENDENT MULTICOLOR MECHANOCHROMISM FROM A SINGLE MECHANOPHORE

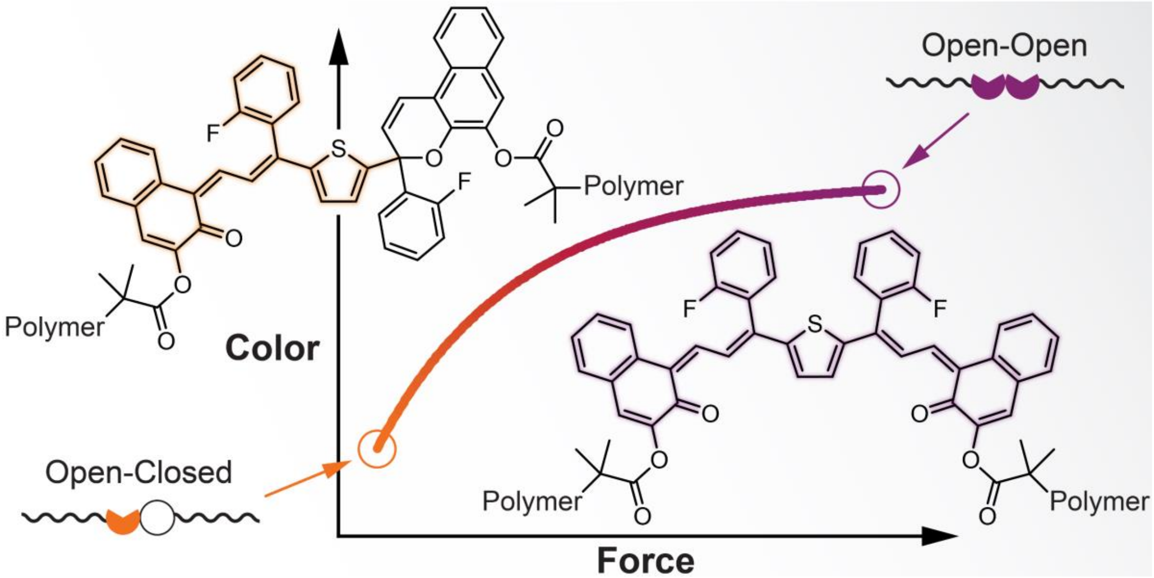

ABSTRACT: We report a bis-naphthopyran mechanophore that exhibits force-dependent changes in visible absorption. A series of polymers incorporating a chain-centered bis-naphthopyran mechanophore are activated using ultrasonication. By varying the length of the polymer chains, the force delivered to the mechanophore is modulated systematically. We demonstrate that the relative distribution of two distinctly colored merocyanine products is altered predictably with different magnitudes of applied force, resulting in gradient multicolor mechanochromism. The mechanochemical reactivity of bis-naphthopyran is supported by DFT calculations and described by a theoretical model that provides insight into the force-color relationship.

This chapter has been adapted with permission from McFadden, M. E.; Robb, M. J. Force-Dependent Multicolor Mechanochromism from a Single Mechanophore. *J. Am. Chem. Soc.* **2019**, *141*, 11388–11392. DOI: 10.1021/jacs.9b05280

Investigation

Mechanophores are molecules that undergo specific and productive chemical transformations under mechanical stress.[1] In polymer mechanochemistry, force is transduced to a mechanophore through covalently linked polymer chains.[2,3] Mechanophores that exhibit changes in color or luminescence, for example, enable the straightforward visible detection of stress and/or strain in polymers and polymeric materials.[4–10] A diverse library of mechanochromic molecular force probes has emerged including spiropyran[11–18] and naphthopyran,[19] which undergo 6π electrocyclic ring-opening reactions under force to generate colored merocyanine dyes. In addition, mechanophores that homolytically cleave to generate colored radical species,[20–23] the force-activated unzipping of polyladderene to form conjugated polyacetylene,[24] and the ring-opening reaction of rhodamine[25,26] have also been recently reported.

Scheme 4.1. Electrocyclic reactions of bis-naphthopyran produce distinctly colored merocyanine products via photochemical, thermal, and mechanochemical processes.

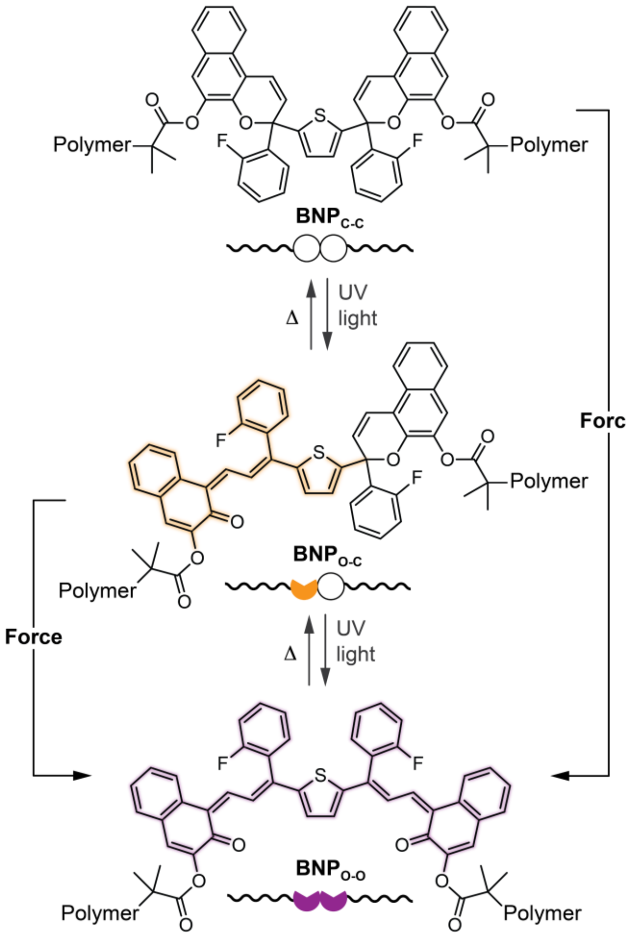

The development of mechanochromic mechanophores that are capable of distinguishing between different magnitudes of force through discrete visual signals remains an important challenge. Spiropyran[17,27] and rhodamine[26] exhibit a unique color transition in materials under active stress and after relaxation due to presumed changes in *cis–trans* isomerization and conformational torsion, respectively. Furthermore, taking advantage of the unique properties of phase-separated polymer and composite materials, differential activation of two different mechanochromic mechanophores introduced into hard and soft domains has been demonstrated under varying degrees of mechanical stimulation.[28,29] A single mechanophore, however, that is capable of achieving a force-dependent, gradient multicolor response is a desirable target.

We were intrigued by reports of multicolor photochromism in bis-naphthopyran (BNP) chromophores (Scheme 2.1).[30–33] The two pyran rings, which are initially in the closed-closed state ($\mathrm{BNP_{C\text{-}C}}$), open sequentially under extended irradiation with UV light to generate distinctly colored merocyanine dyes. A single ring-opening reaction produces the open-closed form ($\mathrm{BNP_{O\text{-}C}}$) with absorption properties characteristic of typical merocyanine dyes; however, the ring-opening reaction of the second pyran unit generates the open-open bis-merocyanine species ($\mathrm{BNP_{O\text{-}O}}$) that absorbs at longer wavelengths due to conjugation through the thiophene linker. Here, we report the mechanochemical reactivity of a BNP mechanophore that exhibits force-dependent multicolor mechanochromism. Interestingly, the mechanochemical behavior of the BNP mechanophore is distinct from its photochemical reactivity. In contrast to the sequential ring-opening behavior with light, $\mathrm{BNP_{O\text{-}O}}$ appears to be generated directly with force. A dynamic equilibrium is achieved under mechanical activation in which the distribution of merocyanine products is increasingly biased toward $\mathrm{BNP_{O\text{-}O}}$ with greater force applied to the BNP mechanophore. The trend in mechanochemical reactivity is described by a mechanistic model that captures the experimentally determined force-color relationship.

Density functional theory (DFT) calculations using the easily implemented constrained geometries simulate external force (CoGEF) method[34,35] were initially performed to evaluate the mechanochemical activity of bis-naphthopyran (see Section III of the Experimental section for details). Encouragingly, the calculations predict successful ring-opening reactions of both pyran units upon molecular elongation. To experimentally evaluate the mechanochemical reactivity of bis-naphthopyran, we synthesized a series of poly(methyl acrylate) (PMA) polymers incorporating a BNP unit near the center of the polymer chain (Scheme 4.2). An *ortho*- fluorophenyl group was incorporated into the BNP structure, which reduces the rate of thermal ring-closure and extends the lifetime of the merocyanine species.[36] Polymers with number average molecular weights (M_n) in the range 22–330 kDa were prepared (Table 4.1)

Scheme 4.2. Synthesis of poly(methyl acrylate) polymers containing a chain-centered bis-naphthopyran unit.

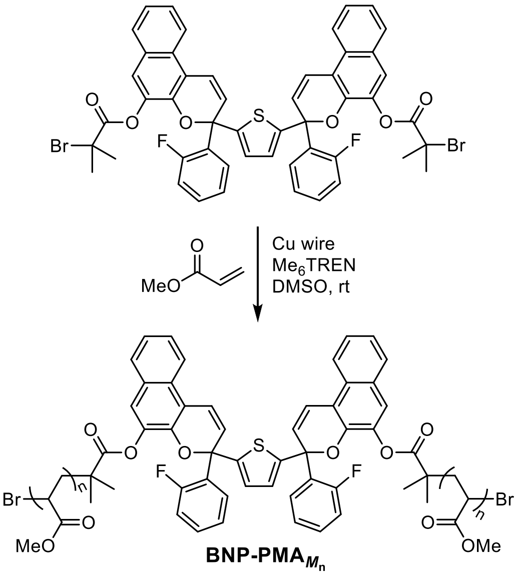

According to the bead–rod model, the force experienced by a polymer under these conditions is dependent upon the length of the chain.[37] Thus, the magnitude of force applied to a BNP molecule during ultrasonication is tuned by varying the degree of polymerization (DP) of the attached polymer

Table 4.1. Polymer characterization and quantification of force-dependent mechanochromism.

Polymer	M_n (kDa)^a	DP^b	$Đ^a$	B_{620}/B_{460}^{c}
BNP-PMA$_{22}$	21.5	250	1.19	0.24 ± 0.010
BNP-PMA$_{40}$	40.0	465	1.10	0.32 ± 0.025
BNP-PMA$_{53}$	53.1	617	1.10	0.40 ± 0.033
BNP-PMA$_{73}$	73.2	850	1.10	0.44 ± 0.014
BNP-PMA$_{98}$	97.6	1130	1.20	0.51 ± 0.068
BNP-PMA$_{165}$	165	1920	1.15	0.62 ± 0.047
BNP-PMA$_{330}$	330	3830	1.24	0.75 ± 0.024

^{a}Determined from GPC-MALS. ^{b}M_n/M_0. ^{c}Average values from absorbance data fitted to eq. 4.1. Standard deviation from a minimum of three trials.

chains, with longer polymers transducing greater force. Accordingly, the activation rate of mechanochemical reactions is directly proportional to DP above a threshold chain length.[35] Although DP is a better descriptor of mechanical activation,[38,39] we refer to polymer molecular weight as a more identifiable metric since only PMA was used in this study.

The photochromic properties of a 330 kDa polymer containing a chain-centered bis-naphthopyran molecule (**BNP-PMA$_{330}$**) were initially investigated and compared to its mechanochemical reactivity. Photochemical and mechanochemical reactions were monitored in real-time by UV-vis absorption spectroscopy using a peristaltic pump to continuously circulate a polymer solution between a reaction vessel and a UV-vis flow cell.[15a] A THF solution of **BNP-PMA$_{330}$** at −45 °C was irradiated with UV light (λ = 311 nm) and absorption spectra were acquired over time (Figure 4.1a). At early irradiation times, a new peak with an absorption maximum at approximately 460 nm emerges, corresponding to the BNP$_{\text{O-C}}$ species.[11a] A longer wavelength absorption signal appears after extended UV irradiation that corresponds to the BNP$_{\text{O-O}}$ form. To better characterize the formation of each species over time, the absorbance at two characteristic wavelengths of 460 nm and 620 nm were monitored continuously. The latter wavelength was chosen to minimize overlap with the absorption

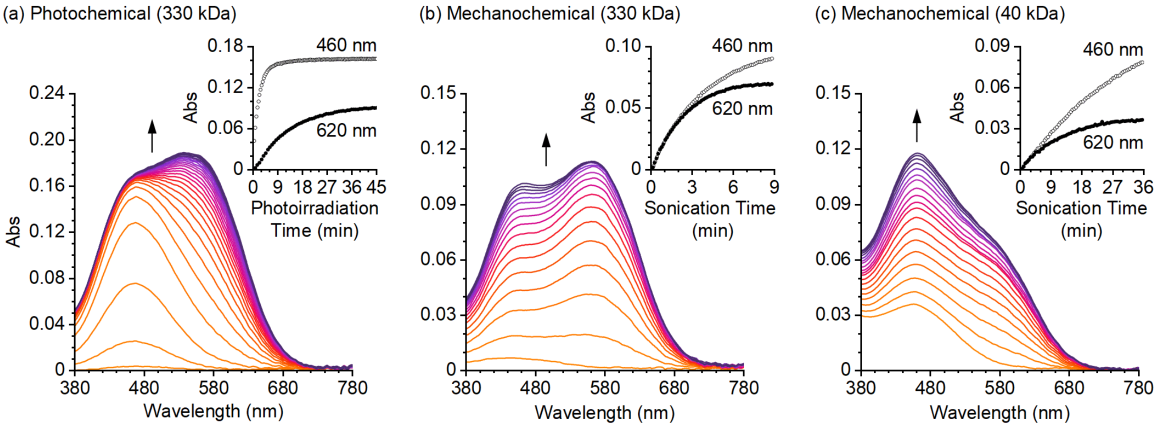

Figure 4.1. UV-vis absorption behavior of bis-naphthopyran under photochemical and mechanochemical activation. (a) Absorption spectra of 330 kDa **BNP-PMA$_{330}$** upon increasing exposure to UV light (λ = 311 nm) illustrating sequential ring-opening behavior. Insets show absorbance monitored at characteristic wavelengths of 460 nm and 620 nm during the reactions. UV-vis absorption behavior of (b) 330 kDa **BNP-PMA$_{330}$** and (c) 40 kDa **BNP-PMA$_{40}$** subjected to ultrasound-induced mechanochemical activation demonstrating a non-sequential ring-opening process and force-dependent visible absorption. Polymer concentrations are 2 mg/mL in THF.

of $BNP_{O\text{-}C}$, allowing for the selective detection of $BNP_{O\text{-}O}$. Under constant photoirradiation of **$BNP\text{-}PMA_{330}$**, the absorbance at 460 nm increases rapidly and reaches a maximum well before the absorbance at 620 nm. These observations are consistent with a sequential photoactivation mechanism in which $BNP_{C\text{-}C}$ undergoes a single ring-opening reaction to generate $BNP_{O\text{-}C}$, followed

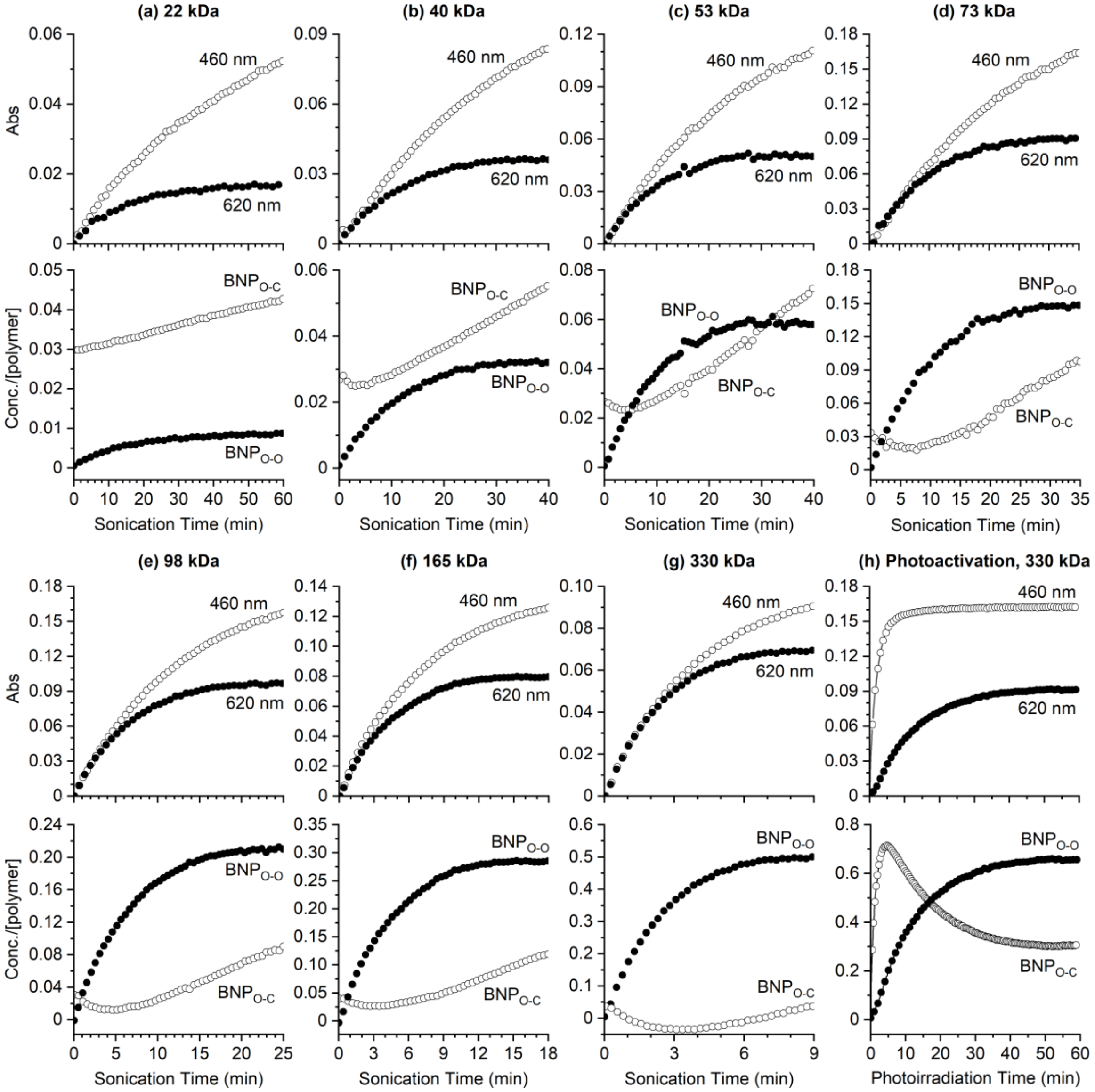

Figure 4.2. (a–g) Representative absorbance (*top*) and concentration (*bottom*) data for the mechanochemical activation of all polymers. (h) Absorbance and concentration data collected during photochemical activation of **$BNP\text{-}PMA_{330}$** with 311 nm UV light. Concentrations of merocyanine species $BNP_{O\text{-}C}$ and $BNP_{O\text{-}O}$ were determined from the absorption data using estimated extinction coefficients (see Section VI of the Experimental section for details). All reactions were conducted at −45 °C with 2 mg/mL polymer in THF. Concentrations of $BNP_{O\text{-}C}$ and $BNP_{O\text{-}O}$ are scaled to the total molar concentration of polymer in solution.

by transformation of the second pyran ring to produce $BNP_{O\text{-}O}$. Tracking the concentration of each species as a function of photoirradiation time using extinction coefficients estimated from similar isolated small molecules[11a,b] further supports this mechanism (Figure 4.2).

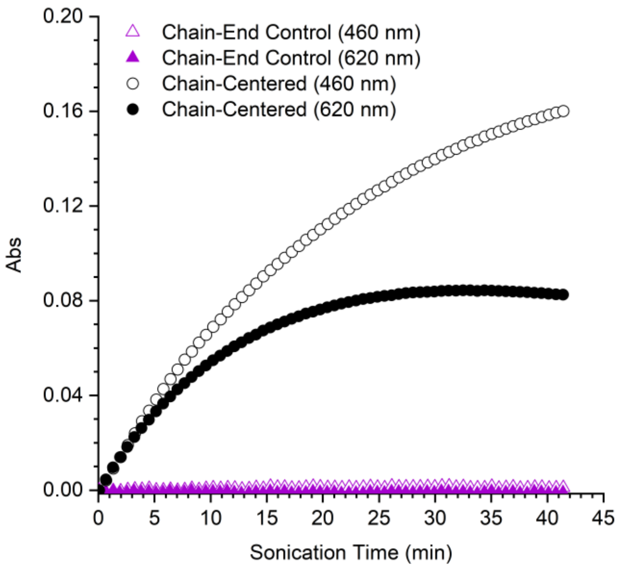

Figure 4.3. Absorbance monitored at 460 nm and 620 nm during continuous ultrasonication (−45 °C, 2 mg/mL in THF) of a 73 kDa chain-centered polymer (**BNP-PMA$_{73}$**) and a 71 kDa chain-end functional control polymer (**BNP-PMA$_{Control}$**) . In contrast to the polymer with a chain-centered BNP unit, no changes in the absorbance at 460 nm or 620 nm are observed for the control polymer containing a BNP unit at the chain-end, confirming that mechanical force is responsible for the observed activation of the BNP mechanophore during ultrasonication.

Mechanochemical activation of PMA chain-centered bis-naphthopyran was investigated by subjecting polymers in THF at −45 °C to continuous ultrasonication (8.2 W/cm^2) using the same analytical flow setup employed in the photoirradiation experiments. In contrast to the sequential photoactivation behavior, mechanochemical activation of **BNP-PMA$_{330}$** occurs via a different mechanism (Figure 4.1b). The absorbance at 620 nm reaches a maximum value early, while the absorbance at 460 nm continues to increase more slowly with longer ultrasonication exposure. These data indicate that $BNP_{O\text{-}O}$ is formed relatively quickly in the mechanochemical reaction compared to $BNP_{O\text{-}C}$, which is generated relatively slowly. Ultrasound-induced mechanical activation of lower molecular weight **BNP-PMA$_{40}$** under the same conditions exhibits a similar trend in absorbance over time with the population of $BNP_{O\text{-}O}$ reaching a steady state before $BNP_{O\text{-}C}$; however, the absorption spectra are markedly different (Figure 4.1c). Remarkably, these results suggest that the relative distribution of $BNP_{O\text{-}C}$ and $BNP_{O\text{-}O}$ resulting from the mechanochemical reaction and the correlated visible absorption spectrum are force-dependent (*vide infra*). Control experiments performed on a chain-end functional polymer confirm the mechanical origin of the observed ultrasound-induced reactivity (Figure 4.3).

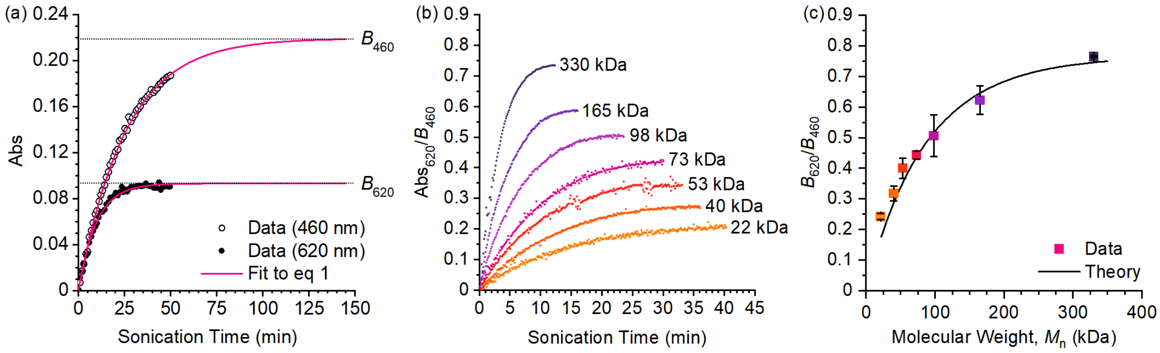

Figure 4.4. Evaluation of force-dependent mechanochromism of the BNP mechanophore. (a) Representative kinetic plots for **BNP-PMA$_{73}$** demonstrating the determination of steady-state absorbance values. Absorbance at 460 nm and 620 nm was recorded for each polymer during ultrasound-induced mechanical activation and fitted to eq. 4.1 to calculate B_{460} and B_{620}. (b) Representative traces of absorbance at 620 nm as a function of sonication time for each polymer scaled to their respective values of B_{460}. (c) Ratios of B_{620}/B_{460} determined for polymers of varying M_n describe the overall distribution of BNP$_{\text{O-C}}$ and BNP$_{\text{O-O}}$ and are consistent with a theoretical model that predicts the force-color relationship.

To further quantify how varying force affects the dynamic equilibrium of the system and the distribution of merocyanine species at the mechanostationary state,[15a] the series of polymers was subjected to ultrasound-induced mechanical activation as described above, the absorbance at 460 nm and 620 nm was plotted as a function of sonication time, and the curves were fitted to eq. 4.1:

$$Abs(t) = B\left(1 - e^{-kt}\right) \tag{4.1}$$

where *Abs(t)* is the absorbance at a specific wavelength at time *t*, *B* is the amplitude (the maximum absorbance value), and *k* is the effective rate constant. A representative example is illustrated in Figure 4.4a. Average values of *B* measured at 460 nm (B_{460}) and 620 nm (B_{620}) were determined from a minimum of three trials for each polymer and are reflective of the steady-state concentration of merocyanine species. More importantly, as discussed below, the ratio of B_{620} to B_{460} for each polymer provides a consistent measure of the ensemble average steady-state distribution of $\mathrm{BNP_{O\text{-}C}}$ and $\mathrm{BNP_{O\text{-}O}}$ at a particular applied force (Table 4.1).

Representative traces of absorbance at 620 nm scaled to respective values of B_{460} as a function of sonication time are shown for each polymer in Figure 4.4b. These data reveal how the populations of merocyanine species change over time to reach a steady-state concentration of $\mathrm{BNP_{O\text{-}C}}$ and $\mathrm{BNP_{O\text{-}O}}$. The relative spectral contribution from the $\mathrm{BNP_{O\text{-}O}}$ state becomes greater with increasing molecular weight of the attached polymers, and thus with greater force applied to the BNP mechanophore. Additionally, the steady-state concentration of $\mathrm{BNP_{O\text{-}O}}$ is reached faster with higher molecular weight polymers, which is consistent with longer chains being activated more quickly in mechanochemical reactions.

We constructed a theoretical model to further understand the force-color relationship observed for the BNP mechanophore (Figure 4.4c). As mentioned above, the average ratio of B_{620}/B_{460} determined for each polymer serves as a proxy to describe the overall distribution of $\mathrm{BNP_{O\text{-}C}}$ and $\mathrm{BNP_{O\text{-}O}}$ resulting from the mechanochemical reaction. In the model, the relative steady-state concentrations (φ) of $\mathrm{BNP_{O\text{-}C}}$ and $\mathrm{BNP_{O\text{-}O}}$ given by eq. 4.2:

$$\varphi_{\text{O-O}} = 1 - \varphi_{\text{O-C}} = \frac{[\mathrm{BNP_{O\text{-}O}}]}{[\mathrm{BNP_{O\text{-}C}}] + [\mathrm{BNP_{O\text{-}O}}]} \tag{4.2}$$

are related to M_n according to eq. 4.3:

$$\varphi_{\text{O-O}} = 1 - e^{-c(M_\mathrm{n}/M_0)} \tag{4.3}$$

where c is a constant and M_0 is the molecular weight of the monomer unit (DP = M_n/M_0). The concentration of each merocyanine species can be calculated from the experimentally determined absorbance values at 460 nm and 620 nm using the Beer-Lambert relationship and previously estimated extinction coefficients to predict the dependence of B_{620}/B_{460} on M_n (see the Experimental section for details). The goal of this model is not to describe the system exactly, but rather capture the overall trend observed for the changes in visible absorption resulting from mechanical activation of BNP with varying force. This simple model is in good agreement with the data.

The experimental results presented above demonstrating force-dependent, gradient multicolor mechanochromism of the BNP mechanophore are consistent with a non-sequential activation mechanism in which $\mathrm{BNP_{C\text{-}C}}$ is converted directly to $\mathrm{BNP_{O\text{-}O}}$ (see the Experimental section for details). Biased by external force, $\mathrm{BNP_{C\text{-}C}}$ exists in equilibrium with $\mathrm{BNP_{O\text{-}C}}$ and $\mathrm{BNP_{O\text{-}O}}$ and the distribution of the two merocyanine species is dictated by the balance between the forward rate of mechanochemical activation and thermal electrocyclization, resulting in a mechanostationary state. Although the complex interconversion processes preclude an exact solution of the rate law, numerical modeling supports the proposed mechanism and suggests that $\mathrm{BNP_{O\text{-}C}}$ is produced predominately, if not exclusively, from thermal electrocyclization of $\mathrm{BNP_{O\text{-}O}}$. The data and the kinetic model also indicate that $\mathrm{BNP_{O\text{-}C}}$ can be activated mechanochemically to regenerate $\mathrm{BNP_{O\text{-}O}}$. As the average DP, or M_n, of the polymers attached to the BNP mechanophore increases, the rate of electrocyclic ring-opening increases, which shifts the merocyanine distribution at the mechanostationary state toward $\mathrm{BNP_{O\text{-}O}}$. This feature is reflected in a greater spectral contribution from $\mathrm{BNP_{O\text{-}O}}$ relative to $\mathrm{BNP_{O\text{-}C}}$ and a larger ratio of B_{620}/B_{460}. This mechanism also accounts for the more rapid mechanochemical generation of $\mathrm{BNP_{O\text{-}O}}$ compared to $\mathrm{BNP_{O\text{-}C}}$. With the exception of **BNP-PMA$_{22}$**, polymer chain scission occurs with extended ultrasonication as expected, leading to irreversible loss of $\mathrm{BNP_{O\text{-}O}}$. This degradation pathway is included explicitly in the kinetic model; however, it appears to have a minimal effect on the value of B_{620}/B_{460}.

In summary, we have developed a bis-naphthopyran (BNP) mechanophore that exhibits force-dependent, gradient multicolor mechanochromism. The BNP mechanophore was incorporated into a series of polymers with different degrees of polymerization and mechanically activated in solution using ultrasonication. By changing the length of the attached polymer chains, the amount of force delivered to the mechanophore was varied systematically. Mechanical activation of BNP proceeds via a mechanistically distinct pathway compared to the photochemical process. Increasing the force applied to the BNP mechanophore predictably alters the relative distribution of two distinctly colored merocyanine products, resulting in a graded change in the overall visible absorption spectrum. The mechanochemical behavior of the BNP mechanophore is described by a theoretical model that provides insight into the force-color relationship.

Acknowledgements

Financial support from Caltech and the Dow Next Generation Educator Fund is gratefully acknowledged. We thank Corey Husic, Anna Overholts, and Dr. Scott Virgil for helpful discussions and the Caltech Center for Catalysis and Chemical Synthesis of the Beckman Institute at Caltech for access to equipment. MEM was supported by a NSF Graduate Research Fellowship (DGE-1745301).

EXPERIMENTAL DETAILS

I. General Experimental Details

Reagents from commercial sources were used without further purification unless otherwise stated. Methyl acrylate was passed through a short plug of basic alumina to remove inhibitor immediately prior to use. Dry THF was obtained from a Pure Process Technology solvent purification system. All reactions were performed under a N_2 or argon atmosphere unless specified otherwise. Column chromatography was performed on a Biotage Isolera system using SiliCycle SiliaSep HP flash cartridges.

NMR spectra were recorded using a 400 MHz Bruker Avance III HD with Prodigy Cryoprobe, a 400 MHz Bruker Avance Neo, or Varian Inova 500 or 600 MHz spectrometers. All ^1H NMR spectra are reported in δ units, parts per million (ppm), and were measured relative to the signals for residual $CHCl_3$ (7.26 ppm) or CH_2Cl_2 (5.32 ppm) in deuterated solvent. All ^{13}C NMR spectra were measured in deuterated solvents and are reported in ppm relative to the signals for $^{13}CDCl_3$ (77.16 ppm) or $^{13}CD_2Cl_2$ (54.00 ppm). Multiplicity and qualifier abbreviations are as follows: s = singlet, d = doublet, m = multiplet, br = broad, app = apparent. Peaks were assigned on the basis of 2D NMR experiments (COSY, HSQC, and HMBC). ^1H–^{19}F coupling constants were determined from $^1H\{^{19}F\}$ NMR spectra acquired on a 400 MHz Bruker Avance Neo spectrometer.

High resolution mass spectra (HRMS) were obtained from an Agilent 6200 series time-of-flight mass spectrometer equipped with an Agilent G1978A multimode source (ESI+).

Analytical gel permeation chromatography (GPC) was performed using an Agilent 1260 series pump equipped with two Agilent PLgel MIXED-B columns (7.5 x 300 mm), an Agilent 1200 series diode array detector, a Wyatt 18-angle DAWN HELEOS light scattering detector, and a Optilab rEX differential refractive index detector. The mobile phase was THF at a flow rate of 1 mL/min. Molecular weights and molecular weight distributions were calculated by light scattering using a dn/dc value of 0.062 mL/g (25 °C) for poly(methyl acrylate). Preparative HPLC was performed on a Agilent 1100 Series apparatus using three Eclipse XDB-C18 9.4 x 250 mm columns in series.

UV-vis absorption spectra were recorded on a Thermo Scientific Evolution 220 spectrometer.

Ultrasound experiments were performed using a Vibra Cell 505 liquid processor equipped with a 0.5-inch diameter solid probe (part #630-0217), sonochemical adapter (part #830-00014), and a Suslick reaction vessel made by the Caltech glass shop (analogous to vessel #830-00014 from Sonics and Materials). UV irradiation was performed using a Philips PL-S 9W/01/2P UVB bulb with a narrow emission of 305–315 nm and a peak at 311 nm under ambient conditions unless indicated otherwise. A Thermo Scientific EK45 Immersion Cooler (part #3281452) was used to maintain a constant temperature bath for sonication and photoirradiation experiments. Polymer solutions were continuously sampled for UV-vis analysis using a Cole Parmer Masterflex L/S pump system (item #EW-77912-10) composed of an L/S pump head (part #77390-00) and L/S precision variable speed drive (part #07528-20) using 4x6 mm PTFE tubing (part #77390-60) and a quartz flow-through cell (Starna, part #583.4-Q-10/Z8.5), which was connected using M6-threaded PTFE tubing (Starna, part #M6-SET).

II. Synthetic Details

Scheme 4.3. Synthesis of bis-naphthopyran initiator **1**.

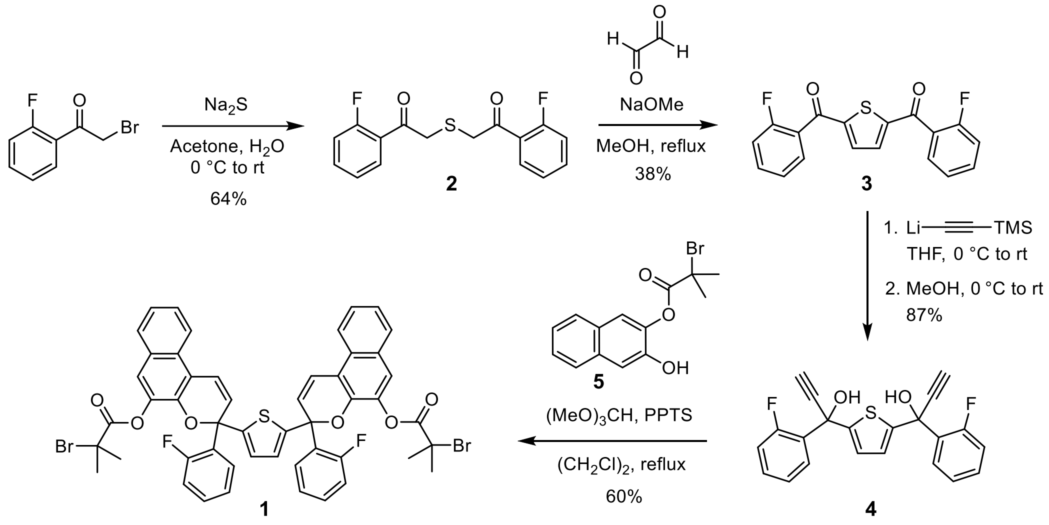

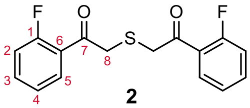

2

2,2′-Thiobis(1-(2-fluorophenyl)ethan-1-one) (2). A round bottom flask equipped with a stir bar was charged with 2-bromo-2′-fluoroacetophenone (13.6 g, 62.3 mmol) dissolved in acetone (150 mL). The solution was cooled to 0 °C in an ice bath followed by the dropwise addition of sodium sulfide nonahydrate (7.53 g, 31.4 mmol) dissolved in DI water (17 mL). The reaction was allowed to warm to room temperature and stirred for 25 h. The solution was concentrated under reduced pressure and the aqueous solution was extracted into dichloromethane, dried over $MgSO_4$, filtered, and concentrated. The crude material was purified by column chromatography on silica gel (30% EtOAc/hexanes) to provide the title compound as pale-yellow crystals (6.16 g, 64%).

TLC (20% EtOAC/hexanes): $R_f = 0.43$

<u>^{1}H NMR (500 MHz, CD_2Cl_2) δ:</u> 3.92 (d, J_{HF} = 2.4 Hz, 4H, C_8), 7.16 (ddd, J_{HF} = 11.4 Hz, J_{HH} = 8.4 Hz, 1.1 Hz, 2H, C_2), 7.26 (ddd, J_{HH} = 7.8, 7.3, 1.1 Hz, 2H, C_4), 7.57 (dddd, J_{HF} = 5.1 Hz, J_{HH} = 8.3, 7.1, 1.9 Hz, 2H, C_3), 7.88 (ddd, J_{HF} = 7.6 Hz, J_{HH} = 7.6, 1.9 Hz, 2H, C_5).

<u>$^{13}C\{^1H\}$ NMR (101 MHz, $CDCl_3$) δ:</u> 42.0 (d, J_{CF} = 8.3 Hz, C_8), 116.8 (d, J_{CF} = 23.9 Hz, C_2), 124.1 (d, J_{CF} = 12.6 Hz, C_6), 124.8 (d, J_{CF} = 3.3 Hz, C_4), 131.4 (d, J_{CF} = 2.5 Hz, C_5), 135.3 (d, J_{CF} = 9.2 Hz, C_3), 161.9 (d, J_{CF} = 254.6 Hz, C_1), 192.0 (d, J_{CF} = 4.6 Hz, C_7).

<u>HRMS (ESI, *m/z*):</u> calcd for $[C_{16}H_{13}F_2O_2S]^+$ $(M+H)^+$, 307.0599; found, 307.0604.

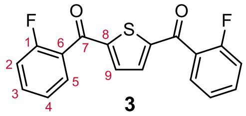

3

2,5-Di(*o*-fluorobenzoyl)thiophene (3). A flame-dried round bottom flask equipped with a condenser and stir bar was charged with 2,3-dihydroxy-1,4-dioxane (0.922 g, 7.68 mmol) and evacuated/backfilled with nitrogen (3x). Anhydrous methanol (50 mL) was added via syringe and the mixture was heated to reflux for 1.5 h to generate glyoxal. In a separate flame-dried round bottom flask equipped with a condenser and stir bar, sodium metal (340 mg, 14.8 mmol) was dissolved in anhydrous methanol (15 mL) under nitrogen at 0 °C in an ice bath to form sodium methoxide. Compound **2** (3.795 g, 12.31 mmol) was dissolved in anhydrous dichloromethane (15 mL) under nitrogen and transferred via syringe to the warm glyoxal solution, followed by the dropwise addition of the sodium methoxide solution via syringe (the solution turned orange, then yellow, then dark green). The reaction mixture was returned to reflux (turning dark red) and stirred for 16 h. The reaction was cooled to room temperature, concentrated under reduced pressure, and dissolved in EtOAc (100 mL). The organic layer was washed with 1 M aqueous HCl (100 mL), distilled water (100 mL), 10% aqueous $NaHCO_3$ (100 mL), 2 M aqueous NaOH (100 mL), and brine (100 mL). The organic layer was dried over $MgSO_4$, filtered, and concentrated under reduced pressure. The crude material was purified by column chromatography on silica gel (10–40% EtOAc/hexanes) and subsequently recrystallized from EtOAc/hexanes to provide the title compound as white needles (1.52 g, 38%).

TLC (20% EtOAc/hexanes): $R_f = 0.35$

^{1}H NMR (500 MHz, $CDCl_3$) δ: 7.21 (ddd, J_{HF} = 9.6 Hz, J_{HH} = 8.3, 1.0 Hz, 2H, C_2), 7.29 (ddd, J_{HH} = 7.5 Hz, 7.5, 1.0 Hz, 2H, C_4), 7.54–7.59 (m, 4H, C_3 and C_9), 7.61 (ddd, J_{HF} = 6.9 Hz, J_{HH} = 7.7, 1.8 Hz, 2H, C_5).

^{13}C{^{1}H} NMR (101 MHz, $CDCl_3$) δ: 116.8 (d, J_{CF} = 21.5 Hz, C_2), 124.6 (d, J_{CF} = 3.7 Hz, C_4), 126.4 (d, J_{CF} = 14.5 Hz, C_6), 130.5 (d, J_{CF} = 2.5 Hz, C_5), 133.9 (d, J_{CF} = 8.4 Hz, C_3), 134.4 (d, J_{CF} = 2.9 Hz, C_9), 149.8 (C_8), 159.9 (d, J_{CF} = 253.5 Hz, C_1), 185.4 (C_7).

HRMS (ESI, *m/z*): calcd for $[C_{18}H_{11}F_2O_2S]^+$ $(M+H)^+$, 329.0442; found, 329.0444.

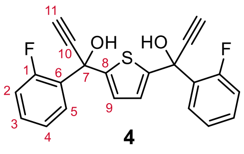

4

2,5-Di[hydroxyl-1-(*o*-fluorophenyl)-prop-2-ynyl]thiophene (4). A flame-dried round bottom flask equipped with a stir bar under nitrogen was charged with anhydrous THF (4 mL) and ethynyltrimethylsilane (0.160 mL, 1.15 mmol). The solution was cooled to 0 °C in an ice bath and n-butyllithium (2.5 M in hexanes, 0.450 mL, 1.13 mmol) was added dropwise via syringe. After 1 h, compound **3** (131 mg, 0.399 mmol) dissolved in anhydrous THF (1 mL) was added to the reaction mixture and it was allowed to warm to room temperature. After 21 h, the solution was cooled to 0 °C in an ice bath. Methanol (3 mL) was added to the solution via syringe and the reaction mixture was allowed to warm to room temperature and stirred for 5 h. The reaction mixture was neutralized with 1 M HCl and extracted into EtOAc (50 mL). The organic layer was washed with 10% aqueous NH_4Cl (50 mL), 10% aqueous $NaHCO_3$ (50 mL), and brine (50 mL). The organic layer was dried over $MgSO_4$, filtered, and concentrated under vacuum. The crude material was purified by column chromatography on silica gel (5–40%

EtOAc/hexanes) to provide the title compound (mixture of diastereomers) as a light-brown viscous oil (132 mg, 87%). R_f = 0.15 (20% EtOAc/hexanes). HRMS (ESI, *m/z*): calcd for $[C_{22}H_{13}F_2O_2S]^+$ $(M-OH)^+$, 363.0650; found, 363.0649. An analytical sample was further separated to characterize each diastereomer individually.

Diastereomer 1:

^{1}H NMR (400 MHz, $CDCl_3$) δ: 2.85 (d, J_{HF} = 0.6 Hz, 2H, C_{11}), 3.29 (d, J_{HF} = 3.3 Hz, 2H, OH), 7.00 (s, 2H, C_9), 7.05 (ddd, J_{HF} = 11.6 Hz, J_{HH} = 8.1, 1.4 Hz, 2H, C_2), 7.16 (ddd, J_{HH} = 7.6, 7.6, 1.2 Hz, 2H, C_4), 7.33 (dddd, J_{HF} = 5.0 Hz, J_{HH} = 8.1, 7.5, 1.9 Hz, 2H, C_3), 7.67 (ddd, J_{HF} = 8.0 Hz, J_{HH} = 8.0, 1.7 Hz, 2H, C_5).

^{13}C{^{1}H} NMR (101 MHz, $CDCl_3$) δ: 69.22 (C_7), 74.8 (d, J_{CF} = 2.4 Hz, C_{11}), 83.99 (C_{10}), 116.52 (d, J_{CF} = 21.7 Hz, C_2), 124.1 (d, J_{CF} = 3.6 Hz, C_4), 125.31 (d, J_{CF} = 1.5 Hz, C_9), 127.2 (d, J_{CF} = 2.2 Hz, C_5), 130.50 (d, J_{CF} = 10.0 Hz, C_6), 130.55 (d, J_{CF} = 8.5 Hz, C_3), 148.50 (C_8), 160.09 (d, J_{CF} = 249.4 Hz, C_1).

Diastereomer 2:

^{1}H NMR (400 MHz, $CDCl_3$) δ: 2.84 (d, J_{HF} = 0.6 Hz, 2H, C_{11}), 3.28 (d, J_{HF} = 3.0 Hz, 2H, OH), 6.94 (s, 2H, C_9), 7.05 (ddd, J_{HF} = 11.5 Hz, J_{HH} = 8.1, 1.4 Hz, 2H, C_2), 7.16 (ddd, J_{HH} = 7.6, 7.6, 1.2 Hz, 2H, C_4), 7.34 (dddd, J_{HF} = 5.0 Hz, J_{HH} = 8.1, 7.5, 1.8 Hz, 2H, C_3), 7.69 (ddd, J_{HF} = 8.0 Hz, J_{HH} = 8.0, 1.8 Hz, 2H, C_5).

^{13}C{^{1}H} NMR (101 MHz, $CDCl_3$) δ: 69.18 (C_7), 74.9 (d, J_{CF} = 2.2 Hz, C_{11}), 84.03 (C_{10}), 116.51 (d, J_{CF} = 21.6 Hz, C_2), 124.1 (d, J_{CF} = 3.6 Hz, C_4), 125.27 (d, J_{CF} = 1.4 Hz, C_9), 127.3 (d, J_{CF} = 2.3 Hz, C_5), 130.4 (d, J_{CF} = 9.9 Hz, C_6), 130.57 (d, J_{CF} = 8.4 Hz, C_3), 148.47 (C_8), 160.06 (d, J_{CF} = 249.4 Hz, C_1).

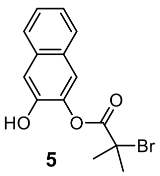

5

3-Hydroxynaphthalen-2-yl 2-bromo-2-methylpropanoate (5). An oven-dried round bottom flask equipped with a stir bar was charged with 2,3-dihydroxynaphthalene (3.0 g, 19 mmol) and evacuated/backfilled with nitrogen (3x). Anhydrous THF (54 mL) was added via syringe under nitrogen. The solution was cooled to 0 °C in an ice bath, followed by the consecutive dropwise addition of triethylamine (2.6 mL, 19 mmol) and α-bromoisobutyryl bromide (2.3 mL, 19 mmol) via syringe, resulting in formation of a white precipitate. The reaction mixture was allowed to warm to room temperature and stirred for 19 h. The mixture was extracted into EtOAc (120 mL) and washed with distilled water (50 mL) and brine (50 mL). The organic layer was dried over $MgSO_4$, filtered, and concentrated under reduced pressure. The crude material was purified by column chromatography on silica gel (5–38% EtOAc/hexanes) followed by recrystallization from EtOAc/hexanes to provide the title compound as colorless, transparent crystals (2.1 g, 36%).

TLC (20% EtOAc/hexanes): $R_f = 0.38$

^{1}H NMR (400 MHz, CD_2Cl_2) δ: 2.14 (s, 6H), 5.75 (s, 1H), 7.34 (d, *J* = 0.7 Hz, 1H), 7.38 (ddd, *J* = 8.1, 6.9, 1.3 Hz, 1H), 7.45 (ddd, *J* = 8.3, 6.9, 1.4 Hz, 1H), 7.62 (d, *J* = 0.7 Hz, 1H), 7.70 (ddddd, *J* = 8.2, 1.3, 0.6, 0.6, 0.6 Hz, 1H), 7.76 (ddddd, *J* = 8.2, 1.3, 0.7, 0.7, 0.7 Hz, 1H).

^{13}C{^{1}H} NMR (101 MHz, $CDCl_3$) δ: 30.8, 56.0, 112.3, 120.1, 124.5, 126.55, 126.58, 127.6, 128.6, 132.9, 138.7, 146.2, 170.0.

HRMS (ESI, *m/z*): calcd for $[C_{14}H_{17}{}^{79}BrO_3N]^+$ $(M-OH)^+$, 326.0386; found, 326.0388.

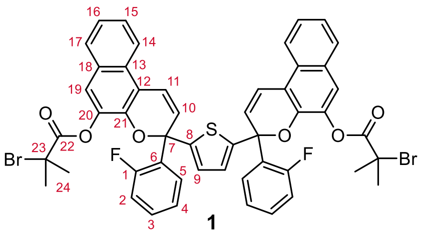

1

Thiophene-2,5-diylbis(3-(2-fluorophenyl)-3*H*-benzo[*f*]chromene-3,5-diyl) bis(2-bromo-2-methylpropanoate) (1). Naphthopyrans were synthesized according to the procedure by Zhao and Carreira.[40] A flame-dried two-neck round bottom flask equipped with a stir bar and condenser was charged with compound **5** (584 mg, 1.89 mmol) and pyridinium *p*-toluenesulfonate (20 mg, 0.080 mmol) and evacuated/ backfilled with nitrogen (3x). Compound **4** (290 mg, 0.762 mmol) dissolved in anhydrous 1,2-dichloroethane (5 mL) was added via syringe. Trimethyl orthoformate (0.38 mL, 3.5 mmol) was added via syringe and the solution was refluxed for 22 h. The solution was poured into water (50 mL) and extracted into EtOAc (50 mL). The organic layer was washed with 10% aqueous $NaHCO_3$ (50 mL), 10% aqueous NH_4Cl (50 mL), and brine (50 mL), dried over Na_2SO_4, filtered, and concentrated under reduced pressure. The crude product was purified by column chromatography (5–40% EtOAc/hexanes). It was further purified by precipitation from hexanes and isolated by filtration to provide the title compound (mixture of diastereomers) as a magenta powder (440 mg, 60%). $R_f = 0.51$ (20% EtOAC/hexanes). An analytical sample was separated by preparative HPLC to characterize each diastereomer individually.

Diastereomer 1:

^{1}H NMR (400 MHz, CD_2Cl_2) δ: 1.87 (s, 6H, C_{24}), 1.96 (s, 6H, C_{24}), 6.43 (dd, J_{HF} = 4.0 Hz, J_{HH} = 10.0 Hz, 2H, C_{10}), 6.90 (s, 2H, C_9), 7.02 (ddd, J_{HF} = 11.6 Hz, J_{HH} = 8.2, 1.2 Hz, 2H, C_2), 7.13 (ddd, J_{HF} = 7.4 Hz, J_{HH} = 7.9, 1.2 Hz, 2H, C_4), 7.25–7.35 (m, 4H, C_3 and C_{11}), 7.41 (ddd, J_{HH} = 8.0, 6.9, 1.2 Hz, 2H, C_{16}), 7.47–7.54 (m, 4H, C_{15} and C_{19}), 7.67 (ddd, J_{HF} = 8.0 Hz, J_{HH} = 8.0, 1.8 Hz, 2H, C_5), 7.72–7.76 (m, 2H, C_{17}), 7.97 (dd, J_{HH} = 8.7, 1.0 Hz, 2H, C_{14}).

^{13}C{^{1}H} NMR (101 MHz, CD_2Cl_2) δ: 31.3 (C_{24}), 31.4 (C_{24}), 55.6 (C_{23}), 79.2 (d, J_{CF} = 2.9 Hz, C_7), 115.9 (C_{12}), 117.00 (d, J_{CF} = 21.8 Hz, C_2), 120.3 (C_{11}), 121.17 (C_{19}), 121.97 (C_{14}), 124.45 (d, J_{CF} =

3.1 Hz, C_{4}), 125.4 (C_{16}), 126.1 (d, J_{CF} = 4.3 Hz, C_{10}), 126.3 (d, J_{CF} = 1.4 Hz, C_{9}), 127.3 (C_{15}), 127.6 (d, J_{CF} = 2.6 Hz, C_{5}), 128.4 (C_{18}), 128.71 (C_{17}), 129.4 (C_{12}), 130.69 (d, J_{CF} = 8.5 Hz, C_{3}), 131.0 (d, J_{CF} = 10.6 Hz, C_{6}), 139.39 (C_{20}), 142.5 (C_{21}), 148.5 (C_{8}), 159.6 (d, J_{CF} = 248.3 Hz, C_{1}), 170.3 (C_{22}).

HRMS (ESI, *m/z*): calcd for $[C_{50}H_{40}{}^{79}Br_{2}F_{2}O_{6}SN]^{+}$ $(M+NH_{4})^{+}$, 978.0906; found, 978.0866.

Diastereomer 2:

^{1}H NMR (400 MHz, $CD_{2}Cl_{2}$) δ: 1.91 (s, 6H, C_{24}), 2.02 (s, 6H, C_{24}), 6.40 (dd, J_{HF} = 4.1 Hz, J_{HH} = 10.0 Hz, 2H, C_{10}), 6.78 (s, 2H, C_{9}), 7.01 (ddd, J_{HF} = 12.6 Hz, J_{HH} = 8.2, 1.1 Hz, 2H, C_{2}), 7.12 (ddd, J_{HF} = 7.4 Hz, J_{HH} = 7.9, 1.2 Hz, 2H, C_{4}), 7.27–7.34 (m, 4H, C_{3} and C_{11}), 7.40 (ddd, J_{HH} = 8.1, 7.0, 1.1 Hz, 2H, C_{16}), 7.48–7.54 (m, 4H, C_{15} and C_{19}), 7.66 (ddd, J_{HF} = 8.0 Hz, J_{HH} = 8.0, 1.8 Hz, 2H, C_{5}), 7.68–7.72 (m, 2H, C_{17}), 7.96 (dd, J_{HH} = 8.7, 1.0 Hz, 2H, C_{14}).

$^{13}C\{^{1}H\}$ NMR (101 MHz, $CD_{2}Cl_{2}$) δ: 31.3 (C_{24}), 31.4 (C_{24}), 55.7 (C_{23}), 79.6 (d, J_{CF} = 2.6 Hz, C_{7}), 116.1 (C_{12}), 117.02 (d, J_{CF} = 22.0 Hz, C_{2}), 120.1 (C_{11}), 121.22 (C_{19}), 121.99 (C_{14}), 124.41 (d, J_{CF} = 3.2 Hz, C_{4}), 125.4 (C_{16}), 125.7 (d, J_{CF} = 1.7 Hz, C_{9}), 126.7 (d, J_{CF} = 4.0 Hz, C_{10}), 127.3 (C_{15}), 128.0 (d, J_{CF} = 2.8 Hz, C_{5}), 128.4 (C_{18}), 128.69 (C_{17}), 129.4 (C_{12}), 130.66 (d, J_{CF} = 10.7 Hz, C_{6}), 130.8 (d, J_{CF} = 8.4 Hz, C_{3}), 139.44 (C_{20}), 142.6 (C_{21}), 148.7 (C_{8}), 159.9 (d, J_{CF} = 248.7 Hz, C_{1}), 170.4 (C_{22}).

HRMS (ESI, *m/z*): calcd for $[C_{50}H_{40}{}^{79}Br_{2}F_{2}O_{6}SN]^{+}$ $(M+NH_{4})^{+}$, 978.0906; found, 978.0861.

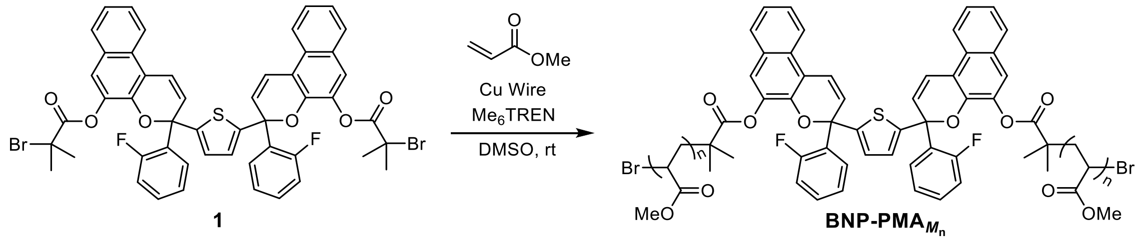

General Procedure for the Synthesis of Polymers Incorporating a Bis-Naphthopyran Mechanophore

A representative procedure is provided for the synthesis of **BNP-PMA$_{73}$**. A 10 mL flame-dried Schlenk flask equipped with a stir bar was charged with initiator **1** (18.3 mg, 0.0204 mmol), DMSO (1.00 mL), methyl acrylate (2.00 mL, 22.2 mmol) and freshly cut copper wire (2.0 cm, 20 gauge). The flask was sealed, the solution was degassed via four freeze-pump-thaw cycles, and then backfilled with nitrogen and warmed to room temperature. Me$_6$TREN (10.5 µL, 0.0393 mmol) was added via microsyringe. After stirring at room temperature for 2 h, the flask was opened to air and the solution was diluted with DCM. The polymer solution was precipitated into methanol cooled with dry ice (3x) and the isolated material was dried under vacuum to provide 1.05 g of polymer (55%). M_n = 73.2 kg/mol, $Đ$ = 1.10.

Scheme 4.4. Synthesis of chain-end functional control polymer **BNP-PMA$_{\text{Control}}$**.

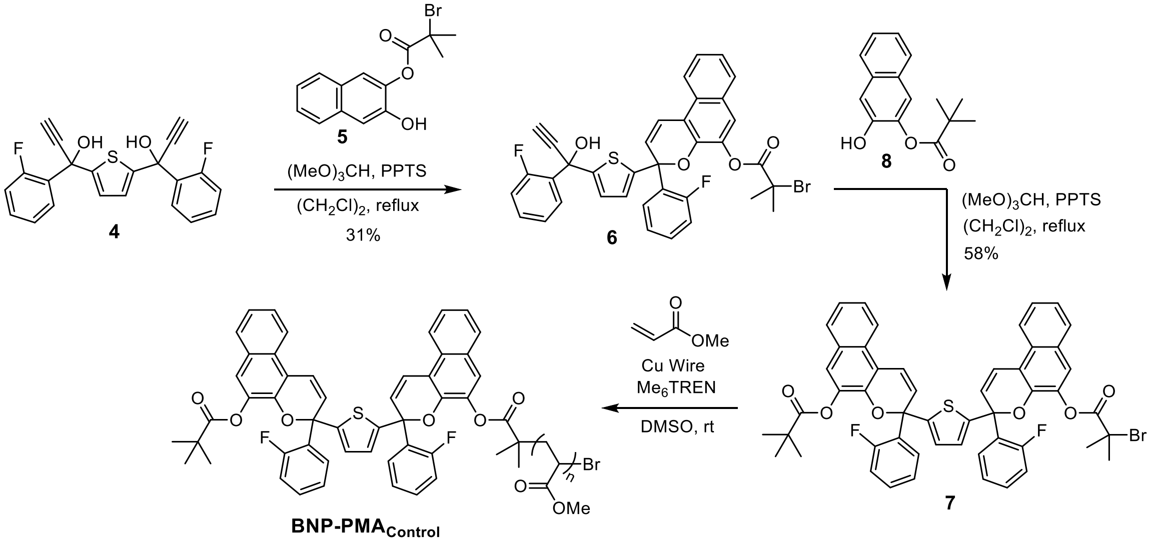

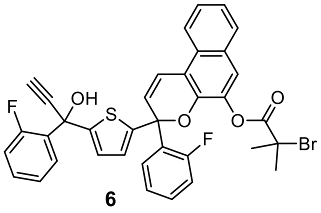

6

3-(2-fluorophenyl)-3-(5-(1-(2-fluorophenyl)-1-hydroxyprop-2-yn-1-yl)thiophen-2-yl)-3*H*-benzo[*f*]chromen-5-yl 2-bromo-2-methylpropanoate (6). A flame-dried two-neck round bottom flask equipped with a condenser and stir bar was charged with compound **5** (594 mg, 1.92 mmol) and pyridinium *p*-toluenesulfonate (27 mg, 0.11 mmol) and evacuated/ backfilled with nitrogen (3x). Compound **4** (729 mg, 1.92 mmol) was dissolved in 1,2-dichloroethane (20 mL) under nitrogen and added to the reaction mixture, followed by addition of trimethyl orthoformate (0.95 mL, 2.7 mmol) via syringe. The reaction was refluxed for 14 h, during which time it became a deep red color. The solution was cooled to room temperature, concentrated under reduced pressure, and dissolved in EtOAc (50 mL). The organic layer was washed with distilled water (50 mL), 1 M aqueous $NaHCO_3$ (50 mL), and brine (50 mL). The organic layer was dried over $MgSO_4$, filtered, and concentrated under reduced pressure. The crude product was purified by column chromatography on silica gel (20–100% DCM/hexanes) to provide the title compound (mixture of diastereomers) as a red foamy solid (400 mg, 31%).

TLC (100% DCM): R_f = 0.32

^{1}H NMR (400 MHz, CD_2Cl_2) δ: 2.00 (s, 1.5H), 2.03 (s, 1.5H), 2.08 (s, 1.5H), 2.10 (s, 1.5H), 2.85 (d, J_{HF} = 0.8 Hz, 0.5H), 2.86 (d, J_{HF} = 0.7 Hz, 0.5H), 3.33 (d, J_{HF} = 1.2 Hz, 0.5H), 3.34 (d, J_{HF} = 1.4 Hz, 0.5H), 6.47 (dd, J_{HF} = 3.9 Hz, J_{HH} = 10.0, 1H), 6.47 (dd, J_{HF} = 3.9 Hz, J_{HH} = 10.0, 1H), 6.85 (d, J_{HH} = 3.8 Hz, 0.5H), 6.90 (d, J_{HH} = 3.8 Hz, 0.5H), 6.92–6.97 (m, 1H), 6.99–7.09 (m, 2H), 7.11–7.21 (m, 2H), 7.29–7.38 (m, 3H), 7.38–7.45 (m, 1H), 7.48–7.56 (m, 2H), 7.63 (dddd, , J_{HF} = 8.0 Hz, J_{HH} = 9.6, 7.8, 1.8 Hz, 1H), 7.70–7.79 (m, 2H), 7.96–8.03 (m, 1H).

^{13}C{^{1}H} NMR (151 MHz, CD_2Cl_2) δ: 31.41, 31.42, 31.45, 55.7 (d, J_{CF} = 2.9 Hz), 69.2, 69.3, 74.8 (d, J_{CF} = 2.5 Hz), 74.9 (d, J_{CF} = 2.4 Hz), 79.3 (d, J = 2.7 Hz), 79.4 (d, J_{CF} = 2.9 Hz), 84.5, 116.20, 116.21, 116.79 (d, J_{CF} = 21.8 Hz), 116.79 (d, J_{CF} = 21.8 Hz), 117.05 (d, J_{CF} = 21.9 Hz), 117.07 (d,

J_{CF} = 21.8 Hz), 120.46, 120.53, 121.30, 121.32, 122.0, 124.5 (d, J_{CF} = 3.1 Hz), 124.6 (d, J_{CF} = 4.7 Hz), 125.5, 125.66 (d, J_{CF} = 1.0 Hz), 125.70 (d, J_{CF} = 0.8 Hz), 126.0 (d, J_{CF} = 1.3 Hz), 126.1 (d, J_{CF} = 1.2 Hz), 126.2 (d, J_{CF} = 4.2 Hz), 126.4 (d, J_{CF} = 4.5 Hz), 127.4, 127.5 (d, J_{CF} = 2.3 Hz), 127.6 (d, J_{CF} = 2.3 Hz), 127.7 (d, J_{CF} = 2.6 Hz), 127.9 (d, J_{CF} = 2.8 Hz), 128.5, 128.7, 129.4, 130.77 (d, J_{CF} = 10.6 Hz), 130.79 (d, J_{CF} = 8.4 Hz), 130.81 (d, J_{CF} = 8.4 Hz), 130.9 (d, J_{CF} = 10.6 Hz), 130.97 (d, J_{CF} = 8.4 Hz), 131.00 (d, J_{CF} = 8.5 Hz), 131.10 (d, J_{CF} = 10.2 Hz), 131.13 (d, J_{CF} = 10.1 Hz), 139.5, 142.58, 142.59, 148.1, 148.3, 149.47, 149.51, 159.79 (d, J_{CF} = 248.1 Hz), 159.84 (d, J_{CF} = 248.4 Hz), 160.40 (d, J_{CF} = 249.3 Hz), 160.44 (d, J_{CF} = 249.4 Hz), 170.53.

HRMS (ESI, *m/z*): calcd for $[C_{36}H_{29}{}^{79}BrF_2O_4SN]^+$ $(M+NH_4)^+$, 688.0963; found, 688.0946.

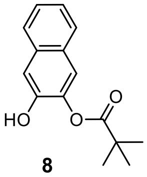

8

3-hydroxynaphthalen-2-yl pivalate (8). A flame-dried two neck round bottom flask equipped with a stir bar was charged with 2,3-dihydroxynaphthalene (3.00 g, 18.7 mmol) and evacuated/backfilled with nitrogen (3x). Anhydrous THF (30 mL) was added via syringe under nitrogen. The solution was cooled to 0 °C in an ice bath, followed by the consecutive dropwise addition of triethylamine (2.65 mL, 19.0 mmol) and pivaloyl chloride (2.30 mL, 18.7 mmol) via syringe, resulting in formation of a white precipitate. The reaction mixture was allowed to warm to room temperature and stirred for 16 h. The precipitate was filtered off and rinsed with EtOAc (100 mL), and the filtrate was collected and washed with DI water (50 mL), 10% aqueous NH_4Cl (50 mL), and brine (50 mL). The organic layer was dried over Na_2SO_4, filtered, and concentrated under reduced pressure. The crude product was purified by column chromatography on silica gel (DCM) to provide the title compound as white crystals (3.10 g, 68%).

TLC (100% DCM): R_f = 0.84

<u>^{1}H NMR (400 MHz, CD_2Cl_2) δ:</u> 1.43 (s, 9H), 7.32 (s, 1H), 5.36–5.39 (m, 1H), 7.36 (ddd, *J* = 8.1, 6.9, 1.3 Hz, 1H), 7.42 (ddd, *J* = 8.2, 6.9, 1.4 Hz, 1H), 7.55 (d, *J* = 0.7, 1H), 7.69 (app br d, *J* = 8.1 Hz, 1H), 7.74 (ddddd, *J* = 8.1, 1.3, 0.6, 0.6, 0.6 Hz, 1H).

<u>$^{13}C\{^1H\}$ NMR (101 MHz, $CDCl_3$) δ:</u> 27.4, 39.6, 112.5, 120.0, 124.4, 126.2, 126.4, 127.4, 128.8, 132.6, 139.8, 146.3, 177.4.

<u>HRMS (ESI, *m/z*):</u> calcd for $[C_{15}H_{20}O_3N]^+$ $(M+NH_4)^+$, 262.1438; found, 262.1439.

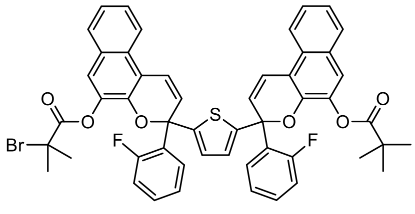

7

3-(5-(5-((2-bromo-2-methylpropanoyl)oxy)-3-(2-fluorophenyl)-3*H*-benzo[*f*]chromen-3-yl)thiophen-2-yl)-3-(2-fluorophenyl)-3*H*-benzo[*f*]chromen-5-yl pivalate (7). A flame-dried two-neck round bottom flask equipped with a condenser and stir bar was charged with compound **8** (51 mg, 0.21 mmol) and pyridinium *p*-toluenesulfonate (2.7 mg, 0.011 mmol) and evacuated/backfilled with nitrogen (3x). Compound **6** (71 mg, 0.11 mmol) was dissolved in anhydrous 1,2-dichloroethane (2.5 mL) under nitrogen and added to the reaction mixture, followed by addition of trimethyl orthoformate (50 µL, 0.46 mmol) via syringe. The reaction was refluxed for 12 h. The solution was cooled to room temperature, extracted into EtOAc (20 mL), and washed with 10% aqueous NH_4Cl (20 mL), 1 M aqueous $NaHCO_3$ (20 mL), and brine (20 mL). The organic layer was dried over Na_2SO_4, filtered, and concentrated under reduced pressure. The crude product was purified by consecutive chromatographic separations on silica gel (10–40% EtOAc/hexanes, then 40–80% DCM/hexanes) to provide the title compound (mixture of diastereomers) as a red foamy solid (55 mg, 58%).

<u>TLC (20% EtOAc/hexanes):</u> $R_f = 0.47$

^{1}H NMR (400 MHz, CD_2Cl_2) δ: 1.25 (s, 4.5H), 1.30 (s, 4.5H), 1.87 (s, 1.5H), 1.93 (s, 1.5H), 1.97 (s, 1.5H), 2.03 (s, 1.5H), 6.38–6.47 (m, 2H), 6.76–6.81 (m, 1H), 6.90 (s, 1H), 6.98–7.06 (m, 2H), 7.09–7.17 (m, 2H), 7.25–7.35 (m, 4H), 7.36–7.56 (m, 6H), 7.63–7.76 (m, 4H), 7.91–7.99 (m, 2H).

^{13}C{^{1}H} NMR (101 MHz, CD_2Cl_2) δ: 27.6, 31.31, 31.32, 31.35, 39.41, 39.5, 55.7, 55.8, 79.0 (d, J = 3.0 Hz), 79.2 (d, J_{CF} = 2.9 Hz), 79.4 (d, J_{CF} = 2.8 Hz), 79.6 (d, J_{CF} = 2.6 Hz), 115.6, 115.8, 115.9, 116.1, 116.97 (d, J_{CF} = 21.8 Hz), 116.98 (d, J_{CF} = 21.8 Hz), 117.02 (d, J_{CF} = 21.9 Hz), 120.12, 120.14, 120.3, 120.4, 121.16, 121.21, 121.5, 121.6, 121.91, 121.93, 121.98, 122.00, 124.39 (d, J_{CF} = 3.0 Hz), 124.42 (d, J_{CF} = 2.8 Hz), 125.2, 125.4, 125.7 (d, J = 1.6 Hz), 125.8 (d, J_{CF} = 1.7 Hz), 125.9 (d, J_{CF} = 4.5 Hz), 126.1 (d, J_{CF} = 4.4 Hz), 126.2 (d, J_{CF} = 1.3 Hz), 126.3 (d, J_{CF} = 1.4 Hz), 126.5 (d, J_{CF} = 4.2 Hz), 126.7 (d, J_{CF} = 3.9 Hz), 127.0, 127.3, 127.58 (d, J_{CF} = 2.5 Hz), 127.59 (d, J_{CF} = 2.9 Hz), 127.9 (d, J_{CF} = 3.0 Hz), 128.0 (d, J_{CF} = 2.7 Hz), 128.2, 128.4, 128.5, 128.6, 128.69, 128.70, 129.4, 129.5, 130.6 (d, J_{CF} = 8.5 Hz), 130.7 (d, J_{CF} = 8.1 Hz), 130.8 (d, J_{CF} = 8.6 Hz), 130.9 (d, J_{CF} = 10.8 Hz), 131.1 (d, J_{CF} = 10.7 Hz), 131.2 (d, J_{CF} = 10.9 Hz), 139.4, 139.5, 139.96, 140.01, 142.55, 142.61, 142.9, 143.0, 148.5, 148.69, 148.71, 148.8, 159.6 (d, J_{CF} = 248.2 Hz), 159.7 (d, J_{CF} = 248.3 Hz), 159.8 (d, J_{CF} = 248.5 Hz), 159.9 (d, J_{CF} = 248.7 Hz), 170.35, 170.41, 176.90, 176.92.

HRMS (ESI, *m/z*): calcd for $[C_{51}H_{43}{}^{79}Br_2F_2O_6SN]^+$ $(M+NH_4)^+$, 914.1957; found, 914.1921.

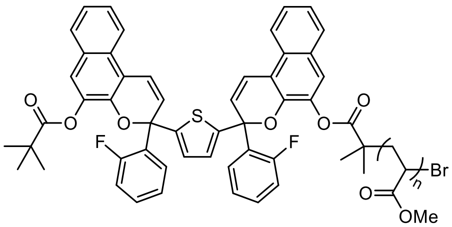

BNP-PMA$_{\text{Control}}$

Chain-end control polymer (BNP-PMA$_{\text{Control}}$). A PMA control polymer containing the bis-naphthopyran mechanophore at the chain-end was synthesized following the general procedure using initiator **7** (19.9 mg, 0.0222 mmol), DMSO (1.20 mL), methyl acrylate (2.40 mL, 26.7 mmol) and freshly cut copper wire (2.0 cm, 20 gauge) to provide 1.18 g of polymer (51%). M_n = 71.2 kg/mol, $Đ$ = 1.14.

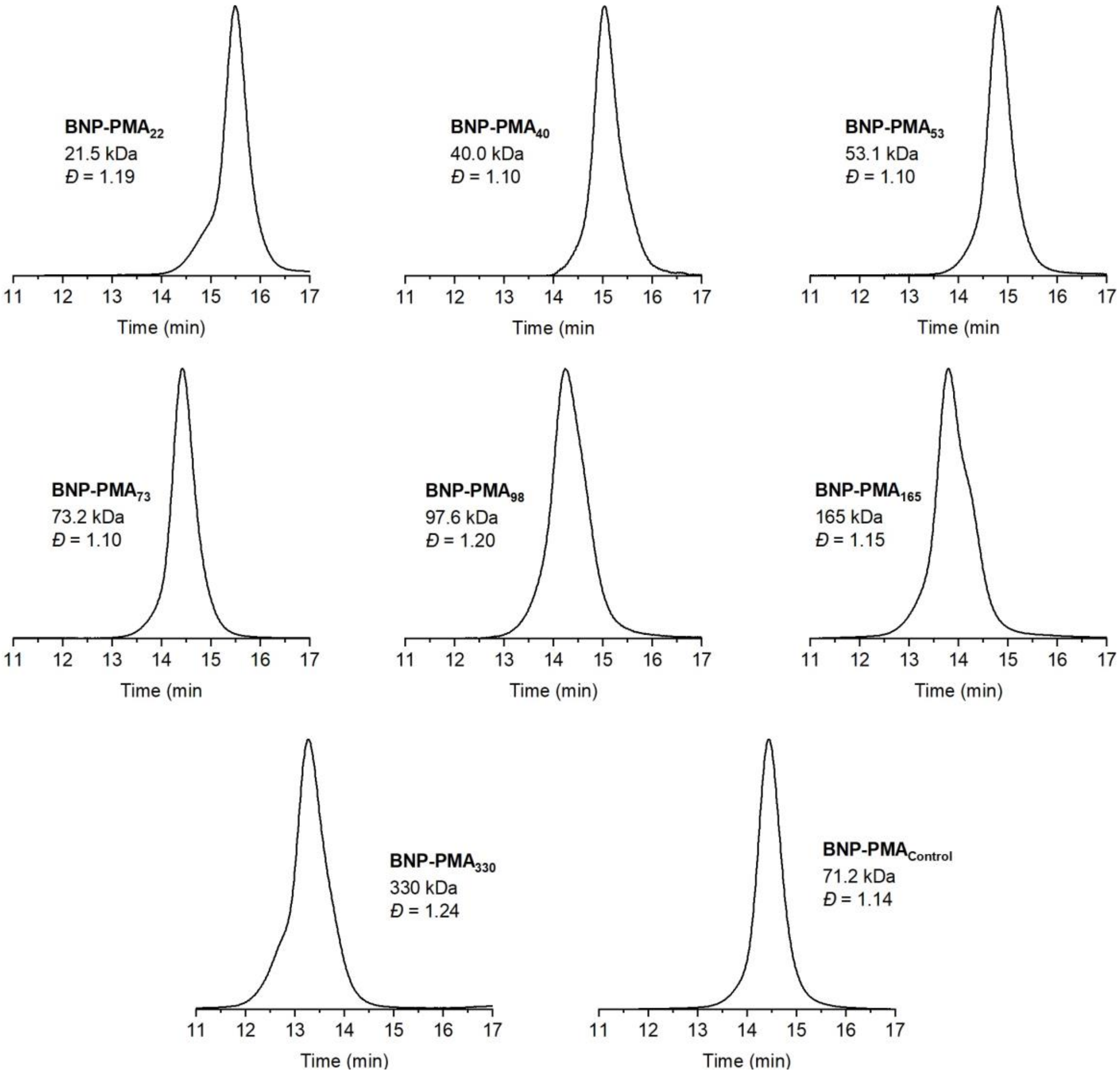

Figure 4.5. GPC traces (refractive index response), M_n, and dispersity for each polymer studied.

III. DFT Calculations (CoGEF)

CoGEF calculations were performed using Spartan ′18 Parallel Suite according to previously reported methods.[19,34,35] Ground state energies were calculated using DFT at the B3LYP/6-31G* level of theory. For both possible diastereomers, the equilibrium conformations of the unconstrained molecules were initially calculated followed by optimization of the equilibrium geometries. Starting from the equilibrium geometry of the unconstrained molecules (energy = 0 kJ/mol), the distance

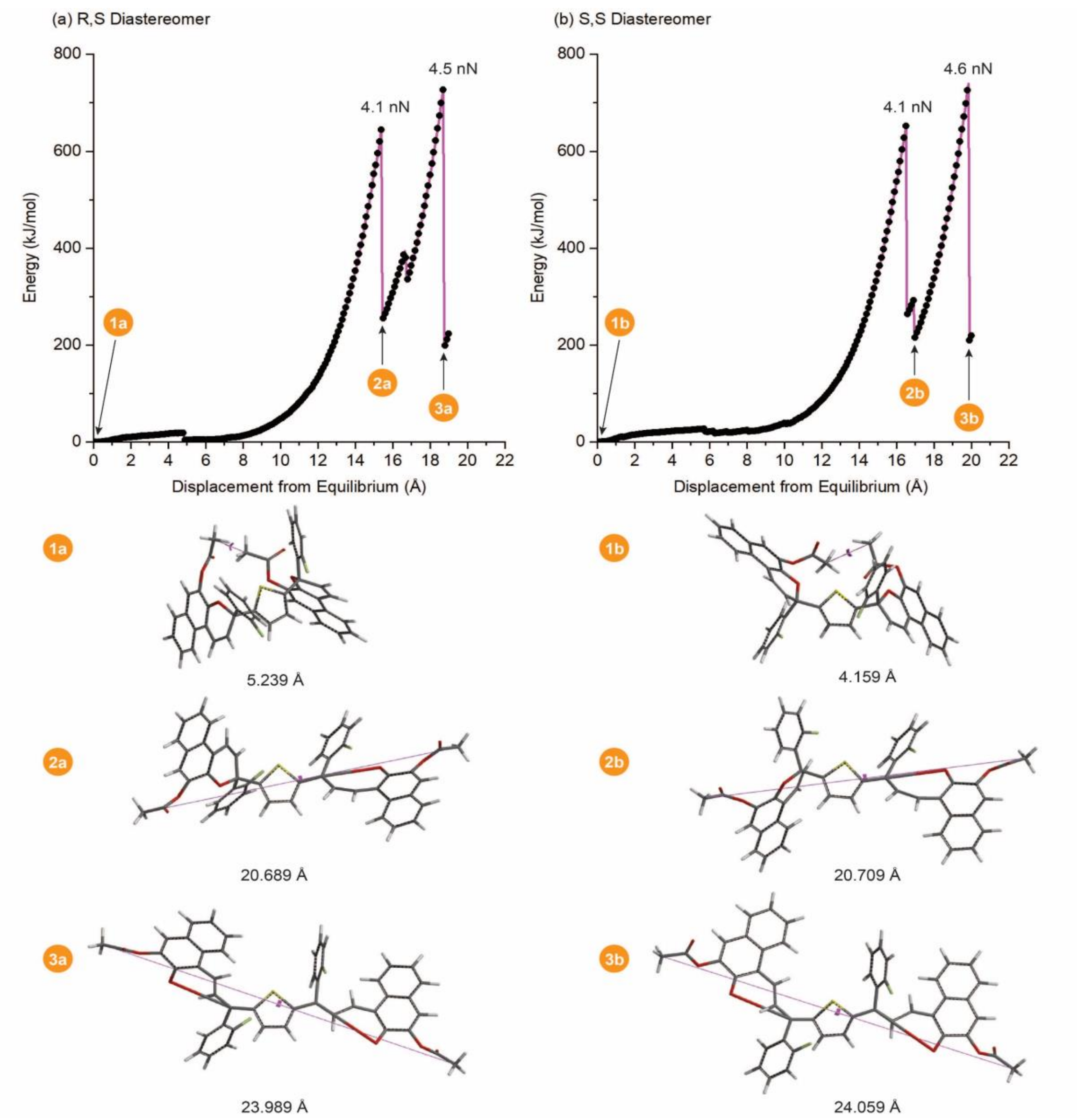

Figure 4.6. DFT calculations using the constrained geometries simulate external force (CoGEF) method at the B3LYP/6-31G* level of theory for the (a) R,S-diastereomer and (b) S,S-diastereomer of the bis-naphthopyran mechanophore. The corresponding computed structures of the truncated molecules at various points of elongation are shown along with the associated constraint distance between the terminal methyl groups.

between the terminal methyl groups of the truncated structures was increased in increments of 0.05 Å and the energy was minimized at each step (Figure 4.6). The maximum force associated with the electrocylic ring-opening reactions was calculated from the slope of the curve immediately prior to C–O bond cleavage. For the S,S-diastereomer, the first ring-opening event is predicted to occur at a maximum force of 4.1 nN and the second occurs at 4.6 nN. For the R,S-diastereomer, the respective forces are 4.1 nN and 4.5 nN for the first and second ring-opening reactions. The relatively small energetic relaxations observed between the two ring-opening transformations correspond to conformational rotations around a single bond in the merocyanine structures.

IV. Details for Photoirradiation and Sonication Experiments

In order to continuously monitor reaction progress by UV-vis absorption spectroscopy, an experimental setup based on previously reported design[38] was assembled using a peristaltic pump to transport solution from the reaction vessel through a quartz flow cell in a UV-vis spectrometer and return the solution to the reaction vessel. The flow rate through the system was maintained at 6 mL/min, corresponding to a setting of 50 RPM on the peristaltic pump. The UV-vis spectrometer was programmed to acquire either full spectra or absorbance at predefined wavelengths at regular time intervals. Absorbance measurements at wavelengths of 460 nm, 620 nm, and 800 nm were acquired every ten seconds during continuous photoirradiation or sonication of polymer solutions. The absorbance values measured at 800 nm were subtracted from the absorbance values monitored at 460 nm and 620 nm at each time point to account for drift during the experiments. Absorbance data was baseline corrected by subtracting the initial absorbance value (t = 0) at each wavelength; however, this step was omitted for determining the concentrations of merocyanine species.

General procedure for photoirradiation experiments. An oven-dried sonication vessel was fitted with a Teflon screw cap sealed with an O-ring and allowed to cool under a stream of dry argon. The vessel was charged with a solution of the polymer in THF (2.0 mg/mL, 20.0 mL). An additional 6.2 mL of polymer solution was pumped into the dead space of the circulatory setup. Teflon inlet and outlet tubes were inserted into the solution in the reaction vessel through a plastic cap sealed with parafilm, and the pump was engaged to start the flow of solution through the system. The sonication vessel was submerged in an ethanol bath maintained at −45 ± 2 °C and a UV light source (λ = 311 nm) was placed 2 inches from the vessel. The total volume of the apparatus was 26.2 mL, with 20.0 mL contained in the reaction vessel. At any given time, only 20.0 mL of solution (out of the total 26.2 mL) was inside of the cuvette and exposed to UV irradiation. Therefore, the actual "irradiation time" was treated as 20/26.2 of real "clock" time, consistent with previously reported methods.5 The entire system was protected from outside light for the duration of the experiment.

General procedure for sonication experiments. An oven-dried sonication vessel was placed onto the sonication probe and allowed to cool under a stream of dry argon. The vessel was charged with a solution of the polymer in THF (2.0 mg/mL, 20.0 mL). An additional 6.2 mL of polymer solution was pumped into the dead space of the circulatory setup. Teflon inlet and outlet tubes were inserted into the solution in the sonication vessel through a plastic cap sealed with parafilm, and the pump was engaged to start the flow of solution through the system. The sonication vessel was submerged in an acetone bath maintained at −45 ± 2 °C. The polymer solution was sparged with argon for 30 minutes prior to sonication and for the duration of the sonication experiment. Solutions were sonicated continuously at 20 kHz (8.20 W cm^{-2}). Sonication intensity was calibrated via the literature method.[6] Similar to the photoirradiation experiments described above, "sonication time" was treated as 20/26.2 of real "clock" time to account for the fraction of polymer solution actually exposed to ultrasound during the experiment. The entire system was kept in the dark for the duration of the experiment.

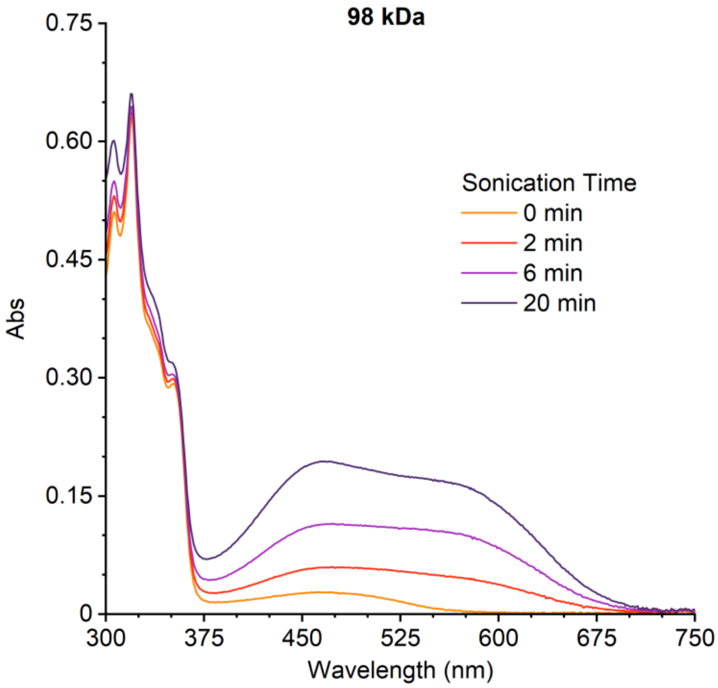

Figure 4.7. Representative absorption spectra in the wavelength range 300–750 nm of **BNP-PMA$_{98}$** subjected to ultrasound-induced mechanochemical activation for varying amounts of time (−45 °C, 2 mg/mL polymer in THF).

Figure 4.8. Photographs of polymer solutions (2 mg/mL in THF) subjected to ultrasound-induced mechanochemical activation. (*left*) **BNP-PMA$_{40}$** after 30 min of sonication, and (*right*) **BNP-PMA$_{330}$** after 9 min of sonication. Immediately after cessation of sonication, the reaction vessel was removed from the cooling bath, sprayed with isopropanol to prevent water condensation, the vessel was illuminated with a fluorescent lamp and immediately photographed. Images were acquired in RAW format to preserve color information.

V. Description of Control Experiments

To confirm that the ring-opening reactions observed for chain-centered BNP molecules exposed to ultrasonication were due to mechanical force,[1] a chain-end functional control polymer (**BNP-PMA$_{\mathbf{Control}}$**) was synthesized and sonicated under identical conditions. As shown in Figure 4.3, no changes in absorption were detected during sonication of the chain-end functional control polymer.

All sonication experiments were performed using polymer solutions with a concentration of 2 mg/mL. A set of control experiments were performed to confirm that changes in the molar concentration of polymers as a result of varying molecular weight at constant mass concentration were not responsible for observed variation in the ratio B_{620}/B_{460} (Figure 4.9). Solutions of **BNP-PMA$_{\mathbf{73}}$** were prepared at 1 mg/mL and 3 mg/mL in THF and sonicated under the same conditions as the 2 mg/mL solution. The average ratios of B_{620}/B_{460} from two separate trials were determined to be 0.44 and 0.43 for concentrations of 1 mg/mL, and 3 mg/mL, respectively, compared to the value of 0.44 measured for the 2 mg/mL solution. These data indicate that variation in the molar concentration of polymers in this range does not significantly affect the distribution of merocyanine products.

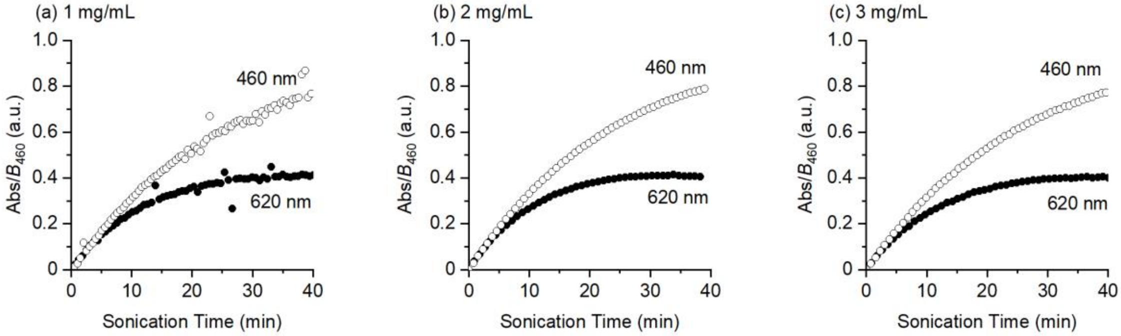

Figure 4.9. Absorbance at 460 nm and 620 nm measured as function of sonication time for **BNP-PMA$_{\mathbf{73}}$** in THF at −45 °C at three different concentrations: (a) 1 mg/mL, (b) 2 mg/mL, (c) 3 mg/mL.

VI. Modeling Force-Dependent Absorption

We constructed a theoretical model to describe the force-color relationship observed for the BNP mechanophore. We use the ratio of the steady-state absorbance at 620 nm (B_{620}) to the steady-state absorbance at 460 nm (B_{460}) as a proxy for the overall distribution of the two distinct merocyanine products resulting from mechanochemical reaction. We first establish that this ratio, B_{620}/B_{460}, scales with the relative concentrations of BNP$_{\text{O-O}}$ and BNP$_{\text{O-C}}$, which are calculated from the experimentally determined absorbance values at 460 nm and 620 nm using the Beer-Lambert relationship and extinction coefficients estimated from similar isolated merocyanine molecules. Based on the reported spectra for isolated merocyanines derived from analogous thiophene-linked[8] and bithiophene-linked[31] bis-naphthopyrans, we estimate the following extinction coefficients, ε, for BNP$_{\text{O-C}}$ and BNP$_{\text{O-O}}$:

Table 4.2 Estimated extinction coefficients for BNP$_{\text{O-C}}$ and BNP$_{\text{O-O}}$

	Wavelength (nm)	**ε (L mol^{-1} cm^{-1})**
BNP$_{\text{O-C}}$	460	26,000
BNP$_{\text{O-O}}$	460	30,000
	620	23,000

The mathematical relationship between absorbance at 460 nm and 620 nm and the concentrations of BNP$_{\text{O-C}}$ and BNP$_{\text{O-O}}$ is given by eq. 4.4:

$$\frac{Abs_{t,460}}{Abs_{t,620}} = \frac{\varepsilon_{\mathrm{O-C},460}[\mathrm{BNP}_{\mathrm{O-C}}]_t + \varepsilon_{\mathrm{O-O},460}[\mathrm{BNP}_{\mathrm{O-O}}]_t}{\varepsilon_{\mathrm{O-O},620}[\mathrm{BNP}_{\mathrm{O-O}}]_t} \tag{4.4}$$

where $Abs_{t,460}$ is the absorbance value measured at 460 nm and time *t*, $\varepsilon_{\mathrm{O-C},460}$ is the extinction coefficient of BNP$_{\text{O-C}}$ at 460 nm, $[\mathrm{BNP}_{\mathrm{O-C}}]_t$ is the concentration of BNP$_{\text{O-C}}$ at time *t*, etc. The expression simplifies to the following linear function in slope-intercept form (eq. 4.5):

$$\frac{Abs_{t,460}}{Abs_{t,620}} = \frac{\varepsilon_{\mathrm{O-C},460}}{\varepsilon_{\mathrm{O-O},620}} \frac{[\mathrm{BNP_{O-C}}]_t}{[\mathrm{BNP_{O-O}}]_t} + R_{\mathrm{O-O}} \tag{4.5}$$

where $R_{\mathrm{O-O}}$ is a constant defined by (eq. 4.6):

$$R_{\mathrm{O-O}} = \frac{\varepsilon_{\mathrm{O-O},460}}{\varepsilon_{\mathrm{O-O},620}} \tag{4.6}$$

We define the relative steady-state concentrations of $\mathrm{BNP_{O\text{-}C}}$ and $\mathrm{BNP_{O\text{-}O}}$ by eq. 4.7 and 4.8:

$$\varphi_{\mathrm{O-O}} = \frac{[\mathrm{BNP_{O-O}}]}{[\mathrm{BNP_{O-C}}] + [\mathrm{BNP_{O-O}}]} \tag{4.7}$$

$$\varphi_{\mathrm{O-O}} + \varphi_{\mathrm{O-C}} = 1 \tag{4.8}$$

Combining equations 4.5, 4.7 and 4.8:gives eq. 4.9:

$$\frac{B_{460}}{B_{620}} = \frac{\varepsilon_{\mathrm{O-C},460}}{\varepsilon_{\mathrm{O-O},620}} \frac{(1-\varphi_{O-O})}{\varphi_{O-O}} + R_{\mathrm{O-O}} \tag{4.9}$$

where B_{460} and B_{620} are the steady-state absorbance values at 460 nm and 620 nm, respectively, determined from fitting the absorbance–time data to an increasing exponential decay function as described in the main text. The ratio of absorbance values at the mechanostationary state, which provides a description of the overall color of the system, is derived in terms of the relative concentration of $\mathrm{BNP_{O\text{-}O}}$. Furthermore, as the concentration of $\mathrm{BNP_{O\text{-}O}}$ becomes large (relative to $\mathrm{BNP_{O\text{-}C}}$), the absorbance ratio B_{460}/B_{620} approaches a constant value, $R_{\mathrm{O\text{-}O}}$.

We next derive a relationship to approximate the dependence of the relative concentration of $\mathrm{BNP_{O\text{-}O}}$ on the degree of polymerization (DP), or M_n, of the attached polymer chains (DP = M_n/M_0). Mechanochemical reactions are described by first-order kinetics with respect to DP, whereby the rate of mechanochemical activation is directly proportional to DP above a threshold chain length.[34,38] The combined experimental and computational data indicate that the relative concentration of $\mathrm{BNP_{O\text{-}O}}$

increases with longer polymer chains, and hence greater applied force.[37] Thus, the relative concentration of $\mathrm{BNP_{O\text{-}O}}$ at the steady-state can be approximated by eq. 4.10:

$$\varphi_{OO} = A(1 - e^{-c(M_{\mathrm{n}}/M_0)}) \tag{4.10}$$

where the constant c is a fit-determined parameter that modifies the dependence of the changing concentration on DP, and the pre-exponential factor, A, is equal to 100% from eq. 4.8. The value of c was determined to be 9×10^{-4}.

Equations 4.9 and 4.10 are then combined to give eq. 4.11, which expresses the dependence of the ratio B_{460}/B_{620} on DP:

$$\frac{B_{460}}{B_{620}} = \frac{\varepsilon_{\mathrm{O-C},460}}{\varepsilon_{\mathrm{O-O},620}} \frac{\left(e^{-c(\frac{M_n}{M_0})}\right)}{\left(1 - e^{-c(\frac{M_n}{M_0})}\right)} + R_{\mathrm{O-O}} \tag{4.11}$$

Up until this point we have derived the relationships relating the ratio B_{460}/B_{620} because it simplifies the expressions; however, it is more intuitive to discuss the increasing ratio of B_{620}/B_{460} as degree of polymerization increases. We therefore take the reciprocal of eq. 4.11, which provides the relationship between the ratio of the steady-state absorption values and DP, or M_{n}, of the polymer according to eq. 4.12:

$$\frac{B_{620}}{B_{460}} = \left(\frac{\varepsilon_{\mathrm{O-C},460}}{\varepsilon_{\mathrm{O-O},620}} \frac{\left(e^{-c(\frac{M_n}{M_0})}\right)}{\left(1 - e^{-c(\frac{M_n}{M_0})}\right)} + R_{\mathrm{O-O}} \right)^{-1} \tag{4.12}$$

The ratio B_{620}/B_{460} is predicted to increase asymptotically toward a value of $\frac{1}{R_{\mathrm{O-O}}}$, or $\frac{\varepsilon_{\mathrm{O-O},620}}{\varepsilon_{\mathrm{O-O},460}}$, as DP becomes infinitely large.

VII. Kinetic Modeling

Scheme 4.5. Proposed mechanism for the dynamic equilibrium achieved upon mechanochemical activation of the bis-naphthopyran mechanophore and associated rate

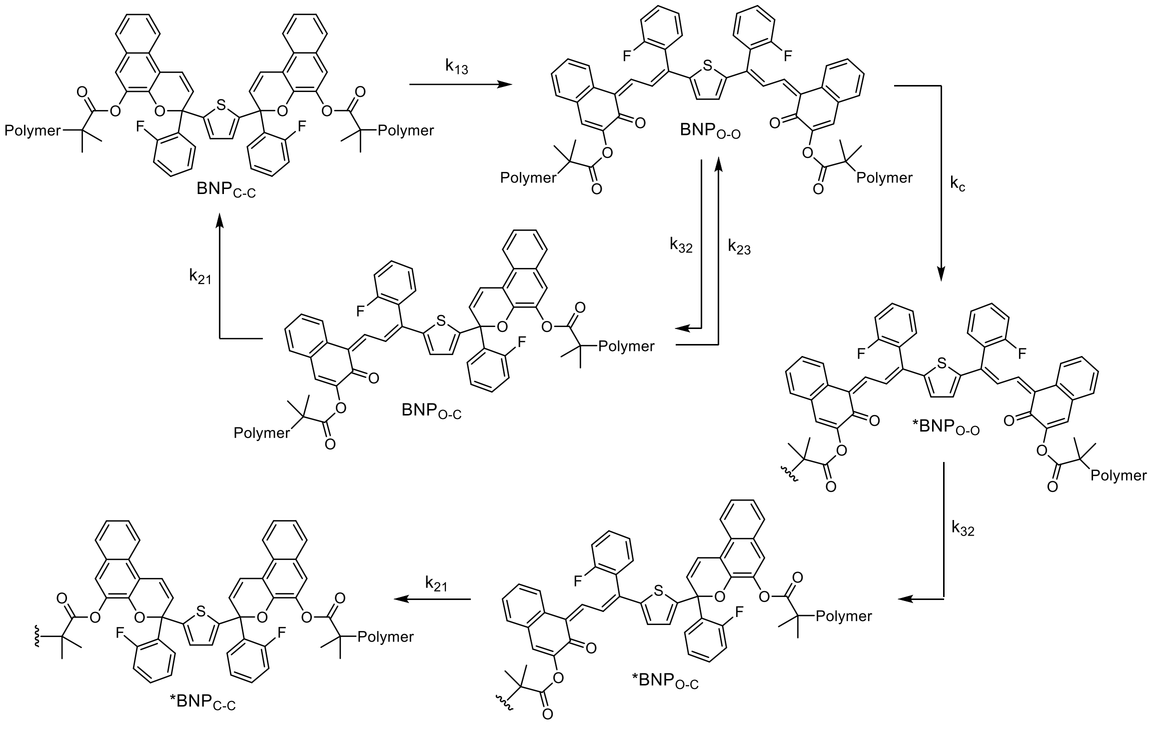

The mechanochemical reactivity of the bis-naphthopyran mechanophore in our system is consistent with the mechanism shown in Scheme 4.5. As detailed below, numerical modeling of the rate expressions describing this system of reactions supports this proposed mechanism in which BNP_{C-C} is effectively converted directly to BNP_{O-O}, in contrast to the photochemical reaction. Biased by external force, BNP_{C-C} exists in equilibrium with BNP_{O-C} and BNP_{O-O} and the distribution of the two merocyanine species is dictated by the balance between the forward rate of mechanochemical activation and thermal electrocyclization. The kinetic model suggests that BNP_{O-C} is produced predominately, if not exclusively, from thermal electrocyclization of BNP_{O-O}. The data and the kinetic model also indicate that BNP_{O-C} can be activated mechanochemically to regenerate BNP_{O-O}. Polymer chain scission occurs for most polymers with extended ultrasonication, leading to irreversible loss of

$\mathrm{BNP_{O\text{-}O}}$. The products resulting from chain cleavage (described by rate constant k_c) are denoted with an asterisk (e.g., $^*\mathrm{BNP_{O\text{-}O}}$). Polymers that undergo chain scission cannot be reactivated by ultrasonication, leading to an irreversible degradation pathway that results in loss of merocyanine via thermal electrocyclization. The corresponding rate expressions for the system of reactions shown in Scheme 4.5 are outlined below in equations 4.13–4.18:

$$\frac{d[\mathrm{BNP_{C\text{-}C}}]_t}{dt} = -k_{13}[\mathrm{BNP_{C\text{-}C}}]_t + k_{21}[\mathrm{BNP_{O\text{-}C}}]_t \tag{4.13}$$

$$\frac{d[\mathrm{BNP_{O\text{-}C}}]_t}{dt} = k_{32}[\mathrm{BNP_{O\text{-}O}}]_t - k_{23}[\mathrm{BNP_{O\text{-}C}}]_t - k_{21}[\mathrm{BNP_{O\text{-}C}}]_t \tag{4.14}$$

$$\frac{d[\mathrm{BNP_{O\text{-}O}}]_t}{dt} = k_{13}[\mathrm{BNP_{C\text{-}C}}]_t + k_{23}[\mathrm{BNP_{O\text{-}C}}]_t - k_{32}[\mathrm{BNP_{O\text{-}O}}]_t - k_c[\mathrm{BNP_{O\text{-}O}}]_t \tag{4.15}$$

$$\frac{d[^*\mathrm{BNP_{O\text{-}O}}]_t}{dt} = k_c[\mathrm{BNP_{O\text{-}O}}]_t - k_{32}[^*\mathrm{BNP_{O\text{-}O}}]_t \tag{4.16}$$

$$\frac{d[^*\mathrm{BNP_{O\text{-}C}}]_t}{dt} = k_{32}[^*\mathrm{BNP_{O\text{-}O}}]_t - k_{21}[^*\mathrm{BNP_{O\text{-}C}}]_t \tag{4.17}$$

$$\frac{d[^*\mathrm{BNP_{C\text{-}C}}]_t}{dt} = k_{21}[^*\mathrm{BNP_{O\text{-}C}}]_t \tag{4.18}$$

The integrated rate law from the system of differential rate equations was solved numerically using the *ParametricNDSolve* function in Wolfram Mathematica 12[41] following the procedure by Collum.[42] The *ParametricNDSolve* function was chosen to allow rate constants to be free parameters. The results provided from the numerical solution of the integrated rate law allow for direct comparison of the expected changes in the concentration of merocyanine species to experimental data. In order to model time-dependent changes in absorbance, the relationships shown in equations 4.19 and 4.20 were employed to convert concentrations to absorbance values using the extinction coefficients presented previously in section VI.

$$Abs_{460} = \varepsilon_{\mathrm{O-C,460}}[\mathrm{BNP_{O-C}}]_t + \varepsilon_{\mathrm{O-C,460}}[{}^*\mathrm{BNP_{O-C}}]_t + \varepsilon_{\mathrm{O-O,460}}[\mathrm{BNP_{O-O}}]_t + \varepsilon_{\mathrm{O-O,460}}[{}^*\mathrm{BNP_{O-O}}]_t \quad (4.19)$$

$$Abs_{620} = \varepsilon_{\mathrm{O-O,620}}[\mathrm{BNP_{O-O}}]_t + \varepsilon_{\mathrm{O-O,620}}[{}^*\mathrm{BNP_{O-O}}]_t \quad (4.20)$$

A snapshot of the code used to generate plots of absorbance as a function of time from the kinetic model is shown below in Figure 4.10. All of the estimated rate constants and parameters used to model time-dependent concentration and absorption are summarized in Table 4.3 and discussed individually in detail below.

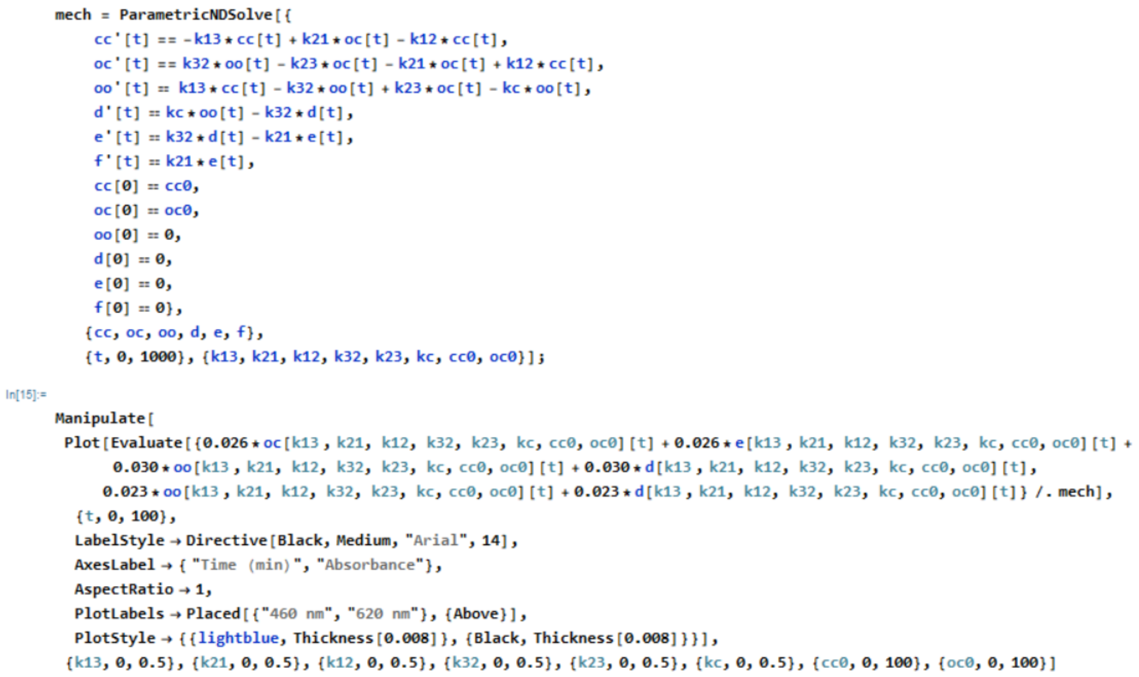

```
mech = ParametricNDSolve[{
    cc'[t] == -k13⋆cc[t] + k21⋆oc[t] - k12⋆cc[t],
    oc'[t] == k32⋆oo[t] - k23⋆oc[t] - k21⋆oc[t] + k12⋆cc[t],
    oo'[t] == k13⋆cc[t] - k32⋆oo[t] + k23⋆oc[t] - kc⋆oo[t],
    d'[t] == kc⋆oo[t] - k32⋆d[t],
    e'[t] == k32⋆d[t] - k21⋆e[t],
    f'[t] == k21⋆e[t],
    cc[0] == cc0,
    oc[0] == oc0,
    oo[0] == 0,
    d[0] == 0,
    e[0] == 0,
    f[0] == 0},
   {cc, oc, oo, d, e, f},
   {t, 0, 1000}, {k13, k21, k12, k32, k23, kc, cc0, oc0}];

In[15]:=
Manipulate[
 Plot[Evaluate[{0.026⋆oc[k13 , k21, k12, k32, k23, kc, cc0, oc0][t] + 0.026⋆e[k13 , k21, k12, k32, k23, kc, cc0, oc0][t] +
      0.030⋆oo[k13 , k21, k12, k32, k23, kc, cc0, oc0][t] + 0.030⋆d[k13 , k21, k12, k32, k23, kc, cc0, oc0][t],
     0.023⋆oo[k13 , k21, k12, k32, k23, kc, cc0, oc0][t] + 0.023⋆d[k13 , k21, k12, k32, k23, kc, cc0, oc0][t]} /. mech],
  {t, 0, 100},
  LabelStyle → Directive[Black, Medium, "Arial", 14],
  AxesLabel → { "Time (min)", "Absorbance"},
  AspectRatio → 1,
  PlotLabels → Placed[{"460 nm", "620 nm"}, {Above}],
  PlotStyle → {{lightblue, Thickness[0.008]}, {Black, Thickness[0.008]}}],
 {k13, 0, 0.5}, {k21, 0, 0.5}, {k12, 0, 0.5}, {k32, 0, 0.5}, {k23, 0, 0.5}, {kc, 0, 0.5}, {cc0, 0, 100}, {oc0, 0, 100}]
```

Figure 4.10. Code used to plot time-dependent absorbance from the kinetic model in Wolfram Mathematica 12.[11,12]

Table 4.3. Summary of parameters used to model time-dependent absorbance and concentration for all polymers.

	k_{13} (min^{-1})	k_{23} (min^{-1})	k_{32} (min^{-1})	k_{21} (min^{-1})	k_c (min^{-1})	Ω
BNP-PMA$_{22}$	0.003	0.003	0.03	0.01	0	0.11
BNP-PMA$_{40}$	0.007	0.007	0.03	0.01	0.0022	0.28
BNP-PMA$_{53}$	0.017	0.017	0.03	0.01	0.0093	0.20
BNP-PMA$_{73}$	0.03	0.03	0.03	0.01	0.020	0.33
BNP-PMA$_{98}$	0.045	0.045	0.03	0.01	0.034	0.39
BNP-PMA$_{165}$	0.15	0.15	0.03	0.01	0.070	0.47
BNP-PMA$_{330}$	0.30	0.30	0.03	0.01	0.16	0.68

	Absorbance Plots	**Concentration Plots**		
	[BNP$_{\text{C-C}}$]$_{t=0,\text{abs}}$ (μM)	[BNP$_{\text{C-C}}$]$_{t=0}$ (μM)	[BNP$_{\text{O-C}}$]$_{t=0}$ (μM)	[BNP$_{\text{O-C}}$]$_{t=0}$ (μM) (*residual*)
BNP-PMA$_{22}$	10	9.71	0.29	2.39
BNP-PMA$_{40}$	14	13.62	0.38	0.97
BNP-PMA$_{53}$	7.5	7.30	0.20	0.81
BNP-PMA$_{73}$	9.0	8.70	0.30	0.62
BNP-PMA$_{98}$	8.0	7.76	0.24	0.38
BNP-PMA$_{165}$	5.7	5.47	0.23	0.26
BNP-PMA$_{330}$	4.1	3.94	0.16	0.08

Determination of parameters for the kinetic model

Scheme 4.6. Thermal electrocyclization reactions of $\mathrm{BNP_{O\text{-}O}}$ and $\mathrm{BNP_{O\text{-}C}}$.

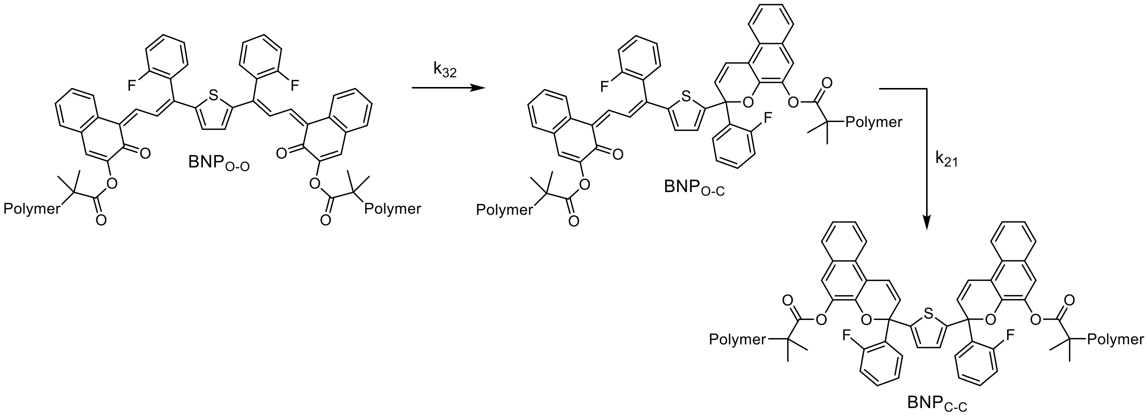

Rates of thermal electrocyclization. Values of k_{32} and k_{21} were determined from thermal fading experiments performed on $\mathrm{BNP\text{-}PMA_{330}}$ following either mechanochemical activation or photochemical activation. Values of k_{32} and k_{21} were determined from each experiment and averaged to provide the values of the rate constants used in the model. Following photochemical or mechanochemical activation as described above, the light source and sonication were turned off (t = 0) and absorbance data was collected. No other conditions were changed from those of the activation experiments. The rate equations describing the thermal ring-closing processes shown in Scheme 4.6 are given by equations 4.21 and 4.22 for the concentration of merocyanine species:

$$\frac{d[\mathrm{BNP_{O\text{-}O}}]_t}{dt} = -k_{32}[\mathrm{BNP_{O\text{-}O}}]_t \tag{4.21}$$

$$\frac{d[\mathrm{BNP_{O\text{-}C}}]_t}{dt} = k_{32}[\mathrm{BNP_{O\text{-}O}}]_t - k_{21}[\mathrm{BNP_{O\text{-}C}}]_t \tag{4.22}$$

The *DSolve* function in Mathematica was used to analytically solve the integrated rate laws to model the time-dependent concentration of merocyanine species, which are provided as equations 4.23 and 4.24:

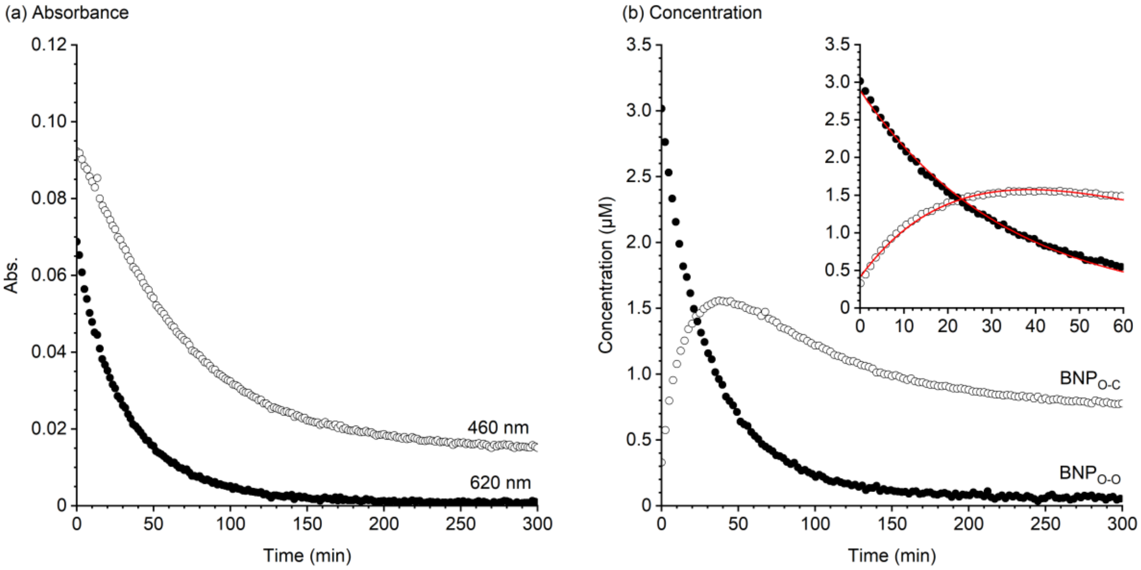

Figure 4.11. Determination of k_{32} and k_{21} from (a) absorbance and (b) concentration data acquired for thermal fading of BNP$_{O-C}$ and BNP$_{O-O}$ after mechanical activation of **BNP-PMA$_{330}$** and cessation of sonication. Time-dependent concentration curves were fitted to equations S20 and S21 (inset) to calculate values of k_{32} and k_{21}.

$$[\mathrm{BNP}_{\mathrm{O-O}}]_t = [\mathrm{BNP}_{\mathrm{O-O}}]_{t=0} * e^{-k_{32}t} \tag{4.23}$$

$$[\mathrm{BNP}_{\mathrm{O-C}}]_t = \frac{[\mathrm{BNP}_{\mathrm{O-C}}]_{t=0} * k_{21}e^{-k_{21}t} - ([\mathrm{BNP}_{\mathrm{O-C}}]_{t=0} + [\mathrm{BNP}_{\mathrm{O-O}}]_{t=0}) * k_{32}e^{-k_{21}t} + [\mathrm{BNP}_{\mathrm{O-O}}]_{t=0} * k_{32}e^{-k_{32}t}}{k_{21} - k_{32}} \tag{4.24}$$

The absorbance data measured for the thermal electrocyclization of mechanochemically activated **BNP-PMA$_{330}$** are shown in Figure 4.11. The time-dependent absorbance data was converted to concentration of BNP$_{O-C}$ and BNP$_{O-O}$ and the first 60 minutes of data were fitted to equations 4.23 and 4.24 to obtain k_{32} and k_{21}. The same procedure was performed on the photochemically activated sample, and the average values of k_{32} and k_{21} from these experiments were determined to be 0.03 min^{-1} and 0.01 min^{-1}, respectively.

As shown in Figure 4.11b, after sonication is stopped, the concentration of $\mathrm{BNP_{O\text{-}O}}$ decreases as it is converted to $\mathrm{BNP_{O\text{-}C}}$. Consequently, the concentration of $\mathrm{BNP_{O\text{-}C}}$ increases initially and then subsequently decreases as it is converted to $\mathrm{BNP_{C\text{-}C}}$. However, in contrast to $\mathrm{BNP_{O\text{-}O}}$ which is ultimately completely converted to $\mathrm{BNP_{O\text{-}C}}$, the concentration of $\mathrm{BNP_{O\text{-}C}}$ decreases more slowly at later times. This observation is consistent with previous studies of similar merocyanine dyes that identify different rates of thermal ring-closure for different merocyanine isomers, with the *transoid-cis* isomer of the merocyanine species fading faster than the trans-trans isomer.[30,31] The generation of some slow fading *transoid-trans* $\mathrm{BNP_{O\text{-}C}}$ species would account for the small fraction of the absorbance at 460 nm that is persistent on the time scale of the reaction. The *transoid-cis* and *transoid-trans* isomers of similar $\mathrm{BNP_{O\text{-}C}}$ species have nearly identical absorption spectra, making it difficult to differentiate the two compounds spectroscopically. Because we do not account for isomerization in the kinetic model, the measured value of k_{21} that we employ in the model only captures the fast-fading component of $\mathrm{BNP_{O\text{-}C}}$ and the slow fading fraction is neglected. Despite this simplification, the kinetic model aligns well with the experimental data and reflects the time-dependent changes in absorbance and merocyanine concentration.

Determination of rates of ring-opening. After defining k_{32} and k_{21} in the model, the values of k_{13} and k_{23} for each polymer were determined empirically by adjusting the parameters, along with $[\mathrm{BNP_{C\text{-}C}}]_{t=0,\mathrm{abs}}$, until the predicted values of B_{620} and B_{460} were consistent with average values determined experimentally. For the purposes of the model, we assume that k_{13} and k_{23} are equal. Figure 4.2 demonstrates that a small amount of $\mathrm{BNP_{O\text{-}C}}$ present at the start of the reaction is immediately lost, indicating that $\mathrm{BNP_{O\text{-}C}}$ is converted mechanochemically to $\mathrm{BNP_{O\text{-}O}}$. The rate of ring-opening is dependent upon the force applied to the mechanophore, and thus the length of the polymer chains attached to the mechanophore. Therefore, we assume that upon thermal electrocyclization of $BNP_{O\text{-}O}$ to $BNP_{O\text{-}C}$, the rate of reactivation and associated rate constant k_{23}, will be approximately equal to the original forward rate of ring-opening described by k_{13}, since the length of the polymer chains attached to the mechanophore is the same. Not all polymer chains in solution react under ultrasonication,[43] so the boundary condition $[BNP_{C\text{-}C}]_{t=0,abs}$ reflects the concentration of polymer that is activated, rather than the total concentration of polymer in solution. All other initial concentrations were set to zero to model time-dependent changes in absorption, consistent with our treatment of the experimental absorbance data.

Determination of chain scission rates. The rate of polymer chain scission induced by ultrasonication is typically determined from changes in molecular weight averages measured by GPC.[35] However, rates determined by this method are not comparable to rates determined spectroscopically.[43] Accordingly, the rate constant for polymer chain cleavage, k_c, was first estimated for $BNP\text{-}PMA_{165}$ by adjusting the parameter so that the model reflected the experimental data at extended sonication times (see Figure 4.21). This value of k_c was then used to determine a scaling factor so that previously reported relationships for the molecular-weight-dependent rate of polymer chain scission measured by GPC could be converted to appropriate values for the kinetic model. We derived eq. 4.25 based on reported chain cleavage rates of PMA by Kryger et al.[35] Using this relationship, we then calculated the estimated rate constant for chain cleavage based on GPC measurements, $k_{c,GPC}$, expected for each polymer in our study (Table 4.4). We note that these rate constants have units of min^{-1} kDa^{-1} and must be multiplied by the molecular weight of the polymer repeat unit, M_o (for PMA, $M_o = 0.0861$ kg/mol). A scaling factor of 8150 was then determined by dividing the value of k_c determined for $BNP\text{-}PMA_{165}$ by the corresponding calculated value of $k_{c,GPC}$. This scaling factor was used to convert calculated values of $k_{c,GPC}$ (with units of min^{-1}) for each polymer of varying molecular weight to appropriate values of k_c to be used in the kinetic model.

$$k_{c,GPC} = 7.73 \text{ x } 10^{-7} * M_n - 2.78 \text{ x } 10^{-5} \qquad (4.25)$$

Table 4.4. Molecular-weight-dependent rate constants for polymer chain scission.

Molecular Weight (M_n, kDa)	$\boldsymbol{k}_{\mathbf{c,GPC}}$ calculated from eq. 4.25 (min^{-1} kDa^{-1})	$\boldsymbol{M_o}$*$\boldsymbol{k}_{\mathbf{c,GPC}}$ (min^{-1})	$\boldsymbol{k}_{\mathbf{c}}$ (8150*M_o*$k_{\text{c,GPC}}$) (min^{-1})
22	0	0	0
40	3.1×10^{-6}	2.7×10^{-7}	0.0022
53	1.3×10^{-5}	1.1×10^{-6}	0.0093
73	2.9×10^{-5}	2.5×10^{-6}	0.020
98	4.8×10^{-5}	4.1×10^{-6}	0.034
165	1.0×10^{-4}	8.6×10^{-6}	0.070
330	2.3×10^{-4}	2.0×10^{-5}	0.16

Initial concentrations in the time-dependent concentration kinetic model. A small amount of $\text{BNP}_{\text{O-C}}$ is present in solution prior to ultrasound-induced mechanochemical activation of each polymer. In order to monitor changes in absorbance resulting from mechanochemical activation of the BNP mechanophore, the absorbance at t=0 was subtracted from the time-dependent absorbance values as described above. However, it is useful to characterize the concentration of merocyanine species at any point in the reaction, and therefore this step was omitted when converting time-dependent absorbance to concentration of $\text{BNP}_{\text{O-C}}$ and $\text{BNP}_{\text{O-O}}$. In order to account for this in the kinetic model, the initial fractional concentration of polymer that is activated during sonication (% activation, Ω) was calculated from the empirically determined values of $[\text{BNP}_{\text{C-C}}]_{t=0,\text{abs}}$ identified from the time-dependent absorbance models relative to the total concentration of polymer in solution according to eq. 4.26:

$$\Omega = \frac{[\text{BNP}_{\text{C-C}}]_{t=0,abs}}{[\text{polymer}]} \tag{4.26}$$

Only a fraction of the polymer chains subjected to sonication reacts. Likewise, only a portion of $\mathrm{BNP_{O\text{-}C}}$ present at the start of ultrasonication is expected to contribute to the dynamic equilibrium. This fractional concentration of active $\mathrm{BNP_{O\text{-}C}}$, $[\mathrm{BNP_{O-C}}]_{t=0}$, is defined according to eq. 4.27 with respect to the concentration of $\mathrm{BNP_{O\text{-}C}}$ determined from the experimental data, $[\mathrm{BNP_{O-C}}]_{t=0,observed}$. The residual $\mathrm{BNP_{O\text{-}C}}$ that is present in the reaction but does not become activated is defined according to eq. 4.28. This quantity was determined for each polymer and added as a constant to the calculated concentration of $\mathrm{BNP_{O\text{-}C}}$ in each time-dependent concentration model. The fractional concentration of active $\mathrm{BNP_{C\text{-}C}}$ at t=0 was finally calculated according to eq. 4.29. The values of all parameters that were used in the kinetic model are presented in Table 4.3.

$$[\mathrm{BNP_{O\text{-}C}}]_{t=0} = \Omega * [\mathrm{BNP_{O\text{-}C}}]_{t=0,observed} \tag{4.27}$$

$$[\mathrm{BNP_{O\text{-}C}}]_{t=0,residual} = (1-\Omega) * [\mathrm{BNP_{O\text{-}C}}]_{t=0,observed} \tag{4.28}$$

$$[\mathrm{BNP_{C\text{-}C}}]_{t=0} = \Omega * [\mathrm{Polymer}] - [\mathrm{BNP_{O\text{-}C}}]_{t=0} \tag{4.29}$$

$\mathrm{BNP_{O\text{-}C}}$ and $^*\mathrm{BNP_{O\text{-}C}}$, as well as $\mathrm{BNP_{O\text{-}O}}$ and $^*\mathrm{BNP_{O\text{-}O}}$, are spectroscopically indistinguishable. Thus, the relationships presented in eq. 4.30 and 4.31 were used to plot the modeled time-dependent concentration of each merocyanine species relative to the total concentration of polymer:

$$\frac{[\mathrm{BNP_{O\text{-}C}}]_{t,apparent}}{[\mathrm{polymer}]} = \frac{[\mathrm{BNP_{O\text{-}C}}]_t + [^*\mathrm{BNP_{O\text{-}C}}]_t}{[\mathrm{polymer}]} \tag{4.30}$$

$$\frac{[\mathrm{BNP_{O\text{-}O}}]_{t,apparent}}{[\mathrm{polymer}]} = \frac{[\mathrm{BNP_{O\text{-}O}}]_t + [^*\mathrm{BNP_{O\text{-}O}}]_t}{[\mathrm{polymer}]} \tag{4.31}$$

Results of kinetic modeling. Experimentally measured time-dependent absorbance at 460 and 620 nm and the corresponding data for the concentration of $BNP_{O\text{-}C}$ and $BNP_{O\text{-}O}$ as a function of sonication time is shown below and compared directly to the results of the kinetic model for each polymer (Figure 4.12–Figure 4.18). The kinetic model closely reproduces the experimental results for the force-dependent mechanochemical activation of bis-naphthopyran supporting the proposed mechanism.

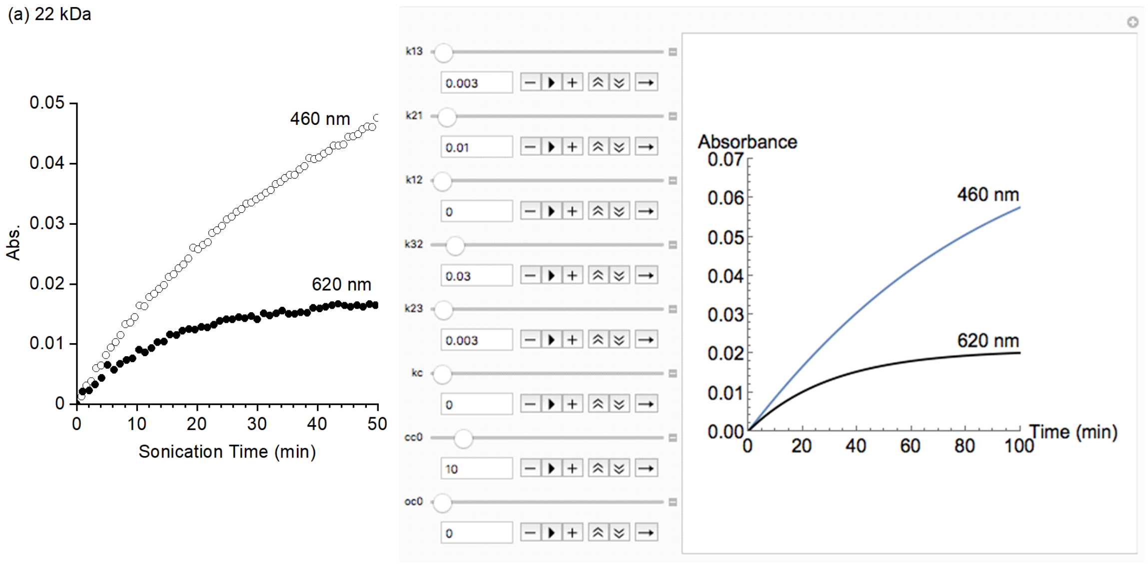

(a) 22 kDa

k13 0.003
k21 0.01
k12 0
k32 0.03
k23 0.003
kc 0
cc0 10
oc0 0

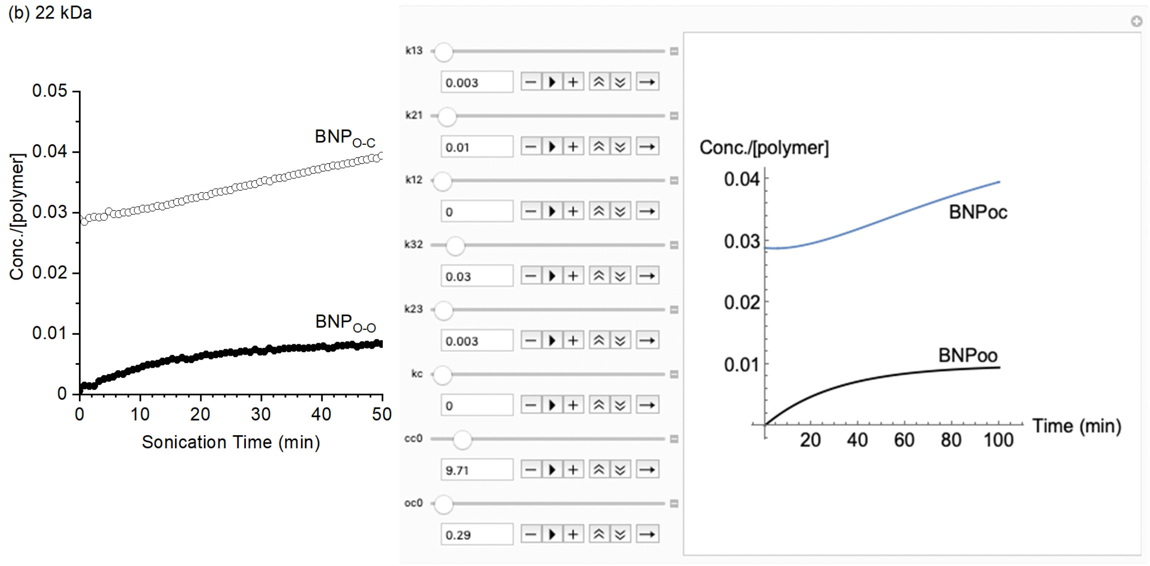

(b) 22 kDa

k13 0.003
k21 0.01
k12 0
k32 0.03
k23 0.003
kc 0
cc0 9.71
oc0 0.29

Figure 4.12. Time-dependent (a) absorbance at 460 and 620 nm, and (b) concentration of BNP$_{O\text{-}C}$ and BNP$_{O\text{-}O}$ for the mechanochemical activation of **BNP-PMA$_{22}$**. Experimental data (*left*) is compared to results from the kinetic model (*right*).

(a) 40 kDa

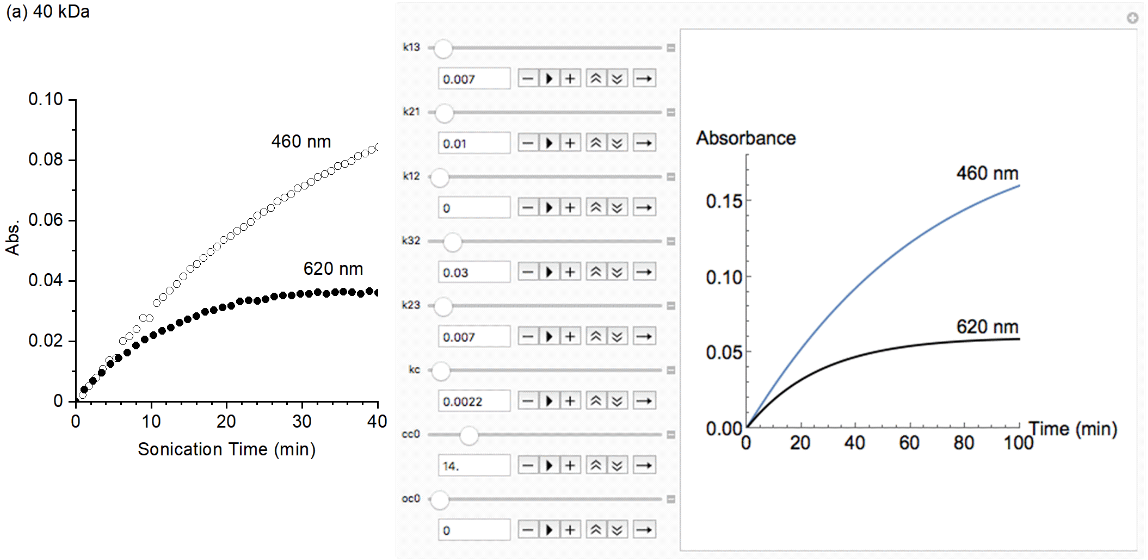

k13 0.007
k21 0.01
k12 0
k32 0.03
k23 0.007
kc 0.0022
cc0 14.
oc0 0

(b) 40 kDa

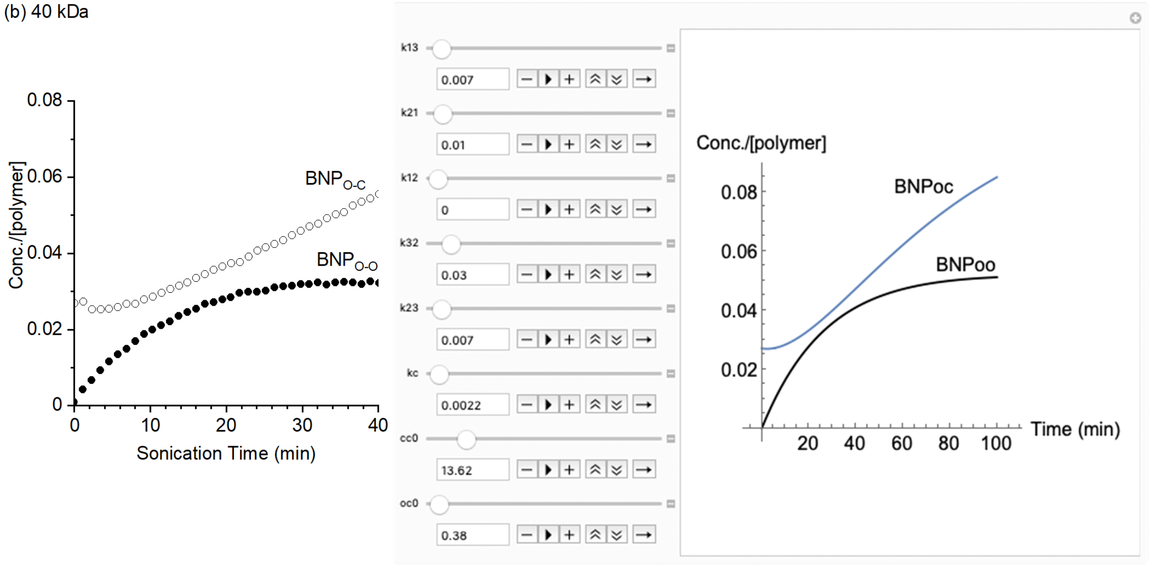

k13 0.007
k21 0.01
k12 0
k32 0.03
k23 0.007
kc 0.0022
cc0 13.62
oc0 0.38

Figure 4.13. Time-dependent (a) absorbance at 460 and 620 nm, and (b) concentration of BNP$_{O\text{-}C}$ and BNP$_{O\text{-}O}$ for the mechanochemical activation of **BNP-PMA$_{40}$**. Experimental data (*left*) is compared to results from the kinetic model (*right*).

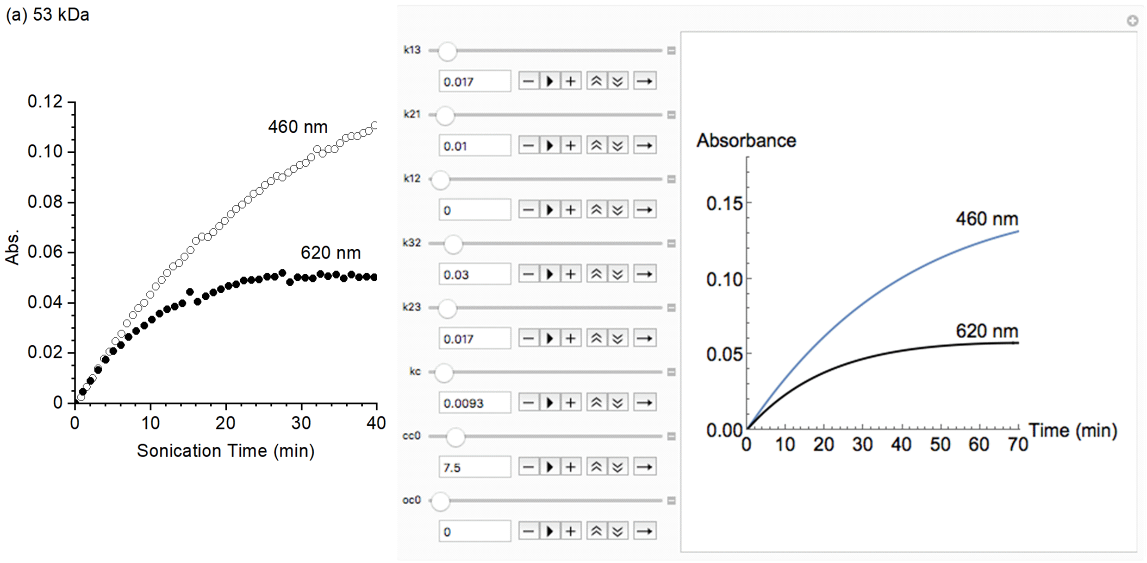

k13 0.017
k21 0.01
k12 0
k32 0.03
k23 0.017
kc 0.0093
cc0 7.5
oc0 0

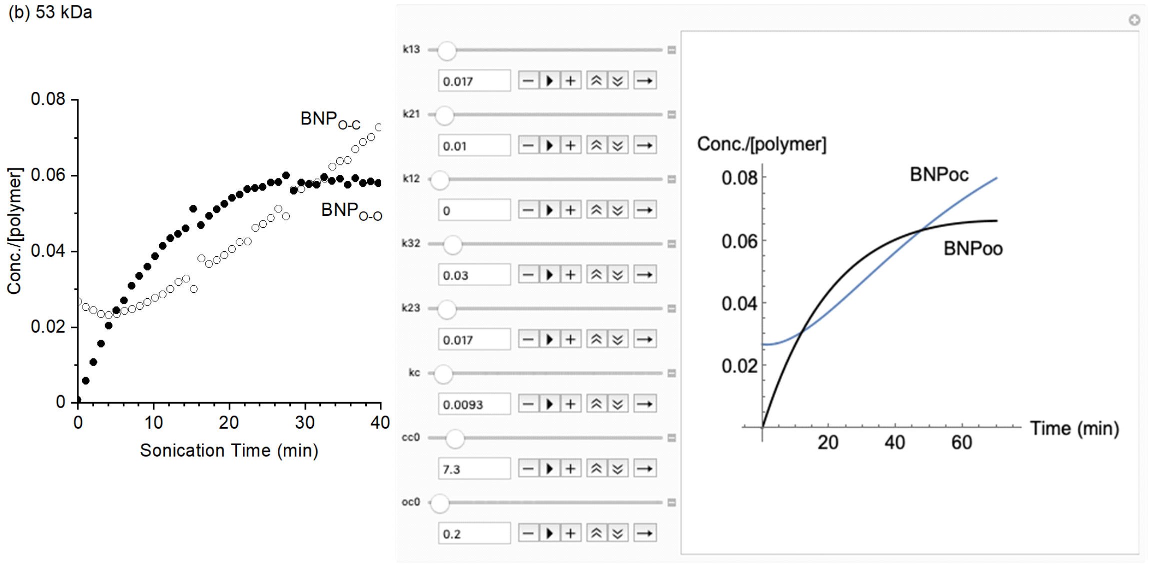

k13 0.017
k21 0.01
k12 0
k32 0.03
k23 0.017
kc 0.0093
cc0 7.3
oc0 0.2

Figure 4.14. Time-dependent (a) absorbance at 460 and 620 nm, and (b) concentration of BNP$_{O\text{-}C}$ and BNP$_{O\text{-}O}$ for the mechanochemical activation of **BNP-PMA$_{53}$**. Experimental data (*left*) is compared to results from the kinetic model (*right*).

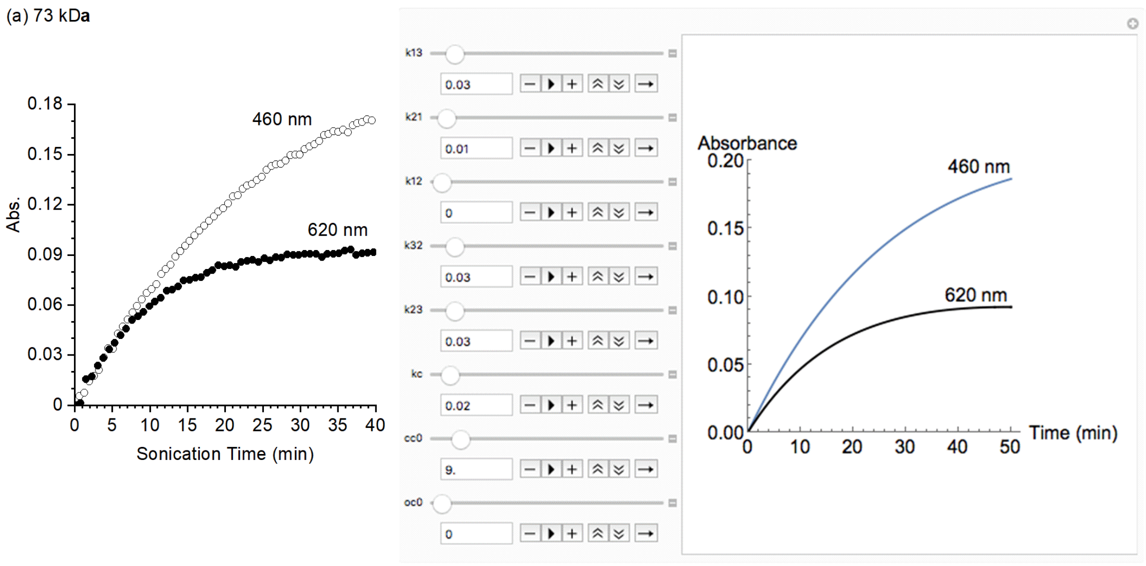

k13 0.03
k21 0.01
k12 0
k32 0.03
k23 0.03
kc 0.02
cc0 9.
oc0 0

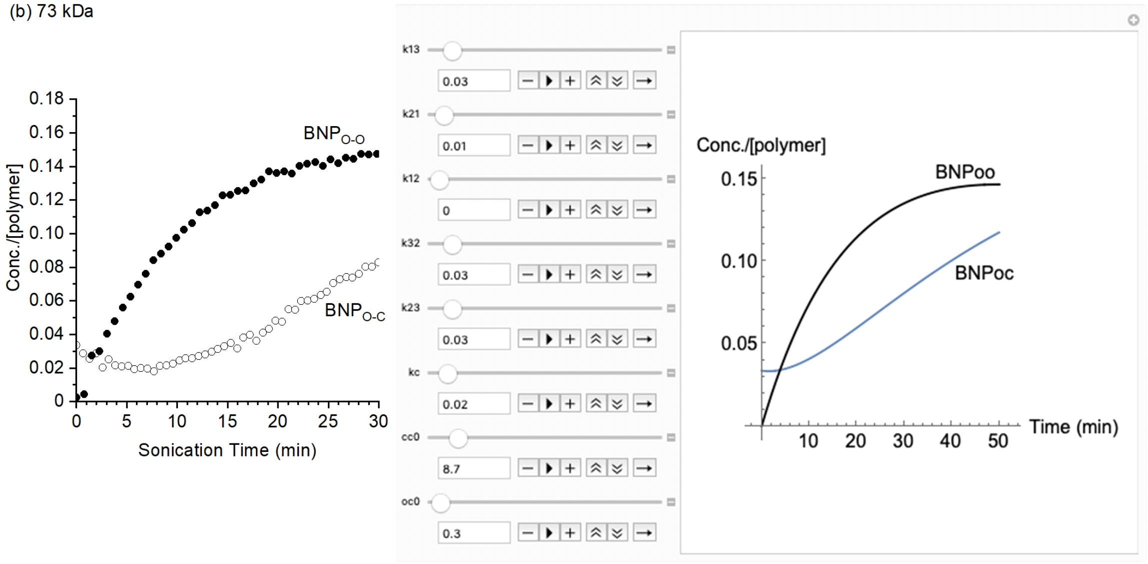

k13 0.03
k21 0.01
k12 0
k32 0.03
k23 0.03
kc 0.02
cc0 8.7
oc0 0.3

Figure 4.15. Time-dependent (a) absorbance at 460 and 620 nm, and (b) concentration of BNP$_{O\text{-}C}$ and BNP$_{O\text{-}O}$ for the mechanochemical activation of **BNP-PMA$_{73}$**. Experimental data (*left*) is compared to results from the kinetic model (*right*).

(a) 98 kDa

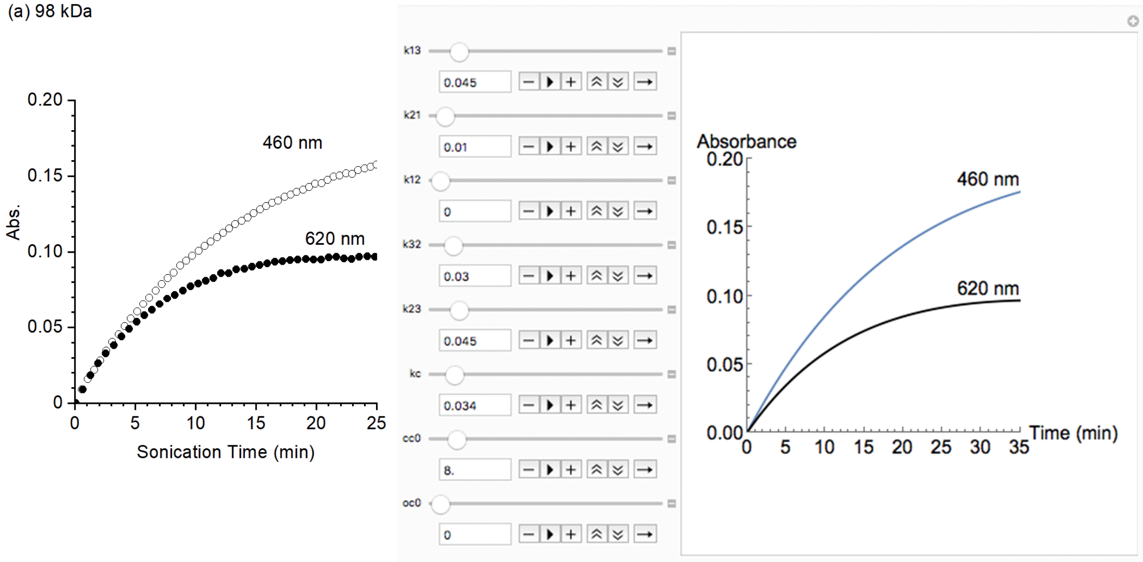

k13 0.045
k21 0.01
k12 0
k32 0.03
k23 0.045
kc 0.034
cc0 8.
oc0 0

(b) 98 kDa

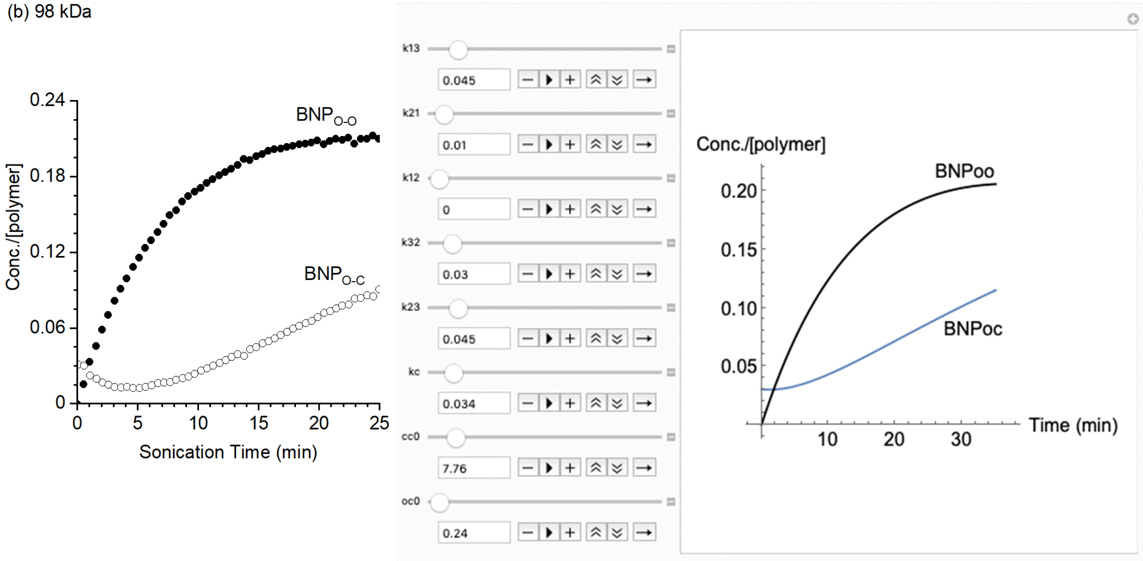

k13 0.045
k21 0.01
k12 0
k32 0.03
k23 0.045
kc 0.034
cc0 7.76
oc0 0.24

Figure 4.16. Time-dependent (a) absorbance at 460 and 620 nm, and (b) concentration of BNP$_{O\text{-}C}$ and BNP$_{O\text{-}O}$ for the mechanochemical activation of **BNP-PMA$_{98}$**. Experimental data (*left*) is compared to results from the kinetic model (*right*).

(a) 165 kDa

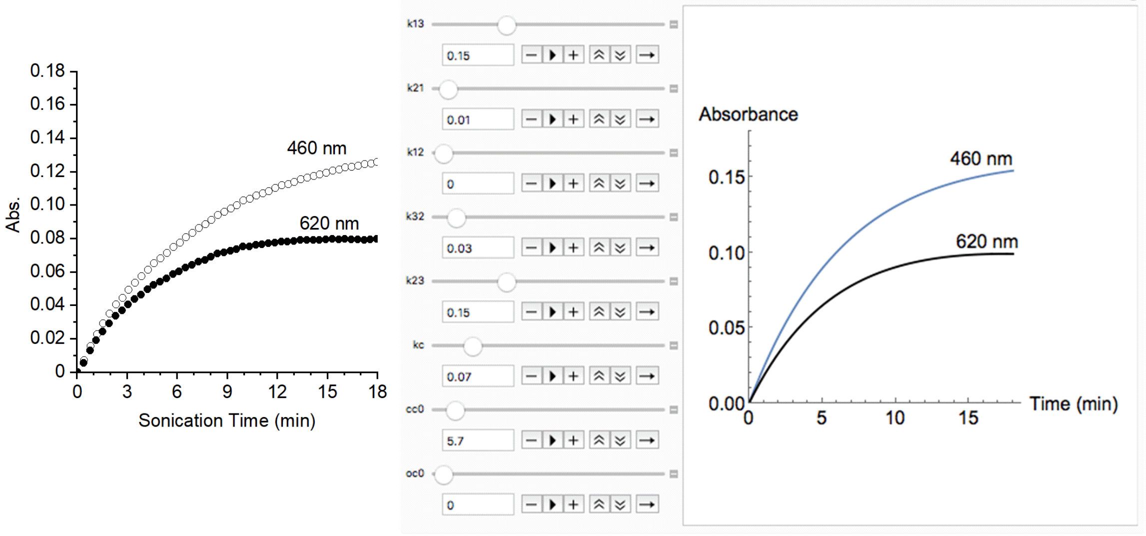

k13 0.15
k21 0.01
k12 0
k32 0.03
k23 0.15
kc 0.07
cc0 5.7
oc0 0

(b) 165 kDa

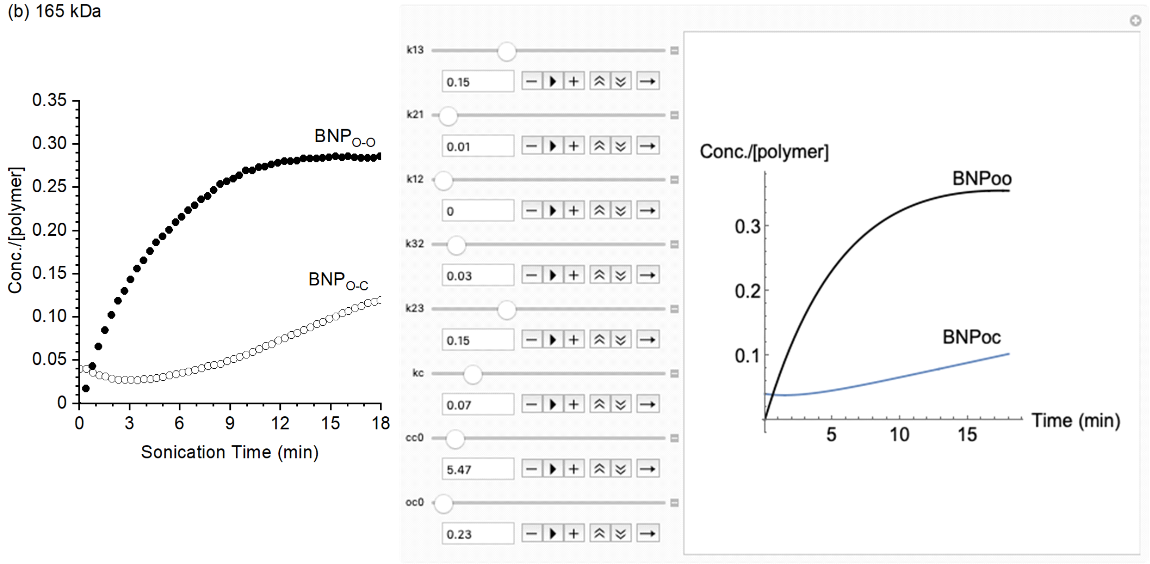

k13 0.15
k21 0.01
k12 0
k32 0.03
k23 0.15
kc 0.07
cc0 5.47
oc0 0.23

Figure 4.17. Time-dependent (a) absorbance at 460 and 620 nm, and (b) concentration of $BNP_{O\text{-}C}$ and $BNP_{O\text{-}O}$ for the mechanochemical activation of **BNP-PMA$_{165}$**. Experimental data (*left*) is compared to results from the kinetic model (*right*).

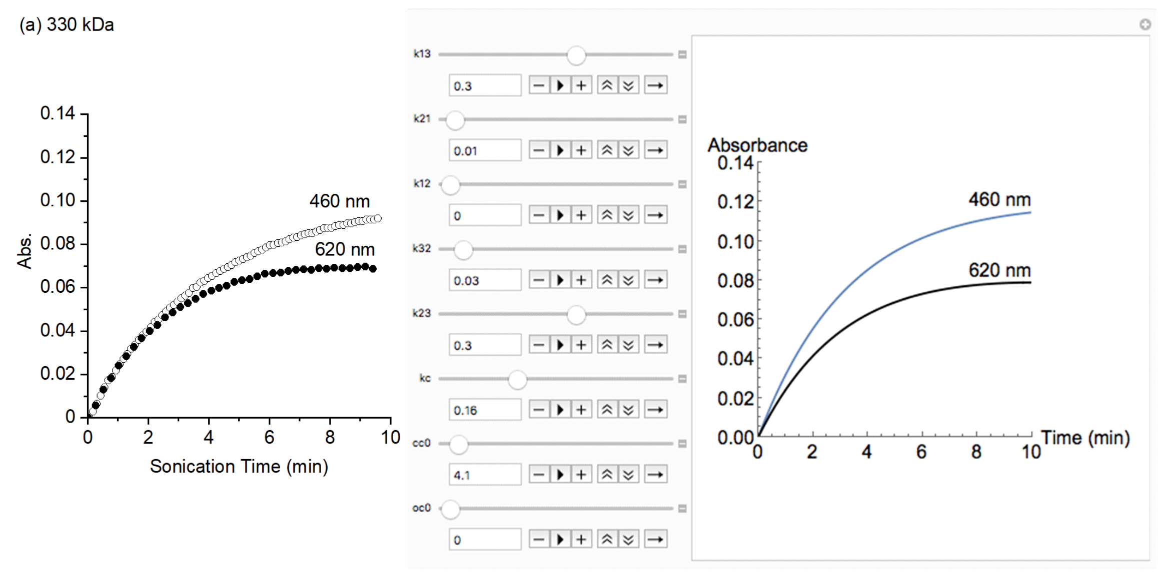

(a) 330 kDa

k13 0.3
k21 0.01
k12 0
k32 0.03
k23 0.3
kc 0.16
cc0 4.1
oc0 0

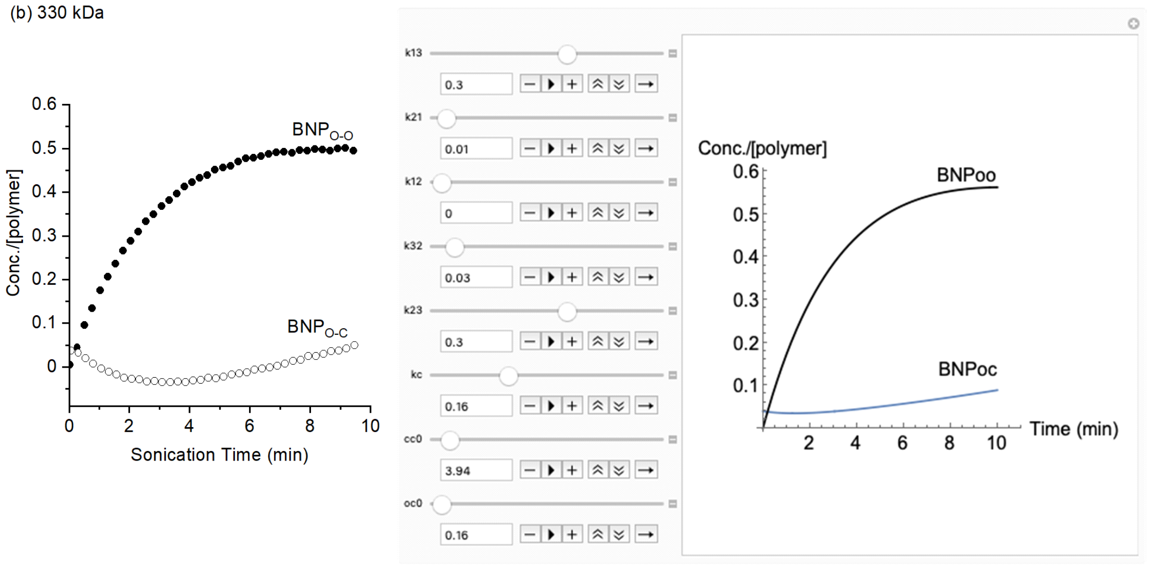

(b) 330 kDa

k13 0.3
k21 0.01
k12 0
k32 0.03
k23 0.3
kc 0.16
cc0 3.94
oc0 0.16

Figure 4.18. Time-dependent (a) absorbance at 460 and 620 nm, and (b) concentration of BNP$_{O-C}$ and BNP$_{O-O}$ for the mechanochemical activation of **BNP-PMA$_{330}$**. Experimental data (*left*) is compared to results from the kinetic model (*right*).

Effect of polymer chain scission. Chain scission occurs for polymers subjected to ultrasonication. We demonstrate below that the kinetic model closely reproduces the experimental data when chain scission is explicitly included and that the effect of chain scission on the value of B_{620}/B_{460} is minimal. BNP-PMA$_{22}$, BNP-PMA$_{98}$, and BNP-PMA$_{165}$ presenting a large range of molecular weights were subjected to extended ultrasonication treatment for 150, 65, and 70 min respectively (Figure 4.19–Figure 4.21). Changes in molecular weight for these polymers at various sonication times were characterized by GPC (Table 4.5).

Table 4.5. Molecular weight (M_n) and dispersity measured by GPC-MALLS for polymers after ultrasonication.

	BNP-PMA$_{22}$	**BNP-PMA$_{98}$**		**BNP-PMA$_{165}$**
Sonication Time (min)	85	17	31	23
M_n (kDa)	21	78	55	78
$Đ$	1.18	1.16	1.24	1.21

Ultrasonication of **BNP-PMA$_{22}$** for extended time results in negligible chain scission. The molecular weight and dispersity of the polymer is unchanged after 85 minutes of sonication. Furthermore, the time-dependent absorbance and associated concentration data shows that the concentration of BNP$_{O\text{-}O}$ reaches a constant value that is maintained for the duration of the sonication experiment, consistent with the absence of irreversible degradation caused by chain cleavage (Figure 4.19). These results for the mechanochemical activation of **BNP-PMA$_{22}$** demonstrate that chain scission is not required for the system to reach a mechanostationary state.

Extended ultrasound-induced mechanical activation of higher molecular weight **BNP-PMA$_{98}$** and **BNP-PMA$_{165}$** results in appreciable amounts of chain scission as expected. The molecular weight of **BNP-PMA$_{98}$** is reduced to 78 kDa after 17 min and 55 kDa after 31 min of sonication. **BNP-PMA$_{165}$** exhibits a faster rate of chain cleavage. After 23 min of sonication, the molecular weight was reduced to 78 kDa. Nevertheless, the experimental results for the mechanochemical reaction are reliably captured by the kinetic model when chain scission is explicitly included (Figure 4.20 and Figure 4.21).

The impact of chain cleavage on the outcome of mechanochemical activation of each polymer and its effect on the ratio of B_{620}/B_{460} was investigated by comparing time-dependent absorbance plots generated from the kinetic model that include and omit the chain scission parameter (Figure 4.22–Figure 4.28). Time-dependent absorbance traces for both mechanisms were modeled for each polymer and their corresponding values of B_{620}/B_{460} were calculated. In Figure 4.23–Figure 4.28, a model that explicitly incorporates chain cleavage is shown on the left using values of k_c from Table 4.3. The model that omits chain cleavage is displayed on the right (k_c = 0). This comparison demonstrates that while chain cleavage impacts how quickly the maximum absorbance values are reached and the rate at which irreversible degradation occurs, the value of B_{620}/B_{460} is not significantly affected.

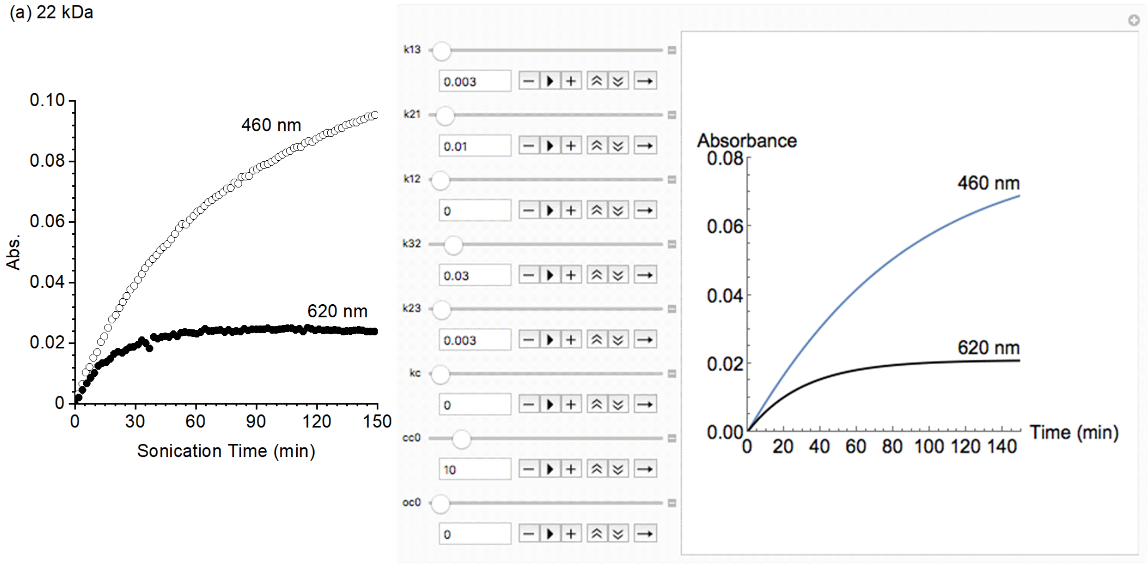
(a) 22 kDa

k13 0.003
k21 0.01
k12 0
k32 0.03
k23 0.003
kc 0
cc0 10
oc0 0

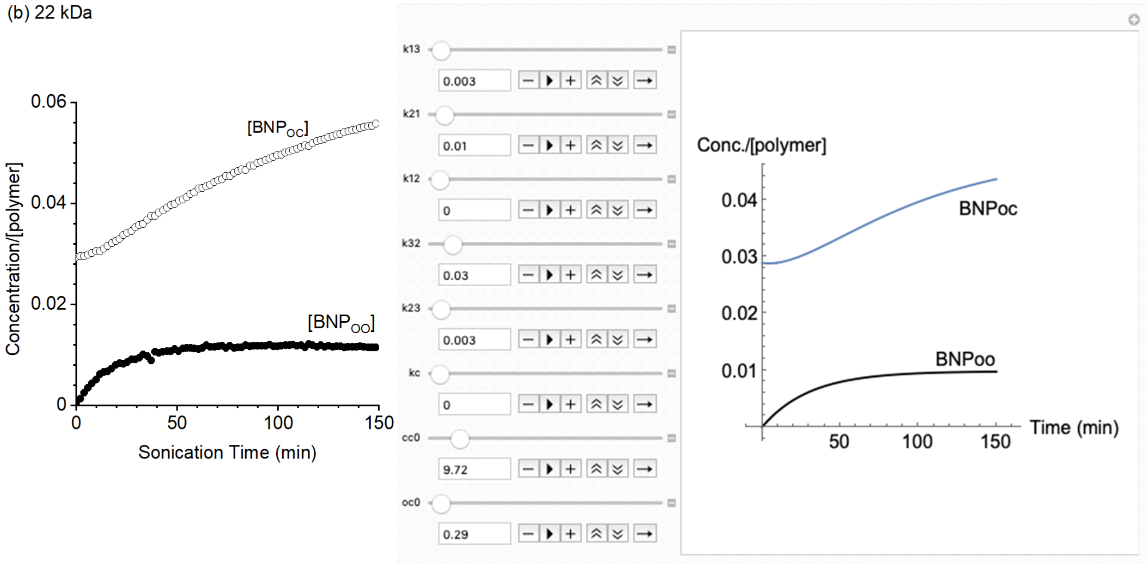
(b) 22 kDa

k13 0.003
k21 0.01
k12 0
k32 0.03
k23 0.003
kc 0
cc0 9.72
oc0 0.29

Figure 4.19. Time-dependent (a) absorbance at 460 and 620 nm, and (b) concentration of $BNP_{O\text{-}C}$ and $BNP_{O\text{-}O}$ for the mechanochemical activation of **$BNP\text{-}PMA_{22}$** for extended sonication time. Experimental data (*left*) is compared to results from the kinetic model (*right*).

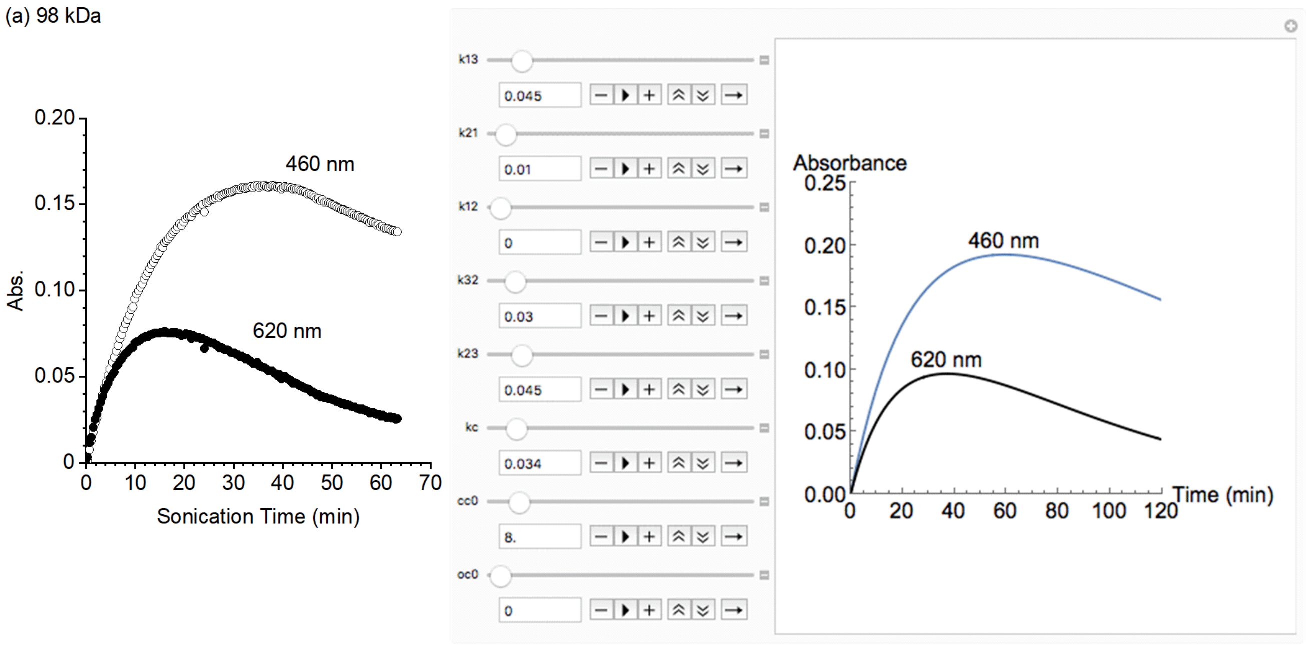
(a) 98 kDa

k13 0.045
k21 0.01
k12 0
k32 0.03
k23 0.045
kc 0.034
cc0 8.
oc0 0

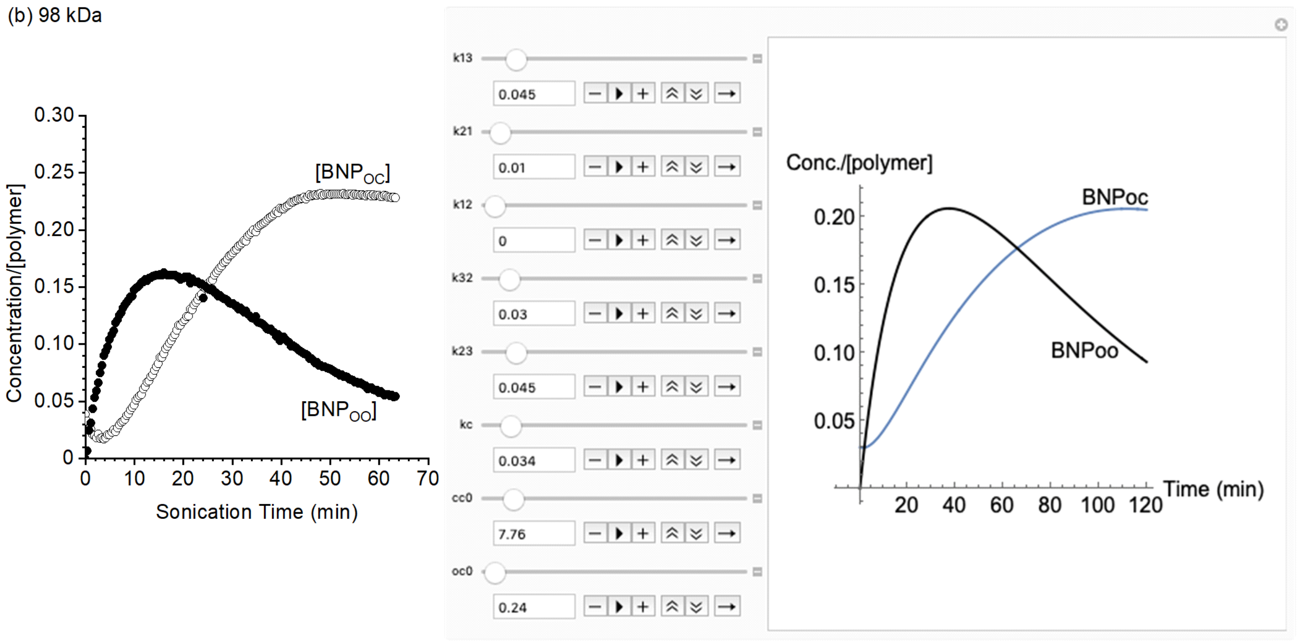
(b) 98 kDa

k13 0.045
k21 0.01
k12 0
k32 0.03
k23 0.045
kc 0.034
cc0 7.76
oc0 0.24

Figure 4.20. Time-dependent (a) absorbance at 460 and 620 nm, and (b) concentration of BNP$_{O\text{-}C}$ and BNP$_{O\text{-}O}$ for the mechanochemical activation of **BNP-PMA$_{98}$** for extended sonication time. Experimental data (*left*) is compared to results from the kinetic model (*right*).

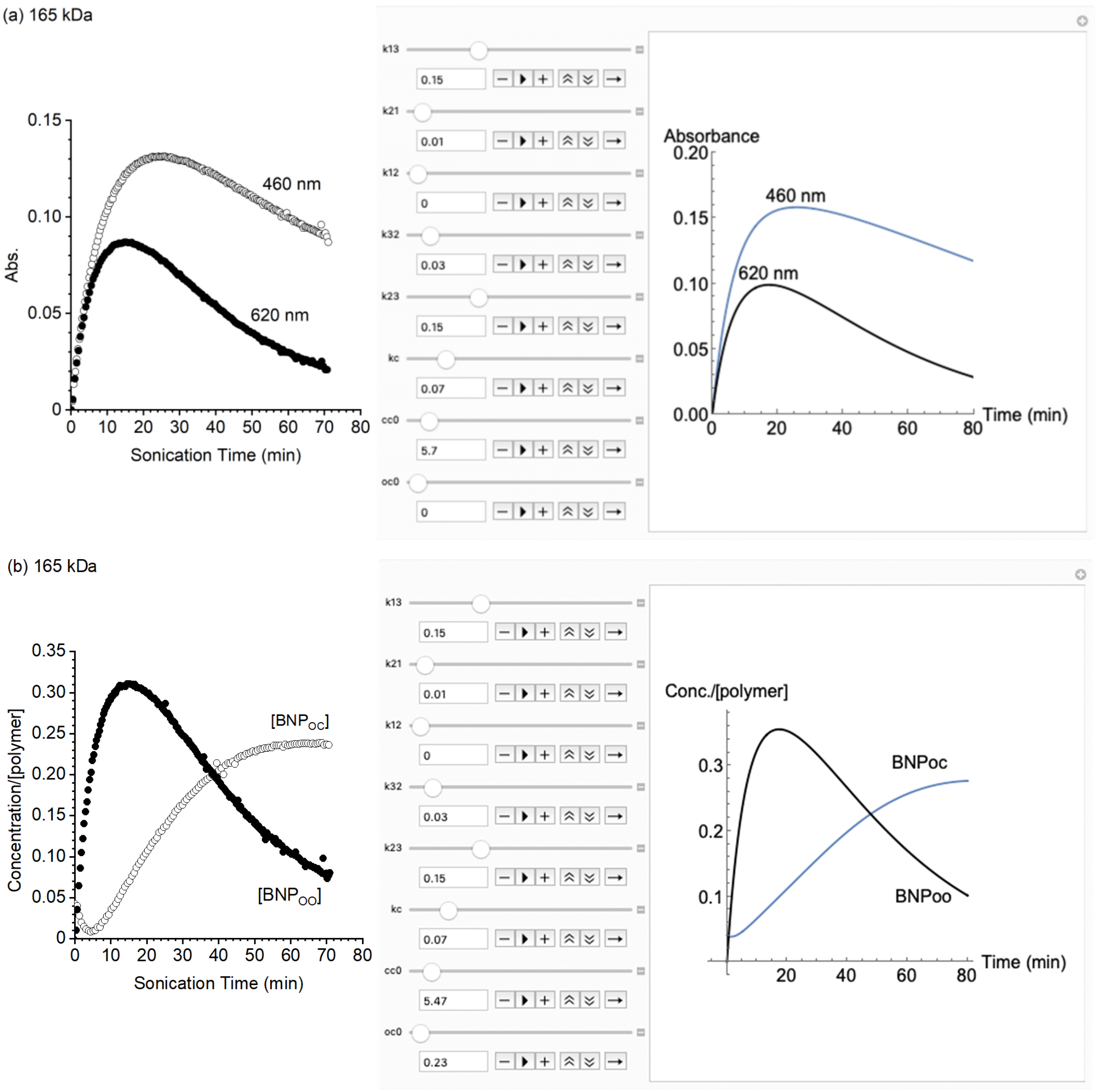

(a)
k13 0.15
k21 0.01
k12 0
k32 0.03
k23 0.15
kc 0.07
cc0 5.7
oc0 0

(b)
k13 0.15
k21 0.01
k12 0
k32 0.03
k23 0.15
kc 0.07
cc0 5.47
oc0 0.23

Figure 4.21. Time-dependent (a) absorbance at 460 and 620 nm, and (b) concentration of BNP$_{O\text{-}C}$ and BNP$_{O\text{-}O}$ for the mechanochemical activation of **BNP-PMA$_{165}$** for extended sonication time. Experimental data (*left*) is compared to results from the kinetic model (*right*).

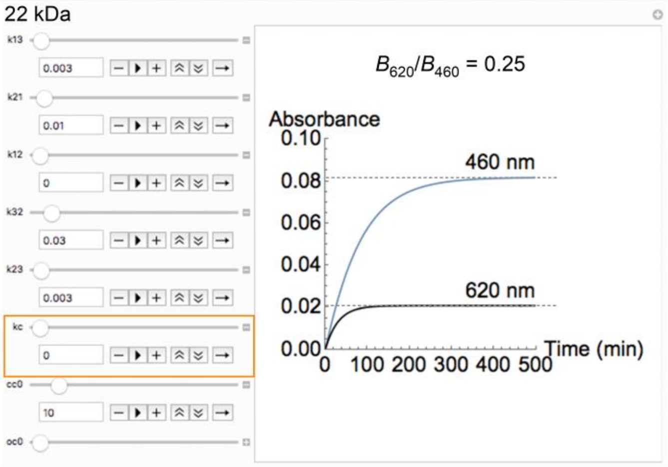

22 kDa

k13 0.003
k21 0.01
k12 0
k32 0.03
k23 0.003
kc 0
cc0 10
oc0

B_{620}/B_{460} = 0.25

Figure 4.22. Comparison of the effect of chain cleavage on the values of B_{620}/B_{460} calculated from the kinetic model. Chain scission is not observed for sonication of **BNP-PMA$_{22}$**. The ratios of B_{620}/B_{460} predicted from the model closely match the experimentally determined values.

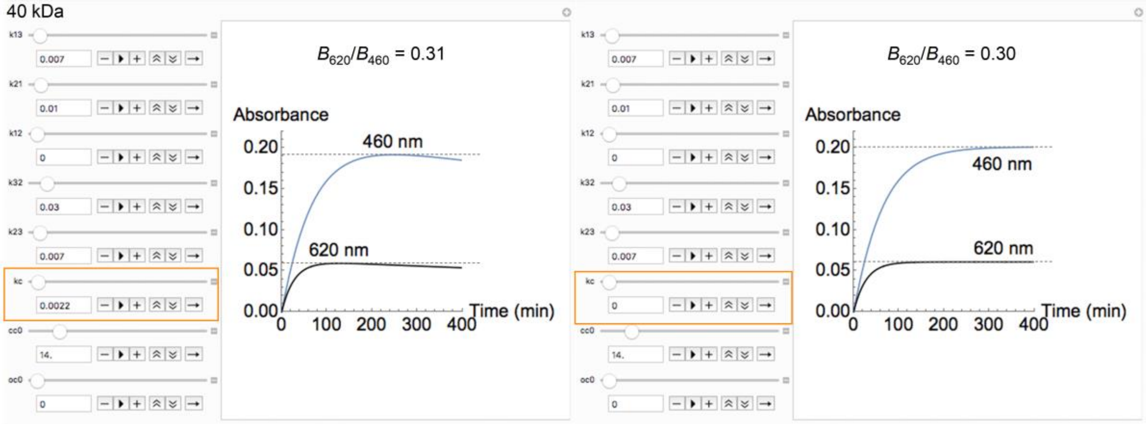

40 kDa

k13 0.007
k21 0.01
k12 0
k32 0.03
k23 0.007
kc 0.0022
cc0 14.
oc0 0

B_{620}/B_{460} = 0.31

k13 0.007
k21 0.01
k12 0
k32 0.03
k23 0.007
kc 0
cc0 14.
oc0 0

B_{620}/B_{460} = 0.30

Figure 4.23. Comparison of the effect of chain cleavage on the values of B_{620}/B_{460} calculated for **BNP-PMA$_{40}$** from the kinetic model. The ratios of B_{620}/B_{460} predicted from the model closely match the experimentally determined values. Chain scission has a minimal impact on the value of B_{620}/B_{460}.

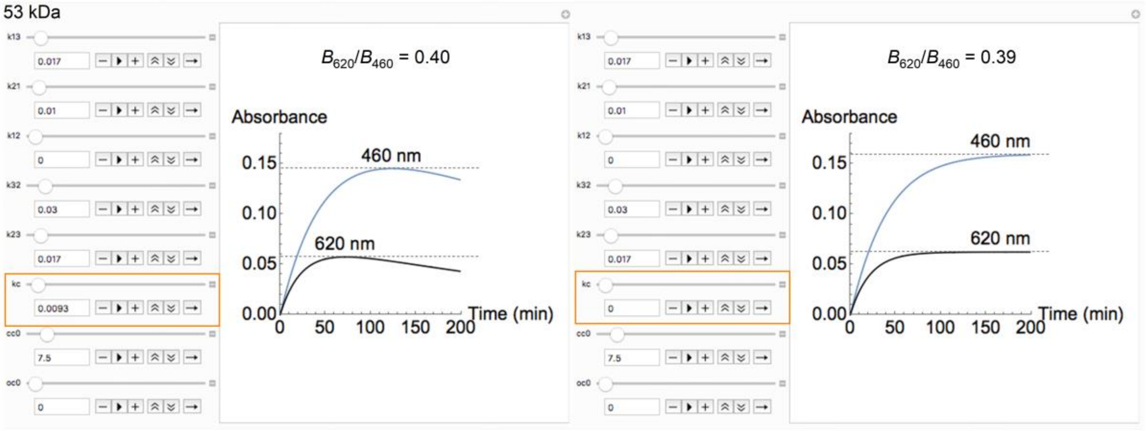

53 kDa

k13 0.017
k21 0.01
k12 0
k32 0.03
k23 0.017
kc 0.0093
cc0 7.5
oc0 0

B_{620}/B_{460} = 0.40

k13 0.017
k21 0.01
k12 0
k32 0.03
k23 0.017
kc 0
cc0 7.5
oc0 0

B_{620}/B_{460} = 0.39

Figure 4.25. Comparison of the effect of chain cleavage on the values of B_{620}/B_{460} calculated for **BNP-PMA$_{53}$** from the kinetic model. The ratios of B_{620}/B_{460} predicted from the model closely match the experimentally determined values. Chain scission has a minimal impact on the value of B_{620}/B_{460}.

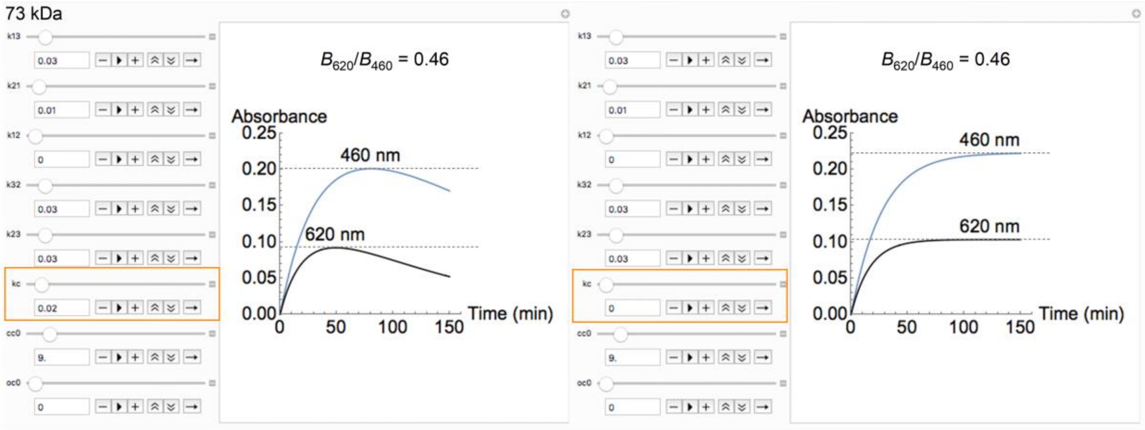

73 kDa

k13 0.03
k21 0.01
k12 0
k32 0.03
k23 0.03
kc 0.02
cc0 9.
oc0 0

B_{620}/B_{460} = 0.46

k13 0.03
k21 0.01
k12 0
k32 0.03
k23 0.03
kc 0
cc0 9.
oc0 0

B_{620}/B_{460} = 0.46

Figure 4.24. Comparison of the effect of chain cleavage on the values of B_{620}/B_{460} calculated for **BNP-PMA$_{73}$** from the kinetic model. The ratios of B_{620}/B_{460} predicted from the model closely match the experimentally determined values. Chain scission has a minimal impact on the value of B_{620}/B_{460}.

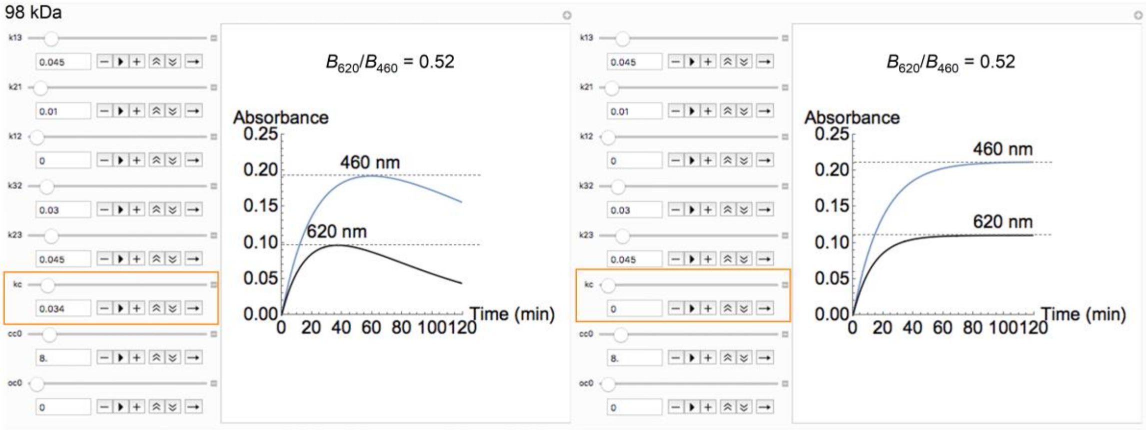
98 kDa

k13 0.045
k21 0.01
k12 0
k32 0.03
k23 0.045
kc 0.034
cc0 8.
oc0 0

k13 0.045
k21 0.01
k12 0
k32 0.03
k23 0.045
kc 0
cc0 8.
oc0 0

Figure 4.26. Comparison of the effect of chain cleavage on the values of B_{620}/B_{460} calculated for **BNP-PMA$_{98}$** from the kinetic model. The ratios of B_{620}/B_{460} predicted from the model closely match the experimentally determined values. Chain scission has a minimal impact on the value of B_{620}/B_{460}.

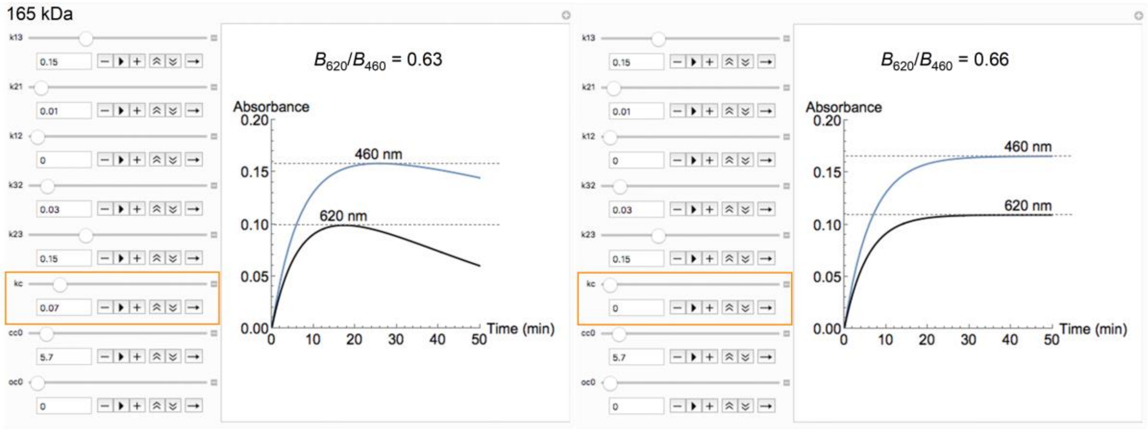
165 kDa

k13 0.15
k21 0.01
k12 0
k32 0.03
k23 0.15
kc 0.07
cc0 5.7
oc0 0

k13 0.15
k21 0.01
k12 0
k32 0.03
k23 0.15
kc 0
cc0 5.7
oc0 0

Figure 4.27. Comparison of the effect of chain cleavage on the values of B_{620}/B_{460} calculated for **BNP-PMA$_{165}$** from the kinetic model. The ratios of B_{620}/B_{460} predicted from the model closely match the experimentally determined values. Chain scission has a minimal impact on the value of B_{620}/B_{460}.

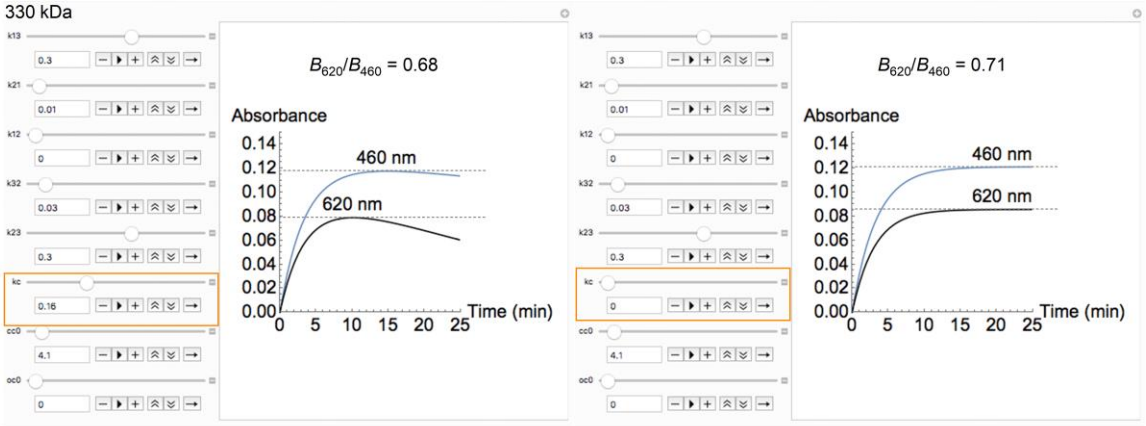
330 kDa

k13 0.3
k21 0.01
k12 0
k32 0.03
k23 0.3
kc 0.16
cc0 4.1
oc0 0

k13 0.3
k21 0.01
k12 0
k32 0.03
k23 0.3
kc 0
cc0 4.1
oc0 0

Figure 4.28. Comparison of the effect of chain cleavage on the values of B_{620}/B_{460} calculated for **BNP-PMA$_{330}$** from the kinetic model. The ratios of B_{620}/B_{460} predicted from the model closely match the experimentally determined values. Chain scission has a minimal impact on the value of B_{620}/B_{460}.

Analysis of the predicted effect of k$_{12}$. experimental data and the results of kinetic modeling are consistent with a mechanism in which BNP$_{C\text{-}C}$ is converted directly to BNP$_{O\text{-}O}$. The experimentally observed formation of BNP$_{O\text{-}C}$ and BNP$_{O\text{-}O}$ under mechanical activation is mechanistically distinct from the sequential process observed from photochemical activation (see Figure 4.2).

To further investigate whether the formation of BNP$_{O\text{-}C}$ directly from BNP$_{C\text{-}C}$ was occurring (with corresponding rate constant k_{12}) to any significant extent with mechanical force, time-dependent concentrations of merocyanine products were compared to models in which k_{12} was either included or omitted (Figure 4.29). The concentration of BNP$_{O\text{-}C}$ present in solution prior to sonication is observed to decrease immediately upon initiating sonication, which manifests as a concave up region in the curve for the concentration of BNP$_{O\text{-}C}$ at early sonication times. This feature in the experimental data is replicated when k_{12} is omitted from the kinetic model. When the reaction pathway for the direct formation BNP$_{O\text{-}C}$ from BNP$_{C\text{-}C}$ is included in the model (with a non-zero value for k_{12}), this concave up feature is no longer observed. While a mechanism in which BNP$_{C\text{-}C}$ is first converted to BNP$_{O\text{-}C}$ followed by rapid conversion to BNP$_{O\text{-}O}$ cannot be completely ruled out, the results of the model indicate that k_{12} is either zero or very small compared to k_{23}. The time-dependent absorption and concentration data shows immediate generation of $BNP_{O\text{-}O}$ in all sonication experiments, in direct contrast to the photoactivation experiment in which $BNP_{O\text{-}C}$ is clearly generated first, followed by the production of $BNP_{O\text{-}O}$ (Figure 4.2).

It is also possible that a small fraction of chains is only able to convert $BNP_{C\text{-}C}$ to $BNP_{O\text{-}C}$, which cannot react further to generate $BNP_{O\text{-}O}$. This situation would arise if the force required, and thus the threshold chain length, for generating $BNP_{O\text{-}O}$ from $BNP_{O\text{-}C}$ is greater than that for conversion of $BNP_{C\text{-}C}$ to $BNP_{O\text{-}C}$. Importantly, however, differences in threshold chain length for mechanophores with varying reactivity are statistically small.[35] Therefore, under this hypothetical mechanism, it is reasonable to expect that the majority of chains in solution that are long enough to be activated mechanochemically to form $BNP_{O\text{-}C}$ would also experience enough force to ultimately be converted to $BNP_{O\text{-}O}$. The features we observe in the experimental absorption data and the supporting evidence provided by the kinetic model are consistent with a dominant mechanism in which $BNP_{C\text{-}C}$ is effectively converted directly to $BNP_{O\text{-}O}$, and $BNP_{O\text{-}C}$ is generated via thermal electrocyclization.

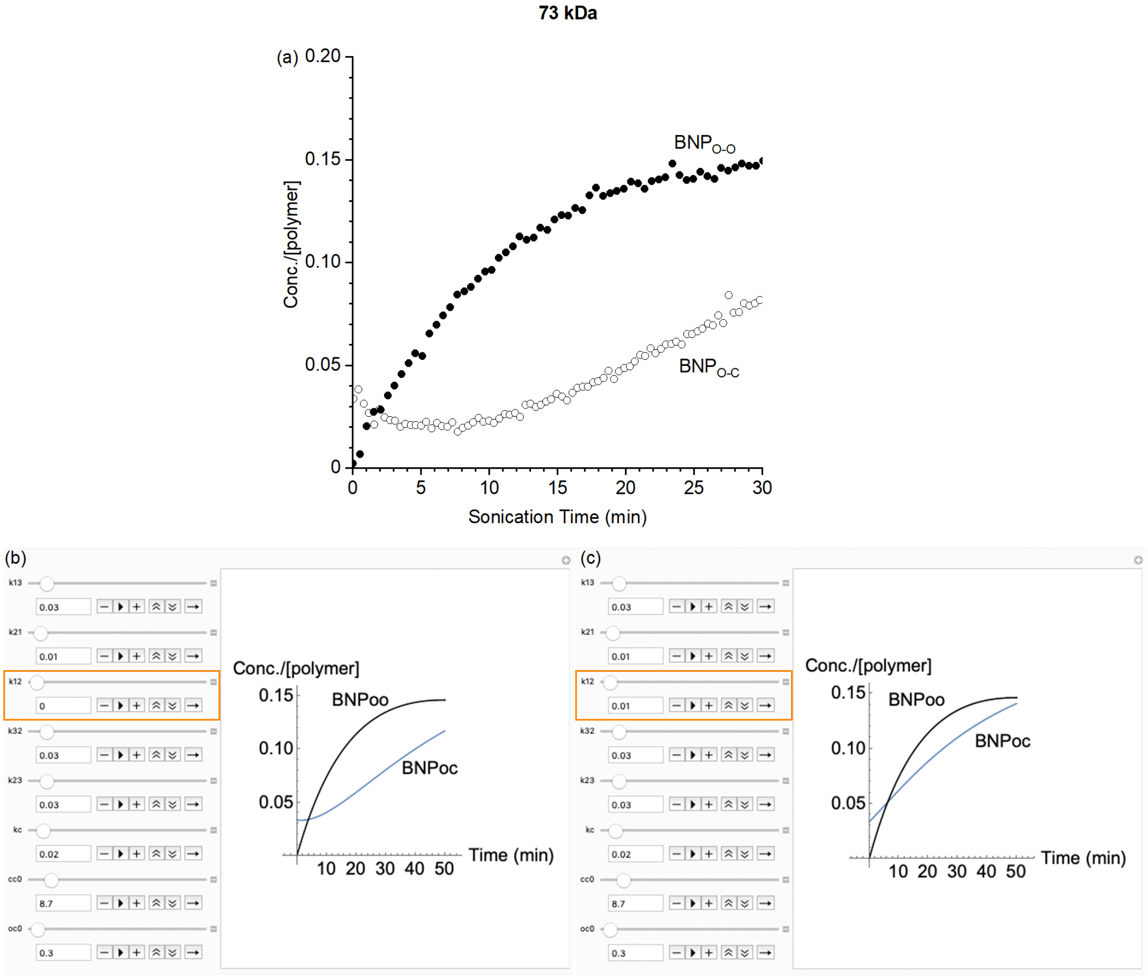

(b)
k13 0.03
k21 0.01
k12 0
k32 0.03
k23 0.03
kc 0.02
cc0 8.7
oc0 0.3

(c)
k13 0.03
k21 0.01
k12 0.01
k32 0.03
k23 0.03
kc 0.02
cc0 8.7
oc0 0.3

Figure 4.29. Comparison of the mechanochemical activation data acquired for **BNP-PMA$_{73}$** and the predicted effect of k_{12} from the kinetic model. (a) Concentration of merocyanine species as a function of sonication time, compared to results of the kinetic model (b) with k_{12} = 0 and (c) with k_{12} = 0.01 min^{-1}. The kinetic model suggests that the direct formation of BNP$_{O-C}$ from BNP$_{C-C}$, with associated rate constant k_{12}, is insignificant compared to the rate of conversion of BNP$_{O-C}$ to BNP$_{O-O}$ with associated rate constant k_{23}. These results support that BNP$_{C-C}$ is effectively converted directly to BNP$_{O-O}$.

References

(1) Li, J.; Nagamani, C.; Moore, J. S. Polymer Mechanochemistry: From Destructive to Productive. *Acc. Chem. Res.* **2015**, *48*, 2181–2190.

(2) Beyer, M. K.; Clausen-Schaumann, H. Mechanochemistry: The Mechanical Activation of Covalent Bonds. *Chem. Rev.* **2005**, *105*, 2921–2948.

(3) Caruso, M. M.; Davis, D. A.; Shen, Q.; Odom, S. A.; Sottos, N. R.; White, S. R.; Moore, J. S. Mechanically-Induced Chemical Changes in Polymeric Materials. *Chem. Rev.* **2009**, *109*, 5755–5798.

(4) Chen, Y.; Spiering, A. J. H.; Karthikeyan, S.; Peters, G. W. M.; Meijer, E. W.; Sijbesma, R. P. Mechanically Induced Chemiluminescence from Polymers Incorporating a 1,2-Dioxetane Unit in the Main Chain. *Nat. Chem.* **2012**, *4*, 559–562.

(5) Zhang, H.; Gao, F.; Cao, X.; Li, Y.; Xu, Y.; Weng, W.; Boulatov, R. Mechanochromism and Mechanical-Force-Triggered Cross-Linking from a Single Reactive Moiety Incorporated into Polymer Chains. *Angew. Chem. Int. Ed.* **2016**, *55*, 3040–3044.

(6) Li, Z.; Toivola, R.; Ding, F.; Yang, J.; Lai, P.-N.; Howie, T.; Georgeson, G.; Jang, S.-H.; Li, X.; Flinn, B. D.; Jen, A. K.-Y. Highly Sensitive Built-In Strain Sensors for Polymer Composites: Fluorescence Turn-On Response through Mechanochemical Activation. *Adv. Mater.* **2016**, *28*, 6592–6597.

(7) Clough, J. M.; Creton, C.; Craig, S. L.; Sijbesma, R. P. Covalent Bond Scission in the Mullins Effect of a Filled Elastomer: Real-Time Visualization with Mechanoluminescence. *Adv. Funct. Mater.* **2016**, *26*, 9063–9074.

(8) Göstl, R.; Sijbesma, R. P. π-Extended Anthracenes as Sensitive Probes for Mechanical Stress. *Chem. Sci.* **2016**, *7*, 370–375.

(9) Sagara, Y.; Karman, M.; Verde-Sesto, E.; Matsuo, K.; Kim, Y.; Tamaoki, N.; Weder, C. Rotaxanes as Mechanochromic Fluorescent Force Transducers in Polymers. *J. Am. Chem. Soc.* **2018**, *140*, 1584–1587.

(10) Sagara, Y.; Karman, M.; Seki, A.; Pannipara, M.; Tamaoki, N.; Weder, C. Rotaxane-Based Mechanophores Enable Polymers with Mechanically Switchable White Photoluminescence. *ACS Cent. Sci.* **2019**, acscentsci.9b00173.

(11) Potisek, S. L.; Davis, D. A.; Sottos, N. R.; White, S. R.; Moore, J. S. Mechanophore-Linked Addition Polymers. *J. Am. Chem. Soc.* **2007**, *129*, 13808–13809.

(12) Davis, D. A.; Hamilton, A.; Yang, J.; Cremar, L. D.; Van Gough, D.; Potisek, S. L.; Ong, M. T.; Braun, P. V.; Martínez, T. J.; White, S. R.; Moore, J. S.; Sottos, N. R. Force-Induced Activation of Covalent Bonds in Mechanoresponsive Polymeric Materials. *Nature* **2009**, *459*, 68–72.

(13) Lee, C. K.; Beiermann, B. A.; Silberstein, M. N.; Wang, J.; Moore, J. S.; Sottos, N. R.; Braun, P. V. Exploiting Force Sensitive Spiropyrans as Molecular Level Probes. *Macromolecules* **2013**, *46*, 3746–3752.

(14) Gossweiler, G. R.; Hewage, G. B.; Soriano, G.; Wang, Q.; Welshofer, G. W.; Zhao, X.; Craig, S. L. Mechanochemical Activation of Covalent Bonds in Polymers with Full and Repeatable Macroscopic Shape Recovery. *ACS Macro Lett.* **2014**, *3*, 216–219.

(15) Zhang, H.; Chen, Y.; Lin, Y.; Fang, X.; Xu, Y.; Ruan, Y.; Weng, W. Spiropyran as a Mechanochromic Probe in Dual Cross-Linked Elastomers. *Macromolecules* **2014**, *47*, 6783–6790.

(16) Peterson, G. I.; Larsen, M. B.; Ganter, M. A.; Storti, D. W.; Boydston, A. J. 3D-Printed Mechanochromic Materials. *ACS Appl. Mater. Interfaces* **2014**, *7*, 577–583.

(17) Gossweiler, G. R.; Kouznetsova, T. B.; Craig, S. L. Force-Rate Characterization of Two Spiropyran-Based Molecular Force Probes. *J. Am. Chem. Soc.* **2015**, *137*, 6148–6151.

(18) Lin, Y.; Barbee, M. H.; Chang, C. C.; Craig, S. L. Regiochemical Effects on Mechanophore Activation in Bulk Materials. *J. Am. Chem. Soc.* **2018**, *140*, 15969–15975.

(19) Robb, M. J.; Kim, T. A.; Halmes, A. J.; White, S. R.; Sottos, N. R.; Moore, J. S. Regioisomer-Specific Mechanochromism of Naphthopyran in Polymeric Materials. *J. Am. Chem. Soc.* **2016**, *138*, 12328–12331.

(20) Imato, K.; Irie, A.; Kosuge, T.; Ohishi, T.; Nishihara, M.; Takahara, A.; Otsuka, H. Mechanophores with a Reversible Radical System and Freezing-Induced Mechanochemistry in Polymer Solutions and Gels. *Angew. Chem. Int. Ed.* **2015**, *54*, 6168–6172.

(21) Verstraeten, F.; Göstl, R.; Sijbesma, R. P. Stress-Induced Colouration and Crosslinking of Polymeric Materials by Mechanochemical Formation of Triphenylimidazolyl Radicals. *Chem. Commun.* **2016**, *52*, 8608–8611.

(22) Ishizuki, K.; Oka, H.; Aoki, D.; Goseki, R.; Otsuka, H. Mechanochromic Polymers That Turn Green Upon the Dissociation of Diarylbibenzothiophenonyl: The Missing Piece toward Rainbow Mechanochromism. *Chem. Eur. J.* **2018**, *24*, 3170–3173.

(23) Sakai, H.; Sumi, T.; Aoki, D.; Goseki, R.; Otsuka, H. Thermally Stable Radical-Type Mechanochromic Polymers Based on Difluorenylsuccinonitrile. *ACS Macro Lett.* **2018**, *7*, 1359–1363.

(24) Chen, Z.; Mercer, J. A. M.; Zhu, X.; Romaniuk, J. A. H.; Pfattner, R.; Cegelski, L.; Martinez, T. J.; Burns, N. Z.; Xia, Y. Mechanochemical Unzipping of Insulating Polyladderene to Semiconducting Polyacetylene. *Science* **2017**, *357*, 475–479.

(25) Wang, Z.; Ma, Z.; Wang, Y.; Xu, Z.; Luo, Y.; Wei, Y.; Jia, X. A Novel Mechanochromic and Photochromic Polymer Film: When Rhodamine Joins Polyurethane. *Adv. Mater.* **2015**, *27*, 6469–6474.

(26) Wang, T.; Zhang, N.; Dai, J.; Li, Z.; Bai, W.; Bai, R. Novel Reversible Mechanochromic Elastomer with High Sensitivity: Bond Scission and Bending-Induced Multicolor Switching. *ACS Appl. Mater. Interfaces* **2017**, *9*, 11874–11881.

(27) Kim, T. A.; Robb, M. J.; Moore, J. S.; White, S. R.; Sottos, N. R. Mechanical Reactivity of Two Different Spiropyran Mechanophores in Polydimethylsiloxane. *Macromolecules* **2018**, *51*, 9177–9183.

(28) Ishizuki, K.; Aoki, D.; Goseki, R.; Otsuka, H. Multicolor Mechanochromic Polymer Blends That Can Discriminate between Stretching and Grinding. *ACS Macro Lett.* **2018**, *7*, 556–560.

(29) Kosuge, T.; Zhu, X.; Lau, V. M.; Aoki, D.; Martinez, T. J.; Moore, J. S.; Otsuka, H. Multicolor Mechanochromism of a Polymer/Silica Composite with Dual Distinct Mechanophores. *J. Am. Chem. Soc.* **2019**, *141*, 1898–1902.

(30) Lu, X.; Dong, Q.; Dong, X.; Zhao, W. Synthesis and Sequential Photochromism of Thiophene-Linked Bis-Pyrans. *Tetrahedron* **2015**, *71*, 4061–4069.

(31) Zhao, W.; Carreira, E. M. Oligothiophene-Linked Bisnaphthopyrans: Sequential and Temperature- Dependent Photochromism. *Chem. Eur. J.* **2007**, *13*, 2671–2688.

(32) Zhao, W.; Carreira, E. M. Synthesis and Photochromism of Novel Phenylene-Linked Photochromic Bispyrans. *Org. Lett.* **2006**, *8*, 99–102.

(33) Zhao, W.; Carreira, E. M. A Smart Photochromophore through Synergistic Coupling of Photochromic Subunits. *J. Am. Chem. Soc.* **2002**, *124*, 1582–1583.

(34) Beyer, M. K. The Mechanical Strength of a Covalent Bond Calculated by Density Functional Theory. *J. Chem. Phys.* **2000**, *112*, 7307–7312.

(35) Kryger, M. J.; Munaretto, A. M.; Moore, J. S. Structure-Mechanochemical Activity Relationships for Cyclobutane Mechanophores. *J. Am. Chem. Soc.* **2011**, *133*, 18992–18998.

(36) Gabbutt, C. D.; Heron, B. M.; Instone, A. C. Control of the Fading Properties of Photochromic 3,3-Diaryl-3H-Naphtho[2,1-b]Pyrans. *Heterocycles* **2003**, *60*, 843–855.

(37) Odell, J. A.; Keller, A. Flow-Induced Chain Fracture of Isolated Linear Macromolecules in Solution. *J. Polym. Sci. Pol. Phys.* **1986**, *24*, 1889–1916.

(38) May, P. A.; Munaretto, N. F.; Hamoy, M. B.; Robb, M. J.; Moore, J. S. Is Molecular Weight or Degree of Polymerization a Better Descriptor of Ultrasound-Induced Mechanochemical Transduction? *ACS Macro Lett.* **2016**, *5*, 177–180.

(39) Schaefer, M.; Icli, B.; Weder, C.; Lattuada, M.; Kilbinger, A. F. M.; Simon, Y. C. The Role of Mass and Length in the Sonochemistry of Polymers. *Macromolecules* **2016**, *49*, 1630–1636.

(40) Zhao, W.; Carreira, E. M. Facile One-Pot Synthesis of Photochromic Pyrans. *Org. Lett.* **2003**, *5*, 4153–4154.

(41) Wolfram Research, Inc. Mathematica. Version 12.0.; Wolfram Research, Inc.: Champaign, Illinois, 2019.

(42) Collum, D. B. Numerical Integration - Simulation of Chemical Kinetics Using Mathematica 6.0. Numerical Integration - Simulation of Chemical Kinetics Using Mathematica 6.0 https://collum.chem.cornell.edu/files/2019/10/numerical_integration.pdf (accessed Jun 15, 2019).

(43) Akbulatov, S.; Boulatov, R. Experimental Polymer Mechanochemistry and Its Interpretational Frameworks. *ChemPhysChem* **2017**, *18*, 1422–1450.

^{1}H and ^{13}C NMR Spectra

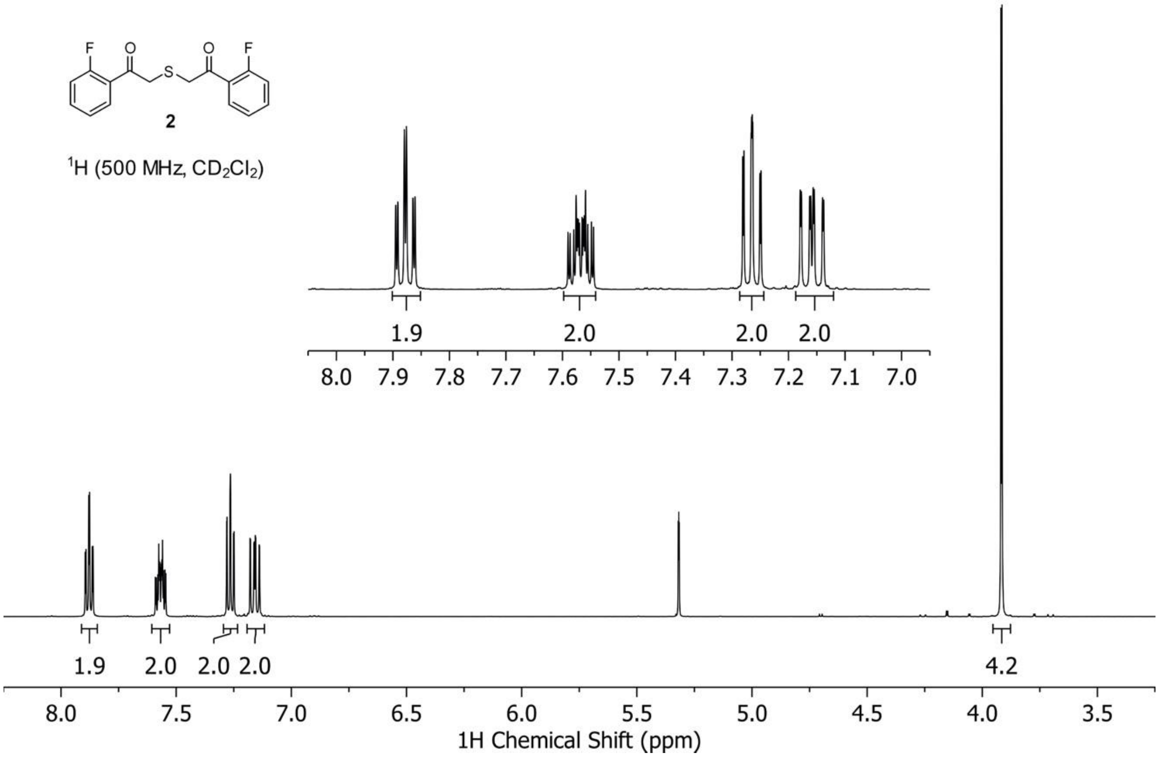

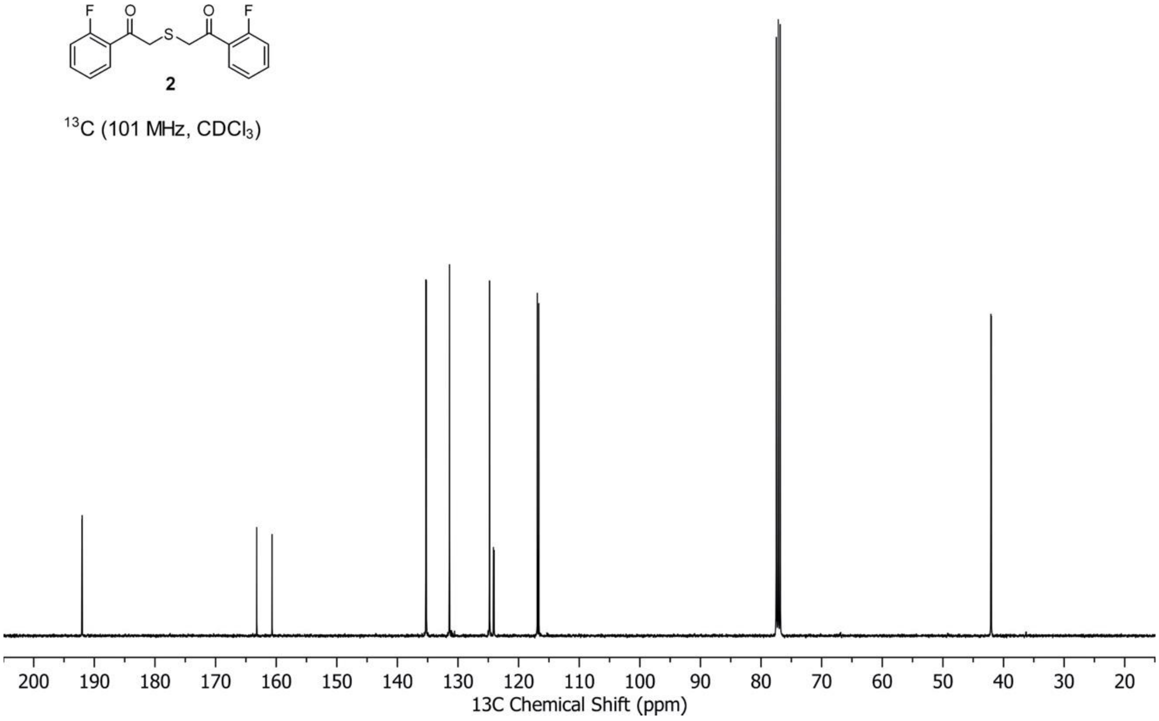

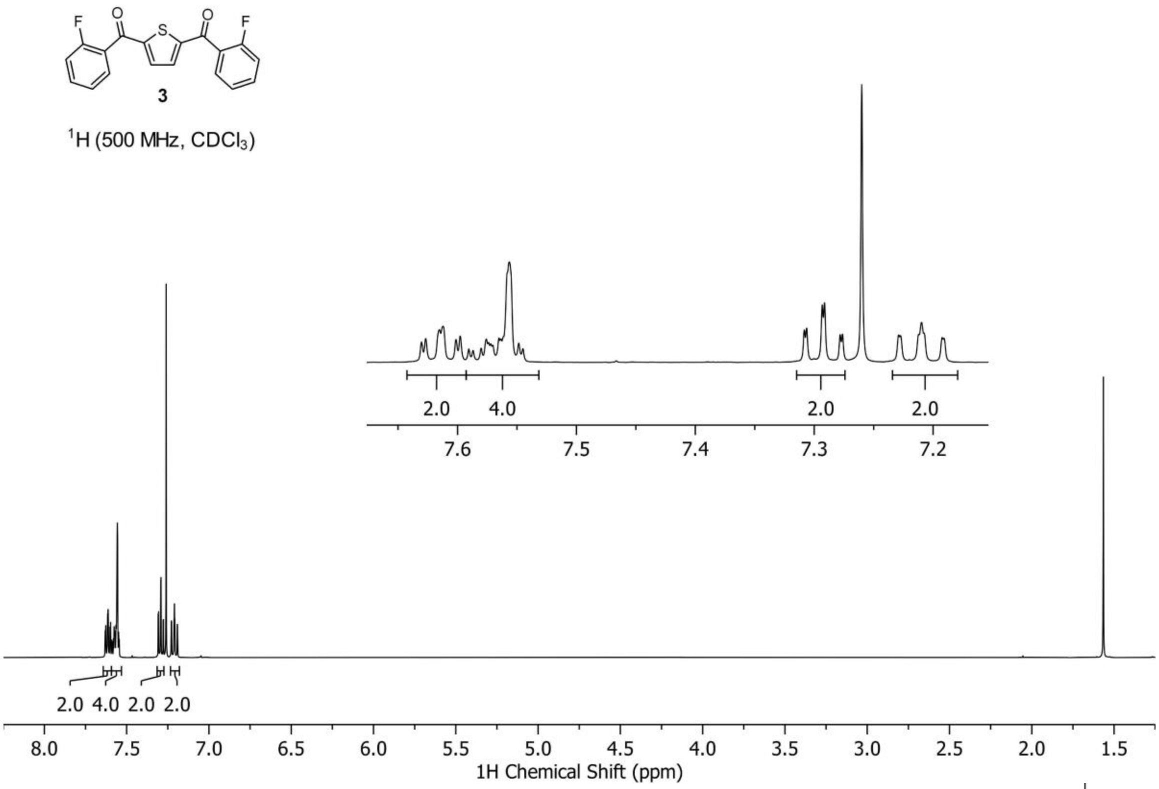
F
O
S
O
F
3
^{1}H (500 MHz, CDCl$_3$)
2.0 4.0
2.0
2.0
7.6 7.5 7.4 7.3 7.2
2.0 4.0 2.0 2.0
8.0 7.5 7.0 6.5 6.0 5.5 5.0 4.5 4.0 3.5 3.0 2.5 2.0 1.5
1H Chemical Shift (ppm)

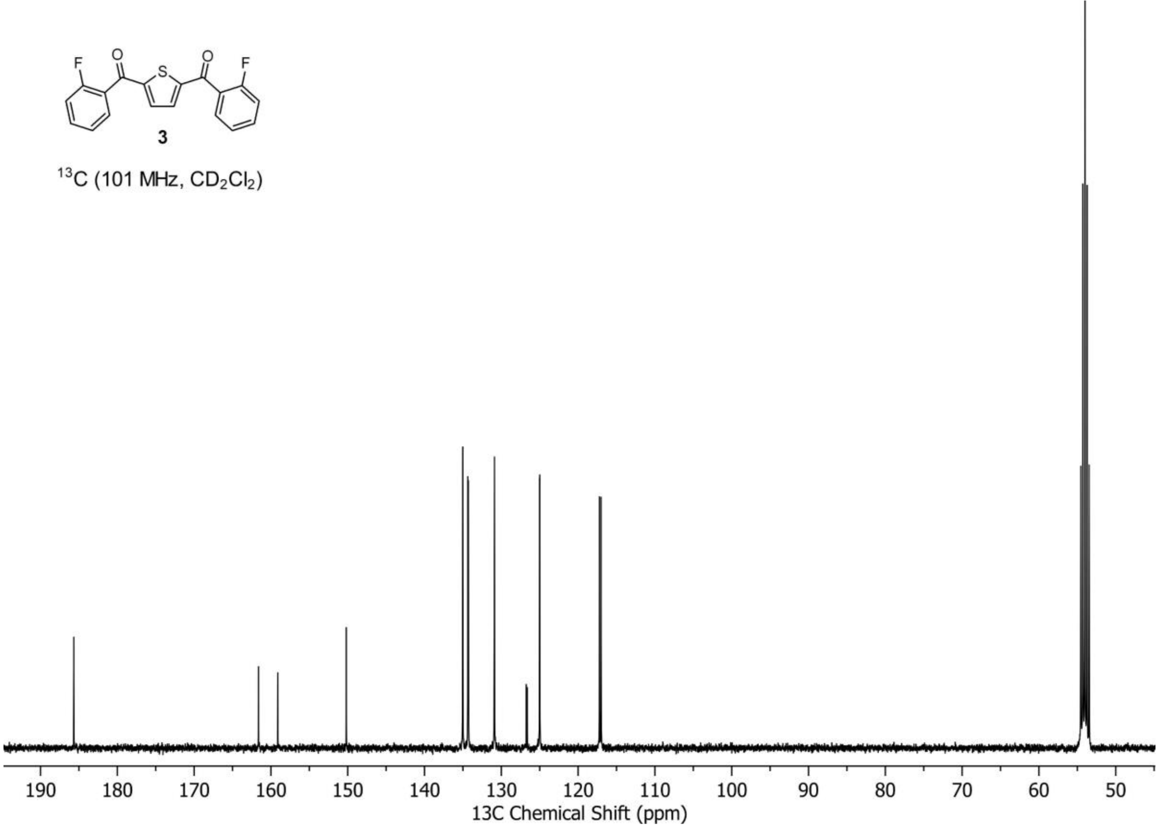
F
O
S
O
F
3
^{13}C (101 MHz, CD$_2$Cl$_2$)
190 180 170 160 150 140 130 120 110 100 90 80 70 60 50
13C Chemical Shift (ppm)

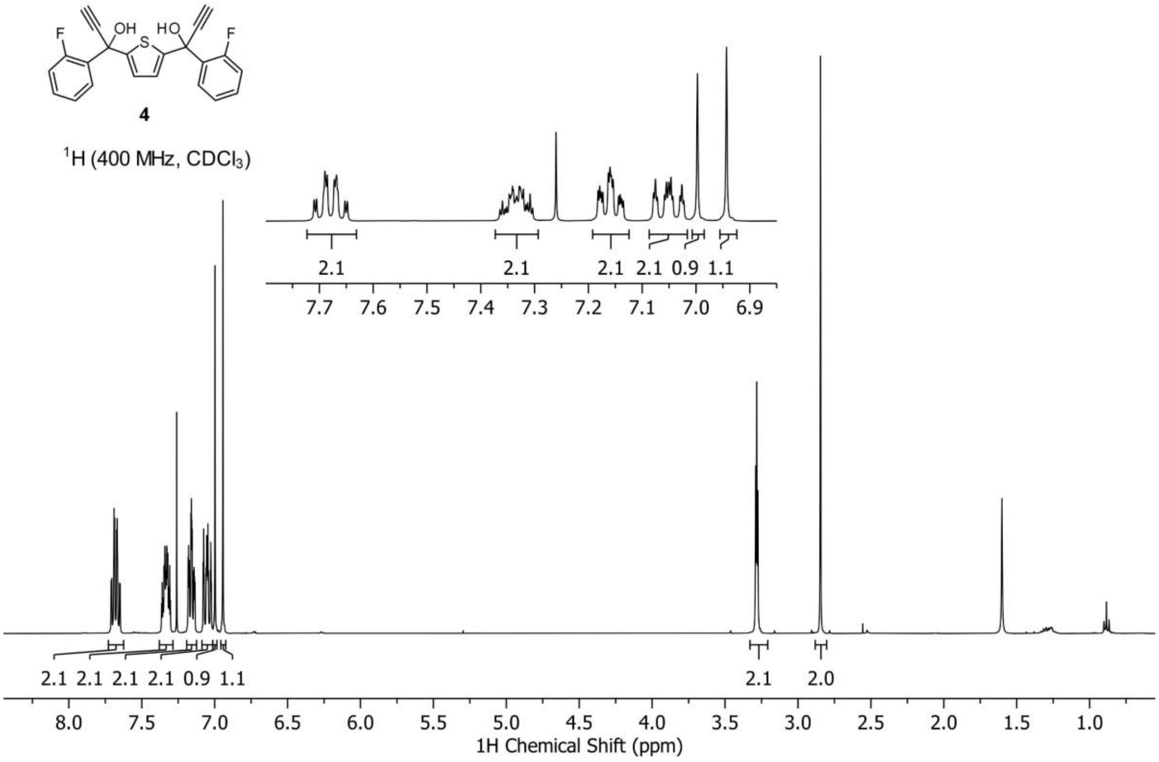
F
OH
S
HO
F
4
^{1}H (400 MHz, CDCl$_3$)
2.1
2.1
2.1
2.1
0.9
1.1
7.7
7.6
7.5
7.4
7.3
7.2
7.1
7.0
6.9
2.1
2.1
2.1
2.1
0.9
1.1
2.1
2.0
8.0
7.5
7.0
6.5
6.0
5.5
5.0
4.5
4.0
3.5
3.0
2.5
2.0
1.5
1.0
1H Chemical Shift (ppm)

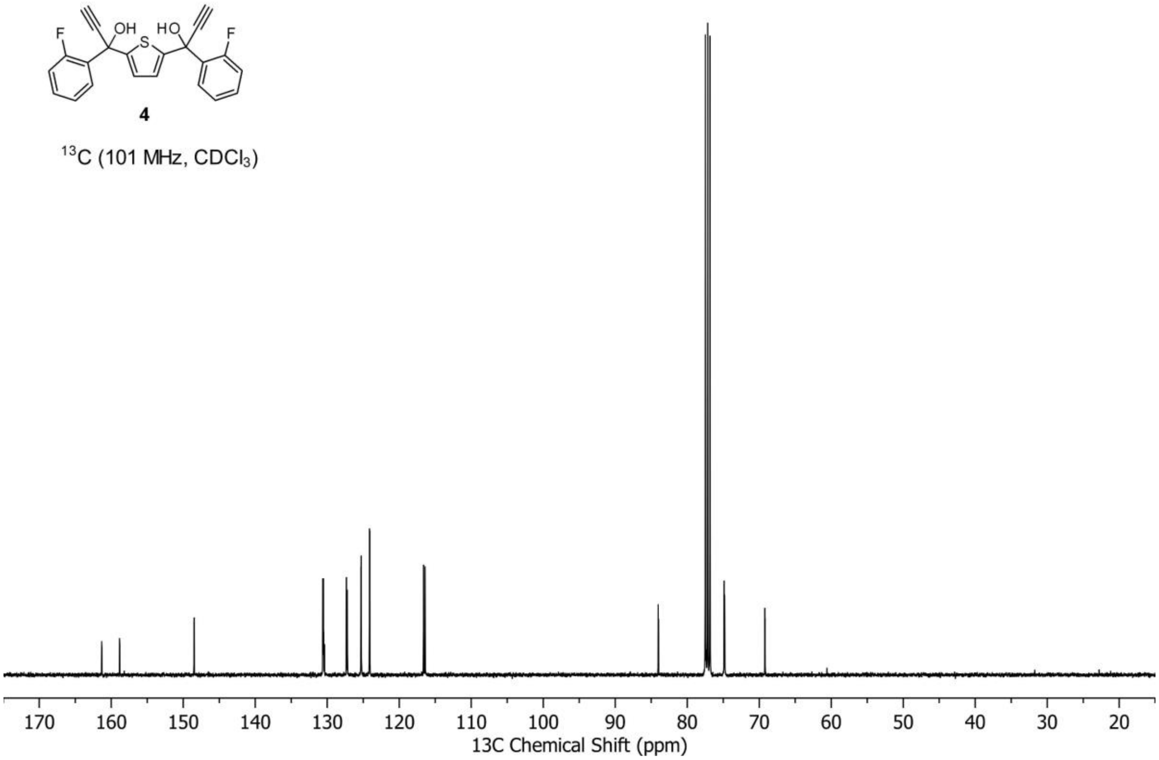
F
OH
S
HO
F
4
^{13}C (101 MHz, CDCl$_3$)
170
160
150
140
130
120
110
100
90
80
70
60
50
40
30
20
13C Chemical Shift (ppm)

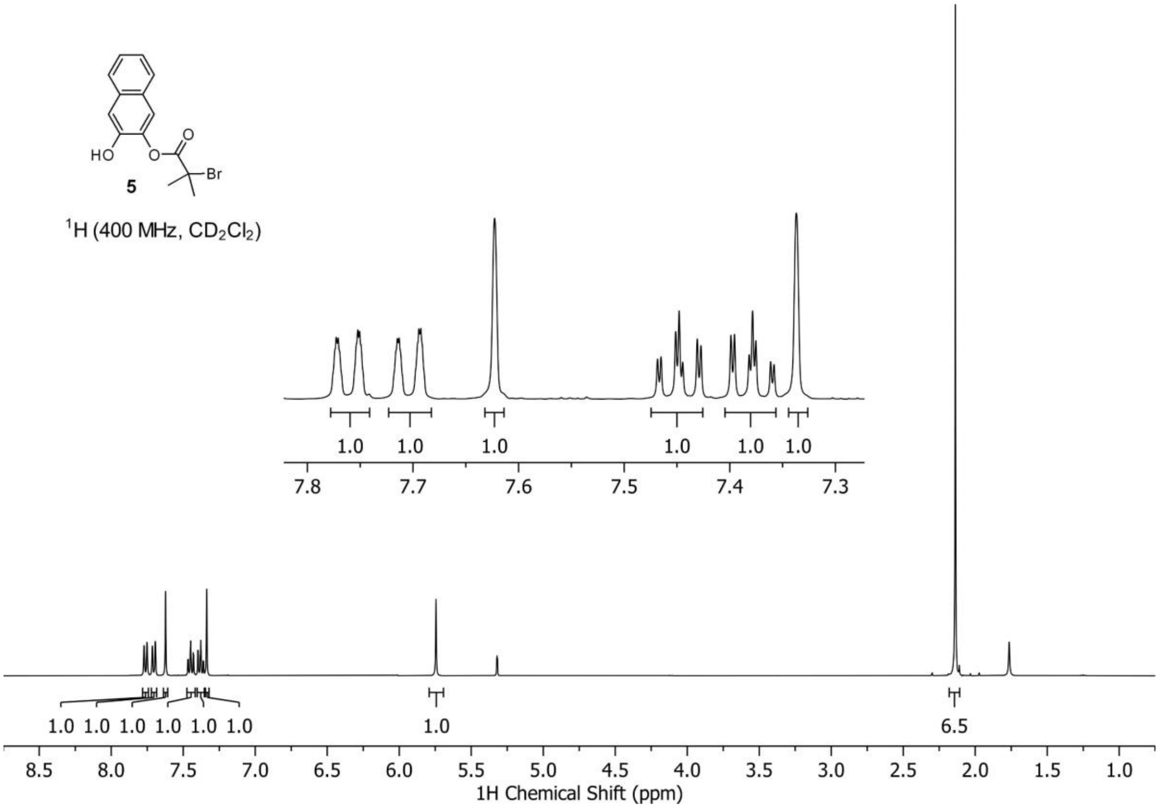
HO
O
O
Br
5
1H (400 MHz, CD2Cl2)
1.0 1.0 1.0 1.0 1.0 1.0
7.8 7.7 7.6 7.5 7.4 7.3
1.0 1.0 1.0 1.0 1.0 1.0
1.0
6.5
8.5 8.0 7.5 7.0 6.5 6.0 5.5 5.0 4.5 4.0 3.5 3.0 2.5 2.0 1.5 1.0
1H Chemical Shift (ppm)

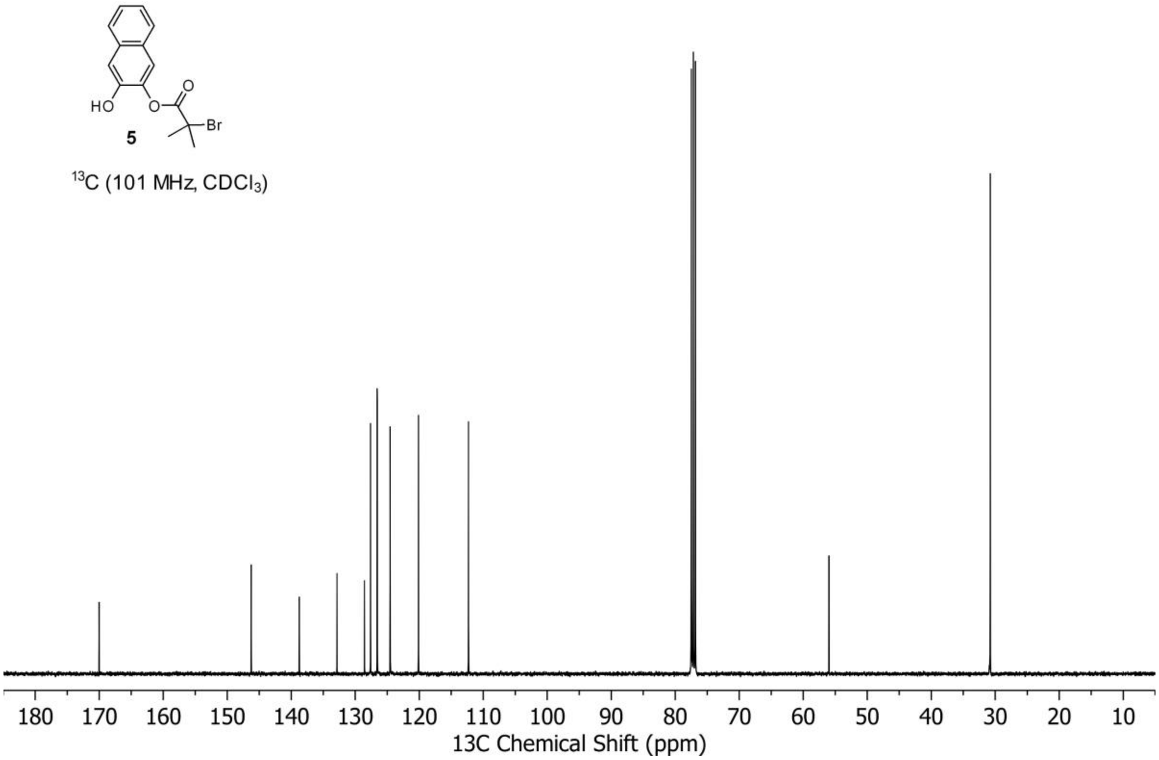
HO
O
O
Br
5
13C (101 MHz, CDCl3)
180 170 160 150 140 130 120 110 100 90 80 70 60 50 40 30 20 10
13C Chemical Shift (ppm)

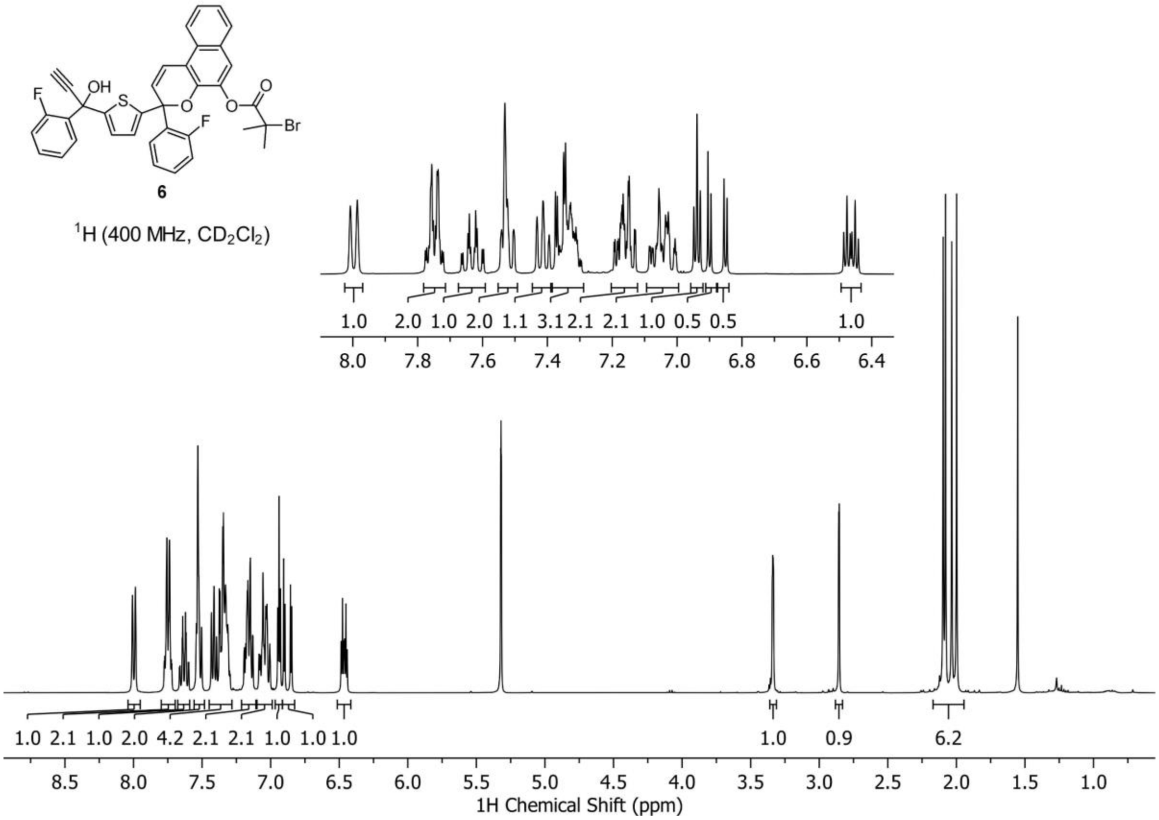

6

^{1}H (400 MHz, CD$_2$Cl$_2$)

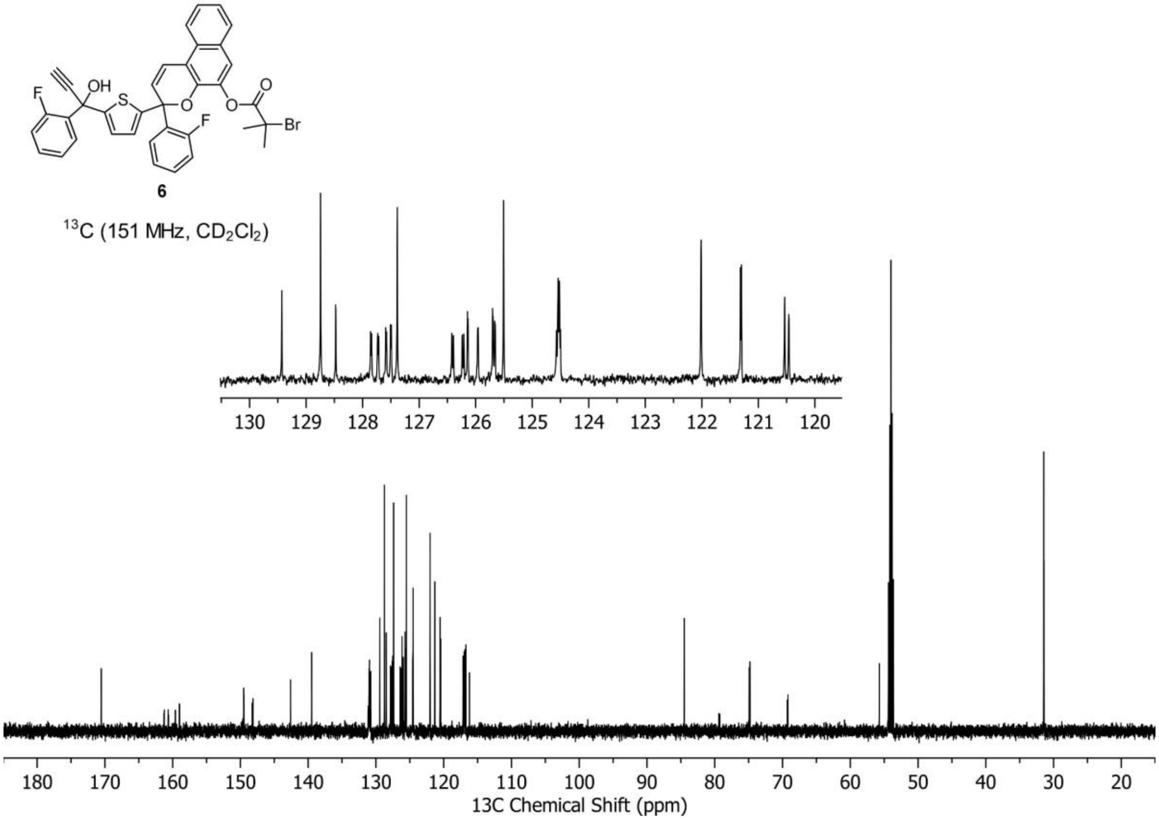

6

^{13}C (151 MHz, CD$_2$Cl$_2$)

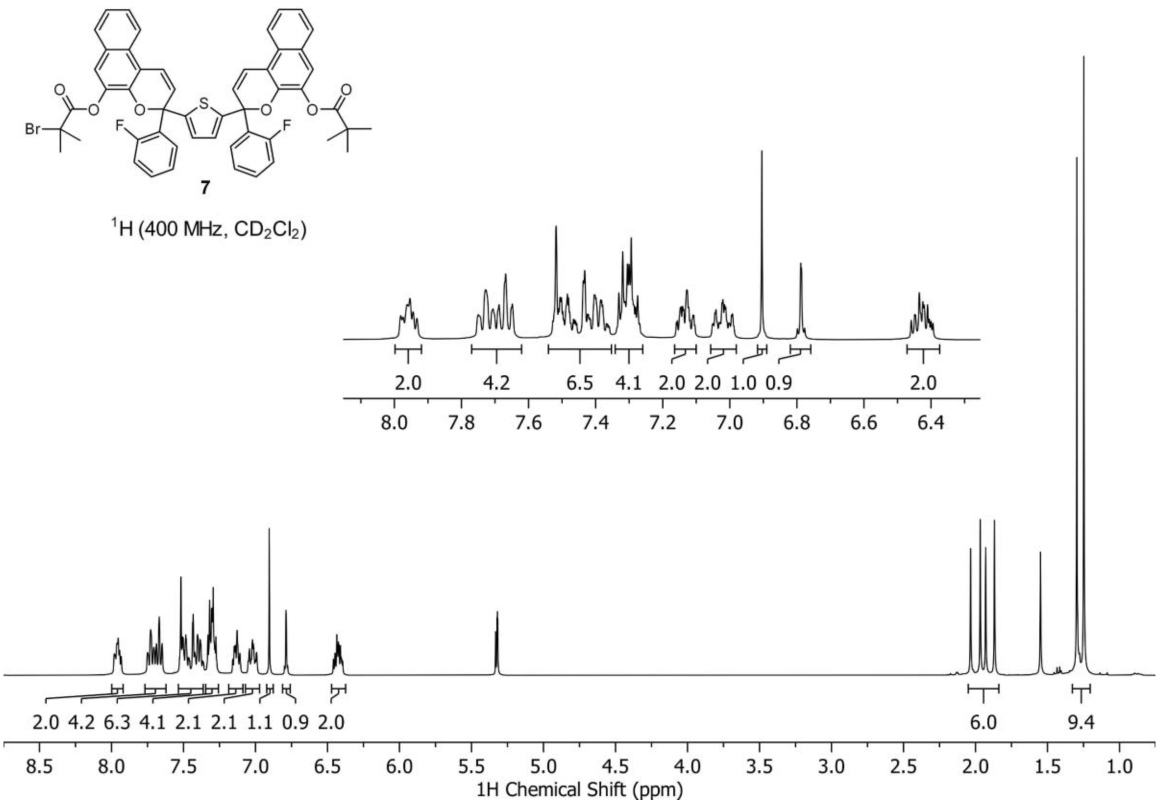

7

^{1}H (400 MHz, CD_2Cl_2)

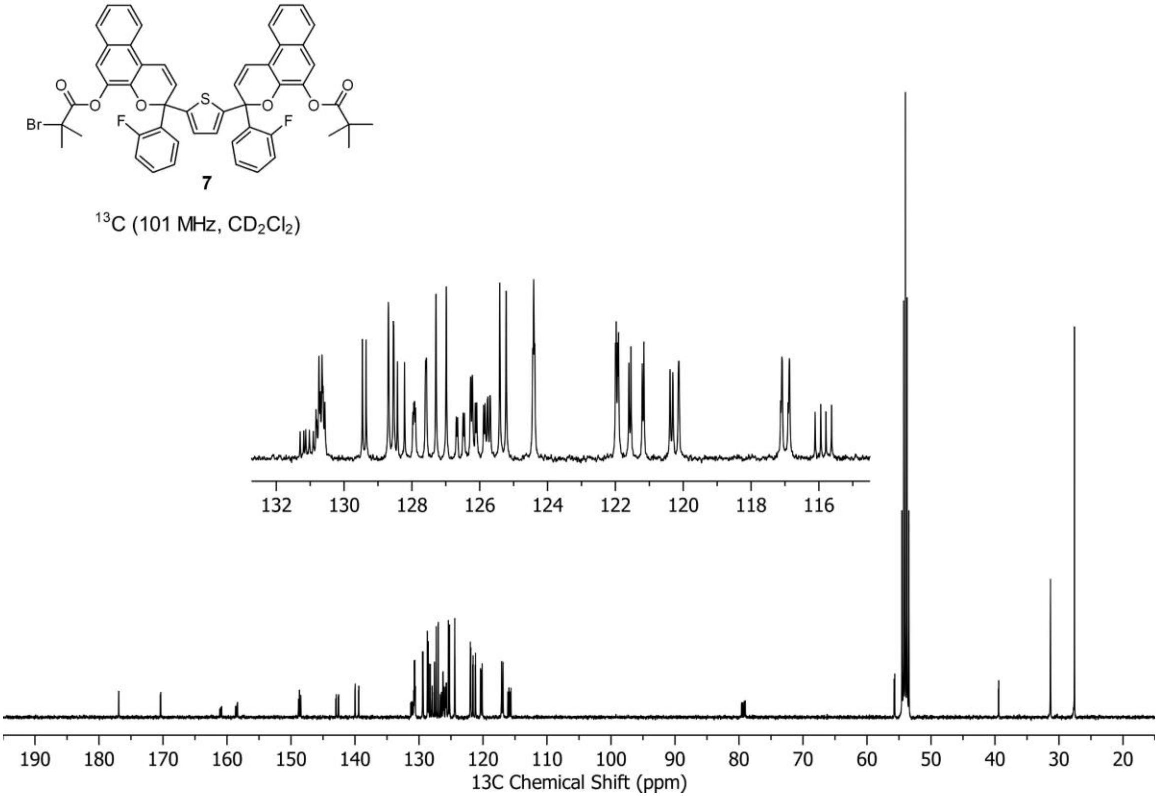

7

^{13}C (101 MHz, CD_2Cl_2)

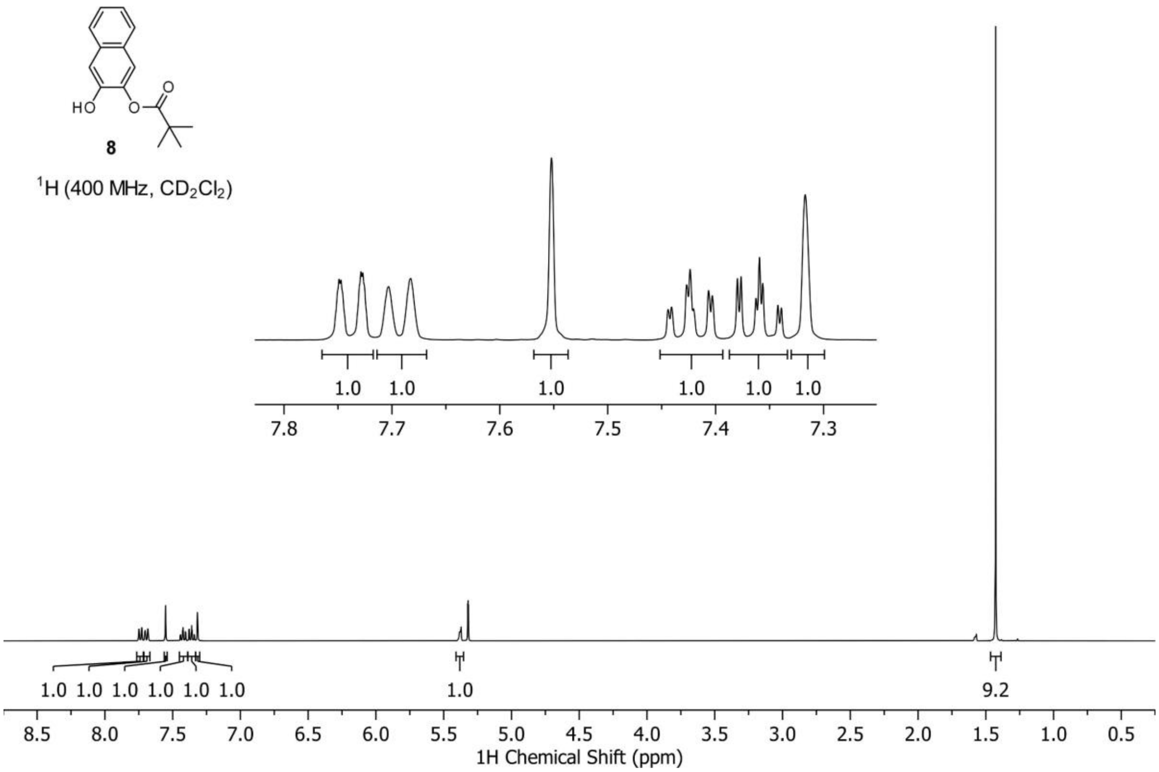
HO
O
O
8
^{1}H (400 MHz, CD$_2$Cl$_2$)
1.0 1.0 1.0 1.0 1.0 1.0
7.8 7.7 7.6 7.5 7.4 7.3
1.0 1.0 1.0 1.0 1.0 1.0 1.0 9.2
8.5 8.0 7.5 7.0 6.5 6.0 5.5 5.0 4.5 4.0 3.5 3.0 2.5 2.0 1.5 1.0 0.5
1H Chemical Shift (ppm)

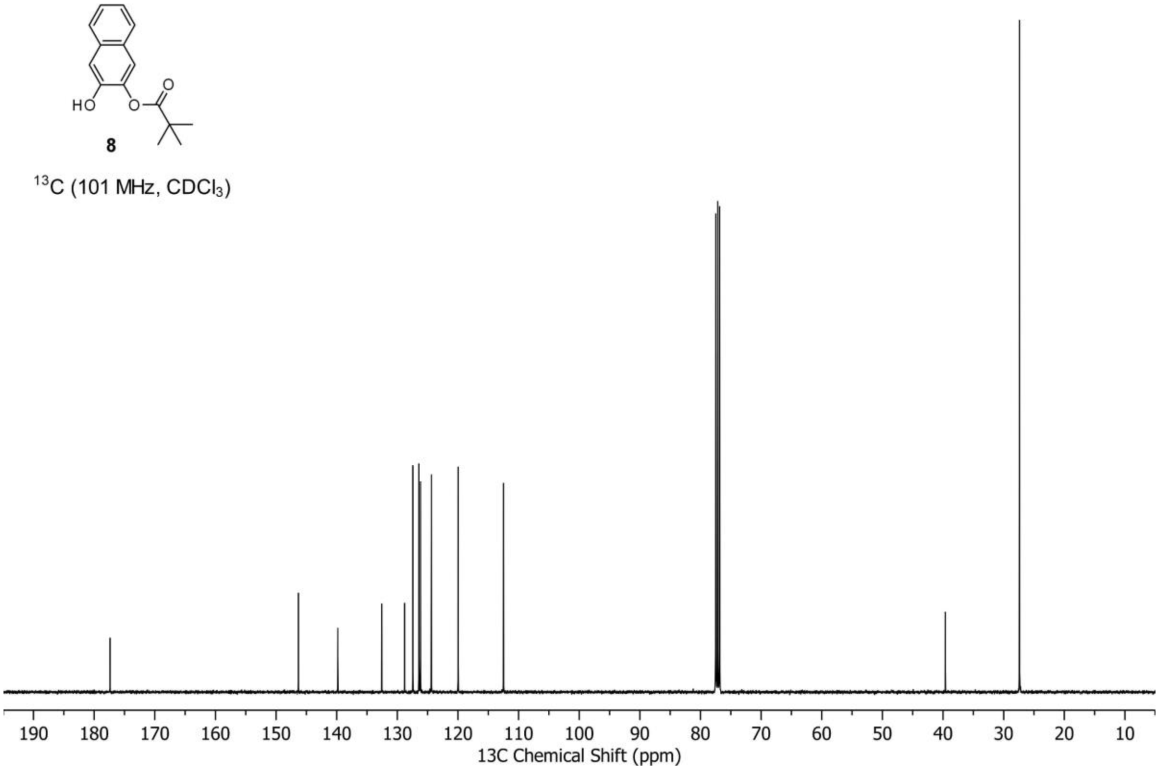
HO
O
O
8
^{13}C (101 MHz, CDCl$_3$)
190 180 170 160 150 140 130 120 110 100 90 80 70 60 50 40 30 20 10
13C Chemical Shift (ppm)

Chapter 5

MECHANICAL FORCE ENABLES AN ANOMALOUS DUAL RING-OPENING REACTION OF NAPHTHODIPYRAN

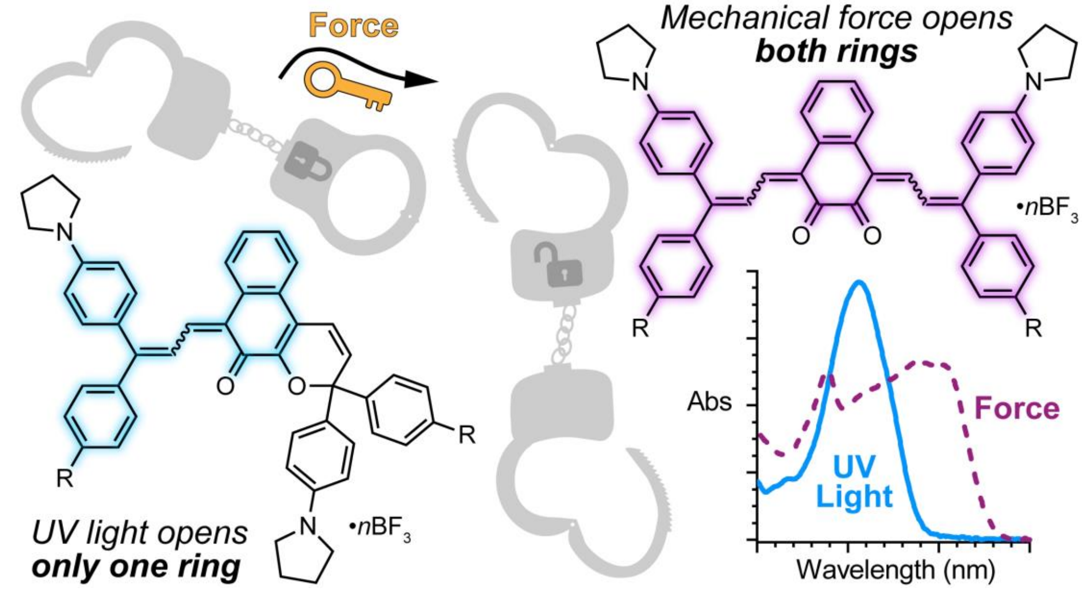

ABSTRACT: Multimodal mechanophores that exhibit complex mechanochromic behavior beyond the typical binary response are capable of distinguishing between multiple stress states through discrete changes in color. Naphthodipyran photoswitches contain two pyran rings fused to a central naphthalene core and represent a potentially promising framework for multimodal reactivity. However, the concurrent ring opening of both pyran moieties has previously proven inaccessible via photochemical activation. Here, we demonstrate that mechanical force supplied to naphthodipyran through covalently bound polymer chains generates the elusive dual ring-opened dimerocyanine product with unique near-infrared absorption properties. Trapping with boron trifluoride renders the merocyanine dyes thermally persistent and reveals unusual sequential ring-opening behavior that departs from the reactivity of previously studied mechanophores under the high strain rates imposed by ultrasound-induced solvodynamic chain extension.

This chapter has been adapted with permission from McFadden, M. E.; Osler, S. K.; Sun, Y.; Robb, M. J. Mechanical Force Enables an Anomalous Dual Ring-Opening Reaction of Naphthodipyran. *J. Am. Chem. Soc.* **2022**, *144*, 22391–22396. DOI: 10.1021/jacs.2c08817

Investigation

Mechanical force has been demonstrated to promote unusual reaction pathways that often diverge from those obtained under more conventional thermal or photochemical processes.[1–3] Stress-sensitive molecules termed mechanophores are designed to selectively transduce mechanical force into a wide variety of productive chemical transformations.[4] The development of mechanochromic mechanophores in particular has attracted significant interest as these molecular force probes enable the straightforward detection of stress and/or strain in polymers through changes in color. Naphthopyrans are molecular switches that undergo a ring-opening reaction upon external stimulation to generate intensely colored merocyanine dyes.[5] The photochemical reactivity of naphthopyrans has been studied extensively, producing a rich array of structurally diverse and commercially important photoswitches.[6] More recently it was discovered that the ring-opening reaction of naphthopyrans can be achieved using mechanical force.[7–9] While relatively rare, multimodal mechanophores that exhibit more complex mechanochromic behavior beyond a binary on–off response are capable of distinguishing between different stress states through discrete visual cues.[10–12] To this end, our group previously developed a bis-naphthopyran mechanophore incorporating two separate naphthopyran subunits joined by a conjugated linker that displays transient changes in color via a force-dependent dynamic equilibrium.[13]

Naphthodipyrans are compounds that contain two separate pyran rings fused to a central naphthalene nucleus. In contrast to bis-naphthopyrans, however, concurrent ring opening of both pyran units is inaccessible upon photochemical activation (Figure 5.1a).[14–16] Given the proclivity for mechanical force to facilitate otherwise unattainable reactions, we hypothesized that mechanochemical activation of naphthodipyran could enable the ring-opening reactions of both pyrans to produce the elusive dimerocyanine species with extended π-conjugation. The potential reactivity of naphthodipyran endowed with two mechanochemically active pyran rings and distinctly colored merocyanine states would render it an alluring new multimodal mechanophore.

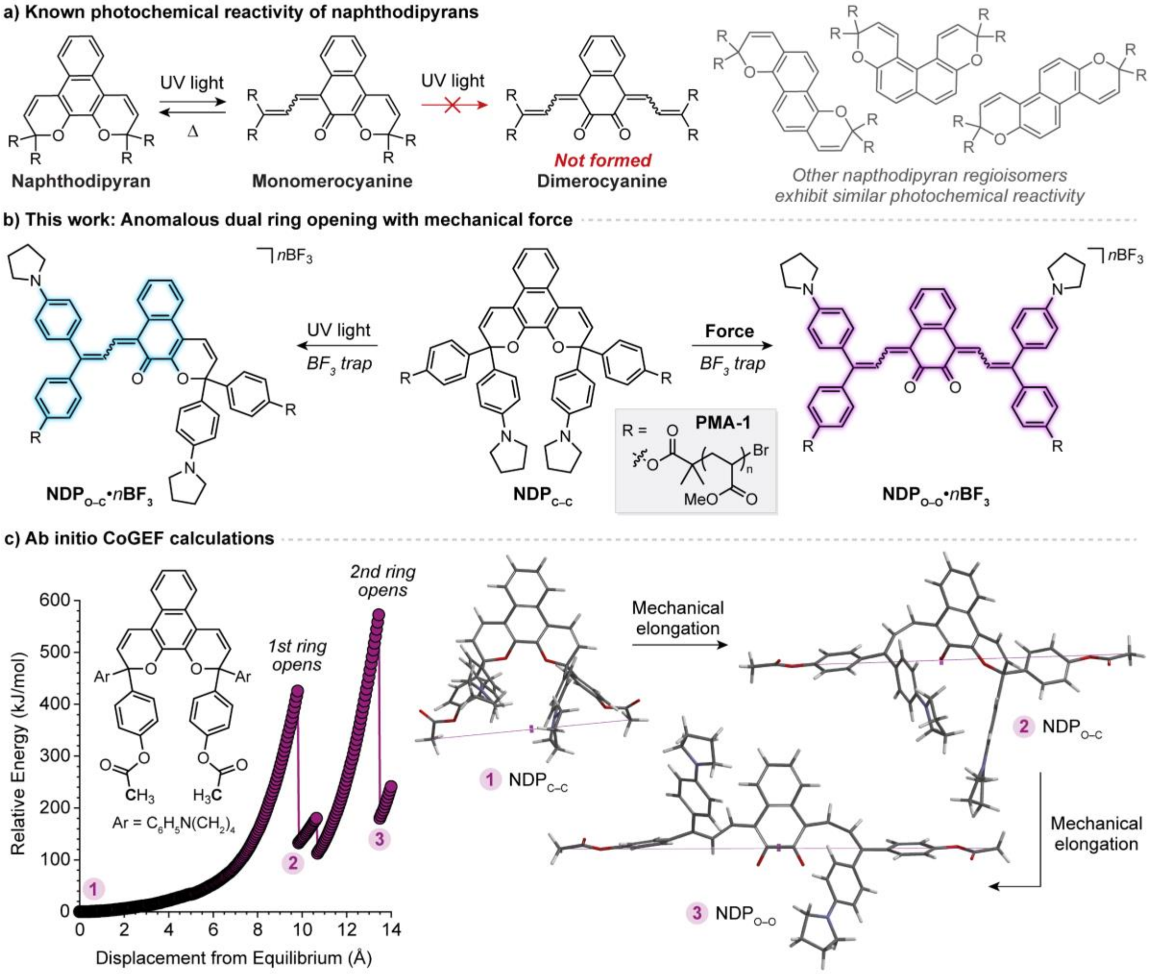

Figure 5.1. a) Naphthodipyran photoswitches undergo a single ring-opening reaction with UV light. b) Divergent photochemical and mechanochemical reactivity of a 3*H*-naphthodipyran moiety incorporated near the center of a polymer chain. c) CoGEF calculations (B3LYP/6-31G*) performed on a naphthodipyran model predict ring opening of both pyran units upon mechanical elongation.

The 3*H*-naphthodipyran scaffold was identified as an ideal target as it possesses the requisite geometry for transmitting force selectively across the C–O bonds in each pyran ring (Figure 5.1b). We initiated our investigation by examining the computationally predicted mechanochemical reactivity of a series of 3*H*-naphthodipyran derivatives using the *ab initio* constrained geometries simulate external force (CoGEF) method.[17,18] The calculations revealed that several substituted naphthodipyran derivatives were predicted to undergo a dual ring-opening reaction upon mechanical elongation, including a model incorporating aryl substituents with *para*-pyrrolidine groups (Figure 5.1c and Figure 5.2 and Figure 5.3). Conveniently, merocyanine dyes derived from simple 3*H*-napthopyrans containing similar tertiary amines on the aryl substituents can be trapped using $BF_3 \cdot Et_2O$,[19] precluding possible complications in reaction analysis due to fast thermal reversion processes.[9]

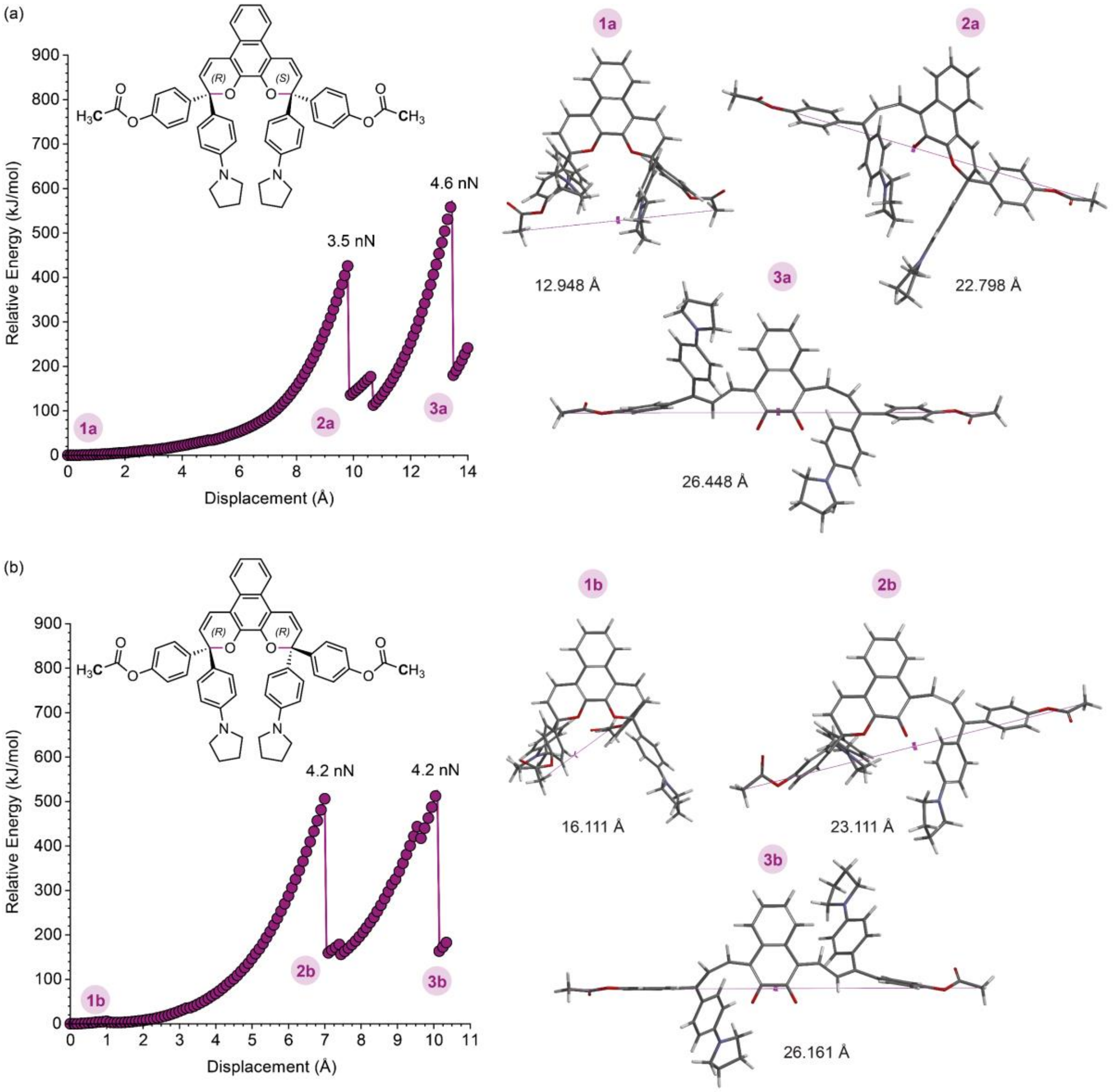

Figure 5.2. DFT calculations using the constrained geometries simulate external force (CoGEF) method at the B3LYP/6-31G* level of theory for truncated models reflecting two diastereomers of the naphthodipyran mechanophore in polymer **PMA-1**. (a) Calculations for the *R*,*S*-isomer predict the first ring-opening reaction with an $F_{\max}$ value of 3.5 nN followed by further elongation that results in the second ring-opening reaction at a predicted $F_{\max}$ value of 4.6 nN. (b) Calculations for the *R*,*R*-isomer predict the first ring-opening reaction with an $F_{\max}$ value of 4.2 nN followed by further elongation that results in the second ring-opening reaction at a predicted $F_{\max}$ value of 4.2 nN. The corresponding computed structures at various points of elongation are shown at right along with the associated constraint distance between the terminal methyl groups.

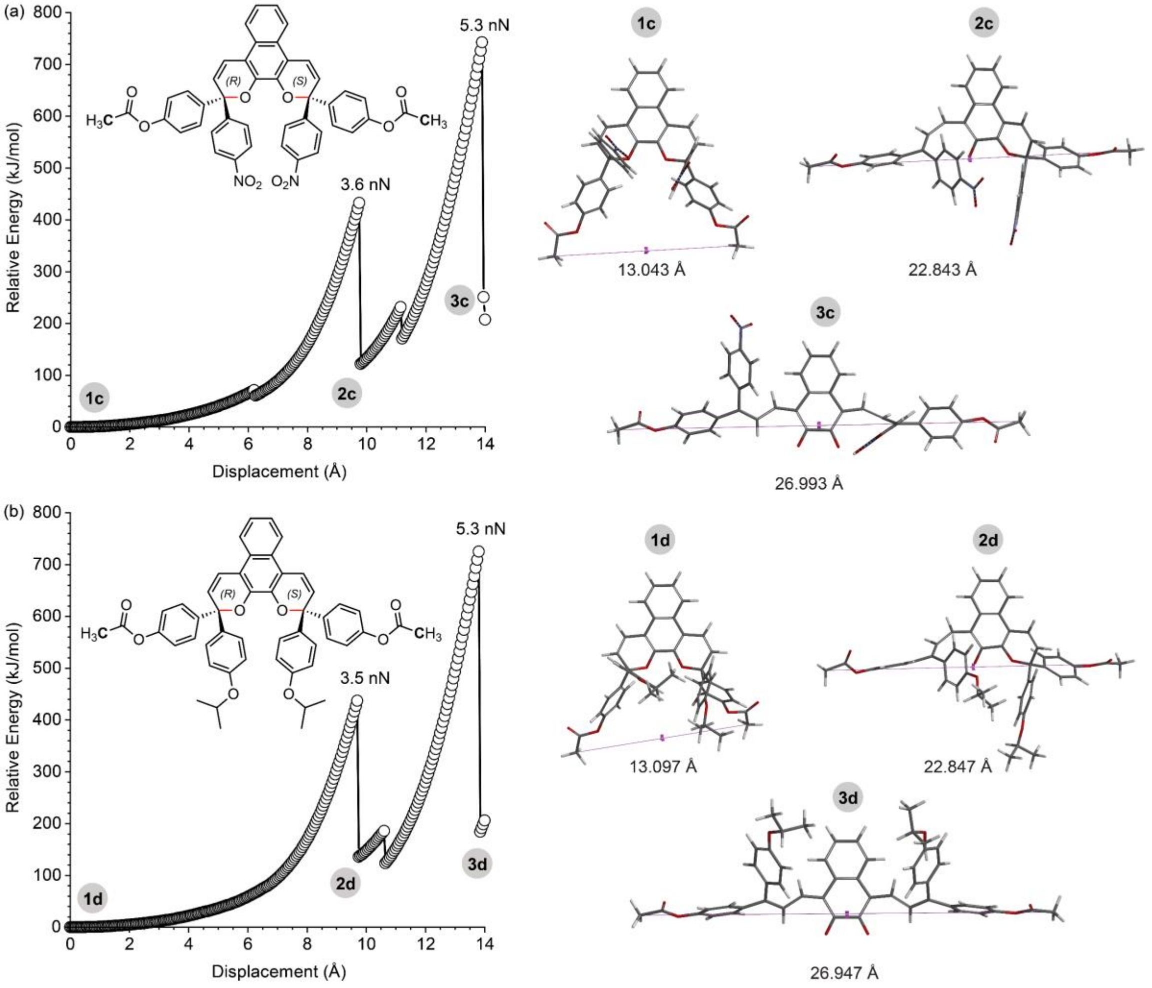

Figure 5.3. CoGEF calculations at the B3LYP/6-31G* level of theory predicting dual ring-opening reactions of naphthodipyran models with different aryl substituents. (a) Calculations for a nitro-substituted naphthodipyran predict the first and second ring-opening reactions with F_{max} values of 3.6 nN and 5.3 nN, respectively. (b) Calculations for an isopropoxy-substituted naphthodipyran predict the first and second ring-opening reactions with F_{max} values of 3.5 nN and 5.3 nN, respectively. The corresponding computed structures at various points of elongation are shown at right along with the associated constraint distance between the terminal methyl groups.

With these insights, we set out to experimentally investigate the mechanochemical reactivity of naphthodipyran using solution-phase ultrasonication for direct comparison to the photochemical reactivity under ultraviolet (UV) light. Polymers in dilute solution subjected to high intensity ultrasound undergo rapid extension with elongational forces maximized near the chain midpoint.[20] Therefore, we designed and synthesized a naphthodipyran bis-initiator that was used in the controlled radical polymerization of methyl acrylate to generate linear **PMA-1** (M_{n} = 185 kDa, *Đ* = 1.23) incorporating the naphthodipyran motif near the center of the polymer chain (Figure 5.1b, see the Experimental section for details). A continuous flow setup enabled monitoring of both mechanochemical and photochemical reactions in real-time by UV–vis–near-infrared absorption spectroscopy.[13,21] Photoirradiation of **PMA-1** (5.8 µM in CH_3CN stabilized with 30 mM BHT) with 365 nm UV light in the presence of $BF_3\cdot Et_2O$ (1.5 mM) generates a thermally persistent merocyanine dye with a single visible absorption peak at 625 nm (Figure 5.4a and Figure 5.5). Additional irradiation with UV light does not produce any further spectral changes (Figure 5.6). The absorption spectrum is consistent with the expected BF_3-coordinated monomerocyanine ($NDP_{O\text{–}C}\cdot nBF_3$) wherein one pyran ring has opened and the other remains closed (Figure 5.1b). The absorption maximum is bathochromically shifted by 65 nm in

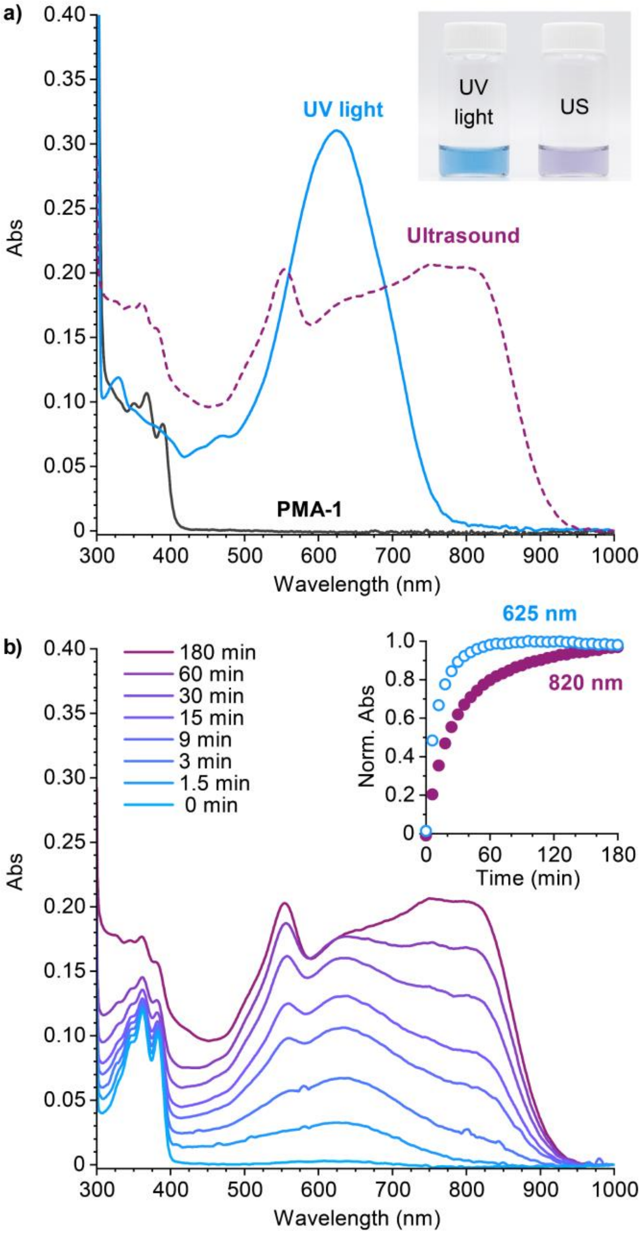

Figure 5.4. a) UV–vis–near-infrared absorption spectra of **PMA-1** (5.8 µM in CH_3CN, 30 mM BHT, 1.5 mM $BF_3\cdot Et_2O$) before and after photoirradiation with 365 nm UV light (15 min, −30 °C) or ultrasonication (180 min, −15 °C). The photograph shows the two solutions after activation with UV light or ultrasound (US). b) Spectral evolution during sonication of **PMA-1** and time-dependent absorption profiles at 625 nm and 820 nm characteristic of monomerocyanine $NDP_{O\text{–}C}\cdot nBF_3$ and dimerocyanine $NDP_{O\text{–}O}\cdot nBF_3$, respectively.

comparison to the spectrum acquired after photoirradiation of **PMA-1** in the absence of $BF_3 \cdot Et_2O$ (Figure 5.8), in excellent agreement with similar experiments performed on a simple 3*H*-naphthopyran.[19]

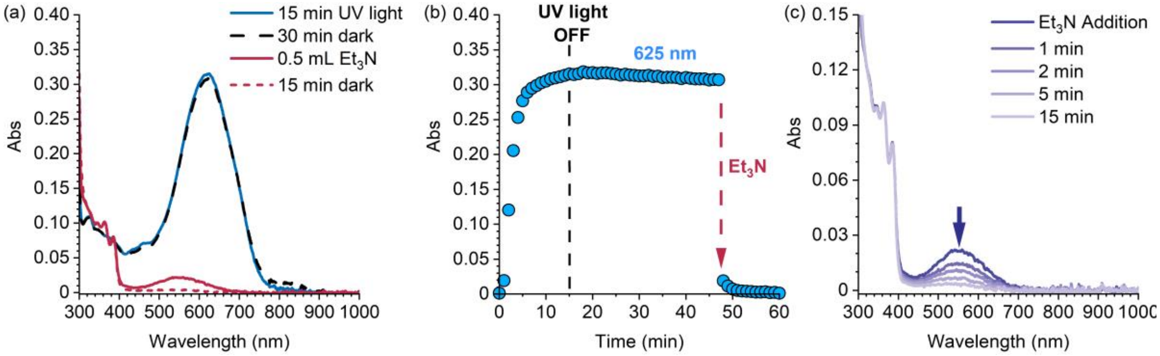

Figure 5.5. Photoirradiation (365 nm UV light) of **PMA-1** (5.8 µM in CH_3CN, 30 mM BHT, 1.5 mM $BF_3 \cdot Et_2O$, 15 min, −30 °C) produces a thermally persistent monomerocyanine species (NDP$_{\text{O–C}}$•nBF$_3$) that reverts upon the addition of triethylamine. (a) UV-vis-near-IR absorption spectra illustrate minimal thermal reversion of the merocyanine dye after 30 min post-activation. Addition of 0.5 mL Et_3N (140 mM final concentration) competitively coordinates BF_3, resulting in a small amount of unbound monomerocyanine (λ_{max} = 560 nm) that thermally reverts after 15 minutes. (b) Time-dependent absorption profiles at 625 nm for the process illustrated in (a). (c) Spectra demonstrating thermal reversion of residual unbound monomerocyanine following the addition of triethylamine. See Section 0 of the Experimental section for additional details.

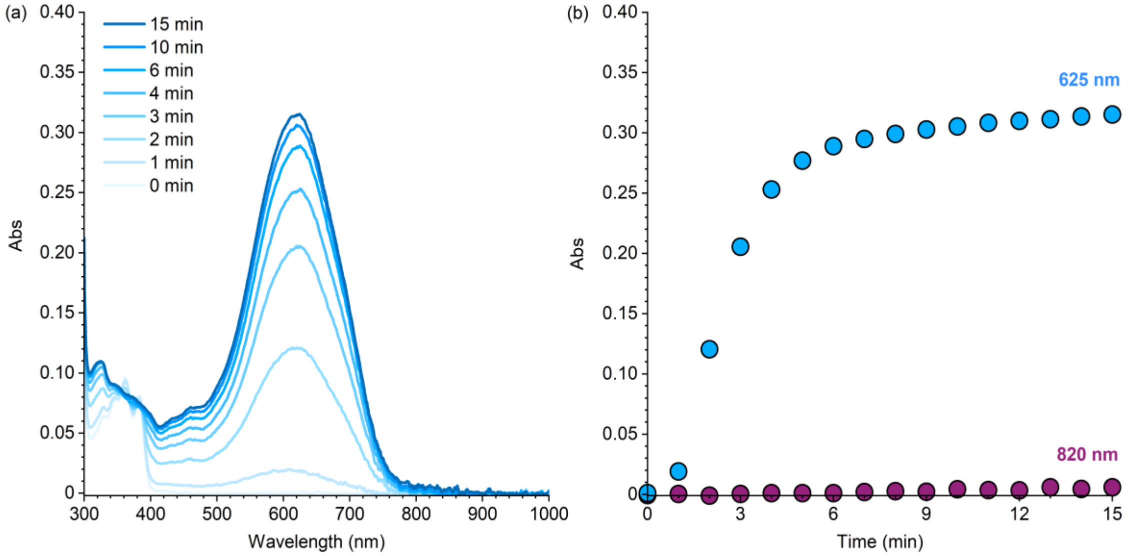

Figure 5.6. A single visible absorption feature with a peak maximum at 625 nm is observed upon extended UV photoirradiation (365 nm) of **PMA-1** (5.8 µM in CH_3CN with 30 mM BHT and 1.5 mM $BF_3 \cdot Et_2O$). (a) UV-vis-near-IR absorption spectra acquired over 15 min of photoirradiation. (b) Time-dependent absorption profiles at 625 and 820 nm.

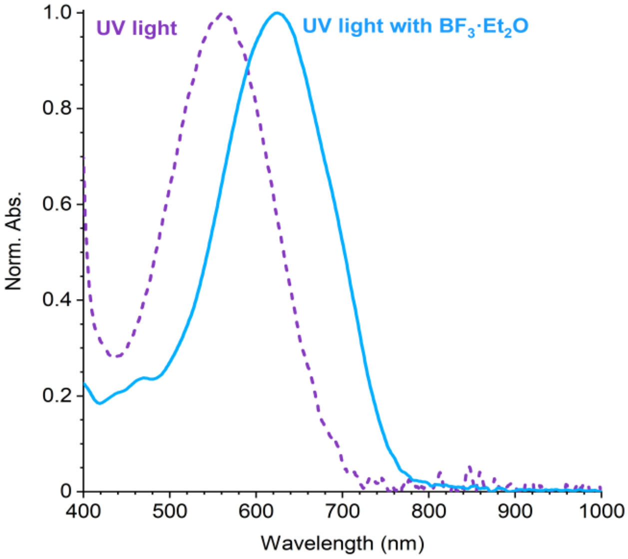

Figure 5.8. Photoirradiation of **PMA-1** (5.8 µM in CH_3CN, 30 mM BHT, −30 °C) using 365 nm UV light in the absence of a trapping agent produces a single visible absorption feature (λ_{max} = 560 nm), while irradiation under the same conditions in the presence of 1.5 mM BF_3·Et_2O produces a peak with λ_{max} = 625 nm.

In contrast to the photochemical reaction, ultrasound-induced mechanochemical activation of **PMA-1** with BF_3·Et_2O produces a unique absorption spectrum with longer wavelength features that extend into the near-infrared region, consistent with generation of the dimerocyanine product in which both pyran rings have opened ($NDP_{O\text{–}O}$·$n$$BF_3$) (Figure 5.4a). Again, the mechanochemical reaction product is thermally persistent (Figure 5.9). This unique absorption is not observed without BF_3·Et_2O, consistent with the anticipated transience of the untrapped dimerocyanine (Figure 5.7). Intriguingly, the kinetics of mechanochemical activation observed for the naphthodipyran

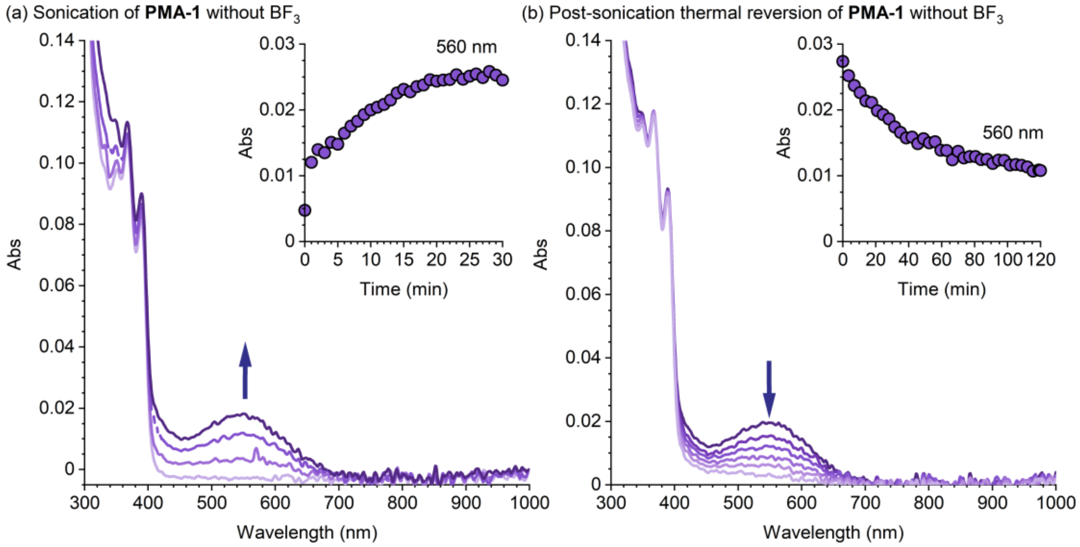

Figure 5.7. Absorption spectra obtained from a solution of **PMA-1** (5.8 µM in CH_3CN, 30 mM BHT) in the absence of any trapping agent upon (a) ultrasound-induced mechanochemical activation, and (b) subsequent thermal reversion. Ultrasound-induced mechanical activation results in the growth of a peak with λ_{max} = 560 nm. In contrast to the behavior in the presence of BF_3·Et_2O, these spectra are consistent with the exclusive accumulation of a monomerocyanine product.

mechanophore report colorimetrically on temporal exposure to ultrasound-induced mechanical force (Figure 5.4b). At early reaction times, only monomerocyanine product $NDP_{O–C}\cdot nBF_3$ is observed; the longer wavelength absorption features associated with dimerocyanine $NDP_{O–O}\cdot nBF_3$ emerge later in the reaction and increase with extended sonication time. This apparent sequential ring-opening behavior juxtaposes the mechanochemical reactivity of our previously studied bis-naphthopyran mechanophore.[13] In that system, bis-naphthopyran is converted directly to the bis-merocyanine species, consistent with recently discovered dynamic effects whereby the momenta derived from extrinsic force drive reaction trajectories that completely bypass reactive intermediates.[22] While the observed kinetic behavior of naphthodipyran is effectively indistinguishable from a sequential ring-opening mechanism, we speculate that both pyran rings open during a single chain extension event;[23] however, the lifetime of the free dimerocyanine may be too transient for efficient trapping. Instead, rapid reversion of the dimerocyanine species to the more stable monomerocyanine upon chain relaxation would permit BF_3 coordination. A second

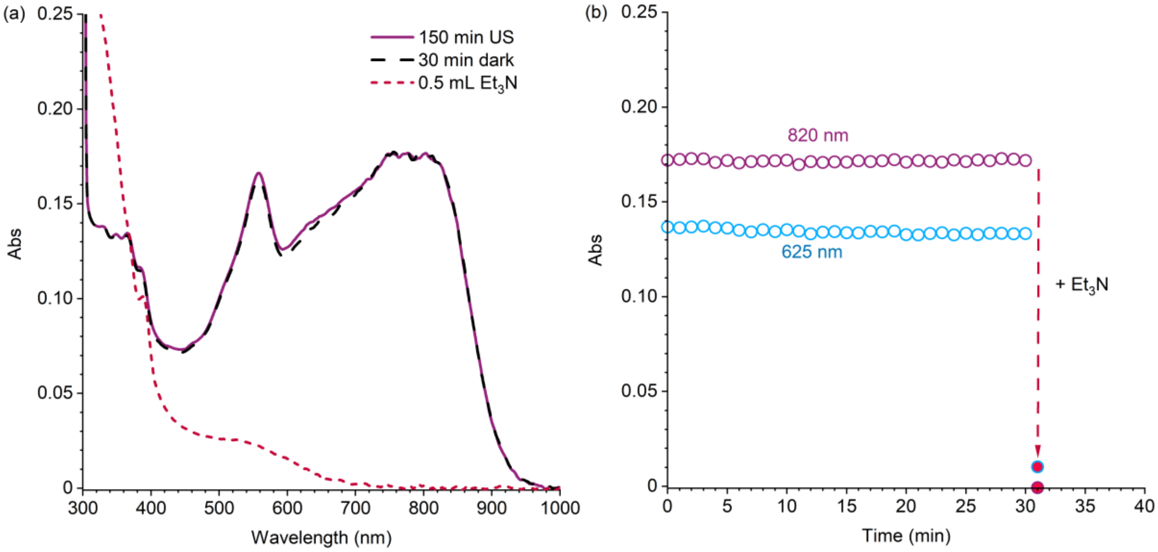

Figure 5.9. (a) UV-vis-near-IR absorption spectra measured after mechanochemical activation of **PMA-1** (5.8 µM in CH_3CN with 30 mM BHT and 1.5 mM $BF_3\cdot Et_2O$) and after the addition of triethylamine (140 mM final concentration). (b) Time-dependent absorption profiles at 625 and 820 nm acquired after mechanochemical activation illustrate no change in the dark until the addition of triethylamine. See Section 0 of the Experimental section for additional details.

Scheme 5.1. Proposed Mechanism for the Dual Ring-Opening Reaction of Naphthodipyran and Trapping Upon Ultrasound-Induced Mechanochemical Activation

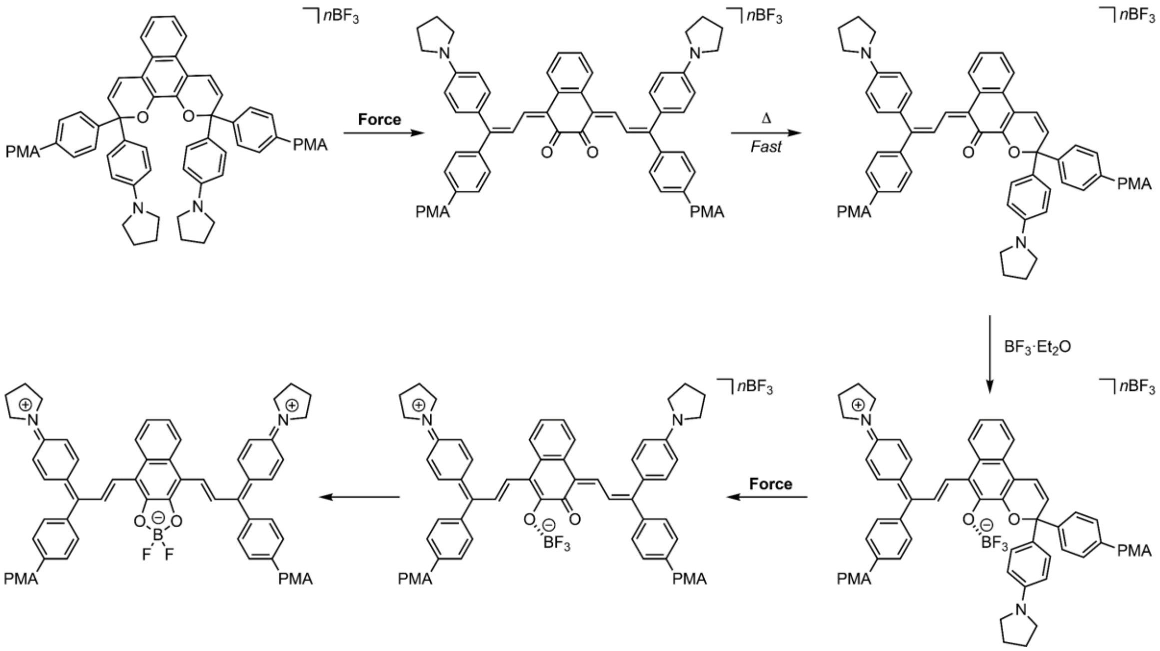

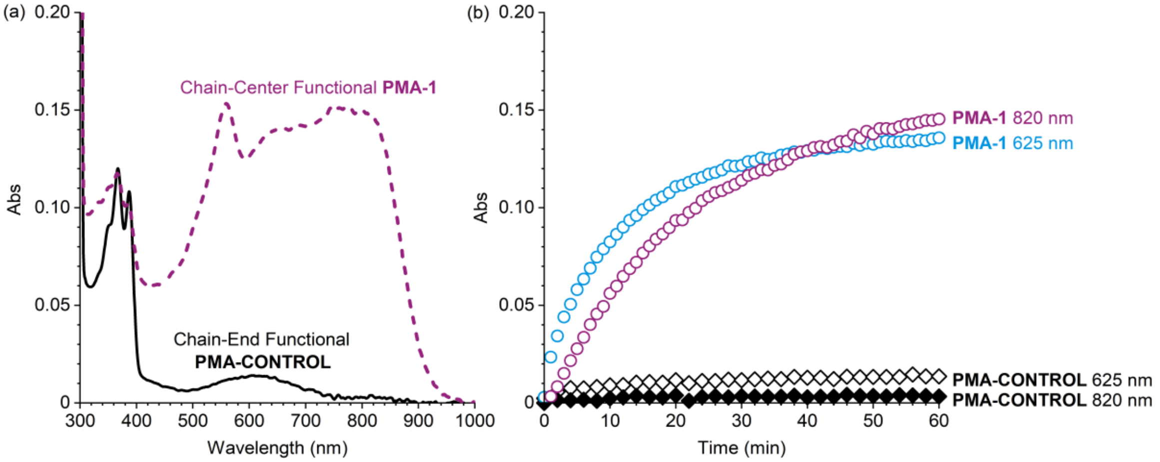

Figure 5.10. Comparison of sonication experiments performed on solutions (5.8 µM in CH_3CN with 30 mM BHT and 1.5 mM $BF_3\cdot Et_2O$) of **PMA-1** with a chain-centered naphthodipyran unit and the chain-end functional polymer **PMA-Control**. (a) UV-vis-near-IR absorption spectra acquired after ultrasonication of **PMA-1** for 60 min demonstrate significant merocyanine generation, in contrast to spectral data acquired under the same conditions for **PMA-Control**, supporting that ring-opening reactions of naphthodipyran are mechanochemically mediated. (b) Time-dependent absorption profiles at wavelengths characteristic of $\mathrm{NDP_{O–C}}\cdot n\mathrm{BF_3}$ (625 nm) and $\mathrm{NDP_{O–O}}\cdot n\mathrm{BF_3}$ (820 nm) showing an increase with sonication for **PMA-1**, with negligible changes observed for **PMA-Control**.

chain extension is then primed for a relatively facile intramolecular trapping process to form dimerocyanine $\mathrm{NDP_{O–O}}\cdot n\mathrm{BF_3}$ (Scheme 5.1). Although we cannot rule out that BF_3 coordination is necessary for the second ring-opening reaction, this hypothesis is inconsistent with the observed

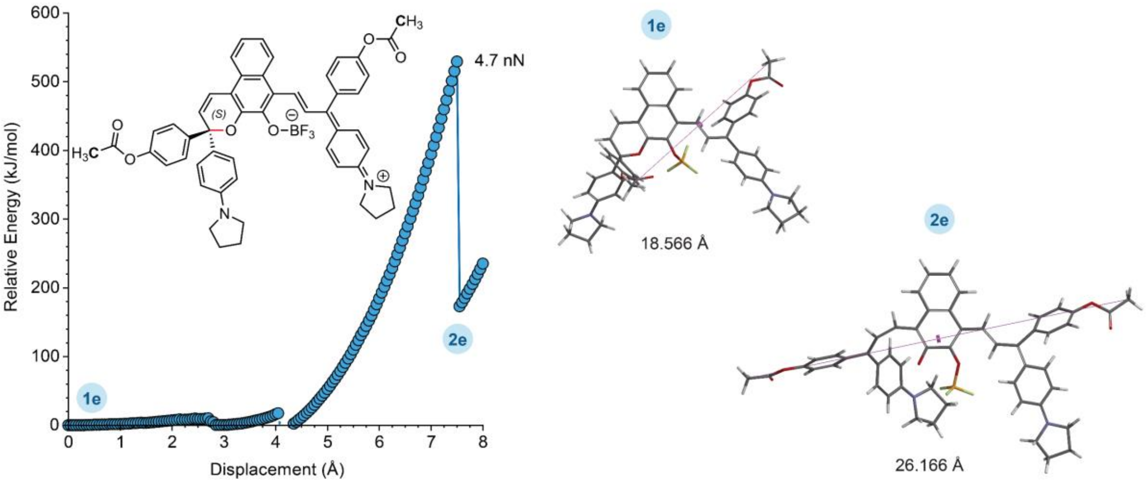

Figure 5.11. CoGEF calculations performed on a model reflecting one possible structure for the monomerocyanine complex $\mathrm{NDP_{O\text{–}C}}\cdot n\mathrm{BF_3}$ in the zwitterionic state. Calculations predict the mechanochemical ring-opening reaction of the pyran with an F_{max} value of 4.7 nN, similar to the Fmax values observed for the second ring-opening reaction in the absence of an explicit BF_3 binding model (see Figure 5.2). The corresponding computed structures at various points of elongation are shown at right along with the associated constraint distance between the terminal methyl groups. See Section III of the Experimental section for additional data and details.

photochemical reactivity of monomerocyanine $\mathrm{NDP_{O\text{–}C}}\cdot n\mathrm{BF_3}$ as well as DFT calculations employing an explicit BF_3-binding model (Figure 5.11).

Control experiments confirmed that the spectral changes ascribed to the dual ring-opening reactions of naphthodipyran are uniquely enabled by mechanical activation. First, negligible changes in absorption were observed upon ultrasonication of control polymer **PMA-Control** (M_n = 173 kDa, $Đ$ = 1.20) incorporating the naphthodipyran moiety at the chain-end, which is not subjected to mechanical force (Figure 5.10). Given the unprecedented nature of the second ring-opening reaction, we sought additional evidence to support that the transformation attributed to the conversion of $\mathrm{NDP_{O\text{–}C}}\cdot n\mathrm{BF_3}$ to $\mathrm{NDP_{O\text{–}O}}\cdot n\mathrm{BF_3}$ observed for **PMA-1** was indeed mechanochemically mediated (Figure 5.12a and Figure 5.14). A solution of **PMA-1** in the presence of $BF_3\cdot Et_2O$ was irradiated with 365 nm UV light to generate the trapped monomerocyanine species, $\mathrm{NDP_{O\text{–}C}}\cdot n\mathrm{BF_3}$, near the center of the polymer chains (Figure 5.12b). After 10 min, UV light was turned off and ultrasonication was applied to the solution, causing the attenuation of the absorption peak at 625 nm and the concurrent appearance of longer wavelength absorption features, consistent with the conversion of NDP$_{\mathrm{O–C}}$·nBF$_3$ to dimerocyanine NDP$_{\mathrm{O–O}}$·nBF$_3$. In direct contrast, the same experiment performed on **PMA-Control**, in which NDP$_{\mathrm{O–C}}$·nBF$_3$ is photochemically generated at the polymer chain-end, resulted in no changes to the absorption spectrum after initiation of ultrasound (Figure 5.12c). The time-dependent changes in absorbance at characteristic wavelengths of 625 nm (NDP$_{\mathrm{O–C}}$·nBF$_3$) and 820 nm (NDP$_{\mathrm{O–O}}$·nBF$_3$) clearly illustrate the divergent reactivity of **PMA-1** and **PMA-Control** upon ultrasonication and the critical role of mechanical force in the activation of the putative second ring-opening reaction (Figure 5.12d).

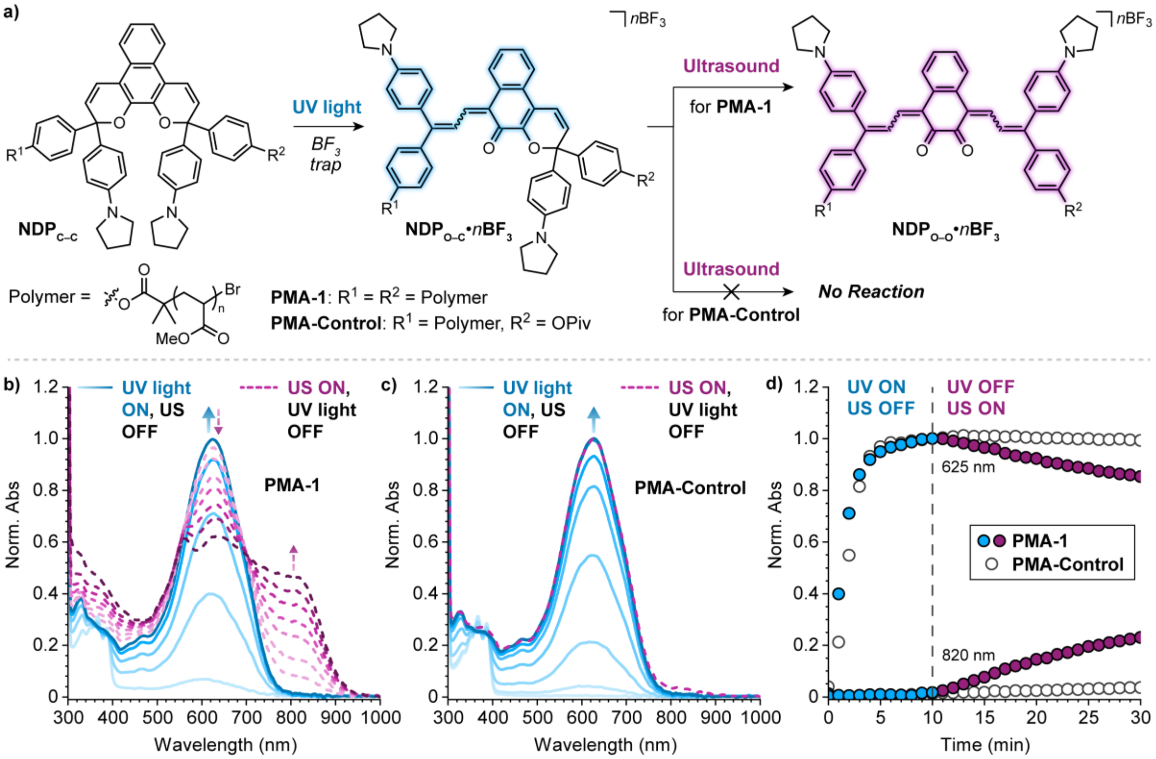

Figure 5.12. a) Reaction scheme for the photochemical conversion of naphthodipyran to monomerocyanine NDP$_{\mathrm{O–C}}$·nBF$_3$ in chain-centered polymer **PMA-1** and chain-end functional control polymer **PMA-control** followed by ultrasonication. UV–vis–near-infrared absorption spectra of b) **PMA-1**, and c) **PMA-Control** during photoirradiation and subsequent ultrasonication. d) Time-dependent changes in absorbance at characteristic wavelengths of 625 nm (NDP$_{\mathrm{O–C}}$·nBF$_3$) and 820 nm (NDP$_{\mathrm{O–O}}$·nBF$_3$) for **PMA-1** and **PMA-Control**.

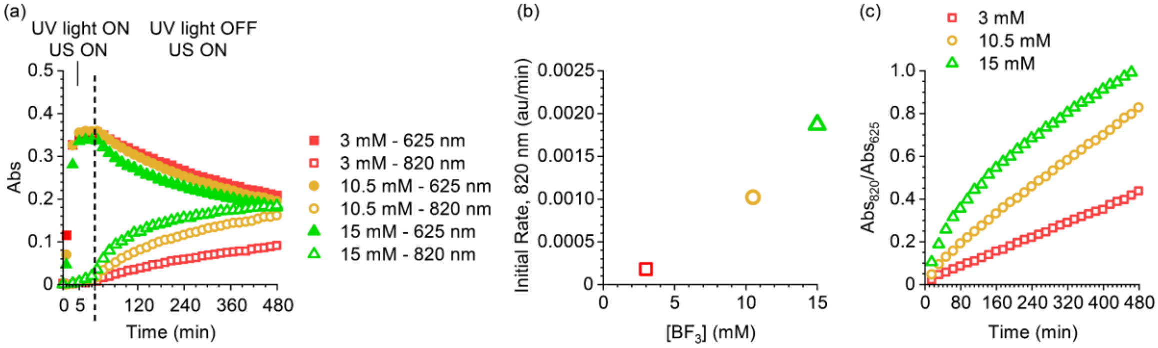

Figure 5.13. Characterization of the thermal conversion of monomerocyanine $\mathrm{NDP_{O\text{–}C}}\cdot n\mathrm{BF_3}$ to dimerocyanine $\mathrm{NDP_{O\text{–}O}\cdot nBF_3}$ with higher concentrations of $\mathrm{BF_3\cdot Et_2O}$, in contrast to the results presented above. Under constant ultrasonication, chain-end functional **PMA-Control** (5.8 µM in $\mathrm{CH_3CN}$, 30 mM BHT) was subjected to an initial period of UV photoirradiation (365 nm, 10 min) to produce the monomerocyanine, which is subsequently thermally converted to the dimerocyanine with higher concentrations of $\mathrm{BF_3\cdot Et_2O}$ (see Section V for details). (a) Concurrent photoirradiation and ultrasonication for 10 min produces monomerocyanine $\mathrm{NDP_{O\text{–}C}}\cdot n\mathrm{BF_3}$ (625 nm). Upon cessation of photoirradiation, $\mathrm{NDP_{O\text{–}C}}\cdot n\mathrm{BF_3}$ is thermally converted in the dark to $\mathrm{NDP_{O\text{–}O}}\cdot n\mathrm{BF_3}$ (820 nm) with increasing efficiency at higher $\mathrm{BF_3\cdot Et_2O}$ concentrations. (b) The initial rate of dimerocyanine formation as monitored at 820 nm as a function of $\mathrm{BF_3\cdot Et_2O}$ concentration. (c) Ratio of the absorbance values characteristic of $\mathrm{NDP_{O\text{–}O}}\cdot n\mathrm{BF_3}$ (820 nm) and $\mathrm{NDP_{O\text{–}C}}\cdot n\mathrm{BF_3}$ (625 nm) demonstrating changes in merocyanine distribution with varying concentrations of $\mathrm{BF_3\cdot Et_2O}$.

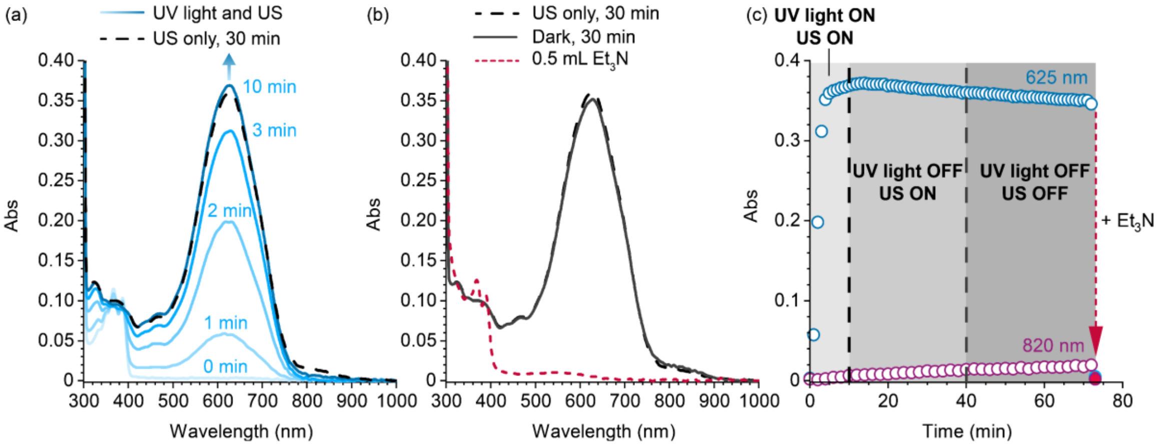

Figure 5.14. Concurrent photoirradiation (λ = 365 nm) and ultrasonication of chain-end functional **PMA-Control** (5.8 µM in $\mathrm{CH_3CN}$, 30 mM BHT, 1.5 mM $\mathrm{BF_3\cdot Et_2O}$) exclusively generates absorption features consistent with monomerocyanine $\mathrm{NDP_{O\text{–}C}\cdot BF_3}$. (a) Photoirradiation of **PMA-Control** under identical conditions experienced by **PMA-1** during ultrasonication produces only a single visible absorption feature with λ_{max} = 625 nm. Upon cessation of UV irradiation, negligible change in the spectrum is observed over 30 min of continued ultrasonication. (b) Minimal reversion of the photochemical merocyanine product occurs after 30 min in the dark, but the addition of 0.5 mL $\mathrm{Et_3N}$ (final concentration 140 mM) results in nearly complete reversion. (c) Time-dependent absorption profiles at wavelengths characteristic of $\mathrm{NDP_{O\text{–}C}}\cdot n\mathrm{BF_3}$ (625 nm) and $\mathrm{NDP_{O\text{–}O}}\cdot n\mathrm{BF_3}$ (820 nm) during the experiment.

To confirm the identity of the photochemical and mechanochemical reaction products, a series of characterization experiments were performed on the small molecule naphthodipyran bis-initiator used to prepare **PMA-1**. Photoirradiation of the naphthodipyran (0.5 mM in CD_3CN) with 365 nm UV light in the presence of $BF_3 \cdot Et_2O$ (1.5 mM) produces an absorption spectrum with a peak at 625 nm that matches the spectrum obtained upon similar treatment of **PMA-1** (Figure 5.15a). Analysis of the same sample by ^{1}H NMR spectroscopy supports the photochemical generation of monomerocyanine $\mathrm{NDP_{O–C}} \cdot n\mathrm{BF_3}$. The ^{1}H NMR spectrum of the naphthodipyran starting material contains two diagnostic doublets at 6.52 (J = 10.0 Hz) and 6.55 ppm (J = 9.9 Hz) corresponding to one pyran alkene proton on each of two diastereomers (Figure 5.15b). After UV irradiation, two new doublets appear concurrently at 8.70 ppm (J = 15.2 Hz) and 6.55 ppm (J = 10.0 Hz) characteristic of an olefin proton on the merocyanine and a unique pyran resonance, respectively (Figure 5.15c). We found that at sufficiently high concentrations of $BF_3 \cdot Et_2O$,

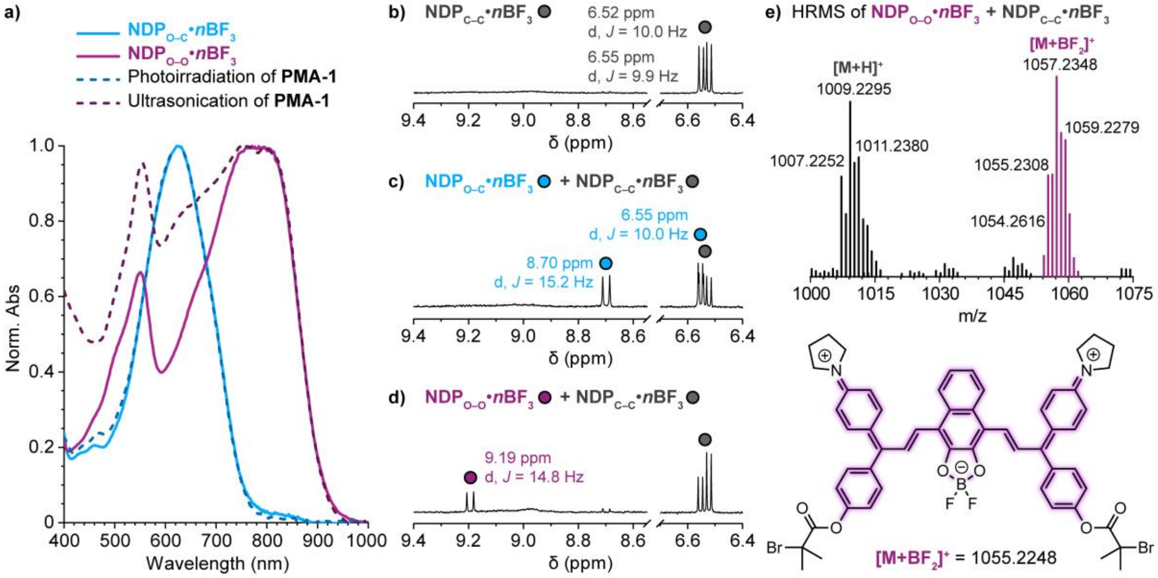

Figure 5.15. a) UV–vis–near-infrared absorption spectra of small molecule merocyanine species $\mathrm{NDP_{O–C}} \cdot \mathrm{nBF_3}$ and $\mathrm{NDP_{O–O}} \cdot \mathrm{nBF_3}$ obtained from the naphthodipyran bis-initiator compared to spectra of **PMA-1** after photochemical and mechanochemical activation. ^{1}H NMR spectra (CD_3CN, 600 MHz) of naphthodipyran bis-initiator b) in the presence of $BF_3 \cdot Et_2O$ (1.5 mM), and c) the same solution after irradiation with 365 nm UV light (2 min, rt). d) Similar experiment as (c) using 3.0 mM $BF_3 \cdot Et_2O$ illustrating the thermal conversion of $\mathrm{NDP_{O–C}} \cdot \mathrm{nBF_3}$ to $\mathrm{NDP_{O–O}} \cdot \mathrm{nBF_3}$. e) High resolution mass spectrometry data from a similar experiment as (d) using 7.8 mM $BF_3 \cdot Et_2O$ and the proposed structure of the trapped dimerocyanine cation.

photochemically-generated monomerocyanine $\mathrm{NDP}_{\mathrm{O–C}}\cdot n\mathrm{BF}_3$ is thermally converted to trapped dimerocyanine $\mathrm{NDP}_{\mathrm{O–O}}\cdot n\mathrm{BF}_3$ (Figure 5.13). This behavior is not unexpected[24] and is similar to the

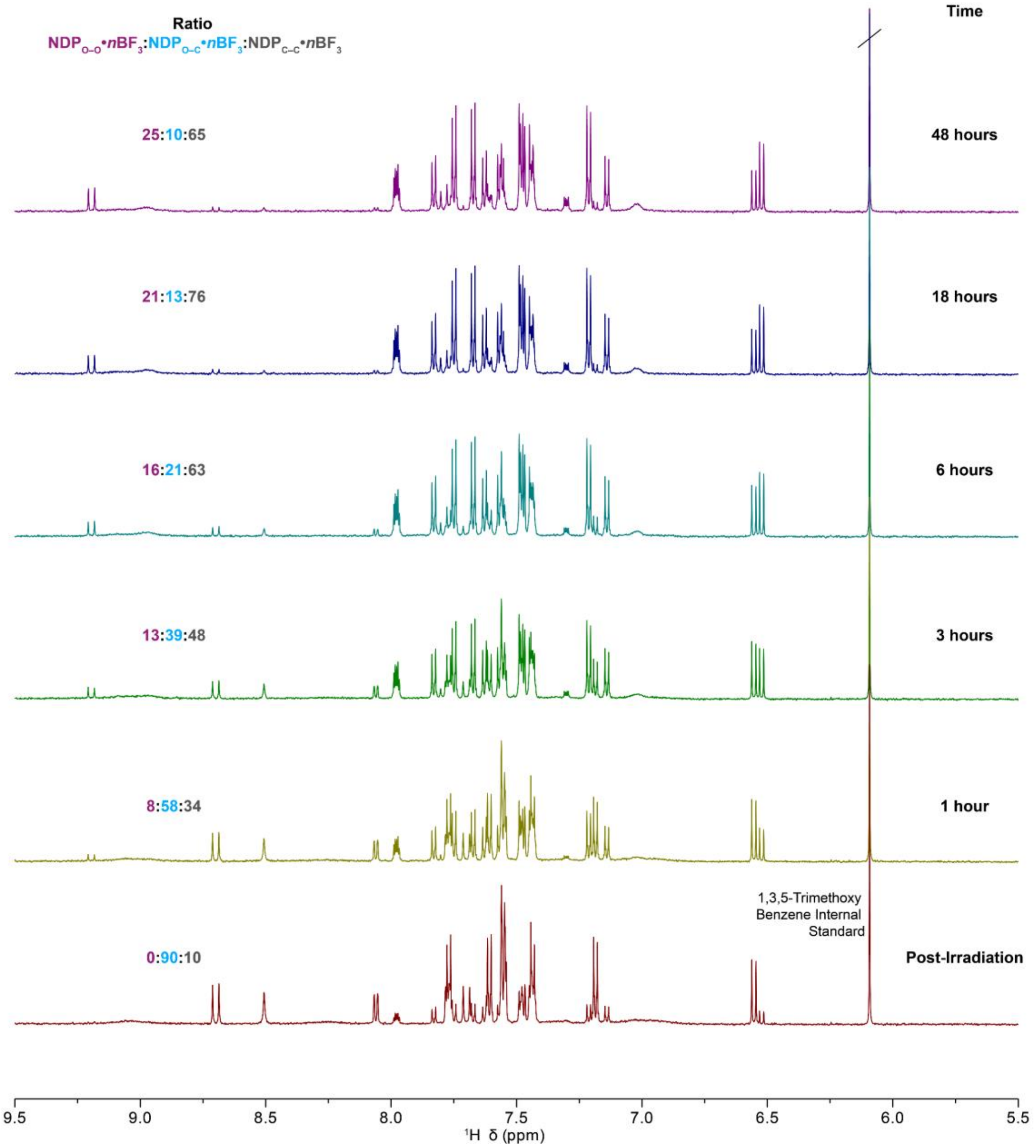

Figure 5.16. ^{1}H NMR (600 MHz) spectra characterizing conversion of $\mathrm{NDP}_{\mathrm{O–C}}\cdot n\mathrm{BF}_3$ to either $\mathrm{NDP}_{\mathrm{O–O}}\cdot n\mathrm{BF}_3$ or $\mathrm{NDP}_{\mathrm{C–C}}\cdot n\mathrm{BF}_3$. A solution of naphthodipyran bis-initiator (0.5 mM in $\mathrm{CD_3CN}$, 0.5 mM 1,3,5-trimethoxy benzene as internal standard, 3 mM $\mathrm{BF_3\cdot Et_2O}$) was irradiated with 365 nm UV light for 2 min at room temperature. While the formation of $\mathrm{NDP}_{\mathrm{O–O}}\cdot n\mathrm{BF}_3$ is not observed immediately after photoirradiation, the high concentration of $\mathrm{BF_3\cdot Et_2O}$ facilitates thermal ring-opening of the second pyran ring to generate $\mathrm{NDP}_{\mathrm{O–O}}\cdot n\mathrm{BF}_3$ over time in the dark. Loss of monomerocyanine $\mathrm{NDP}_{\mathrm{O–C}}\cdot n\mathrm{BF}_3$ was monitored by the attenuation of the doublet at 8.70 ppm (J = 15.2 Hz) while production of $\mathrm{NDP}_{\mathrm{O–O}}\cdot n\mathrm{BF}_3$ was monitored by growth of the doublet at 9.19 ppm (J = 14.8 Hz).

strong thermodynamic driving force responsible for acidochromic and metallochromic phenomena commonly observed for spiropyrans.[25] After increasing the concentration of $BF_3{\cdot}Et_2O$ to 3 mM, additional photoirradiation replenished the monomerocyanine, which is thermally transient without a sufficient stoichiometric excess of trapping agent. The ^{1}H NMR spectrum slowly transformed in the dark at room temperature with loss of the resonances associated with monomerocyanine $NDP_{O–C}{\cdot}nBF_3$ and the concomitant appearance of a new doublet at 9.19 ppm (J = 14.8 Hz) consistent with the formation of dimerocyanine $NDP_{O–O}{\cdot}nBF_3$ (Figure 5.15d and Figure 5.16). As illustrated in Figure 5.15a, the absorption spectrum of this chemically generated small molecule closely matches the spectrum acquired after extended ultrasonication of **PMA-1**, providing further support that the mechanochemical reaction product is the same dimerocyanine species.

High resolution mass spectrometry provided additional insight into the structure of trapped dimerocyanine $NDP_{O–O}{\cdot}nBF_3$. Analysis of a solution containing a mixture of small molecule

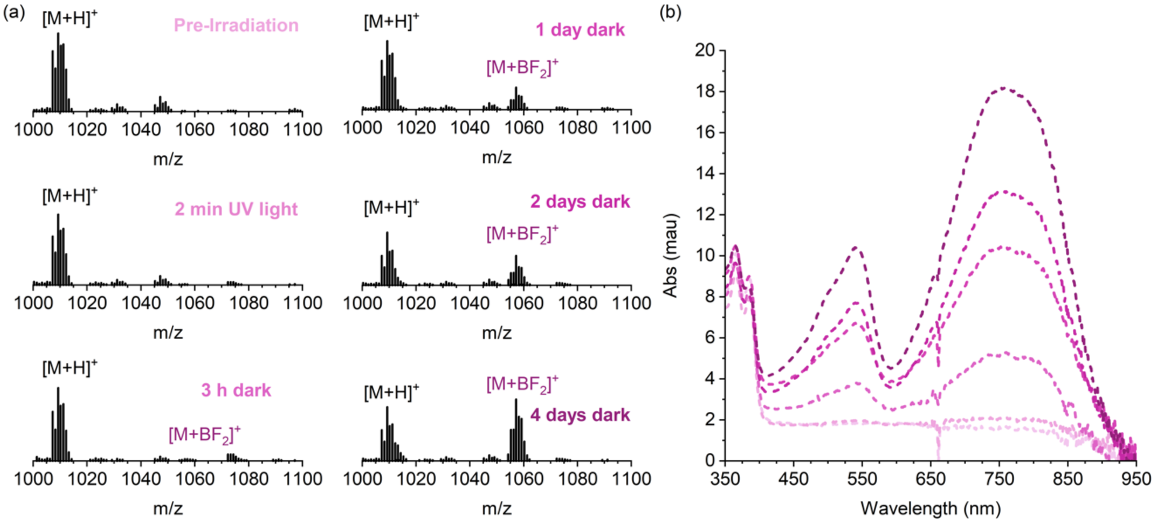

Figure 5.17. A solution of naphthodipyran bis-initiator (0.078 mM in CH_3CN with 7.8 mM $BF_3{\cdot}Et_2O$) was exposed to 365 nm UV light (2 min) and then stored in the dark and analyzed by high resolution mass spectroscopy and synchronous UV-vis absorption spectroscopy periodically over 4 days via direct injection with 70% CH_3CN/H_2O. (a) m/z and isotope patterns consistent with $[M+H]^+$ are present prior to irradiation, while those of $[M+BF_2]^+$ gradually increase after photoirradiation. (b) Concurrent with increases in the m/z signals for $[M+BF_2]^+$, absorption features consistent with dimerocyanine $NDP_{O–O}{\cdot}nBF_3$ are also observed. Notably, shorter wavelength absorption features characteristic of monomerocyanine $NDP_{O–C}{\cdot}nBF_3$ are not observed in the UV-vis-near-IR spectra, presumably due to hydrolytic instability in the 70% CH_3CN/H_2O environment used for direct injection analysis.

naphthodipyran bis-initiator and chemically-generated $\mathrm{NDP_{O\text{–}O}}\cdot n\mathrm{BF_3}$ analogous to the sample that produced the ^{1}H NMR spectrum in Figure 5.15d provided the expected $[\mathrm{M+H}]^+$ peaks of the naphthodipyran as well as new signals corresponding to $[\mathrm{M+BF_2}]^+$ (Figure 5.15e). In addition, synchronous visible–near-infrared absorption measurements demonstrated the concomitant increase of the long-wavelength spectral features characteristic of the trapped dimerocyanine product (Figure 5.17). We hypothesize that the 1,2-diketone subunit of the dimerocyanine species forms a thermally and hydrolytically stable 5-membered difluoroborocyclic motif upon reaction with BF_3, which is presumably charge-balanced by a BF_4^- counterion (Figure 5.15e). Taken together, these results provide compelling support for the mechanochemical generation of an unprecedented dimerocyanine species from naphthodipyran.

Mechanical force has been demonstrated to bias reaction pathways, promoting chemical transformations that are not attainable using light or heat alone. Our results complement previous work revealing that mechanochemical activation can formally override orbital symmetry rules conventionally governing the electrocyclic ring-opening reactions of benzocyclobutene and *gem*-dihalocyclopropranes to yield products with unexpected stereochemistry.[1,26] Here, we show that mechanical force promotes a previously elusive and photochemically inaccessible dual ring-opening reaction of naphthodipyran to generate a unique dimerocyanine species with near-infrared absorption. More broadly, we envision that the newly unveiled multimodal reactivity of naphthodipyran coupled with unusual mechanochemical activation kinetics will enable the design and study of additional mechanophores and force-responsive polymers with multicolor mechanochromic function.

Acknowledgements

Financial support from Caltech and an NSF CAREER award (CHE-2145791) is gratefully acknowledged. M.E.M. was supported by an NSF Graduate Research Fellowship (DGE-1745301) and a Barbara J. Burger Fellowship. S.K.O. was supported by an Institute Fellowship from Caltech.

We thank Dr. Scott Virgil and the Center for Catalysis and Chemical Synthesis of the Beckman institute at Caltech for access to equipment and Dr. David VanderVelde for technical assistance with NMR spectroscopy. We thank the Fu laboratory at Caltech for use of their mass spectrometer.

EXPERIMENTAL DETAILS

I. General Experimental Details

Reagents from commercial sources were used without further purification unless otherwise stated. Methyl acrylate was passed through a short plug of basic alumina to remove inhibitor immediately prior to use. Copper wire was soaked in 1 M HCl for 10 min and then rinsed consecutively with water and acetone immediately prior to use. Dry THF and toluene were obtained from a Pure Process Technology solvent purification system. All reactions were performed under a N_2 or Ar atmosphere unless specified otherwise. Column chromatography was performed on a Biotage Isolera system using SiliCycle SiliaSep HP flash cartridges.

NMR spectra were recorded using a 400 MHz Bruker spectrometer with Prodigy broadband cryoprobe, a 400 MHz Bruker spectrometer with broadband iProbe, a Varian 400 MHz spectrometer with broadband OneProbe, or a 600 MHz Varian spectrometer with 5 mm triple resonance inverse probe. All ^{1}H NMR spectra are reported in δ units, parts per million (ppm), and were measured relative to the signals for residual chloroform (7.26 ppm), acetone (2.05 ppm), dichloromethane (5.32 ppm), DMSO (2.50), or THF (3.58 ppm) in deuterated solvent. All ^{13}C NMR spectra were measured in deuterated solvents and are reported in ppm relative to the signals for chloroform (77.16 ppm), acetone (206.26 ppm), dichloromethane (53.84 ppm), DMSO (39.52 ppm), or THF (67.57 ppm). All ^{19}F NMR spectra were acquired using a 1 s relaxation delay (unless noted otherwise) in CD_3CN and are reported in ppm relative to the signals for internal standard 1,2,3,4,5-pentafluorotoluene (–143.9 ppm, –160.2 ppm, and –164.7 ppm) and $CFCl_3$ (0.0 ppm). Multiplicity and qualifier abbreviations are as follows: s = singlet, d = doublet, t = triplet, m = multiplet, br = broad, app = apparent.

High resolution mass spectra (HRMS) were obtained via direct injection on an Agilent 1260 Infinity II Series HPLC coupled to a 6230 LC/TOF system in electrospray ionization (ESI+) mode.

Analytical gel permeation chromatography (GPC) was performed using an Agilent 1260 series pump equipped with two Agilent PLgel MIXED-B columns (7.5 x 300 mm), an Agilent 1200 series diode array detector, a Wyatt 18-angle DAWN HELEOS light scattering detector, and a Optilab rEX differential refractive index detector. The mobile phase was THF at a flow rate of 1 mL/min. Molecular weights and molecular weight distributions were calculated by light scattering using a dn/dc value of 0.062 mL/g (25 °C) for poly(methyl acrylate).

UV-Vis absorption spectra were recorded on a Thermo Scientific Evolution 220 spectrometer.

Ultrasound experiments were performed using a Vibra Cell 505 liquid processor equipped with a 0.5-inch diameter solid probe (part #630-0217), sonochemical adapter (part #830-00014), and a Suslick reaction vessel made by the Caltech glass shop (analogous to vessel #830-00014 from Sonics and Materials). Polymer solutions were continuously sampled for UV-vis analysis using a Cole Parmer Masterflex L/S pump system (item #EW-77912-10) composed of an L/S pump head (part #77390-00) and L/S precision variable speed drive (part #07528-20) using 4x6 mm PTFE tubing (part #77390-60) and a quartz flow-through cell (Starna, part #583.4-Q-10/Z8.5), which was connected using M6-threaded PTFE tubing (Starna, part #M6-SET). A Thermo Scientific EK45 Immersion Cooler (part #3281452) was used to maintain a constant temperature bath for sonication and photoirradiation experiments. Photoirradiation with UV light was performed using a DR/9W-UVA 365 nm lamp under ambient conditions unless indicated otherwise.

II. Synthetic Details

Scheme 5.2. Synthesis of all compounds used in this study.

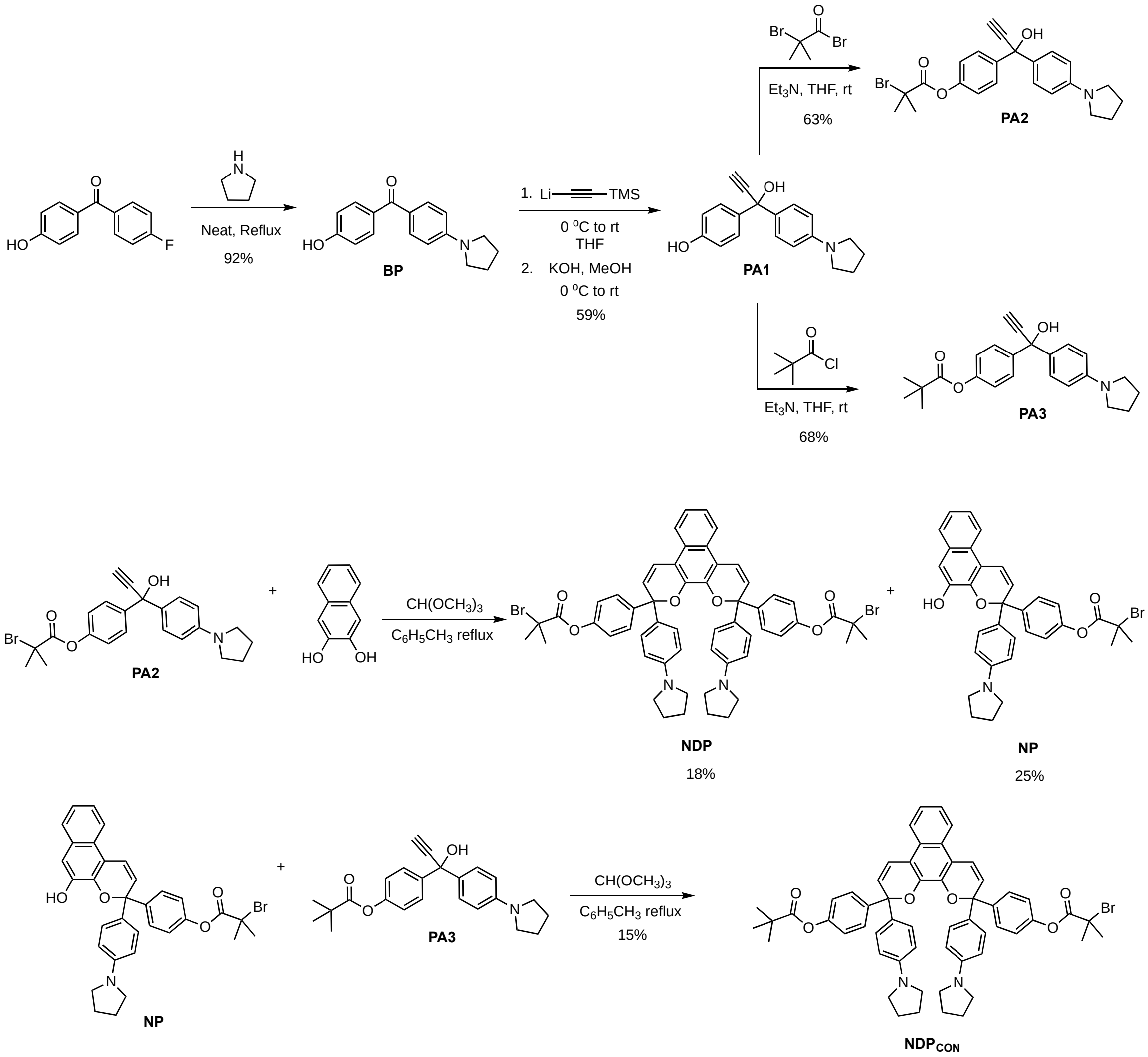

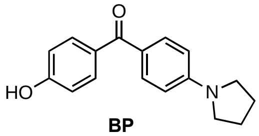

BP

(4-hydroxyphenyl) (4-(pyrrolidin-1-yl)phenyl)methanone (BP). A flame-dried two-neck round-bottom flask equipped with a stir bar and condenser was charged with 4-fluoro-4'-hydroxybenzophenone (3.998 g, 18.50 mmol). The flask was purged and backfilled with N_2 (3x), followed by the addition of pyrrolidine (10 mL, 120 mmol). After stirring at reflux for 17 h, the flask was removed from heat, and the crude mixture was partitioned between water (300 mL) and ethyl acetate (300 mL). The aqueous layer was extracted with additional ethyl acetate (3 x 300 mL) and the combined organic layers were washed with water (200 mL) then dried over $MgSO_4$, filtered, and concentrated under reduced pressure to afford the title product as a yellow-orange solid (4.55 g, 92%).

TLC (5% MeOH/CH_2Cl_2): $R_f = 0.29$

^{1}H NMR (400 MHz, DMSO-d_6) δ: 7.59 (d, *J* = 8.8 Hz, 2H), 7.54 (d, *J* = 8.6 Hz, 2H), 6.86 (d, *J* = 8.6 Hz, 2H), 6.56 (d, *J* = 8.9 Hz, 2H), 3.28 (m, 4H), 1.94 (m, 4H).

^{13}C{^{1}H} NMR (101 MHz, DMSO-d_6) δ: 192.8, 160.8, 150.5, 132.2, 131.8, 129.8, 124.1, 115.0, 110.8, 47.4, 25.1.

HRMS (ESI, *m/z*): calcd for $[C_{17}H_{18}NO_2]^+$ $(M+H)^+$, 268.1332; found, 268.1337.

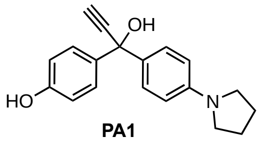

PA1

4-(1-hydroxy-1-(4-(pyrrolidin-1-yl) phenyl)prop-2-yn-1-yl)phenol (PA1). A flame-dried round-bottom flask equipped with a stir bar was charged with dry THF (120 mL) and trimethylsilyl acetylene (6.60 mL, 46.8 mmol) and cooled to 0 °C in an ice bath. *n*-Butyllithium (2.5 M in hexanes, 18.7 mL, 46.8 mmol) was then added slowly with stirring. After 2 h, benzophenone **BP** (5.0 g, 19 mmol) was added via syringe as a slurry in dry THF. The flask was then allowed to warm to room temperature. After stirring for 17 h, the flask was cooled to 0 °C and a solution of KOH (5.0 g, 94 mmol) in methanol (20 mL) was added. The mixture was warmed to room temperature and stirred in the dark for 4 h. The flask was again cooled to 0 °C, diluted with ethyl acetate (500 mL), and then neutralized with a saturated solution of ammonium chloride (700 mL). The organic layer was washed with brine (100 mL) and dried over Na_2SO_4, filtered over a glass frit, and concentrated under reduced pressure. Recrystallization from diethyl ether/hexanes provided the title compound as pale pink crystals (3.24 g, 59%).

TLC (25% EtOAc/hexanes): $R_f = 0.38$

^{1}H NMR (400 MHz, Acetone-*d*$_6$) δ: 7.39 (d, *J* = 8.7 Hz, 2H), 7.36 (d, *J* = 8.8 Hz, 2H), 6.75 (d, *J* = 8.7 Hz, 2H), 6.47 (d, *J* = 8.8 Hz, 2H), 5.15 (br s, 1H), 3.26 – 3.21 (m, 4H), 3.20 (d, *J* = 0.6 Hz, 1H), 2.02 – 1.94 (m, 4H).

^{13}C{^{1}H} NMR (101 MHz, Acetone-*d*$_6$) δ: 206.2, 157.3, 148.2, 138.8, 133.9, 128.2, 127.8, 115.2, 111.7, 89.2, 75.0, 73.8, 48.2, 26.0.

HRMS (ESI, *m/z*): calcd for $[C_{19}H_{20}NO_2]^+$ $(M+H)^+$, 294.1489; found, 294.1495.

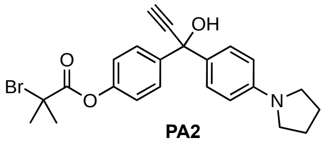

PA2

4-(1-hydroxy-1-(4-(pyrrolidin-1-yl)phenyl)prop-2-yn-1-yl)phenyl 2-bromo-2-methylpropanoate (PA2). An oven-dried two neck 100 mL round bottom flask equipped with a stir bar was charged with propargyl alcohol **PA1** (2.48 g, 8.45 mmol). The flask was evacuated and backfilled with N_2 three times. Anhydrous THF (45 mL) and triethylamine (1.80 mL, 12.9 mmol) were added in sequence via syringe, followed by the dropwise addition of α-bromoisobutyryl bromide (1.20 mL, 9.76 mmol) over 10 min under N_2 at room temperature. After stirring for 16 h, the reaction was diluted with ethyl acetate (150 mL) and washed with water (100 mL), saturated aqueous $NaHCO_3$ (2 x 100 mL), and brine (100 mL). The organic layer was dried over Na_2SO_4, filtered, and concentrated under reduced pressure. The solid was redissolved in a minimal amount of dichloromethane and then precipitated into hexanes. The precipitate was isolated by filtration using a nylon membrane and washed with hexanes to provide the title compound as a beige solid (2.37 g, 63%).

TLC (25% EtOAc/hexanes): $R_f = 0.69$

^{1}H NMR (400 MHz, CD_2Cl_2) δ: 7.63 (dd, J = 8.8, 0.9 Hz, 2H), 7.38 (dd, J = 8.9, 0.9 Hz, 2H), 7.08 (dd, J = 8.8, 0.9 Hz, 2H), 6.51 (d, J = 8.6 Hz, 2H), 3.26 (ddd, J = 6.6, 5.0, 2.0 Hz, 4H), 2.92 (m, 2H), 2.06 (s, 6H), 1.98 (ddd, J = 6.7, 4.8, 1.9 Hz, 4H).

$^{13}C\{^1H\}$ NMR (101 MHz, CD_2Cl_2) δ: 170.6, 150.4, 148.2, 143.9, 131.2, 127.5, 127.3, 121.0, 111.5, 87.1, 75.4, 74.1, 56.1, 48.0, 30.8, 25.8.

HRMS (ESI, *m/z*): calcd for $[C_{23}H_{25}{}^{79}Br\,NO_3]^+$ $(M+H)^+$, 442.1012; found, 442.1010.

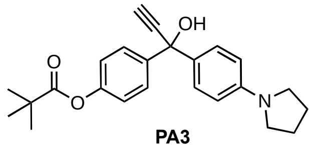

PA3

4-(1-hydroxy-1-(4-(pyrrolidin-1-yl)phenyl)prop-2-yn-1-yl)phenyl pivalate (PA3). A flame-dried two neck 100 mL round bottom flask equipped with a stir bar was charged with propargyl alcohol **PA1** (500 mg, 1.70 mmol). The flask was evacuated and backfilled with N_2 three times. Anhydrous THF (25 mL) and triethylamine (0.36 mL, 2.6 mmol) were added in sequence via syringe under N_2. The flask was cooled to 0 °C in an ice bath, then pivaloyl chloride (0.27 mL, 2.2 mmol) was added dropwise via syringe over 10 min and the solution was warmed to room temperature. After stirring for 20 h, the reaction was diluted with ethyl acetate (100 mL) and washed with saturated aqueous $NaHCO_3$ (100 mL), water (100 mL), and brine (50 mL). The organic layer was dried over Na_2SO_4, filtered over a glass frit, and precipitated from hexanes to provide the title compound as a gray solid (436 mg, 68%).

<u>TLC (25% EtOAc/hexanes):</u> $R_f = 0.75$

<u>^{1}H NMR (400 MHz, Acetone-d_6) δ:</u> 7.61 (d, J = 8.8 Hz, 2H), 7.38 (d, J = 8.8 Hz, 2H), 7.03 (d, J = 8.7 Hz, 2H), 6.48 (d, J = 8.9 Hz, 2H), 5.39 (d, J = 0.9 Hz, 1H), 3.28 (d, J = 0.6 Hz, 1H), 3.27 – 3.18 (m, 5H), 2.01 – 1.94 (m, 4H), 1.32 (s, 9H).

<u>^{13}C{^{1}H} NMR (101 MHz, Acetone-d_6) δ:</u> 177.2, 151.2, 148.4, 145.21, 145.18, 133.4, 128.0, 127.9, 121.8, 111.9, 88.7, 88.6, 75.7, 73.9, 73.8, 48.3, 39.6, 27.4, 26.1.

<u>HRMS (ESI, *m/z*):</u> calcd for $[C_{24}H_{28}NO_3^+]^+$ $(M+H)^+$, 378.2064; found, 378.2069.

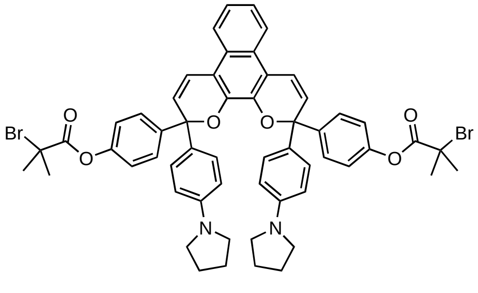

NDP

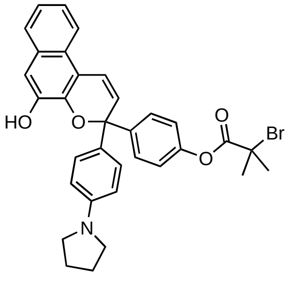

NP

(2,11-bis(4-(pyrrolidin-1-yl)phenyl)-2,11-dihydrobenzo[*f*]pyrano[3,2-*h*]chromene-2,11-diyl)bis(4,1-phenylene) bis(2-bromo-2-methylpropanoate) (NDP) and **4-(5-hydroxy-3-(4-(pyrrolidin-1-yl)phenyl)-3*H*-benzo[*f*]chromen-3-yl)phenyl 2-bromo-2-methylpropanoate (NP).** A flame-dried two neck round bottom flask equipped with a stir bar and reflux condenser was charged with propargyl alcohol **PA2** (507 mg, 1.14 mmol) and 2,3-dihydroxynaphthalene (79 mg, 0.49 mmol). The flask was evacuated and backfilled with N_2 three times followed by the sequential addition of toluene (5 mL) and trimethyl orthoformate (0.30 mL, 2.7 mmol) via syringe. The reaction was heated to reflux. After stirring for 6 h, the reaction was cooled to room temperature, concentrated under reduced pressure with celite, and purified directly by column chromatography on silica gel (20–

100% CH_2Cl_2/hexanes) to produce the title compounds **NDP** as a pale blue solid (mixture of two diastereomers, 88 mg, 18%) and **NP** as a dark blue solid (71 mg, 25%).

NDP:

TLC (70% CH_2Cl_2/hexanes): $R_f = 0.66$

^{1}H NMR (400 MHz, CD_2Cl_2) δ: 7.91 (dd, *J* = 6.5, 3.3 Hz, 2H), 7.66 (d, *J* = 8.7 Hz, 2H), 7.60 (d, *J* = 8.7 Hz, 2H), 7.44 – 7.33 (m, 6H), 7.30 (d, *J* = 10.0 Hz, 2H), 7.15 (d, *J* = 8.7 Hz, 2H), 7.10 (d, *J* = 8.6 Hz, 2H), 6.53 (d, *J* = 8.8 Hz, 2H), 6.46 (d, *J* = 8.8 Hz, 2H), 6.33 (dd, *J* = 9.9, 1.5 Hz, 2H), 3.32 – 3.17 (m, 8H), 2.09 (s, 6H), 2.07 (s, 6H), 2.00 – 1.92 (m, 8H).

^{13}C{^{1}H} NMR (101 MHz, CD_2Cl_2) δ: 170.6, 170.5, 150.2, 150.1, 147.9, 147.8, 144.5, 144.3, 141.79, 141.77, 130.9, 129.2, 129.1, 128.5, 128.4, 128.3, 128.2, 125.54, 125.52, 124.82, 124.81, 122.1, 121.0, 120.9, 119.9, 119.8, 116.5, 111.48, 111.45, 82.7, 82.6, 56.2, 56.1, 48.0, 47.9, 30.85, 30.83, 25.82, 25.79.

HRMS (ESI, *m/z*): calcd for $[C_{56}H_{53}{}^{79}Br_2N_2O_6{}^+]^+$ $(M+H)^+$, 1007.2265; found, 1007.2256.

NP:

TLC (70% CH_2Cl_2/hexanes): $R_f = 0.50$

^{1}H NMR (400 MHz, THF-*d*8) δ: 8.20 (br s, 1H), 7.88 (dd, *J* = 7.5, 1.6 Hz, 1H), 7.56 (d, *J* = 8.7 Hz, 2H), 7.51 (dd, *J* = 8.0, 1.6 Hz, 1H), 7.35 (d, *J* = 10.0 Hz, 1H), 7.31 (d, *J* = 8.8 Hz, 2H), 7.24 – 7.15 (m, 2H), 7.08 (d, *J* = 8.8 Hz, 2H), 7.05 (s, 1H), 6.45 (d, *J* = 8.8 Hz, 2H), 6.29 (d, *J* = 9.9 Hz, 1H), 3.24 – 3.16 (m, 4H), 2.02 (s, 6H), 1.98 – 1.90 (m, 4H).

^{13}C{^{1}H} NMR (101 MHz, THF-*d*8) δ: 170.4, 151.3, 148.6, 147.2, 144.8, 142.3, 131.4, 131.3, 129.8, 129.4, 129.2, 127.6, 125.7, 124.7, 124.3, 122.2, 121.2, 120.5, 116.1, 112.1, 111.9, 84.2, 57.0, 48.4, 30.9, 26.4.

HRMS (ESI, *m/z*): calcd for $[C_{33}H_{31}{}^{79}BrNO_4{}^+]^+$ $(M+H)^+$, 584.1431; found, 584.1460.

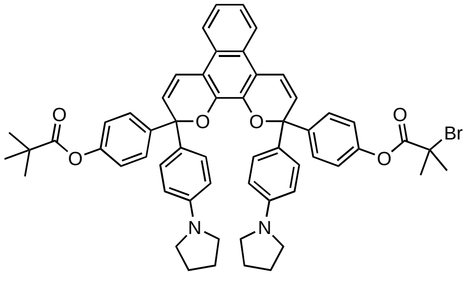

NDP$_{CON}$

4-(11-(4-((2-bromo-2-methylpropanoyl)oxy)phenyl)-2,11-bis(4-(pyrrolidin-1-yl)phenyl)-2,11-dihydrobenzo[*f*]pyrano[3,2-*h*]chromen-2-yl)phenyl pivalate (NDP$_{CON}$). A flame-dried two neck round bottom flask equipped with a stir bar and reflux condenser was charged with propargyl alcohol **PA3** (63 mg, 0.17 mmol) and naphthopyran **NP** (50 mg, 0.086 mmol). The flask was evacuated and backfilled with N_2 three times followed by the sequential addition of toluene (3 mL) and trimethyl orthoformate (0.07 mL, 0.64 mmol) via syringe. The reaction was heated to reflux. After stirring for 11 h, the reaction was cooled to room temperature, concentrated under reduced pressure with celite, and purified directly by column chromatography on silica gel (20–100% CH_2Cl_2/hexanes) to produce the title compound as a pale blue solid (mixture of two diastereomers, 12 mg, 15%).

TLC (70% CH_2Cl_2/hexanes): $R_f = 0.67$

^{1}H NMR (400 MHz, CD_2Cl_2) δ: 7.88 (dd, *J* = 6.4, 3.3 Hz, 2H), 7.60 (d, *J* = 8.8 Hz, 1H), 7.55 (app t, *J* = 8.7 Hz, 2H), 7.51 (d, *J* = 8.7 Hz, 1H), 7.40 – 7.24 (m, 8H), 7.10 (d, *J* = 8.8 Hz, 1H), 7.03 (app t, *J* = 8.5 Hz, 2H), 6.97 (d, *J* = 8.7 Hz, 1H), 6.49 (d, *J* = 8.4 Hz, 2H), 6.43 (d, *J* = 8.3 Hz, 2H), 6.29 (d, *J* = 10.0 Hz, 1H), 6.29 (d, *J* = 9.9 Hz, 1H), 3.33 – 3.15 (m, 8H), 2.05 (s, 3H), 2.04 (s, 3H), 1.92 – 1.82 (m, 8H), 1.33 (s, 4.5H), 1.32 (s, 4.5H).

^{13}C{^{1}H} NMR (101 MHz, CD_2Cl_2) δ: 177.35, 177.28, 170.61, 170.55, 150.6, 150.5, 150.2, 150.1, 148.0, 147.8, 144.4, 144.3, 143.7, 143.6, 141.8, 130.9, 129.3, 129.2, 129.13, 129.08, 128.5, 128.4, 128.24, 128.19, 128.1, 128.0, 125.5, 124.8, 122.1, 121.5, 121.4, 121.0, 120.9, 119.8, 119.7, 116.5, 116.4, 111.4, 82.7, 82.63, 82.61, 56.2, 56.1, 48.0, 39.3, 30.8, 27.27, 27.25, 25.8.

HRMS (ESI, *m/z*): calcd for $[C_{57}H_{56}BrN_2O_6]^+$ $(M+H)^+$, 943.3316; found, 943.3361.

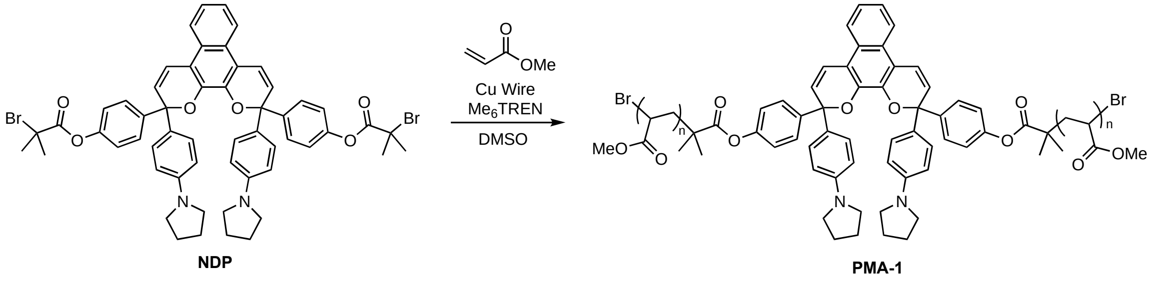

Synthesis of PMA-1. Polymers were synthesized by controlled radical polymerization following the procedure by Nguyen *et al.*[27] A flame-dried Schlenk flask was charged with freshly cut 20 G copper wire (2 cm), naphthodipyran bis-initiator **NDP** (11.6 mg, 0.0115 mmol), DMSO (2.80 mL), and methyl acrylate (2.80 mL, 31.1 mmol). The flask was sealed and the solution was degassed via three freeze-pump-thaw cycles, then backfilled with nitrogen and warmed to room temperature. Me$_6$TREN (30 µL, 0.11 mmol) was added via microsyringe and the reaction was stirred at room temperature for 2.5 h. Upon completion of the polymerization, the flask was opened to atmosphere and diluted with a minimal amount of CH_2Cl_2. The polymer was precipitated 3x into methanol cooled with dry ice and then dried under vacuum to afford the title polymer as a tacky pale purple solid (0.933 g, 33% yield). M_n = 185 kg/mol, *Đ* = 1.23. The GPC trace is shown below in Figure 5.18.

Synthesis of PMA-1$_{174}$. A second polymer closely matching **PMA-1** was prepared for additional experiments following the same procedure as above using freshly cut 20 G copper wire (2 cm), naphthodipyran bis-initiator **NDP** (10.0 mg, 0.00991 mmol), DMSO (3.6 mL), methyl acrylate (3.5 mL, 38.9 mmol), and Me$_6$TREN (15 µL, 0.056 mmol). Reaction for 2.33 h afforded the title polymer as a tacky pale purple solid (0.998 g, 29% yield). M_n = 174 kg/mol, $Đ$ = 1.14. The GPC trace is shown below in Figure 5.18.

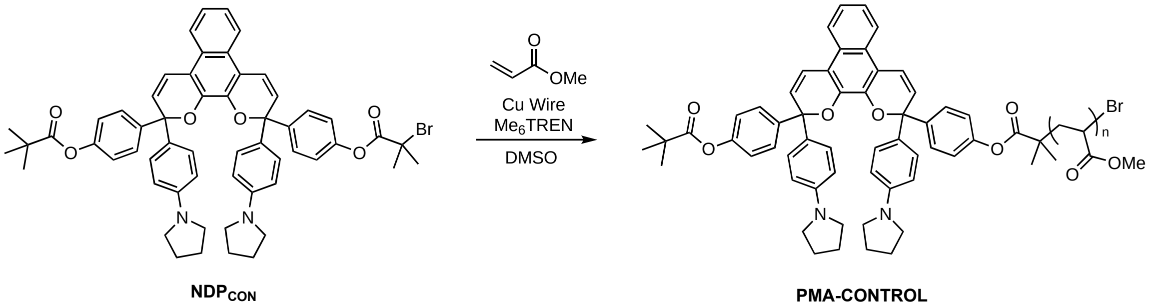

Synthesis of PMA-Control. A flame-dried Schlenk flask was charged with freshly cut 20 G copper wire (2 cm), naphthodipyran initiator **NDP_{CON}** (10.1 mg, 0.017 mmol), DMSO (3.20 mL), and methyl acrylate (3.20 mL, 35.5 mmol). The flask was sealed, and the solution was degassed via three freeze-pump-thaw cycles, then backfilled with nitrogen and warmed to room temperature. Me_6TREN (14 µL, 0.052 mmol) was added via microsyringe and the reaction was stirred at room temperature for 2 h. Upon completion of the polymerization, the flask was opened to atmosphere and diluted with a

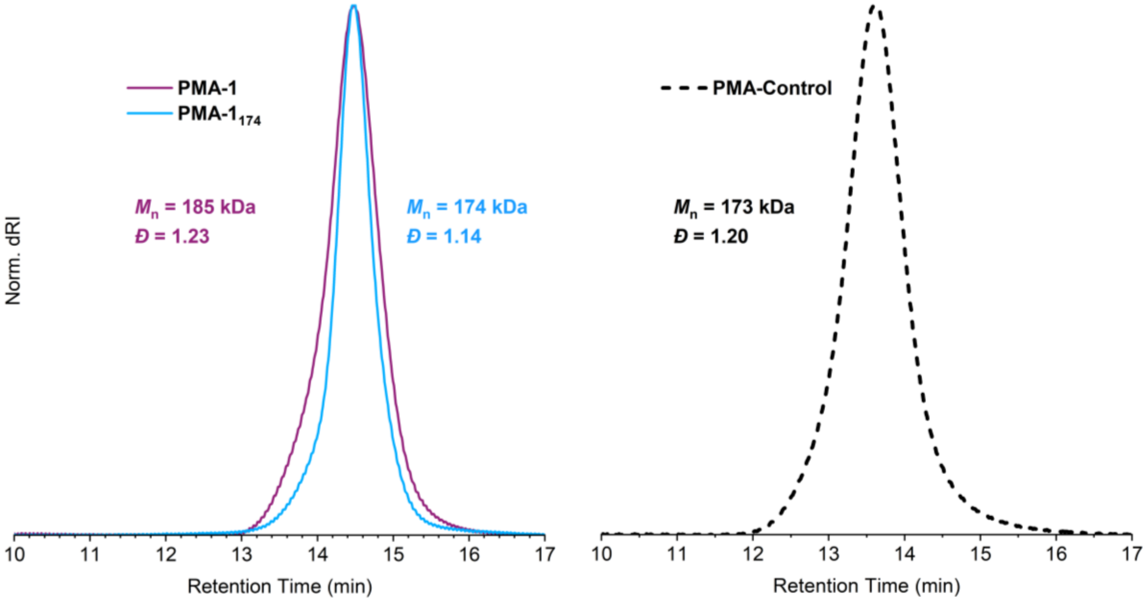

Figure 5.18. GPC traces (RI response) normalized to peak height for **PMA-1**, **$PMA-1_{174}$**, and **PMA-Control**.

minimal amount of CH_2Cl_2. The polymer was precipitated 3x into methanol cooled with dry ice and then dried under vacuum to afford the title polymer as a tacky pale purple solid (0.925 g, 29% yield). M_n = 173 kg/mol, $Đ$ = 1.20. The GPC trace is shown below in Figure 5.18.

III. DFT Calculations (CoGEF)

CoGEF calculations were performed using Spartan ′18 Parallel Suite according to previously reported methods.[17,18] Ground state energies were calculated using DFT at the B3LYP/6-31G* level of theory. Unless noted otherwise, the equilibrium conformations of the unconstrained molecules were initially calculated using molecular mechanics (MMFF) followed by optimization of the equilibrium geometries using DFT (B3LYP/6-31G*). Starting from the equilibrium geometry of the unconstrained molecules (energy = 0 kJ/mol), the distance between the terminal methyl groups of the truncated structures was increased in increments of 0.05 Å and the energy was minimized at each step. The maximum force associated with the mechanochemical reaction was calculated from the slope of the curve immediately prior to bond cleavage.

CoGEF results are shown in Figure 5.1c and Figure 5.2 for a truncated model reflecting the two possible diastereomers of the naphthodipyran mechanophore in **PMA-1**, each of which is predicted to undergo dual ring-opening reactions. Three structures with alternative substitution at the *para* position of the pendant aryl rings were also subjected to CoGEF analysis to evaluate the generality of naphthodipyran mechanochemical reactivity. In each case, the equilibrium geometry structure of the of the corresponding pyrrolidine-substituted naphthodipyran was used as the starting model. The pyrrolidine groups were replaced in Spartan with the appropriate substituent, followed by another equilibrium geometry optimization. CoGEF calculations illustrated in Figure 5.3 for two alternative substitution patterns (*para*-nitro or *para*-isopropoxy groups) also predict dual ring-opening reactions. In contrast, a naphthodipyran model substituted with simple phenyl substituents (*i.e.*, *para*-H groups) is predicted to only undergo one ring-opening reaction upon mechanical elongation at an $F_{\max}$ of 3.6

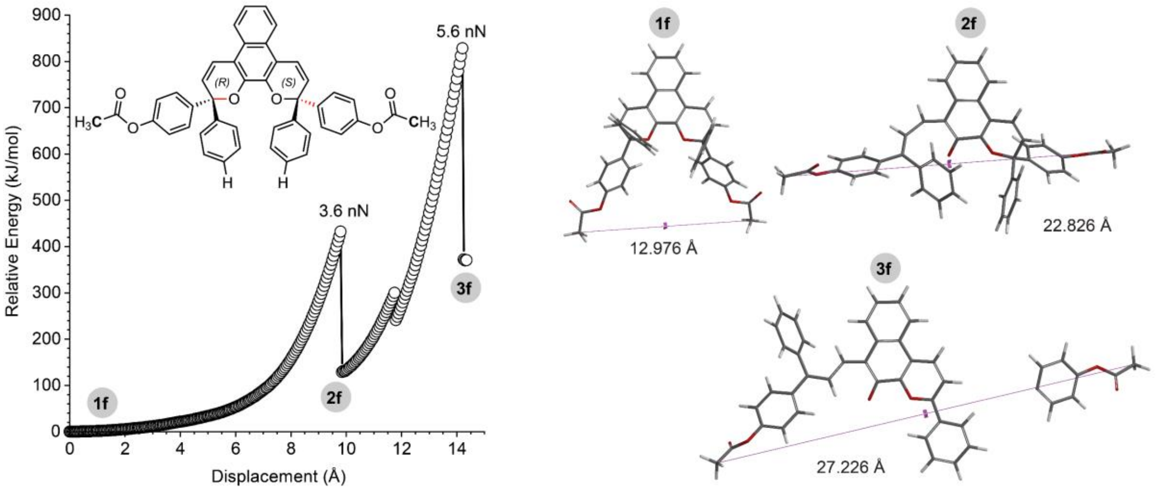

Figure 5.19. CoGEF calculations at the B3LYP/6-31G* level of theory predict that naphthodipyran (R,S-isomer) with phenyl substituents undergoes a single ring-opening reaction followed by C–C bond scission, in contrast to the dual ring-opening reactivity predicted for other substituted derivatives (See Figure 5.3 and Figure 5.5). The first ring-opening reaction occurs at an $F_{\max}$ value of 3.6 nN, and further elongation results in C–C bond scission at an $F_{\max}$ value of 5.6 nN. The corresponding computed structures at various points of elongation are shown at right along with the associated constraint distance between the terminal methyl groups.

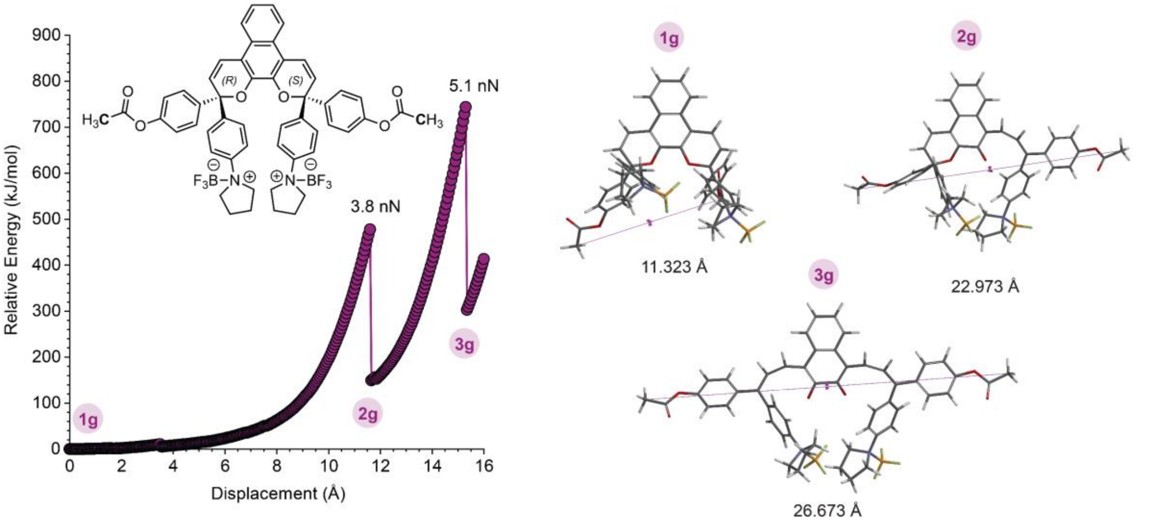

Figure 5.20. CoGEF calculations at the B3LYP/6-31G* level of theory predict a dual ring-opening reaction for a naphthodipyran model with aryl substituents containing *para*-pyrrolidine groups explicitly bound at the nitrogen atom to BF_3. The first ring-opening reaction occurs at an F_{max} value of 3.6 nN while the second ring-opening reaction occurs at an F_{max} value of 5.1 nN, similar to the naphthodipyran model without BF_3 coordination. The corresponding computed structures at various points of elongation are shown at right along with the associated constraint distance between the terminal methyl groups.

nN (Figure 5.19). Instead of a second ring-opening reaction, C–C bond scission is predicted between the pendant aryl ring and the pyran *sp*^{3} carbon at an F_{max} of 5.6 nN.

CoGEF calculations were also performed on a model of monomerocyanine $NDP_{O–C}·nBF_3$ with explicit BF_3 binding to the merocyanine oxygen (see **Figure 5.11**). Upon mechanical elongation, the second pyran ring is predicted to open at an F_{max} of 4.7 nN, similar to the F_{max} value of 4.6 nN predicted for the second ring-opening reaction of the unbound model. In addition, a CoGEF

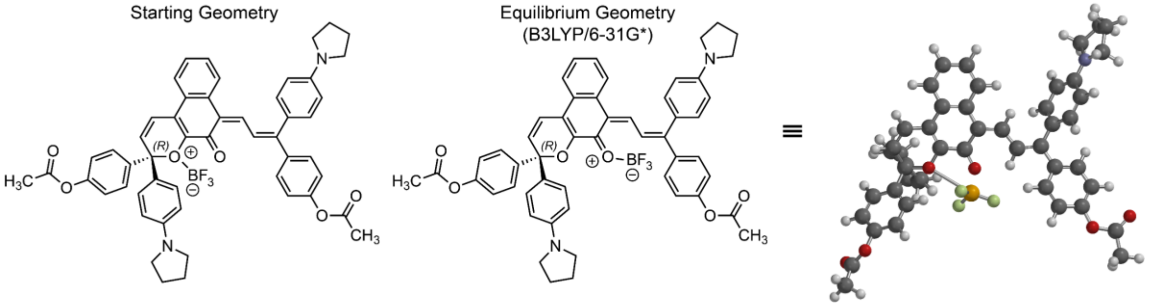

Figure 5.21. Equilibrium geometry calculation (B3LYP/6-31G*) performed on a model reflecting one possible structure for the monomerocyanine complex $NDP_{O–C}·nBF_3$. The BF_3 unit initially associated with the pyran oxygen atom migrates to the oxygen atom of the adjacent merocyanine ketone after geometry optimization.

calculation performed on a hypothesized model structure of naphthodipyran bound to BF_3 at each pyrrolidine nitrogen ($NDP_{C–C}\cdot nBF_3$) predicts dual ring-opening reactions with F_{max} values of 3.8 nN and 5.1 nN for the first and second ring-openings, respectively (Figure 5.20).

Additional computations were performed to investigate the possibility of BF_3 coordination to the pyran oxygen in the monomerocyanine and any effect on the second mechanochemical ring-opening reaction. One potential model of monomerocyanine $NDP_{O–C}\cdot nBF_3$ was constructed with BF_3 association at the pyran oxygen, as illustrated in Figure 5.21. Upon geometry optimization (B3LYP/6-31G*), the BF_3 unit migrates to the adjacent merocyanine oxygen atom. This result supports the BF_3-binding model used in the CoGEF calculation in Figure 5.11. A similar result is achieved for a model in which a BF_3 unit is associated with each pyrrolidine N atom (Figure 5.22). Performing a similar geometry optimization on a model with a BF_3 unit associated with the pyran oxygen atom and another BF_3 unit already coordinated to the merocyanine oxygen also predicts BF_3 migration to form a second coordination to the merocyanine oxygen atom (Figure 5.23). More generally, coordination between the pyran oxygen atom and a BF_3 unit was not observed in any equilibrium geometry calculation, suggesting that BF_3 coordination at that position is unlikely. A CoGEF calculation performed on the geometry-optimized model in Figure 5.23 containing two BF_3 units coordinated to the oxygen of the merocyanine first predicts a bond rotation at an extension of approximately 3.65 Å that occurs with

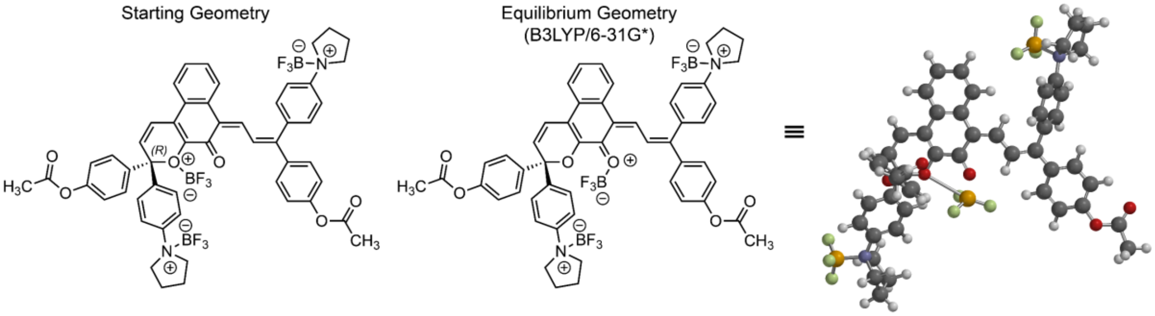

Figure 5.22. Equilibrium geometry calculation (B3LYP/6-31G*) performed on a model reflecting one possible structure for the monomerocyanine complex $NDP_{O–C}\cdot nBF_3$ including a BF_3 unit coordinated to each pyrrolidine nitrogen atom. The BF_3 unit initially associated with the pyran oxygen atom migrates to the oxygen atom of the adjacent merocyanine ketone after geometry optimization.

an F_{max} of 3.1 nN, followed by the expected second ring-opening reaction occurring with an F_{max} of 5.1 nN (Figure 5.24), similar to the CoGEF predictions for alternative BF_3-binding models above.

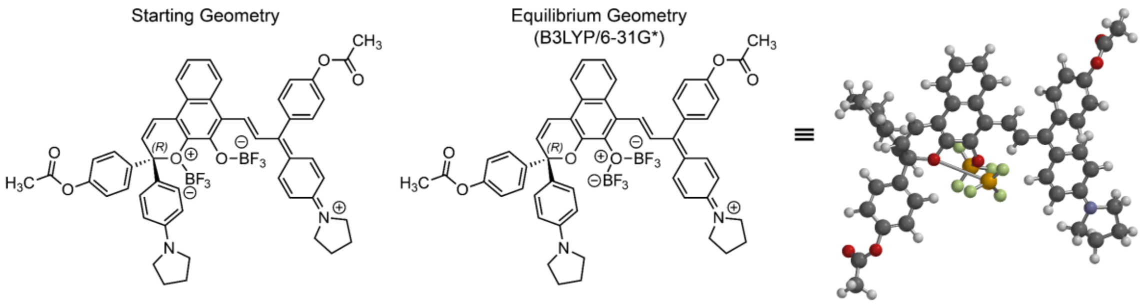

Figure 5.23. Equilibrium geometry calculation (B3LYP/6-31G*) performed on a model reflecting one possible structure for the monomerocyanine complex $NDP_{O\text{–}C}\cdot nBF_3$ including a BF_3 unit coordinated to the merocyanine oxygen atom. The BF_3 unit initially associated with the pyran oxygen atom migrates to the oxygen atom of the adjacent merocyanine after geometry optimization to form a second coordination.

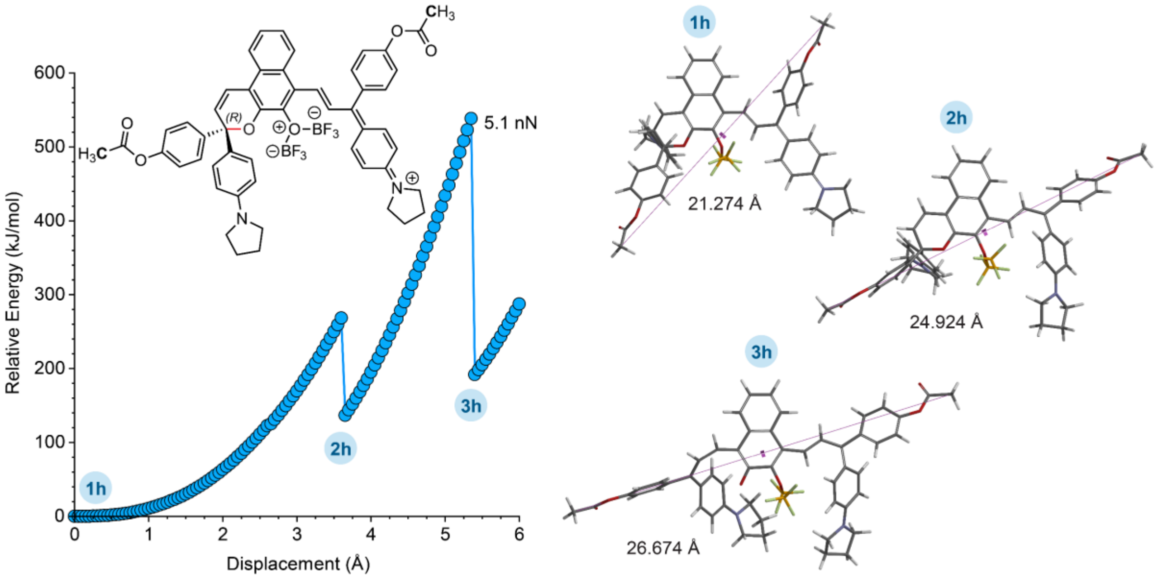

Figure 5.24. CoGEF calculations at the B3LYP/6-31G* level of theory performed on a model reflecting one possible structure for the monomerocyanine complex $NDP_{O\text{–}C}\cdot nBF_3$ based on predictions illustrated in Figure 5.23. The second mechanochemical ring-opening reaction is predicted to occur with an F_{max} value of 5.1 nN. The first transition, which occurs at an elongation of approximately 3.65 Å, corresponds to a bond rotation (F_{max} = 3.1 nN). The corresponding computed structures at various points of elongation are shown at right along with the associated constraint distance between the terminal methyl groups.

IV. Details for Photoirradiation and Sonication Experiments

In order to continuously monitor reaction progress by UV–vis–near-IR absorption spectroscopy, a previously reported experimental setup[13,21] was assembled using a peristaltic pump to transport solution from the reaction vessel through a quartz flow cell in a spectrometer and return the solution to the reaction vessel. The flow rate through the system was maintained at 8 mL/min, corresponding to a setting of 50 RPM on the peristaltic pump at the selected occlusion. The UV-vis spectrometer was programmed to acquire full spectra (280–1100 nm) at regular time intervals. The absorbance values measured at 1000 nm were subtracted from the absorbance values across the rest of the spectrum at each time point to account for drift during the experiments.

General Procedure for Sonication Experiments. A sonication vessel previously stored in an oven maintained at 150 °C was placed onto the sonication probe and allowed to cool under a stream of dry nitrogen. The vessel was charged with a 5.8 µM solution of polymer in CH_3CN containing 30 mM BHT (20.0 mL) to avoid decomposition side reactions resulting from free radicals generated during sonication.[28,29] An additional 6.2 mL of solution was pumped into the dead space of the circulatory setup. If applicable, $BF_3 \cdot Et_2O$ was added to the sonication vessel via microsyringe to give a final concentration of 1.5 mM $BF_3 \cdot Et_2O$ unless another concentration is specified. Teflon inlet and outlet tubes were inserted into the solution in the sonication vessel through punctured septa, and the pump was engaged to start the flow of solution through the system. The sonication vessel was submerged in a −45 °C bath and degassed by sparging with N_2 for 30 minutes prior to sonication, after which the gas line was removed from the solution and into the headspace to maintain an inert atmosphere throughout the sonication experiment. Continuous sonication at 20 kHz (20% amplitude, 6.84 ± 0.46 W/cm^2) was then initiated. The temperature inside the reaction vessel equilibrated to −15 °C, as measured by a thermocouple inserted into the solution (Digi-Sense EW-91428-02 thermometer with Digi-Sense probe EW-08466-83). Reaction progress was monitored by UV–vis–near-IR absorption spectroscopy. Sonication intensity was calibrated via the literature method.[20] The entire system was

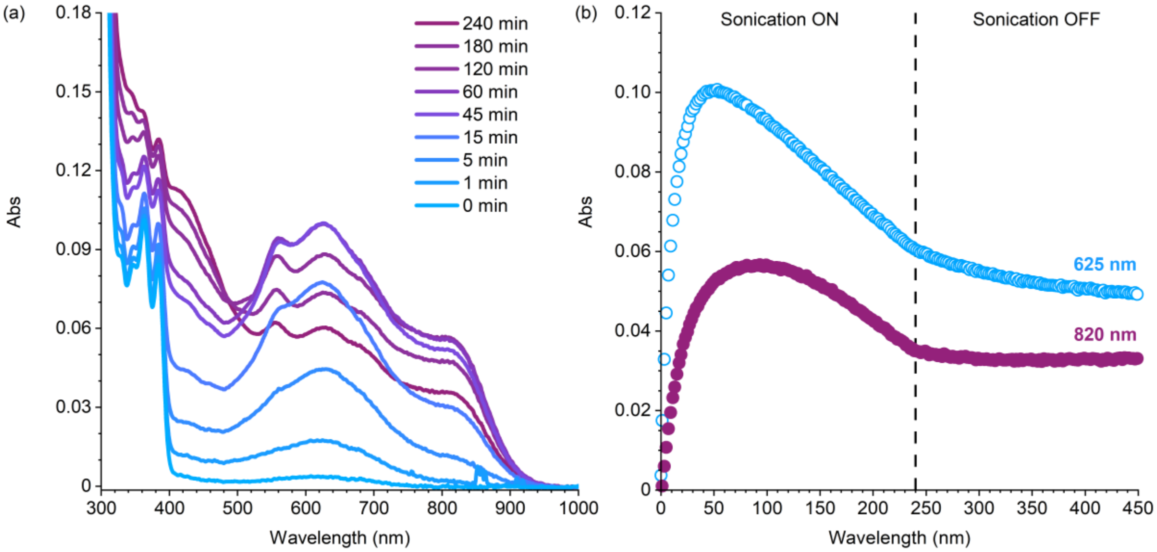

Figure 5.25. Absorption spectra obtained from a solution of **PMA-1** (5.8 µM in CH_3CN, 1.5 mM $BF_3{\cdot}Et_2O$) in the absence the radical trap BHT upon ultrasound-induced mechanochemical activation and subsequent cessation of ultrasound. (a) Ultrasound-induced mechanical activation results initially in the sequential growth of the absorption features of $\mathrm{NDP}_{\mathrm{O–C}}{\cdot}n\mathrm{BF}_3$ and $\mathrm{NDP}_{\mathrm{O–O}}{\cdot}n\mathrm{BF}_3$, however extended ultrasonication results in bleaching of the colored products. (b) Time-dependent absorption profiles at 625 nm and 820 nm shown during and after cessation of ultrasonication.

kept in the dark for the duration of the experiment. After completion of each experiment involving $BF_3{\cdot}Et_2O$, the flow cell was purged in sequence with CH_3CN, deionized water, a saturated aqueous solution of $Ca(OH)_2$, deionized water, and finally CH_3CN to safely remove $BF_3{\cdot}Et_2O$ and any potentially hazardous byproducts of sonication.

Sonication in the Absence of Radical Inhibitor. As shown in Figure 5.25, ultrasonication of **PMA-1** in the absence of BHT results in the same sequential appearance of $\mathrm{NDP}_{\mathrm{O–C}}{\cdot}n\mathrm{BF}_3$ and $\mathrm{NDP}_{\mathrm{O–O}}{\cdot}n\mathrm{BF}_3$ observed in the presence of the radical inhibitor (see Figure 5.4). However, extended exposure to ultrasound results in attenuation of the visible absorption signals, suggesting that the trapped merocyanine species are susceptible to radical-mediated decomposition. Bleaching is significantly slowed upon cessation of ultrasound (Figure 5.21b), further supporting that sonochemically generated radicals are responsible for decomposition.

Comparison of Polymer Chain Scission Kinetics to Dimerocyanine Formation Kinetics. To determine relative rates of polymer chain scission and dimerocyanine formation, sonication experiments were performed on **PMA-1** following the procedures described above, during which aliquots (1 mL) were removed at regular time intervals for GPC analysis. Aliquots were removed from the sonication reactions via a N_2-flushed syringe during continuous sonication. After evaporation of the CH_3CN overnight under vacuum, the sample was redissolved in THF and submitted for GPC analysis. UV-vis absorption data and GPC traces for the sonication of **PMA-1** are shown in Figure 5.26. The kinetics associated with formation of dimerocyanine $NDP_{O–O}\cdot nBF_3$ were determined by fitting the time-dependent absorbance values at 820 nm to 5.1. Rates of polymer chain scission were determined according to the literature method.[29] Briefly, GPC traces were normalized by area and the rate of chain scission was determined by plotting the attenuation of the RI response at the retention time (t_R) corresponding to the initial polymer peak as a function of sonication time. The time dependent GPC-RI response is fitted to eq. 5.2 to determine the rate of chain scission. The observed rate constant for $NDP_{O–O}\cdot nBF_3$ formation (0.038 min^{-1}) is greater than the rate constant for polymer chain scission (0.018 min^{-1}).

$$A(t) = A\left(1 - e^{-kt}\right) + c \tag{5.1}$$

$$A(t) = A\left(e^{-k_r t}\right) + c \tag{5.2}$$

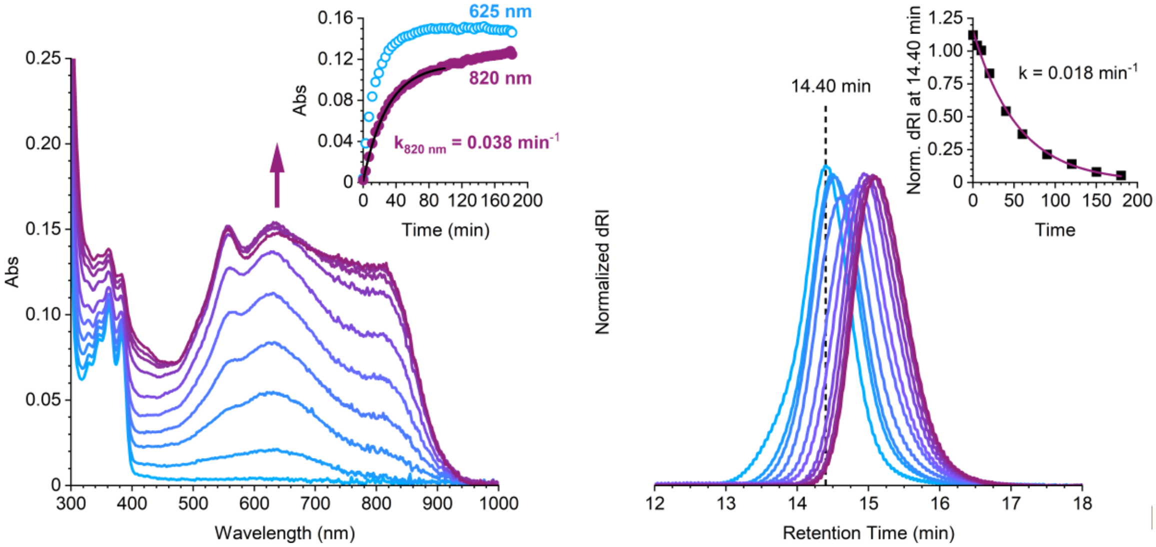

Figure 5.26. Kinetics of ultrasound-mediated mechanochemical merocyanine formation and polymer chain cleavage in **PMA-1** (5.8 µM in CH_3CN, 30 mM BHT, 1.5 mM $BF_3 \cdot Et_2O$) monitored by UV-vis absorption spectroscopy and GPC measurements (a) UV-vis absorption data shows growth of the absorption features of $NDP_{O\text{–}C} \cdot nBF_3$ and $NDP_{O\text{–}O} \cdot nBF_3$. The time-dependent absorption profile at 820 nm shows an observed rate constant of 0.038 min^{-1} for $NDP_{O\text{–}O} \cdot nBF_3$ generation. (b) Time dependent attenuation of the RI signal at t_r = 14.40 min reports a rate of chain scission of 0.018 min^{-1}.

Sonication Experiments with Varying Concentrations of $BF_3{\cdot}Et_2O$. To systematically study the effect of $BF_3{\cdot}Et_2O$ concentration on product formation and kinetics, **PMA-1$_{174}$** was subjected to ultrasonication as described above using different concentrations of $BF_3{\cdot}Et_2O$. As shown in Figure 5.27, absorption spectra recorded at regular intervals demonstrate that accumulation of $NDP_{O\text{–}O}{\cdot}n BF_3$ increases with increasing $BF_3{\cdot}Et_2O$ concentration up to a critical point, above which negligible

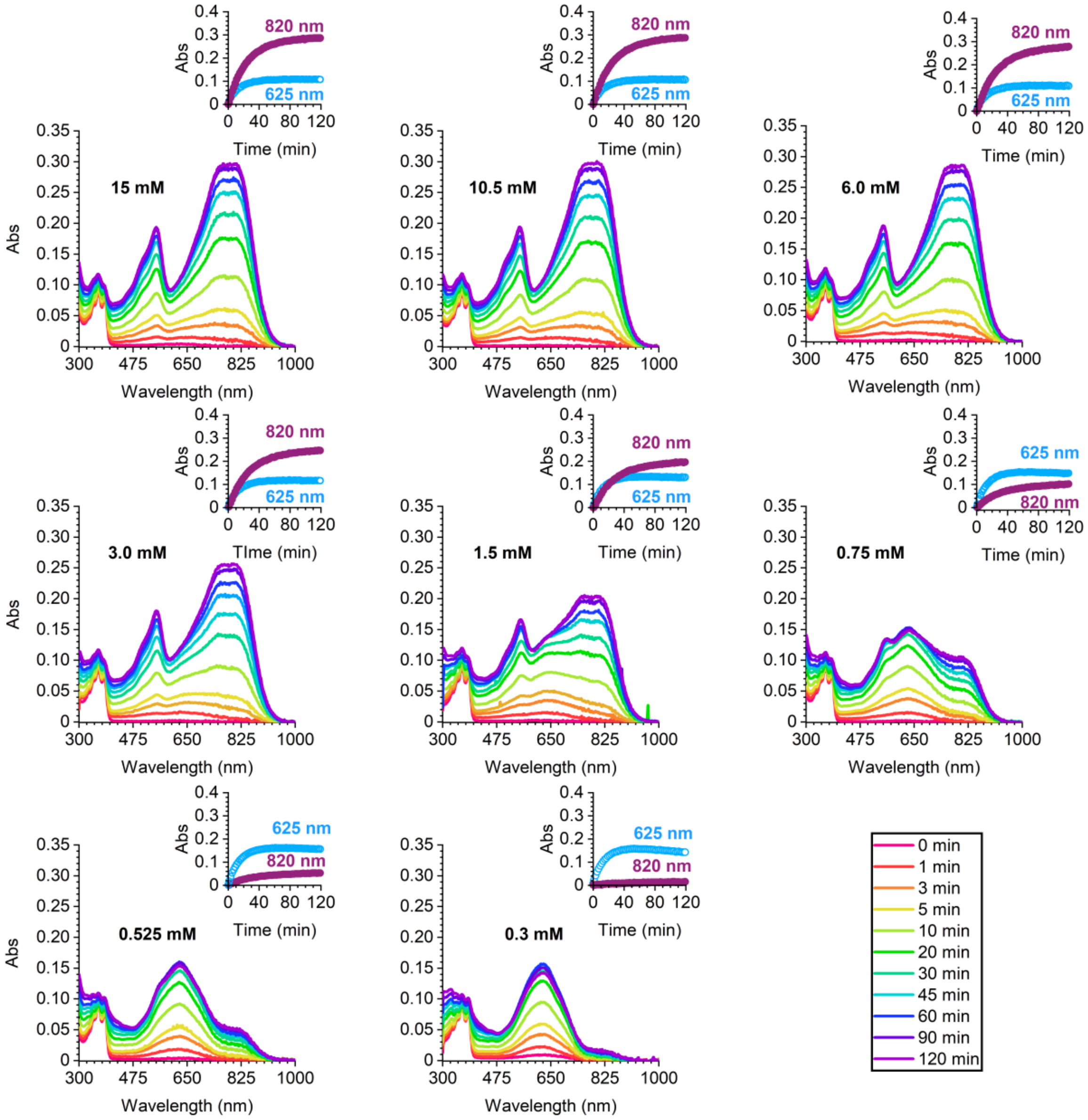

Figure 5.27. Absorption spectra during ultrasound-induced mechanochemical activation of **PMA-1$_{174}$** (5.8 μM in CH_3CN, 30 mM BHT) with varying concentrations of $BF_3{\cdot}Et_2O$.

changes in product distribution are observed. Above this point, time-dependent absorption profiles and comparison of spectra at equivalent timepoints also show that no changes in kinetics are observed.

Time-dependent absorption measurements at wavelengths characteristic of $\mathrm{NDP_{O\text{–}C}}\cdot n\mathrm{BF_3}$ (625 nm, Figure 5.28a) and $\mathrm{NDP_{O\text{–}O}}\cdot n\mathrm{BF_3}$ (820 nm, Figure 5.28b) support this finding. The total accumulation of $\mathrm{NDP_{O\text{–}O}}\cdot n\mathrm{BF_3}$ varies at concentrations of $\mathrm{BF_3 \cdot Et_2O}$ below 6 mM (Figure 5.28b); however, normalizing the traces to the absorbance value at 120 min demonstrates that the observed rate constant varies minimally with $\mathrm{BF_3 \cdot Et_2O}$ concentration (Figure 5.28c). This result is consistent with higher concentrations of $\mathrm{BF_3 \cdot Et_2O}$ leading to greater trapping of $\mathrm{NDP_{O\text{–}O}}\cdot n\mathrm{BF_3}$, but without significantly altering the kinetics associated with $\mathrm{NDP_{O\text{–}O}}\cdot n\mathrm{BF_3}$ formation. We note that the coordination between untrapped monomerocyanine $\mathrm{NDP_{O\text{–}C}}$ and $\mathrm{BF_3}$ is reversible (see Figure 5.16 and Figure 5.17 above). Thus, we hypothesize that increasing the concentration of $\mathrm{BF_3 \cdot Et_2O}$ shifts the equilibrium between $\mathrm{NDP_{O\text{–}C}}$ and $\mathrm{NDP_{O\text{–}C}}\cdot n\mathrm{BF_3}$ toward the $\mathrm{BF_3}$-coordinated monomerocyanine species, which would promote formation of the trapped dimerocyanine species during a second force extension event according to the proposed mechanism in Scheme 5.1.

Values of k_{obs} at 820 nm describing the mechanochemical generation of dimerocyanine were obtained from fitting the first 80 min of the absorption–time profile to eq. 5.1 and exhibit only a slight increase with increasing concentration of $\mathrm{BF_3 \cdot Et_2O}$ between 0.5 and 15 mM (Figure 5.29a). Notably,

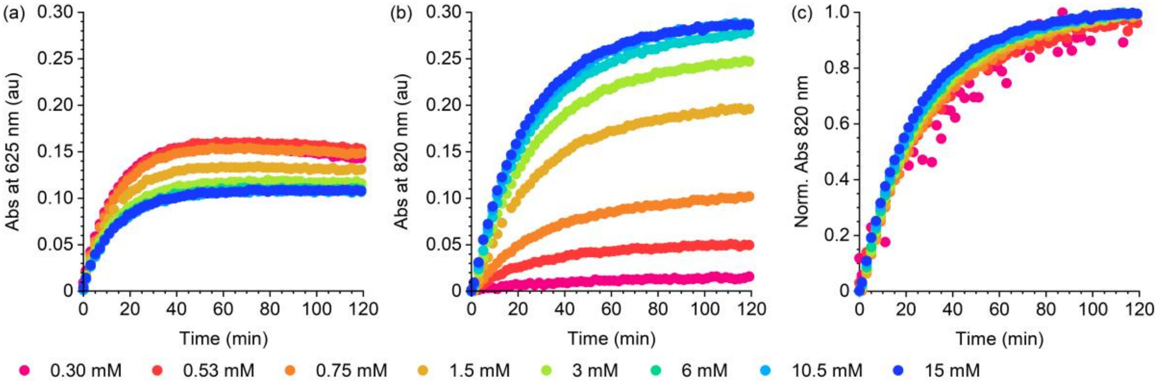

Figure 5.28. Time-dependent absorption profiles during ultrasound-mediated mechanochemical activation of $\mathbf{PMA\text{-}1_{174}}$ (5.8 µM in $\mathrm{CH_3CN}$, 30 mM BHT) with varying concentrations of $\mathrm{BF_3 \cdot Et_2O}$ measured at (a) 625 nm, and (b) 820 nm. (c) Time-dependent absorption profiles measured at 820 nm normalized to the absorbance value for each trace at 120 min of ultrasonication.

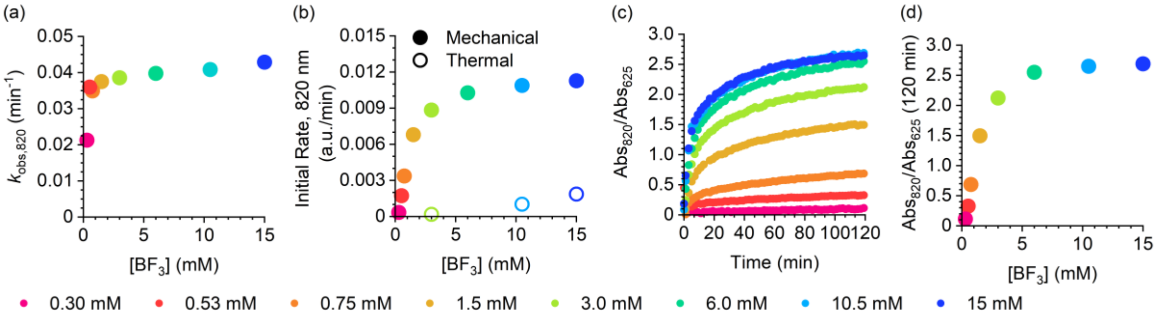

Figure 5.29. (a) Observed rate constant for the mechanochemical accumulation of dimerocyanine NDP$_{\mathrm{O–O}}$·nBF$_3$ measured at 820 nm upon ultrasonication of **PMA-1$_{174}$** at varying concentrations of BF$_3$·Et$_2$O. (b) Initial rate of change at 820 nm for the ultrasound-induced mechanochemical activation of **PMA-1$_{174}$** compared to the thermal conversion of monomerocyanine NDP$_{\mathrm{O–C}}$·nBF$_3$ in **PMA-Control** at varying concentrations of BF$_3$·Et$_2$O (see Section V for additional details). (c) Time-dependent absorbance ratio of wavelengths characteristic of NDP$_{\mathrm{O–O}}$·nBF$_3$ and NDP$_{\mathrm{O–C}}$·nBF$_3$ (820 nm and 625 nm) for **PMA-1$_{174}$** at varying concentrations of BF$_3$·Et$_2$O. (d) Ratio of absorbance values at 820 nm and 625 nm ultrasonication of **PMA-1$_{174}$** for 120 min at varying concentrations of BF$_3$·Et$_2$O.

the lower value of k_{obs} at 0.3 mM BF$_3$·Et$_2$O concentration followed by nearly constant values of k_{obs} above 0.5 mM BF$_3$·Et$_2$O is consistent with the expected trend if BF$_3$·Et$_2$O is acting solely as a trap in a 2nd-order reaction that follows a 1st-order pre-equilibrium.[30] That is, the reversible mechanochemical generation of thermally transient NDP$_{\mathrm{O–O}}$ followed by the irreversible trapping reaction with BF$_3$. Initial rates of NDP$_{\mathrm{O–O}}$·nBF$_3$ accumulation were determined by fitting the first 30 min of the absorption–time curve at 820 nm to a third order polynomial function, $f(x) = ax^2 + bx + c$, following the procedure by Collum where initial rate = $f'(0) = b$.[31] In contrast to the relatively static rate constants, the initial rate of dimerocyanine accumulation increases with higher concentrations of BF$_3$·Et$_2$O up to a maximum rate attained around 6.0 mM BF$_3$·Et$_2$O (Figure 5.29b). We hypothesize that this apparent contrast with the trend in k_{obs} is not due to acceleration of the ring-opening reaction, but rather reflects the diminished overall generation of NDP$_{\mathrm{O–O}}$·nBF$_3$ with lower concentrations of BF$_3$·Et$_2$O whereby trapping is less competitive with thermal reversion. Importantly, the initial rates of mechanochemical formation of NDP$_{\mathrm{O–O}}$·nBF$_3$ are significantly faster than the rate of NDP$_{\mathrm{O–O}}$·nBF$_3$ formation due to the thermal conversion of monomerocyanine NDP$_{\mathrm{O–C}}$·nBF$_3$ at these relatively high concentrations of BF$_3$·Et$_2$O (Figure 5.29b, see Figure 5.13 and Section V for experimental details).

With higher concentrations of $BF_3 \cdot Et_2O$, we hypothesized that trapping of the thermally transient dimerocyanine will become increasingly competitive with thermal reversion to the monomerocyanine species, resulting in merocyanine product distributions that shift further toward $NDP_{O–O} \cdot nBF_3$. The ratio of absorbance values (Abs_{820}/Abs_{625}) at wavelengths characteristic of $NDP_{O–O} \cdot nBF_3$ (820 nm) and $NDP_{O–C} \cdot nBF_3$ (625 nm) reflects the overall distribution of the two merocyanine products. The time-dependent change in this absorbance ratio illustrates a shift in product distribution toward dimerocyanine $NDP_{O–O} \cdot nBF_3$ with increasing sonication time at all concentrations of $BF_3 \cdot Et_2O$ (Figure 5.29c). The final product distribution is further shifted toward dimerocyanine $NDP_{O–O} \cdot nBF_3$ with increasing concentration of $BF_3 \cdot Et_2O$ up to approximately 6.0 mM. Above this concentration of $BF_3 \cdot Et_2O$, the product distribution remains relatively unchanged upon ultrasound-induced mechanochemical activation of the naphthodipyran in **PMA-1$_{174}$** (Figure 5.29d), consistent with the variation in initial rates. These results are consistent with increased concentrations of $BF_3 \cdot Et_2O$ enabling more efficient trapping of the thermally transient uncoordinated dimerocyanine species.

Based on the data presented above and in combination with data from control experiments characterizing the thermal conversion of monomerocyanine $NDP_{O–C} \cdot nBF_3$ to the dimerocyanine species at varying concentrations of $BF_3 \cdot Et_2O$ (Section V), we selected a concentration of 1.5 mM $BF_3 \cdot Et_2O$ for the key experiments in the study. At this concentration of $BF_3 \cdot Et_2O$, the thermal conversion of monomerocyanine is minimized while still enabling relatively efficient trapping of the dimerocyanine species produced via the mechanochemical ring-opening reaction. In addition, the sequential accumulation of monomerocyanine and dimerocyanine species is clearly observed at this lower concentration of $BF_3 \cdot Et_2O$.

Ultrasonication Experiments in the Absence of $BF_3 \cdot Et_2O$. As shown in Figure 5.7, ultrasonication of **PMA-1** in the absence of $BF_3 \cdot Et_2O$ produces a single absorption feature (λ_{max} = 560 nm) that is consistent with the uncoordinated monomerocyanine species. While the dimerocyanine is not observed in these experiments in the absence of trapping agent, it is possible that the species is still formed under force, but its lifetime is too short to be observed. Similar behavior has been reported previously for the ultrasound-induced mechanochemical activation of simple naphthopyrans.[9]

General Procedure for Photoirradiation Experiments. A sonication vessel previously stored in an oven maintained at 150 °C was placed onto the sonication probe and allowed to cool under a stream of dry nitrogen. The vessel was charged with a 5.8 μM solution of polymer in CH_3CN containing 30 mM BHT (20.0 mL) for consistency with ultrasonication experiments. An additional 6.2 mL of solution was pumped into the dead space of the circulatory setup. If applicable, 5 μL of $BF_3{\cdot}Et_2O$ was added to the sonication vessel via microsyringe to give a final concentration of 1.5 mM $BF_3{\cdot}Et_2O$. Teflon inlet and outlet tubes were inserted into the solution in the sonication vessel through punctured septa, and the pump was engaged to start the flow of solution through the system. The sonication vessel was submerged in a −45 °C bath and degassed by sparging with N_2 for 30 minutes prior to sonication, after which the gas line was removed from the solution and into the headspace to maintain an inert atmosphere throughout the photoirradiation experiment. Without sonication, the temperature inside the reaction vessel equilibrated to −30 °C. The vessel was then exposed to a UV light source (λ = 365 nm) positioned 2 in away, which was also submerged in the cooling bath encased within a

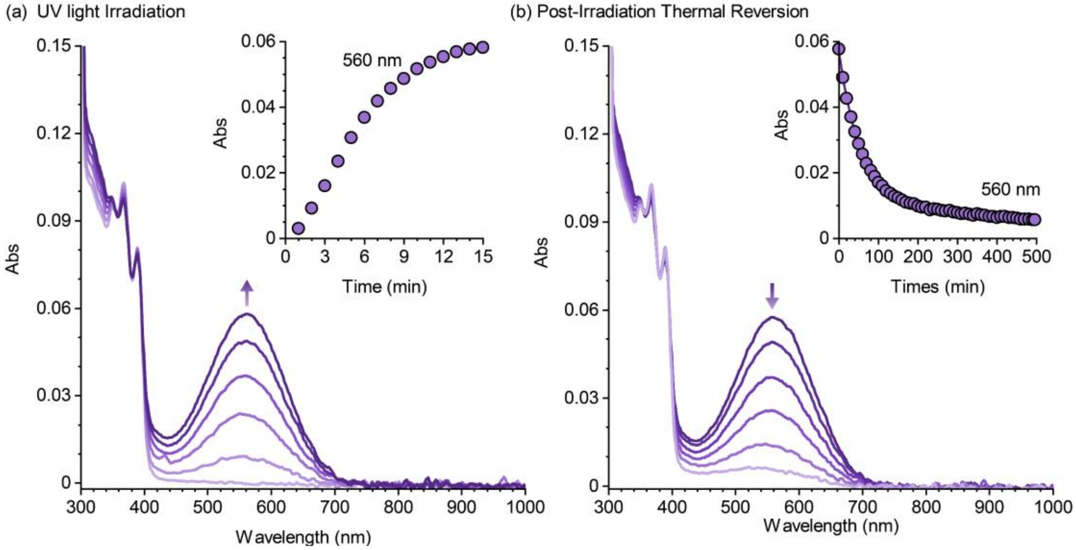

Figure 5.30. Absorption spectra obtained from a solution of **PMA-1** (5.8 μM in CH_3CN, 30 mM BHT) in the absence of any trapping agent upon (a) photoirradiation with 365 nm UV light, and (b) subsequent thermal reversion upon cessation of photoirradiation. Photochemical activation under these conditions produces a peak with λ_{max} = 560 nm.

quartz tube. In applicable experiments, continuous sonication was initiated either simultaneously with UV irradiation (see Figure 5.14) or after cessation of UV irradiation (Figure 5.12, main text). Reaction progress was monitored by absorption spectroscopy. The entire system was protected from outside light for the duration of the experiment.

Photoirradiation of **PMA-1** in the absence of trapping agent produces a peak with λ_{max} = 560 nm, while irradiation under the same conditions in the presence of $BF_3 \cdot Et_2O$ produces an absorption spectrum with λ_{max} = 625 nm (Figure 5.8 and Figure 5.30). This bathochromic shift is consistent with prior reports on the absorption of naphthopyran-derived merocyanines upon BF_3 coordination.[19]

Persistence and Chemical Reversion of BF_3-Coordinated Merocyanines. After photoirradiation of **PMA-1** with UV light (15 min) as described above, the photochemically generated monomerocyanine species ($NDP_{O–C} \cdot nBF_3$) was found to be thermally persistent in the dark over 30 min (Figure 5.5a and b). Consistent with prior reports of similar naphthopyran-derived merocyanines trapped with BF_3,[19] the addition of triethylamine (0.50 mL providing a concentration of 140 mM) caused a rapid attenuation of the absorbance at 625 nm, presumably through competitive coordination of BF_3 (Figure 5.5a and b). Immediately after the addition of triethylamine, a residual absorption peak was observed with λ_{max} = 560 nm, consistent with the unbound merocyanine, $NDP_{O–C}$ (Figure 5.5a and c). This remaining colored species fully reverted after an additional 15 min in the dark (Figure 5.5c). The addition of triethylamine to a solution of dimerocyanine $NDP_{O–O} \cdot nBF_3$ generated by ultrasound-induced mechanical activation of **PMA-1** resulted in similar bleaching behavior (Figure 5.9).

V. Description of Chain-End Control Experiments

To confirm that the ring-opening reactions observed for **PMA-1** containing a chain-centered naphthodipyran mechanophore were due to mechanical force, a chain-end functional control polymer (**PMA-Control**) was synthesized and exposed to ultrasound under identical conditions. As shown in Figure 5.10, minimal changes in absorption are detected during sonication of **PMA-Control** in the presence of 1.5 mM $BF_3{\cdot}Et_2O$, supporting that the first ring-opening reaction is mechanically mediated.[4] Sonication of **PMA-Control** under the same conditions, but using a significantly higher concentration of $BF_3{\cdot}Et_2O$ (15 mM), also resulted in minimal changes in absorption (see Figure 5.31). As described in the main text, a second control experiment was performed to confirm that the second ring-opening reaction of naphthodipyran in **PMA-1** was a mechanically mediated process. A solution of **PMA-Control** was first irradiated with UV light (10 min) as described above to generate $NDP_{O–C}{\cdot}nBF_3$ at the polymer chain-end and subsequently subjected to continuous ultrasonication (Figure 5.12b). While chain-center functional polymer **PMA-1** exposed to the same sequence generated long wavelength features characteristic of $NDP_{O–O}{\cdot}nBF_3$ upon ultrasonication, the spectra of photoirradiated **PMA-Control** remained unchanged under ultrasonication, indicating that the second ring-opening reaction is also mechanochemically mediated.

To further study the effect of UV light irradiation on naphthodipyran under conditions that perfectly mimic the conditions experienced by **PMA-1** during ultrasound-mediated mechanochemical activation, a solution of **PMA-Control** was also exposed to simultaneous UV irradiation and ultrasonication according to the procedures described above in Section 0 (Figure 5.14). Again, only absorption features characteristic of monomerocyanine $NDP_{O–C}{\cdot}nBF_3$ were observed, supporting that the second ring-opening reaction is mechanochemically mediated.

Thermal Conversion of $NDP_{O–C}{\cdot}nBF_3$ and Dependence on Lewis Acid Concentration. To evaluate the impact of $BF_3{\cdot}Et_2O$ concentration on the thermal conversion of monomerocyanine $NDP_{O–C}{\cdot}nBF_3$ to dimerocyanine $NDP_{O–O}{\cdot}nBF_3$, **PMA-Control** was subjected to simultaneous UV irradiation and ultrasonication as described above at varying concentrations of $BF_3{\cdot}Et_2O$ (see Figure 5.13). After 10 min, the generation of monomerocyanine $NDP_{O–C}{\cdot}nBF_3$ reached a maximum and photoirradiation was ceased. Ultrasonication was maintained for the duration of the experiment to mimic the thermal conditions experienced during mechanical activation of naphthodipyran in the chain-centered polymers. Absorption profiles at 625 and 820 nm demonstrate that higher

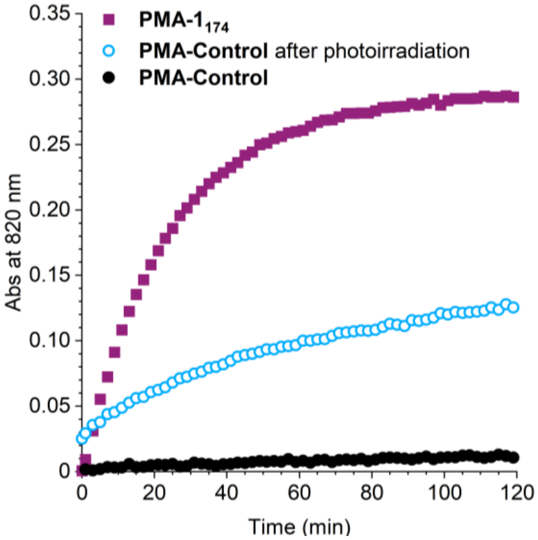

Figure 5.31. Time-dependent absorption profiles measured at 820 nm for a series of ultrasonication experiments performed using 15 mM $BF_3{\cdot}Et_2O$. Ultrasonication of **PMA-1**$_{\mathbf{174}}$ containing a chain-centered naphthodipyran generates significant coloration characteristic of dimerocyanine $NDP_{O\text{–}O}{\cdot}n BF_3$. Photoirradiation of chain-end functional **PMA-Control** (10 min, 365 nm UV light) to generate monomerocyanine $NDP_{O\text{–}C}{\cdot}n BF_3$ followed by ultrasonication results in significantly less dimerocyanine formation. Ultrasonication of **PMA-Control** without prior photoirradiation produces minimal dimerocyanine.

concentrations of $BF_3{\cdot}Et_2O$ result in increased accumulation of dimerocyanine $NDP_{O\text{–}O}{\cdot}n BF_3$ (Figure 5.13a). The initial rate of change at 820 nm increases with increasing $BF_3{\cdot}Et_2O$ concentration as shown in (Figure 5.13b; however, thermal conversion is significantly slower than the mechanochemical process at all studied concentrations of $BF_3{\cdot}Et_2O$ (up to 15 mM) (see Figure 5.25d and Figure 5.31). Higher concentrations of $BF_3{\cdot}Et_2O$ also result in a pronounced shift in the distribution of merocyanine products toward dimerocyanine $NDP_{O\text{–}O}{\cdot}n BF_3$ as discussed in greater detail above in Section 0 (Figure 5.13c).

Additional experiments were performed using high concentrations of alternative Lewis acids, BCl_3 and $Al(OTf)_3$, to investigate how different Lewis acids affect the thermal accumulation of dimerocyanine from the photogenerated monomerocyanine species (Figure 5.32). Both BCl_3 and $Al(OTf)_3$ are stronger Lewis acids than BF_3.[32] The Lewis acid was added to a quartz cuvette containing 1.0 mL of a solution of **PMA-1**$_{\mathbf{174}}$ (5.8 µM in CH_3CN with 30 mM BHT) at room temperature under ambient conditions. As observed previously with $BF_3{\cdot}Et_2O$, minimal dimerocyanine was produced without prior photoirradiation in each case. The cuvette was exposed to UV photoirradiation (365 nm, 30 s) under ambient conditions and then placed inside the UV-vis spectrometer and monitored continuously. Trapped dimerocyanine accumulates relatively quickly in the presence of high concentrations of BCl_3 (Figure 5.32a). We note, however, that this species is thermally transient at lower concentrations of BCl_3 (1.5 mM) and is also hydrolytically unstable, in contrast to the dimerocyanine species formed using $BF_3{\cdot}Et_2O$. The experiment with $BF_3{\cdot}Et_2O$ is shown in Figure 5.32b for comparison. Interestingly, minimal thermal accumulation of trapped dimerocyanine occurs with $Al(OTf)_3$ even though reversion of the monomerocyanine is relatively slow (Figure 5.32c and d). These results suggest that Lewis acid strength is not a determining factor in the rate of thermal dimerocyanine accumulation.

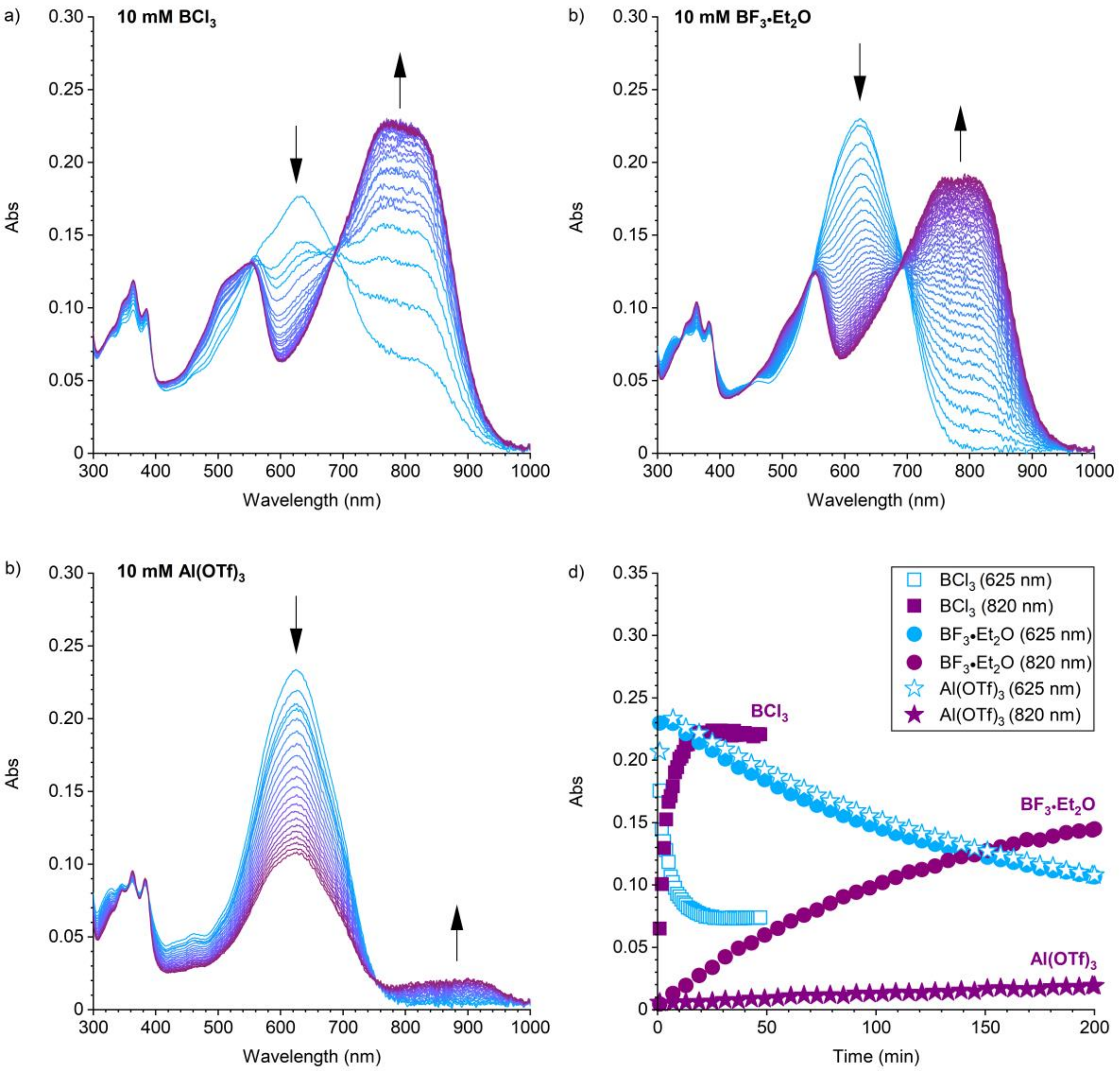

Figure 5.32. Characterization of the thermal conversion of photogenerated monomerocyanine to dimerocyanine using high concentrations (10 mM) of Lewis acid traps (a) BCl_3, (b) $BF_3{\cdot}Et_2O$, or (c) $Al(OTf)_3$. Under ambient conditions, **PMA-1$_{174}$** (5.8 µM in CH_3CN, 30 mM BHT) was subjected to an initial period of UV photoirradiation (365 nm, 30 s) to produce the monomerocyanine species and then spectra were subsequently recorded at room temperature to monitor thermal conversion. (d) The corresponding time-dependent absorbance values monitored at wavelengths characteristic of dimerocyanine (820 nm) and monomerocyanine (625 nm) demonstrating changes in merocyanine distribution post-irradiation for different Lewis acid traps. Notably, minimal dimerocyanine accumulates in the experiment using $Al(OTf)_3$ despite it being a stronger Lewis acid than BF_3. Spectra shown were recorded in intervals of 1 min (a) and 10 min (b,c).

VI. Details for NMR Experiments

A solution of small molecule naphthodipyran bis-initiator **NDP** (0.5 mM in CD_3CN, 0.5 mM 1,3,5-trimethoxybenzene as internal standard) was prepared. The ^1H NMR spectrum contains two doublets characteristic of a proton on the *cis* alkene of the pyran ring on the two naphthodipyran diastereomers at 6.39 ppm (J = 9.9 Hz, 1H) and 6.40 ppm (J = 9.8 Hz, 1H) (Figure 5.33a). Two more well-resolved doublets are observed just downfield at 6.44 ppm (J = 8.9 Hz, 2H) and 6.52 ppm (J = 8.9 ppm, 2H) attributed to aryl protons *ortho* to the electron-rich pyrrolidine group. Also notable are resonances at 3.16–3.25 ppm (m, 8H) attributed to the alkyl protons of the pyrrolidine ring alpha to nitrogen. Addition of $BF_3 \cdot Et_2O$ to the sample (final concentration 1.5 mM) induces significant spectral changes (Figure 5.33b). While the pyran protons are roughly unchanged with peaks at 6.55 ppm (d, J = 9.9 Hz, 1H) and 6.52 ppm (d, J = 10.0 ppm), the aryl protons *ortho* to the pyrrolidine group appear to shift downfield, while the alkyl protons of the pyrrolidine ring alpha to nitrogen change from a sharp multiplet to three broad resonances, shifting slightly downfield to 3.78–4.07 ppm and 3.45–3.65 ppm. These changes are consistent with coordination of BF_3 to the pyrrolidine nitrogen atoms.

The same sample was then exposed to UV light (λ = 365 nm, 2 min, room temperature). A drop of the sample was immediately taken from the irradiated NMR tube, diluted with CH_3CN, and analyzed immediately by UV-vis-near-IR absorption spectroscopy. The remaining sample was immediately frozen in liquid nitrogen and transferred to the instrument for NMR analysis (Figure 5.33c). At sufficiently low *equivalents* of $BF_3 \cdot Et_2O$ relative to substrate, $NDP_{O–C} \cdot nBF_3$ exhibits some thermal reversibility. Due to the detection limits of ^1H NMR spectroscopy, which imposes a lower limit on the concentration of **NDP**, and the limiting upper concentration of $BF_3 \cdot Et_2O$ that induces chemical conversion of $NDP_{O–C} \cdot nBF_3$ to $NDP_{O–O} \cdot nBF_3$, the permissible stoichiometric excess of $BF_3 \cdot Et_2O$ in this experiment is limited. After NMR analysis, another drop of the NMR sample was diluted again in CH_3CN and analyzed by UV-vis-near-IR absorption spectroscopy, which illustrated minimal change before and after NMR analysis and confirmed that the NMR and absorption spectra were representative of the same compound (Figure 5.34). To chemically generate and characterize dimerocyanine species $\mathrm{NDP_{O\text{–}O}}\cdot n\mathrm{BF_3}$, additional $\mathrm{BF_3\cdot Et_2O}$ was added to the same sample to yield a final concentration of 3 mM, and the sample was subsequently irradiated for another 2 min with 365 nm UV light to regenerate $\mathrm{NDP_{O\text{–}C}}\cdot n\mathrm{BF_3}$. After 2 days in the dark *at room temperature*, all $\mathrm{NDP_{O\text{–}C}}\cdot n\mathrm{BF_3}$ had either undergone thermal ring-closure or the chemically-induced ring-opening reaction, yielding a sample containing solely $\mathrm{NDP_{O\text{–}O}}\cdot n\mathrm{BF_3}$ and $\mathrm{BF_3}$-coordinated starting material $\mathrm{NDP_{C\text{–}}}$

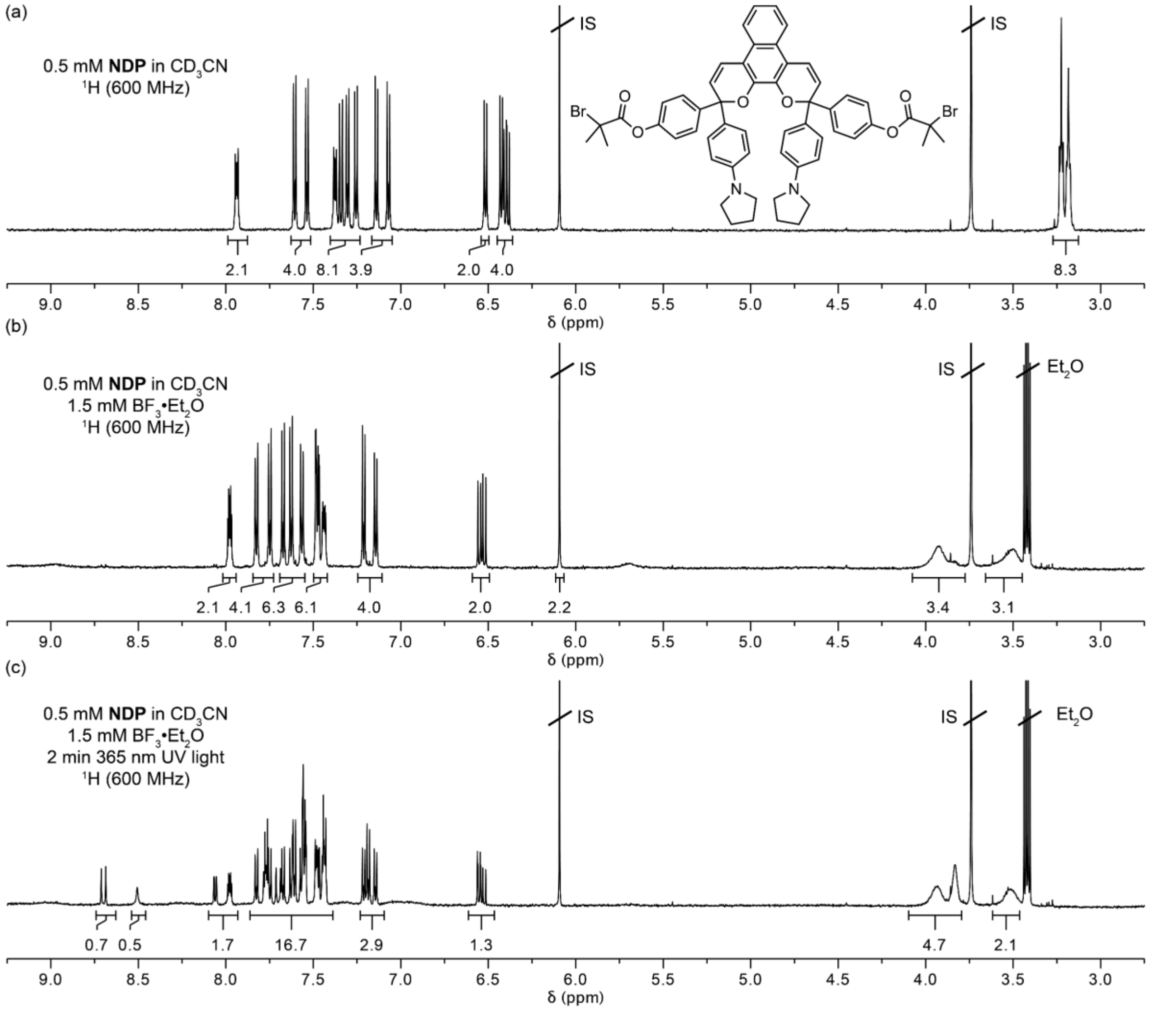

Figure 5.33. ^{1}H NMR spectra (600 MHz, $\mathrm{CD_3CN}$ with 0.5 mM 1,3,5-trimethoxybenzene) of a 0.5 mM solution of naphthodipyran bis-initiator **NDP** (a) before and (b) after addition of 1.5 mM $\mathrm{BF_3\cdot Et_2O}$, and (c) after photoirradiation of with 365 nm UV light for 2 min. See Section VI for detailed description.

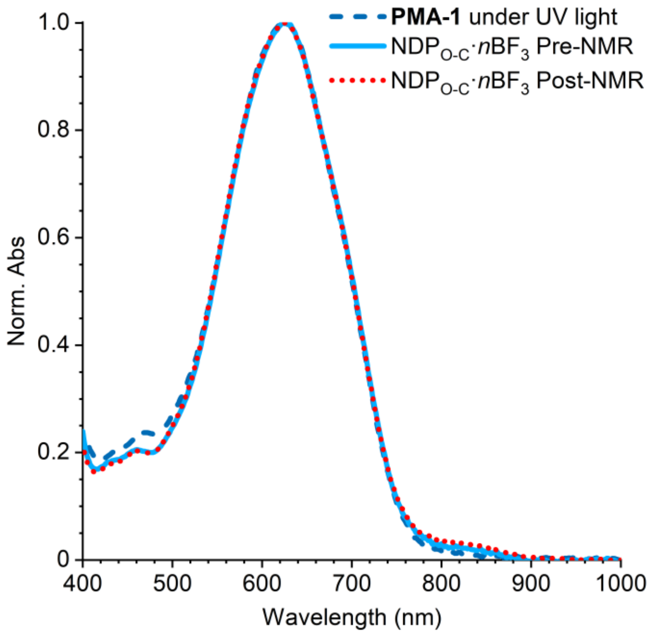

Figure 5.34. UV-vis-near-IR absorption spectra acquired from the NMR sample of naphthodipyran bis-initiator **NDP** shown in Figure 5.33c before and after NMR analysis in comparison to a photoirradiated sample of **PMA-1** (365 nm UV light, 10 min, –30 °C).

$_C$·nBF$_3$ (Figure 5.16 and Figure 5.12d). Notably, dimerocyanine NDP$_{O–O}$·nBF$_3$ was not observed to be thermally reversible.

^{19}F{^{1}H} NMR spectroscopy was used to further characterize the interaction between the naphthodipyran/merocyanine species and BF$_3$ (Figure 5.35). A solution of small molecule naphthodipyran bis-initiator **NDP** (0.5 mM in CD$_3$CN) containing 0.5 mM pentafluorotoluene (PFT) as internal standard was prepared and a ^{1}H NMR spectrum was acquired (Figure 5.35a). Separately, a ^{19}F NMR spectrum was acquired for a solution of BF$_3$·Et$_2$O and PFT in CD$_3$CN (Figure 5.35b), which was referenced to the furthest upfield signal of PFT (–143.9 ppm, 2F).[33] The two signals for BF$_3$ in solution observed at –149.1 and –149.2 ppm represent ^{19}F atoms bound to either ^{10}B (20% isotopic abundance) or ^{11}B (80% isotopic abundance). The addition of BF$_3$·Et$_2$O to the **NDP** sample (1.5 mM BF$_3$·Et$_2$O) induces the same ^{1}H NMR spectral changes observed in Figure 5.33, consistent with BF$_3$ binding at the pyrrolidine nitrogen atoms (Figure 5.35c, see above for further discussion). A new broad peak is also observed upfield of B^{19}F$_3$ in the ^{19}F NMR spectrum at –150.6 ppm, again consistent with BF$_3$ coordinated to a tertiary amine (Figure 5.35d).[34,35]

The addition of more $BF_3 \cdot Et_2O$ to the sample (to afford a final concentration of 3.0 mM) followed by photoirradiation with 365 nm UV light (2 min) at room temperature produces new signals associated with monomerocyanine $NDP_{O–C} \cdot nBF_3$ in the ^1H NMR spectrum (Figure 5.35e). However, no new peaks were observed in the ^{19}F NMR spectrum, suggesting that the ^{19}F signals of $NDP_{O–C} \cdot nBF_3$ are not resolved from either BF_3 in solution or $NDP_{C–C} \cdot nBF_3$, or alternatively, that dynamic coordination between BF_3 and $NDP_{O–C}$ generates a broad resonance that is not readily detected (Figure 5.35f). As described in detail above, upon storing this sample in the dark overnight at room temperature, some of $NDP_{O–C} \cdot nBF_3$ is thermally converted to dimerocyanine $NDP_{O–O} \cdot nBF_3$ while a fraction also reverts back to naphthodipyran $NDP_{C–C} \cdot nBF_3$. Integrating the ^1H NMR resonances for each species indicates a final ratio of 15:85 for $NDP_{O–O} \cdot nBF_3$:$NDP_{C–C} \cdot nBF_3$ (Figure 5.35g). Two new ^{19}F signals are observed for this sample at –142.6 and –142.7 ppm in an approximately 1:4 ratio, again consistent with ^{19}F bound to boron (Figure 5.35h). Three additional cycles of UV photoirradiation (2 min) followed by incubation overnight in the dark were performed to increase the accumulation of $NDP_{O–O} \cdot nBF_3$ (Figure 5.35i–n). Notably, the integration of the ^{19}F signals increases from 0.5 to 0.9 relative to internal standard, which is proportional to the increase in accumulation of $NDP_{O–O} \cdot nBF_3$ (15% to 30%) measured by ^1H NMR spectroscopy. These results suggest that the ^{19}F NMR signals at –142.6 and –142.7 ppm correspond to the fluorine atoms on the trapped dimerocyanine species. Finally, these chemical shifts are consistent with chemical shifts reported previously for difluorodioxaborolane compounds, which resonate downfield of free $B^{19}F_3$, supporting the proposed structure of the trapped dimerocyanine species.[36–38]

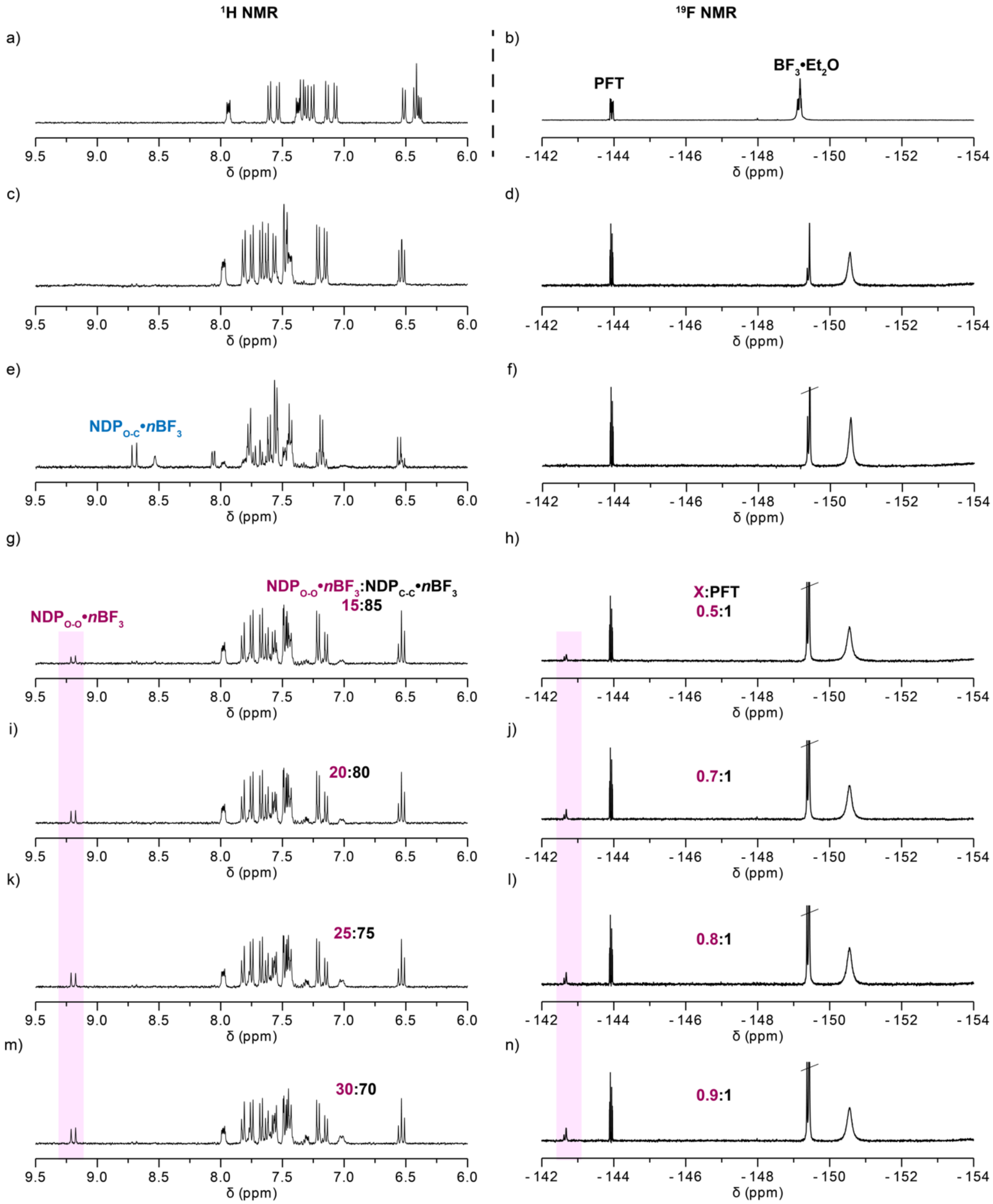

Figure 5.35. ^{1}H (400 MHz, CD_3CN) and ^{19}F (376 MHz, CD_3CN) NMR spectra of (a) naphthodipyran bis-initiator **NDP**, (b) $BF_3{\cdot}Et_2O$ in CD_3CN, (c,d) **NDP** in the presence of $BF_3{\cdot}Et_2O$ before, and (e,f) immediately after photoirradiation with 365 nm UV light. (g,h) Spectra of the same photoirradiated solutions after incubation overnight in the dark, and (i–n) after 3 additional cycles of photoirradiation and incubation in the dark. See Section VI for details.

Additional NMR experiments were performed to determine the stoichiometry between BF_3 and pyran or merocyanine species. A 60 s relaxation delay was employed to ensure quantitative integrations. T1 relaxation times were determined to be < 5 s for all ^{19}F and ^{1}H resonances of interest. As a control, a solution of model compound 4,N,N-trimethylaniline (~1 mM in CD_3CN) containing ~2.4 equiv of PFT as internal standard was prepared and a ^{1}H NMR spectrum was acquired (Figure 5.36a). The addition of $BF_3{\cdot}Et_2O$ to the sample (~3.9 equiv based on ^{1}H NMR integrations) induces similar ^{1}H NMR spectral changes observed in Figure 5.33 and Figure 5.35 consistent with BF_3 coordination to the pyrrolidine nitrogen (Figure 5.36b). Signals for the methyl protons attached to nitrogen shift downfield from 2.85 ppm to 3.19 and 3.21 ppm upon addition of $BF_3{\cdot}Et_2O$ to the sample. Signals for aromatic protons also shift downfield from to 7.41 ppm upon $BF_3{\cdot}Et_2O$ addition.

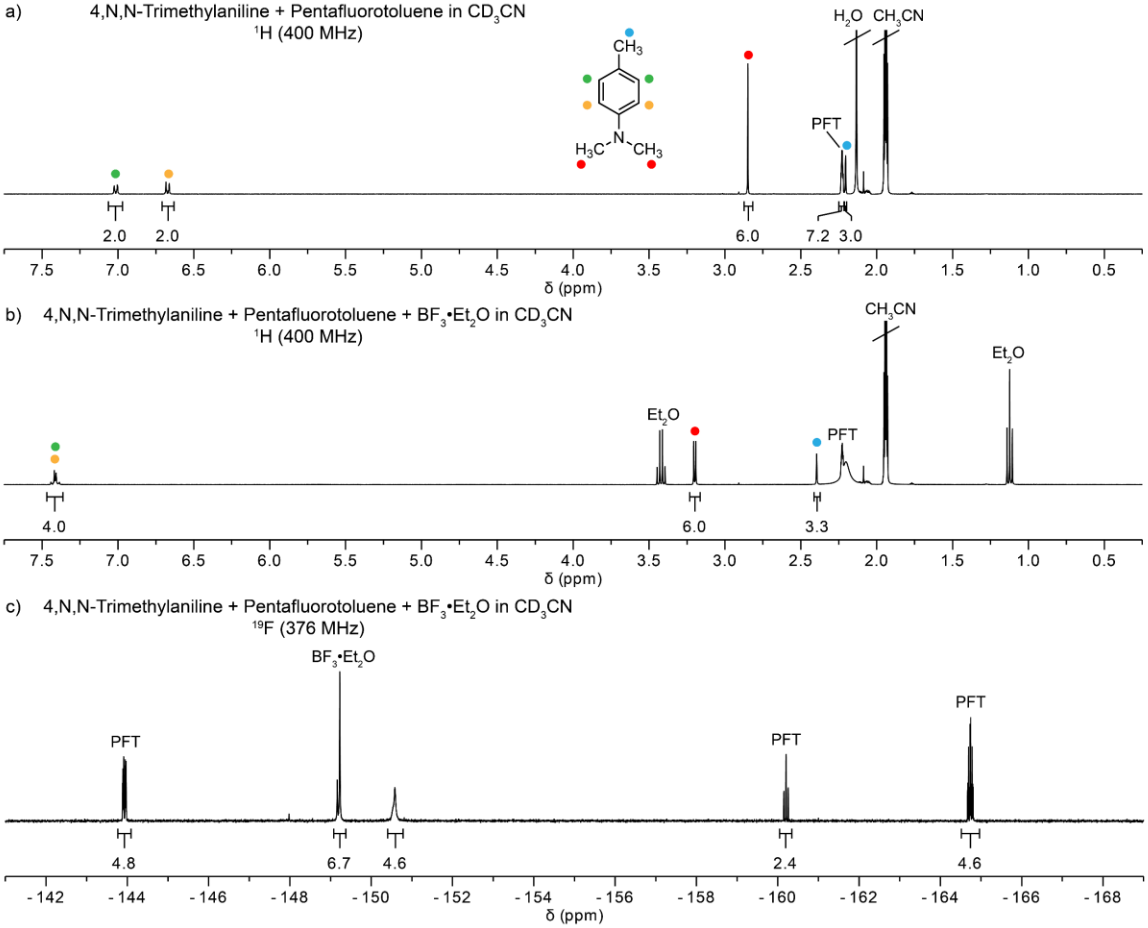

Figure 5.36. ^{1}H (400 MHz) and ^{19}F (376 MHz) NMR spectra of a solution of 4,N,N-trimethylaniline (~1 mM in CD_3CN) with ~2.4 equiv pentafluorotoluene (a) before, and (b,c) after addition of ~3.9 equiv $BF_3{\cdot}Et_2O$. See Section VI for details.

A new broad peak is also observed upfield of free $B^{19}F_3$in the ^{19}F NMR spectrum at –150.6 ppm (Figure 5.36c), again consistent with BF_3 coordinated to a tertiary amine[34,35] and consistent with the spectra obtained upon addition of $BF_3 \cdot Et_2O$ to **NDP** (see Figure 5.35 above). The peak at –150.6 ppm integrates to 4.6F, suggesting each tertiary amine coordinates ~1.5 units BF_3.

The same experiment was next performed on naphthodipyran. A solution of small molecule naphthodipyran bis-initiator **NDP** (~0.5 mM in CD_3CN) containing ~4.5 equiv of PFT as internal standard was prepared and a ^{1}H NMR spectrum was acquired (Figure 5.37a). The addition of $BF_3 \cdot Et_2O$ to the sample (~7.6 equiv) induces the same ^{1}H NMR spectral changes illustrated above in Figure 5.33 and Figure 5.35 (Figure 5.37b, see above for further discussion). The broad peak observed in the ^{19}F NMR spectrum at –150.5 ppm attributed to BF_3 coordinated to the pyrrolidine nitrogen

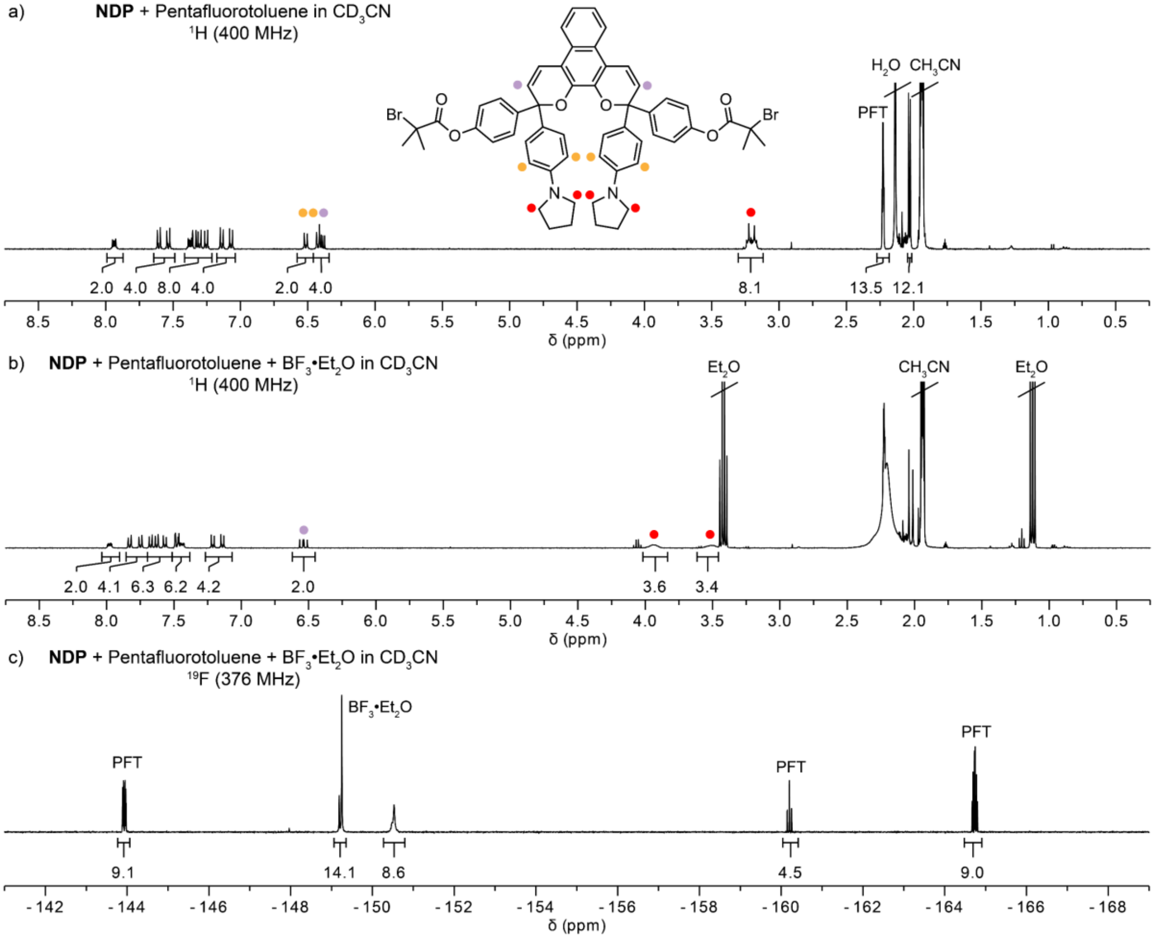

Figure 5.37. ^{1}H (400 MHz) and ^{19}F (376 MHz) NMR spectra of naphthodipyran bis-initiator **NDP** (~0.5 mM in CD_3CN) with ~4.5 equiv pentafluorotoluene (a) before, and (b,c) after addition of ~7.6 equiv $BF_3 \cdot Et_2O$. See Section VI for details.

(Figure 5.37c) integrates to ~8.6F, suggesting each tertiary amine coordinates ~1.5 units of BF_3, consistent with the results for 4,N,N-trimethylaniline illustrated in Figure 5.36.

A similar experiment was next performed to assess BF_3 coordination to the dimerocyanine. A solution of small molecule naphthodipyran bis-initiator **NDP** (~2 mM in CD_3CN) containing ~8.8 equiv of PFT as internal standard was prepared and a ^{1}H NMR spectrum was acquired (Figure 5.38a). The addition of $BF_3{\cdot}Et_2O$ to the sample (~7.9 equiv) induces the same ^{1}H NMR spectral changes observed in Figure 5.33, Figure 5.35, and Figure 5.37 (Figure 5.38b). A high concentration of $BF_3{\cdot}Et_2O$ was used to achieve significant accumulation of thermally generated $NDP_{O\text{–}O}{\cdot}nBF_3$. Similar to the procedure detailed above, the sample was then exposed to multiple cycles of UV photoirradiation followed by incubation in the dark to accumulate dimerocyanine $NDP_{O\text{–}O}{\cdot}nBF_3$. Analysis by ^{1}H NMR spectroscopy indicates that the final sample is comprised of approximately 90% dimerocyanine $NDP_{O\text{–}O}{\cdot}nBF_3$ and 10% starting material $NDP_{C\text{–}C}{\cdot}nBF_3$ (Figure 5.38c). The two new ^{19}F NMR signals observed at –142.5 and –142.6 ppm attributed to the difluorodioxaborolane moiety integrate to 1.7F, consistent with the BF_2 subunit expected for this heterocycle (Figure 5.38d). T1 values for these ^{19}F resonances were measured to be ~1.2 s for ^{19}F–^{10}B and ~0.5 s for ^{19}F–^{11}B. These T1 values are significantly smaller than measured T1 values for the signals attributed to BF_3 in solution (2.9 s), consistent with covalent attachment to the large dimerocyanine compound. Notably, the inversion recovery curves for these resonances do not fit perfectly to monoexponential decay, an unusual phenomenon potentially related to quadrupolar effects from boron. The broad peak observed in the ^{19}F NMR spectrum at –150.5 ppm attributed to BF_3 coordinated to the pyrrolidine nitrogen integrates to 6.5F, suggesting that each pyrrolidine nitrogen in the trapped dimerocyanine coordinates ~1 unit of BF_3.

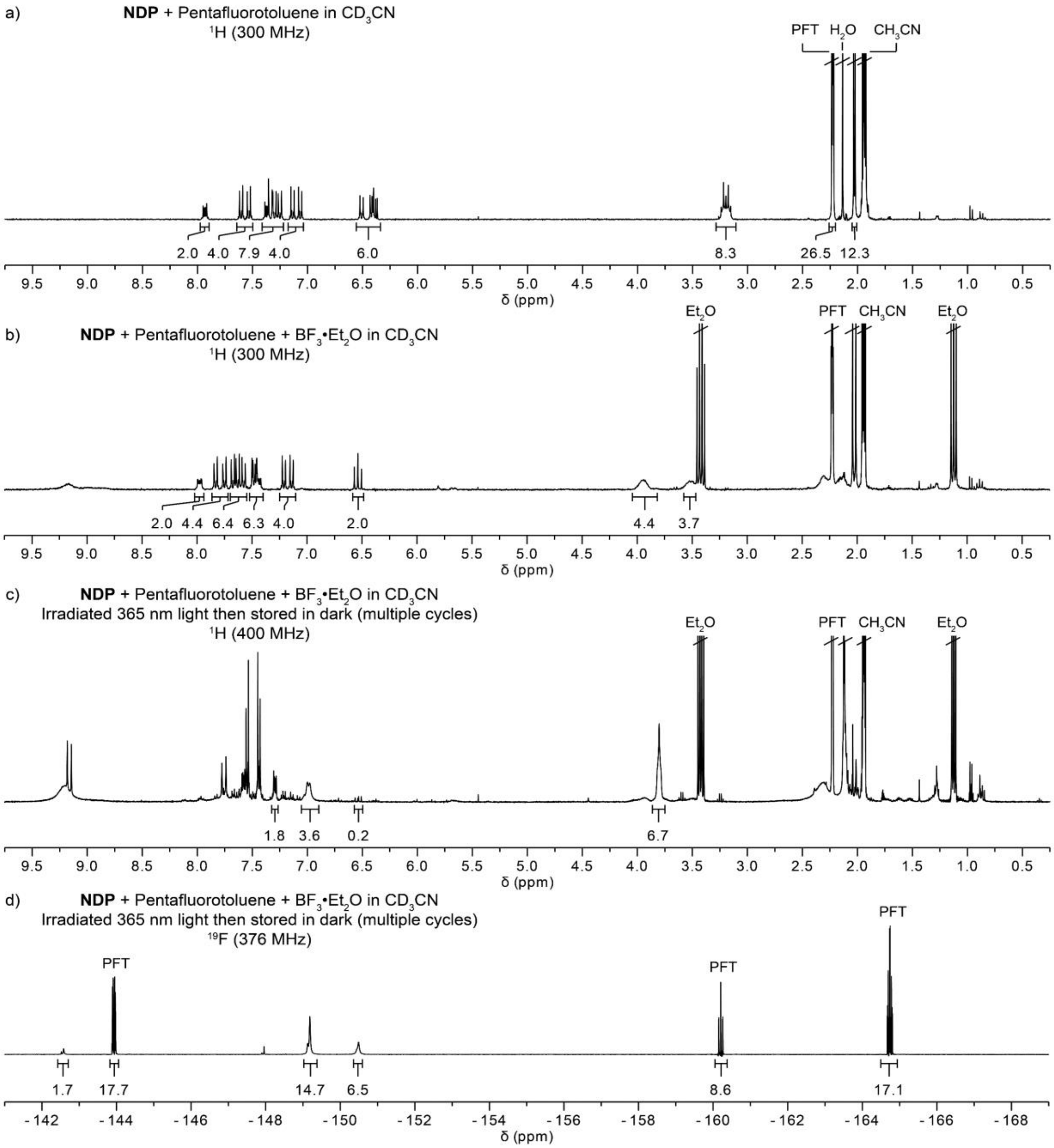

Figure 5.38. ^{1}H NMR (400 MHz) spectra of naphthodipyran bis-initiator **NDP** (~2 mM in CD_3CN) with ~8.8 equiv pentafluorotoluene (a) before, and (b) after addition of ~7.9 equiv $BF_3 \cdot Et_2O$. (c,d) ^{1}H (400 MHz) and ^{19}F (376 MHz) NMR spectra of the sample after exposure to multiple cycles of UV photoirradiation (365 nm light) and incubation in the dark to accumulate dimerocyanine. See Section VI for details.

VII. Details for High Resolution Mass Spectrometry (HRMS) Experiments

A sample of naphthodipyran bis-initiator **NDP** in CH_3CN (0.078 mM, 7.8 mM $BF_3 \cdot Et_2O$) was prepared and analyzed by high resolution mass spectrometry (HRMS) via direct injection in 70% CH_3CN/H_2O with in-line UV-vis absorption spectroscopy (Figure 5.17). The expected $[M+H]^+$ peak was observed (calcd for $[C_{56}H_{53}{}^{79}Br_2N_2O_6]^+$, 1007.2265; found, 1007.2256) with a characteristic Br_2 isotope pattern. No significant visible absorption features were observed. The sample was then exposed to 365 nm UV light at ambient temperatures for 2 min and subsequently analyzed again by HRMS and UV-vis spectroscopy. Similar to the NMR time course experiment, features of dimerocyanine $NDP_{O\text{–}O} \cdot n BF_3$ were not immediately observed; rather, they grew in slowly in the dark over a period of approximately 4 days. A new set of peaks including m/z = 1055.2308 was observed that grew in concurrently with the increase of long-wavelength absorption features attributed to $NDP_{O\text{–}O} \cdot n BF_3$. The peaks in the mass spectrum are attributed to $[M+BF_2]^+$ (calcd for $[C_{56}H_{52}{}^{79}Br_2N_2O_6BF_2]^+$: 1055.2248), with an isotope pattern consistent with the proposed structure, including a diagnostic “M−1” peak at 1054.2616 characteristic of the 20% isotopic abundance of ^{10}B. We note that although $NDP_{O\text{–}C} \cdot n BF_3$ was expected to be present in the sample after photoirradiation, as also suggested by the intense blue color of the solution, its characteristic absorption at λ_{max} = 625 nm was not observed. We hypothesize that the coordination in $NDP_{O\text{–}C} \cdot n BF_3$ is relatively weak and hydrolytically unstable, and thus dissociation occurs upon contact with 70% CH_3CN/H_2O during injection. This is also consistent with the thermal reversibility observed for that species in the absence of a large stoichiometric excess of trapping agent. We propose that the 1,2-diketone motif of the dimerocyanine forms a relatively stable, covalent 5-membered difluoroborocycle through the expulsion of one equivalent of fluoride (main text Figure 5.15e). Future work will investigate applications of mechanically-triggered release of fluoride ions.

References

(1) Hickenboth, C. R.; Moore, J. S.; White, S. R.; Sottos, N. R.; Baudry, J.; Wilson, S. R. Biasing Reaction Pathways with Mechanical Force. *Nature* **2007**, *446*, 423–427.

(2) Lenhardt, J. M.; Ong, M. T.; Choe, R.; Evenhuis, C. R.; Martinez, T. J.; Craig, S. L. Trapping a Diradical Transition State by Mechanochemical Polymer Extension. *Science* **2010**, *329*, 1057–1060.

(3) McFadden, M. E.; Robb, M. J. Generation of an Elusive Permanent Merocyanine via a Unique Mechanochemical Reaction Pathway. *J. Am. Chem. Soc.* **2021**, *143*, 7925–7929.

(4) Li, J.; Nagamani, C.; Moore, J. S. Polymer Mechanochemistry: From Destructive to Productive. *Acc. Chem. Res.* **2015**, *48*, 2181–2190.

(5) Hepworth, J. D.; Heron, B. M. Photochromic Naphthopyrans. Photochromic Naphthopyrans. In *Functional Dyes*; Elsevier Science, 2006; pp 85–135.

(6) Corns, S. N.; Partington, S. M.; Towns, A. D. Industrial Organic Photochromic Dyes: Industrial Organic Photochromic Dyes. *Color. Technol.* **2009**, *125*, 249–261.

(7) Robb, M. J.; Kim, T. A.; Halmes, A. J.; White, S. R.; Sottos, N. R.; Moore, J. S. Regioisomer-Specific Mechanochromism of Naphthopyran in Polymeric Materials. *J. Am. Chem. Soc.* **2016**, *138*, 12328–12331.

(8) Versaw, B. A.; McFadden, M. E.; Husic, C. C.; Robb, M. J. Designing Naphthopyran Mechanophores with Tunable Mechanochromic Behavior. *Chem. Sci.* **2020**, *11*, 4525–4530.

(9) Osler, S. K.; McFadden, M. E.; Robb, M. J. Comparison of the Reactivity of Isomeric 2H- and 3H-Naphthopyran Mechanophores. *J. Polym. Sci.* **2021**, *59*, 2537–2544.

(10) Gossweiler, G. R.; Hewage, G. B.; Soriano, G.; Wang, Q.; Welshofer, G. W.; Zhao, X.; Craig, S. L. Mechanochemical Activation of Covalent Bonds in Polymers with Full and Repeatable Macroscopic Shape Recovery. *ACS Macro Letters* **2014**, *3*, 216–219.

(11) Wang, T.; Zhang, N.; Dai, J.; Li, Z.; Bai, W.; Bai, R. Novel Reversible Mechanochromic Elastomer with High Sensitivity: Bond Scission and Bending-Induced Multicolor Switching. *ACS Applied Materials and Interfaces* **2017**, *9*, 11874–11881.

(12) Raisch, M.; Maftuhin, W.; Walter, M.; Sommer, M. A Mechanochromic Donor-Acceptor Torsional Spring. *Nat Commun* **2021**, *12*, 4243.

(13) McFadden, M. E.; Robb, M. J. Force-Dependent Multicolor Mechanochromism from a Single Mechanophore. *J. Am. Chem. Soc.* **2019**, *141*, 11388–11392.

(14) Van Gemert, B. Benzo and Naphthopyrans (Chromenes). Benzo and Naphthopyrans (Chromenes). In *Organic Photochromic and Thermochromic Compounds*; Springer: Boston, MA, 2002; pp 111–140.

(15) Hepworth, J. D.; Heron, B. M. Synthesis and Photochromic Properties of Naphthopyrans. Synthesis and Photochromic Properties of Naphthopyrans. In *Progress in Heterocyclic Chemistry*; Elsevier Ltd, 2005; Vol. 17, pp 33–62.

(16) Hepworth, J. D.; Heron, B. M. Photochromic Naphthopyrans. Photochromic Naphthopyrans. In *Functional Dyes*; Elsevier Science, 2006; pp 85–135.

(17) Beyer, M. K. The Mechanical Strength of a Covalent Bond Calculated by Density Functional Theory. *J. Chem. Phys.* **2000**, *112*, 7307–7312.

(18) Klein, I. M.; Husic, C. C.; Kovács, D. P.; Choquette, N. J.; Robb, M. J. Validation of the CoGEF Method as a Predictive Tool for Polymer Mechanochemistry. *J. Am. Chem. Soc.* **2020**, *142*, 16364–16381.

(19) Guo, K.; Chen, Y. 'Locking and Unlocking Control' of Photochromism of Naphthopyran Derivative. *Journal of Physical Organic Chemistry* **2010**, *23*, 207–210.

(20) Berkowski, K. L.; Potisek, S. L.; Hickenboth, C. R.; Moore, J. S. Ultrasound-Induced Site-Specific Cleavage of Azo-Functionalized Poly(Ethylene Glycol). *Macromolecules* **2005**, *38*, 8975–8978.

(21) May, P. A.; Munaretto, N. F.; Hamoy, M. B.; Robb, M. J.; Moore, J. S. Is Molecular Weight or Degree of Polymerization a Better Descriptor of Ultrasound-Induced Mechanochemical Transduction? *ACS Macro Letters* **2016**, *5*, 177–180.

(22) Liu, Y.; Holm, S.; Meisner, J.; Jia, Y.; Wu, Q.; Woods, T. J.; Martinez, T. J.; Moore, J. S. Flyby Reaction Trajectories: Chemical Dynamics under Extrinsic Force. *Science* **2021**, *373*, 208–212.

(23) Lin, Y.; Zhang, Y.; Wang, Z.; Craig, S. L. Dynamic Memory Effects in the Mechanochemistry of Cyclic Polymers. *J. Am. Chem. Soc.* **2019**, *141*, 10943–10947.

(24) Harié, G.; Samat, A.; Guglielmetti, R.; van Parys, I.; Saeyens, W.; de Keukeleire, D.; Lorenz, K.; Mannschreck, A. Chiral 2-Aryl-2-Methyl-2 H -1-Benzopyrans: Synthesis, Characterization of Enantiomers, and Barriers to Thermal Racemization. *Helv. Chim. Acta* **1997**, *80*, 1122–1132.

(25) Kortekaas, L.; R. Browne, W. The Evolution of Spiropyran: Fundamentals and Progress of an Extraordinarily Versatile Photochrome. *Chemical Society Reviews* **2019**, *48*, 3406–3424.

(26) Wang, J.; Kouznetsova, T. B.; Niu, Z.; Ong, M. T.; Klukovich, H. M.; Rheingold, A. L.; Martinez, T. J.; Craig, S. L. Inducing and Quantifying Forbidden Reactivity with Single-Molecule Polymer Mechanochemistry. *Nat. Chem.* **2015**, *7*, 323–327.

(27) Nguyen, N. H.; Rosen, B. M.; Lligadas, G.; Percec, V. Surface-Dependent Kinetics of Cu(0)-Wire-Catalyzed Single-Electron Transfer Living Radical Polymerization of Methyl Acrylate in DMSO at 25 °C. *Macromolecules* **2009**, *42*, 2379–2386.

(28) Yang, J.; Horst, M.; Werby, S. H.; Cegelski, L.; Burns, N. Z.; Xia, Y. Bicyclohexene-Peri-Naphthalenes: Scalable Synthesis, Diverse Functionalization, Efficient Polymerization, and Facile Mechanoactivation of Their Polymers. *J. Am. Chem. Soc.* **2020**, *142*, 14619–14626.

(29) Overholts, A. C.; McFadden, M. E.; Robb, M. J. Quantifying Activation Rates of Scissile Mechanophores and the Influence of Dispersity. *Macromolecules* **2022**, *55*, 276–283.

(30) Collum, D. B. *XI. 1st-Order Pre-Equilibrium, 2nd-Order Reaction.* Collum Group Website (Cornell University): 1st-Order Pre-Equilibrium, 2nd-Order Reaction https://collum.chem.cornell.edu/resources/kinetics/ (accessed August 16, 2022).

(31) Collum, D. B. *Determining Initial Rates*. Collum Group Website (Cornell University): Initial Rates, 2009. https://collum.chem.cornell.edu/resources/kinetics/ (accessed August 16, 2022).

(32) Gaffen, J. R.; Bentley, J. N.; Torres, L. C.; Chu, C.; Baumgartner, T.; Caputo, C. B. A Simple and Effective Method of Determining Lewis Acidity by Using Fluorescence. *Chem* **2019**, *5*, 1567–1583.

(33) Colomban, C.; Kudrik, E. V.; Afanasiev, P.; Sorokin, A. B. Catalytic Defluorination of Perfluorinated Aromatics under Oxidative Conditions Using N-Bridged Diiron Phthalocyanine. *J. Am. Chem. Soc.* **2014**, *136*, 11321–11330.

(34) NMR Spectroscopy :: 19F NMR Chemical Shifts. NMR Spectroscopy :: 19F NMR Chemical Shifts https://organicchemistrydata.org/hansreich/resources/nmr/?index=nmr_index%2F19F_shift#f-data02 (accessed Oct 4, 2022).

(35) Fox, A.; Hartman, J. S.; Humphries, R. E. Mixed Boron Trihalide Adducts of Amines: A Multinuclear Nuclear Magnetic Resonance Study. *J. Chem. Soc., Dalton Trans.* **1982**, No. 7, 1275–1283.

(36) Kumar, G. R.; Thilagar, P. Triarylborane Conjugated AcacH Ligands and Their BF2 Complexes: Facile Synthesis and Intriguing Optical Properties. *Dalton Trans.* **2014**, *43*, 3871–3879.

(37) Yang, Y.; Su, X.; Carroll, C. N.; Aprahamian, I. Aggregation-Induced Emission in BF2–Hydrazone (BODIHY) Complexes. *Chem. Sci.* **2012**, *3*, 610–613.

(38) Xu, C.; Xu, J. An Expeditious Method to Synthesize Difluoroboron Complexes of β-Keto Amides from β-Keto Nitriles and BF3·OEt2. *Org. Biomol. Chem.* **2017**, *15*, 6375–6383.

^{1}H and ^{13}C NMR Spectra

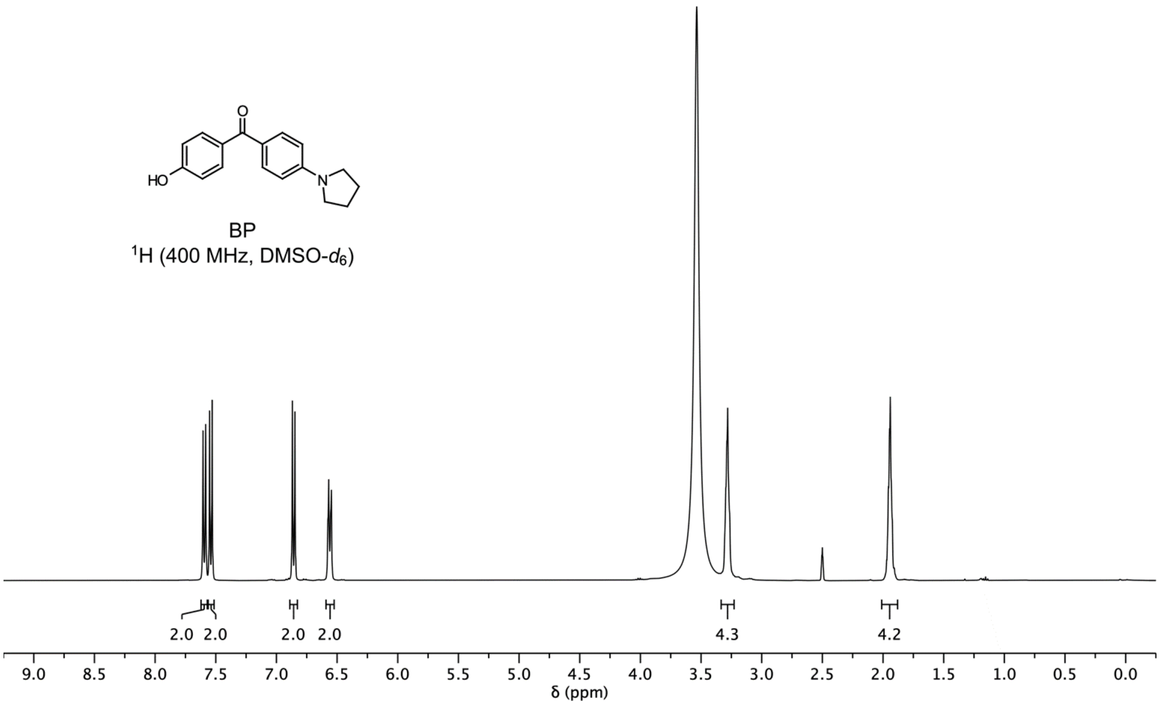

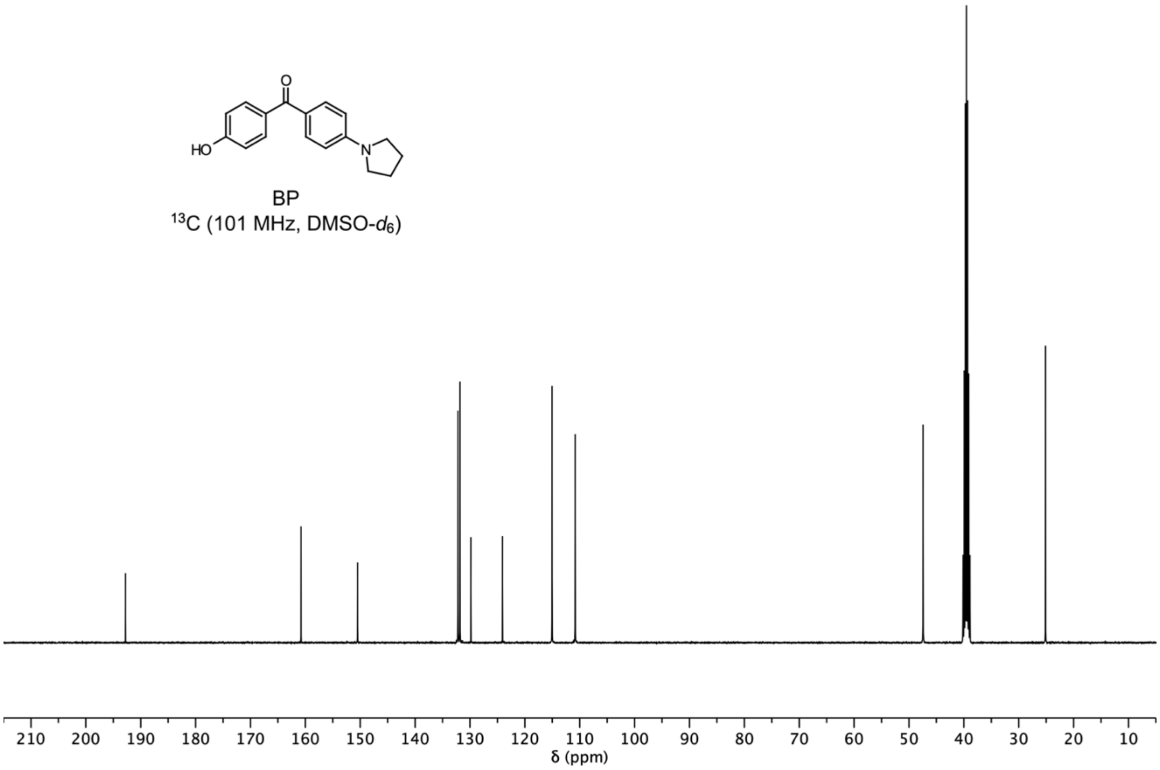

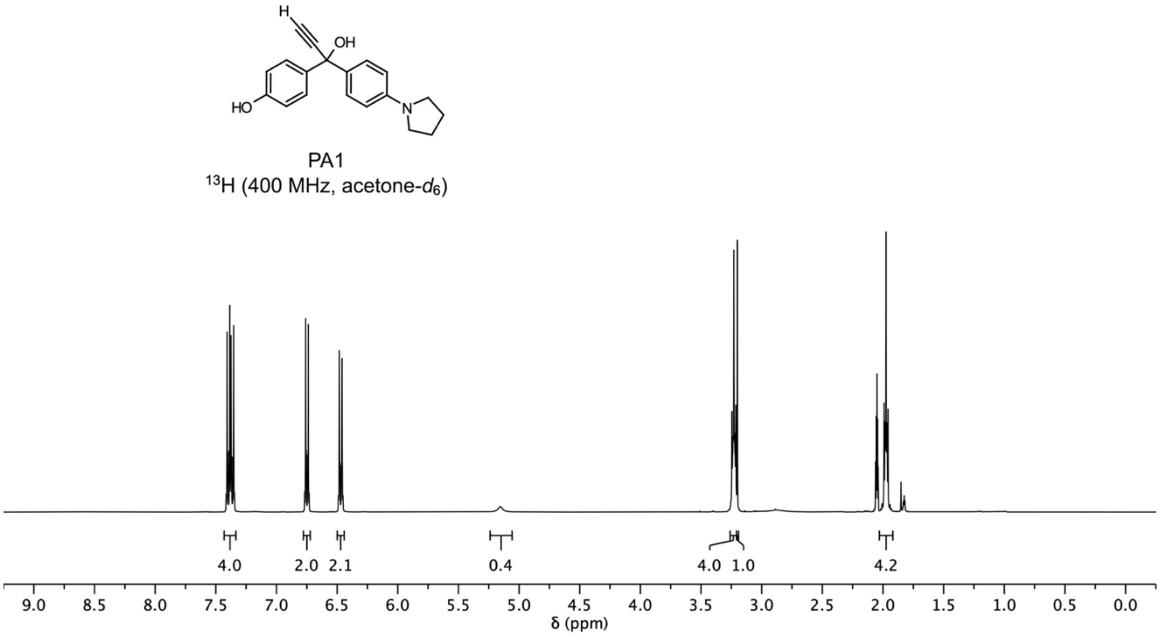
H
OH
HO
N
PA1
^{13}H (400 MHz, acetone-d_6)
4.0
2.0
2.1
0.4
4.0
1.0
4.2
9.0
8.5
8.0
7.5
7.0
6.5
6.0
5.5
5.0
4.5
4.0
3.5
3.0
2.5
2.0
1.5
1.0
0.5
0.0
δ (ppm)

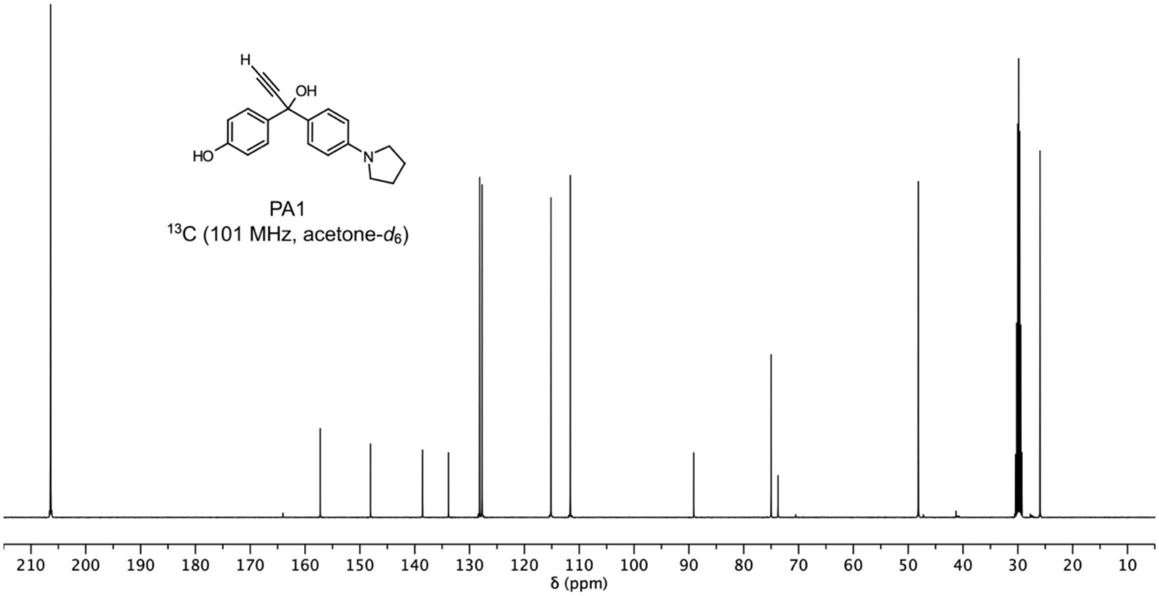
H
OH
HO
N
PA1
^{13}C (101 MHz, acetone-d_6)
210
200
190
180
170
160
150
140
130
120
110
100
90
80
70
60
50
40
30
20
10
δ (ppm)

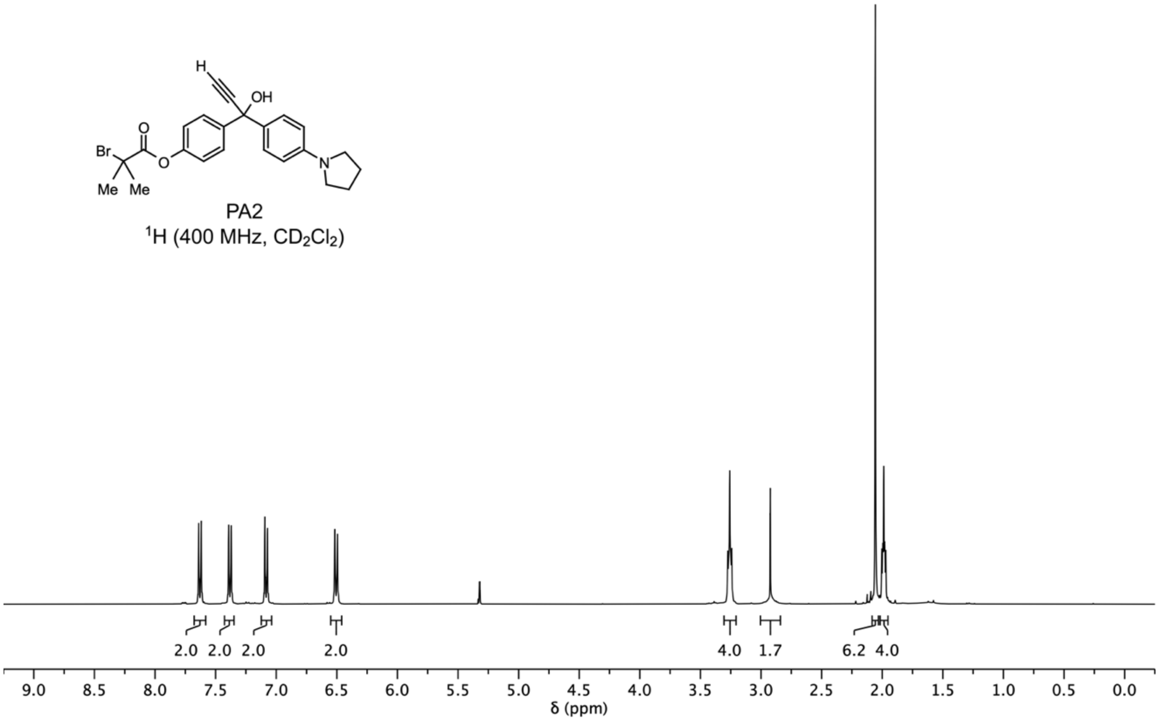
H
OH
O
Br
O
Me Me
N
PA2
1H (400 MHz, CD2Cl2)
2.0 2.0 2.0 2.0 4.0 1.7 6.2 4.0
9.0 8.5 8.0 7.5 7.0 6.5 6.0 5.5 5.0 4.5 4.0 3.5 3.0 2.5 2.0 1.5 1.0 0.5 0.0
δ (ppm)

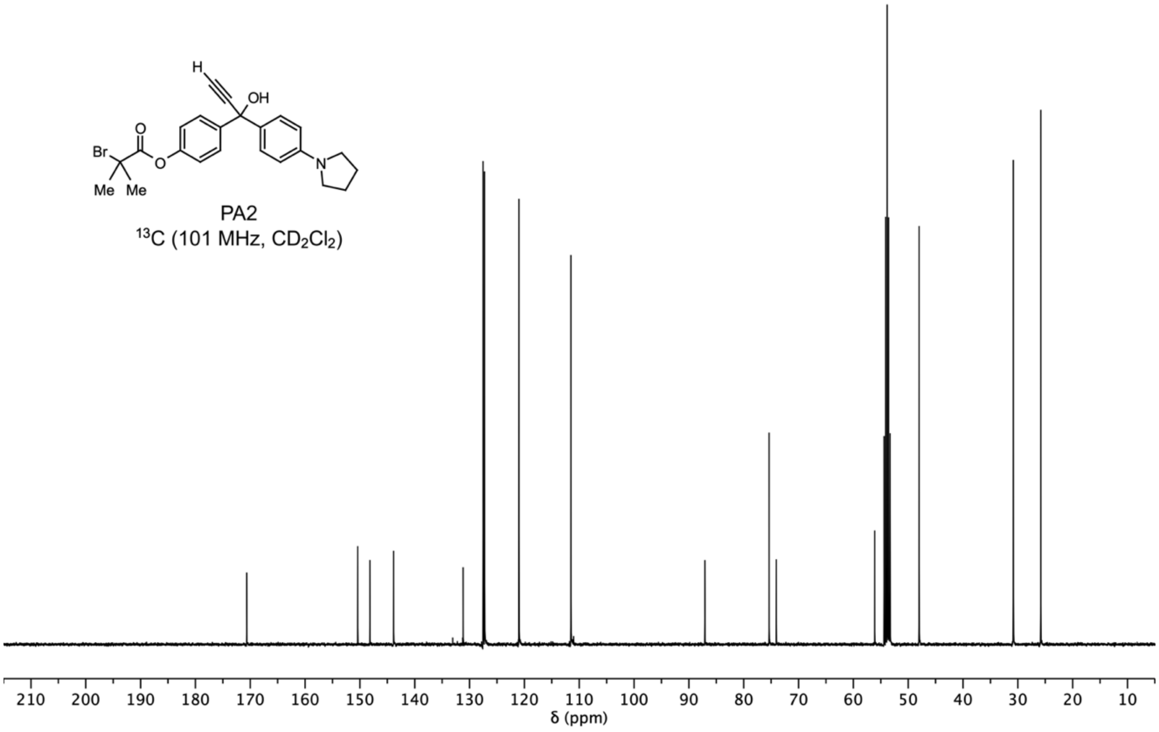
H
OH
O
Br
O
Me Me
N
PA2
13C (101 MHz, CD2Cl2)
210 200 190 180 170 160 150 140 130 120 110 100 90 80 70 60 50 40 30 20 10
δ (ppm)

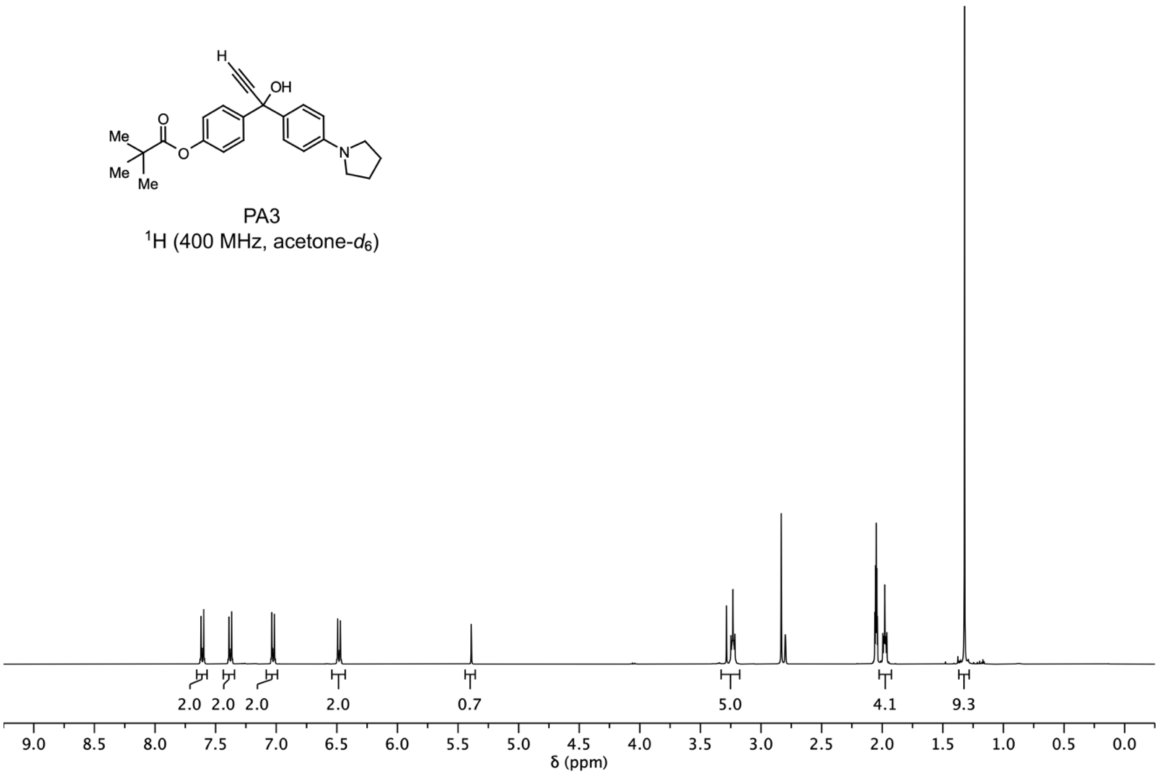
H
OH
O
Me
Me
Me
O
N
PA3
1H (400 MHz, acetone-d6)
2.0
2.0
2.0
2.0
0.7
5.0
4.1
9.3
9.0
8.5
8.0
7.5
7.0
6.5
6.0
5.5
5.0
4.5
4.0
3.5
3.0
2.5
2.0
1.5
1.0
0.5
0.0
δ (ppm)

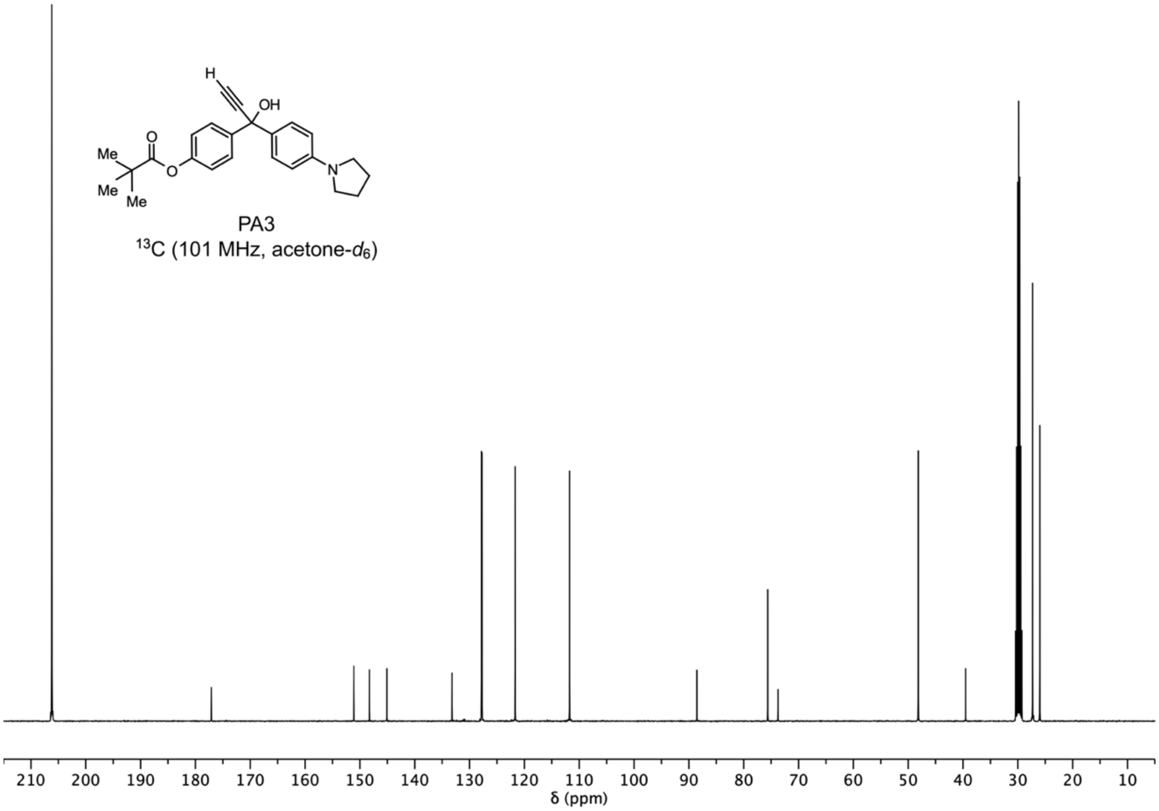
H
OH
O
Me
Me
Me
O
N
PA3
13C (101 MHz, acetone-d6)
210
200
190
180
170
160
150
140
130
120
110
100
90
80
70
60
50
40
30
20
10
δ (ppm)

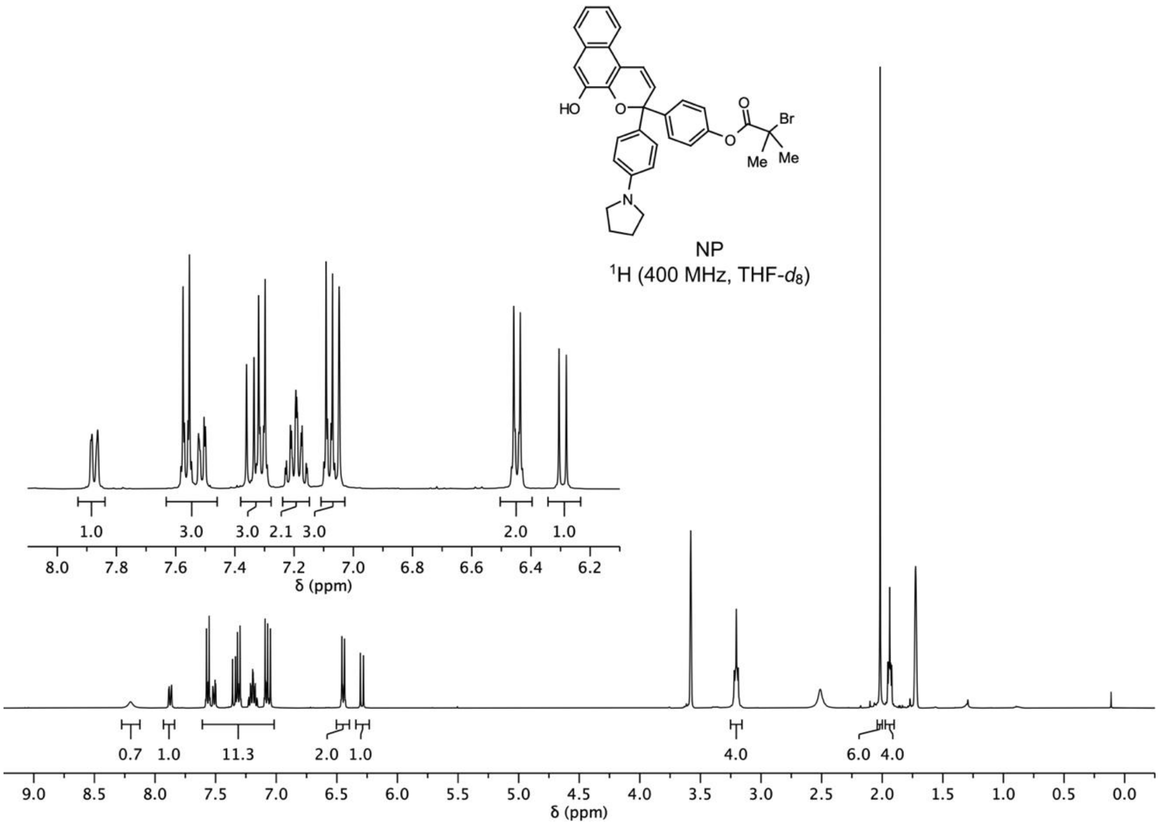
HO
O
O
O
Br
Me
Me
N
NP
^{1}H (400 MHz, THF-d_8)
1.0
3.0
3.0
2.1
3.0
2.0
1.0
8.0
7.8
7.6
7.4
7.2
7.0
6.8
6.6
6.4
6.2
δ (ppm)
0.7
1.0
11.3
2.0
1.0
4.0
6.0
4.0
9.0
8.5
8.0
7.5
7.0
6.5
6.0
5.5
5.0
4.5
4.0
3.5
3.0
2.5
2.0
1.5
1.0
0.5
0.0
δ (ppm)

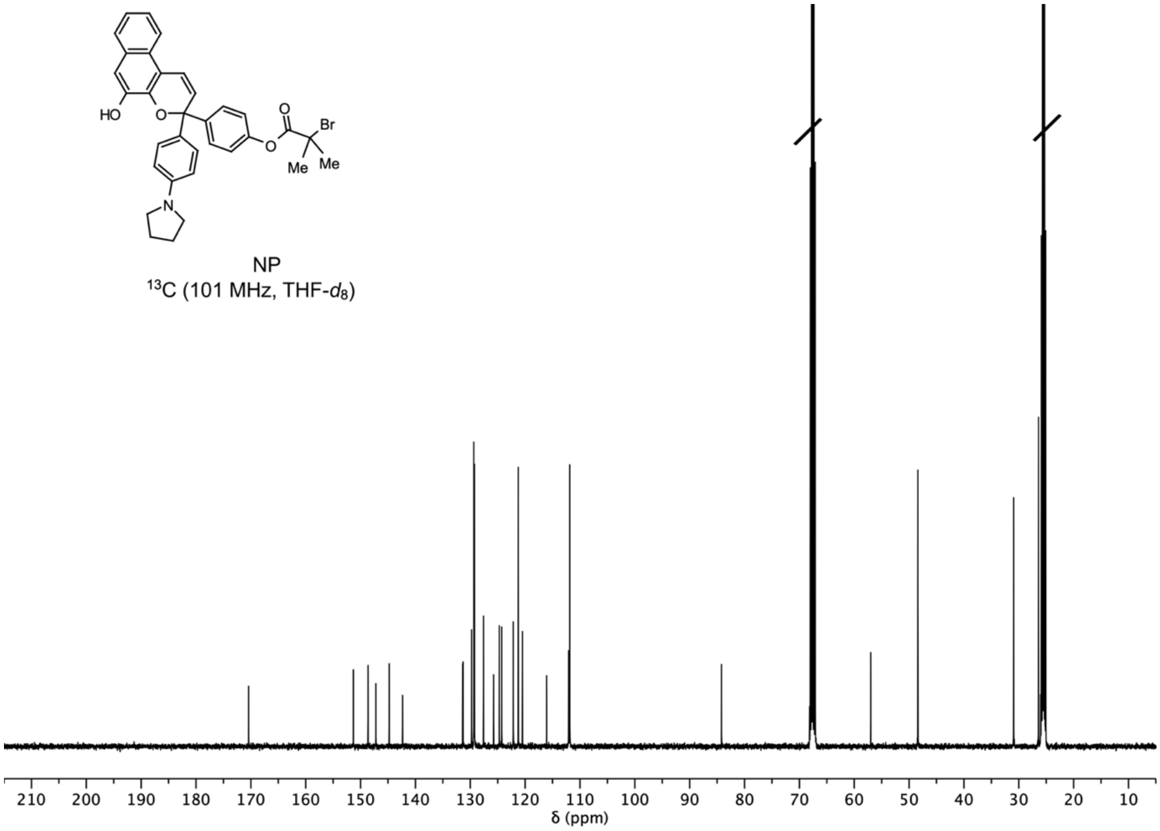
HO
O
O
O
Br
Me
Me
N
NP
^{13}C (101 MHz, THF-d_8)
210
200
190
180
170
160
150
140
130
120
110
100
90
80
70
60
50
40
30
20
10
δ (ppm)

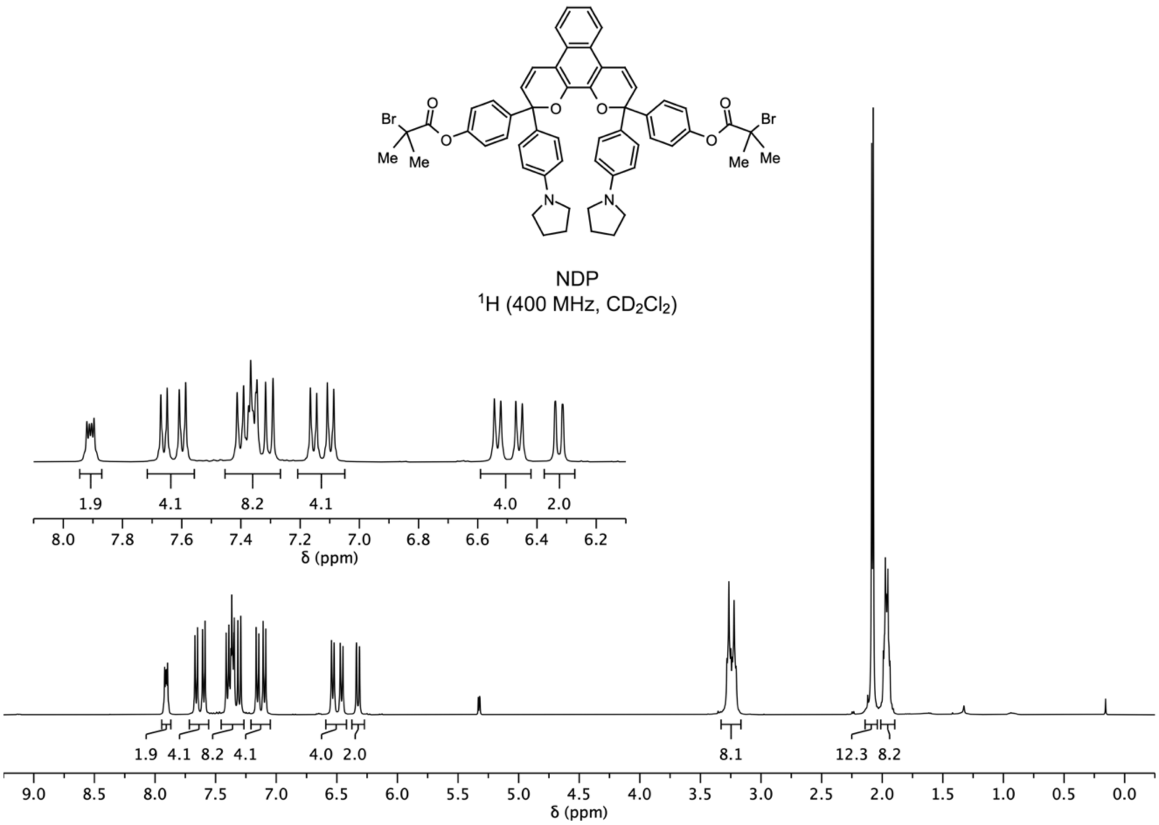
Br
O
Me
Me
O
O
N
NDP
¹H (400 MHz, CD₂Cl₂)
1.9
4.1
8.2
4.1
4.0
2.0
8.0 7.8 7.6 7.4 7.2 7.0 6.8 6.6 6.4 6.2
δ (ppm)
1.9 4.1 8.2 4.1 4.0 2.0
8.1
12.3 8.2
9.0 8.5 8.0 7.5 7.0 6.5 6.0 5.5 5.0 4.5 4.0 3.5 3.0 2.5 2.0 1.5 1.0 0.5 0.0
δ (ppm)

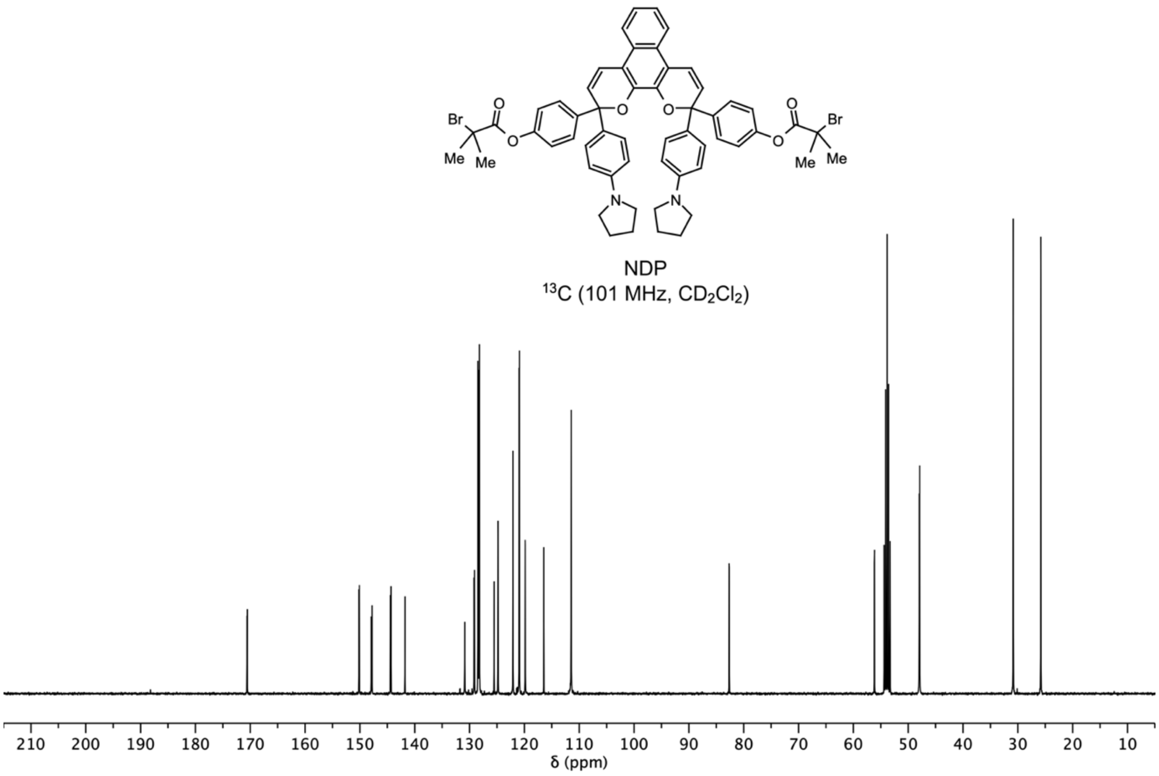
Br
O
Me
Me
O
O
N
NDP
¹³C (101 MHz, CD₂Cl₂)
210 200 190 180 170 160 150 140 130 120 110 100 90 80 70 60 50 40 30 20 10
δ (ppm)

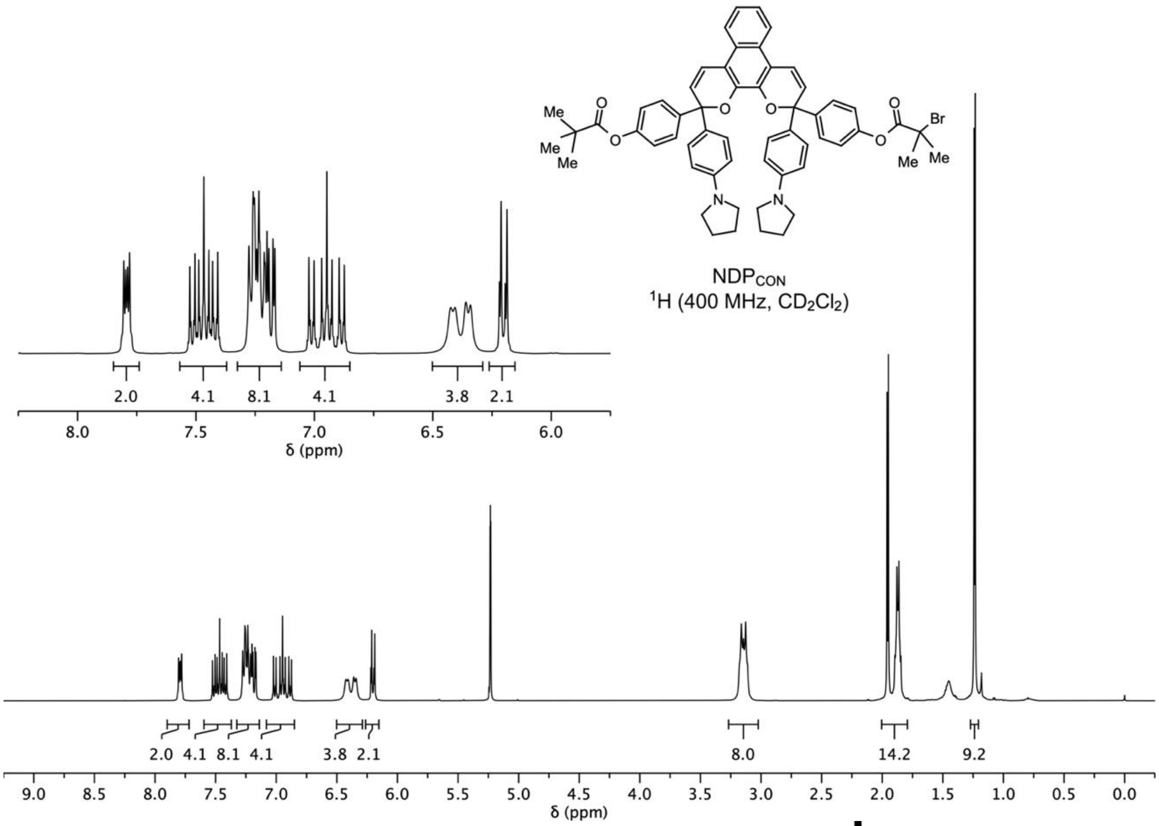
Me
Me
Me
O
O
O
O
O
O
Br
Me
Me
N
N
NDP$_{CON}$
^{1}H (400 MHz, CD_2Cl_2)
2.0
4.1
8.1
4.1
3.8
2.1
8.0
7.5
7.0
6.5
6.0
δ (ppm)
2.0
4.1
8.1
4.1
3.8
2.1
8.0
14.2
9.2
9.0
8.5
8.0
7.5
7.0
6.5
6.0
5.5
5.0
4.5
4.0
3.5
3.0
2.5
2.0
1.5
1.0
0.5
0.0
δ (ppm)

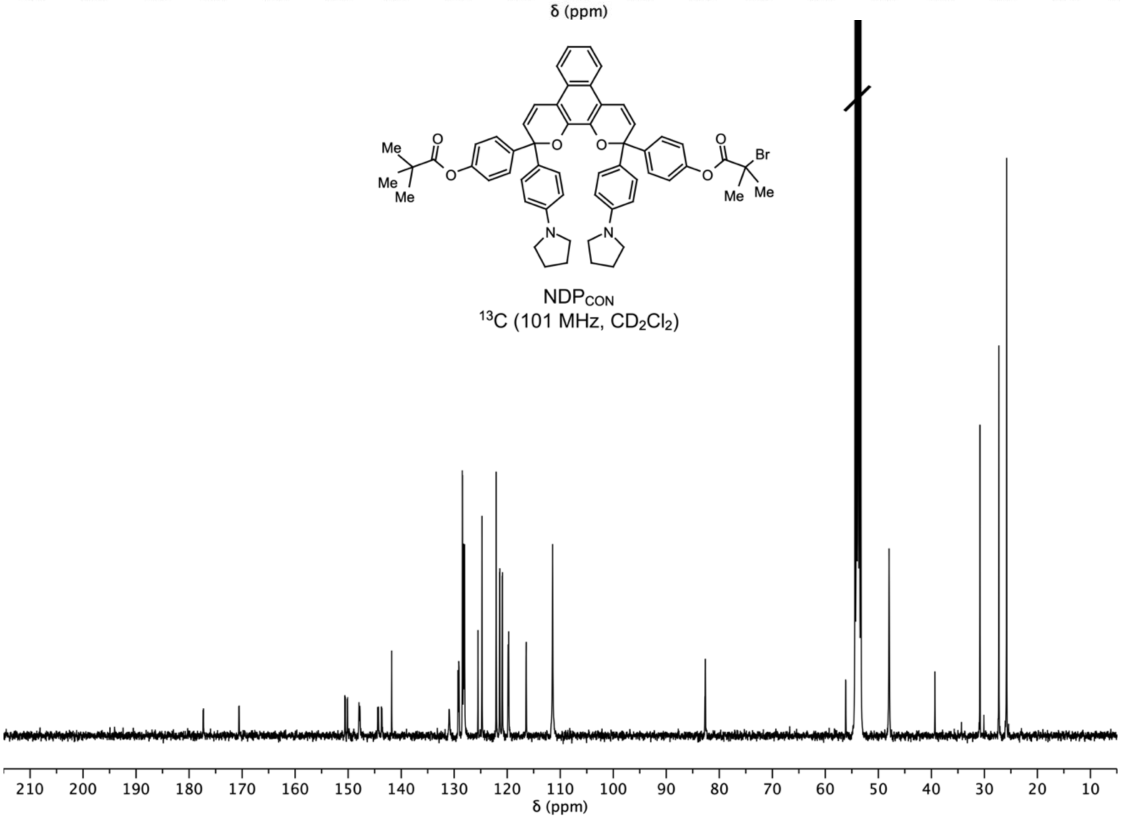
Me
Me
Me
O
O
O
O
O
O
Br
Me
Me
N
N
NDP$_{CON}$
^{13}C (101 MHz, CD_2Cl_2)
210
200
190
180
170
160
150
140
130
120
110
100
90
80
70
60
50
40
30
20
10
δ (ppm)